

Fiscal Year 2022: Second Quarter

Progress Reports:
**Advanced Battery Materials Research
(BMR) Program
&
Battery500 Consortium**

Released July 2022
for the period of January – March 2022

Approved by

Tien Q. Duong

Manager, Advanced Battery Materials Research Program & Battery500 Consortium
Batteries & Electrification R&D

Office of Energy Efficiency and Renewable Energy – Vehicle Technologies Office
U.S. Department of Energy

ACKNOWLEDGMENTS

This report has been edited by the following team members:

- **T. A. Zachry**, Energy & Environmental Resources Group
- **Patricia H. Smith**, Naval Sea Systems Command – Carderock Division

TABLE OF CONTENTS

A Message from the Manager:

Advanced Battery Materials Research and Battery500 Consortium..... xxv

Advanced Battery Materials Research Program

Task 1 –Solid-State Electrolytes	1
Task 1.1 – Multifunctional Gradient Coatings for Scalable, High-Energy-Density Sulfide-Based Solid-State Batteries (Justin Connell, Argonne National Laboratory)	4
Task 1.2 – Electrolytes for High-Energy, All-Solid-State, Lithium-Metal Batteries (Guiliang Xu, Argonne National Laboratory)	8
Task 1.3 – Thioborate Solid-State Electrolytes for Practical All-Solid-State Batteries (Yi Cui, Stanford University)	12
Task 1.4 – Substituted Argyrodite Solid Electrolytes and High-Capacity Conversion Cathodes for All-Solid-State Batteries (Jagjit Nanda, Oak Ridge National Laboratory)	14
Task 1.5 – Stable Solid-State Electrolyte and Interface for High-Energy, All-Solid-State, Lithium-Sulfur Battery (Dongping Lu, Pacific Northwest National Laboratory)	17
Task 1.6 – Development of Thin, Robust, Lithium-Impenetrable, High-Conductivity, Electrochemically Stable, Scalable, and Low-Cost Glassy Solid Electrolytes for Solid-State Lithium Batteries (Steve Martin, Iowa State University of Science and Technology)	20
Task 1.7 – All-Solid-State Batteries Enabled by Multifunctional Electrolyte Materials (Pu Zhang, Solid Power Inc.)	27
Task 1.8 – Developing Materials for High-Energy-Density Solid-State Lithium-Sulfur Batteries (Donghai Wang, Pennsylvania State University)	30
Task 1.9 – Hot Pressing of Reinforced Lithium-NMC All-Solid-State Batteries with Sulfide Glass Electrolyte (Thomas Yersak, General Motors, LLC)	33
Task 1.10 – Three-Dimensional Printing of All-Solid-State Lithium Batteries (Jianchao Ye, Lawrence Livermore National Laboratory)	37
Task 1.11 – Physical and Mechano-Electrochemical Phenomena of Thin-Film Lithium-Ceramic Electrolyte Constructs (Jeff Sakamoto, University of Michigan)	42
Task 1.12 – Low Impedance Cathode/Electrolyte Interfaces for High-Energy-Density Solid-State Batteries (Eric Wachsman and Yifei Mo, University of Maryland)	45
Task 1.13 – Development of All-Solid-State Battery Using Anti-Perovskite Electrolytes (Zonghai Chen and Tao Li, Argonne National Laboratory)	49

Task 1.14 – Lithium Halide-Based Superionic Solid Electrolytes and High-Voltage Cathode Interface (Jagjit Nanda, Oak Ridge National Laboratory).....	53
Task 1.15 – Developing an <i>In Situ</i> Formed Dynamic Protection Layer to Mitigate Lithium Interface Shifting: Preventing Dendrite Formation on Metallic Lithium Surface to Facilitate Long Cycle Life of Lithium Solid-State Batteries (Deyang Qu, University of Wisconsin, Milwaukee)	56
Task 1.16 – Polyester-Based Block Copolymer Electrolytes for Lithium-Metal Batteries (Nitash Balsara, University of California, Berkeley).....	59
Task 1.17 – Advanced Polymer Materials for Batteries (Zhenan Bao and Yi Cui, Stanford University)	62
Task 1.18 – Molecular Ionic Composites: A New Class of Polymer Electrolytes to Enable All-Solid-State and High-Voltage Lithium Batteries (Louis Madsen, Virginia Polytechnic Institute and State University).....	66
Task 1.19 – Synthesis of Composite Electrolytes with Integrated Interface Design (Sanja Tepavcevic, Argonne National Laboratory)	71
Task 1.20 – Polymer Electrolytes for Stable, Low-Impedance, Solid-State Battery Interfaces (X. Chelsea Chen, Oak Ridge National Laboratory)	74
Task 1.21 – Ion Conductive High Li ⁺ Transference Number Polymer Composites for Solid-State Batteries (Bryan McCloskey, University of California, Berkeley)	79
Task 1.22 – Inorganic-Polymer-Composite Electrolyte with Architecture Design for Lithium-Metal Solid-State Batteries (Enyuan Hu, Brookhaven National Laboratory)	81
Task 1.23 – Solid-State Batteries with Long Cycle Life and High Energy Density through Materials Design and Integration (Gerbrand Ceder, University of California, Berkeley)	84
Task 1.24 – Low-Pressure All-Solid-State Cells (Anthony Burrell, National Renewable Energy Laboratory).....	87
Task 1.25 – Precision Control of the Lithium Surface for Solid-State Batteries (Andrew Westover, Oak Ridge National Laboratory).....	94
Task 2 – Diagnostics.....	99
Task 2.1 – Characterization and Modeling of Lithium-Metal Batteries: Model-System Synthesis and Advanced Characterization (Guoying Chen, Lawrence Berkeley National Laboratory)	101
Task 2.2 – Interfacial Processes – Diagnostics (Robert Kostecki, Lawrence Berkeley National Laboratory)	104
Task 2.3 – Advanced <i>In Situ</i> Diagnostic Techniques for Battery Materials (Xiao-Qing Yang and Enyuan Hu, Brookhaven National Laboratory)	107
Task 2.4 – Probing Interfacial Processes Controlled Electrode Stability in Rechargeable Batteries (Chongmin Wang, Pacific Northwest National Laboratory)	110

Task 2.5 – Integrated Atomic-, Meso-, and Micro-Scale Diagnostics of Solid-State Batteries (Yi Cui, William Chueh, and Michael Toney; Stanford University/SLAC National Accelerator Laboratory)	115
Task 2.6 – Fundamental Understanding of Interfacial Phenomena in Solid-State Batteries (Xingcheng Xiao, General Motors)	118
Task 2.7 – Multidimensional Diagnostics of the Interface Evolutions in Solid-State Lithium Batteries (Yan Yao, University of Houston)	121
Task 3 – Modeling	124
Task 3.1 – Characterization and Modeling of Lithium-Metal Batteries: First-Principles Modeling and Machine Learning (Kristin Persson, Lawrence Berkeley National Laboratory)	125
Task 3.2 – Electrode Materials Design and Failure Prediction (Venkat Srinivasan, Argonne National Laboratory).....	129
Task 3.3 – Modeling of Amorphous Solid-State Conductors (Gerbrand Ceder, University of California, Berkeley).....	132
Task 3.4 – <i>In Situ</i> and <i>Operando</i> Thermal Diagnostics of Buried Interfaces in Beyond Lithium-Ion Cells (Ravi Prasher, Lawrence Berkeley National Laboratory).....	135
Task 3.5 – Multi-Scale Modeling of Solid-State Electrolytes for Next-Generation Lithium Batteries (Anh Ngo, Larry A. Curtiss, and Venkat Srinivasan, Argonne National Laboratory).....	139
Task 3.6 – First-Principles Modeling of Cluster-Based Solid Electrolytes (Puru Jena, Virginia Commonwealth University)	142
Task 3.7 – Predictive Engineering of Interfaces and Cathodes for High-Performance All-Solid-State Lithium-Sulfur Batteries (Badri Narayanan, University of Louisville)	146
Task 3.8 – Predicting the Nucleation and Evolution of Interphases in All-Solid-State Lithium Batteries (Sabrina (Liwen) Wan, Lawrence Livermore National Laboratory)	150
Task 3.9 – Design of Strain Free Cathode – Solid-State Electrolyte Interfaces Using Chemistry-Informed Deep Learning (Hakim Iddir, Argonne National Laboratory)	154
Task 3.10 – Tackling Solid-State Electrochemical Interfaces from Structure to Function Utilizing High-Performance Computing and Machine-Learning Tools (Shinjae Yoo, Feng Wang, and Deyu Lu, Brookhaven National Laboratory; Nongnuch Artrith and Alexander Urban, Columbia University)	159
Task 3.11 – Integrated Multiscale Model for Design of Robust, Three-Dimensional, Solid-State Lithium Batteries (Brandon Wood, Lawrence Livermore National Laboratory).....	163

Task 4 – Metallic Lithium	167
Task 4.1 – Lithium Dendrite Prevention for Lithium Batteries (Wu Xu and Ji-Guang Zhang, Pacific Northwest National Laboratory).....	168
Task 4.2 – Prelithiation for High-Energy Lithium-Ion Batteries (Yi Cui, Stanford University)	171
Task 4.3 – Anode-Free Lithium Batteries (Jiguang Zhang and Xia Cao, Pacific Northwest National Laboratory)	174
Task 5 – Lithium-Sulfur Batteries	177
Task 5.1 – Novel Chemistry: Lithium Selenium and Selenium Sulfur Couple (Khalil Amine, Argonne National Laboratory)	180
Task 5.2 – Development of High-Energy Lithium-Sulfur Batteries (Dongping Lu and Jun Liu, Pacific Northwest National Laboratory).....	183
Task 5.3 – Nanostructured Design of Sulfur Cathodes for High-Energy Lithium-Sulfur Batteries (Yi Cui, Stanford University)	186
Task 5.4 – Investigation of Sulfur Reaction Mechanisms (Enyuan Hu, Brookhaven National Laboratory; Deyang Qu, University of Wisconsin, Milwaukee).....	189
Task 5.5 – New Electrolytes for Lithium-Sulfur Battery (Gao Liu, Lawrence Berkeley National Laboratory).....	192
Task 5.6 – Strategies to Enable Lean Electrolytes for High Loading and Stable Lithium- Sulfur Batteries (Y. Shirley Meng, University of California, San Diego).....	195
Task 5.7 – New Engineering Concepts to High-Energy-Density Lithium-Sulfur Batteries (Prashant N. Kumta, University of Pittsburgh)	203
Task 5.8 – Development of Lithium-Sulfur Battery Cells with High Energy Density and Long Cycle Life (Donghai Wang, Pennsylvania State University)	207
Task 6 – Lithium-Air Batteries	211
Task 6.1 – Lithium-Air Batteries (Khalil Amine, Larry A. Curtiss, and Jun Lu, Argonne National Laboratory)	212
Task 6.2 – Lithium Oxygen Battery Design and Predictions (Larry A. Curtiss/Anh Ngo, Argonne National Laboratory; Amin Salehi-Khojin, University of Illinois, Chicago).....	215
Task 6.3 – Development of a High-Rate Lithium-Air Battery Using a Gaseous CO ₂ Reactant (Amin Salehi-Khojin, University of Illinois, Chicago)	218
Task 7 – Sodium-Ion Batteries	221
Task 7.1 – Exploratory Studies of Novel Sodium-Ion Battery Systems (Xiao-Qing Yang and Enyuan Hu, Brookhaven National Laboratory)	222
Task 7.2 – Development of a High-Energy Sodium-Ion Battery with Long Life (Chris Johnson and Khalil Amine, Argonne National Laboratory)	225

Task 7.3 – Tailoring High-Capacity, Reversible Anodes for Sodium-Ion Batteries
(Marca M. Doeff, Lawrence Berkeley National Laboratory) 229

Task 7.4 – Electrolytes and Interfaces for Stable High-Energy Sodium-Ion Batteries
(Phung M. L. Le, Pacific Northwest National Laboratory) 233

Battery500 Consortium Program

Innovation Center for Battery500
(Jun Liu, Pacific Northwest National Laboratory; Yi Cui, Stanford University) 236

Appendix – Acronym Guide 264

TABLE OF FIGURES

Figure 1. (a) X-ray diffraction (XRD) patterns for pristine $\text{Li}_6\text{PS}_5\text{Cl}$ (LPSCI) from ANL, NEI, and Ampcera; the XRD pattern for the Kapton background is shown for comparison. (b) Arrhenius plots for total Li^+ conductivity of LPSCI from NEI in the temperature range of -20°C to 100°C . (c) Cycling stability of pristine LPSCI from ANL (black) and NEI (green) in $\text{Li} \text{Li}$ symmetric cells at 65°C	5
Figure 2. (a) Sulfur 2p, (b) phosphorus 2p, (c) chlorine 2p, and (d) oxygen 1s X-ray photoelectron spectroscopy core level spectra for the NEI LPSCI solid-state electrolyte.	6
Figure 3. Digital photo of vacuum sealing set up for the synthesis of solid-state electrolytes.	9
Figure 4. (a) Digital photo of <i>in situ</i> synchrotron X-ray diffraction set up at Advanced Photon Source to probe synthesis of sulfide solid-state electrolytes. (b) Snapshot photo during heating process.	9
Figure 5. (a) Two-dimensional contour plot of <i>in situ</i> synchrotron X-ray diffraction patterns during formation of LPSBr. (b) Zoom-in view of 2θ range of 6.0 - 9.5°	10
Figure 6. Rietveld refinement of <i>in situ</i> synchrotron X-ray diffraction pattern at 600°C	10
Figure 7. Two-dimensional contour plot of <i>in situ</i> synchrotron X-ray diffraction patterns during formation of O-doped LPSBr: (a) heating from room temperature to 550°C ; and (b) 550°C holding for 8 hours followed by quenching.	11
Figure 8. (a) Unique X-ray diffraction spectra of $\text{Li}_2\text{B}_2\text{S}_5$, Li_3BS_3 , and $\text{Li}_{10}\text{B}_{10}\text{S}_{20}$. Fourier transform infrared spectra of $\text{Li}_2\text{B}_2\text{S}_5$ (b), Li_3BS_3 (c), and $\text{Li}_{10}\text{B}_{10}\text{S}_{20}$ (d) in the B-S bonding range, showing symmetric and asymmetric B-S vibrations.	13
Figure 9. Li^+ conductivity measurements for $\text{Li}_6\text{PS}_5\text{X}$ ($\text{X} = \text{Cl}, \text{Br}$) prepared by hand grinding (HG) and planetary milling (PM).	15
Figure 10. (a) Raman spectra and (b) powder X-ray diffraction patterns for $\text{Li}_6\text{PS}_5\text{X}$ ($\text{X} = \text{Cl}, \text{Br}$) prepared by hand grinding (HG) and planetary milling (PM) methods.	16
Figure 11. (a) Formation of H_2S . (b) Electrochemical impedance spectra. (c) X-ray diffraction patterns. (d) High-resolution carbon 1s spectra of $\text{Li}_7\text{P}_2\text{S}_8\text{Br}_{0.5}\text{I}_{0.5}$ powders with/without amphipathic organic molecules (AOM) coating exposed to air with relative humidity of 0.5% in a dry room.	18
Figure 12. Raman spectra of ISU-6 glasses. The blue spectrum corresponds to “good” quality glasses that would be used in scale-up synthesis, and the red spectrum corresponds to “bad” quality glasses that would contain defect structures that would be excluded from scale-up synthesis.	21
Figure 13. ISU-6 preform made using new high-quality small-scale synthesis route.	22
Figure 14. ISU-6 thin-film that has been drawn and collected for further testing.	23
Figure 15. Solid-state cathode composite mixing methods. Method 1 is a simple single-step mixing, while methods 2-4 are two-step mixing methods, where two materials are mixed first and the final material is mixed in the second step. Schematics of the likely microstructure resulting are shown below each method’s steps.	24
Figure 16. Temperature-dependent conductivities of solid-state cathode composites synthesized through Methods 1-4 described in Figure 15.	24
Figure 17. (a) Temperature-dependent conductivity of cathode composites milled for different lengths of time. (b) Temperature-dependent electronic conductivities of cathode composites synthesized with different carbon morphologies.	25

Figure 18. Tape-cast solid-state cathode utilizing the glassy solid electrolyte and LiFePO_4 composite cathode developed.....	25
Figure 19. (a) X-ray diffractogram of $\text{Li}_2\text{S-C}$ nanocomposite powder showing peaks that match the literature diffractogram. (b) Energy-dispersive X-ray spectroscopy map of the synthesized $\text{Li}_2\text{S-C}$ powder showing homogenous mixing of the carbon and sulfur signal.	26
Figure 20. Cross-section images of a slurry-cast solid-state electrolyte separator film $< 40 \mu\text{m}$	28
Figure 21. Cycle life of an NMC/Li-metal solid-state pouch cell with the multifunctional solid-state electrolyte at 45°C	28
Figure 22. All-solid-state 2-Ah Li-NMC pouch cells.	29
Figure 23. The (a) Arrhenius and (b) Nyquist plots of SE-1 solid electrolyte at different temperatures from 25°C to 100°C	31
Figure 24. (a) Charge-discharge voltage profiles and (b) cycling performance of sulfur cathode with high areal sulfur loading of 5.205 mg cm^{-2} at room temperature.	31
Figure 25. Long-term cycling performance of the newly synthesized Li-alloy anodes for all-solid-state Li-S batteries under 0.1 C charge/ discharge at 60°C . The specific capacity is based on the weight of sulfur.	32
Figure 26. (a) Picture of experimental setup used to expose sulfide solid-state electrolyte (SSE) powders to a dry-room environment. The setup includes a 300-liter volume tabletop glovebox, a cartridge-based desiccant system, a microcontroller system to control the moisture setpoint, a personal H_2S detector, and a fan to continuously mix the glovebox air. (b) H_2S generation of different SSEs in a -40°C dew point dry room as a function of time. (c) Reduction in ionic conductivity versus maximum H_2S reading for different sulfide SSEs.	34
Figure 27. Ionic conductivity of LPSI sulfide solid-state electrolyte (SSE) after exposure as a dry powder to different dry-room environments for 30 minutes. The star marks the ionic conductivity of LPSI sulfide SSE after exposure to a -40°C dew point dry room for 30 minutes while immersed in anhydrous dodecane.....	35
Figure 28. Scanning electron microscopy images of (a) pristine LLZTO film and (b) solid polymer electrolyte (SPE) infilled LLZTO films. (c) Backscattered electron image of the LLZTO/SPE system.	38
Figure 29. X-ray photoelectron spectroscopy (XPS) survey scan of (a) pristine LLZTO film and acid-treated LLZTO films, HCl and H_3PO_4 . (b) High-resolution lithium 1s XPS spectra. (c) High-resolution carbon 1s XPS spectra. (d) High-resolution lanthanum 3D XPS spectra. (e) High-resolution phosphorus 2p XPS spectra. (f) High-resolution chlorine 2p XPS spectra.	39
Figure 30. (a-c) DC polarization curves for determining the Li^+ transference number under an applied voltage of 0.04 V at 60°C . (a) Pristine LLZTO film. (b) H_3PO_4 treated films. (c) HCl treated film. Inset: impedance taken just before and immediately after the DC polarization experiment. The curves were fitted with a decay function, and the steady state at the end of the curve was extrapolated. (d-f) Voltage versus time plots of plating-stripping at different current densities. (d) Pristine LLZTO film. (e) H_3PO_4 treated films. (f) HCl treated film.	39

Figure 31. Voltage versus time plots at 60°C of the four model systems assembled to understand the conductivity differences: (a) single solid polymer electrolyte (SPE) layer. (b) SPE infilled porous LLZTO film (H ₃ PO ₄ treated). (c) Stacked SPE, densified LLZTO pellet (H ₃ PO ₄ treated) and SPE. (d) Stacked SPE and densified LLZTO pellet (H ₃ PO ₄ treated) bilayers with the polymer side initially connected to the positive electrode. Their corresponding cycling stability tests showing symmetric and asymmetric cycling behaviors.	40
Figure 32. Characterization of the stripping behavior of thin lithium using simultaneous direct current (DC) and <i>operando</i> alternating current (AC) analysis. (a) Voltage responses of stripping thin lithium on LLZO at 0.4 mA/cm ² . (b) AC impedance analysis at salient points in the DC polarization curve (a). (c) Schematic representation of what is believed to be the lithium morphological evolution at the Li-LLZO interface during discharge.....	43
Figure 33. Thermal gravimetric analysis results of (a) NMC-811, (b) NMC-622, (c) NMC-111, and (d) Al ₂ O ₃ -coated NMC-622 in both argon and O ₂ atmospheres.....	46
Figure 34. (a) X-ray diffraction spectra of sintered cathodes of NMC-622 and LLZ with and without excess lithium. Backscatter scanning electron microscopy images of (b) 10 mol% excess lithium from Li ₂ CO ₃ and (c) no excess lithium, deposited onto the thin porous LLZ structure. These samples were heated to 900°C for 3 hours in argon atmosphere.....	47
Figure 35. (a) Nyquist plot and (b) distribution of relaxation times analysis of milled NMC/LLZ composite cathodes sintered at 900°C with and without Li ₂ CO ₃ addition.	47
Figure 36. (a) X-ray diffraction (XRD) results of the anti-perovskite electrolytes with different chlorine and bromine ratios. Red arrows indicate the LiCl impurities in Li ₂ OHCl. (b) XRD spectra near (110) and (200) peaks. Peak splitting can be clearly seen in Li ₂ OHCl.	50
Figure 37. Scanning electron microscopy and energy-dispersive X-ray spectroscopy results of (a) Li ₂ OHCl and (b) Li ₂ OHCl _{0.5} Br _{0.5}	51
Figure 38. Differential scanning calorimetry results of anti-perovskite electrolytes with different chlorine and bromine ratios. Red arrow points to endothermic peak from orthorhombic to cubic phase transformation in Li ₂ OHCl.....	51
Figure 39. Results of the large-scale Li ₃ InCl ₆ synthesis with 10% excess InCl ₃ from ethanol solution. (top) X-ray diffraction shows no impurities other than aluminum substrate. (lower left) Nyquist plot shows electrolyte is highly conductive with some grain boundaries present after pressing at 5 bar. (lower right) Arrhenius plot shows product is a superionic conductor with low activation energy.	54
Figure 40. (a) Flexibility test of free-standing solid-state electrolyte (SSE) membrane. (b) Cross-sectional scanning electron microscopy images of SSE membrane (b) before and (c) after cold pressing. (d) Ionic conductivity measurement of SSE membrane at 25°C. (e) Galvanostatic voltage profiles and (f) cycling performance of sheet-type PI Li ₆ PS ₅ Cl LiIn cell at 60°C.....	57
Figure 41. (a) Structures of a series of poly(alkyl malonates) synthesized for this project. (b) Ionic conductivity (κ , blue squares) and glass transition temperature (T _g , red circles) of polymer electrolytes comprising 40 wt% of LiTFSI salt at 90°C.	60
Figure 42. The effect of salt concentration r on ionic conductivity, κ , of PPM/LiTFSI (blue circles) and PEO/LiTFSI (black squares) electrolytes at 90°C. Data for PEO/LiTFSI electrolytes were taken from previous work. ^[1]	60

Figure 43. Selectivity of PyTFSI and salt affinity solvent phobic (SASP) polymer. (a) Experimental set-up for H-cell experiments. (b) H-cell experiment with the polymer sandwiched in the middle, with images taken after 3 hours with the measured LiTFSI concentration labeled on the graph; rheological frequency sweep of the polymer after soaked in 1 M LiTFSI DME electrolyte for 8 hours, with the $\tan(\delta)$ at 10 rad s^{-1} marked: (c) PyTFSI. (d) SASP, (e) conductivity (25°C) of the polymer before and after soaked in 1 M LiTFSI DME for 8 hours, and (f) oxygen 1s X-ray photoelectron spectroscopy of SEI on the anode. The signals attributed to either salt or solvent decomposition were separated with their relative percentage marked out.....	64
Figure 44. Specific discharge capacity of LiFePO_4 electrodes prepared with 3% PBBDT (red) and 3% PVDF (black) as binder over long-term cycling at 22°C . Performances of three cells are shown for each type of electrode. The cells are cycled at 0.2C for 5 cycles followed by 1000 cycles at 4C rate. Occasional pausing of the battery tester causes a few inconsistent data points in the plot. Electrodes with PBBDT binder demonstrate better long-term cycling stability despite their slightly inferior capacity compared to their PVDF counterparts.....	67
Figure 45. Specific discharge capacity of five LiFePO_4 electrodes with 3 wt% PBBDT as binder when cycled at 22°C . The cells are cycled at 0.2C for 5 cycles followed by 2000 cycles at 4C rate. Capacity decay is only observed after 1100 ~ 1500 cycles; capacity retention after 2000 cycles at 4C rate is as high as 89%.....	67
Figure 46. Images of the electrodes before and after tape peeling tests. The electrodes are pressed on an adhesive tape and then peeled off. The thin carbon coating layer on the aluminum substrate stays intact after the peeling test when using PVDF as the binder. However, when using PBBDT as the binder, the majority of the carbon coating layer is peeled off along with the LiFePO_4 and carbon particles, exposing the metallic luster of the aluminum substrate. These tests strongly indicate that PBBDT has higher binding strength than PVDF.....	68
Figure 47. Electrochemical performance of different concentrations of Nb_2O_5 -coated NMC-622 materials cycled in liquid electrolyte systems (LP57 + 2%VC). The capacity of the 50 th cycle is used to calculate capacity retention.	68
Figure 48. X-ray fluorescence imaging and X-ray absorption spectroscopy results of pristine and cycled molecular ionic composite (MIC) electrolytes. The cycled MIC sample displayed a heterogeneous distribution of sulfur species compared to the pristine sample. The evolution of decomposed sulfur species is revealed from distinct X-ray absorption near-edge spectroscopy.	69
Figure 49. Electrolyte membrane synthesis and optimization schematics of cold pressing, drop casting, and slot-die coating techniques with optical photographs of the membranes.	72
Figure 50. Characterization of composite membranes cross-section scanning electron microscopy of a flexible, dense LLZO fiber-PEO CPE prepared by (a) drop casting and (b) slot-die coating. (c) Critical current density determination for drop-casted (red) and slot-die coated (blue) membranes in Li-PEO-LiTFSI-LLZO-Cu cell configuration. (d) Arrhenius plot of bulk ionic conductivity for composite and polymer solid-state electrolytes.....	73

Figure 51. (a) Photograph of a decrimped cell made with cross-linked PEO-filled partially sintered Ohara ceramic composite electrolyte membrane, showing its fracture and darkening due to reaction with lithium. (b) Nyquist impedance plots of blocking-electrode cells made with an xPEO-filled partially sintered ceramic tape before plasticizing, and after plasticizing the same sample with TEGDME followed by thoroughly drying it off. The inset photograph shows the membrane becoming flexible after plasticizing.	75
Figure 52. (a) Schematic of trilayer composite electrolyte containing xPEO-filled 3D-interconnected Ohara ceramic as the middle layer, and linear PEO+LiTFSi electrolyte as the top and bottom layers. (b) Photographs of a cell after decrimping show no major fractures in the trilayer membrane (left), and no darkening of composite membrane could be seen after lithium electrode was scraped off. (c) Voltage profile of a Li//Li symmetric cell made with the trilayer membrane and cycled at 0.2 mA/cm ² , 2.5 hours each half cycle, at 70°C. (d) Voltage profile of the last two cycles shown in (c).	76
Figure 53. (a-b) Scanning electron microscopy images of 60w:40w perfluoropolyether (PFPE) : poly (ethylene oxide) (PEO) membranes made using (a) acetonitrile (ACN) / hexafluorobenzene (HFB) and (b) tetrahydrofuran (THF) / n-methyl-2-pyrrolidone (NMP) mixed solvents. (c-d) Ionic conductivity of PFPE/PEO membranes as a function of inverse temperature. The membranes were made using (c) ACN/HFB and (d) THF/NMP mixed solvents, respectively.	77
Figure 54. Conversion and molecular weight data from a 20 K PLiMTFSI synthesis.	80
Figure 55. X-ray diffraction data showing characteristic amorphous peak for both the 60 K (red) and 20 K (blue) PLiMTFSI.	80
Figure 56. (a) Schematic illustration showing the UV-polymerization route to synthesize the single Li-ion conducting (SIC) solid polymer electrolyte (SPE) from the anionic monomer, crosslinker, and plasticizer. (b) Li ⁺ transference number measured by the potentiostatic polarization method of SIC-SPE. (c) Voltage-time profile of the Li-Li symmetric cells when cycling at 0.2 mA/cm ² and 0.1 mAh/cm ² showing the concentration overpotential of SIC-SPE. (d) Li ⁺ transference number measured by the potentiostatic polarization method of mixed ion-conducting SPE. (e) Voltage-time profile of the Li-Li symmetric cells when cycling at 0.2 mA/cm ² and 0.1 mAh/cm ² showing the concentration overpotential of mixed-ion conducting SPE.	82
Figure 57. Schematics of (a) amorphous carbon and (b) graphitic carbon electrodes. (c) Schematic of an asymmetric cell with active buffer layer (ABL). (d) Discharging profile of the asymmetric cell. (e-f) Optical microscopy images of (e) amorphous carbon and (f) graphitic carbon ABLs after lithium plating.	85
Figure 58. Materials and structural concepts for polymer incorporation in solid-state electrolytes.	88

Figure 59. Schematic illustration of the virtual electrode (VE) X-ray photoelectron spectroscopy (XPS) approach for studying solid-state electrolyte (SSE) materials. The VE-XPS approach employs (1) low-energy electron and (2) Li ⁺ ion gun sources to drive electrochemical currents at the surface of exposed battery materials and structure. Additionally, various ultraviolet (UV) and vacuum UV (VUV) light sources are available to extract electrons from the valence-band of the exposed surface. By combining these current-bias sources, it is possible to perform electrochemical cycling on all-solid-state battery materials to probe the formation and evolution of electrochemical properties of the SEI that forms at the Li/SSE interface.	89
Figure 60. First iteration of design for an <i>in situ</i> nano – computed tomography cell with (left) a full view of <i>in situ</i> cell with piezo-electric motion controller on top and (right) a magnified view of the cell enclosure.....	90
Figure 61. Schematics of (a) the nm-scale ionic and electronic transport imaging and (b) kelvin probe force microscopy (KPFM) potential imaging on space charges at interfaces. (c) Photograph of the atomic force microscopy – based nanoprobe set up in an argon glove box.	91
Figure 62. (a) Graphite composite anode with solid-state electrolytes (SSE) overlayer. (b) Coated LCO composite cathode with SSE overlayer. (c) Thin Li-metal film rolled onto stainless-steel foil. (e) SSE layer printed onto non-woven fabric.....	92
Figure 63. Load frames for applying digitally measured pressured to all-solid-state pouch or coin-cell batteries.....	93
Figure 64. FTIR-ATR data of the five lithium sources studied: Supplier #1, Supplier #2, Supplier #3, Supplier #4, and ORNL evaporated lithium, from 400 cm ⁻¹ to 4000 cm ⁻¹	95
Figure 65. Initial X-ray photoelectron data of the five lithium sources studied: Supplier #1, Supplier #2, Supplier #3, Supplier #4, and ORNL evaporated lithium focused on the (a) lithium 1s, (b) carbon 1s, and (c) oxygen 1s peaks.	96
Figure 66. Depth profiling X-ray photoelectron spectroscopy data of the 5 lithium sources studied: Supplier #1, Supplier #2, Supplier #3, Supplier #4, and ORNL evaporated lithium, focused on the lithium 1s (a), the carbon 1s (b), and the oxygen 1s (c) peaks with the different lithium, carbon, and oxygen species denoted as a function of etching time. The estimated etching rate based on a SiO ₂ standard was 12 nm/min for an estimated etch depth of ~ 200 nm per 1000s.....	97
Figure 67. (a-b) Scanning electron microscopy images of polycrystalline (PC) NMC-811 and single crystalline (SC) NMC-811 particles, respectively. (c-d) Voltage profiles collected on PC NMC-811 and SC NMC-811 cells cycled at 0.5C. Li ₃ YCl ₆ was used as electrolyte and Li-In alloy used as anode. (e) Comparison of discharge capacity as a function of cycle number. (f) Rate capability comparison of the cells.....	102
Figure 68. Post-mortem analysis of the interface between Li ₃ YCl ₆ (LYC) and Li-In anode after 1000 cycles. (a) Cross-sectional scanning electron microscopy image. (b-d) Energy-dispersive X-ray spectroscopy maps of In-Li, Y-Li, and Cl-K, respectively. (e) Yttrium K-edge X-ray absorption spectra collected on yttrium metal, pristine LYC, and the interface after cycling. (f) Chemical map obtained from X-ray fluorescence imaging.	103

Figure 69. Schematic of experimental and device setup for graphene-liquid electrochemical <i>in situ</i> cell for infrared near-field imaging and nanospectroscopy, previously used by this team.....	105
Figure 70. Comparison of attenuated total reflectance – Fourier transform infrared (ATR-FTIR) of 2 M LiClO ₄ in propylene carbonate (top, green trace) and nano-FTIR spectra of the graphene / 2 M LiClO ₄ in propylene carbonate interface (bottom, black trace). Light blue bars and black vertical lines highlight measured differences in infrared absorption between the bulk and interface.....	105
Figure 71. (a) Spatially-resolved nano – Fourier transform infrared (nano-FTIR) spectra across the graphene / 2 M LiClO ₄ in propylene carbonate interface. Noted with the black lines are changes in the shoulder of the peaks (b) biased nano-FTIR data collected over single location.....	105
Figure 72. (a) Cryo – high-angle annular dark field (HAADF) scanning transmission electron microscopy (STEM) of plated lithium dendrite in baseline electrolyte without LiNO ₃ additive. (b) Cryo – bright field STEM of plated lithium particles in electrolyte with LiNO ₃ additive. (c) Cryo – transmission electron microscopy and selected area diffraction of the SEI formed in electrolyte with LiNO ₃ additive.....	108
Figure 73. Low-magnification transmission electron microscopy images of lithium deposits in (a) carbonate-based electrolyte and (b) ether-based localized high-concentration electrolyte.....	111
Figure 74. Microstructure of lithium deposits and SEI formed in the different electrolytes. (a-c) Cryogenic – transmission electron microscopy (cryo-TEM) images of lithium deposits formed in the carbonate-based electrolyte: (a) TEM image of lithium deposits with whisker morphology. (b) High-resolution TEM (HRTEM) images acquired from the stem region of the lithium whisker. (c) HRTEM images acquired from the tip region of the lithium whisker. (d-f) Cryo-TEM images of lithium deposits formed in the ether-based LHCE: (d) TEM image of lithium deposits with whisker morphology. (e) HRTEM images acquired from the stem region of the lithium whisker. (f) HRTEM images acquired from the tip region of the lithium whisker.....	111
Figure 75. Structure and elemental composition of lithium deposits and their SEIs formed in the carbonate-based electrolyte. (a) Scanning transmission electron microscopy – high-angle annular dark field image showing the lithium whisker. (b) Electron energy loss spectroscopy (EELS) elemental mapping showing the elemental distribution of SEI. (c) EELS acquired from stem and tip region of the whisker. (d) EELS of lithium. (e) EELS of phosphorus. (f) EELS of carbon. (g) EELS of oxygen. (h) EELS of fluorine.....	112
Figure 76. Composition of lithium deposit and SEI layer formed in the ether-based localized high-concentration electrolyte (LHCE). (a) Electron energy loss spectroscopy (EELS) elemental maps from the tip region of the whisker showing distribution of lithium, sulfur, carbon, nitrogen, fluorine, and oxygen. (b) EELS elemental maps from the stem region of the whisker showing distribution of lithium, sulfur, carbon, nitrogen, fluorine, and oxygen. (c) Comparison of EELS of lithium K-edge, oxygen K-edge, and carbon K-edge from the stem and tip region of the lithium whisker.....	113

Figure 77. (a) Schematic of scanning electron microscopy (SEM) microprobe Li-metal deposition experiment showing electrostatic potential profile contours. (b) Example linear sweep voltammetry experiments from SEM experiment. (c) Colorized SEM images of lithium plating experiments outlined in (a), with each image corresponding to the positions on plot (b).	116
Figure 78. Indentation modulus results on different thin films on lithium foil.....	119
Figure 79. Histogram of the moduli in Figure 78.....	119
Figure 80. Three atomic force microscopy images at different locations of the DME 2-hour sample.....	119
Figure 81. Schematic illustration of an <i>in situ</i> time-of-flight – secondary ion mass spectrometry stage and open-cell setup on the stage.	122
Figure 82. Time-of-flight – secondary ion mass spectrometry (TOF-SIMS) and scanning electron microscopy characterization of Cu/Ag-C/LPSCI/Li cell inside TOF-SIMS.....	122
Figure 83. Electrochemical measurements of Cu/Ag-C/ LPSCI/Li cell mounted on a biasing stage inside time-of-flight – secondary ion mass spectrometry.....	122
Figure 84. Li-Al-O phase diagrams. (a) The first phase-region (green triangle) formed by LiAl_5O_8 , LiAlO_2 , and aluminum for LiAl_5O_8 lithiation. The dash line represents the lithiation path of LiAl_5O_8 . (b) The first phase-region (green triangle) formed by LiAl_5O_8 , Al_2O_3 , and aluminum for Al_2O_3 lithiation. The dash line represents the lithiation path of Al_2O_3	127
Figure 85. Li-ion transport mechanism study in PEO-LATP composite electrolyte at temperature 90°C . (a) Schematic representation of polymer and ceramic particles in composite electrolyte. Ceramic particles, polymer, and interphase are represented in green, orange, and red, respectively. The zoomed-in view of ceramic particle depicts ceramic and polymer interface and interphase region near ceramic particle surface. (b) Effective conductivity of the composite electrolyte at a varying interface charge transfer resistance for different volume fractions of ceramics in polymer matrix. Solid lines represent case 1: $k_{\text{interphase}} = k_{\text{PEO}}$, and dotted lines represent case 2: $k_{\text{interphase}} = (1/2) k_{\text{PEO}}$. (c) Effective conductivity of the composite electrolyte at varying volume fractions of ceramics in polymer matrix at different interface charge transfer resistance. Solid lines represent case 1: $k_{\text{interphase}} = k_{\text{PEO}}$ and case 2: $k_{\text{interphase}} = (1/2) k_{\text{PEO}}$. (d) Transference number and effective conductivity at low (solid line) and high (dotted line) interfacial charge transfer resistance. (e) Required ionic conductivity for polymer electrolytes at different transference number for electric vehicle applications. Composite electrolytes are represented by the blue oval patch. A yellow asterisk represents the current state of LATP-PEO system for $R_{\text{CT}} = 0.004 \Omega\text{m}^2$	130
Figure 86. Typical crystal structures of known superionic conductors with corner-sharing frameworks. (a) Structure of $\text{Li}_{1+x}\text{Al}_x\text{Ti}_{2-x}(\text{PO}_4)_3$. (b) Structure of LiTa_2PO_8 . (c) Structure of $\text{Li}_{1+x}\text{Ta}_{1-x}\text{Zr}_x\text{SiO}_5$	133
Figure 87. Degree of distortion of octahedral lithium environment in quaternary lithium oxide materials with (a) corner-sharing framework, and (b) non-corner-sharing frameworks.	133
Figure 88. (a) Variation of the thermal contact resistance with pressure in good agreement with the contact resistance model (M. R. Sridhar and M. M. Yovanovich; see Reference [1]). Extracted mean contact spot size (b) and contact number density (c) from the model of Yovanovich, and (d) the electrochemical impedance spectroscopy Nyquist plot at different stack pressure showing no significant pressure dependence.	136

Figure 89. (a) Variation of the thermal contact resistance with cell cycling and the extracted mean contact spot size (b) and contact number density (c). With cycling, the number of contacts decreases while the mean contact spot size increases, indicating preferential lithium deposition.	137
Figure 90. (a) Schematic of the symmetric cell. (b) Electrochemical impedance spectroscopy Nyquist plot of the cell impedance. (c) 2ω multiharmonic electrothermal spectroscopy (METS) fitting related to the resistances at the interface and the transport in the electrolyte. (d) 1ω METS fitting related to the entropy change of the charge transfer reaction.	138
Figure 91. The snapshots of the interface between a S-C cathode and a $\text{Li}_7\text{P}_3\text{S}_{11}$ amorphous glass-ceramic solid-state electrolyte (a) S-graphene (GRA) and (b) S-carbon nanotube (CNT) based systems and mean square displacement of Li^+ in system GRA and CNT calculated by means of ab initio molecular dynamics simulation at (c) 300 K and (d) 600 K.	140
Figure 92. (a) Interface model between $\text{Li}_6\text{PS}_5(\text{BH}_4)$ and Li-metal anode with terminal atoms of H_2 at the interfacial contact. Lithium atoms are in green, BH_4 units are in light blue with hydrogen in pink, and PS_4 units are in purple with sulfur in yellow. (b) Evolution of P-S and B-H bonds versus simulation time.....	143
Figure 93. (a) Calculated radial distribution function of P-S at the interface compared to those of the bulk $\text{Li}_6\text{PS}_5(\text{BH}_4)$ and the stable polysulfide phases in the Li-P-S chemical space. (B) Calculated radial distribution function of Li-Li at the interface compared to those of its decomposition phases predicted under full thermodynamic equilibrium. (C) Calculated radial distribution function of B-H and B-Li at the interface compared to those of the bulk $\text{Li}_6\text{PS}_5(\text{BH}_4)$ and LiBH_4	144
Figure 94. Electrochemical performance of quasi-solid-state Li-S battery at high-S loading (4 mg/cm^2). (a) Cycling behavior and (b) discharge curves at selected cycles are shown for a quasi-solid-state Li-S battery made up of Li-anode, $\text{Li}_6\text{PS}_5\text{F}_{0.5}\text{Cl}_{0.5}$ SSE, and super-P cathode with sulfur loading of 4 mg/cm^2 containing 2 wt% AB + 9 wt % CNT, and 2 wt% LATP. The battery was cycled at C/20.....	147
Figure 95. Scanning electron microscopy characterization of SP-S cathodes (with AB 7 wt%, CNT 5 wt%) at various sulfur loadings. (a-f) Low-magnification images, (g-l) high-magnification images, and (m-l) cross-sectional view taken at 60° tilts.	148
Figure 96. Scanning electron microscopy characterization of SP-S cathodes (with AB 7 wt%, CNT 5 wt%) with (a/h) no LATP, (b/i) 0.5 wt%, (c/j) 1 wt%, (d/k) 1.5 wt%, (e/l) 2 wt%, (f/m) 2.5 wt%, and (g/n) 5 wt%. (a-g) Images of the surface. (h-n) Cross-sectional view taken at 60° tilts.....	148
Figure 97. (a) Example energy variation plot for different iterative structures sampled for La_2CoO_4 using the Basin Hopping approach. (b) Distribution of energies, with corresponding atomic structures for selected local minima (highlighted region) from the energy variation plot. Lanthanum, cobalt, and oxygen are represented by yellow, blue, and red spheres, respectively, in the structure representation.	151
Figure 98. Example of stable structures obtained for (a-c) $\text{Li}_{1.5}\text{La}_{0.5}\text{CoO}_3$ and (d-e) $\text{Li}_{1.5}\text{LaCo}_{0.5}\text{O}_3$. Lithium, lanthanum, cobalt, and oxygen ions are represented by green, yellow, blue, and red spheres, respectively, in the structure representations.....	152

Figure 99. (a) Distribution of calculated kinetic energy barrier for 10 distinct nucleation pathways to form LaCoO_3 . (b) Examples of relatively low-energy and high-energy nucleation pathways. The structural evolutions along these two nucleation pathways are also presented from the starting nuclei to the stable structure predicted for LaCoO_3 .	152
Figure 100. Probability of occurrence of a given configuration of Zr-doped $\text{LiNi}_{0.8}\text{Mn}_{0.1}\text{Co}_{0.1}\text{O}_2$: (a) one dopant per cell [3.7% of total transition metal content], and (b) two dopants per cell [7.4% of total transition metal content].	156
Figure 101. Parity plots of machine learning model energies for (a) Al-doped NMC-811 and (b) Mg-doped NMC-811.	157
Figure 102. Comparison of the hydroxyl bonds for the proton defect in NiO_2 for O1 stacking and O3 stacking. The dashed line shows the hydrogen bonding between layers.	157
Figure 103. Cyclic voltammetry (CV) profiles of (a) $\text{Li}_6\text{PS}_5\text{Cl}$, (b) $\text{Li}_6\text{PS}_5\text{Cl}_{0.5}\text{Br}_{0.5}$, and (c) $\text{Li}_6\text{PS}_5\text{Br}$. Cycle range is 0-5 V, and voltage sweep rate is 0.1 mV/s. In each experiment, the voltage sweep starts first from open-circuit voltage (~ 2 V) toward the higher voltage, hence the oxidation (delithiation) direction.	160
Figure 104. (a) Phosphorus K-edge, (b) sulfur K-edge, and (c) chlorine K-edge X-ray absorption spectra of sulfide electrolytes before and after cycling. In each panel, the black, red, green, and blue curves are from Li_3PS_4 , $\text{Li}_6\text{PS}_5\text{Cl}$, $\text{Li}_6\text{PS}_5\text{Cl}_{0.5}\text{Br}_{0.5}$, and $\text{Li}_6\text{PS}_5\text{Br}$, respectively, with solid lines representing the pristine samples and dashed lines representing cycled samples. The cyan curve in (c) is a reference chlorine K-edge spectra of LiCl compound from Reference [1].	161
Figure 105. (a) The k-space and (b) R-space extended X-ray absorption fine structure of phosphorus K-edge. Black curve: Li_3PS_4 ; red curve: $\text{Li}_6\text{PS}_5\text{Cl}$; and black dashed curve: cycled Li_3PS_4 .	162
Figure 106. (a) Lattice parameters. (b) Total lithium diffusivity under hydraulic pressures. (c) Lithium diffusivity along strain axis under mechanical strain of LLZO as a function of temperature.	164
Figure 107. (a) Radial distribution functions and (b) mean squared displacement of bulk $\text{Li}_{0.75}\text{CoO}_2$ at 2000 K. (c) LCO $\Sigma 2(-1104)/[11-20]$ tilt grain boundary (GB) model. (d) Histogram of diffusivity of lithium atoms that stayed at GB area.	165
Figure 108. A workflow for generating two-phase particulate microstructures for modeling the composite cathode consisting of LLZO solid electrolyte and LCO active particles. (a) Generation of multiphase particulate microstructure with controlled size distributions of two-phase mixtures using the open-source software <i>Particula</i> . (b) Voxelization and labeling of the two-phase particulate microstructure to convert it into a readable format for <i>MesoMicro</i> . (c) Simulation of the transport of lithium in the composite cathode and calculation of the effective diffusivity and mechanical elastic modulus by a self-consistent model considering chemo-mechanical couplings.	166
Figure 109. Differential scanning calorimetry curves of $\text{Li} \parallel \text{NMC-622}$ cells using a single-layer 20- μm polyethylene separator and 7 μm polyethylene + polyimide separator. (NMC-622 was charged to 4.4 V.)	169
Figure 110. Thermal stabilities of (a) 20- μm single-layer polyethylene, (b) electrospun polycarbonate, and (c) electrospun polysulfone separators. (d) Cycling performance of $\text{Li} \parallel \text{NMC-622}$ cells using 20- μm single-layer polyethylene, 7- μm polyethylene + polycarbonate, and 7- μm polyethylene + polysulfone dual separators.	170

Figure 111. (a) Digital photos of the designed prelithiation reagents with porosity of 80% and 70%, respectively, and their corresponding capacity. (b) The initial Coulombic efficiency of silicon anode with and without prelithiation.	172
Figure 112. Schematic of lithium reserve on copper (lithium from cathode) by voltage optimization.	175
Figure 113. Cu NMC-622 cell performance at different cutoff-discharge voltages.	175
Figure 114. (a) Calculated specific energy versus areal sulfur loading for Li-S pouch cells with different E/S ratios assuming that the specific capacity and the average discharge voltage are 1,000 mAh/g and 2.05 V, respectively. (b) Configuration of interdigitated type battery winding for the pouch cell stacking.	181
Figure 115. (a) Charge/discharge curves of 1.2 g-sulfur pouch cell using sulfur/macroporous host with double-end binding cathode under different current densities ranging from 41.67 mA/g to 166.67 mA/g. (b) Cycling performance of 1.2-g-sulfur pouch cell using sulfur/macroporous host with double-end binding cathode at 83.33 mA/g.	181
Figure 116. Weight analysis pie chart of the 1.2-g-sulfur pouch cell through interdigitated type battery winding.	182
Figure 117. (a) Schematic of a single-particle-layer electrode with low tortuosity in vertical and planar direction. (b) Scanning electron microscopy image of sulfur/carbon materials around 50 μm . (c) Reconstructed micro- computed tomography image of single-particle-layer electrode. (d) Discharge and charge curves of the single-particle-layer electrode during 1 st cycle. (e) Cycling performance of single-particle-layer electrode at different porosity. (f) Cycling performance of single-/multi-particle-layer electrodes.	184
Figure 118. <i>Operando</i> X-ray absorption (XAS) to understand redox mediator (RM) chemistry in all-solid-state Li-S batteries (ASSLSBs). <i>Operando</i> sulfur K-edge XAS spectra of (a) bare Li ₂ S cathodes and (d) Li ₂ S@AQT cathodes in polymer-based ASSLSBs for the first charge process. XAS spectra of Li ₂ S (2473.5 eV) and sulfur (2472.7 eV) shown in the bottom are used as references. The pre-edge feature at 2470.7 eV is identified as the fingerprint of lithium polysulfides from the terminal sulfur. (b) Contents of Li ₂ S and sulfur calculated from two-phase fitting of the XAS spectra in (a) as a function of test time. The corresponding charge curve shows a high energy barrier of ~ 4 V for Li ₂ S activation. Schematics for proposed Li-S reaction mechanism in ASSLSBs, using Li ₂ S cathodes (c) without / (f) with AQT RM. (e) The average chain length of lithium polysulfides as a function of the state of charge for Li ₂ S@AQT cathodes during the first charging.	187
Figure 119. (a) Prolonged cycling performance at 60°C. (b) Galvanostatic voltage profiles of high active mass loading PMTH cathode and (c) its cycling performance at 0.05 C. (d) Energy density comparison of the state-of-the-art organic cathodes reported in Li-organic all-solid-state batteries.	190
Figure 120. (a) The scanning electron microscopy surface image of nickel foam and multiwalled carbon nanotube composite electrode. The inset is optical photo of the electrode. (b) The composite electrode after first full charge. (c) The electrode after first full discharge.	193
Figure 121. (a) Schematics of preparing the polysulfide retaining interlay. (b) Scanning electron microscopy image of the surface of the glass fiber separator. (c) The polyamic-coated glass fiber separator interlayer.	193

Figure 122. The laboratory synthesis setup of the (a) HATN monomer and (b) polymer. (c) The field emission scanning electron microscopy image of HATN-S composite and (d) the energy dispersive X-ray spectrum of the yellow circled area. (e) Voltage profiles of high-loading HATN-S cathode in lean lithium and electrolyte conditions, showing the high areal loadings achieved.....	197
Figure 123. (a) Voltage profiles of C/S composite electrodes at different C-rates using 100 μm lithium and E/S ratio of 10 $\mu\text{L mg}_{\text{sulfur}}^{-1}$ and (b) the corresponding cycling stability. (c) Schematic of passivation layer originated from LiNO_3 consumption and (d) the formation of insulating layer due to polysulfide shuttle.....	198
Figure 124. (a) Photo of lithium metal from the disassembled cell after 200 cycles. (b) Schematic of titration gas chromatography quantification of lithium metal loss. (c) Sample of lithium metal by polysulfide shuttle. (d) Photo of C/S cathode from the disassembled cell after 200 cycles and immersed in DOL/DME solvents. (e) Thermal gravimetric analysis curves.....	200
Figure 125. (a) Image of MTI E1300 roll-to-roll coater for kg-scale coating at GM. (b) Image of sulfur cathode electrode with areal sulfur loading of $\sim 5.2 \text{ mg-sulfur/cm}^2$	201
Figure 126. Electrochemical performance of 5.2 mg-sulfur/ cm^2 sulfur cathode electrode (a) charge-discharge profiles, and (b) discharge-discharge capacities and Coulombic efficiency versus cycle number.	201
Figure 127. (a) The charge-discharge curves of C/S cathode in 1 M LiTFSI in a DOL/DME mixture (1:1, v/v) and in (b) New Electrolyte, using (c) cycling performance of C/S cathode cycling in New Electrolyte.....	202
Figure 128. Electrochemical cycling performance and Coulombic efficiency of <i>complex framework materials – sulfur</i> cycled between 1.7-2.8 V.	205
Figure 129. Electrochemical cycling performance and Coulombic efficiency of <i>inorganic-organic framework materials – sulfur</i> cycled between 1.7-2.8 V.	205
Figure 130. (a) Non-lithiated phase stability of alloys. (b) Lithiated phase stability.....	206
Figure 131. (a) Galvanostatic discharge-charge curves of SPZ-1a cathode at different cycles. (b-d) Cycling performance of (b) SPZ-1a, (c) SPZ-1b, and (d) SPZ-1c cathodes. The areal active material loading is $\sim 2 \text{ mg cm}^{-2}$. The cells were activated at 0.03 A g^{-1} (based on composite weight) for the 1 st cycle and then cycled at 0.1 A g^{-1}	208
Figure 132. (a) Initial capacities of SPZ-2a, SPZ-2b, and SPZ-2c cathodes. (b-d) Cycling performance of (b) SPZ-2a2, (c) SPZ-2a6, and (d) SPZ-2a10 cathodes in carbonate electrolytes. The areal active material loading is $\sim 2 \text{ mg cm}^{-2}$. The cells were activated at 0.05 A g^{-1} (based on composite weight) for the 1 st cycle and then cycled at 0.1 A g^{-1}	209
Figure 133. Attenuated total reflectance – Fourier transform infrared spectroscopy of (a) as-formed SEI catalytic layer, (b) SEI exposed to oxygen for 6 hours, (c) SEI deposited with Li_2O_2 , (d) SEI with Li_2O_2 delithiated, and (e) the separator used in the cell of panel (d).....	213
Figure 134. X-ray photoelectron spectroscopy of the SEI-coated cathode before and after exposure to O_2 at (a) carbon 1s and (b) oxygen 1s.....	213
Figure 135. Density functional theory calculations for six O_2 adsorption sites on tin sulfide (SnS). (top) Example of O_2 adsorption structure is given for C1 site. (bottom) O_2 adsorption energies for the six sites shown for SnS surface (top figure).....	216
Figure 136. G4MP2 free energies for LiO_2 disproportionation to Li_2O_2 in DMSO solvent.	216

Figure 137. Electrochemical performance of Li-CO ₂ battery. (a) Discharge/charge curves at current density and capacity of 0.3 mA/cm ² and 0.3 mAh/cm ² (corresponding to 3000 mAh/g), respectively. (b) Discharge/charge curves at current density of 0.5 mA/cm ² and capacity of 0.2 mAh/cm ² (2000 mAh/g). (c) Discharge/charge curves in CO ₂ chamber at the current density of 0.5 mA/cm ² and capacity of 0.5 mAh/cm ² (5000 mAh/g), respectively. (d) Rate capability results of (NbTa) _{0.5} BiS ₃ . (e) Cycling stability of batteries with (NbTa) _{0.5} BiS ₃ with ZnI ₂ , only (NbTa) _{0.5} BiS ₃ , (NbTa) _{0.5} BiS ₃ with LiI, and MoS ₂ with LiI. (f) Comparison of current density versus capacity of the Li-CO ₂ battery for the team's work (black stars) with other references.....	219
Figure 138. <i>In situ</i> X-ray diffraction with up cut-off voltage of 4.1 V.....	223
Figure 139. (a-c) Powder X-ray diffraction patterns of Na[(Ni _{0.5} Mn _{0.5}) _{1-x} Fe _x]O ₂ (x = 0, 1/3, and 2/3), and (d) changes in the c/a lattice parameter ratio before and after air-exposure.....	226
Figure 140. Scanning electron microscopy particle morphologies of Na[(Ni _{0.5} Mn _{0.5}) _{1-x} Fe _x]O ₂ (x = 0, 1/3, 1/2, 2/3, and 0.8) before and after air-exposure for five days.....	227
Figure 141. X-ray photoelectron spectroscopy nickel 2p spectra of the pristine and air-exposed (a) Na[Ni _{0.5} Mn _{0.5}]O ₂ , (b) Na[Ni _{0.25} Mn _{0.25} Fe _{0.5}]O ₂ , and (c) Na[Ni _{0.1} Mn _{0.1} Fe _{0.8}]O ₂ . (d) Open-circuit voltage profiles of Na[(Ni _{0.5} Mn _{0.5}) _{1-x} Fe _x]O ₂	227
Figure 142. (a) Two-dimensional contour plot and (b) selected high-temperature synchrotron X-ray diffraction (XRD) patterns of Na _{0.74} Ti _{1.815□0.185} O ₄ ·nH ₂ O collected from room temperature to 775°C during the heating process in air. Le Bail fitting of XRD patterns collected at (c) 200°C using space group <i>Cmcm</i> and (d) 775°C using space group <i>C 2/m</i>	230
Figure 143. Le Bail fitting of X-ray diffraction (XRD) patterns collected at (a) room temperature, (b) 100°C, (c) 125°C, and (d) 150°C during the high-temperature synchrotron XRD measurement by adopting the <i>Immm</i> space group.....	231
Figure 144. <i>Ex situ</i> Raman spectra of Na _{0.74} Ti _{1.815□0.185} O ₄ ·nH ₂ O heated in air at different temperatures.....	232
Figure 145. Le Bail fitting of X-ray diffraction (XRD) patterns collected at (a) 500°C and (b) 600°C during the high-temperature synchrotron XRD measurement by adopting the <i>C 2/m</i> space group.....	232
Figure 146. Electrochemical performance of hard carbon (HC) NaNMC full cells. (a) Electrochemical stability window. (b) Cycling performance of HC NaNMC full cells using different electrolytes cycled at 0.2 C after three formation cycles at 0.1 C. The cathode loading is 1.5 mAh cm ⁻² . (c–e) Voltage curves as a function of cycle number of HC NaNMC full cells using NaPF ₆ /EC:EMC (c), NaFSI/TFP (d), and NaFSI/DMC:TFP (e) electrolytes.....	234
Figure 147. X-ray photoelectron (XPS) characterization to identify SEI dissolution. (a/d) The absolute value of difference of quantified SEI atomic composition ratios between the cycled and cycled-soaked hard carbon (HC) anodes as a function of the sputtering thickness. (b/c/e/f) XPS spectra of carbon 1s (b/e), phosphorus 2p (c), and nitrogen 1s (f) of the HC anodes (signal depth = 0 nm). The cycled HC anodes were cycled in NaPF ₆ / EC:EMC (a; upper of b/c), NaFSI/TFP (d; upper of e/f) electrolytes for 100 cycles. The cycled-soaked HC anodes were soaking cycled HC electrodes with EC:EMC (a; bottom of b/c) and TFP (d; bottom of e/f) solvents for 50 hours.....	235

Figure 148. Capacity retention for NMC-9055 and Nb-coated/substituted NMC-9055. Cycling conditions: 2.8 V to 4.4 V, tap density 3.0 g/cm ³ , lithium foil as anode, (left) 1 M LiPF ₆ in EC/DMC, and (right) M47 electrolyte.	237
Figure 149. Evolution of the cell impedance of NMC-9055 and Nb-coated / substituted NMC-9055 during cycling in carbonate electrolyte.	237
Figure 150. Cross-sectional and top-view scanning electron microscopy (SEM) images of (a) DL-3@Li and (b) bare lithium after deposition for a capacity of 4 mAh cm ⁻² at a current density of 2 mA cm ⁻² . (c) Charge rate capability of Li NMC-622 cells at various charge current densities from C/10 to 1.5C (1C = 4.6 mAh cm ⁻²) with the same constant discharge current density of C/10. (d) Galvanostatic intermittent titration technique profiles of Li NMC-622 cells (4 mAh cm ⁻²) at a current density of 1.5C and variation in internal cell resistance as a function of state of charge. Cross-sectional and top-view SEM images of (e) DL-3@Li and (f) bare lithium after charging at 1.5C, as pointed out in panel (c).....	239
Figure 151. (a) The 10 th charge/discharge curves and (b) Coulombic efficiency of Li/Cu batteries in high-concentration electrolyte, localized high-concentration electrolyte, and F5DEE electrolytes (at 1 mA cm ⁻² current density and 1 mAh cm ⁻² areal capacity).	239
Figure 152. Electrochemical performance of Li NMC-811 battery cells in Electrolytes A, B, and C between 2.8-4.3 V. (a) Initial voltage profiles of Li NMC-811 coin cells at 0.1 C. (b) Cycling performance of Li NMC-811 coin cells at 0.2C for charge and 0.5 C for discharge. (c) Cycling performance of Li NMC-811 coin cells at 0.2C for charge and 0.5 C for discharge in Electrolyte C. 50- μ m Li-metal anode and 30 μ L of electrolytes were used. 1 C = 4 mA/cm ²	240
Figure 153. Nyquist plots of Li NMC-811 coin cells in Electrolytes A, B, and C at different cycles.	240
Figure 154. (a) Scanning electron spectroscopy (SEM) images and (b) X-ray diffraction patterns of LNO, NM, NC, and NA cathodes. (c) Cycling performances and (d) relationship between the specific capacities (C/3 rate) and cycle life (100 cycles) of LNO, NM, NC, and NA cathodes cycled between 2.8 V and 4.4 V. (e) Charge-discharge curves of LNO, NM, NC, and NA cathodes cycled with a cutoff energy density of 750 W h kg ⁻¹ . Cyclability evaluation in (f) coin cells with baseline LP57 electrolyte for 100 cycles at a C/3 rate and in (g) pouch cells with a localized high-concentration electrolyte (LHCE) for 300 cycles at a C/3 rate with a cutoff energy density of 750 W h kg ⁻¹ . The scale bars in (a) are 20 μ m. LHCE electrolyte in (g) consists of LiFSI, DME, and TTE with a molar ratio of 1:1.2:3.....	241
Figure 155. Functional groups and structure for sulfurized polyacrylonitrile (SPAN). (a) X-ray photoelectron spectra (XPS) for SPAN synthesized at different temperature. (b) Compositional ratio in SPAN derived from XPS results shown in (a). (c) Molecular structure of SPAN.....	243
Figure 156. Roles of sulfur and nitrogen for sulfurized polyacrylonitrile (SPAN) cathode (SPAN:CMC:Super-P 8:1:1) in Li-metal battery (a) gas chromatography – mass spectrometry of SPAN in the chemical lithiation solution. (b) Scanning transmission electron microscopy (STEM) – electron energy loss spectroscopy of the SPAN cathode after the 1 st discharge in battery. (c) STEM – energy dispersive X-ray spectroscopy of the SPAN cathode after the 1 st discharge and charge; X-ray photoelectron spectroscopy (d) sulfur 2p and (e) nitrogen 1s spectra for the SPAN cathode after the 1 st discharge and charge. (f-g) Discharge and charge mechanism of the sulfur and nitrogen functional groups in SPAN.	244

Figure 157. (a-b) Selected galvanotactic charge and discharge curves and Coulombic efficiency versus cycle number of Li Cu coin cell using LTO@PE separator. The electrolyte is the 1.49 M lithium bis(fluorosulfonyl)imide (LiFSI) in a mixture of 1,2-dimethoxyethane (DME) and 1,1,2,2-tetrafluoroethyl-2,2,3,3-tetrafluoropropyl ether (TTE), with DME and TTE a molar ratio of 1.2:3. The deposition capacity is 1 mAh cm ⁻² at a current density of 1 mA cm ⁻² with a volume of 60 μL for each coin cell. In this testing procedure, a given amount of lithium metal is plated on a copper foil and then stripped off with a cutoff voltage of 1 V versus Li/Li ⁺	245
Figure 158. (a-b) Selected galvanotactic charge and discharge curves of 50 μm Li NMC-622 (4 mAh cm ⁻²) full cell using polyethylene and LTO@PE separators. (c) Capacity versus cycle number of 50 μm Li NMC-622 full cell. All cells were charged and discharged at C/10 for the 1 st formation cycle and then cycled at a C/3 charge and discharge in the voltage window of 2.7–4.4 V. The electrolyte was localized high-concentration electrolyte, with a volume of 60 μL for each coin cell.	246
Figure 159. (a) Potential energy profile for Reaction 1 (Li ₂ S → LiS + Li). (b) Potential energy profile for Reaction 2 (Li ₂ S ₂ → Li ₂ S + S).....	248
Figure 160. Electrochemical performance of sulfur cathodes with areal sulfur loading of (a-b) 3.75 mgS/cm ² and (c-d) 5.2 mgS/cm ²	249
Figure 161. Analysis of the formation cycle of a Li–NMC-622 cell using the eCAD technique. (a) The charge and discharge voltage profiles and the associated infrared-free voltage (VIR-free) profiles. Also presented is the pseudo – open circuit voltage versus state-of-charge (SOC) curve, which is obtained from a validated Li-NMC-622 cell during an initial reference performance test at C/20. (b) The reconciled charge and discharge VIR-free versus SOC profiles in correspondence with the lithium content in NMC-622.	250
Figure 162. (a) Charge capacity retention curve of the Li-NMC-622 cell in the cycle aging test. (b) Projections of useful life based on charge capacity retention as a function of cycle number. (c) Projections of useful life based on the lithium inventory retention and cathode active material utilization as a function of cycling rate.	251
Figure 163. Galvanostatic charge and discharge voltage profiles of Li SPAN coin cell across 50 cycles using (a) UCSD electrolyte and (b) baseline electrolyte: 1 M LiTFSI in DOL/DME. Cycling performance and Coulombic efficiency of Li//SPAN battery cycling in (c) UCSD electrolyte and (d) 1 M LiTFSI in DOL/DME electrolyte. Cells were cycled at C/10 (1C = 550 mA h g ⁻¹).	253
Figure 164. Pair distribution function results comparing SPAN structural changes during cycling in the UCSD electrolyte (left) and the DOL/DME electrolyte (right), with the peak corresponding to the C-S bond distance highlighted.	254
Figure 165. Pair distribution function results for S-S bonding changes while cycling SPAN (a) in UCSD electrolyte and (b) in DOL/DME baseline electrolyte. (c) Illustration of interatomic distances in S-S and S-S-S. (d) Proposed structural changes in SPAN during 1 st cycle, providing insights into two different charge storage mechanisms.....	255
Figure 166. (a) Comparison of electrochemical performance for Li Cu cell in baseline electrolyte with and without LiNO ₃ additive. (b) X-ray fluorescence mapping of copper electrode after cycling. (c) X-ray absorption results of SEI from electrolytes with and without LiNO ₃ additive.....	256

Figure 167. Evolution of SEI morphology at the Li-metal surface in 5 M LiFSI in DMC solution from <i>ab initio</i> molecular dynamics / classical molecular dynamics simulations. (left) Well-defined regions of amorphous lithium oxide connected by less dense regions of LiF_x and LiS_xN_y structures. (right) Blue and gray are outer and inner surfaces enclosing lithium oxide volumes.....	257
Figure 168. (a) High-performance liquid chromatography – ultra violet (HPLC-UV) chromatograms of five different standards of elemental sulfur in DME: 0.0151 mM, 0.0756 mM, 0.378 mM, 0.7556 mM, and 0.9445 mM. (b) Calibration curve obtained by plotting the area under the sulfur peak in HPLC-UV chromatogram against the sulfur concentration. (c) HPLC-UV chromatogram of derivatized polysulfides using methyl triflate as a derivatization agent. (d) Plot of logarithm of retention time of a particular derivatized polysulfide against the number of sulfur atoms in it.	258
Figure 169. 3D reconstruction of deposited lithium metal plated under different stacking pressures resulting in different lithium porosities: (a) 50 kPa and 43.57% porosity; (b) 150 kPa and 36.90% porosity; (c) 250 kPa and 8.61% porosity, and (d) 350 kPa and 0.68% porosity. (e) Li-metal corrosion rate and its correlation with the porosity of the freshly deposited lithium. All lithium is plated in Gen 2 electrolyte. A total amount of 0.318 mAh of lithium is plated at a rate of 0.5 mA/cm ² for each sample.	259
Figure 170. <i>Operando</i> atomic force microscopy of lithium plating in three stages. (a) SEI growth on copper at +30 mV versus Li/Li ⁺ potential prior to lithium plating. Measurement over 25 hours reveals dual microstructure (grain + particles) that roughens with time. (b) Lithium nucleation showing a broad distribution of nuclei sizes. (c) Later-stage lithium growth showing faceted grain structure. The amount of charge passed is indicated.....	260

TABLE OF TABLES

Table 1. Summary of Raman spectroscopic data of sulfide and oxysulfide glass solid-state electrolytes before and after exposure to a dry-room environment. Fractional peak areas are assigned to the vibrational modes of different glass structural units.	35
Table 2. Ionic conductivity (σ_{Li}) at room temperature and 60°C, activation energy (E_a) at 60°C, transference number (t_{Li^+}) at 60°C, and critical current density at 60°C of the polymer solid electrolyte and hybrid system (LLZTO/polymer) with different acid treatments conducted on LLZTO films.....	38
Table 3. Space group and lattice parameters analyzed from X-ray diffraction for each electrolyte.....	50
Table 4. Summary of differential scanning calorimetry results of the anti-perovskite electrolytes. (MP: melting point)	51
Table 5. Surface composition from X-ray photoelectron spectroscopy (at%) before etching.....	96
Table 6. X-ray photoelectron spectroscopy surface composition (at%) after etching.....	98
Table 7. Summary of the electrochemical impedance spectroscopy (EIS) and multiharmonic electrothermal spectroscopy (METS) measurements.....	137
Table 8. Comparison of density functional theory calculated NiO ₂ oxygen stacking relative energy and structural parameters.	157
Table 9. Summarized performance of Cu NMC-622 cell at different cutoff-discharge voltages.	176

A MESSAGE FROM THE MANAGER: ADVANCED BATTERY MATERIALS RESEARCH AND BATTERY500 CONSORTIUM

Congratulations to Jiguang (Jason) Zhang of Pacific Northwest National Laboratory (PNNL) for receiving the Distinguished Achievement Award during the Vehicle Technology Office Annual Merit Review meeting (June 21 to 23, 2022). Jason, a Lab fellow, has been a member of the BMR Team for 13 years. During this time, he led pioneering work in developing energy storage devices including lithium-metal and solid-state batteries. His Team developed novel electrolytes that allow lithium-metal batteries to achieve higher cycling efficiencies than today's conventional lithium-ion electrolytes. More recently, he has broadened his research to include sodium batteries. Jason has been awarded 36 U. S. patents and published more than 360 papers in professional journals.

The new Solid-State Electrolyte projects and the Lithium-Air and Sulfur projects are off to a good start, and a synopsis of their progress is presented in this report. A review of the solid-state projects will be held at Lawrence Berkeley National Laboratory on August 18-19, 2022. A few notable achievements of these and the more seasoned efforts during this quarter are summarized below:

- J. Nanda's team at Oak Ridge National Laboratory (ORNL) used solution-based synthesis techniques to make Li_3InCl_6 electrolytes on the gram scale with ionic conductivities of up to ~ 1 mS/cm. They found that the best ionic conductivities were obtained using 10% excess InCl_3 in the synthesis.
- N. Balsara's team at University of California, Berkeley, successfully synthesized multiple polyester-based polymer electrolytes. They demonstrated that increasing the diol length yielded higher conductivity up to a diol chain length of $n = 5$. The best ionic conductivity measured was 1 mS/cm at 90°C , on par with PEO-based electrolytes.
- P. Zhang's team at Solid Power demonstrated the synthesis of a thin sulfide-based electrolyte ($25\ \mu\text{m}$) on a carrier film. Their best Li/NMC pouch cell has cycled for more than 700 cycles between 2.8-4.2 V at a current of $C/5$ at 45°C with a capacity retention of 88%.
- E. Wachsman's team at the University of Maryland sintered LLZO and NMC with 10% excess Li_2CO_3 . The Li_2CO_3 addition was found to decrease the interfacial resistance between the NMC and LLZO by 10 times.
- A. Westover's team at ORNL demonstrated that lithium metal has distinct surface layers from various sources, including rolled lithium from four suppliers, along with ORNL evaporated lithium. The different surfaces include Li_2CO_3 , hydrocarbons, and silicone-based hydrocarbons. All lithium samples studied had a Li_2O layer under the outermost surface, ranging from 50 nm for high purity evaporated lithium to > 500 nm for some rolled samples. The surface species can all be removed through etching processes.
- X-Q. Yang's and E. Hu's team at Brookhaven National Laboratory used cryogenic transmission electron microscopy (cryo-TEM) to demonstrate the ability of LiNO_3 additive in suppressing lithium dendrites. The cryogenic conditions reduce beam damage on deposited materials, allowing the observation of uniformly spherical versus dendritic lithium formations with and without LiNO_3 , respectively.

- Y. Cui's team at Stanford University developed a method of fabricating porous lithium-mesh to optimize and control pre-lithiation of silicon anodes. Their results show that 70% porous lithium-meshes (1.5 mAh cm^{-2}) fully compensate for the initial capacity loss and improve the initial Coulombic efficiency to nearly the ideal 100%. This approach has advantages compared to using thick lithium foil due to significant capacity mismatch between the lithiating electrodes.
- P. Le's team at PNNL developed a low solvation electrolyte NaFSI:DME:TFP (1:1.5:2 in mole) to suppress the SEI dissolution and extend the long cycling performance of high-energy sodium-ion batteries. The HC||NaNi_{0.68}Mn_{0.22}Co_{0.1}O₂ (NaNMC) full cells using NaFSI:DMC:TFP electrolyte with a charge limit of 4.2 V demonstrated 94% capacity retention after 300 cycles.

A few notable achievements from the Battery500 Consortium this quarter include the following:

- The Binghamton University team developed a new niobium treatment process by adding the niobium together with the lithium salt to an in-house synthesized 90% nickel content NMC. The niobium treatment is highly effective in improving capacity retention to reach as high as 95% capacity retention after 200 cycles for the 3.1Nb-NMC-9055 versus the 75% retention for untreated NMC-9055.
- The Pennsylvania State University team developed a novel electrolyte achieving a lithium Coulombic efficiency of 99.0%. The electrolyte was found to improve the cycling performance as well as the cell stability of Li/NMC-811 cells.
- The University of California, San Diego, team demonstrated that the aromatic C-S and pyridine-N in SPAN (sulfurized polyacrylonitrile) are the main contributors to its reversible capacity. Other components are either involved in irreversible structural change and/or irreversible capacity loss.
- The SLAC/Stanford team developed a new *operando* electrochemical atomic force microscopy (EC-AFM) to study lithium plating. This technique allows the *operando* study of microstructural evolution during lithium plating in various electrolyte systems with approximately 1 nm spatial resolution (x, y, and z).

On behalf of the VTO team,

Tien Q. Duong

Tien Q. Duong
Manager, Advanced Battery Materials Research Program & Battery500 Consortium
Batteries & Electrification R&D
Energy Efficiency and Renewable Energy
U.S. Department of Energy

TASK 1 – Solid-State Electrolytes

Team Lead: Andrew Westover, Oak Ridge National Laboratory

Summary and Highlights

The U. S. Department of Energy (DOE) has made a clear goal of realizing next-generation batteries with an energy density greater than 500 Wh/kg, that can cycle for more than 300 cycles, and that can demonstrate high-rate capabilities. To achieve this step-change in battery performance, a significant change in the battery chemistry and cell design is needed. This task focuses on developing solid-state electrolytes (SSEs) that enable Li-metal anodes and high-energy cathodes to achieve just such a step change. This task includes 12 projects centered in DOE national laboratories and 13 in companies and universities. These projects span the gamut of different materials for SSEs, interfacial design strategies to enable Li-metal anodes, and high-energy cathodes. Together, they can significantly impact the successful realization of the DOE battery performance targets.

In summary, the projects focus on research and development of a range of solid electrolytes (SEs), including:

- sulfur ceramics and glasses (1.1 – 1.9),
- oxide ceramics (1.10 – 1.13),
- halides and anti-perovskites (1.13 – 1.15),
- polymers (1.16 – 1.18),
- composites (1.19 – 1.22),
- multiple electrolytes / full cells (1.23 – 1.24), and
- Li-metal – SSE interface (1.25).

These projects encompass common research themes essential to achieving high-energy solid-state batteries (SSBs), including:

- engineering high ionic conductivity > 1 mS/cm,
- developing electrolytes that are stable with various high-energy cathodes, including layered oxide cathodes, high-voltage spinels, and conversion cathodes such as sulfur and FeF_3 ,
- developing electrolytes or interfaces that are stable with lithium metal,
- developing thin SEs 20-100 μm thick, and
- understanding the mechanics of SSBs.

Highlights

The highlights for this quarter are as follows:

- J. Connell's group at Argonne National Laboratory (ANL) characterized multiple argyrodite SEs from NEI, Ampcera, and ANL. The argyrodite powders had similar ionic conductivities of ~ 1 mS/cm with the same crystallographic structure and minimal impurities.
- G. Xu's ANL team made significant progress toward completion of a sulfide SE synthesis lab. They also performed *in situ* synchrotron X-ray diffraction (XRD) during synthesis, showing the crystallizing of pure argyrodite sulfide SE O-doped argyrodites. They found that oxygen inclusion prevents Li_2S and LiBr from fully dissolving to form the desired phase.
- Y. Cui's group at Stanford University successfully made each of the novel SEs, that is, Li_3BS_4 , $\text{Li}_2\text{B}_2\text{S}_5$, and $\text{Li}_{10}\text{Bi}_{10}\text{S}_{20}$, in > 10 -g quantities.

- J. Nanda's Oak Ridge National Laboratory (ORNL) team made both Cl-doped and Br-doped argyrodites. They compared two synthesis routes relying on hand grinding and planetary milling. Both methods yielded the same phase, but the electrolytes produced using the planetary milling had higher ionic conductivity. They proposed that amorphous phases not detected by XRD likely play a role in the improved ionic conductivity.
- D. Lu's group at Pacific Northwest National Laboratory coated halide-doped sulfide electrolytes (with $\text{Li}_7\text{P}_2\text{S}_8\text{Br}_{0.5}\text{I}_{0.5}$) with an amphipathic organic molecular coating. The coating had a minimal drop in conductivity, but significantly improved air stability in a dry room.
- S. Martin's Iowa State University (ISU) team performed glass drawing of 150-g preforms into glass films ~ 150- μm thick. They also compared the conductivity of cathodes using the ISU-6 glass and various conductive carbon additives, finding that carbon-nanotube-based cathodes had the best overall conductivity.
- P. Zhang's group at Solid Power demonstrated the synthesis of a thin electrolyte 25- μm -thick on a carrier film. They also continued a long-term cycling test of their sulfide electrolyte. The best cell has cycled for more than 700 cycles between 2.8-4.2 V at a current of C/5 at 45°C with a capacity retention of 88%. Finally, they made 2 Ah test pouch cells. Initial cycling results will be reported next quarter.
- D. Wang's Pennsylvania State University team synthesized a new sulfide-based SE with conductivity of 3 mS/cm. They also began evaluating a new sulfide cathode with > 5 mg/cm² loading, but it had poor initial Coulombic efficiency, which needs to be resolved. Finally, they tested the cycling stability of two Li-alloy anodes, which both had respectable capacity retention over 50 cycles.
- T. Yersak's General Motors group tested the moisture stability of several sulfide SEs, demonstrating that PS_4^{-3} was the most stable sulfide unit in dry-room environments. Despite minimal H₂S generation for some electrolytes, all the electrolytes had a significant drop in ionic conductivity, emphasizing that H₂S generation alone is not a sufficient stability indicator. They also demonstrated that handling the sulfide electrolytes in an anhydrous solvent mitigates H₂S generation and preserves the original ionic conductivity.
- J. Ye's team at Lawrence Livermore National Laboratory compared the effect of different acid treatments on printed $\text{Li}_7\text{La}_3\text{Zr}_2\text{O}_{12}$ (LLZO) films used in composite SEs. Both HCl and H₃PO₄ acid treatments decreased the overall ionic conductivity, but the H₃PO₄-treated LLZO composites had a higher overall transference number and the best critical current density (CCD) of 0.28 mA/cm².
- J. Sakamoto's University of Michigan group used *in situ* electrochemical impedance spectroscopy (EIS) measurements to track void formation during stripping during symmetric Li/LLZO/Li testing. As lithium is stripped, voids form, as evidenced by a second semicircle in the plating/stripping that also shows up as an increase in the stripping overpotential.
- E. Wachsman's team at University of Maryland sintered LLZO and Ni-Mn-Co (NMC) with 10% excess Li_2CO_3 . The Li_2CO_3 addition decreased interfacial resistance between the NMC and LLZO by ten times.
- Z. Chen and T. Li's ANL group investigated the effect of bromine substitution into the antiperovskite SE Li_2OHCl . Substituting even small amounts of bromine into the Li_2OHCl structure stabilizes the cubic phase, which has higher ionic conductivity. Differential scanning calorimetry confirmed the prior observations and identified a phase transition from orthorhombic to cubic at 42°C for the undoped phase and a melting temperature of ~ 296°C.
- J. Nanda's team at ORNL used solution-based synthesis techniques to make Li_3InCl_6 electrolytes on the gram scale with ionic conductivities of up to ~ 1 mS/cm. They found that the best ionic conductivities were obtained using 10% excess InCl_3 in the synthesis.
- D. Qu's University of Wisconsin, Madison group made a 45- μm -thick electrolyte with 0.2 wt% polytetrafluoroethylene (PTFE) binder that was freestanding and mechanically robust. Full cells with a Li-In alloy are shown as well with an argyrodite SE that has a capacity of 180 mAh/g over 30 cycles.

- N. Balsara's team at University of California, Berkeley (UCB) successfully synthesized multiple polyester-based polymer electrolytes (PEs). They reported that increasing diol length yields higher conductivity up to a diol chain length of $n = 5$. Beyond this point, ionic conductivity begins to drop. The best ionic conductivity measured was 1 mS/cm at 90°C, on par with poly(ethylene oxide) (PEO)-based electrolytes. They also observed that the ionic conductivity drops in the polyester-based electrolytes as the salt concentration is increased.
- Z. Bao and Y. Cui's Stanford University group developed an H cell to test the effectiveness of their SASP (salt affinity solvent phobic) electrolyte. The tests effectively showed that the SASP electrolyte allows ions to pass through, but prevents almost all of the solvent from crossing the membrane.
- L. Madsen's team at Virginia Polytechnic Institute and State University compared the cycling behavior of lithium iron oxide (LFP) cathodes synthesized with both PBDT [poly(2,2'-disulfonyl-4,4'-benzidine terephthalamide)] and PVDF [polyvinylidene (di)fluoride] binders. The PVDF-based cathodes had a higher initial capacity, but the PBDT-based cathodes had improved cyclability. They also used X-ray absorption spectroscopy and X-ray fluorescence imaging to study the homogeneity of molecular ionic composite (MIC) electrolytes before and after cycling. Cycling causes the MIC electrolytes to become more heterogeneous.
- S. Tepavcevic's ANL group compared different methods to make electrospun LLZO fibers into membranes, including drop-casting with PEO, slot-die coating with PEO, and cold pressing. Slot-die coating and drop-casting gave virtually identical ionic conductivities, but the slot-die-coated LLZO composites had a slightly improved CCD of 0.16 mA/cm². EIS measurements suggest that the polymer phase dominates the conductivity.
- X. C. Chen's team at ORNL successfully demonstrated Li//Li plating and stripping through the partially sintered ceramic/PEO composite, with good cyclability >100 cycles for 0.5 mAh/cm² at 0.25 mA/cm² at 70°C. They also successfully synthesized mixed PEO/fluorinated polyether (PFPE) membranes, which are expected to improve interfacial stability. They developed two sets of mixed solvents that can enable the co-casting of PEO-PFPE electrolytes.
- B. McCloskey's UCB group tailored the synthesis of PLiMTFSI [poly((trifluoromethanesulfon)imide lithium methacrylate)] electrolytes. The polymers are completely amorphous and do not have a glass transition between -80°C and 250°C. They are, however, relatively brittle and challenging to make freestanding.
- E. Hu's Brookhaven National Laboratory team developed plasticized single-ion conducting (SIC) PEs utilizing ultraviolet crosslinked. The SIC polymers had a more ideal square plating and stripping profile than the comparable mixed ionic conductor.
- G. Cedar's team at UCB compared two active buffer layers (ABLs) between Li₃PS₄ SEs and lithium anodes. The two buffer layers were amorphous carbon and graphitic carbon. For the amorphous carbon, plating occurred between the amorphous carbon and the copper, but it occurred between the ABL and the electrolyte for the graphitic carbon.
- A. Burrell's National Renewable Energy Laboratory group developed a polysulfide-based polymer binder for sulfide electrolytes that helps improve ionic conductivity while under low pressures. They also initiated efforts to cast pouch-cell-scale SEs, lithium anode, and LCO cathodes. Finally, they developed a testing setup for 5 cm × 6 cm single-layer pouch cells that can vary temperature and pressure.
- A. Westover's team at ORNL demonstrated that lithium metal has distinct surface layers from various sources, including rolled lithium from four suppliers, and ORNL evaporated lithium. The different surfaces include Li₂CO₃, hydrocarbons, and silicone-based hydrocarbons. All lithium samples studied also had a Li₂O layer under the outermost surface, ranging from 50 nm for high purity evaporated lithium to > 500 nm for some rolled samples. The surface species can all be removed through etching processes.

Task 1.1 – Multifunctional Gradient Coatings for Scalable, High-Energy-Density Sulfide-Based Solid-State Batteries (Justin Connell, Argonne National Laboratory)

Project Objective. This task seeks to develop scalable approaches to synthesize gradient-coated sulfide solid-state-electrolyte (SSE) particles to improve their air/moisture tolerance and provide chemical compatibility with Li-metal anodes and high-voltage oxide cathodes. The compositional gradient is targeted to provide the additional advantage of lower interfacial impedance due to mitigation of detrimental, spontaneously formed space-charge layers and/or elemental interdiffusion at the sulfide SSE-oxide cathode interface.

Impact. Development of coated SSE materials that provide stable, low-impedance interfaces with both anode and cathode will enable high-energy-density, all-solid-state full cells with improved cyclability at high rates relative to benchmarked, uncoated materials. Coating the SSE directly will also remove the need for separate anode and cathode coatings, significantly reducing the cost and complexity associated with materials processing while maintaining compatibility with roll-to-roll manufacturing.

Approach. The team will leverage a surface science-based, integrated experimental-theoretical approach to synthesize gradient-coated SSE powders, characterize the structure, composition, and intrinsic stability of coated SSEs in contact with reactive electrodes, and directly correlate this understanding with their electrochemical performance. Gradient coatings will be developed using atomic layer deposition (ALD) and/or physical mixing methodologies viable at the kg/ton scale, ensuring technical and commercial relevance of the final, optimized coating process. Well characterized, model surfaces will be used to understand the electronic structure and chemical stability of the gradient coatings as a function of gradient composition and thickness to understand the effect of space-charge layers and chemical reactions on interface resistance. They will accelerate development and optimization of the gradient coatings for improved performance in full cells by establishing a tight feedback loop between materials synthesis and experimental/computational characterization of interfacial (electro)chemistry.

Out-Year Goals. The out-year goals are to demonstrate high-energy-density, low-impedance full cells assembled from fully optimized, gradient-coated SSE powders, high-energy-density cathodes, and Li-metal anodes. The team will also significantly improve the ability to manipulate the formation of space-charge layers at sulfide SSE-oxide cathode interfaces based on mechanistic understanding of the extent to which they can be mitigated to reduce overall cell impedance.

Collaborations. This project funds work within multiple divisions and directorates at Argonne National Laboratory (ANL) and includes in-kind contributions from Solid Power.

Milestones

1. Baseline Li|Li symmetric cell testing and characterization of uncoated argyrodite SSEs. (Q2, FY 2022; In progress)
2. Chemical stability characterization of gradient coatings for argyrodite SSEs. (Q3, FY 2022; In progress).
3. Computational assessment of electronic structure of candidate gradient coating chemistries. (Q4, FY 2022)
4. Identification of multiple gradient coating chemistries that deliver > 50% reduction in weight gain during humidified air exposure. (Q1, FY 2023)

Progress Report

Among the classes of SSEs investigated to date, sulfide-based SSEs deliver the highest Li-ion conductivities (≥ 10 mS/cm in some cases) compared to polymer and oxide SSEs across a wide range of temperatures with favorable mechanical properties and low-temperature processability. Argyrodite-based SSEs, with the general formula $\text{Li}_{7-y}\text{PS}_{6-y}\text{X}_y$ (LPSX; X = Cl, Br, I), have emerged as one of the most promising families of sulfide-based materials due to the wide range of compositional control and structural (dis)order achievable depending on the nature and chemistry of the halide dopant incorporated into the material. To set reasonable performance baselines for symmetric cells employing the project's gradient-coated SSEs, the team has focused on initial characterization of the structural, chemical, and electrochemical properties of uncoated, argyrodite-based SSEs.

All materials studied have the nominal formula $\text{Li}_6\text{PS}_5\text{Cl}$ (LPSCI), and the team has evaluated LPSCI materials synthesized in-house at ANL, as well as material obtained from commercial suppliers (that is, NEI and Ampcera). Figure 1a shows representative X-ray diffraction (XRD) patterns for LPSCI from ANL, NEI, and Ampcera. An XRD pattern of the Kapton background signal is also provided for comparison. In all three SSEs, the powder crystallizes in the cubic F-43m space group, as expected, with no detectable impurity phases. Electrochemical impedance spectroscopy (EIS) measurements of pellets pressed from each SSE powder indicate room-temperature ionic conductivities of 0.71 mS/cm, 0.90 mS/cm, and 2.8 mS/cm for the ANL, NEI, and Ampcera materials, respectively. Temperature-dependent conductivity measurements derived from EIS analysis (Figure 1b) allow for determination of the activation energy (E_a) for Li^+ transport according to the Arrhenius equation $\sigma(T) = A \exp(-E_a/kT)$, where A is a pre-exponential factor, k is the Boltzmann constant, and T is the absolute temperature. The E_a for the LPSCI SSEs from NEI was calculated to be 0.31 eV, providing

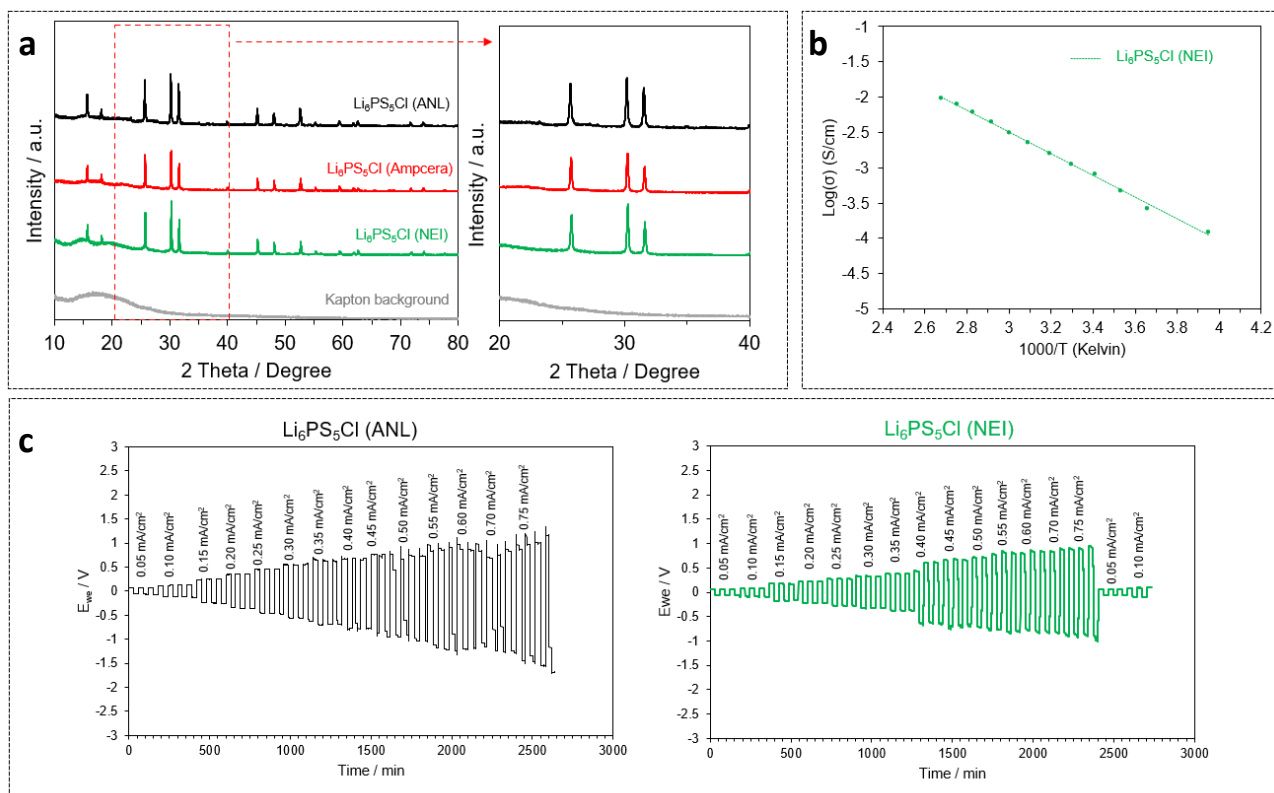


Figure 1. (a) X-ray diffraction (XRD) patterns for pristine $\text{Li}_6\text{PS}_5\text{Cl}$ (LPSCI) from ANL, NEI, and Ampcera; the XRD pattern for the Kapton background is shown for comparison. (b) Arrhenius plots for total Li^+ conductivity of LPSCI from NEI in the temperature range of -20°C to 100°C . (c) Cycling stability of pristine LPSCI from ANL (black) and NEI (green) in Li||Li symmetric cells at 65°C .

a baseline for Li^+ mobility to compare against coated SSE materials. The representative electrochemical characterization data for $\text{Li}|\text{LPSCl}|\text{Li}$ symmetric cells made from the ANL-synthesized LPSCl and NEI SSE are summarized in Figure 1c. In both cases, the LPSCl materials exhibit close-to-uniform plating/stripping profiles at current densities up to 0.35 mA/cm^2 . At current densities $> 0.35 \text{ mA/cm}^2$, the plating/stripping profiles of both LPSCl materials become unstable, showing sharp voltage drops indicative of nonuniform lithium plating and/or internal short-circuiting. Returning to lower current densities ($\leq 0.1 \text{ mA/cm}^2$) with the NEI material recovers the same symmetric plating/stripping behavior observed initially, indicating hard short-circuits do not form up to 0.75 mA/cm^2 ($\sim 1.8 \text{ }\mu\text{m}$ lithium plated per cycle). Similar Arrhenius and cycling evaluation of the Ampcera material is ongoing and will be completed shortly, as this material was only recently received. Overall, these baseline measurements will serve as a comparison for forthcoming work related to ALD of ceramic coatings on sulfide-based powders.

Surface characterization of LPSCl materials via X-ray photoelectron spectroscopy (XPS) was also performed to assess the nominal composition and surface chemistry of the starting materials and establish a baseline before applying coatings (Figure 2). Utilizing the project's glovebox-connected ultrahigh vacuum (UHV) system, it is possible to analyze the LPSCl materials without any ambient air exposure prior to analysis. XPS core-level spectra of the as-received NEI LPSCl powders reveal a surface speciation consistent with reports elsewhere in the literature,^[1] exhibiting little to no impurity phases and minimal (but non-zero) surface oxidation. The dominant species observed in both the sulfur 2p and phosphorus 2p core levels (Figure 2a-b) are assigned to PS_4^{3-} tetrahedra in LPSCl. Evidence of S^{2-} species is also present in the sulfur 2p, and has been attributed previously to anionic S^{2-} species present in the LPSCl lattice.^[1] Negligible ($\leq 0.5 \text{ at}\%$) amounts of S^0 and $\text{P}_2\text{S}_5/\text{Li}_3\text{PO}_4$ can also be fit to the spectra, indicating possible residual precursor materials or some degree of surface oxidation, but are within the experimental error and are therefore not confidently assigned as present. The chlorine 2p core level (Figure 2c) indicates a single species that is consistent with Cl in the LPSCl structure. Surface oxide species (Figure 2d) are partially due to carbonaceous contaminants that are inherent to XPS analysis (R-C-O and O-C-O) as well and suggest a small amount of surface carbonate or phosphate formation, perhaps due to some air exposure during the materials manufacturing and/or shipment. Quantitative composition analysis indicates the surface oxygen content is $\sim 5\%$ of the total signal, suggesting only a very thin layer of surface oxidation is present. Materials stoichiometry analysis further indicates a slightly Cl-enriched material, with a nominal composition of $\text{Li}_{5.8}\text{PS}_5\text{Cl}_{1.2}$. This additional chlorine content could come from multiple sources. It is possible that the additional chlorine content was added intentionally to improve the total Li-ion conductivity; however, it is also possible that it is due to a small amount of excess LiCl that remains from the synthesis. Processing temperatures used to synthesize LPSCl ($\geq 450^\circ\text{C}$) may also cause some surface enrichment of chlorine. Nevertheless, the materials composition falls within expected ranges, and indicates high-quality materials with which to proceed with testing the impact of SSE coating on (electro)chemical stability and performance.

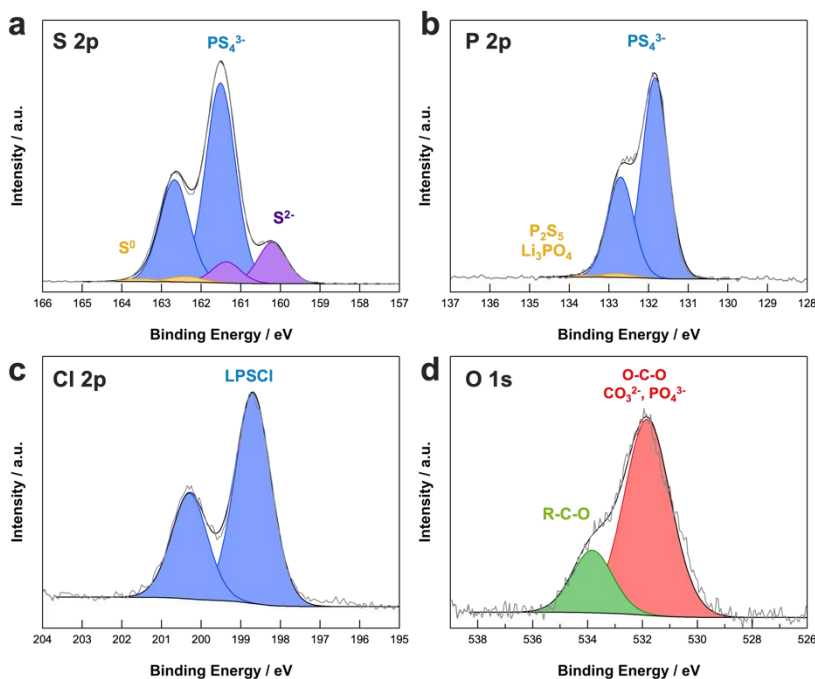


Figure 2. (a) Sulfur 2p, (b) phosphorus 2p, (c) chlorine 2p, and (d) oxygen 1s X-ray photoelectron spectroscopy core level spectra for the NEI LPSCl solid-state electrolyte.

Reference

- [1] Walther, F., et al. *Chemistry of Materials* 31 (2019): 3745–3755.

Patents/Publications/Presentations

The project has no patents, publications, or presentations to report this quarter.

Task 1.2 – Electrolytes for High-Energy, All-Solid-State, Lithium-Metal Batteries (Guiliang Xu, Argonne National Laboratory)

Project Objective. The project objective is to develop ultra-thin ($< 30 \mu\text{m}$) sulfide SSEs with high room-temperature ionic conductivity ($> 0.01 \text{ S/cm}$) and high chemical/mechanical/electrochemical stability, and further integrate them with lithium metal and high-loading selenium-doped sulfur (Se-S) cathodes through rational interface engineering to develop all-solid-state Li-S batteries (ASSLSBs) with high energy density and long cycle life.

Impact. The project is related to development and mass production of high-performance sulfide SSEs for high-energy all-solid-state Li-S pouch cells. The project's success in meeting or exceeding U. S. Department of Energy (DOE) targets can promote practical implementation of Li-S battery in electric vehicles (EVs), electric aviation, and grid energy storage, and hence significantly reduce oil dependence and emissions of carbon dioxide. It can also mitigate the domestic supply challenge on the critical raw battery materials (for example, nickel and cobalt).

Approach. The thickness and chemical/interfacial stability of sulfide SSEs are the critical challenges for energy density, cycle life, and mass production of all-solid-state Li-S pouch cells. The team will combine innovative material design, electrode architecture fabrication, and advanced diagnostics tools to address these challenges. Specifically, the approaches include: (1) improving air stability and ionic conductivity of sulfides through synthetic control and cation/anion doping, and (2) fabrication of flexible thick SeS cathode supported thin sulfide electrolytes to ensure intimate contact and increase energy density, (3) stabilizing Li-metal/sulfide electrolytes interface via interlayer and additives design to increase critical current density (CCD) of lithium stripping/plating, (4) advanced Li-S pouch-cell design, and (5) multiscale advanced diagnostic such as *in situ* XRD, X-ray absorption spectroscopy (XAS), X-ray imaging, and focused ion beam – scanning electron microscopy (FIB-SEM) to understand and overcome the degradation pathways.

Out-Year Goals. The out-year goals are to scale up the optimal sulfide SSEs to develop Ah-level all-solid-state Li-S pouch cells that can reach a cell energy density of $> 500 \text{ Wh/kg}$ with 80% capacity retention for > 300 cycles at a current density of $> 1 \text{ mA/cm}^2$.

Collaborations. The team is closely collaborating with top scientists at University of Chicago (X. Huang) and at Advanced Photon Source (APS; C. Sun, W. Xu, D. Zhang, and J. Deng) and Center for Nanoscale Materials (CNM; Y. Liu and M. Chan) of ANL for *in situ* diagnostics on the synthesis and aging mechanism of the proposed sulfide SSEs.

Milestones

1. Set up a dedicated lab for synthesis, processing, and characterization of sulfide SSEs. (Q1, FY 2022; In progress)
2. Reveal the formation and degradation mechanism of sulfide SSE. (Q2, FY 2022; In progress)
3. Complete composition tuning of sulfide SSE. (Q3, FY 2022; In progress)
4. Develop doped sulfide SSE with high room-temperature ionic conductivity ($> 1 \text{ mS/cm}$) and air stability. (Q4, FY 2022; In progress)

Progress Report

This quarter, the team has begun work on developing high-performance sulfide SSEs for ASSLSBs. Their strategy for sulfide SSEs with high ionic conductivity and air stability includes: (1) improving air stability of sulfide SSEs that have inherently higher ionic conductivity (for example, argyrodite-type $\text{Li}_2\text{S-P}_2\text{S}_5\text{-LiX}$; X = Cl, Br, I) through anion doping; (2) increasing ionic conductivity of sulfide SSEs that have inherently higher air stability (for example, $\text{Li}_2\text{S-MS}_2$; M = Sn, Ge, Si...) through cation doping. The method they used to synthesize these sulfide SSEs is high-energy ball milling followed by thermal treatment.

At ANL, the team has an existing Li-S lab that focuses on development of advanced sulfur cathode and liquid electrolytes (LEs) to push up the energy density and cycle life of liquid Li-S batteries. To prevent contamination between LEs and solid electrolytes (SEs), they have been setting up another lab that is dedicated for synthesis, processing, and characterization of sulfide SSEs. They have secured a lab from their division and obtained the required equipment, including a glovebox, PM-200 ball milling, electrochemical testing cells, two box furnaces, a tube furnace, a pellet presser, a vacuum oven, etc. They have also built a vacuum sealing system (Figure 3), which allows them to seal the precursor of sulfide SSEs in quartz tubes under vacuum for the subsequent heat treatment. They are also setting up a system for evaluation of air stability of the developed sulfide SSEs. They expect the lab to be ready for full operation by next quarter.



Figure 3. Digital photo of vacuum sealing set up for the synthesis of solid-state electrolytes.

Meanwhile, the team is investigating the solid-state synthesis process of sulfide SSEs by using *in situ* synchrotron X-ray diffraction (SXR) at APS. Unlike the conventional approach based on many trial-and-error experiments, the *in situ* SXR experiment could allow the team to directly probe the phase transition and crystal structure evolution during formation of sulfide SSEs. They could also observe the structural evolution during holding (for example, effect of time) and cooling process (quenching versus slow cooling). Moreover, through Rietveld refinement, they are able to obtain evolution of cell lattice parameters, and microstrain during these processes. This all relies on collaboration with the APS beamline scientist. Figure 4a shows the *in situ* SXR set up built at APS, with an X-ray beam, gas-blower heater, and camera. They loaded samples into quartz tubes and sealed them with Kapton tape to prevent moisture contamination during the experiment. Figure 4b shows a snapshot during the experiment, in which the gas blower directly heated the sample, while X-ray penetrated the sample to collect the XRD pattern.

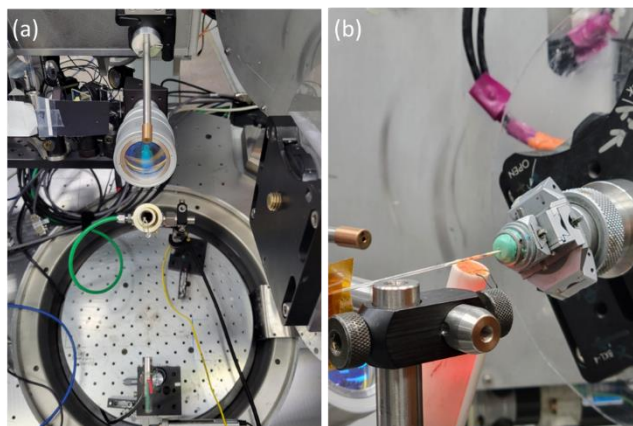


Figure 4. (a) Digital photo of *in situ* synchrotron X-ray diffraction set up at Advanced Photon Source to probe synthesis of sulfide solid-state electrolytes. (b) Snapshot photo during heating process.

Unlike $\text{Li}_6\text{PS}_5\text{I}$ comprising fully ordered S^{2-} and I⁻ and $\text{Li}_6\text{PS}_5\text{Cl}$ comprising fully disordered S^{2-} and Cl⁻, $\text{Li}_6\text{PS}_5\text{Br}$ (LPSBr) comprises a mixture of ordered and disordered structures, thus demonstrating the fastest theoretical Li^+ mobility in the $\text{Li}_6\text{PS}_5\text{X}$ family. Therefore, the team has started the study of LPSBr SSEs.

Through *in situ* SXR, the team would like to clarify the effect of synthesis conditions (for example, heating rate, temperature, atmosphere, and cooling process) on site-disorder and ionic conductivity. They will also explore the effect of oxygen doping and composition (change of bromine content) on air stability and ionic conductivity of optimal LPSBr SSEs.

Before the *in situ* SXRDXRD experiment, the team mixed Li_2S , LiBr , and P_2S_5 in a designated weight ratio to form a homogeneous mixture by high-energy ball milling. Figure 5a shows the *in situ* SXRDXRD pattern during formation of LPSBr during heating from room temperature to 600°C , followed by rapid cooling. As shown, the reaction process can be separated into three regions: (1) starting materials, (2) formation of LPSBr, and (3) quenching process. Figure 5b shows the zoom-in view at 2θ range of $6\text{--}9.5^\circ$. As shown, on heating, the peaks of Li_2S (111 and 200), LiBr (111 and 200), and P_2S_5 (012 and 2-2-1) gradually decreased. At a temperature of $\sim 270^\circ\text{C}$, three new peaks corresponding to the (220), (311), and (222) peaks of LPSBr emerged, indicating formation of LPSBr. Further heating from 270°C to 600°C results in increase of XRD peak intensity due to the growth of particle size and disappearance of other impurities. The team has conducted Rietveld refinement on the XRD pattern at 600°C . As shown in Figure 6, the formed LPSBr is very consistent with the standard LPSBr with a space group of F-43m and cell lattice parameter of $a = b = c = 10.097443 \text{ \AA}$ and $\alpha = \beta = \gamma = 90^\circ$. During quenching (rapid cooling), they can see there is no phase transition, indicating the reservation of pure LPSBr phase.

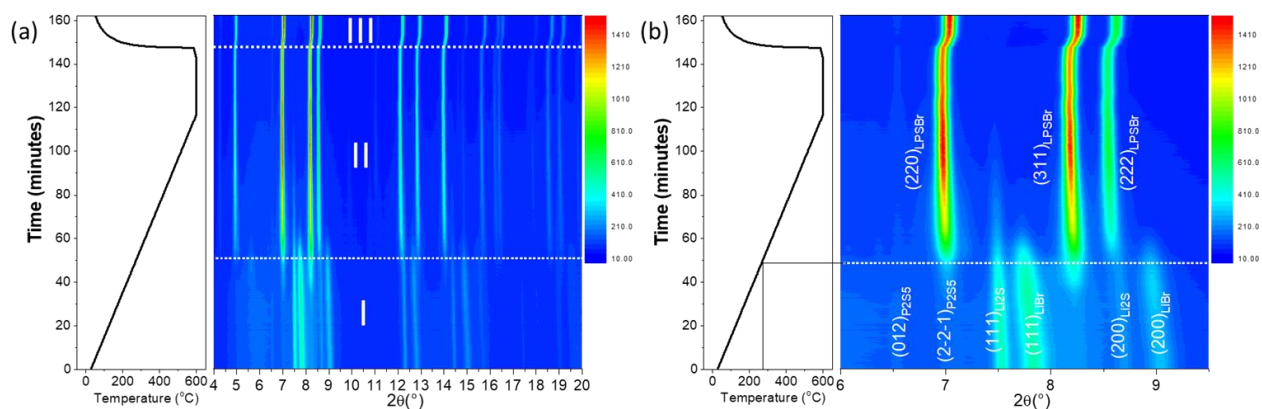


Figure 5. (a) Two-dimensional contour plot of *in situ* synchrotron X-ray diffraction patterns during formation of LPSBr. (b) Zoom-in view of 2θ range of $6.0\text{--}9.5^\circ$.

The team has performed another experiment by incorporation of oxygen doping ($\text{Li}_6\text{PS}_{4.8}\text{O}_{0.2}\text{Br}$) during *in situ* SXRDXRD experiment. The results are shown in Figure 7a. It generally follows a similar reaction process by converting Li_2S , LiBr , P_2S_5 , and Li_2O to form $\text{Li}_6\text{PS}_{4.8}\text{O}_{0.2}\text{Br}$. However, compared to the result for LPSBr without oxygen doping, the starting temperature for the evolution of (220) peak of LPSBr was postponed to around 300°C . Meanwhile, it can be clearly seen that even after heating to 550°C , there are still some peaks remaining, which are corresponding to Li_2S and LiBr , respectively. The results indicate that the incorporation of Li_2O will compete with Li_2S and LiBr for site occupancy during the formation of $\text{Li}_6\text{PS}_{4.8}\text{O}_{0.2}\text{Br}$. Even after heating at 550°C for 8 hours, the peaks of Li_2S and LiBr still remained. It is still not clear about the effect of residual Li_2S and LiBr on ionic conductivity and air stability, which will be explored next quarter.

In brief, using *in situ* SXRDXRD, the team can obtain the real-time phase transition during solid-state synthesis of LiPSBr electrolytes. This information has provided them with valuable guidelines to prepare LiPSBr SSEs with different structures. Meanwhile, they will analyze the microstructure changes (that is, lattice parameter and microstrain) by Rietveld refinement next quarter for further synthetic condition optimization. They will also explore the effect of different oxygen content and different bromine content by using *in situ* SXRDXRD to obtain the best composition. Based on these results, they will synthesize and evaluate the ionic conductivity and air stability of LiPSBr SSEs.

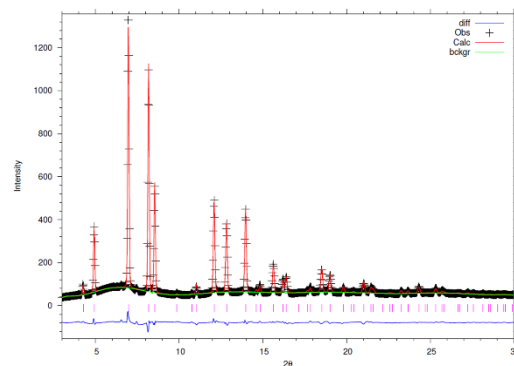


Figure 6. Rietveld refinement of *in situ* synchrotron X-ray diffraction pattern at 600°C .

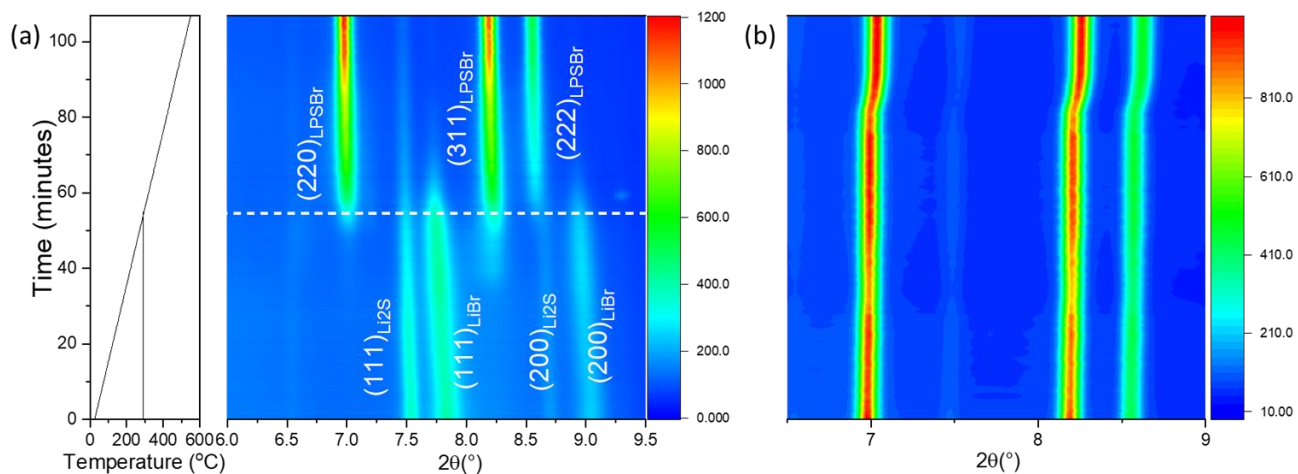


Figure 7. Two-dimensional contour plot of *in situ* synchrotron X-ray diffraction patterns during formation of O-doped LPSBr: (a) heating from room temperature to 550°C; and (b) 550°C holding for 8 hours followed by quenching.

Patents/Publications/Presentations

The project has no patents, publications, or presentations to report this quarter.

Task 1.3 – Thioborate Solid-State Electrolytes for Practical All-Solid-State Batteries (Yi Cui, Stanford University)

Project Objective. This project aims to develop novel lithium thioborates (lithium-boron-sulfur, LBS) as a new class of SSEs to realize high-performance all-solid-state batteries (ASSBs), with a particular focus on addressing the technical challenges in electrolyte synthesis, cell integration, failure diagnostics, and scale-up. The approach will be technologically transformative to the current solutions for ASSB development. For the final deliverables, ASSBs with the ability to reach an energy density of 500 Wh/kg and maintain 80% capacity for at least 300 cycles will be demonstrated.

Impact. The project approaches provide new directions toward developing high-conductivity and electrochemically stable sulfur-based electrolytes for ASSBs. Such high-performance electrolytes can enable the practical realization of ASSBs with a high energy density and improved safety.

Approach. The long-term project has a multi-step approach toward integration of LBS with high-voltage cathodes, with steps 1-3 as the focus for this year:

1. Fabricate undoped LBS powders using an all-solid-state synthesis method to achieve high ionic conductivity, low electronic conductivity, and a wide operational voltage window.
2. Integrate LBS SSEs into symmetric Li/LBS/Li cells and into full batteries using high-voltage cathodes including lithium Ni-Mn-Co (NMC) oxide.
3. Study atomic, particle, and cell-scale Li-metal-SSE interface development and dendrite growth mechanisms in SSEs using advanced characterization tools. Use knowledge to better develop SSEs and modify interfaces for stable cycling in full cells.
4. Fabricate doped LBS powders and develop particle/surface modifications to increase ionic conductivity as well as stability in full batteries and in air for glovebox-free synthesis.
5. Use density functional theory (DFT) to guide development of new doped LBS materials and to explore interactions at solid-solid interfaces.

Out-Year Goals. In the following year, the team will develop solid-state reaction methods to synthesize undoped LBS powders and construct Li/LBS/Li symmetric cells to test the electrochemical performance of synthesized LBS. Meanwhile, the team will utilize advanced characterization tools [for example, cryogenic electron microscopy (cryo-EM), X-ray computed tomography (CT), etc.] to resolve the nanostructure of Li/LBS interphase and investigate the electrochemical stability between LBS and lithium metal.

Collaborations. The Y. Cui group is collaborating with W. Chueh's group (advanced characterization) and E. Reed's group (crystal structure computation) at Stanford University as well as with Y. Liu (advanced characterization) at SLAC National Accelerator Laboratory (SLAC).

Milestones

1. Develop solid-state reaction methods to synthesize undoped LBS powders with high ionic conductivity. (Q1, FY 2022; Completed)
2. Construct Li/LBS/Li symmetric cells for electrochemical characterizations. (Q2, FY 2022; Completed)
3. Study the evolution of Li/LBS interphase. (Q3, FY 2022; In progress)
4. Resolve the nanostructure of Li/LBS interphase using advanced characterizations (for example, cryo-EM, CT, etc.). Achieve ionic conductivity of LBS SSE of $1.0 \times 10^{-3} \text{ S cm}^{-1}$. (Q4, FY 2022; In progress)

Progress Report

In a collaboration with the E. Reed group at Stanford University, the team discovered that the theoretical ionic conductivity of LBS SSEs can reach 74 mS cm^{-1} . Motivated by these calculations and by the possibility of discovering a new class of SSEs made from earth-abundant elements, they are working to develop LBS SSEs with high ionic conductivity and high stability for application in full batteries. First, they worked to synthesize high-purity $\text{Li}_{10}\text{B}_{10}\text{S}_{20}$ SSE (Figure 8). Now, they are working to synthesize high-purity $\text{Li}_{10}\text{B}_{10}\text{S}_{20}$, Li_3BS_3 , and $\text{Li}_2\text{B}_2\text{S}_5$ SSE. By altering the ratio of starting materials, high-temperature sintering procedure, and total length of sintering, the team has been able to synthesize mixed-phase $\text{Li}_3\text{BS}_3/\text{Li}_{10}\text{B}_{10}\text{S}_{20}$ and $\text{Li}_2\text{B}_2\text{S}_5/\text{Li}_{10}\text{B}_{10}\text{S}_{20}$ SSEs. Another important task of this project is to increase the yield of the reaction to grams scale. Using a new reactor setup, they have increased the quantity that can be produced in one reaction to > 10 grams. Once optimizations of the synthesis have been completed, they will select LBS candidates to study the electrochemistry and cyclability in batteries with Li-metal anodes.

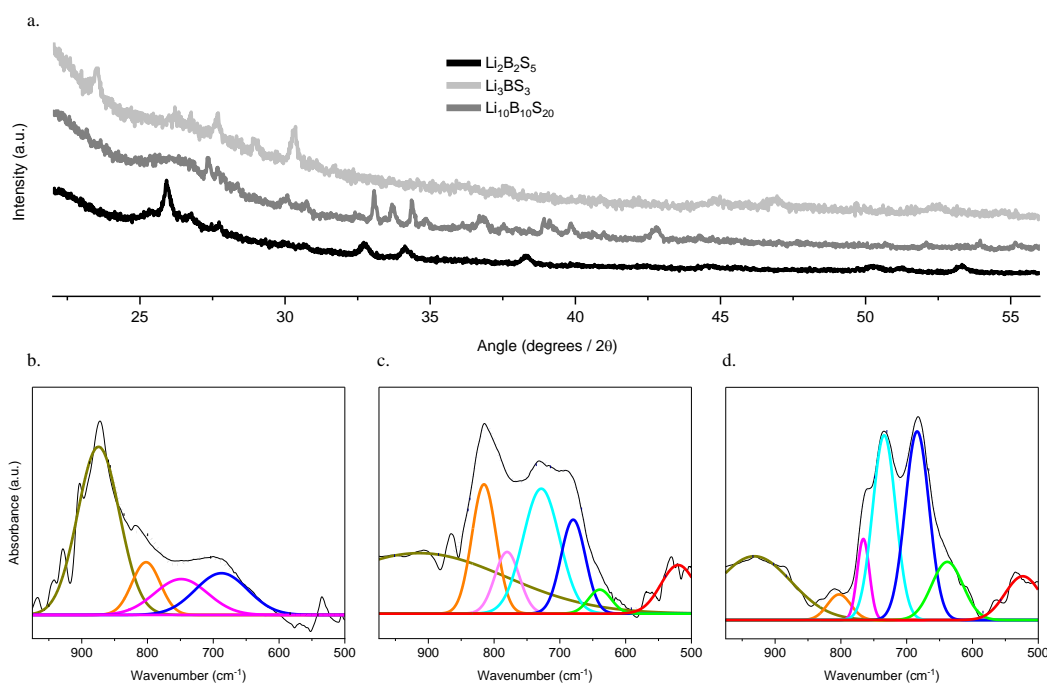


Figure 8. (a) Unique X-ray diffraction spectra of $\text{Li}_2\text{B}_2\text{S}_5$, Li_3BS_3 , and $\text{Li}_{10}\text{B}_{10}\text{S}_{20}$. Fourier transform infrared spectra of $\text{Li}_2\text{B}_2\text{S}_5$ (b), Li_3BS_3 (c), and $\text{Li}_{10}\text{B}_{10}\text{S}_{20}$ (d) in the B-S bonding range, showing symmetric and asymmetric B-S vibrations.

Patents/Publications/Presentations

The project has no patents, publications, or presentations to report this quarter.

Task 1.4 – Substituted Argyrodite Solid Electrolytes and High-Capacity Conversion Cathodes for All-Solid-State Batteries (Jagjit Nanda, Oak Ridge National Laboratory)

Project Objective. The project aims at synthesis and fabrication of Li-ion conducting argyrodite SEs with nominal composition $\text{Li}_6\text{PS}_5\text{X}$, where X = chlorine and/or bromine. The team will combine EIS with complementary *in situ* spectroscopy and microscopy to identify buried interfacial side-reaction products and quantify the voltage losses associated with these side reactions. Specifically, they plan to investigate the interfacial reaction between various $\text{Li}_6\text{PS}_5\text{X}$ SE and Li-ion cathodes belonging to different structural families [transition metal (TM)-based sulfides and fluorides (for example, FeS_2 and FeF_2) and high-voltage layered oxides (for example, $\text{LiNi}_{0.8}\text{Mn}_{0.1}\text{Co}_{0.1}\text{O}_2$, NMC-811)]. New dopants such as niobium and partial substitution of sulfur with oxygen will be explored to improve stability of argyrodite SEs against lithium metal and high-voltage cathodes.

Impact. The proposed work addresses key technical barriers to achieve Li-metal SSBs with energy densities of > 450 Wh/kg and 1,000 Wh/L, which are critical for next-generation EVs. Integrating new sulfide SEs prepared through scalable, low-cost solvent-mediated routes with high capacity, earth abundant conversion cathodes (for example, sulfur, FeF_3 , and FeS_2) will lower solid-state battery (SSB) cost to \$80/kWh and eliminate use of critical materials such as cobalt and nickel.

Approach. Scalable solution-based processing routes will be developed to produce freestanding sulfide/binder solid-state separators with thicknesses < 50 μm and area specific resistance (ASR) < 50 Ωcm^2 . These ultra-thin separators will be integrated with Li-metal anodes and high areal capacity conversion cathodes (for example, sulfur, FeS_2 , and FeF_3) to demonstrate lab-scale prototype SSBs. As a cross-cut activity, various *in situ* and *ex situ* passivation methods will be combined with enabling characterization techniques to facilitate Li^+ transport across electrode/SE interfaces.

Out-Year Goals. Optimize SSB performance by: (1) varying cathode composition, particle size, and porosity, (2) applying halide-rich and carbon layers at electrode/electrolyte interfaces, and (3) evaluating how stack pressure (0.1-10 MPa) and temperature (25-75°C) impact performance. Targets: room-temperature cycling with areal capacities > 5 mAh/cm², current densities > 2 mA/cm², stack pressures < 1 MPa, and $< 20\%$ capacity fade over 300 cycles.

Collaborations. D. Hallinan and his group are funded collaborators to develop the binder system for sulfide SEs and evaluate compatibility with cathode and Li-metal. P. Jena from Virginia Commonwealth University will be an unfunded collaborator on DFT modeling of bulk Li-ion transport and *ab initio* molecular dynamics (AIMD) at SE interfaces.

Milestones

1. Produce $\text{Li}_6\text{PS}_5\text{X}$ (X = Cl, Br, and/or I) SEs using solvent-mediated routes with ionic conductivity $\geq 1 \times 10^{-3}$ S/cm⁻¹ at room temperature. (Q1, FY 2022; Completed)
2. Optimize synthesis and annealing conditions to obtain phase-pure SE $\text{Li}_6\text{PS}_5\text{X}$ powders. Evaluate structure using XRD, Raman, and neutron scattering. (Q2, FY 2022; Completed)
3. Compare the structure and Li^+ conductivity of $\text{Li}_6\text{PS}_5\text{X}$ prepared through solvent-mediated versus mechano-chemical and solid-state routes. (Q3, FY 2022)
4. Integrate SSB using $\text{Li}_6\text{PS}_5\text{X}$ SE with a working cathode and thin Li-metal anode for testing and capacity optimization. (Q4, FY 2022)

Progress Report

Precursor mixing has a major impact on key properties (for example, phase purity, morphology, and ionic conductivity) of SEs synthesized through solid-state routes. Activities this quarter focused on solid-state synthesis of $\text{Li}_6\text{PS}_5\text{X}$ ($\text{X} = \text{Cl}, \text{Br}$) SEs where two precursor mixing strategies were explored. The first method involved hand grinding (HG) stoichiometric amounts of Li_2S , LiCl , and P_2S_5 in an agate mortar and pestle followed by pelletizing and heating at 550°C ($5^\circ\text{C}/\text{min}$) for 10 hours under flowing argon. To investigate the effect of higher energy mixing on the product's conductivity and purity, the team also used a planetary mill (PM) assisted route where precursors were blended with zirconia milling media for 1 hour at 100 RPM. After milling, the resulting mixtures were pelletized and annealed at the same conditions as the HG samples.

The ionic conductivity of the SEs was evaluated using EIS in a blocking cell configuration. As shown in Figure 9, all samples had ionic conductivities on the order of $1 \text{ mS}/\text{cm}$ at room temperature. The $\text{Li}_6\text{PS}_5\text{Cl}$ samples exhibited higher ionic conductivities across both the HG and PM samples. This trend is attributed to greater anion site disorder for the Cl-based sample, which facilitated Li^+ transport as reported previously.^[1] For a given composition, the ionic conductivity of the PM samples exhibited higher conductivity, presumably due to more intimate precursor mixing prior to annealing.

Raman spectroscopy and XRD were used to characterize the materials' bulk and local structures. Figure 10a shows a Raman spectrum of each sample highlighting the principal Raman band near 430 cm^{-1} , which is indexed to the ortho-thiophosphate unit PS_4^{3-} . This band was slightly blue shifted for the Cl-containing samples, suggesting that different halide substitutions influence P-S bond lengths. XRD patterns in Figure 10b show that all samples had the expected argyrodite peaks along with minor phase impurities, including LiCl and Li_2S . Sloping backgrounds near $2\theta = 30^\circ$ are due to Kapton tape, which was used to prevent air exposure during the measurements. Overall, these results demonstrate that HG and PM blending routes did not have a discernable impact on the materials' structure as determined by Raman and XRD. These findings suggest that the differences in ionic conductivity may be influenced by amorphous phases or other structural variations, which were not readily accessible by these techniques.

To better understand how local structure influences Li^+ conductivity of $\text{Li}_6\text{PS}_5\text{X}$ SEs, experiments next quarter will investigate changes in anion disorder and relative amounts of amorphous versus crystalline phases using nuclear magnetic resonance (NMR) spectroscopy and neutron total scattering. Follow-up work will also characterize the materials as separators and catholytes for Li-metal SSBs.

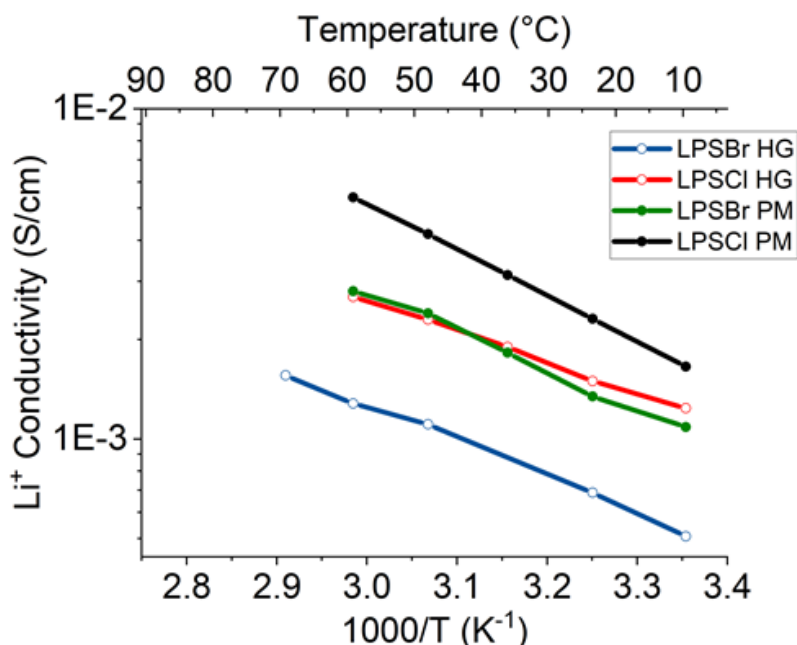


Figure 9. Li^+ conductivity measurements for $\text{Li}_6\text{PS}_5\text{X}$ ($\text{X} = \text{Cl}, \text{Br}$) prepared by hand grinding (HG) and planetary milling (PM).

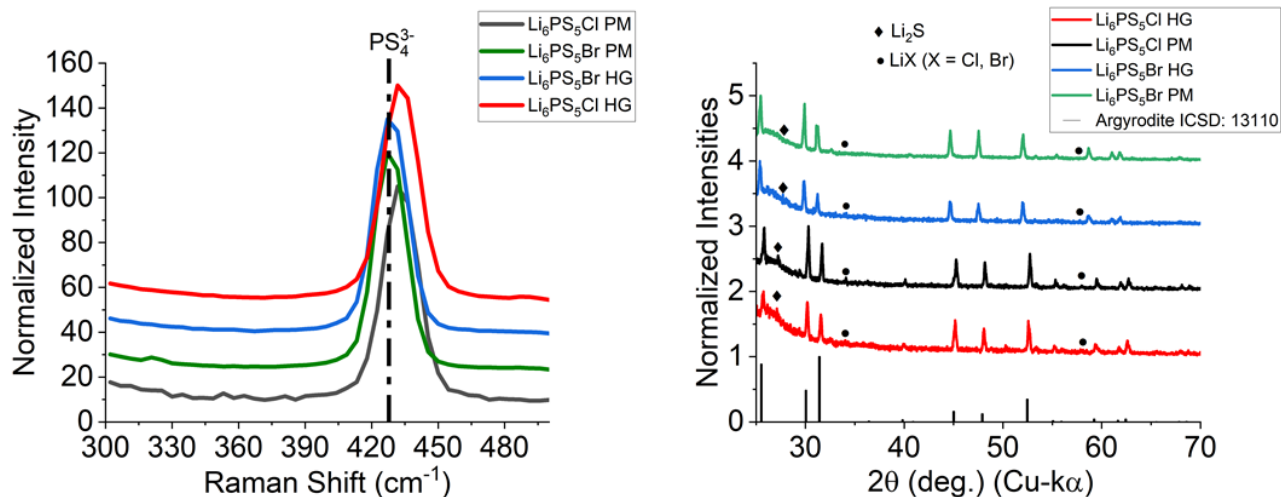


Figure 10. (a) Raman spectra and (b) powder X-ray diffraction patterns for Li₆PS₅X (X = Cl, Br) prepared by hand grinding (HG) and planetary milling (PM) methods.

Reference

- [1] Kraft, M. A., et al. "Influence of Lattice Polarizability on the Ionic Conductivity in the Lithium Superionic Argyrodites Li₆PS₅X (X = Cl, Br, I)." *Journal of the American Chemical Society* 139, no. 31 (2017): 10909–10918.

Patents/Publications/Presentations

Publication

- Feng, X., H. Fang, N. Wu, P. Liu, P. Jena, J. Nanda, and D. Mitlin. "Review of Structure and Interface Modification Strategies in Emerging Inorganic Solid-State Electrolytes (SSEs) for Lithium, Sodium, and Potassium Batteries." *Joule* 6 (2022): 543–587.

Task 1.5 – Stable Solid-State Electrolyte and Interface for High-Energy, All-Solid-State, Lithium-Sulfur Battery (Dongping Lu, Pacific Northwest National Laboratory)

Project Objective. The project objective is to address material and interfacial barriers of sulfide-based solid-state electrolyte (S-SSE) for deep cycling of Li-metal anode in all-solid-state lithium batteries (ASSLBs). All proposed work will be focused on development of highly conductive sulfide Li^+ conductors with extremely low Li/SSE interfacial resistance and ultra-thin multifunctional interlayer to enable deep and stable lithium cycling. The SEs and interlayer assembly achieved in the project will be tested at practical conditions and validated in realistic Li-S pouch cells.

Impact. ASSLBs have the potential to achieve higher energy and power densities, extending the range of EVs and reducing charging time simultaneously. The success of the project would advance the research and deployment of superionic SEs and protective Li-compatible interlayers to support the DOE Vehicle Technologies Office (VTO) target of developing next-generation ASSLBs for EVs, accelerating market acceptance of long-range EVs required by the EV Everywhere Grand Challenge.

Approach. The project proposes the following approach: (1) to develop Li-compatible superionic sulfide-based SSEs and effective coating approaches, (2) to stabilize Li/SSE interface by employing a multifunctional interlayer, (3) to enable robust Li^+/e^- mixed conduction network for a high-loading sulfur cathode, (4) to develop dry processing for SSE film, cathode, and interlayer fabrication, and (5) to advance the mechanism study of the sulfur cathode, lithium anode, and interfaces by multiscale characterization and multiscale modeling.

Out-Year Goals. This project has the following out-year goals:

- Development of Li-metal-compatible S-SSEs with Li/SSE interfacial resistance $< 5 \Omega\text{cm}^2$ and room-temperature Li^+ conductivity $> 5 \text{ mS/cm}$.
- Operation of lithium anode at CCD $> 1 \text{ mA/cm}^2$, and lithium cycling for at least 400 cycles.
- Ultra-thin multifunctional interlayer to enable deep lithium cycling $> 4 \text{ mAh/cm}^2$ to couple high areal-capacity cathode.
- Dry processing of an SSE/interlayer assembly with an overall ionic conductivity $> 1 \text{ mS/cm}$.
- Validation of the S-SSE, high-areal capacity cathode, and bilayer assembly in a realistic Li-S pouch cell.

Collaborations. This project engages in collaboration with the following: D. Y. Qu (University of Wisconsin, Madison, or UWM), Z. K. Liu (Pennsylvania State University, or PSU), C. M. Wang (Pacific Northwest National Laboratory, or PNNL), J. Bao (PNNL), H. Du (Ampcera Inc.), and Z. Liu (Thermo Fisher Scientific).

Milestones

1. Synthesis of lithium halides doped S-SSE to realize low Li/SSE areal interfacial resistance (AIR $< 5 \Omega\text{cm}^2$) and high room-temperature Li^+ conductivity ($\sigma \sim 6 \text{ mS/cm}$). (Q1, FY 2022; Completed)
2. Development of surface treatment approach to improve moisture stability of S-SSE. (Q2, FY 2022; Completed)
3. Optimization, characterization, and simulation of Li/SSE interface and its dynamics. (Q3, FY 2022; In progress)
4. Optimization of external pressure to improve CCD ($> 1 \text{ mA/cm}^2$) and Li/SSE/Li cycle life (> 400 cycles). (Q4, FY 2022)

Progress Report

S-SSEs have merits of low density, high ionic conductivity, and favorable mechanical properties compared to oxide ceramic and polymer materials. However, mass production and processing of S-SSEs remain an ongoing challenge due to their poor moisture stability. This quarter, the team developed a reversible surface coating strategy for enhancing the moisture stability of S-SSEs by using amphipathic organic molecules (AOMs). An ultra-thin amphipathic organic layer was coated on the S-SSE surface (for example, $\text{Li}_7\text{P}_2\text{S}_8\text{Br}_{0.5}\text{I}_{0.5}$, or LPSBI) via van der Waals forces, where the hydrophobic long-chain alkyl tail can repel water molecules. The weight gained after the process was measured at 0.97 wt%, indicating that a very thin layer of molecules was coated on the surface of LPSBI. Moreover, this amphipathic molecular layer has a negligible effect on ionic conductivity and can be removed reversibly by heating at low temperatures (for example, 160°C).

To investigate effects of AOM coating on moisture stability of LPSBI, the team monitored H_2S generation from LPSBI and LPSBI-AOM during dry-room exposure (relative humidity of 0.5%) for 120 minutes. As shown in Figure 11a, the concentration of H_2S gas released from the pristine LPSBI increases to 8.9 ppm at 120 minutes. In sharp contrast, the concentration of H_2S gas is as low as 1.6 ppm for LPSBI-AOM during the 120-minute exposure, which is 82% less than the amount from pristine LPSBI. When comparing the accumulated H_2S in the first 40 minutes, (a typical processing time for electrodes or solid separators in mass production), the H_2S concentration is below the detection limit. This indicates that the AOM coating almost completely shuts down the reactions between LPSBI and H_2O and dramatically enhances the moisture stability of LPSBI. Figure 11b compares the EIS of LPSBI before and after exposure to air with relative humidity of 0.5%, which is analyzed by fitting the spectra to an equivalent electrical circuit, composed of a constant phase element in parallel with an Ohmic resistance (R), representing the impedance of Li-ion transport through the bulk/grain and grain boundary (GB), and a Warburg impedance (W_o), representing impedance contributions from the electrode. On exposure, a semicircle is detected in the EIS of LPSBI-0.5%, corresponding to an overall impedance due mainly to the reactions between LPSBI and H_2O . The calculated ionic conductivity of LPSBI-0.5% is 0.8 mS cm^{-1} , an 85% drop compared with that of the pristine LPSBI before exposure (5.3 mS cm^{-1}). In contrast, the calculated ionic conductivity for LPSBI-AOM-0.5% is 2.5 mS cm^{-1} , which is three times higher than that for LPSBI-0.5%. The powder XRD patterns of the exposed LPSBI with/without AOM are presented in Figure 11c. Compared to the pristine LPSBI, additional peaks are observed in both LPSBI-0.5% and LPSBI-AOM-0.5%, some of which are

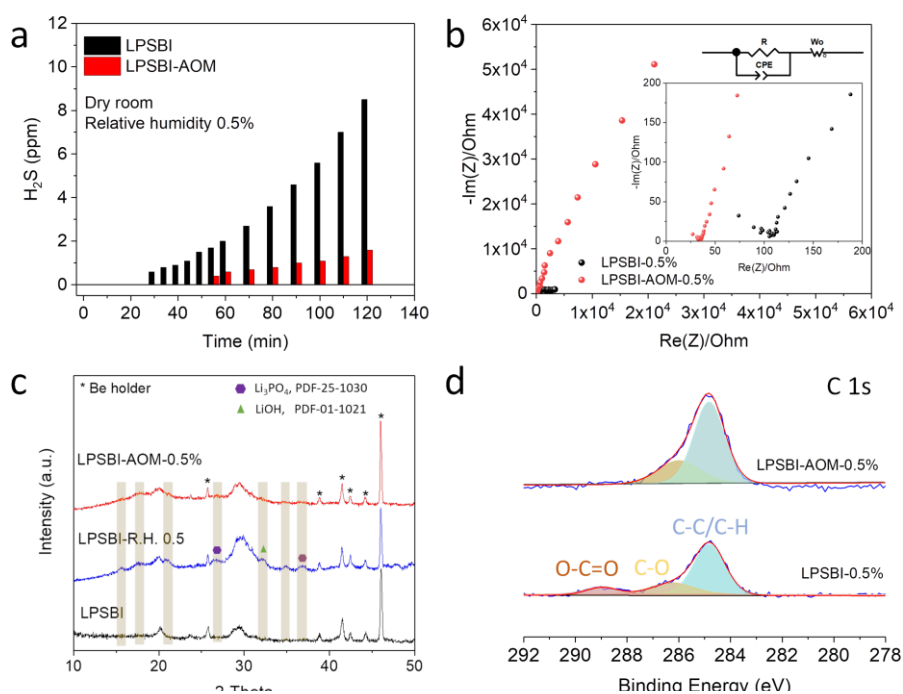


Figure 11. (a) Formation of H_2S . (b) Electrochemical impedance spectra. (c) X-ray diffraction patterns. (d) High-resolution carbon 1s spectra of $\text{Li}_7\text{P}_2\text{S}_8\text{Br}_{0.5}\text{I}_{0.5}$ powders with/without amphipathic organic molecules (AOM) coating exposed to air with relative humidity of 0.5% in a dry room.

indexed to Li_3PO_4 and LiOH , indicating reactions between sulfide samples and moisture. In addition, these peaks appear to be much sharper in the LPSBI-0.5% sample, especially for the peaks corresponding to Li_3PO_4 and LiOH , suggesting more severe reactions between LPSBI and moisture, which corresponds with the observations of H_2S formation. To study details of the surfaces of these samples before and after exposure, XPS measurements were conducted on LPSBI-0.5% and LPSBI-AOM-0.5% powders. Figure 11d shows the high-resolution carbon 1s spectra of these powders. In comparison to LPSBI-AOM-0.5% XPS results, a peak centered at ~ 288.8 eV, corresponding to $\text{O-C}=\text{O}$, is detected in LPSBI-0.5%, indicating that carbonate species could be the products of the reactions between LPSBI and $\text{H}_2\text{O}/\text{CO}_2$ in air.

Patents/Publications/Presentations

Patent

- Yu, Z., D. Lu, J. Xiao, and J. Liu. “Air-Stable Solid-State Electrolyte.” U. S. Application No. 17/507,432.

Task 1.6 – Development of Thin, Robust, Lithium-Impenetrable, High-Conductivity, Electrochemically Stable, Scalable, and Low-Cost Glassy Solid Electrolytes for Solid-State Lithium Batteries (Steve Martin, Iowa State University of Science and Technology)

Project Objective. The project objective is to develop new Li⁺-conducting mixed oxy-sulfide nitride (MOSN) glassy solid electrolytes (GSEs) that are impermeable to lithium dendrites, have high conductivities, are scalable through low-cost glass manufacturing, are chemically and electrochemically stable, and will enable low-cost, high-energy-density solid-state lithium batteries (SSLBs). The SSLBs constructed from these new GSEs will meet and exceed all program objectives: usable specific energy @ C/3 \geq 350 Wh/kg, calendar life of 15 years, cycle life (C/3 deep discharge with < 20% energy fade) of 1000, and cost \leq \$100/kWh.

Project Impact. This project will enable the team to demonstrate the following: (1) thin MOSN GSE films yield superior performance in a much safer, lower-cost, and Li-dendrite impenetrable form, and (2) high rate and long cycle life can be achieved in SSLBs using thin-film MOSN GSEs. The new GSEs in SSLBs are anticipated to increase energy density (anode basis) from \sim 300 mAh/g to \sim 4,000 mAh/g, enabling replacement of internal combustion engines in both light-duty and heavy-duty vehicles. Each 20% reduction in the \sim 1.6 billion l of gasoline used per day in the United States would reduce CO₂ emissions by \sim 4 billion kg or 2×10^{12} l of CO₂ per day. The team will also increase scientific and engineering knowledge of thin-film GSEs in SSLBs.

Approach. The MOSN mixed glass former (MGF) glasses used for the GSEs in this project were developed in previous work to have the necessary thermal stability and high ionic conductivity for successful use as a drawn-film electrolyte. In this project, the glass chemistry will be tuned for even more desirable properties, by investigating structure-property relationships and testing variations in glass chemistry.

Out-Year Goals. Work will progress toward developing a glass capable of being drawn to 100- μ m thickness, while having high conductivity and electrochemical stability and good cycling ability.

Collaborations. The team is collaborating with S. Kalnaus and G. Veith (Oak Ridge National Laboratory, ORNL) on the physical and mechanical properties of oxy-nitride glasses and with Y. Cui (Stanford University) and A. Sendek (Avionics) on new classes of polycrystalline lithium thioborate SE. The team is also collaborating with General Motors (GM; Tom Versak) on testing of the GSEs in their solid-state cells.

Milestones

1. Accomplish: Large MOSN MGF GSE preforms (10 cm \times 0.5 cm \times 30 cm) demonstrate < 1 vol% crystallization at 90°C above the glass transition temperature (T_g). (Q1, FY 2022; Completed)
2. Accomplish: Optimize draw conditions for MOSN GSE to achieve 5 m \times 5 cm \times < 50 μ m thin films. (Q2, FY 2022; In progress)
3. Accomplish: Fabricate MOSN MGF Li|GSE|Li cells in intermediate area format, \sim 2 cm². (Q3, FY 2022; In progress)
4. *Go/No-Go Decision*: Fabricate MOSN MGF GSE cells in large format \sim 5 cm². Cells achieve targeted performance metrics. Analysis indicates technical approach capable of achieving performance targets. (Q4, FY 2022; In progress)

Progress Report

Development of Optimized High Li⁺ Conductivity MOSN MGF GSEs

Initiate Development of Preforms of MOSN MGF GSEs That Do Not Crystallize

To optimize the Iowa State University (ISU)-6 (the team’s current best-performing GSE) preform, it was important to test the quality of the small-scale batches (~ 5-15 g) that would be used to synthesis the large batch (~ 150 g). These small-scale batches were tested using Raman spectroscopy and differential scanning calorimetry (DSC). Figure 12 displays the Raman spectra of two separate (~ 10 g) batches of the project’s ISU-6 GSE. The blue curve represents an example of a “good” ISU-6 glass, and the red curve represents an example of a “bad” ISU-6 glass. The common feature in both glasses is the presence of a vibrational mode due to the symmetric stretch of the PS₄³⁻ short range order (SRO) structure at ~ 420 cm⁻¹. However, the red spectrum of the “bad” ISU-6 GSE shows the presence of a shoulder to the left of the main peak at ~ 390 cm⁻¹, which corresponds to the impurity P₂S₆⁴⁻. This species is a defect structure that may lead to a decrease in the Li⁺ ion conductivity and an increase in crystallization tendencies of these glasses on drawing. The criteria then follow that ISU-6 glasses, whose Raman spectra do not show the presence of this defect structure, would be used in scale-up synthesis.

However, further compositional exploration has slowed in the team’s research lab due to glass quality issues. There has been a significant amount of carbon contamination in these glasses, and work is being done to reduce contamination to bolster future efforts to synthesize them. It seems that the glovebox atmosphere has changed and led to an increase in carbon in the glasses synthesized. The team is searching for the source, and they are testing different solutions to continue compositional development.

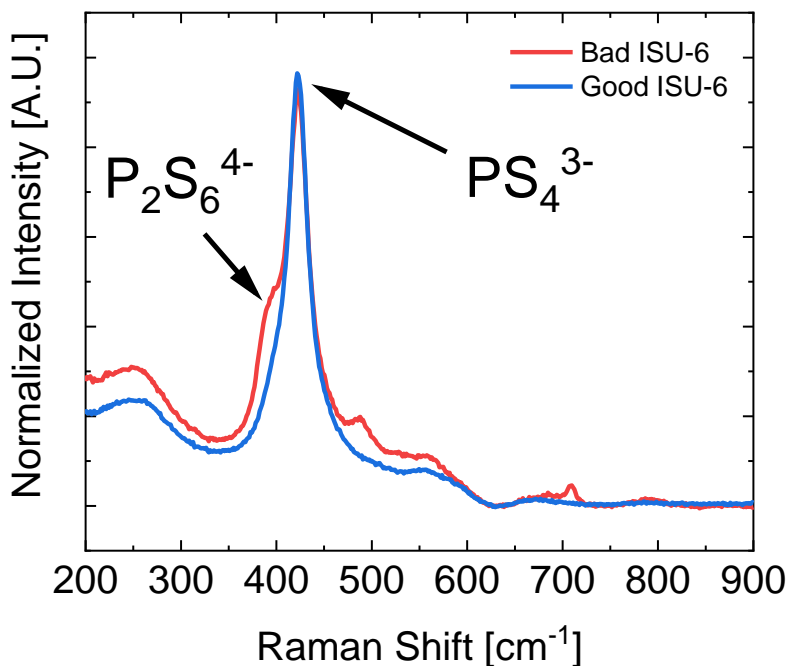


Figure 12. Raman spectra of ISU-6 glasses. The blue spectrum corresponds to “good” quality glasses that would be used in scale-up synthesis, and the red spectrum corresponds to “bad” quality glasses that would contain defect structures that would be excluded from scale-up synthesis.

Develop Micro-Sheet Glass Ribbon Processing Facility for GSEs

Continue to Develop and Optimize GSE Micro-Sheet Glass Ribbon Processing Facility

The micro-sheet glass ribbon processing facility has previously been optimized for drawing high-quality thin films of various GSE compositions. Work is now being done to convert the working gas used inside the glovebox containing the draw tower from nitrogen to argon to prevent surface contamination of the GSEs when the glass is transferred to a second glovebox for fabrication of thin-film cells. Furthermore, it was determined that tightening the screws on the baffles at the top of the thin-film drawing furnace on the draw tower helped to smooth out the left-to-right temperature difference across the furnace from $\sim 25^{\circ}\text{C}$ to $\sim 5^{\circ}\text{C}$. Such temperature gradients inside the furnace used to heat the glass preform to draw it into thin films have been shown in the team's work to produce poor quality glass with nonuniform thickness across the drawn thin ribbon.

Develop Processing Conditions for Micro-Sheet Ribbons of MOSN MGF GSEs

Complete Optimization of Draw Conditions for Optimized MOSN MGF GSEs < 50 μm

Several high-quality, small-scale batches of ISU-6 glass, characterized as described above by Raman spectroscopy, were synthesized and combined into a single melt to create one high-quality GSE preform (~ 150 g). Each small-scale batch (5-15 g) was tested through DSC and Raman spectroscopy to determine the consistencies of the GSE batches. Only batches that match the nominal ISU-6 Tg and glass crystallization temperature (Tc), and the Raman spectra, were used. An image of the new ISU-6 preform is shown in Figure 13. A small sample of the preform was broken off and tested in the DSC, and the Tg and Tc matched the expected values.



Figure 13. ISU-6 preform made using new high-quality small-scale synthesis route.

The new preform was loaded into the custom-built draw tower and was heated slowly to just above the Tg, and film drawing was attempted. Previous attempts on ISU-6 GSE preforms of noticeably poorer quality than this most current one experienced crystallization during this process. This new high-quality preform was able to be drawn into a thin-film, and several sections of this film were collected to be tested further. Images of the film being drawn (left) and some of the collected pieces of film (right) are shown in Figure 14. Analysis indicates that this film reached about $150\ \mu\text{m}$ in thickness, and it is believed that increasing the drawing temperature by a few degrees and drawing slightly faster will allow for further thickness reduction while retaining a film width of 3-5 cm and uniformity of the film thickness across the ribbon. The extra/leftover glass from the preform was collected and will be remelted, recast, and then drawn again. This is an incredible advantage to glass processing of SE films. The leftover glass can be easily remelted and reused to make new films. Indeed, the team is finding, as is commonplace in traditional glass melting and forming operations, that the use of this leftover glass,

called cullet, actually improves the quality of the glass preform and ultimately also improves the quality of the glass film being made. It is commonplace to add in ~ 20-30 wt% of recycled glass cullet to make new glass, and the team is seeing the benefits of recycling their GSEs here as well.



Figure 14. ISU-6 thin-film that has been drawn and collected for further testing.

Fabricate and Test ASSLBs using GSEs in Large Area Planar Formats

Complete Testing of Optimized MOSN MGF GSE in Intermediate-Cell-Format and Large-Cell-Format ASSLBs

To test the full-cell performance of MOSN MGF GSE cells, a solid-state cathode composite first needs to be developed. A solid-state cathode composite is comprised of the cathode active material (CAM), an ionic conductor, an electronic conductor, and typically an organic binder to give the compact mechanical strength during processing. The materials selected for cathode composite synthesis are lithium iron phosphate (LiFePO_4) as the CAM, ISU-6 GSE as the lithium-ion conductor (LIC), and carbon as an electronic conductor. It is important to have both good ionic and electronic conductivity throughout the cathode composite so that lithium ions and electrons can flow through the entire volume of the cathode composite. As such, the morphology of the powder mixture can have a significant impact on the overall performance of the cathode. A study was conducted based on a paper, published by S. Noh, which investigated the effect of different mixing methods on performance of the cathode composite.^[1] Solid-state cathode composites were synthesized using the mixing methods shown in Figure 15 in a planetary ball mill.

Each cathode composite was synthesized with 79 wt% LiFePO_4 , 19 wt% ISU-6, and 2 wt% carbon. After synthesizing these four cathode composites, pellets were pressed for EIS testing to determine the ionic conductivity. The Nyquist plots were fitted using an equivalent circuit consisting of a resistor and constant phase element in series. As shown in the Arrhenius plots in Figure 16, mixing Method 4 exhibited a higher conductivity than the other methods.

Once the best mixing method for optimization of ionic conductivity was identified, the effects of mixing time and carbon morphology were also investigated. It was found the carbon nanotubes (CNTs) mixed for a short amount of time (30 minutes) produced the highest conductivity cathode composite, as shown in Figure 17a-b.

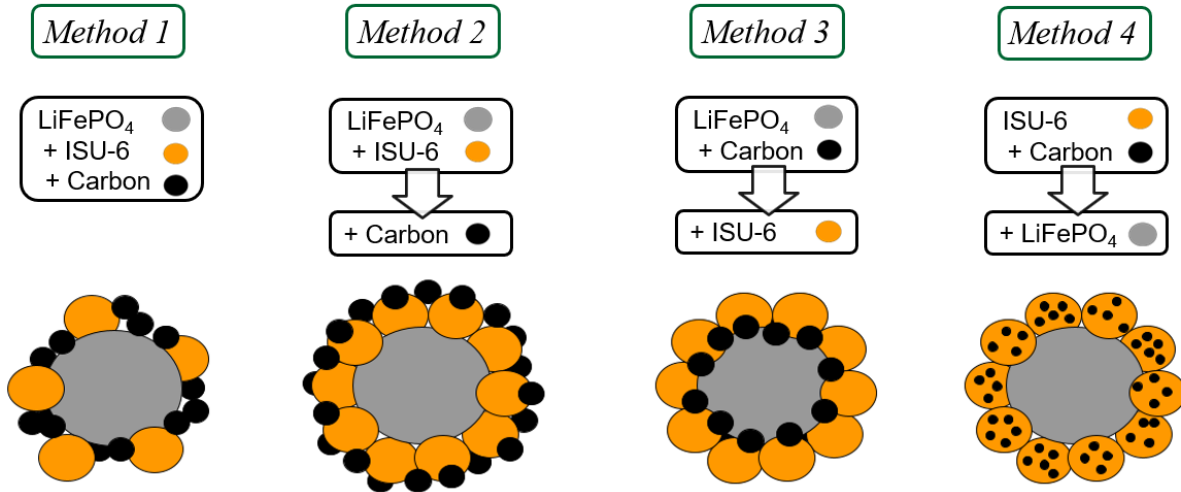


Figure 15. Solid-state cathode composite mixing methods. Method 1 is a simple single-step mixing, while methods 2-4 are two-step mixing methods, where two materials are mixed first and the final material is mixed in the second step. Schematics of the likely microstructure resulting are shown below each method's steps.

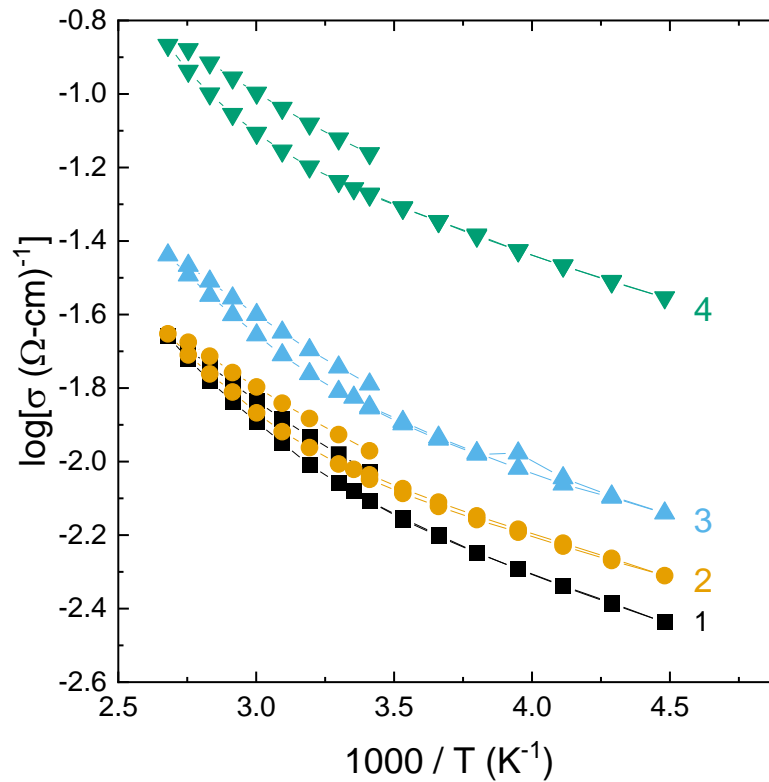


Figure 16. Temperature-dependent conductivities of solid-state cathode composites synthesized through Methods 1-4 described in Figure 15.

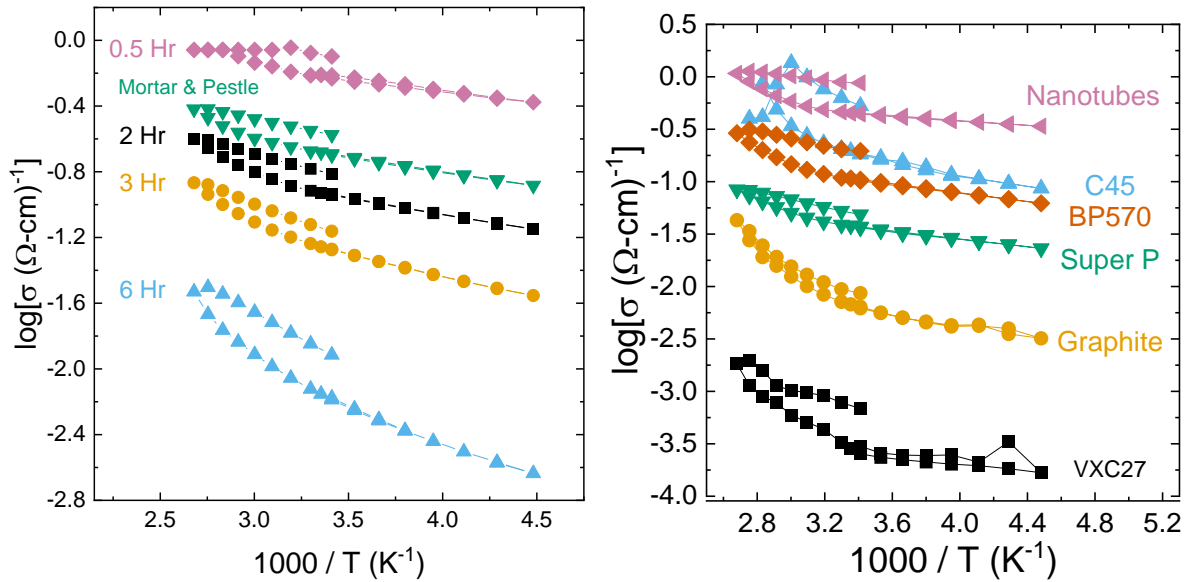


Figure 17. (a) Temperature-dependent conductivity of cathode composites milled for different lengths of time. (b) Temperature-dependent electronic conductivities of cathode composites synthesized with different carbon morphologies.

Based on these results, mixing Method 4 with CNTs and a 30-minute mixing time has been chosen as the optimized cathode composite synthesis method that will be used going forward with the LiFePO_4 cathode. In assembling full cells, cathode composite powder is mixed into a solution of styrene-butadiene rubber (SBR) dissolved in m-xylene to form a slurry. The SBR acts as a binder, holding the dry cathode together after the xylene evaporates. In moving toward intermediate-cell-format ASSLBs, a THINKY ARM-310 Mixer was purchased. This mixer enables the production of larger batches of slurries and allows for the synthesis of more viscous and homogenous slurries than a stir bar can achieve. These slurries were then tape cast onto aluminum foil where they were punched out to accommodate small-sized and intermediate-sized cells. A tape-cast cathode electrode is shown in Figure 18.

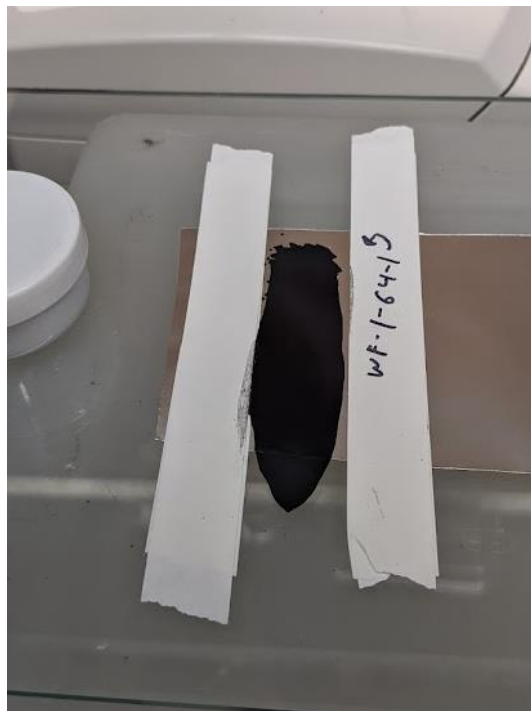


Figure 18. Tape-cast solid-state cathode utilizing the glassy solid electrolyte and LiFePO_4 composite cathode developed.

In addition to the team's work to develop cathodes based on traditional, but low-capacity LiFePO_4 active materials, they are also developing a new cathode material using a method similar to that used by F. Wu et al.^[2] This C-S nanocomposite was synthesized using a precipitation process of Li_2S and polyvinylpyrrolidone (PVP) dissolved in ethanol in an argon glovebox. The PVP was pyrolyzed to carbon in a quartz ampoule under a low vacuum backfilled with nitrogen to produce micron-sized particles of nanocrystalline Li_2S covered with carbon in a core-shell microstructure. XRD analysis, Figure 19a, of this synthesized powder showed a diffractogram nearly identical to that of the literature. Energy-dispersive X-ray spectroscopy (EDS) mapping in Figure 19b shows a powder with uniformly distributed sulfur and carbon signals, with minimal contaminants. No lithium signal is shown due to the low atomic mass of lithium. Work is under way to make cathode composites using this synthesized active material, GSE, and binder.

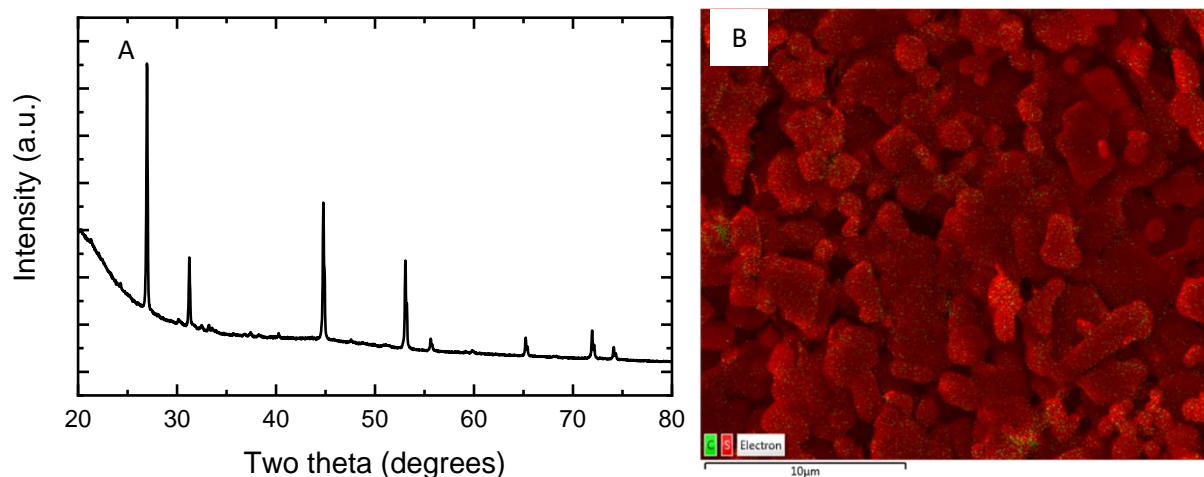


Figure 19. (a) X-ray diffractogram of Li_2S -C nanocomposite powder showing peaks that match the literature diffractogram. (b) Energy-dispersive X-ray spectroscopy map of the synthesized Li_2S -C powder showing homogenous mixing of the carbon and sulfur signal.

References

- [1] Noh, S., W. T. Nichols, M. Cho, and D. Shin. "Importance of Mixing Protocol for Enhanced Performance of Composite Cathodes in All-Solid-State Batteries using Sulfide Solid Electrolyte." *Journal of Electroceramics* 40, no. 4 (2018): 293–299.
- [2] Wu, F., H. Kim, A. Magasinski, J. T. Lee, H-T. Lin, and G. Yushin. "Harnessing Steric Separation of Freshly Nucleated Li_2S Nanoparticles for Bottom-Up Assembly of High-Performance Cathodes for Lithium-Sulfur and Lithium-Ion Batteries." *Advanced Energy Materials* 4, no. 11 (2014): 1400196.

Patents/Publications/Presentations

The project has no patents, publications, or presentations to report this quarter.

Task 1.7 – All-Solid-State Batteries Enabled by Multifunctional Electrolyte Materials (Pu Zhang, Solid Power Inc.)

Project Objective. The project objective is to develop Li-metal SSBs enabled by multifunctional SSEs for EV application. The ultimate goal is scalable production of large-format ASSBs able to deliver ≥ 350 Wh/kg specific energy, ≥ 1000 cycle life, and $\leq \$100/\text{kWh}$ cost.

Project Impact. The project is enabling scalable production of large-format ASSBs required by the vehicle market and is building domestic battery manufacturers as leaders in the global vehicle ASSB production. The proposed technology will address key limitations of state-of-the-art lithium batteries to meet DOE EV battery targets and accelerate their adoption as large-format EV batteries for sustainable transportation technology.

Approach. The project will develop a high-performance Li-metal solid-state cell enabled by a multifunctional SSE. The new SSE will (1) have high conductivity (up to 10 mS/cm), (2) be stable against lithium metal and high-voltage cathodes (0-4.5 V), (3) promote uniform lithium plating (enabling $> 2\text{C}$ charge rate), and (4) be compatible with large-scale manufacturing processes. The specific cell chemistry to be demonstrated will be the SSE with Li-metal anode and high-nickel-content Li-metal oxide cathode. The solid-state cell will be assembled by scalable roll-to-roll processes developed by Solid Power.

Out-Year Goals. In Year 1, a multifunctional SSE will be developed with lithium ionic conductivity of $\geq 3 \times 10^{-3} \text{ S/cm}$. A CCD of $\geq 6 \text{ mA/cm}^2$ will be achieved in a symmetric lithium cell. The SSE design concept will be proven by demonstrating a cycle life of ≥ 200 in a full cell. In Year 2, a SSE material will be optimized with lithium ionic conductivity of $\geq 5 \times 10^{-3} \text{ S/cm}$. Scalable cell assembly processes will be developed. A cycle life of ≥ 500 will be demonstrated in a full cell. In Year 3, large-format solid-state cells ($> 2\text{Ah}$) will be assembled/tested to meet the final goal: $\geq 350 \text{ Wh/kg}$, ≥ 1000 cycles, and $\leq \$100/\text{kWh}$ cost.

Collaborations. The proposed team consists of Solid Power and a subcontractor, University of California, San Diego (UCSD). Solid Power (Principal Investigator, or PI: P. Zhang) will develop the multifunctional SSE and other cell components, assemble cells, and conduct cell tests. UCSD (PI: Y. S. Meng) will carry out material characterization by using advanced techniques such as XPS, cryogenic – scanning transmission electron microscopy (cryo-STEM) imaging, cryo-STEM EDS, electron energy loss spectroscopy (EELS), and cryogenic – focused ion beam (cryo-FIB) milling. The UCSD team seeks to quantify the kinetics and evolution of each contributing factor and its impact on battery performance.

Milestones

1. Charge rate $\geq 2\text{C}$. (Q1, FY 2022; Completed)
2. SSE film $\geq 10 \text{ m}$ and $\leq 40 \text{ }\mu\text{m}$. (Q2, FY 2022; Completed)
3. Pouch cell $\geq 2 \text{ Ah}$. (Q3, FY 2022; In progress)
4. Cycle life ≥ 1000 . (Q4, FY 2022; In progress)

Progress Report

SSE Separator Fabrication

The SSE separator coating process has been developed at pilot scale. A separator slurry was prepared by mixing the SSE powder, a binder, and a solvent using a planetary mixer. The slurry was then cast on a carrier film on a slot-die coater. The separator length and thickness target (≥ 10 m and ≤ 40 μm) was demonstrated last quarter. Figure 20 shows a separator film of 25 μm under SEM. The separator film has been assembled into a full cell for testing. The team will report the performance data next quarter.

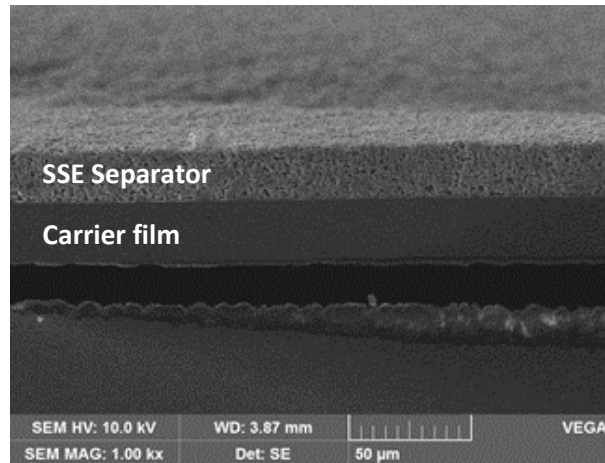


Figure 20. Cross-section images of a slurry-cast solid-state electrolyte separator film < 40 μm .

Full-Cell Cycle Life Demonstration

The team continued evaluation cycle life of the electrolyte in a lab-scale lithium – nickel manganese cobalt oxide (Li-NMC) pouch cell to meet the final project goal > 1000 cycles. When tested at 2.8-4.2 V, C/5 – C/5, and 45°C, the pouch cell showed 88% capacity retention after 700 cycles (Figure 21). A cycle life of > 1000 is projected based on the trend.

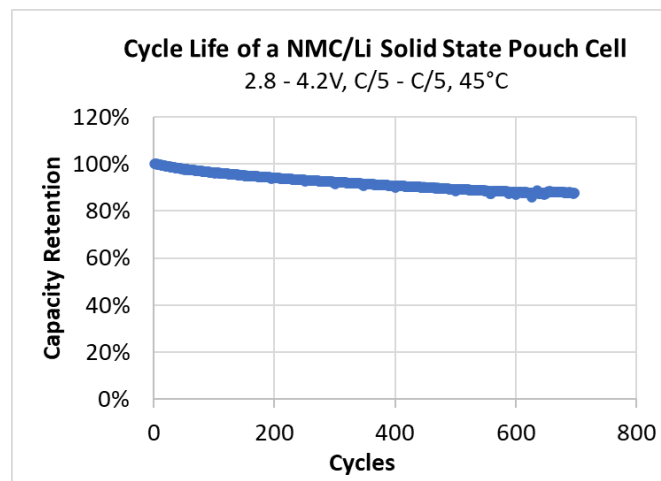


Figure 21. Cycle life of an NMC/Li-metal solid-state pouch cell with the multifunctional solid-state electrolyte at 45°C.

Large-Format 2-Ah Pouch-Cell Assembly

NMC cathodes and SSE separators have been coated by using a slot-die coater. Multilayer cell stacks including lithium anode, separator, and NMC cathode layers were fabricated by using a roll-to-roll process. Large-format 2-Ah pouch cells were assembled by tabbing and sealing the multilayer cell stacks in pouches. Figure 22 shows the initial batch of pouch cells. Cell testing will begin next quarter.



Figure 22. All-solid-state 2-Ah Li-NMC pouch cells.

Patents/Publications/Presentations

The project has no patents, publications, or presentations to report this quarter.

Task 1.8 – Developing Materials for High-Energy-Density Solid-State Lithium-Sulfur Batteries (Donghai Wang, Pennsylvania State University)

Project Objective. The project objectives are to develop materials involving advanced S-C composite materials, solid additives, and sulfide-based SSEs and also to acquire knowledge for ASSLSBs. These batteries—with large areal sulfur loading ($\geq 5 \text{ mg cm}^{-2}$) and high sulfur content ($\geq 50 \text{ wt\%}$ in cathode), and paired with lithium or Li-alloy anode—will deliver a high initial specific capacity $> 1200 \text{ mAh g}^{-1}$ at high charge/discharge rate ($> 0.3 \text{ C}$) for 500 cycles with over 80% capacity retention.

Project Impact. This project aims to develop new materials to enable ASSLSBs with high energy density, excellent cycling stability, and good rate performance, and thus to build knowledge for fabrication of prototype ASSLSBs. Specifically, the developed new materials will greatly increase the specific capacity of sulfur and sulfur utilization at high areal sulfur loading, alleviate the interfacial problem between S-C composite and SSE within sulfur cathode, boost Li-ion conductivity, and improve moisture stability of glass and glass-ceramic sulfide-based SSE. Meeting the technical targets will potentially promote development of high-energy-density ASSLSBs and their practical application in EVs and plug-in hybrid EVs (PHEVs) and will also reduce petroleum consumption in the transportation sector by helping battery-powered vehicles become more accepted by consumers as a reliable source of transportation.

Approach. The project goal will be accomplished through developing new materials, together with in-depth characterization of sulfur cathodes. Specifically, approaches to realize the project objectives include the following: (1) development of new carbon material with unique structure, high surface area, and large pore volume; (2) development of new S-C and S-C- M_xS_y materials ($\text{M} = \text{Li, Co, Ti, Mo, etc.}$) to facilitate electron/ion transport; (3) development of novel additives to tune interfacial behavior among components in the cathode; (4) development and optimization of new SSE through cation and anion doping with superior properties such as high ionic conductivity, good moisture, and stability; and (5) diagnostics, characterization, and cell tests on the developed new material or advanced sulfur cathode.

Out-Year Goals. The out-year goals are as follows: (1) develop and optimize sulfur cathode materials and synthesize new SEs (ionic conductivity $> 5 \text{ mS cm}^{-1}$ at room temperature), and (2) conduct characterization and performance tests on both material and electrode levels. The final demonstration will be all-solid-state sulfur cathodes with $> 1200 \text{ mAh g}^{-1}$ discharge capacity at 0.3 C discharge rate and 50 wt\% sulfur content for 500 cycles at room temperature.

Collaborations. There are no active collaborations.

Milestones

1. Demonstrate sulfur cathode with high areal sulfur loading ($\geq 5 \text{ mg cm}^{-2}$) and 50 wt\% sulfur content over 1000 mAh g^{-1} discharge capacity at 0.1 C rate at 25°C for 10 cycles. (Q1, FY 2022; In progress)
2. Demonstrate new SE with ionic conductivity $> 3 \text{ mS cm}^{-1}$ at 25°C . (Q2, FY 2022; Completed)
3. Demonstrate sulfur cathode with high areal sulfur loading ($\geq 5 \text{ mg cm}^{-2}$) and above 50 wt\% sulfur content over 1000 mAh g^{-1} discharge capacity at 0.3 C rate at 25°C for 50 cycles. (Q3, FY 2022; In progress)
4. Demonstrate sulfur cathode with high sulfur content ($> 50 \text{ wt\%}$) and over 1200 mAh g^{-1} at 0.3 C rate for 500 cycles ($< 20\%$ capacity decay) at room temperature, and new SEs with ionic conductivity $> 5 \text{ mS cm}^{-1}$ at 25°C . (Q4, FY 2022; In progress)

Progress Report

New SE Development

This quarter, the team worked on developing new thiophosphate SE with high ionic conductivity for ASSLSBs. Based on experience accumulated from previous years, they developed a new thiophosphate SE (SE-1). The synthesis procedures were optimized, such as synthesis temperature and chemical compositions. The newly developed SE-1 possesses a high ionic conductivity of 4.01 mS cm^{-1} at room temperature with a low activation energy of 0.212 eV . Figure 23 shows the Arrhenius and Nyquist plots of SE-1 at different temperatures (25°C to 100°C). The result of high room-temperature ionic conductivity meets this quarter's milestone. Next quarter, they will try to further optimize the synthesis procedures to obtain SE with even higher room-temperature ionic conductivity.

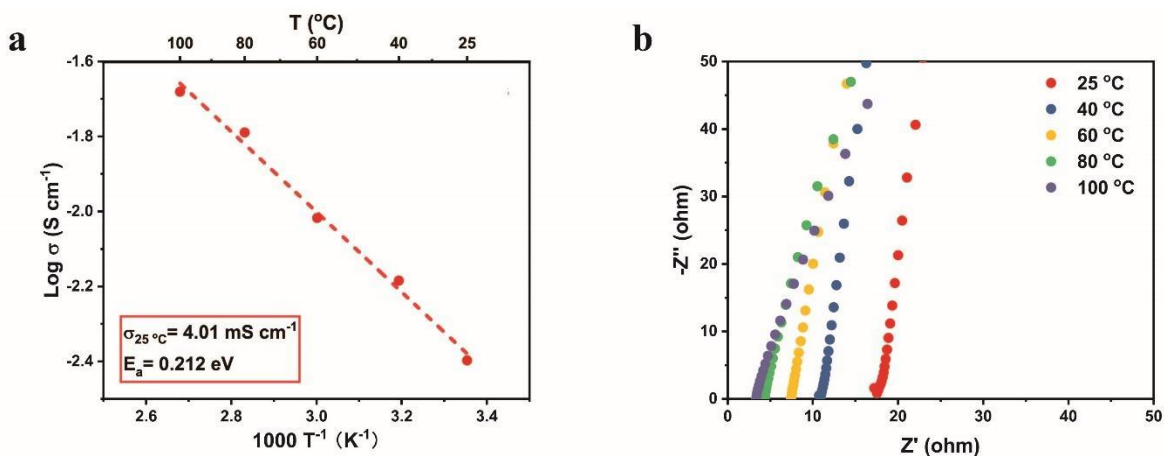


Figure 23. The (a) Arrhenius and (b) Nyquist plots of SE-1 solid electrolyte at different temperatures from 25°C to 100°C .

Advanced Sulfur Cathode Fabrication and Evaluation

In addition to developing new SE, the team is also developing and evaluating an advanced sulfur cathode with high sulfur loading $> 5 \text{ mg cm}^{-2}$. The developed sulfur cathode demonstrated a high initial discharge specific capacity of 1294 mAh g^{-1} at room temperature (Figure 24a). However, due to the large polarization of the cell, the charge specific capacity is merely 858 mAh g^{-1} , leading to the capacity loss in the following cycles (Figure 24b). Next quarter, the team will try to investigate the cause of such low 1st cycle Coulombic efficiency (CE) and thus improve the performance of the cell.

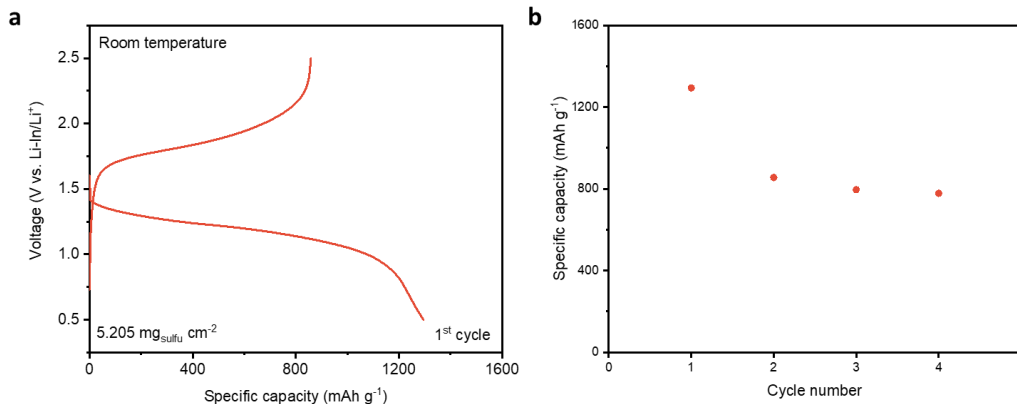


Figure 24. (a) Charge-discharge voltage profiles and (b) cycling performance of sulfur cathode with high areal sulfur loading of 5.205 mg cm^{-2} at room temperature.

Li-Alloy Anodes for ASSLSBs

In addition to the new SE and advanced sulfur cathode, the team also developed Li-alloy anodes that are stable and suitable for ASSLSBs. The lithium alloys are prepared by the high-energy ball-milling method with optimization of composition and synthesis time. The prepared lithium alloys with various compositions possess different open circuit voltages (OCVs) and long-term cycling behavior. As shown in Figure 25, two types of Li-alloy anodes can deliver high initial discharge specific capacity and maintain good reversibility for 50 cycles under 0.1 C at 60°C (the sulfur loading is $\sim 2.19 \text{ mg cm}^{-2}$). They are investigating the relationship between chemical property and electrochemical performance to deeply understand the mechanism of lithium stripping and plating. It shows that the Li-alloy anodes have potential to be utilized in ASSLSBs and can have stable long-term cycling performance.

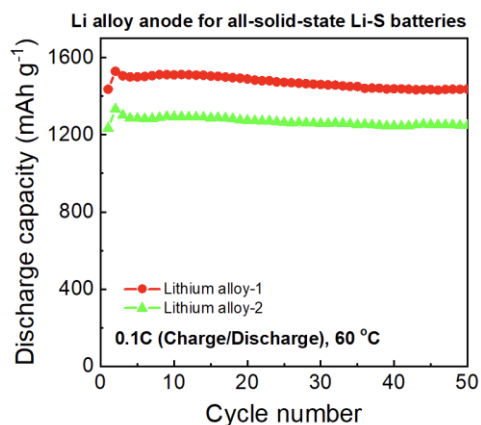


Figure 25. Long-term cycling performance of the newly synthesized Li-alloy anodes for all-solid-state Li-S batteries under 0.1 C charge/discharge at 60°C. The specific capacity is based on the weight of sulfur.

Patents/Publications/Presentations

The project has no patents, publications, or presentations to report this quarter.

Task 1.9 – Hot Pressing of Reinforced Lithium-NMC All-Solid-State Batteries with Sulfide Glass Electrolyte (Thomas Yersak, General Motors, LLC)

Project Objective. The project objective is to research, develop, and test Li-NMC ASSBs capable of achieving program performance metrics by implementing sulfide glass SSEs and hot-press processing in a dry-room environment. The performance of ASSBs with sulfide SSEs is limited because they are essentially green tapes with up to 20% porosity. In composite cathodes, the porosity limits energy density and power, while porosity in the separator acts as a conduit for Li-metal deposits if cycling conditions (C-rate, operating temperature, and pressure) are not strictly controlled. The project goal is to demonstrate that the hot-pressing method and appropriately formulated sulfide glass SSEs can eliminate porosity to enable Li-NMC ASSBs with energy density of > 350 Wh/kg.

Project Impact. The hot-press processing method and appropriately formulated sulfide glass SSEs may enable Li-NMC ASSBs with improved energy density > 350 Wh/kg. The GM processing technology depends on heating a sulfide glass SSE above its T_g , at which point it can consolidate via viscoplastic flow. In the composite cathode, hot-pressing provides liquid-like contact between the NMC cathode and SSE to increase energy density and power by enabling thick composite cathodes with high active material loading. Furthermore, cathode-supported sulfide glass separators can be made dense and thin by hot-pressing. A dense separator enables the use of Li-metal anodes because lithium deposits may be more effectively blocked, preventing cell shorting.

Approach. The sulfide SSE used in the composite cathode, otherwise known as the catholyte, will dictate the processing specifications for ASSB hot-pressing. Thermal stability can be achieved by NMC passivation and proper catholyte formulation. This project will systematically evaluate different NMC coatings, catholyte formulations, and hot-press processing specifications (temperature, time, and pressure). The performance of hot-pressed ASSBs will be compared to green baseline ASSBs and hot-pressed control ASSBs consisting of the β -Li₃PS₄ and Li₆PS₅Cl model SSEs. Electron microscopy will be employed to understand interfacial phenomena and track composite cathode microstructure before and after hot-pressing.

Out-Year Goals. In the second year of this project, a sulfide glass SSE will be formulated specifically for use as the separator. The separator glass SSE formulation will be designed to achieve full densification under the hot-press processing specifications determined for the catholyte. Separator glass formulation design will also consider cathodic stability, moisture stability, and ionic conductivity. Once a system of separator glass SSE and catholyte has been determined, the third year of the project will demonstrate hot-pressed full cells at the coin-cell and single-layer pouch-cell levels, meeting program target performance metrics.

Collaborations. GM will lead this project with no subrecipients.

Milestones

1. Report ionic conductivity of separators with multifunctional reinforcement. Decide whether to carry forward multifunctional reinforcement for the remainder of the project. (Q1, FY 2022; Completed)
2. Demonstrate that H₂S generation of target separator glasses and catholytes can be cut by 50% in a -40°C dewpoint dry-room environment. Report functional characteristics of SSEs after exposure. (Q2, FY 2022; Completed)
3. Based on results collected during Budget Period 2, the best performing separator glasses will be carried forward for the remainder of the project. (Q3 FY 2022; In progress)
4. Retrofit glovebox: implement a simulated dry-room environment inside an inert glovebox by designing and installing custom equipment. (Q4, FY 2022)

Progress Report

Progress this quarter relates to the moisture stability of sulfide-based SSEs when exposed to a dry-room environment. The poor moisture stability of sulfide SSEs presents a major obstacle to commercialization of SSBs utilizing these SSEs. If SSBs are to be manufactured using the same capital equipment and facilities as those used to make conventional Li-ion batteries, then the moisture stability of sulfide SSEs must be improved. Here, the team reports a systematic study of moisture stability as a function of sulfide SSE composition and dewpoint. They propose that moisture stability should be defined not only as H₂S generation, but also as ionic conductivity reduction. Furthermore, they show that sulfide SSEs composed primarily of PS₄³⁻ structural units are the most stable and that anhydrous solvents protect sulfide SSEs from hydrolysis during processing.

In the first experiment of this study, various sulfide SSE powders were exposed to a -40°C dew point dry-room environment for 30 minutes, as shown in Figure 26a. During this experiment, H₂S gas generation was monitored, and the data are provided in Figure 26b. Their results are consistent with the findings of previous studies with respect to the influence of glass modifier (Li₂S) content, glass co-modifier (Li₂O), and LiI dopant on H₂S generation. First, sulfide SSEs with 75 mol% glass modifier produced the least amount of H₂S gas.^[1] (Li₂S)₇₅(P₂S₅)₂₅ (that is, 75-25 LPS), (Li₂O)₇(Li₂S)₆₈(P₂S₅)₂₅ (that is, 7-68-25 LPSO), and (Li₂S)₇₅(P₂S₅)₂₅ + 20 mol% LiI (that is, 75-25 LPSI) all generated a maximum of 0.1 g/cc H₂S, whereas (Li₂S)₇₀(P₂S₅)₃₀ (that is, 70-30 LPS) and (Li₂O)₇(Li₂S)₆₃(P₂S₅)₃₀ (that is, 7-63-30 LPSO) generated a maximum of 0.6-0.7 g/cc H₂S. Second, a Li₂O co-modifier modestly reduced the H₂S generation of sulfide SSEs.^[2-4]

In addition to monitoring H₂S gas generation, this study reports on the ionic conductivity of sulfide SSEs before and after exposure to a -40°C dew point dry-room environment; the data are provided in Figure 26c. Every sample experienced a significant drop in ionic conductivity, with 70-30 LPS having the largest drop of 76.5% and 7-68-25 LPSO having the smallest drop of 51.6%. The products of sulfide SSE hydrolysis may include compounds such as LiOH,^[1] Li₃PO₄,^[5] and Li·H₂O.^[6] These compounds are poor ionic conductors, and if formed on the surface of sulfide SSE particles will act to substantially increase interparticle impedance once the powders are consolidated into pellets or films. The team concludes that H₂S generation is not a sufficient metric for the moisture stability of sulfide SSEs and that moisture stability should also comprehend functional characteristics like ionic conductivity.

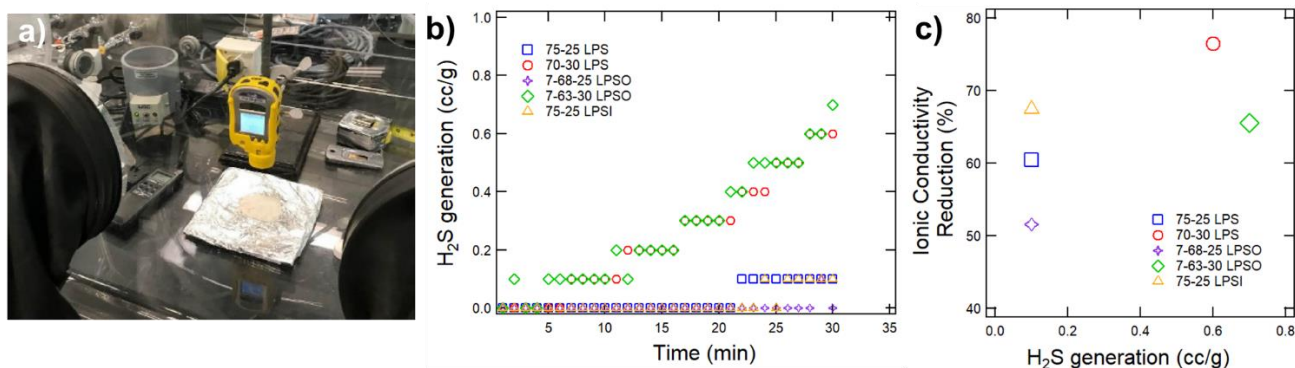


Figure 26. (a) Picture of experimental setup used to expose sulfide solid-state electrolyte (SSE) powders to a dry-room environment. The setup includes a 300-liter volume tabletop glovebox, a cartridge-based desiccant system, a microcontroller system to control the moisture setpoint, a personal H₂S detector, and a fan to continuously mix the glovebox air. (b) H₂S generation of different SSEs in a -40°C dew point dry room as a function of time. (c) Reduction in ionic conductivity versus maximum H₂S reading for different sulfide SSEs.

The local structures of sulfide SSEs before and after exposure were determined by Raman spectroscopy; data are provided in Table 1. The spectra for 70 mol% Li₂S modifier content SSEs are dominated by a single feature, which may be deconvoluted into multiple peaks attributable to PS₄³⁻ (421 cm⁻¹), P₂S₇⁴⁻ (406 cm⁻¹), and P₂S₆⁴⁻ (387 cm⁻¹) structural units. After exposure, the relative abundance of the PS₄³⁻ structural unit increases, which indicates that it is comparatively more stable than P₂S₇⁴⁻ and P₂S₆⁴⁻ structural units. Sulfide SSEs with

75 mol% Li_2S modifier content therefore produce less H_2S because they are primarily composed of PS_4^{3-} structural units, which react with moisture at a slower rate than the larger structural units found in sulfide SSEs with 70 mol% modifier content.

Table 1. Summary of Raman spectroscopic data of sulfide and oxysulfide glass solid-state electrolytes before and after exposure to a dry-room environment. Fractional peak areas are assigned to the vibrational modes of different glass structural units.

Sample	PS_4^{3-} (421 cm^{-1})	$\text{P}_2\text{S}_7^{4-}$ (406 cm^{-1})	$\text{P}_2\text{S}_6^{4-}$ (387 cm^{-1})
Pristine $(\text{Li}_2\text{S})_{70}(\text{P}_2\text{S}_5)_{30}$	27.0%	60.2%	12.8%
Exposed $(\text{Li}_2\text{S})_{70}(\text{P}_2\text{S}_5)_{30}$	28.2%	57.8%	14.0%
Pristine $(\text{Li}_2\text{O})_7(\text{Li}_2\text{S})_{63}(\text{P}_2\text{S}_5)_{30}$	25.3%	59.7%	15.0%
Exposed $(\text{Li}_2\text{O})_7(\text{Li}_2\text{S})_{63}(\text{P}_2\text{S}_5)_{30}$	33.1%	53.3%	13.6%

In the next experiment, the moisture stability of 75-25 LPSI was measured as a function of dew point; data are provided in Figure 27. H_2S generation is not reported since the maximum value at the end of each 30-minute exposure was below the 0.1 ppm detection limit of the team's sensor. Pristine 75-25 LPSI has an ionic conductivity of 1.21 mS/cm at room temperature when only handled inside an inert glovebox with 1 ppm H_2O (-76°C dew point). Exposing 75-25 LPSI powder to a dry-room environment results in degradation of ionic conductivity that trends as the negative log of moisture content. This result implies that over-sizing dry room air handling equipment may not adequately address the poor moisture stability of sulfide SSEs. Fortunately, sulfide SSEs can be handled in a dry room while immersed in an anhydrous solvent. An example would be a slurry prepared for film tape-casting. When 75-25 LPSI is exposed to a dry-room environment while immersed in dodecane, it retains an ionic conductivity of 1.04 mS/cm (Figure 27; star).

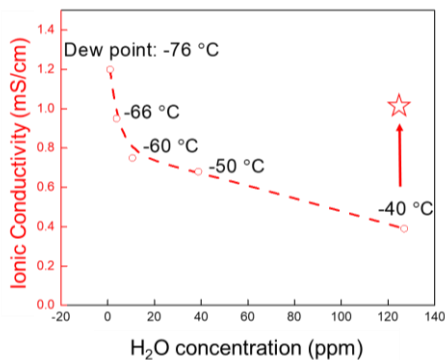


Figure 27. Ionic conductivity of LPSI sulfide solid-state electrolyte (SSE) after exposure as a dry powder to different dry-room environments for 30 minutes. The star marks the ionic conductivity of LPSI sulfide SSE after exposure to a -40°C dew point dry room for 30 minutes while immersed in anhydrous dodecane.

References

- [1] Muramatsu, H., et al. *Solid State Ionics* 182, no. 1 (2011).
- [2] Ohtomo, T., et al. *Journal of Non-Crystalline Solids* 364 (2013).
- [3] Ohtomo, T., et al. *Electrochemistry* 81, no. 6 (2013).
- [4] Ohtomo, T., et al. *Journal of Solid State Electrochemistry* 17, no. 10 (2013).
- [5] Ohtomo, T., et al. *Journal of Materials Science* 48, no. 11 (2013).
- [6] Calpa, M., N. C. Rosero-Navarro, et al. *Applied Materials Today* 22 (2021).

Patents/Publications/Presentations

Publications

- Yersak, T. A., et al. “Consolidation of Composite Cathodes with NCM and Sulfide Solid-State Electrolytes by Hot Pressing for All-Solid-State Li Metal Batteries.” *Journal of Solid State Electrochemistry* 26, no. 5 (2022): 1–10.
- Yersak, T. A., et al. “Sulfide Glass Solid-State Electrolyte Separators for Li Metal Batteries: Using an Interlayer to Increase Rate Performance and Reduce Stack Pressure.” *Materials Advances* 3 (2022): 3562–3570.

Task 1.10 – Three-Dimensional Printing of All-Solid-State Lithium Batteries (Jianchao Ye, Lawrence Livermore National Laboratory)

Project Objectives. The project has two primary objectives: (1) down select three-dimensional (3D) printing and post-processing approaches for SSE/cathode integration, and (2) understand battery failure mechanisms via *ex situ* and *in situ* characterization.

Impact. The adoption of thin separator layer, thick cathode structure, and metallic lithium anode will lead to EV batteries with > 350 Wh/kg energy density for increased mileage per charge. The higher ionic conductivity with suppression of lithium dendrite growth will allow high CCDs for fast charging applications. The improved electrode/electrolyte contact will increase battery cycle life for long-term service.

Approach. The technical approaches include advanced manufacturing based on 3D printing and related techniques, *ex situ* / *in situ* characterizations, and battery testing. Direct-ink writing (DIW) 3D-printing techniques will be employed to fabricate thin-film SSEs (< 100 μm), gradient SSEs, and 3D interfaces for battery performance evaluation. Three approaches including sintering-free, hybrid, and co-sintering will be investigated. The knowledge obtained from these approaches is transferable and complementary to each technique.

Out-Year Goals. The long-term vision of the team is to 3D-print all components of the ASSLBs to facilitate the scale-up of ASSLB manufacturing. In this project, the team will tackle the issues emerging from integrating SE with electrodes. The project goal is to demonstrate a successful 3D-printing approach to integrate SSE into electrodes and show reasonable capacity retention (that is, > 80%) after 300 cycles at current density $\geq 1 \text{ mA/cm}^2$.

Collaborations. The team will work closely with a computational partner (Task 3.11 led by B. Wood) to better understand battery failure mechanisms and design new battery architectures and chemistries for performance improvement.

Milestones

1. Determine the polymer / $\text{Li}_{6.75}\text{La}_3\text{Zr}_{1.75}\text{Ta}_{0.25}\text{O}_{12}$ (LLZTO) interfacial chemistry effects on the total ionic conductivity and Li^+ transference number. (Q2, FY 2022; In progress)
2. Improve conductivity and strength of composite polymer electrolytes (CPEs). (Q3, FY 2022; On schedule)
3. Obtain porous co-sintered LLZTO-SSE/NMC/C electrolyte/cathode bilayer structure. (Q4, FY 2022; On schedule)

Progress Report

In previous studies, it was found that densification of printed LLZTO films by furnace sintering is challenging due to the low packing density of the green films and the severe lithium loss issue at high sintering temperatures. Poor densification will lead to low ionic conductivity and mechanical fragility. The team therefore investigated the possibility of a hybrid electrolyte using the porous LLZTO as scaffold and solid polymer electrolyte (SPE) as flexible and conductive filler, aiming at improving conductivity and cracking resilience. Poly(ethylene glycol) diacrylate (PEGDA) / poly(ethylene glycol) methyl ether acrylate (PEGMEA) / poly(ethylene oxide) (PEO) / lithium bis(trifluoromethanesulfonyl)imide (LiTFSI) SPE was chosen as the infilling polymer electrolyte (PE) based on previous studies on SPEs. Figure 28 shows the SEM images of a pristine LLZTO porous film as well as the hybrid system after infilling and curing of corresponding monomers. Most pores were filled with the SPE, although gaps can be observed in the fracture surface, implying that the wetting between the pristine LLZTO and SPE may be insufficient. The pristine porous LLZTO films show a poor room-temperature ionic conductivity of 1.16×10^{-5} S/cm. After the LLZTO films are acid treated with H_3PO_4 , the

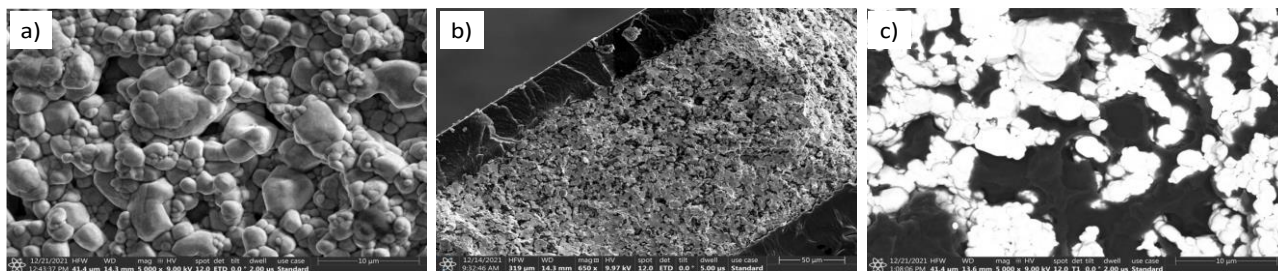


Figure 28. Scanning electron microscopy images of (a) pristine LLZTO film and (b) solid polymer electrolyte (SPE) infilled LLZTO films. (c) Backscattered electron image of the LLZTO/SPE system.

overall resistance decreases due to removal of the surface contaminants such as Li_2CO_3 ; thus, conductivity increases to 3.58×10^{-5} S/cm. By adding SPE in the pores of the LLZTO films, the team expects to introduce extra Li^+ transport channels and thus further improve overall conductivity. As shown in Table 2, the total ionic conductivity of the SPE/infilled pristine LLZTO (SPE/LLZTO/SPE) is 1.27×10^{-5} S/cm, higher than SPE alone (7.1×10^{-6} S/cm). After removing the contributions from the SPE layer top and from the bottom of the SPE/LLZTO/SPE hybrid system, the conductivity of the SPE infilled pristine LLZTO layer is 2.5×10^{-5} S/cm, higher than pristine LLZTO film, but slightly lower than the acid-treated LLZTO film only, which may be partially due to the gaps observed in Figure 28. The ionic conductivity at 60°C, Li^+ transference number, and CCD values are also improved with the LLZTO scaffold, as shown in Table 2.

Table 2. Ionic conductivity (σ_{Li}) at room temperature and 60°C, activation energy (E_a) at 60°C, transference number (t_{Li^+}) at 60°C, and critical current density at 60°C of the polymer solid electrolyte and hybrid system (LLZTO/polymer) with different acid treatments conducted on LLZTO films.

Composition	Total σ_{Li} @ RT (mS/cm)	Total σ_{Li} @ 60°C (mS/cm)	E_a @ 60°C (eV)	t_{Li^+} @ 60°C	CCD @ 60°C (mA/cm ²)
Polymer SE	0.0071±0.002	0.12	-----	0.24±0.03	0.13
SPE/ LLZTO/SPE	0.0127±0.0002	0.173±0.027	0.46	0.41±0.07	0.25±0.02
SPE/HCl- LLZTO/SPE	0.017±0.005	0.171±0.056	0.51	0.44±0.02	0.22±0.04
SPE/ H_3PO_4 -LLZTO/SPE	0.0076±0.0007	0.153±0.051	0.45	0.59±0.01	0.28±0.02

To remove a possible ion-blocking effect due to the presence of the surface Li_2CO_3 contaminant layer, different treatments using HCl acid and H_3PO_4 acid to either remove Li_2CO_3 or convert it into other lithium species were carried out on the porous LLZTO films. Figure 29 shows the XPS analysis of the pristine and acid-treated

LLZTO films. The lanthanum and zirconium peaks in pristine LLZTO are weak due to the existence of Li_2CO_3 surface layer; in contrast, these peaks are observed for the acid-treated LLZTO films. As expected, the surface of the acid-treated film is decorated with either Cl^- from HCl or PO_4^{3-} species from H_3PO_4 (Figure 29e-f).

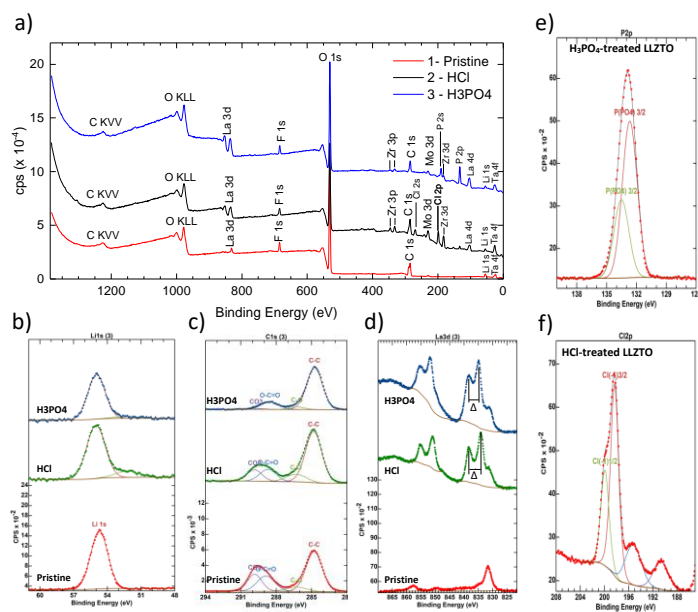


Figure 29. X-ray photoelectron spectroscopy (XPS) survey scan of (a) pristine LLZTO film and acid-treated LLZTO films, HCl and H_3PO_4 . (b) High-resolution lithium 1s XPS spectra. (c) High-resolution carbon 1s XPS spectra. (d) High-resolution lanthanum 3d XPS spectra. (e) High-resolution phosphorus 2p XPS spectra. (f) High-resolution chlorine 2p XPS spectra.

Figure 30a-c shows the chronoamperometry (CA) plots and the EIS plots before and after direct current (DC) polarization. Decreased charge transfer resistances were observed after lithium plating/stripping, implying an improved interfacial contact between lithium and SPE in $\text{Li}/\text{SPE}/\text{LLZTO}/\text{SPE}/\text{Li}$. The transference numbers were further increased, especially for the H_3PO_4 treated sample, up to 0.59 (Table 2). The CCD value for HCl -treated LLZTO film is lower than that of the pristine film ($0.22 \text{ mA}/\text{cm}^2$ versus $0.25 \text{ mA}/\text{cm}^2$), while H_3PO_4 treatment slightly increases the CCD to $0.28 \text{ mA}/\text{cm}^2$. However, the total ionic conductivity of H_3PO_4 -treated LLZTO sample after SPE infilling is the lowest.

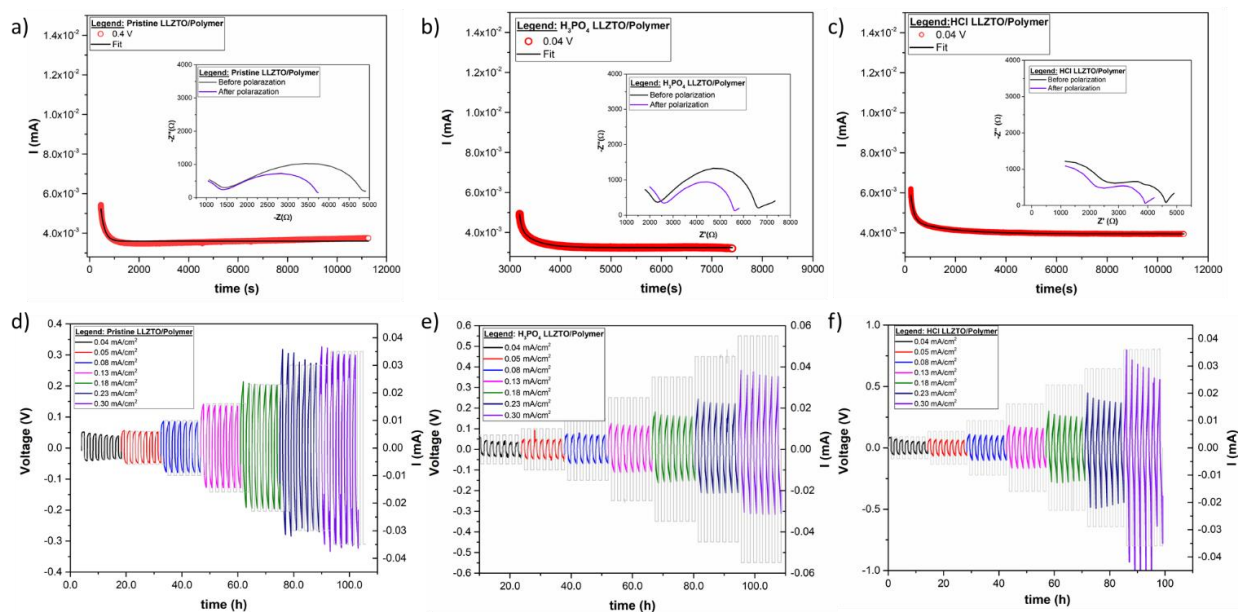


Figure 30. (a-c) DC polarization curves for determining the Li^+ transference number under an applied voltage of 0.04 V at 60°C . (a) Pristine LLZTO film. (b) H_3PO_4 treated films. (c) HCl treated film. Inset: impedance taken just before and immediately after the DC polarization experiment. The curves were fitted with a decay function, and the steady state at the end of the curve was extrapolated. (d-f) Voltage versus time plots of plating-stripping at different current densities. (d) Pristine LLZTO film. (e) H_3PO_4 treated films. (f) HCl treated film.

To simplify the 3D interface problem, the team designed different control experiments to compare the cycling behaviors of four model lithium symmetric cells: (1) Li|SPE|Li; (2) Li|SPE|infilled-LLZTO|SPE|Li; (3) Li|SPE|LLZTO-1100C|Li; and (4) Li|SPE|LLZTO-1100C|SPE|Li. The first two cell configurations (1-2, Figure 31a-b) show symmetric voltage profiles, suggesting Li^+ transport along both directions is similar. This symmetry seems to be intuitive for a symmetric cell setup. However, when the SPE infilled LLZTO layer is replaced with a well densified LLZTO pellet, for example, in the configuration of Li|SPE|LLZTO-1100C|SPE|Li (Figure 31c), the team observed asymmetric cycling behavior. When the cell is cycled at 0.20 mA/cm^2 , the overpotential is greater when the current is negative than it is when the current is positive. This abnormal asymmetry in a symmetric cell is still a mystery. Given the only difference between the above two setups (LLZTO infilled SPE and LLZTO/SPE) is that Li^+ ions can transport in both polymer and LLZTO channels in the infilled LLZTO case, versus that Li^+ ions must transport from polymer to LLZTO and from LLZTO to polymer in the dense LLZTO case, the team suspects that the ion transport via LLZTO/SPE interface is the origin of this asymmetric behavior. In fact, in an SPE asymmetric cell using a densified LLZTO pellet stacked with only one SPE film (Figure 31d), the similar asymmetric behavior is observed, where Li^+ transport in the direction of LLZTO to SPE becomes much more difficult at current densities of 0.13 mA/cm^2 or above. The observed accelerated degradation is found in Li|SPE|Li, Li|SPE|LLZTO-1100C|Li, and Li|SPE|LLZTO-1100C|SPE|Li, but not in Li|SPE|infilled-LLZTO|SPE|Li. The observations suggest an advantage in using the SPE infilled LLZTO, while detailed understanding of the degradation mechanism is still needed. Possible explanations to

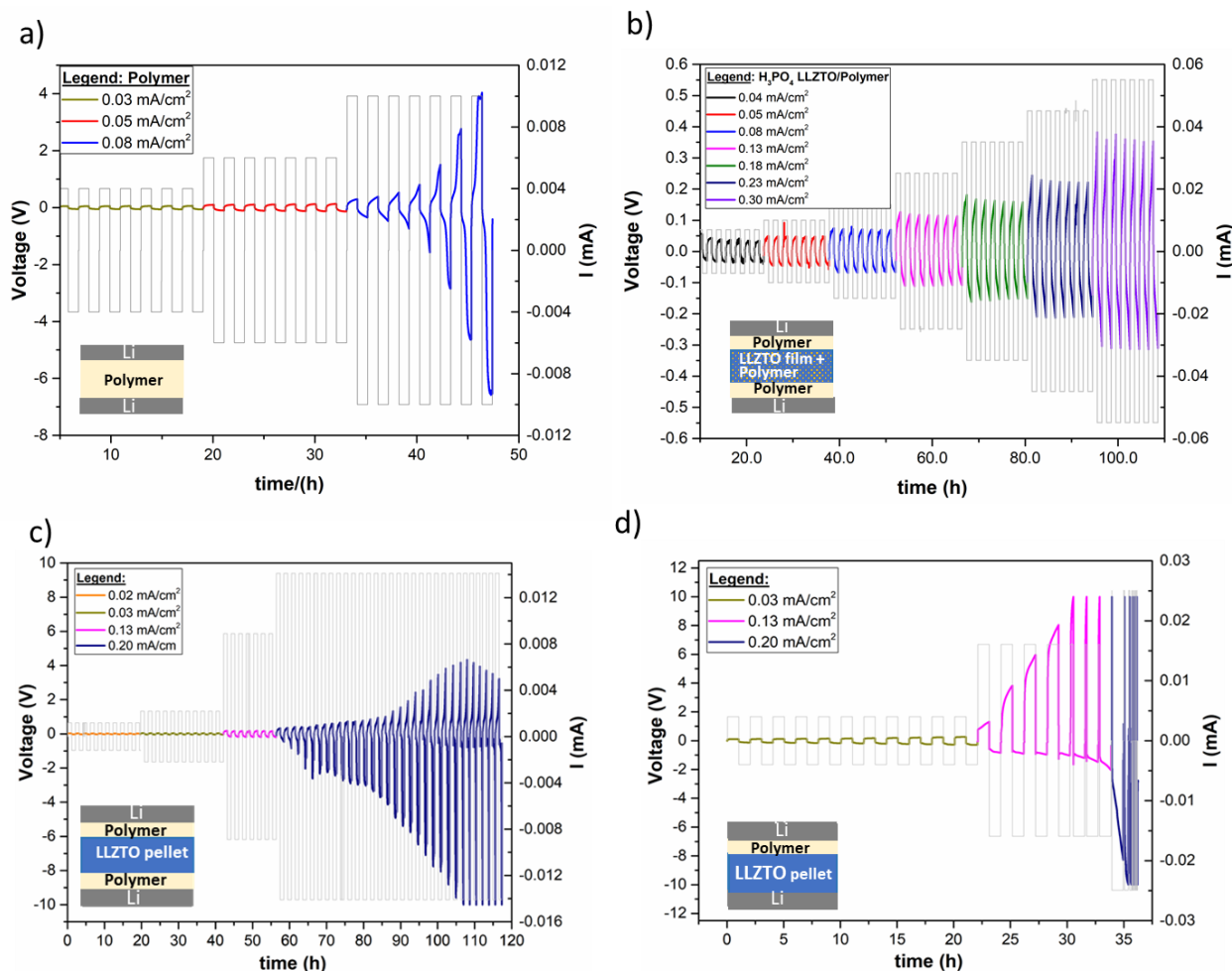


Figure 31. Voltage versus time plots at 60°C of the four model systems assembled to understand the conductivity differences: (a) single solid polymer electrolyte (SPE) layer. (b) SPE infilled porous LLZTO film (H_3PO_4 treated). (c) Stacked SPE, densified LLZTO pellet (H_3PO_4 treated) and SPE. (d) Stacked SPE and densified LLZTO pellet (H_3PO_4 treated) bilayers with the polymer side initially connected to the positive electrode. Their corresponding cycling stability tests showing symmetric and asymmetric cycling behaviors.

be scrutinized in future work include: (1) charge accumulation and clogging at the LLZTO/SPE interface due to sluggish charge transport from LLZTO to SPE; and (2) polymer/Li interface degradation at high voltages. To further enhance performance of the hybrid electrolyte, the ionic conductivity of SPEs and their compatibility with LLZTO shall be improved, which will be the next research focus area.

Patents/Publications/Presentations

Publication

- Hammons, J., J. A. Espitia, E. R. Guzman, R. Shi, F. Meisenkothen, M. Wood, M. R. Ceron, and J. Ye. “Pore and Grain Chemistry during Sintering of Garnet-Type $\text{Li}_{6.4}\text{La}_3\text{Zr}_{1.4}\text{Ta}_{0.6}\text{O}_{12}$ Solid-State Electrolytes.” *Journal of Materials Chemistry A* 10 (2022): 9080–9090.

Task 1.11 – Physical and Mechano-Electrochemical Phenomena of Thin-Film Lithium-Ceramic Electrolyte Constructs (Jeff Sakamoto, University of Michigan)

Project Objective. While a small number of SEs exhibit high ionic conductivity (~ 1 mS cm at 298 K), few are stable against lithium metal. The garnet-type SE, based on the nominal formula $\text{Li}_7\text{La}_3\text{Zr}_2\text{O}_{12}$ (LLZO), is unique in that it is a fast ion conductor and—as demonstrated in the team’s recent project (DE-EE-00006821)—is stable against lithium. Moreover, the team’s former project successfully demonstrated a decrease in Li-LLZO interface resistance from $12,000 \Omega \text{ cm}^2$ to $2 \Omega \text{ cm}^2$ and stable cycling at 1 mA cm^2 for 100 cycles ($\pm 15 \mu\text{m}$ of lithium per cycle). Although the past project demonstrated that LLZO is a viable SE for enabling batteries using metallic lithium, the studies used thick pellets (1 mm) and thick anodes ($\sim 500 \mu\text{m}$). The goal of this project is to acquire a deep fundamental understanding of the physical and mechano-electrochemical phenomena that control the performance of cells consisting of thin LLZO ($\sim 10 \mu\text{m}$), thin lithium anodes ($\sim 20 \mu\text{m}$), and thin solid-state composite cathodes.

Project Impact. If successful, the project will gain knowledge to guide closely related commercialization efforts to scale up the production of LLZO-based SSBs.

Approach. The team believes that to achieve a step increase in technology readiness level (TRL), the same performance characteristics previously shown should be demonstrated in technologically relevant cells, for example, thin LLZO and thin lithium.

Out-Year Goals. Out-year goals involve the following: custom thin-film composite (TFC) development, preliminary cycling studies, Vis cell development, lithium cycling, and polymer gel electrolyte (PGE) screening.

Collaborations. This project collaborates with N. Dasgupta and D. Siegel of University of Michigan (UM), Mechanical Engineering.

Milestones

1. In thin lithium and thin LLZO TFC, determine the maximum plating critical current density ($\text{CCD}^{\text{plating}}$) and stripping critical current density ($\text{CCD}^{\text{stripping}}$) versus depth of discharge (DOD) at fixed lithium thickness ($17 \mu\text{m}$). (Q1, FY 2022; Completed)
2. Long-term cycling tests to demonstrate $\geq 80\%$ energy retention over 1000 cycles. (Q2, FY 2022; In progress)
3. In thin lithium and thin LLZO TFC, determine the max $\text{CCD}^{\text{plating}}$ and $\text{CCD}^{\text{stripping}}$ versus lithium thickness, DOD, stack press, and temperature. (Q3, FY 2022; Complete)
4. Optimize ALD coating technology to suppress reactions between the PGE and LLZO. (Q4, FY 2022; In progress)

Progress Report

In Thin Lithium and Thin LLZO TFC, Determine Max $CCD^{plating}$ and $CCD^{stripping}$ Versus Lithium Thickness, DOD, Stack Press, and Temperature

In Q2, the CCDs for plating and stripping were determined using *in situ* formed lithium and at specific temperature and pressure. It was determined that the behavior of thin *in situ* formed lithium is considerably different compared to relatively thick ($> 50 \mu\text{m}$) Li-foil electrodes. Figure 32 shows the impedance spectra that correspond to salient points in a DC polarization for just the stripping of *in situ* formed lithium on LLZO. As shown in Figure 32, the increase in cell resistance during stripping was mainly attributed to the increase in interfacial resistance. Before stripping, the Li/LLZO interface formed by *in situ* plating exhibited immeasurably small interfacial resistance. However, the interfacial resistance gradually increased during the first phase of stripping. During stripping, the lithium in direct contact with the LLZO is removed, and the stack pressure and diffusion likely transport lithium to the surface to maintain interfacial contact. However, as stripping proceeds, Li-metal deformation is slowed as the thickness decreases, leading to a decreased replenishment rate. It has been shown that a low interfacial resistance can be maintained by applying higher stack pressure and elevating the temperature, which can enhance lithium creep and diffusion. Thus, the reduced lithium flow on stripping of thin lithium results in higher/increasing interfacial resistance. It increases as the current density increases and the thickness of lithium decreases. When the replenishing rate is insufficient to balance the stripping rate, the nucleation of voids is initiated. Small voids grow and merge into larger voids, exacerbating local current focusing near their periphery. Because of the higher local current density, the growth of voids is accelerated, leading to the rapid increase in the interfacial resistance observed final stages of polarization.

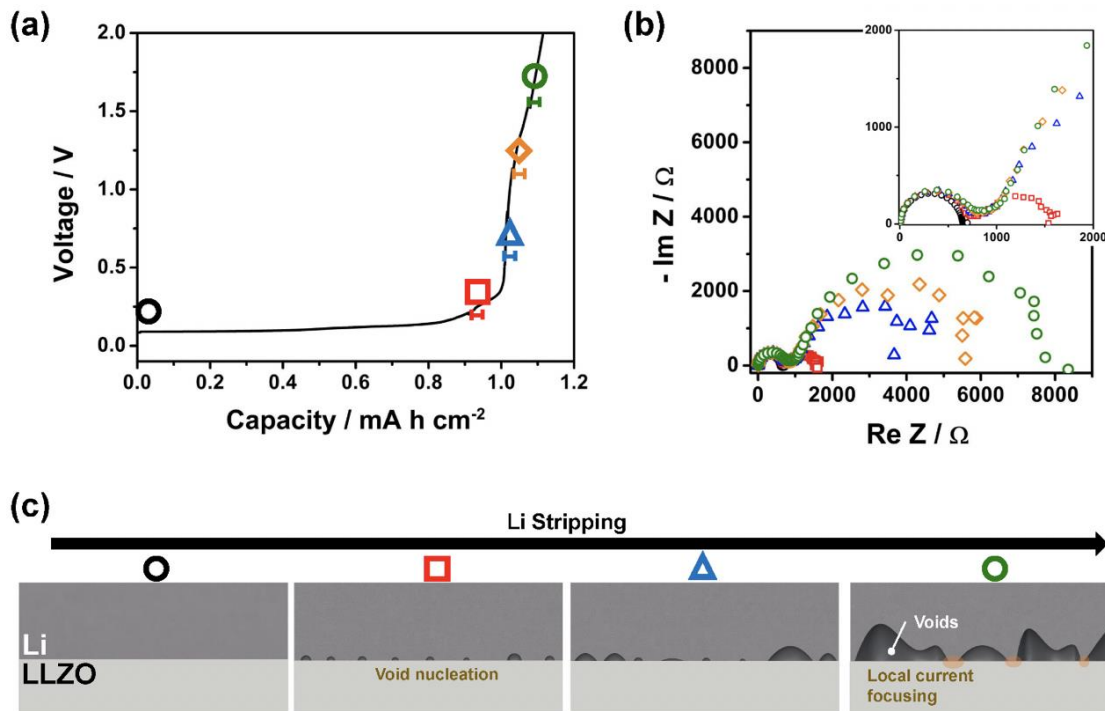


Figure 32. Characterization of the stripping behavior of thin lithium using simultaneous direct current (DC) and *operando* alternating current (AC) analysis. (a) Voltage responses of stripping thin lithium on LLZO at 0.4 mA/cm^2 . (b) AC impedance analysis at salient points in the DC polarization curve (a). (c) Schematic representation of what is believed to be the lithium morphological evolution at the Li-LLZO interface during discharge.

Patents/Publications/Presentations

The project has no patents, publications, or presentations to report this quarter.

Task 1.12 – Low Impedance Cathode/Electrolyte Interfaces for High-Energy-Density Solid-State Batteries

(Eric Wachsman and Yifei Mo, University of Maryland)

Project Objective. The project objective is to research, develop, and test Li-metal-based batteries that implement solid LICs equipped with NMC cathodes integrated into the Li-metal / Li-La-Zr (LLZ) tri-layer architecture. Specifically, the team will achieve the following: (1) identify and demonstrate interfacial layers to achieve low-impedance and stable NMC/LLZ interfaces; (2) develop novel processing techniques to fabricate NMC/LLZ composite cathodes with low interfacial resistance; and (3) enable high-performance ASSBs with an energy density of 450 Wh/kg and 1400 Wh/L and negligible degradation for 500 cycles.

Project Impact. Instability or high resistance at the interface of high-energy cathode materials with Li-garnet SEs limits the high-energy-density ASSBs. This project will lead to a fundamental understanding of solid-electrolyte/solid-cathode interfaces and a unique and transformative LLZ framework to enable high-energy-density, safe Li-metal batteries approaching ~ 400 Wh/kg.

Approach. In this new project, the team will build on their demonstrated expertise with garnet electrolytes and ASSB cells to accomplish the following: (1) engineer interfaces to overcome high NMC/LLZ interfacial impedance and interfacial degradation; (2) develop processing and fabrication techniques to achieve high-loading NMC/LLZ composite cathodes with low resistance and high cyclability; and (3) integrate the NMC/LLZ cathodes into all-solid-state Li-metal/LLZ cells to achieve high-energy-density batteries.

Out-Year Goals. The project will solve the current challenges of integrating garnet SE with a cathode to achieve a high-performance ASSB using a high-energy-density Li-metal anode. The resultant high energy density and stability using both high-energy-density Li-metal anodes and NMC cathodes will open new applications in portable electronics, EVs, and beyond.

Collaborations. This project funds work at University of Maryland (UMD). The PI, E. Wachsman, will have management responsibility and will lead experimental efforts including garnet synthesis, interface processing, cell fabrication, and testing. The Co-PI, Y. Mo, will lead computational efforts on understanding stability between garnet and cathode and on identifying promising coating materials. In addition, E. Wachsman is actively collaborating with several universities and national laboratories through the U.S.–German cooperation on SSB interfaces.

Milestones

1. Thermochemical stability between LLZ and interface-coated NMC experimentally determined. (Q3, FY 2022; In progress)
2. Experimental results compared with computational results, and model refined for side reactions and process optimization. (Q4, FY 2022; In progress)
3. Ten-times reduction in interfacial impedance between coated LLZ/NMC and uncoated LLZ/NMC interfaces demonstrated by co-sintering. (Q4, FY 2022; In progress)
4. Fabricate tri-layer cell with composite NMC-LLZ cathode layer and evaluate. (Q1, FY 2023; In progress)
5. *Go/No-Go Decision*: Demonstrate final cell with achieved performance. (Q2, FY 2023; In progress)

COVID-19 Impact. Progress on experimental results was impacted by COVID-19, which closed labs for several months; this resulted in a six-month no-cost extension reflected in the milestone dates above.

Progress Report

Previous XRD results of sintered NMC/LLZ pellets suggest that NMCs with higher nickel content (for example, NMC-811) are more reactive toward garnet than those with lower amounts of nickel. NMC-811/LLZTO pellets demonstrate near complete loss of peak intensity in XRD when sintered at 1000°C. To further investigate this effect, thermal gravimetric analysis (TGA) / DSC was performed on samples of the pristine NMCs in both argon and O₂ atmosphere, as literature reports indicate NMC loses O₂ from the lattice at high temperatures. The TGA results (Figure 33) show that the higher the nickel content, the greater the mass loss, with an earlier onset temperature at higher nickel content. In addition, the samples heated in an O₂ environment had decreased mass loss with an increase in the onset temperature across all compositions of NMC. This stabilization of the NMC is significant enough that Ni_{1/3}Mn_{1/3}Co_{1/3} (NMC-111) demonstrates nearly no mass loss up to 1100°C in O₂. Additionally, coating Ni_{0.6}Mn_{0.2}Co_{0.2} (NMC-622) with a 4-nm layer of alumina further reduces the mass loss of NMC-622, such that in O₂ atmosphere the sample loses less than 0.5 wt%. This suggests that careful selection of co-sintering environment, use of a protective ALD coating, as well as the NMC composition should be done when co-sintering NMC and LLZ.

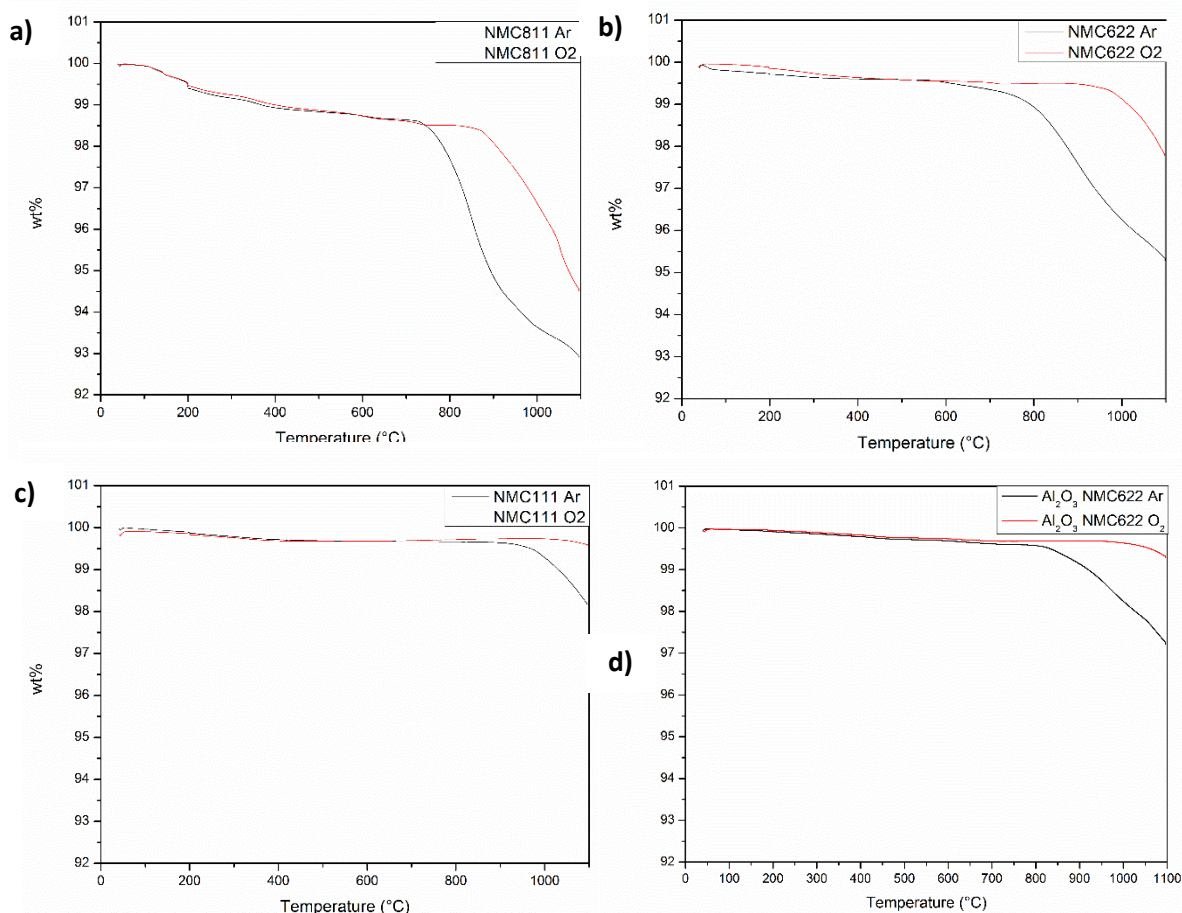


Figure 33. Thermal gravimetric analysis results of (a) NMC-811, (b) NMC-622, (c) NMC-111, and (d) Al₂O₃-coated NMC-622 in both argon and O₂ atmospheres.

Further, the team studied the thermochemical stability between LLZ and NMC-622 with the addition of 10 mol% excess lithium from Li₂CO₃. Previous DSC results indicated the suppression of the reaction between NMC and LLZ when extra lithium is added to the mixture. The LLZ was milled down to < 300 nm, and the NMC-622 was milled down to < 500 nm. Recent XRD results (Figure 34) indicate that there is not a significant degradation of the NMC or the LLZ crystallinity, as the peak intensity of both compounds in both samples is

preserved. Additionally, no new peaks from decomposition products of LLZ and NMC are detected. The backscatter SEM image in Figure 34b shows the presence of an amorphous phase that is darker than NMC, indicating that it is a lower zirconium material. Since this is not observed in the sample without added Li_2CO_3 , it is possible that this is an amorphous Li-rich phase that acts as a Li-conductive pathway between the NMC and LLZ particles.

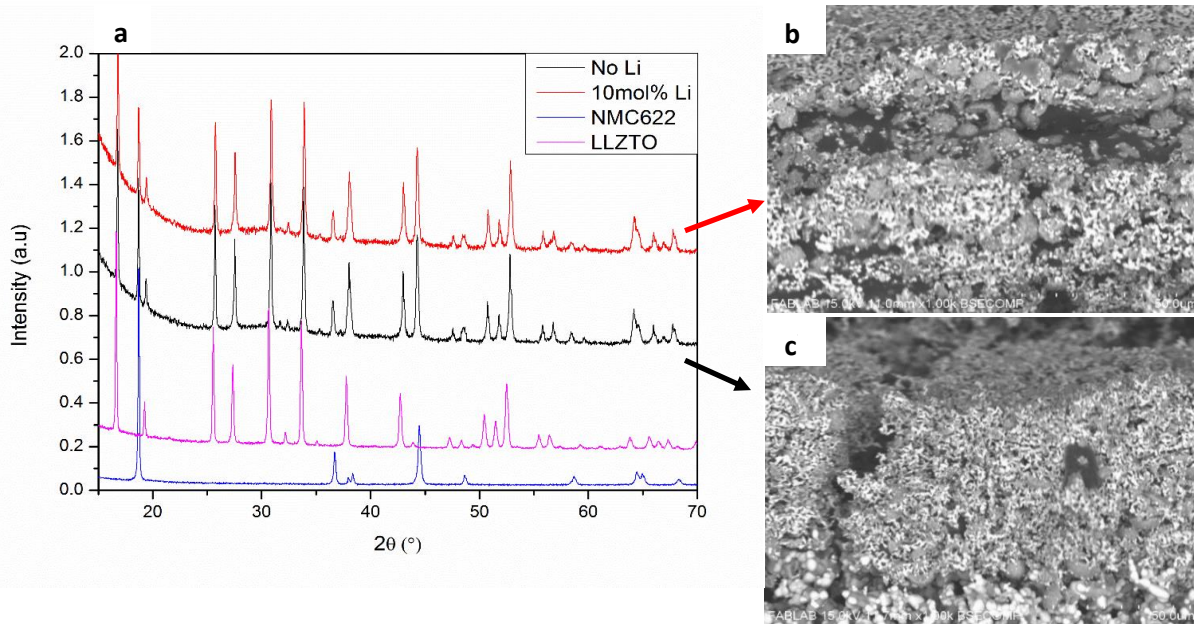


Figure 34. (a) X-ray diffraction spectra of sintered cathodes of NMC-622 and LLZ with and without excess lithium. Backscatter scanning electron microscopy images of (b) 10 mol% excess lithium from Li_2CO_3 and (c) no excess lithium, deposited onto the thin porous LLZ structure. These samples were heated to 900°C for 3 hours in argon atmosphere.

EIS results of symmetric cells with NMC/LLZ composite cathodes with and without excess lithium are shown in Figure 35. From the Nyquist plot (Figure 35a), and the increased peak height from the distribution of relaxation times (DRT) results (Figure 35b), it is clear that the sample without excess lithium has significantly higher ASR. Specifically, the peak in the DRT analysis at $\tau = 5 \times 10^{-4}$ s is attributed to the LLZ/NMC interfacial resistance and decreases from $2.1 \times 10^4 \Omega$ to $2.0 \times 10^3 \Omega$ when excess lithium from Li_2CO_3 is added during sintering, thus demonstrating a 10 \times reduction in interface resistance.

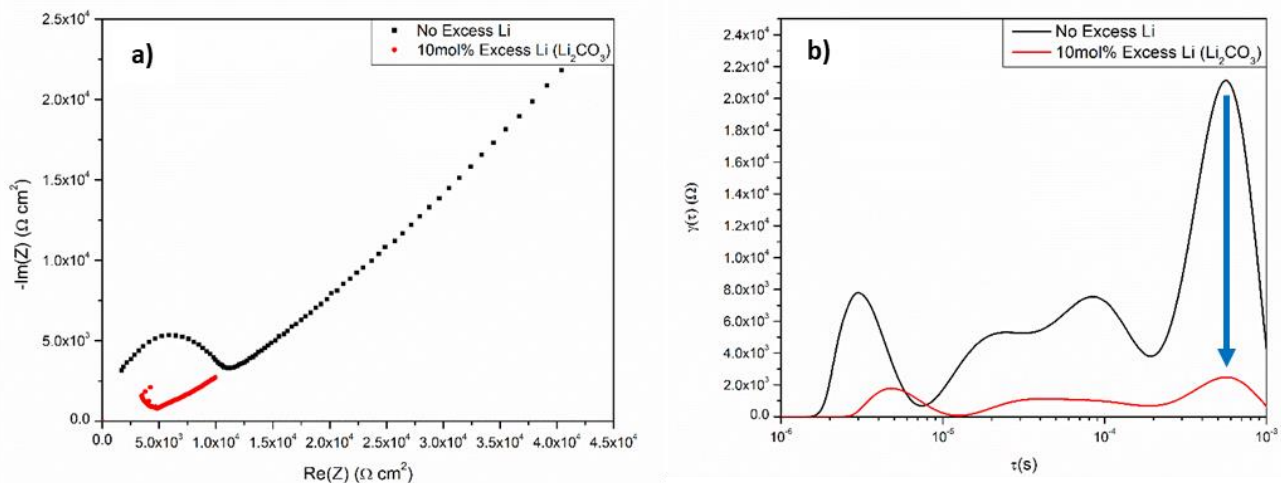


Figure 35. (a) Nyquist plot and (b) distribution of relaxation times analysis of milled NMC/LLZ composite cathodes sintered at 900°C with and without Li_2CO_3 addition.

Patents/Publications/Presentations

Publication

- Ren, Y., and E. D. Wachsman. “All Solid-State Li/LLZO/LCO Battery Enabled by Alumina Interfacial Coating.” *Journal of The Electrochemical Society* 169 (2022): 040529.

Presentation

- Lithium Metal Anodes and their Application in Batteries Webinar, MEET Battery Research Center and the Center for Materials Research, Virtual (February 9–10, 2022): “Enabling High Rate Metal Anodes by Tailored Structures and Interfaces.” Keynote.

Task 1.13 – Development of All-Solid-State Battery Using Anti-Perovskite Electrolytes (Zonghai Chen and Tao Li, Argonne National Laboratory)

Project Objective. The objective of this project is to develop an optimized anti-perovskite electrolyte with a stabilized interface for scalable fabrication of liquid-free SSBs.

Impact. The project will lead to impact on several areas: (1) establishing structure-property relationship of anti-perovskite electrolytes, (2) understanding and quantifying the interaction between the electrolytes and the environment, (3) understanding and mitigating the failure of ASSBs at solid-solid interface, and (4) developing a scalable process for fabrication of ASSBs.

Approach. The project approach is multi-fold: (1) chemistry design: multiple doping at anion sites will be pursued to improve structural stability ionic conductivity and environmental compatibility; (2) interfacial design: surface coating will be deployed to improve the chemical and mechanical stability of solid/solid interface; and (3) process development: a scalable fabrication process based on melt-infiltration or dry lamination will be developed for the fabrication of ASSBs.

Out-Year Goals. The project has the following out-year goals:

- Developing high-performance anti-perovskite electrolytes.
- Accessing the air stability and proton mobility of anti-perovskite electrolytes.
- Stabilizing the solid/solid interface through interfacial engineering.
- Prototyping liquid-free cells using anti-perovskite electrolytes.

Collaborations. This project collaborates with Y. Z. Liu (ANL), W. Q. Xu (ANL), X. H. Xiao (Brookhaven National Laboratory, or BNL), and H. Meng (University of Arkansas).

Milestones

1. Setting up high-throughput (HT) synthesis capability. (Q1, FY 2022; Completed)
2. Optimizing synthesis condition for anti-perovskite electrolytes. (Q2, FY 2022; Completed)
3. Investigating structural stability of doped electrolytes. (Q3, FY 2022; In progress)
4. Investigating transport properties of doped electrolytes. (Q4, FY 2022)

Progress Report

As one simple way to manipulate the structure of anti-perovskite is anion substitution at the dodecahedral site, the team focused this quarter on synthesis of $\text{Li}_2\text{OHCl}_x\text{Br}_{1-x}$ ($0 \leq x \leq 1$) using LiOH and different ratios of LiCl and LiBr salt mixture. Figure 36a shows XRD results of the five products at room temperature. Four Br-substituted products can be indexed to a cubic phase with Pm-3m space group. Some peaks of Li_2OHCl , however, are split into three nearby peaks. The enlarged views near (110) and (200) are shown in Figure 36b. The peak splitting suggests that there is a lattice distortion in the Li_2OHCl lattice, resulting in an orthorhombic phase where $a \neq b \neq c$. It is generally believed that ion conductivity is much lower in the anisometric lattice. These results show that 25% bromine substitution can effectively preserve the cubic phase of anti-perovskite, which may lead to improved ion conductivity at room temperature. Shifting of peaks to the lower angle with increased bromine replacement, shown in Figure 36b, also implies a lattice volume expansion. Detailed refinement results listed in Table 3 reveal a $\sim 2.9\%$ lattice volume increase with every 25% bromine substitution. In addition, a small amount of LiCl impurities was observed in the synthesized Li_2OHCl (highlighted by the red arrows in Figure 36a), indicating a non-negligible loss of LiOH during the synthesis.

The electrolyte powders were cold pressed into pellets and investigated using SEM and EDS. Figure 37 displays the results for Li_2OHCl and $\text{Li}_2\text{OHCl}_{0.5}\text{Br}_{0.5}$. The particles show a plate shape with diameter of $\sim 1 \mu\text{m}$ and thickness of $\sim 300 \text{ nm}$. EDS analyses reveal a local Cl-rich, O-deficient area in the Li_2OHCl pellet (Figure 37a), which can be related to the LiCl impurities in this material detected from XRD. On the contrary, elements in $\text{Li}_2\text{OHCl}_{0.5}\text{Br}_{0.5}$ are uniformly distributed (Figure 37b), and other Br-substituted electrolytes also show similar behavior. Given this, together with the XRD results, the team concludes that a single cubic phase with uniform anion mixing can be achieved when part of the chlorine is replaced by bromine in the anti-perovskite structure.

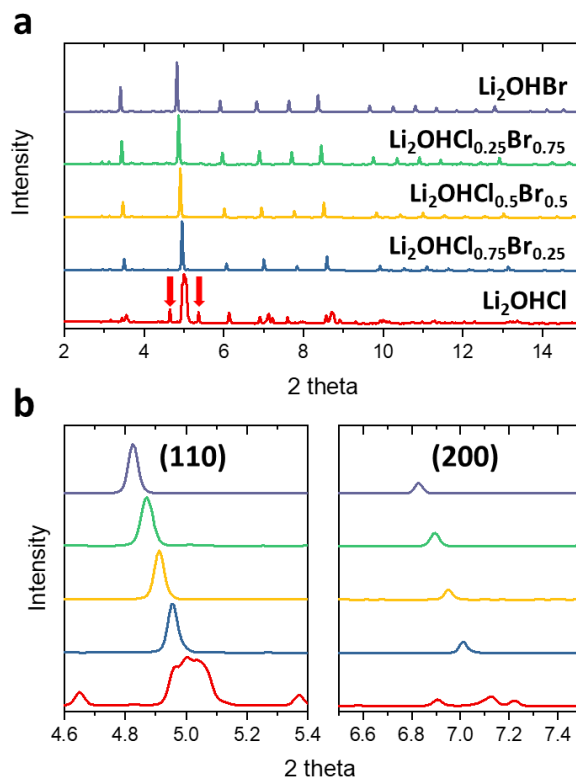


Figure 36. (a) X-ray diffraction (XRD) results of the anti-perovskite electrolytes with different chlorine and bromine ratios. Red arrows indicate the LiCl impurities in Li_2OHCl . (b) XRD spectra near (110) and (200) peaks. Peak splitting can be clearly seen in Li_2OHCl .

Table 3. Space group and lattice parameters analyzed from X-ray diffraction for each electrolyte.

Composition	Space group	a	b	c	V
Li_2OHCl	Pmc21	3.89129	3.83557	8.00373	119.458
$\text{Li}_2\text{OHCl}_{0.75}\text{Br}_{0.25}$	Pm-3m	3.94744			61.51
$\text{Li}_2\text{OHCl}_{0.5}\text{Br}_{0.5}$	Pm-3m	3.98278			63.177
$\text{Li}_2\text{OHCl}_{0.25}\text{Br}_{0.75}$	Pm-3m	4.02081			65.004
Li_2OHBr	Pm-3m	4.05331			66.593

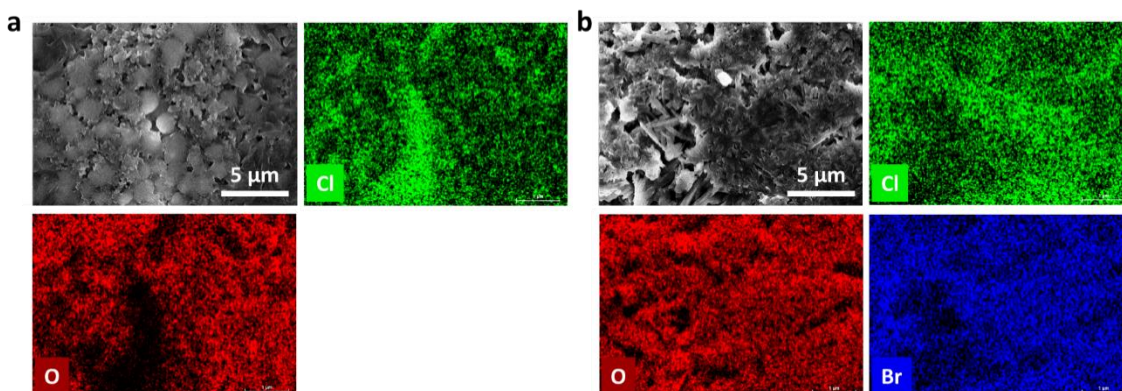


Figure 37. Scanning electron microscopy and energy-dispersive X-ray spectroscopy results of (a) Li_2OHCl and (b) $\text{Li}_2\text{OHCl}_{0.5}\text{Br}_{0.5}$.

The structural changes at elevated temperatures were studied by DSC. Li_2OHCl shows an endothermic peak at 44°C (Figure 38, arrow), caused by the orthorhombic to cubic phase transformation at this temperature. This peak was not seen in other Br-substituted electrolytes, which agrees with their single cubic phase at room temperature observed from XRD measurements. Melting Li_2OHCl gives a single peak at 296°C , while other materials show more than one peak when approaching the melting point, as summarized in Table 4. Phase diagrams clearly show that Li_2OHCl does not experience further phase transformation near the melting point, but Li_2OHBr will decompose to $\text{Li}_4(\text{OH})_3\text{Br}$ and LiBr . Therefore, the three endothermic peaks during heating of Li_2OHBr correspond to (1) deposition of Li_2OHBr , (2) partial salt melt at the eutectic point, and (3) melt of all salts. While the team could not find a phase diagram of the LiOH-LiCl-LiBr ternary system, similar decomposition of $\text{Li}_2\text{OHCl}_x\text{Br}_{1-x}$ at high temperature can be expected, which explains the additional peaks observed before the melt of the electrolyte. Moreover, electrolyte with bromine substitution to 75% ($\text{Li}_2\text{OHCl}_{0.25}\text{Br}_{0.75}$) presents the lowest melting point at 241°C , which is favorable for large-scale cell fabrication.

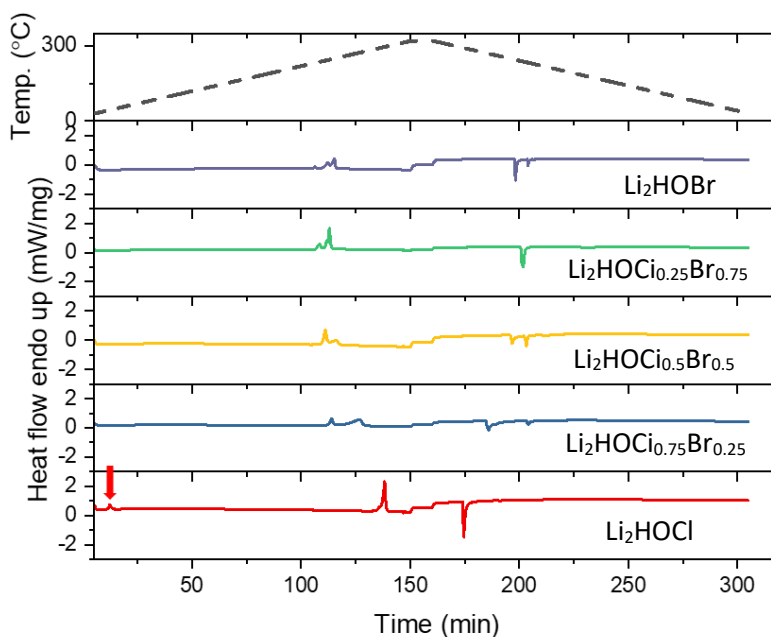


Figure 38. Differential scanning calorimetry results of anti-perovskite electrolytes with different chlorine and bromine ratios. Red arrow points to endothermic peak from orthorhombic to cubic phase transformation in Li_2OHCl .

Table 4. Summary of differential scanning calorimetry results of the anti-perovskite electrolytes. (MP: melting point)

Composition	Low-temp. phase transformation	Number of peaks near MP	MP (heating)	MP (cooling)	MP
Li_2OHCl	Yes @ 43.8°C	1	295.6°C	291.9°C	293.8°C
$\text{Li}_2\text{OHCl}_{0.75}\text{Br}_{0.25}$	No	2	272.3°C	268.9°C	270.6°C
$\text{Li}_2\text{OHCl}_{0.5}\text{Br}_{0.5}$	No	2	251.0°C	247.5°C	249.2°C
$\text{Li}_2\text{OHCl}_{0.25}\text{Br}_{0.75}$	No	3	244.8°C	237.5°C	241.2°C
Li_2OHBr	No	3	249.6°C	244.4°C	247.0°C

Patents/Publications/Presentations

The project has no patents, publications, or presentations to report this quarter.

Task 1.14 – Lithium Halide-Based Superionic Solid Electrolytes and High-Voltage Cathode Interface (Jagjit Nanda, Oak Ridge National Laboratory)

Project Objective. The project aims to develop low-temperature solution-based synthesis strategy for high ionic conducting halide-based SE and to enable approaches to develop a scalable process for integrating halide-based SE within porous high-voltage Li-ion cathode matrix. Years 1 and 2 aim at developing low-cost, solution-based synthesis routes to produce a halide class of superionic conductor belonging to Li_3MX_6 (where $\text{M} = \text{Sc}, \text{Y}, \text{La}, \text{Er}, \text{In}$, and $\text{X} = \text{Cl}, \text{Br}, \text{I}$) along with enabling electrochemical and structural characterization. Parallel efforts in years 2 and 3 target developing synthesis and processing methods where the high-voltage stable halide-based SEs can be readily infiltrated within the porous cathode structures such as NMC-622, high-voltage Mn-Ni spinel ($\text{LiMn}_{1.5}\text{Ni}_{0.5}\text{O}_4$) and recent fluorinated Mn-rich disorder rock salt cathodes. Years 3 and 4 focus on designing and fabricating thin halide SE separators with a thickness of 50 μm or lower and optimizing the cathode microstructure. Finally, years 4 and 5 will develop approaches for anode-free lithium plating and stripping on alloyed or engineered copper current collectors at relatively higher current densities aimed at improving the volumetric energy density of SSB with a high loading cathode and thin halide SE separator.

Impact. The proposed tasks and metrics aim at addressing the long-term VTO goal for developing SSBs at ambient temperature with energy density in the range of 500 Wh/Kg and 1000 Wh/L for electric drive vehicles. Advances in scalable processing of superionic SEs, stabilizing electrode-electrolyte interfaces, and promoting long cycle life are all needed to meet the energy density and cost targets for next-generation batteries for EVs.

Approach. The project employs a multi-faceted approach: (1) conduct solution-based synthesis of the metal halide superionic conductor as the platform to enable robust cathode-electrolyte interface (CEI) processing for SSBs, (2) infiltrate pore structures using solution-based processing that deposits high-conductivity SEs within cathode pores, and (3) facilitate lithium transport and improve stability using cation doping (divalent to introduce lithium vacancies, and lanthanum to prevent indium redox).

Out-Year Goals. Demonstrate single-layer, pouch-cell SSB containing a thin halide SE separator coupled with high-voltage cathodes with 70% capacity retention over 300 cycles at 2 mA/cm^2 in an anode-free SSB configuration that can attain 1000 Wh/L in prototype cells.

Collaborations. Y. Yao and team at University of Houston (UH) are funded collaborators for halide-based SSB fabrication, testing, and interfacial studies. The project also involves unfunded collaboration with SLAC for XAS and SXRD of SEs.

Milestones

1. Produce gram-scale quantities of Li_3InCl_6 SE using solvent-phase synthesis. (Q1, FY 2022; Completed)
2. Obtain phase-pure Li_3InCl_6 thin pellets with $\sim 1 \text{ mS}/\text{cm}^{-1}$ conductivity. (Q2, FY 2022; Completed)
3. Utilize neutron diffraction, XPS, Raman, and electron microscopy to characterize Li_3InCl_6 SE. (Q3, FY 2022)
4. Compare structure and Li^+ conductivity of Li_3InCl_6 prepared through solvent-mediated versus mechanochemical; $> 5\text{g}$ batch with ionic conductivity in the range of $1 \text{ mS}/\text{cm}^{-1}$. (Q4, FY 2022)

Progress Report

This quarter, the major task was understanding how to tune the reaction pathway for full utilization of the LiCl precursor into the Li_3InCl_6 structure for high conductivity. Specifically, this objective included utilizing ethanol and/or water-based synthesis approach.

The team has successfully scaled the synthesis of Li_3InCl_6 in two solvent systems: ethanol and water (Q1 and Q2 objectives). The largest product yield to date was 11 g at > 98% yield, and the conductivity was 0.5 mS cm^{-1} . LiCl is typically the major impurity. Please note that the team cannot quantify impurities smaller than 2% via XRD. Having achieved this result (synthesis method is given at the end), they turned to understanding how an excess amount of InCl_3 affected product purity and overall conductivity.

The team has found that adding 10% stoichiometric excess drastically reduces LiCl impurity level. Interestingly, the addition of up to 50% excess InCl_3 continued to show no additional impurity peaks from XRD. However, incorporation of excessive InCl_3 comes at the cost of conductivity. The best room-temperature conductivity to date is 0.9 mS cm^{-1} , which corresponds to 10% excess InCl_3 . Further excess lowers the conductivity, for example, at 50% excess InCl_3 the room-temperature conductivity is 0.1 mS cm^{-1} .

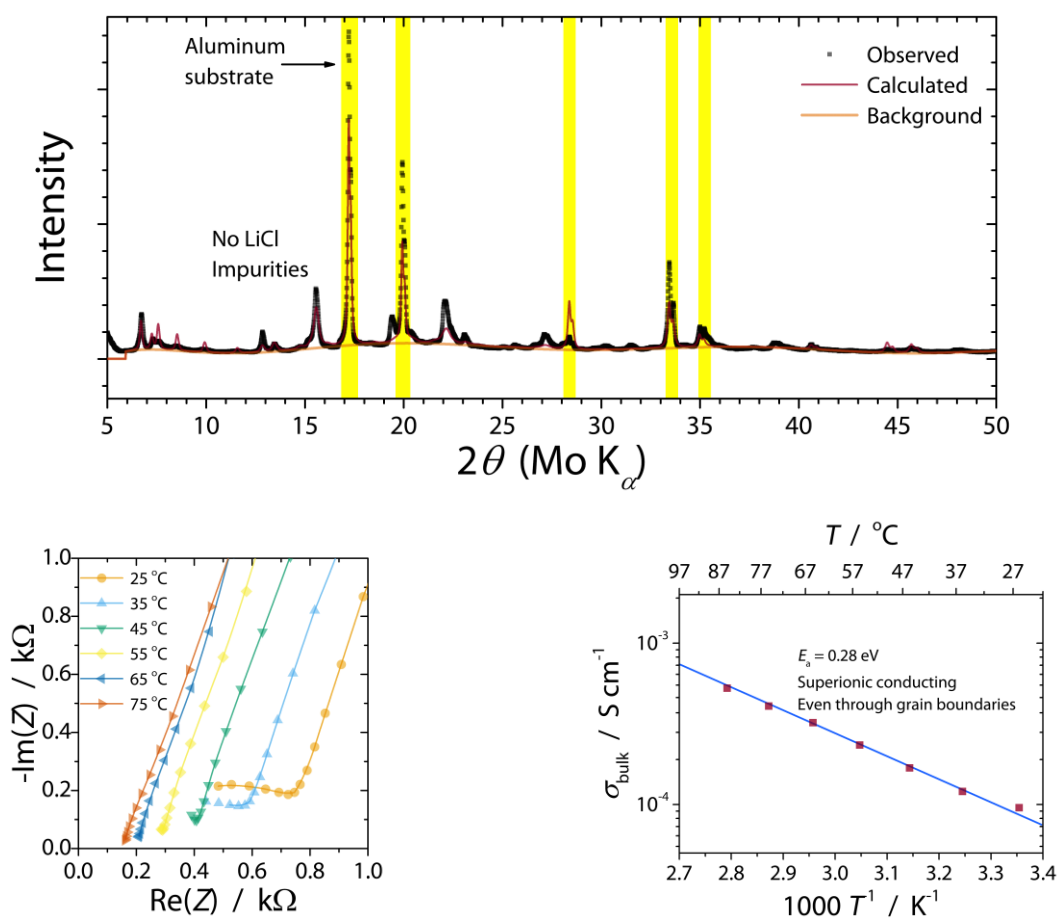


Figure 39. Results of the large-scale Li_3InCl_6 synthesis with 10% excess InCl_3 from ethanol solution. (top) X-ray diffraction shows no impurities other than aluminum substrate. (lower left) Nyquist plot shows electrolyte is highly conductive with some grain boundaries present after pressing at 5 bar. (lower right) Arrhenius plot shows product is a superionic conductor with low activation energy.

The decrease in conductivity due to the addition of excess InCl_3 appears to be a result of additional GB resistance. The team's working hypothesis is that the excess InCl_3 fills in occupancies within the structure, which is a layered structure that houses lithium within the galleries. As all the indium sublattice sites are filled, pressing a pellet introduces anisotropic effects on conductivity. Their next step is to test this hypothesis by combining high-resolution XRD with pressure-resolved impedance spectroscopy on pellets. From this experiment, they should be able to relate excess indium loading with indium site occupancies / anisotropic strain with ionic conductivity. They expect the result to show a "goldilocks" condition, where the pellet is densified enough to show little to no GB impedance, while not pressurized enough to elicit preferential orientation.

They have started synthesis of the material through mechanochemical means to set up the juxtaposition between materials synthesis for reporting in the fourth quarter. They are looking into filling porous polymer membranes with the starting solutions. This will serve as a model system for quickly optimizing the project's pore-filling protocol for Year 2 milestones.

Solution Made Synthesis Method. The team weighed stoichiometric amounts of InCl_3 and LiCl in a 1:3 ratio. They then dissolved this salt mixture in solvent, about 20 mL per 2 g for water or 50 mL per 2 g for alcohols. Solutions were sonicated while heating at 60°C for 1 hour, before loading onto a rotovap for *in vacu* solvent removal. The rotovap bath was set to 50°C for 1 hour, then 80°C for an additional hour. The resulting clear/colorless syrup was then placed in a 10^{-4} torr vacuum over at 80°C overnight. The material was then brought into an Ar-filled glovebox and loaded into a vacuum tube furnace and heated at 150°C for 4 hours (ramp rate was 2 C/min) and naturally cooled to room temperature. Conductivity was measured on a 10-Mpa cold pressed pellet using a SP240 Biologic potentiostat.

Patents/Publications/Presentations

The project has no patents, publications, or presentations to report this quarter.

Task 1.15 – Developing an *In Situ* Formed Dynamic Protection Layer to Mitigate Lithium Interface Shifting: Preventing Dendrite Formation on Metallic Lithium Surface to Facilitate Long Cycle Life of Lithium Solid-State Batteries
(Deyang Qu, University of Wisconsin, Milwaukee)

Project Objective. The objective of this project is to research, develop, and test Li-metal-based batteries that implement solid LICs equipped with a formed dynamic protection layer. The proposed project aims to enable safe, long-cycle lithium anodes to achieve cell performance targets of 400 Wh/Kg, over 100 cycles, with 15-year shelf life, and < \$100/KWh cost.

Project Impact. Project efforts are to contribute an in-depth understanding of the lithium interface and dendrite growth prevention to the field of Li-metal batteries, which will pave the way for eventual development of high-energy-density, low-cost, and long-lasting lithium batteries. This advancement could be a crucial selling point for the greater adoption of EVs. This project will make possible the translation of fundamental research into practical implementation of high-energy lithium anodes, enabling eventual achievement of cell performance targets.

Approach. The novelty of this approach is that the team intends to mitigate the dendrite problem by creating a dynamic protection layer during the interface shift to prevent dendrite formation throughout battery operation.

Out-Year Goals. The project has three *one-year* goals: (1) *in situ* diagnostic tools are verified; (2) thin SSE and cathode are made; and (3) all-solid-state cells are made.

Collaborations. The PI is the Johnson Control Endowed Chair Professor, who has close and frequent collaboration with Johnson Controls’ scientists and engineers. The collaboration enables the team to validate the outcomes of fundamental research in pilot-scale cells. The PI also has been working closely with top scientists at ANL, BNL, Lawrence Berkeley National Laboratory (LBNL), and PNNL and with U. S. industrial collaborators, for example, GM, Millipore, and Clarios. In addition, the team works with international collaborators in China, Japan, and South Korea. These collaborations will be strengthened and expanded to give this project a vision with both today’s state-of-the-art technology and tomorrow’s technology in development, while incorporating feedback from material designers and synthesizers upstream, as well as from industrial end users downstream.

Milestones

1. Coated lithium anode with dendrite suppression demonstrated. Demonstrate effectiveness of inorganic artificial protective layer. (Q1, FY 2022; Completed)
2. Lithium anode with suppressed dendrite growth demonstrated. Demonstrate effectiveness of artificial protective layer. (Q2, FY 2022; Completed)
3. Down select materials and cell fabrication method for final cell build. (Q3, FY 2022; In progress)
4. All-solid-state cell build and test. (Q4, FY 2022; In progress)
5. Dendrite suppression demonstrated; cell performance verified. (Q4, FY 2022; In progress)

Progress Report

Last quarter, the team developed a solvent-free dry-film approach to fabricate thin, flexible SSE with 0.4 wt% fibrous polytetrafluoroethylene (PTFE). The thickness was 55 μm for the SSE membrane, which displayed an ionic conductivity of 1.4 mS cm^{-1} at 25°C after compression.

This quarter, the team constructed and tested an ASSLB. Collaborating with Millipore, polyimide-graphene (PI-G) nanocomposite was synthesized through an *in situ* polycondensation process from two inexpensive stock compounds, 1,4,5,8-naphthalenetetracarboxylic dianhydride and ethylenediamine. Functionalized graphene (Gr) sheets were incorporated during the process to enhance the electronic conductivity of polyimide. The electronic conductivity of the as-synthesised PI-G composite was measured to be 16.5 mS cm^{-1} at 25°C, which outperformed most of the common inorganic cathode materials (10^{-6} - 10^{-4} S cm^{-1}). PI-G was used as the cathode material in the ASSLB using a thin $\text{Li}_6\text{PS}_5\text{Cl}$ SE made with the dry process.

In this study, the dry process was used to manufacture $\text{Li}_6\text{PS}_5\text{Cl}$ membrane. Despite the binder content being merely 0.2 wt%, the as-fabricated SSE membrane in Figure 40a was free-standing and demonstrated high flexibility. After cold pressing, SSE thickness was reduced from 70 μm (Figure 40b) to 46 μm (Figure 40c), with a compaction density of 2.6 g cm^{-3} . As marked by arrows, the PTFE fibrils were well retained within the

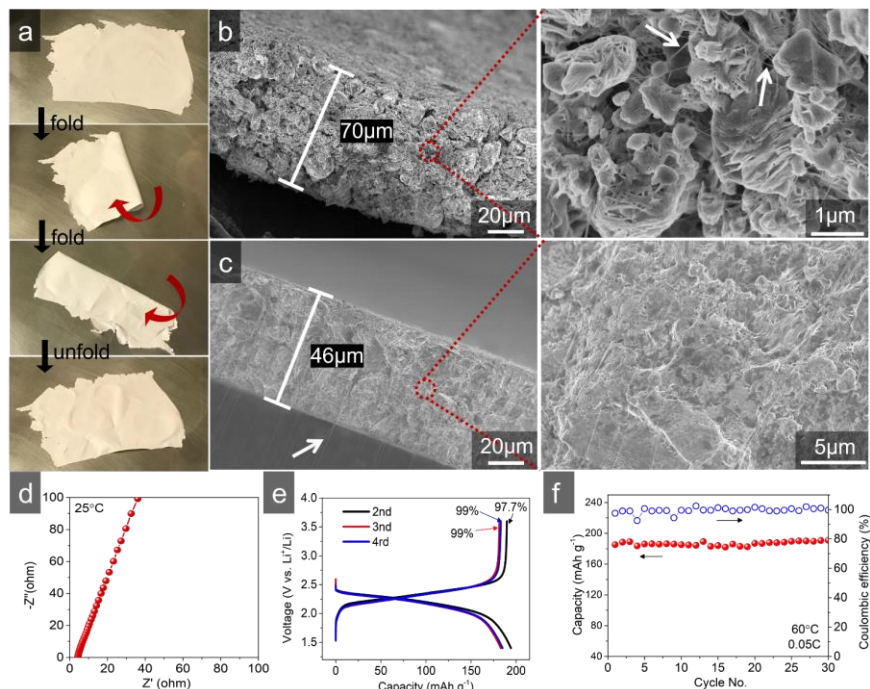


Figure 40. (a) Flexibility test of free-standing solid-state electrolyte (SSE) membrane. (b) Cross-sectional scanning electron microscopy images of SSE membrane (b) before and (c) after cold pressing. (d) Ionic conductivity measurement of SSE membrane at 25°C. (e) Galvanostatic voltage profiles and (f) cycling performance of sheet-type $\text{PI}|\text{Li}_6\text{PS}_5\text{Cl}|\text{LiIn}$ cell at 60°C.

much-densified SSE structure. The ionic conductivity of the SSE membrane was measured to be 1.4 mS cm^{-1} (Figure 40d), slightly lower than that of the binder-free SSE pellet (1.8 mS cm^{-1}), owing to the ionic insulating nature of PTFE. Despite this, the areal resistance was only 3.3 $\Omega \text{ cm}^2$, more than tenfold lower than the SSE pellet (39 $\Omega \text{ cm}^2$; the team used 0.7-mm thickness in the calculation). Sheet-type $\text{PI}|\text{Li}_6\text{PS}_5\text{Cl}|\text{LiIn}$ full cell in Figure 40e shows a discharge plateau of 2.2 V (versus Li^+/Li) and an attainable capacity of $\sim 180 \text{ mAh g}^{-1}$, consistent with that of the pellet-type cells. Cycling performance in Figure 40f shows almost no capacity decay with an average CE > 99% over 30 cycles.

Patents/Publications/Presentations

Publications

- Ji, W., X. Zhang, D. Zhang, H. Huang, T. Lambert, and D. Qu.* “Practically Accessible All-Solid-State Batteries Enabled by Organosulfide Cathodes and Sulfide Electrolytes.” *Advanced Functional Materials* (2022). doi: 10.1002/adfm.202202919.
- Ji, W., X. Zhang, H. Qu, L. Xin, A. T. Luedtke, H. Huang, T. H. Lambert, and D. Qu.* “Polyimide as a Durable Cathode for All-Solid-State Li(Na)–Organic Batteries with Boosted Cell-Level Energy Density.” *Nano Energy* 96 (2022): 107130.

Task 1.16 – Polyester-Based Block Copolymer Electrolytes for Lithium-Metal Batteries (Nitash Balsara, University of California, Berkeley)

Project Objective. The project objective is to design and synthesize polyester-based block copolymer electrolytes that can enable full-cell cycling at 1 mA/cm² or greater for 300 cycles. The cell comprises Li-metal anode, 4.5 V NMC cathode, and thin separators (20-50 μm) casted from the aforementioned block copolymer.

Impact. Polymer electrolytes (PEs) offer increased stability in lithium batteries in comparison to more widely used LEs. Block copolymer-based electrolytes containing both soft, ion-conducting domains and rigid, nonconducting domains offer the opportunity to tune both mechanical and electrical properties separately. Most block copolymer electrolytes studied thus far comprise PEO as the conducting domain. The team hopes to develop polyester-based electrolytes that exhibit much higher transport properties and limiting currents than PEO-based electrolytes. An all-solid full cell with this new block copolymer electrolyte, a Li-metal anode, and an NMC cathode will have much higher energy density than current Li-ion technology.

Approach. The team will begin by synthesizing several series of polyester homopolymers and fully characterizing their blends with lithium salts as PEs in Li-Li symmetric cells. Next, they will make block copolymer electrolytes based on the most promising candidate and measure the electrochemical and mechanical properties thoroughly. Finally, they will assemble full cells with the optimum block copolymer electrolytes together with lithium metal and a 4.5 V NMC cathode.

Out-Year Goals. In the first year, the team will establish an efficient synthesis and characterization platform for polyester electrolytes. Several polyesters will be synthesized, and electrolytes will be made by blending each polymer with lithium salt. Transport properties (such as conductivity and current fraction) and limiting current of resulting electrolytes will be measured in Li-Li symmetric cells. The highest performing PE will be used as the conducting phase in the block copolymer design in the second year.

Collaborations. There are no active collaborations this quarter.

Milestones

1. Establish synthesis platform: synthesize at least two polyester electrolytes. (Q1, FY 2022; Completed)
2. Conductivity: measure conductivity of at least two electrolytes. (Q2, FY 2022; Completed)
3. Symmetric cell characterization: measure salt diffusion coefficient and current fraction of at least two electrolytes. (Q3, FY 2022; In progress)
4. Complete characterization: measure thermodynamic factor and thereby complete characterization of at least one polyester electrolyte. (Q4, FY 2022)

Progress Report

The team completed this quarter's milestone: measure conductivity of at least two electrolytes.

They measured conductivity of electrolytes based on the four polymers they made last quarter, with structures shown in Figure 41a. They made four PEs comprising 40 wt% of LiTFSI salt and 60 wt% of each polymer. They define salt concentration as $r = [\text{Li}]/[\text{O}]$, where all oxygen atoms in the polymer are counted (a total of four in every repeating unit in Figure 41a). Due to the difference in molecular formula of these polymers, r falls between 0.07–0.11. The well-studied PEO/LiTFSI system exhibits a broad maximum in conductivity in this range of r values.^[1] In Figure 41b, they show ionic conductivity (κ) values of these electrolytes measured in Li-polymer-Li symmetric cells at 90°C, along with their glass transition temperature (T_g) values. Ionic conductivity increases drastically with the increasing chain length of diol until $n = 5$. This is expected because ion transport is usually facilitated by low T_g polymers. Poly(pentylene malonate) (PPM) / LiTFSI electrolyte almost has an order of magnitude higher conductivity than the poly(ethylene malonate) (PEM) / LiTFSI electrolyte, reaching 10^{-3} S/cm at 90°C. This is comparable with PEO/LiTFSI electrolytes reported in literature.^[1] The ionic conductivity decreased when n was increased from 5 to 6. This preliminary screening suggests that the PPM/LiTFSI electrolyte has the optimum ionic conductivity among this series of polyester-based electrolytes.

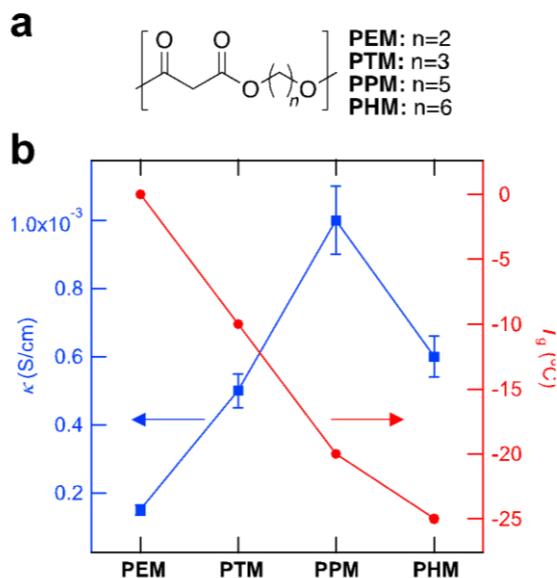


Figure 41. (a) Structures of a series of poly(alkyl malonates) synthesized for this project. (b) Ionic conductivity (κ , blue squares) and glass transition temperature (T_g , red circles) of polymer electrolytes comprising 40 wt% of LiTFSI salt at 90°C.

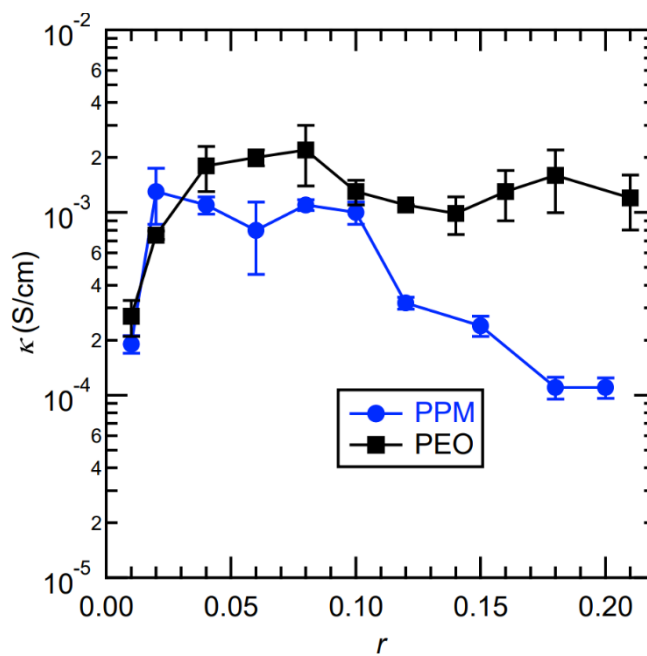


Figure 42. The effect of salt concentration r on ionic conductivity, κ , of PPM/LiTFSI (blue circles) and PEO/LiTFSI (black squares) electrolytes at 90°C. Data for PEO/LiTFSI electrolytes were taken from previous work.^[1]

The effect of salt concentration (r) on κ of PPM/LiTFSI electrolytes is shown in Figure 42. Also shown are values of the same parameters for PEO/LiTFSI electrolytes as reported in literature.^[1] The conductivity of PPM/LiTFSI electrolytes in the range $0.02 \leq r \leq 0.10$ is about 10^{-3} S/cm. These values are close to the conductivity of PEO/LiTFSI electrolytes. In the range $0.10 \leq r \leq 0.20$, κ of PPM/LiTFSI electrolytes drifts toward values that are significantly lower than PEO/LiTFSI electrolytes.

Next quarter, the team will carefully examine the salt diffusion coefficient and current fraction of their polyester electrolytes in Li-Li symmetric cells.

Reference

- [1] Pesko, D. M., Z. G. Feng, S. Sawhney, J. Newman, V. Srinivasan, and N. P. Balsara. “Comparing Cycling Characteristics of Symmetric Lithium-Polymer-Lithium Cells with Theoretical Predictions.” *Journal of The Electrochemical Society* 165 (2018): A3186–A3194.

Patents/Publications/Presentations

The project has no patents, publications, or presentations to report this quarter.

Task 1.17 – Advanced Polymer Materials for Batteries (Zhenan Bao and Yi Cui, Stanford University)

Project Objective. This project will develop new polymer materials for batteries. The team will develop polymer coatings with specific mechanical properties that can accommodate the volume expansion and contraction of the Li-metal anode associated with deposition and stripping (charging and discharging).

Project Impact. The cycling stability and CE of Li-metal electrodes will be increased by implementation of a polymer-based protective layer that functions as an artificial solid electrolyte interphase (SEI) with desired properties. The improved performance will enable further development toward practical utilization of Li-metal anodes with higher cycling efficiency and less susceptibility to dendrite-based failure.

Approach. The project uses soft polymer coatings with dynamic crosslinking to give the resulting polymers liquid-like rheological properties and stretchable and self-healing properties. In previous work, the team has shown that such coatings resulted in uniform deposition/stripping of lithium metal and improved cycling stability of Li-metal electrodes. To understand the design rules for effective polymer coatings, they chose a few representative polymers to systematically understand structure property relationships. Here, they investigate the correlation between surface energy of the polymer and exchange current for lithium deposition.

Out-Year Goals. Work will progress toward the correlation between dielectric constant and exchange current. These findings will enable further understanding and development of various polymer coatings for protecting Li-metal anodes.

Collaborations. The team is collaborating with J. Qin at Stanford University.

Milestones

1. New lithium anode coating design. Design the polymer chemistry through DFT and contact angle measurement to find salt affinitive and solvent phobic moieties. (Q1, FY 2022; Completed)
2. Characterize the selective transport of salt over solvents for this polymer. (Q2, FY 2022; Completed)
3. Characterize the impact of the polymeric coating on lithium deposition morphology and short-term CE. (Q3, FY 2022)
4. Coat thin Li-metal electrodes with the polymeric coating and achieve stable lithium cycling for ≥ 200 cycles at 2.5 mAh/cm² capacity and C/3 D/5 current density in lean electrolyte condition. (Q4, FY 2022)

Progress Report

To demonstrate the selectivity of the salt affinity solvent phobic (SASP) polymer, the team designed an H-cell experiment (Figure 43a). The left-hand side (LHS) of the H-cell was filled with 3 mL of 1 M LiTFSI dimethoxyethane (DME) electrolyte; the right-hand side (RHS) was filled with 6 mL DME solvent. The two sides were separated by two layers of separators with 100 mg of polymer sandwiched. As the system equilibrates, the concentration difference drives the diffusion of salt from LHS to RHS and vice versa for DME. To avoid vacuum build-up on solvent flow, the caps of the H-cell were loosened. Visually, the lowering of the liquid line on the RHS represents DME migration from right to left. The salt concentration was evaluated after 3 hours with ^{19}F NMR, and the measured concentrations of LiTFSI are listed in Figure 43b. When no polymer was present, liquid levels of the two sides matched after 3 hours, indicating significant DME diffusion from right to left. When the SASP polymer was inserted in the H-cell, the liquid level difference was maintained after 3 hours. NMR spectrum revealed that LiTFSI salt has migrated from left to right, resulting in 0.025 M of LiTFSI on RHS. The team noted the LiTFSI concentration remained at 1 M on LHS, instead of lowering, and they argue that the slight evaporation of DME compensated for the salt diffusion and maintained the salt concentration on the LHS. To examine the necessity of introducing a second solvent phobic side chain to the salt affinitive polymer, they conducted an H-cell experiment with only pyrrolidinium (trifluoromethanesulfon)imide (PyTFSI) polymer. When there is only salt affinitive polymer present, the liquid level on the RHS almost matches that of the LHS, indicating significant solvent migration. There is also salt migration from left to right, and the RHS reaches 0.051 M LiTFSI after 3 hours of rest.

The presence of an electrolyte phobic side chain also limited the swelling of the polymer in 1 M LiTFSI DME electrolyte. Specifically, the team compared the mechanical properties and ionic conductivities of the PyTFSI (only salt affinitive polymer, Figure 43c) and SASP (Figure 43d) polymer before and after soaking in the electrolyte for 8 hours. They characterized the frequency dependent modulus of the polymer in rheological measurements: the loss modulus (G'') represents the liquid characteristic, and the storage modulus (G') represents the solid characteristic. Before soaking, both the SASP and the PyTFSI polymer showed viscous behavior, with G'' higher than G' in the characterized frequency range. After swelling, the polymer showed decrease in both storage and loss moduli, indicating reduction in mechanical strength. Specifically, the team characterized the relative liquid-to-solid characteristic of the polymer by calculating the $\tan(\delta)$ (ratio between G'' and G') at the angular frequency of 10 rad s^{-1} . For the PyTFSI polymer, the $\tan(\delta)$ increased close to an order (1.7 to 16) on soaking, while the SASP polymer's $\tan(\delta)$ remained relatively constant (2.3 to 2.4). Although SASP and PyTFSI polymers can both be swelled by the solvent, SASP maintains its relatively solid-liquid characteristics, while the PyTFSI polymer becomes more liquid-like, indicating it is less resistive to solvent swelling.

Beyond changes in mechanical properties, the team also measured the ionic conductivities of the polymer before and after soaking (Figure 43e) with EIS at 25°C . The ionic conductivity in the dry state is attributed to ionic dissociation of PyTFSI moieties, and the wet state ionic conductivity is contributed by both the tethered ionic moieties as well as salt in the electrolyte. After soaking the polymer in the electrolyte, the conductivities of PyTFSI increased an order (0.012 to 0.116 mS cm^{-1}), while the conductivities of SASP remained within one order (0.013 to 0.043 mS cm^{-1}). This is due to the higher solvent resistance for the SASP polymer. Based on both the mechanical characterization and ionic conductivity measurements, they conclude that the addition of solvent phobic side chain can improve the solvent resistance of the polymer.

The team further examined the SASP polymer's ability to induce salt-derived SEI formation with surface analysis technique XPS. They assembled Li|Cu cell with polymer-coated copper current collector. They stripped and plated lithium through the polymer layer in 1 M LiTFSI DME electrolyte for 10 cycles to produce a layer of SEI underneath the polymer coating. After that, the cell was disassembled, and the copper foil was transported to the XPS chamber in an air-free transfer process. The oxygen 1s spectra of the cycled copper electrode after 2 minutes of sputtering are shown in Figure 43f. They attribute the peak at 530.9 eV to $-\text{NO}_x/\text{SO}_x$ (LiTFSI salt breakdown), and the peak at 533.8 eV to $-\text{RO}-\text{CO}_x-\text{Li}$ (DME breakdown). By calculating the

percentage of the peak area attributed to salt/solvent breakdown, they can quantify the polymer coating's ability to form salt-derived SEI. When there was no coating, 56% of the SEI was attributed to salt decomposition. When the PyTFSI polymers were present, the salt-derived SEI content was increased to 63%. This content can be further improved to 73% when SASP coating is presented. Due to the selective transporting ability of the SASP polymer, lithium anode has limited access to solvent molecules, and the percentage of salt-derived SEI content was increased.

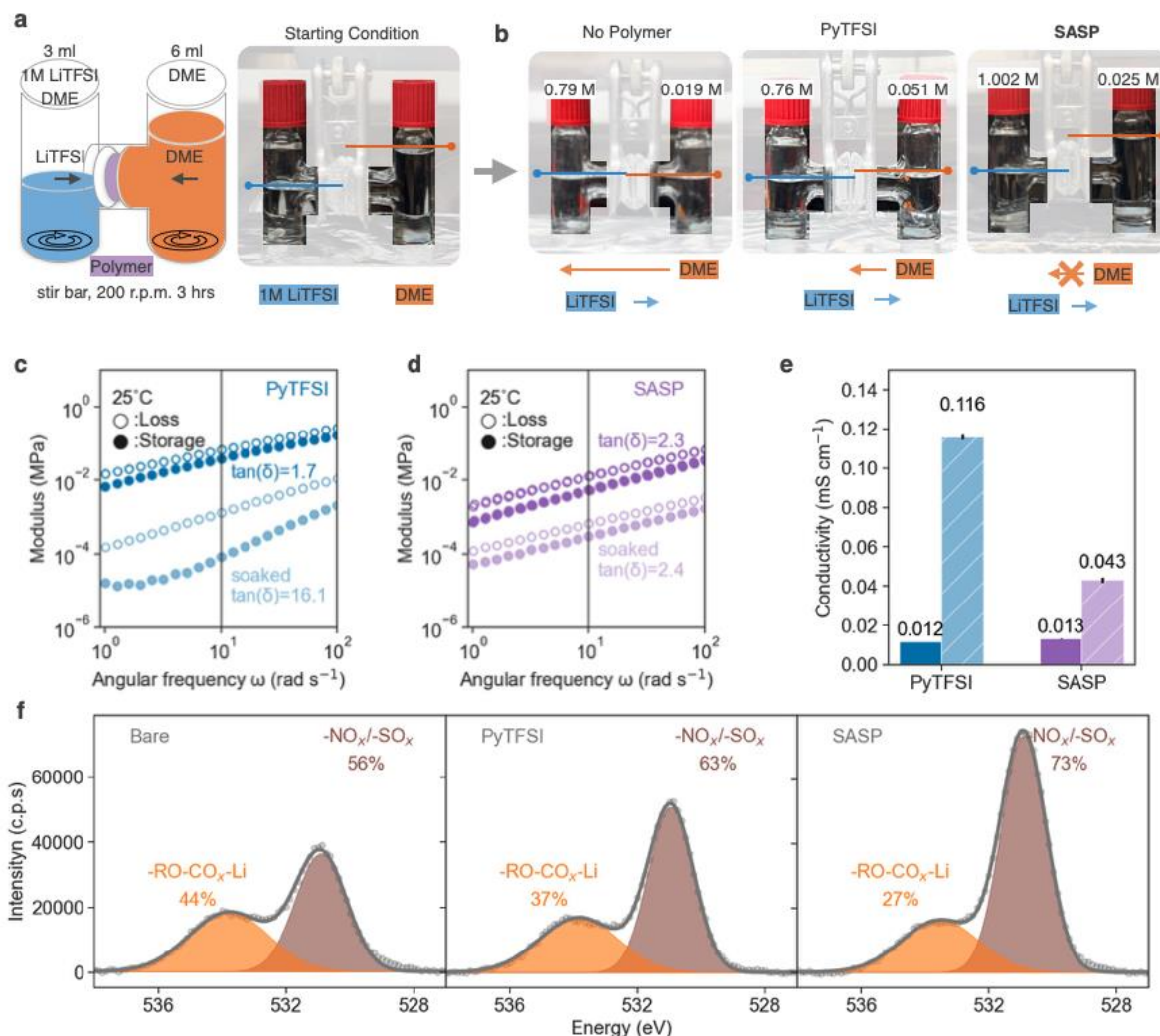


Figure 43. Selectivity of PyTFSI and salt affinity solvent phobic (SASP) polymer. (a) Experimental set-up for H-cell experiments. (b) H-cell experiment with the polymer sandwiched in the middle, with images taken after 3 hours with the measured LiTFSI concentration labeled on the graph; rheological frequency sweep of the polymer after soaked in 1 M LiTFSI DME electrolyte for 8 hours, with the $\tan(\delta)$ at 10 rad s^{-1} marked: (c) PyTFSI. (d) SASP, (e) conductivity (25°C) of the polymer before and after soaked in 1 M LiTFSI DME for 8 hours, and (f) oxygen 1s X-ray photoelectron spectroscopy of SEI on the anode. The signals attributed to either salt or solvent decomposition were separated with their relative percentage marked out.

Patents/Publications/Presentations

Publications

- Yu, Z., P. E. Rudnicki, Z. Zhang, Z. Huang, H. Celik, S. T. Oyakhire, Y. Chen, X. Kong, S. Kim, X. Xiao, H. Wang, Y. Zheng, G. A. Kamat, M. Kim, S. F. Bent, J. Qin, Y. Cui, and Z. Bao. “Rational Solvent Molecule Tuning for High-Performance Lithium Metal Battery Electrolytes.” *Nature Energy* 7 (2022): 94–106.
- Kim, M. S., Z. Zhang, P. E. Rudnicki, Z. Yu, J. Wang, H. Wang, S. T. Oyakhire, Y. Chen, S. C. Kim, W. Zhang, D. T. Boyle, X. Kong, R. Xu, Z. Huang, W. Huang, S. F. Bent, L. Wang, J. Qin, Z. Bao, and Y. Cui. “Suspension Electrolyte with Modified Li⁺ Solvation Environment for Lithium Metal Batteries.” *Nature Materials* 21 (2022): 445–454.
- Wang, H., Z. Yu, X. Kong, S. Kim, D. T. Boyle, J. Qin, Z. Bao, and Y. Cui. “Liquid Electrolyte: The Nexus of Practical Lithium Metal Batteries.” *Joule* 6 (2022): 588–616.
- Zhang, Z., Y. Li, R. Xu, W. Zhou, Y. Li, S. T. Oyakhire, Y. Wu, J. Xu, H. Wang, Z. Yu, D. T. Boyle, W. Huang, Y. Ye, H. Chen, J. Wan, Z. Bao, W. Chiu, and Y. Cui. “Capturing the Swelling of Solid-Electrolyte Interphase in Lithium Metal Batteries.” *Science* 375 (2022): 66–70.

Presentations

- American Chemical Society (ACS) Spring Meeting, San Diego, California (March 2022): “Rationally Designed Liquid Electrolytes for Li Metal and Anode-Free Batteries”; Z. Yu, Y. Cui, and Z. Bao.
- ACS Spring Meeting, San Diego, California (March 2022): “Advanced Polymer Interfaces for Lithium Metal Anode”; Z. Huang, Y. Cui, and Z. Bao.

Task 1.18 – Molecular Ionic Composites: A New Class of Polymer Electrolytes to Enable All-Solid-State and High-Voltage Lithium Batteries (Louis Madsen, Virginia Polytechnic Institute and State University)

Project Objective. Based on a newly discovered class of SPE materials, that is, molecular ionic composites (MICs), the overall objective is to develop solid-state lithium conductors targeted for use in transportation applications. MICs form a mechanically stiff, electrochemically stable, and thermally stable matrix. Specific objectives include the following: (1) development of robust MIC electrolyte thin films (~ 20 μm) to serve as simultaneous nonflammable separators and dendrite-blocking Li^+ conductors, (2) electrochemical quantification of key performance metrics including electrolyte stability, interfacial reactions, and suitability/compatibility with a range of electrode materials, and (3) comprehensive investigation of ion transport mechanisms and electrode-electrolyte interfacial reactivity under practical operating conditions using NMR and synchrotron X-ray analyses.

Project Impact. Commercialization of Li-metal SSBs is hampered by lack of a functional nonflammable SE that can provide high ionic conductivity, wide electrochemical window, favorable mechanical properties to inhibit lithium dendritic growth, and low interfacial resistance. The tunable MIC materials platform has potential to fulfill these requirements with relatively simple fabrication techniques, and thus shows promise for enabling nonflammable SSBs that can be optimized for low cost and high energy density.

Approach. MICs rely on a unique polymer that is similar to Kevlar[®] in its strength, stiffness, and thermal stability, but with densely spaced ionic groups that serve to form an electrostatic network that permeates mobile ions in the MIC. The team can tailor the ion concentrations and types to yield MIC electrolyte films that are electrochemically compatible with Li-metal anode as well as a range of high-voltage layered cathodes. They are searching the composition space of lithium salts, electrochemically compatible ionic liquids (ILs), and polymer [poly(2,2'-disulfonyl-4,4'-benzidine terephthalamide), or PBDT] molecular weight to determine best composition windows for MIC electrolytes. The team is also investigating best methods for casting thin films in terms of temperature, solvent/evaporation conditions, and control over the initial liquid crystalline gel formation point. Concurrently, they are testing MIC films in various electrochemical cells, quantifying transport and structural/morphology parameters with NMR and X-ray techniques, and measuring key mechanical (dynamic mechanical thermal analysis, stress-strain) and thermal (DSC, TGA) properties.

Out-Year Goals. This year, the team will generate a predictive model to understand the relationship between the mobility of all ions and the MIC synthesis parameters. They will establish the testing protocol for NMR measurements under operating conditions. They will also study the surface chemistry of the MIC electrolyte before and after cycling. The team will identify methods to mitigate interfacial degradation. They will then test the final project electrolyte in full cell and develop specifications.

Collaborations. The team is collaborating with T. J. Dingemans' group at University of North Carolina, Chapel Hill, in which they are forming composites based on PBDT polymer and carbon materials such as Gr oxide and are beginning to develop charged rigid-rod polymers building on the PBDT structure. The team is exploring shear rheology and broadband dielectric spectroscopy collaboration with R. H. Colby at PSU. They are collaborating with D. Nordlund and Y. Liu at SLAC and S-M. Bak at BNL to conduct synchrotron X-ray studies on MIC films.

Milestones

1. Multivariant analysis of experimental parameters and electrochemical properties. (Q1 FY 2022; Completed)
2. *In situ* experiments implementing NMR spectroscopy and diffusometry at different cell states of charge. (Q2, FY 2022; In progress)

3. Spectroscopic surface analysis of cathode, anode, and MIC electrolyte after various cycling history. (Q3, FY 2022; In progress)
4. ASR: MIC/Li $\leq 10 \Omega \text{ cm}^2$ and cathode/MIC $\leq 50 \Omega \text{ cm}^2$ / cells. (Q4, FY 2022; In progress)

Progress Report

This quarter, the team continued to evaluate performance of PBDT as a polymer binder for LiFePO₄ (LFP) cathodes (and eventually others). The long-term cycling stability of such cathodes with 3% PBDT binder is compared to cathodes made with 3% polyvinylidene (di)fluoride (PVDF) binder. Figure 44 shows the specific discharge capacity of LFP electrodes cycled at 4C rate for 1000 cycles at 22°C following 5 initial cycles at 0.2C. The team observes that the 3% PVDF-LFP electrodes have slightly higher specific capacity at 4C rate than the 3% PBDT-LFP, which is due to the higher electrolyte uptake of PVDF, as reported previously. However, a notable capacity decay, from 127 mAh/g to 120 mAh/g, is observed for the 3% PVDF-LFP electrodes after 560 ~ 800 cycles, while the capacity of 3% PBDT-LFP remains nearly constant for 1000 cycles. Further experiments show that 3% PBDT-LFP electrodes start to show capacity decay only after 1100 ~ 1500 cycles (Figure 45). Thus, the LiFePO₄ electrode prepared with PBDT as the binder has better cycling stability over PVDF, making PBDT a promising fluorine-free binder material to enable Li-ion batteries with no significant performance decay over long-term cycling.

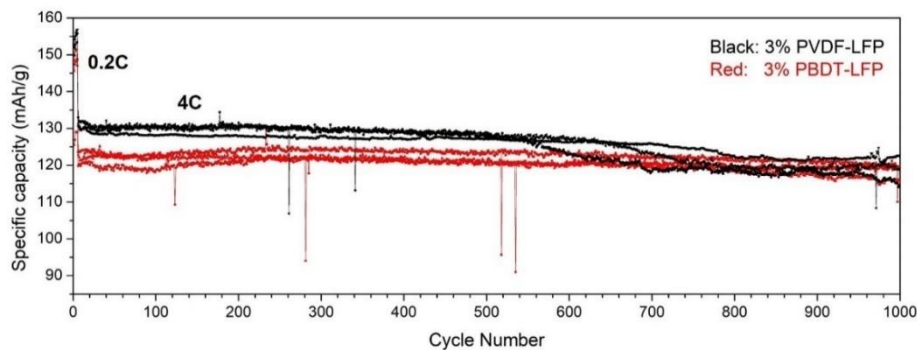


Figure 44. Specific discharge capacity of LiFePO₄ electrodes prepared with 3% PBDT (red) and 3% PVDF (black) as binder over long-term cycling at 22°C. Performances of three cells are shown for each type of electrode. The cells are cycled at 0.2C for 5 cycles followed by 1000 cycles at 4C rate. Occasional pausing of the battery tester causes a few inconsistent data points in the plot. Electrodes with PBDT binder demonstrate better long-term cycling stability despite their slightly inferior capacity compared to their PVDF counterparts.

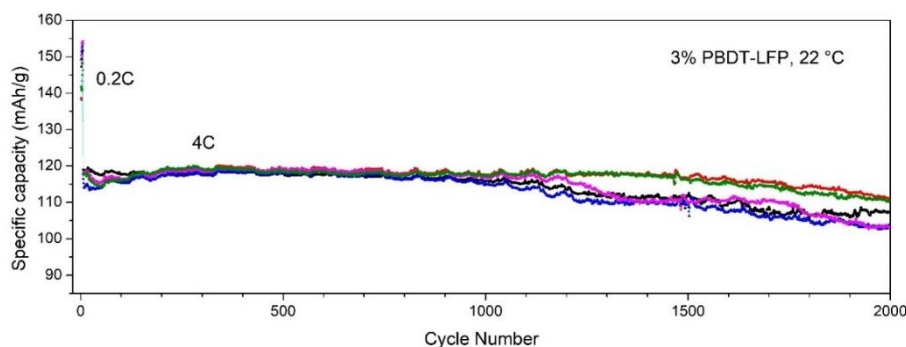


Figure 45. Specific discharge capacity of five LiFePO₄ electrodes with 3 wt% PBDT as binder when cycled at 22°C. The cells are cycled at 0.2C for 5 cycles followed by 2000 cycles at 4C rate. Capacity decay is only observed after 1100 ~ 1500 cycles; capacity retention after 2000 cycles at 4C rate is as high as 89%.

Besides this long-term cycling performance, the team has also evaluated the mechanical integrity of the electrodes to characterize the binding strength of PBBDT versus PVDF. LFP electrodes were cut into slices and adhered to a tape and then peeled off (Figure 46). For the 3% PVDF-LFP electrode, the LiFePO_4 and carbon black particles peel off easily, and the carbon coating layer on the aluminum substrate is almost intact. This suggests that the binding strength between the carbon coating layer and the electrode particles is weak. When using PBBDT as the binder, a higher force is needed to peel the electrode off, as evidenced by the curling of the current collector (carbon-coated aluminum) after the test. Some of the carbon coated on the aluminum also peels off during the test, leading to exposure of the metallic luster of the aluminum. This strongly suggests that PBBDT endows higher binding strength between the electrode particles and the current collector. In combination with the better long-term cycling stability discussed and the similar rate capability of 3% PBBDT-LFP electrodes compared to the 3% PVDF-LFP electrodes, the team believes PBBDT holds great potential as a polymer binder for commercial electrodes.

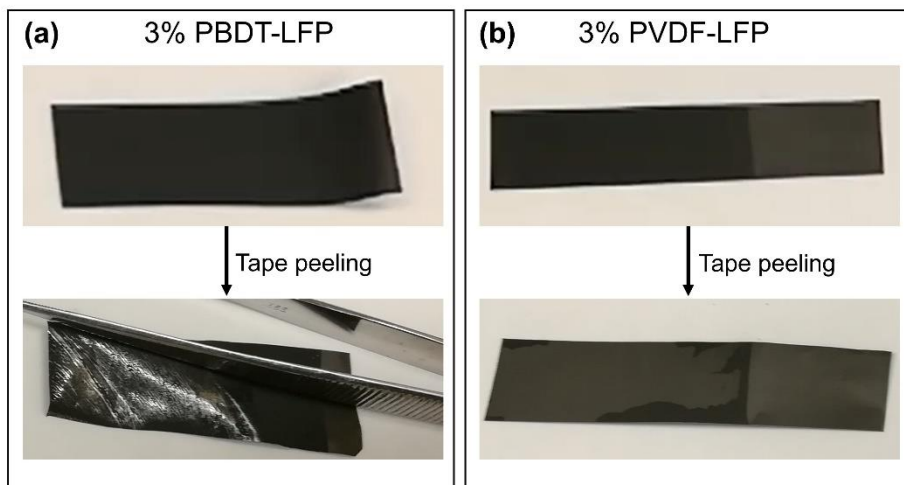


Figure 46. Images of the electrodes before and after tape peeling tests. The electrodes are pressed on an adhesive tape and then peeled off. The thin carbon coating layer on the aluminum substrate stays intact after the peeling test when using PVDF as the binder. However, when using PBBDT as the binder, the majority of the carbon coating layer is peeled off along with the LiFePO_4 and carbon particles, exposing the metallic luster of the aluminum substrate. These tests strongly indicate that PBBDT has higher binding strength than PVDF.

The team is continuing to improve interfacial compatibility between MICs and layered cathodes. To improve the cycle life of MIC-based, high-voltage SSBs, they coated Nb_2O_5 onto pristine NMC-622 materials to further mitigate side reactions at the electrode-electrolyte interfacial region. By tuning the concentration of coating agent and modulating synthesis conditions, they successfully prepared Nb_2O_5 -coated NMC-622 materials with good capacity retention and comparable discharge capacity in LE systems (modified 0.7% material in Figure 47). The team will apply the coated materials to SSBs and determine if the cycle life can be elongated.

The team recently probed the evolution of ionic heterogeneity as well as degradation processes of MIC electrolyte for high-voltage SSLBs. Figure 48 shows examples of XAS and X-ray fluorescence (XRF) imaging obtained at beamline TES (8-BM, tender energy X-ray absorption spectroscopy beamline) at National Synchrotron Light Source – II (NSLS-II). The distinct absorption features of the sulfur K-edge allowed the team to interpret oxidation state, the characteristic bonding between the sulfur atom and its neighboring elements. An energy range of 1 to 5 keV and spatial resolution of $2\ \mu\text{m}$ are

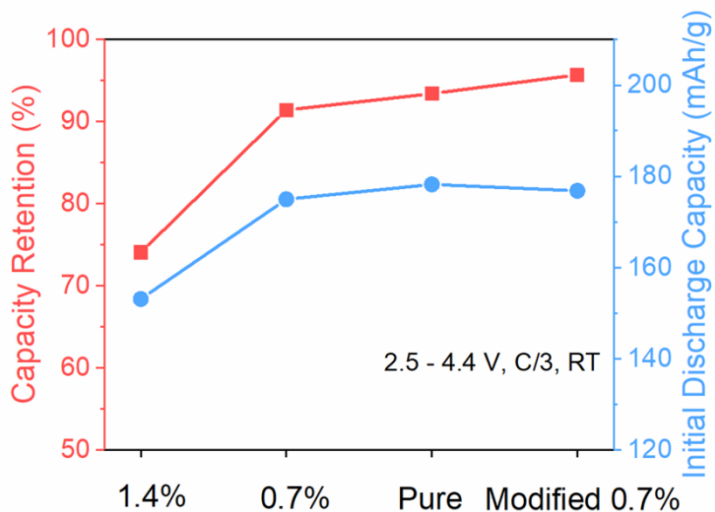


Figure 47. Electrochemical performance of different concentrations of Nb_2O_5 -coated NMC-622 materials cycled in liquid electrolyte systems (LP57 + 2%VC). The capacity of the 50th cycle is used to calculate capacity retention.

suitable for imaging of the ionic species in the MIC electrolyte. The capability of TES 8-BM also facilitates the characterization of spatial heterogeneity of ionic species inside the novel PE via *in situ* 3D fluorescence imaging and tomography. Initial XAS results are enabling identification of the evolution of chemical species from their characteristic X-ray absorption near edge structure (XANES) information. As the team further analyzes and interprets these results, they envision that their discovery will provide fundamental knowledge about the ion dynamics and PE decomposition process to better understand cell failure mechanisms.

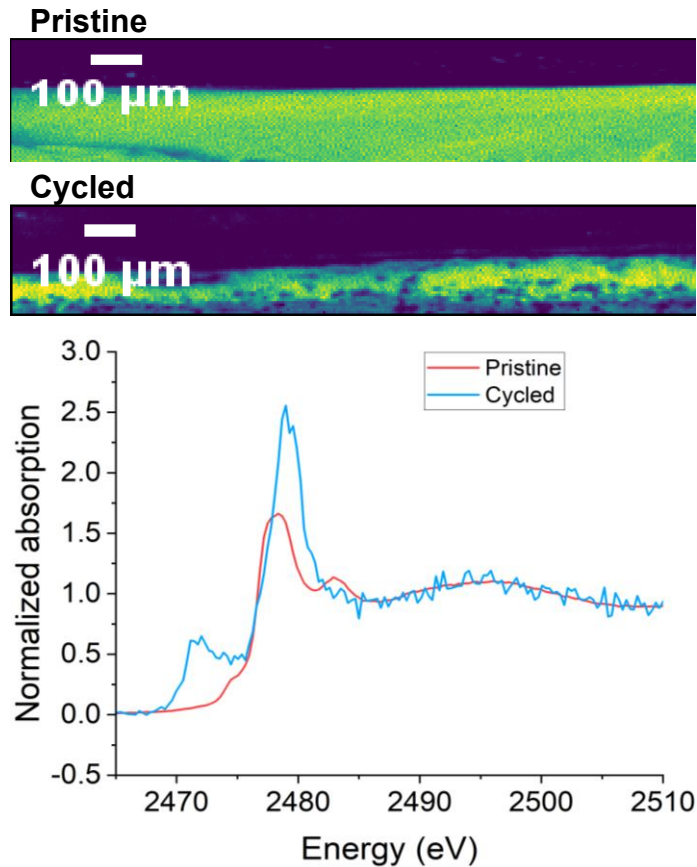


Figure 48. X-ray fluorescence imaging and X-ray absorption spectroscopy results of pristine and cycled molecular ionic composite (MIC) electrolytes. The cycled MIC sample displayed a heterogeneous distribution of sulfur species compared to the pristine sample. The evolution of decomposed sulfur species is revealed from distinct X-ray absorption near-edge spectroscopy.

Patents/Publications/Presentations

Publication

- Bostwick, J. E., C. J. Zanelotti, D. Yu, N. F. Pietra, T. A. Williams, L. A. Madsen, and R. H. Colby. “Ionic Interactions Control the Modulus and Mechanical Properties of Molecular Ionic Composite Electrolytes.” *Journal of Materials Chemistry C* 10 (2022): 947–957. doi: 10.1039/d1tc04119c.

Presentations

- American Physical Society National Meeting, Chicago, Illinois (March 14–18, 2022): “Ion Conduction, Morphology, and Network Formation in a Double-Helix Ionic Polymer Composite Electrolyte”; L. A. Madsen. Invited.
- MII Technical Conference & Review (March 1–3, 2022): “Application of a Rigid-Rod Polyelectrolyte in Energy Storage Technologies”; D. Yu, C. J. Zanelotti, A. G. Korovich, N. F. Pietra, F. Lin, and L. A. Madsen. Poster award.
- MII Technical Conference & Review (March 1–3, 2022): “Polymer Electrolytes for High-Voltage Solid Lithium Batteries”; J. Min, Y. Zhang, M. Yuan, D. Yu, L. A. Madsen, and F. Lin. Poster.

Task 1.19 – Synthesis of Composite Electrolytes with Integrated Interface Design (Sanja Tepavcevic, Argonne National Laboratory)

Project Objective. This project aims to develop well-controlled, scalable LLZO nanofiber and CPE synthesis processes that will address the manufacturing challenges of current SSEs and demonstrate the fabrication of large-area, thin CPE membranes with outstanding electro-chemomechanical properties.

Impact. The outcome of this proposal will be a transformative manufacturing solution that can create large-area, mechanically and (electro)chemically stable SSEs (0 V to 4.5 V versus Li/Li⁺) with Li⁺ conductivity of $\geq 10^{-3}$ S/cm at room temperature enabling ≥ 1 C charging rates.

Approach. To commercialize all-solid-state lithium-ion battery technology, further advances will require the application of knowledge, concepts, and tools from several fields including materials science, physics, engineering, theory, and interfacial electrochemistry. The team’s research philosophy is to establish a synthesis-material characterization-computation cycle that advances synthesis, chemistry, microstructure, interfaces, and transport in CPEs by a coordinated, interdisciplinary approach. The team’s diverse expertise will allow them to understand, create, and rapidly scale up composite electrolytes to meet ambitious conductivity, energy, and power density targets.

Out-Year Goals. The innovative design and synthesis of integrated SSE interfaces include the following goals: (1) achieve high room-temperature conductivity by optimizing composite microstructures, synthetically modifying the LLZO-polymer interface, and reducing CPE membrane thicknesses down to 20 μm ; (2) create a stable and effective interface between the CPE and metallic lithium that yields low charge transfer resistance and enables high CCD (> 3 mA/cm²); and (3) modify the CPE-cathode interface to enable the use of different cathodes [that is, lithium iron phosphate (LFP), LiCoO₂ (LCO), and NMC] and achieve high energy and power density in batteries.

Collaborations. Computational researchers will further help the team to understand and design better ASSBs. They will work closely with L. A. Curtiss, P. Barai, K. Chavan, and V. Srinivasan (ANL) to understand the molecular and mesoscopic characteristics and performance of the team’s CPEs.

Milestones

1. Achieve uniform distribution of LLZO nanofibers within CPEs. (Q1, FY 2022; Completed)
2. Vary LLZO doping (aluminum, germanium, undoped) to improve conductivity and strength. (Q2, FY 2022; In progress)
3. Optimize LLZO nanofibers loading and processing to demonstrate good percolation and maximize conductivity. (Q3, FY 2022; In progress)
4. Use computational methods at the continuum level for the understanding of the improved conduction pathways and lithium deposition mechanisms. (Q4, FY 2022; In progress)

Progress Report

Electrolyte Membrane Synthesis and Optimization. Three routes for electrolyte membrane fabrication were explored (Figure 49). First, the team attempted to create cubic LLZO pellets directly from nanofibers at room temperature by using hydraulic press with 1-inch-diameter die and under 40 MPa pressure. Pure nanofiber pellets were brittle and porous, with highest relative density $\sim 65\%$, high impedance, and low ionic conductivity $\sim 1.3 \times 10^{-5}$ S/cm at 100°C . To achieve improved density, mechanical strength, and electrochemical performance, the team developed LLZO fiber-polymer composites with the polymer matrix reinforced by nanofibers. Interconnected LLZO nanofiber networks form the basis of the composite, with the polymer present within the fiber “scaffold” to increase flexibility and provide soft interfacial contacts for the anode and cathode. Al-doped cubic LLZO nanofibers were formed from electrospun polymer precursor fibers after annealing at 750°C for 2 hours. LLZO fibers of a desired loading (50 wt%) were mixed with a LiTFSI-PEO solution into a well-dispersed slurry [EO:Li⁺ = 15-20 (molar ratio) LLZO : PEO = 1.4 (mass ratio)] and drop cast on aluminum foil or slot-die coated on a fast-moving web to form thin membranes.

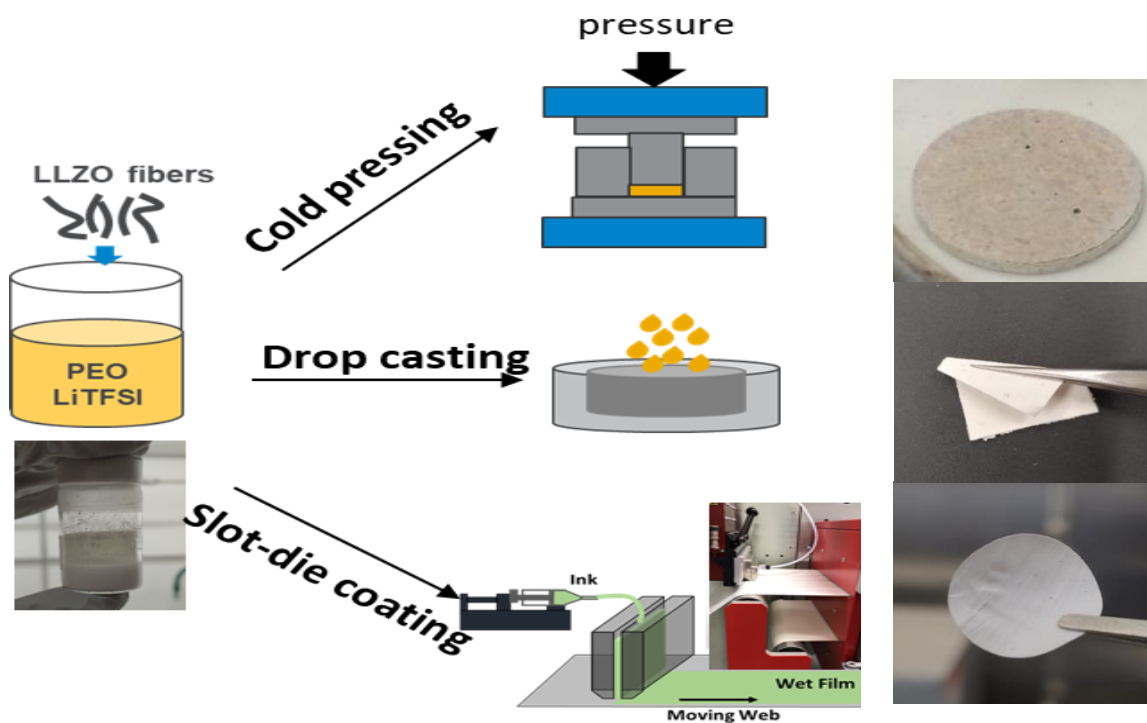


Figure 49. Electrolyte membrane synthesis and optimization schematics of cold pressing, drop casting, and slot-die coating techniques with optical photographs of the membranes.

Cross-sectional SEM images of coated composite membranes are shown in Figure 50. Manually drop-cast samples (Figure 50a) have average thickness of $150\ \mu\text{m}$ and show surface roughness, voids, and non-uniform fiber distribution. Membranes created by slot-die technique (Figure 50b) have average thickness of $150\text{--}80\ \mu\text{m}$ and show good ductility and uniform fiber distribution in the polymer. By accurately controlling coating pressure and gap, as well as web moving speed, uniform membranes of designed thickness ($\leq 20\ \mu\text{m}$) can be obtained. The team will continue to improve microstructure with respect to nanofiber loading and spatial distribution, coating defect control, and membrane thickness by further optimizing ink composition and mechanical fluidic properties and coating process parameters to ensure dense and low-defect membranes with good LLZO fiber percolation networks.

To further determine the impact of coating procedure, the team compared cycling of LLZO-polymer composite membranes with 50 wt% LLZO nanofibers. CCD measurements confirm that superior microstructure resulted in better electrochemical performance by slot-die membranes, with CCD values of $120 \mu\text{A}/\text{cm}^2$ for drop-cast and $160 \mu\text{A}/\text{cm}^2$ for slot-die membranes in Li-PEO-LiTFSI-LLZO-Cu cell configurations (Figure 50c). EIS measurements of slot-die coated electrolytes at various temperatures (Figure 50d) show slightly lower bulk ionic conductivity values for the 50 wt% composite compared to PEO-LiTFSI alone, although with similar activation energies. Interestingly, two regions below and above 55°C (the nominal melting point of the polymer phase) are seen in all samples, with activation energies around 1.2 eV and 0.5 eV, respectively. This indicates further that ionic transport in these electrolytes is still dominated by the PEO-LiTFSI polymer phase. The team will continue to adjust and optimize nanofiber distribution to form a good percolation network to achieve high room-temperature conductivity. Numerous parameters in the composites can be adjusted to improve Li^+ conductivity: LLZO loading and composition (undoped versus doped), nanofiber size and morphology, LiTFSI-to-PEO ratio, and PEO molecular weight.

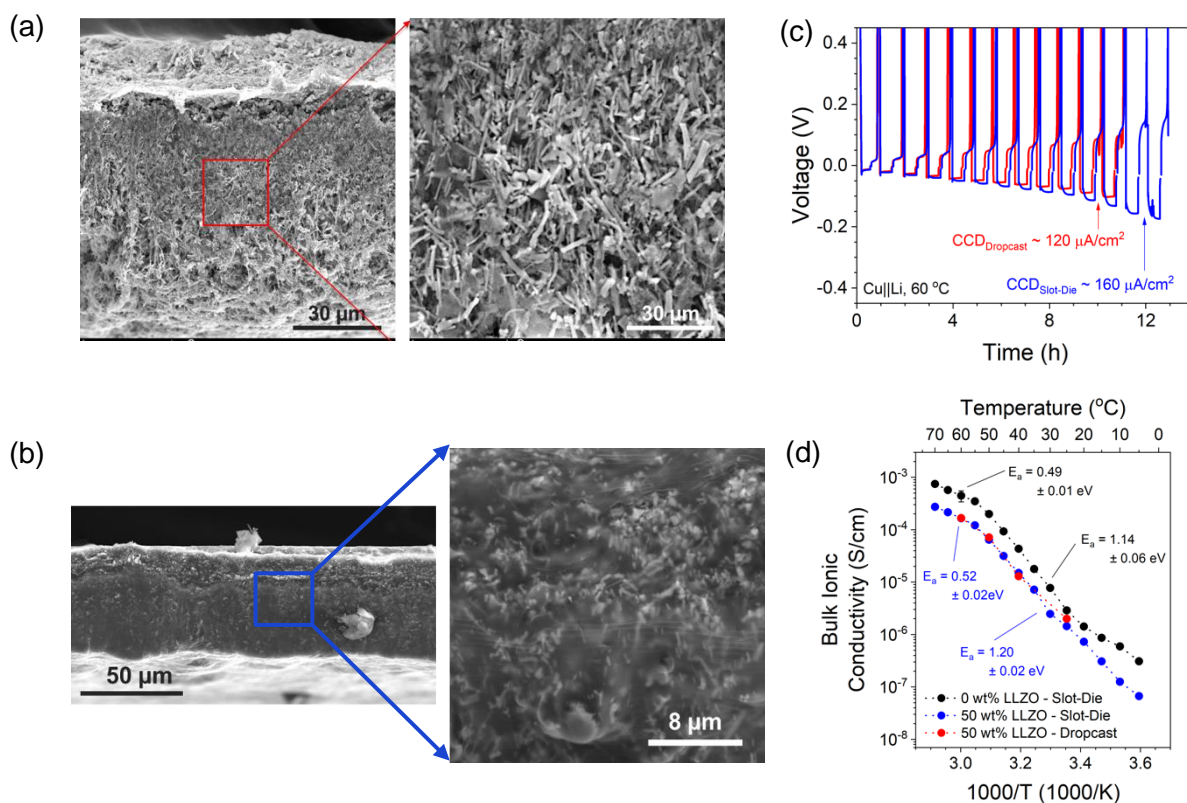


Figure 50. Characterization of composite membranes cross-section scanning electron microscopy of a flexible, dense LLZO fiber-PEO CPE prepared by (a) drop casting and (b) slot-die coating. (c) Critical current density determination for drop-casted (red) and slot-die coated (blue) membranes in Li-PEO-LiTFSI-LLZO-Cu cell configuration. (d) Arrhenius plot of bulk ionic conductivity for composite and polymer solid-state electrolytes.

Patents/Publications/Presentations

Presentation

- Materials Science Division Colloquium, ANL (January 2022): “Interface Reactions and Transport in Polymer and Composite Polymer Electrolytes”; S. Tepavcevic. Invited.

Task 1.20 – Polymer Electrolytes for Stable, Low-Impedance, Solid-State Battery Interfaces (X. Chelsea Chen, Oak Ridge National Laboratory)

Project Objective. The overall project objective is to develop stable polymer/cathode and polymer/anode interfaces with low interfacial impedance for integration of a thin solid composite electrolyte into a battery, to achieve chemical stability at the electrodes, high energy density (500 Wh/kg), high rate (1 mA/cm²), and long cycle life (80% capacity retention for 300 cycles), demonstrated in pouch cells.

Impact. Achieving stable, low-impedance interfaces at both the cathode and anode sides is critical to achieve high energy density with excellent safety, lifetime, and cycling efficiency. This project will identify key design strategies needed to prepare PE to achieve stable, low-impedance polymer/cathode and polymer/Li interfaces and to develop processing procedure to integrate a thin composite electrolyte into a SSB. Success will enable DOE technical targets: energy density of 500 Wh/kg with 80% capacity retention for at least 300 cycles.

Approach. The team's main design principle is to use an oxide ceramic as the main ion transporting phase in the electrolyte and a fluorinated polyether-based PE to form optimized interfaces as well as to provide flexibility to the electrolyte membrane. Compared with inorganic electrolytes, PEs are soft and flexible and capable of maintaining good contact at interfaces. However, several technical barriers remain. On the Li-metal side, the interface between PEs and thin-Li and Li-free anodes is still at an early stage of investigation. Interface optimization using thin-Li and Li-free designs is crucial to reaching the DOE 500 Wh/kg target. On the cathode side, studies on the polymer/cathode interface are scarce. The interface resistance between polymer (catholyte) and CAM is not well understood. In addition, with a target voltage stability of 0-4.5 V versus Li/Li⁺, a polymer with oxidative stability up to 4.5 V is needed. Fluorinated polyethers have the potential to form stable and low impedance interfaces at both the cathode side and the anode side. By systematically examining the effects of fluorine content, polymer chain length and structure, and plasticization on the interfacial resistance with the cathode and the anode, a balance between the desolvation kinetics of Li⁺ and diffusion rate will be achieved to optimize the interface ion transport. A fundamental understanding of the origin of interfacial impedance with the cathode as well as Li-metal anode will be developed alongside the optimization process to generate design rules for polymers with optimized interfaces. The team will also develop a processing procedure to integrate a thin composite electrolyte that was previously developed into a full cell. The composite electrolyte features an interconnected ceramic structure with a thickness of 20 μm. It will be backfilled with the newly developed fluorinated PEs. The mechanical properties of the composite electrolytes will be optimized to accommodate roll-to-roll processing.

Out-Year Goals. In the second and third year of this project, the team will focus on optimizing the cathode/polymer as well as the Li-anode/polymer interface with maximized stability and minimized interfacial impedance. A fundamental understanding of parameters that determine the interfacial impedance and strategies to minimize the interfacial impedance will be developed. The fourth and fifth year of the project will be focused on integration of a thin composite electrolyte into a full cell to achieve high energy density, high rate, and long cycle life, as stated in the overall project objectives. Processing techniques and procedures for electrolyte integration will be investigated to achieve this goal.

Collaborations. Work is being conducted by B. Armstrong, S. Kalnaus, R. Sahore, X. Tang, A. Ullman, and X. C. Chen.

Milestones

1. Synthesize fluoropolyether polymers with four fluorine concentrations. (Q1, FY 2022; Completed)
2. Quantify ionic conductivity, Li⁺ transference number, oxidative stability, thermal stability, glass transition temperature, and mechanical modulus as a function of fluorine concentration. (Q2, FY 2022; In progress)

- Optimize conductivity of composite electrolyte with a 3D interconnected structure (at least 5×10^{-5} S/cm at room temperature). Measure flexural strength of the composite electrolyte with three compositions. (Q3, FY 2022; In progress)
- Quantify interfacial resistance and stability between the fluoropolyether polymers and lithium anode from two different sources. (Q4, FY 2022)
- Build a prototype SSB in a pouch cell using the interconnected composite electrolyte as the electrolyte layer. (FY 2022 Annual Stretch Milestone)

Progress Report

3D Interconnected Ceramic Based CPEs

In previous quarters, the team reported on tuning of solids loadings in the initial ceramic tapes as well as the sintering conditions for optimizing ionic conductivity and porosity of the resulting 3D interconnected partially sintered ceramic tape (PST). However, as also reported, after infiltrating the resulting PST with cross-linked PEO (xPEO), the resulting composite did not have enough mechanical strength or flexibility to survive the crimping pressures during coin-cell fabrication, leading to fracturing of the composite electrolyte membrane and cell shorting (Figure 51a). Furthermore, the infiltration step did not lead to a uniform xPEO layer on either surface of the membrane, which caused reaction between exposed Ohara ceramic and lithium metal, turning the membrane dark. The team had discovered that plasticizing this composite electrolyte with tetraethylene glycol dimethyl ether (TEGDME), resulted in the membrane becoming flexible. However, after systematic investigation of the ionic conductivities before plasticizing and after plasticizing, they concluded that the flexibility was likely a result of microcracking of the ceramic network throughout the membrane (invisible to the eye) due to expansion of the xPEO after plasticizing. Figure 51b shows Nyquist impedance plots of blocking-electrode cells made with an xPEO-filled PST before plasticizing, and after plasticizing the same sample with TEGDME followed by thoroughly drying it off. The room-temperature ionic conductivity of the membrane decreased roughly by half. The inset shows the membrane becoming flexible after plasticizing.

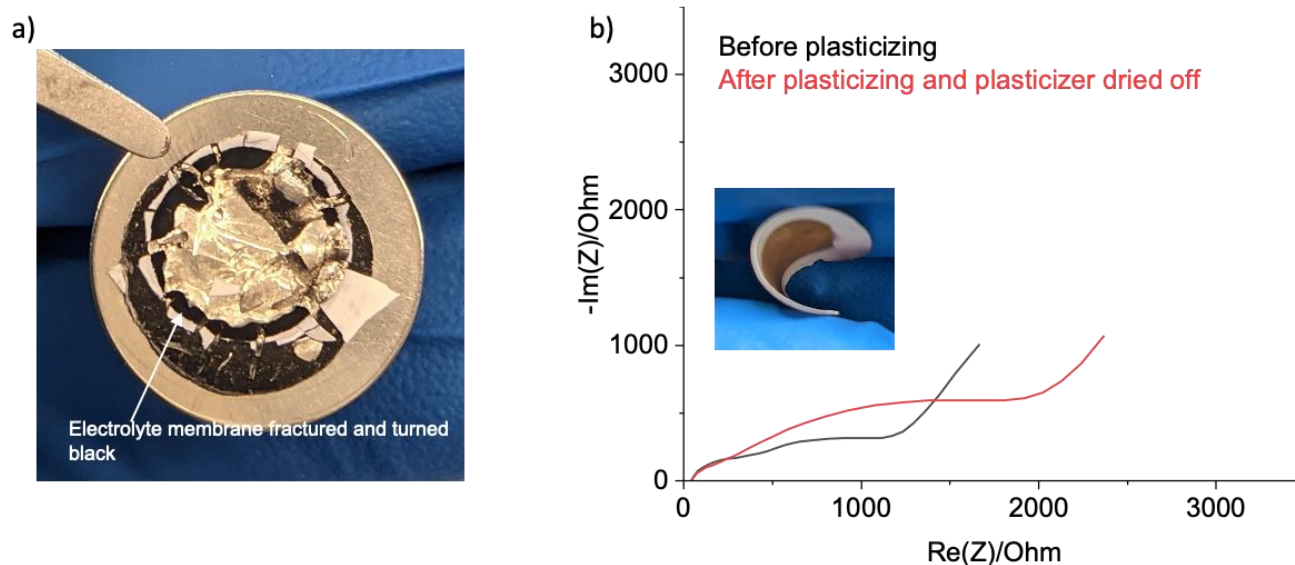


Figure 51. (a) Photograph of a decrimped cell made with cross-linked PEO-filled partially sintered Ohara ceramic composite electrolyte membrane, showing its fracture and darkening due to reaction with lithium. (b) Nyquist impedance plots of blocking-electrode cells made with an xPEO-filled partially sintered ceramic tape before plasticizing, and after plasticizing the same sample with TEGDME followed by thoroughly drying it off. The inset photograph shows the membrane becoming flexible after plasticizing.

To improve the mechanical properties of the composite electrolyte to allow electrochemical testing in coin cells, as well as to obtain a thin uniform polymer layer on both surfaces that can prevent direct contact between lithium metal and Ohara ceramic (which is not stable with lithium), the team deposited 5- μm -thick linear PEO+LiTFSI PE layer on both surfaces of the xPEO-filled PST via spray coating. The final structure is shown schematically in Figure 52a. The thin surface layer allowed cell assembly without fracture; they had also used thin lithium (40 μm) to reduce any bending stresses on membrane due to lithium while crimping, and to act as an effective barrier between the Ohara ceramic and lithium. Figure 52b shows photographs of the membrane after decrimping such a cell after cycling. In a Li//Li symmetric cell (Figure 52c), the PEO protected composite electrolyte cycled for at least 700 hours (100 cycles) without short at 70°C. Stripping/plating was performed at 0.2 mA/cm² for 2.5 hours during each half cycle. A close-up view of the last two cycles is shown in Figure 52d. In contrast, a symmetric cell cycled with a linear PEO-based electrolyte shorted after 6 cycles (data not shown). In addition, the transference number of the trilayer composite electrolyte was measured to be 0.3, which is significantly higher than that of both xPEO and linear PEO (0.08 and 0.14, respectively). This suggests part of the Li-ion transport path is via the interconnected ceramic, which is a single ion conductor (SIC) with unity transference number.

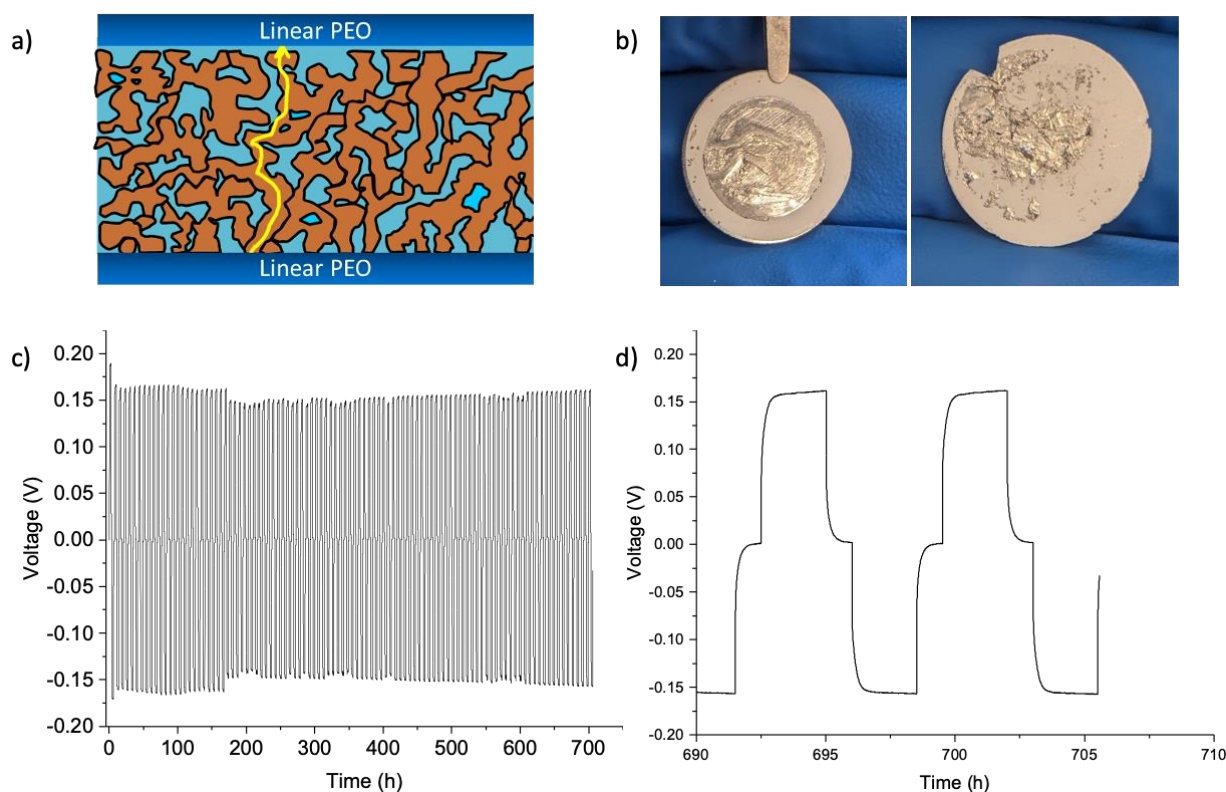


Figure 52. (a) Schematic of trilayer composite electrolyte containing xPEO-filled 3D-interconnected Ohara ceramic as the middle layer, and linear PEO+LiTFSi electrolyte as the top and bottom layers. (b) Photographs of a cell after decrimping show no major fractures in the trilayer membrane (left), and no darkening of composite membrane could be seen after lithium electrode was scraped off. (c) Voltage profile of a Li//Li symmetric cell made with the trilayer membrane and cycled at 0.2 mA/cm², 2.5 hours each half cycle, at 70°C. (d) Voltage profile of the last two cycles shown in (c).

Synthesis of Fluorinated Polyether-Containing PEs

This quarter, the team continued optimizing synthesis of fluorinated polyether-containing PEs. Last quarter, they measured the conductivity of two crosslinked PEO PE membranes with different precursor molecular weights: 1000 g/mol and 500 g/mol. The former exhibited 2-3 orders of magnitude higher ionic conductivity. Therefore, this quarter, the team chose the PEO precursor with 1000 g/mol molecular weight. The fluorinated polyether precursor, denoted as PFPE (perfluoropolyether), was kept the same as used last quarter. Due to the higher molecular weight of the PEO precursor, its miscibility with the PFPE precursor is very poor. After much

trial and error, the team discovered that two mixed solvent systems can be used to co-dissolve PEO/PFPE precursors: an acetonitrile (ACN) / hexafluorobenzene (HFB) mixed solvent system and a tetrahydrofuran (THF) / n-methyl-2-pyrrolidone (NMP) mixed solvent system.

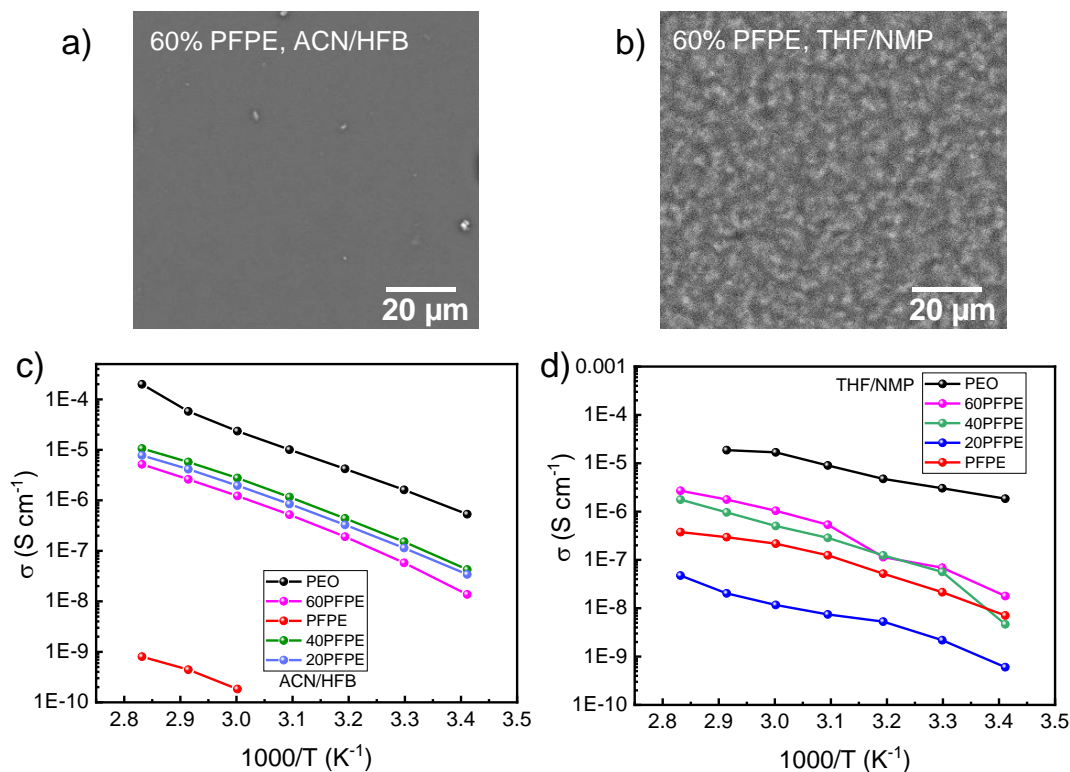


Figure 53. (a-b) Scanning electron microscopy images of 60w:40w perfluoropolyether (PFPE) : poly (ethylene oxide) (PEO) membranes made using (a) acetonitrile (ACN) / hexafluorobenzene (HFB) and (b) tetrahydrofuran (THF) / n-methyl-2-pyrrolidone (NMP) mixed solvents. (c-d) Ionic conductivity of PFPE/PEO membranes as a function of inverse temperature. The membranes were made using (c) ACN/HFB and (d) THF/NMP mixed solvents, respectively.

Five membranes with PFPE to PEO weight ratios of 100:0, 80:20, 60:40, 40:60, and 0:100, were prepared using the two mixed solvent systems, with results shown in Figure 53. For the membranes prepared using the ACN/HFB mixed solvents, lithium salt was infused into the membrane after membrane formation, by soaking the membranes in 1 M Li-salt solution in a mixture of ethylene carbonate (EC) and dimethyl carbonate (DMC) for 24 hours. The membranes were subsequently thoroughly dried. The amount of lithium salt in these membranes varies from 10 wt% to 45 wt%. For the membranes prepared using the THF/NMP mixed solvents, lithium salt was pre-blended into the precursor solutions; the lithium salt weight percentage is 15 wt% in all five membranes.

Figure 53a-b shows the membrane morphology from the two mixed solvent systems. A representative composition, 60:40 w/w PFPE:PEO, is shown. The ACN/HFB solvent system produced homogeneous membranes with no mesoscopic (micrometer level) phase separation (Figure 53a). The THF/NMP solvent system produced membranes with clear phase separation between PFPE and PEO (Figure 53b). In the 60:40 PFPE:PEO membrane, the phase separation length scale is on the order of a few micrometers. The ionic conductivity of these membranes is shown in Figure 53c-d. The PEO membranes without any PFPE showed similar ionic conductivities using the two solvent systems. In contrast, 100% PFPE membrane showed extremely low ionic conductivity (3×10^{-10} S/cm at 70°C) when made using ACN/HFB with the salt infused afterward, while the one made using THF/NMP showed much higher conductivity (3×10^{-7} S/cm at 70°C). Overall, it can be observed that incorporation of PFPE into PEO caused dramatically decreased ionic

conductivity, regardless of the solvent system used. Next quarter, the team will continue investigating the properties and characterizing the structure and morphology of these membranes to gain insight into how to further improve conductivity of these membranes.

Patents/Publications/Presentations

Patent

- U. S. Patent Application 17/675,070. “Gel Composite Electrolyte Membrane for Lithium Metal Batteries.” Filed February 18, 2022; UTB Ref. 4191.1; WNJ Ref. 138974.200994-US.

Presentation

- American Physical Society Meeting (March 16, 2022): “Polymer-Ceramic Composite Electrolyte for High Energy Lithium Batteries”; X. Chelsea Chen. Invited.

Task 1.21 – Ion Conductive High Li⁺ Transference Number Polymer Composites for Solid-State Batteries (Bryan McCloskey, University of California, Berkeley)

Project Objective. This project seeks to develop polymer-inorganic composites that have an optimal combination of conductivity, processability, and low interfacial resistance at both a Li-metal anode and a porous Li[Ni, Co, Mn]O₂ (NMC) cathode. In an effort to enable Li-metal anodes, mechanically rigid solid-state Li⁺ conductors, such as LLZO, Li_{1+x}Al_xTi_{2-x}(PO₄)₃ (LATP), and Li₂S-P₂S₅ (LPS) glasses, have been employed due to their high Li⁺ ion conductivity and, when engineered to eliminate interfacial defects, appropriate stiffness to suppress Li-metal dendrite formation. However, for these materials to result in batteries that compete against current commercial cells in terms of energy density and cost per kWh, they would need to be manufactured at no more than 50- μ m thickness and cost no more than \$5 per square meter. These metrics are daunting for pure thin-film inorganic ion conductors, particularly when a porous, thick cathode also needs to be used to achieve competitive cell energy densities. To overcome these challenges, this project aims to develop polymer-inorganic composites, where high Li⁺ transference number PEs serve as a binder for inorganic ion conducting particles.

Impact. By optimizing the composition of this composite electrolyte, the team aims to marry the processability and interfacial mechanical compliance of polymers with the impressive transport properties of inorganic composites, thereby enabling roll-to-roll manufacturing to allow thin (< 50 μ m) layers of high-conductivity solid-state conductors to be cost-effectively incorporated into batteries.

Approach. The project approach relies on the following key steps in FY 2022: (1) using monomers with (trifluoromethanesulfon)imide (TFSI) anions appended to them, synthesize and characterize polyanionic PEs with high Li⁺ transference number and conductivity; (2) through systematic material structure-property characterization, understand how to reduce interfacial ion transport impedance between inorganic ion conductors (specifically, thin-film inorganic conductors such as LLZTO, LATP, and LPS) and high Li⁺ transference number PEs; and (3) characterize electrode-polymer and electrode-inorganic conductor interfacial resistances at a Li-metal anode.

Out-Year Goals. The overall project goal is to develop an optimized polymer-inorganic LIC with superior conductivity (> 1 mS/cm), thin-film processability, and low electrode interfacial impedance. Of particular interest in the out years is development of a process to fabricate thick, porous, and electrochemically stable NMC cathodes using the polymer-inorganic composite as both the binder and electrolyte. The team aims to integrate the optimized high-loading cathode with a 25- μ m thin-film polymer-inorganic electrolyte to create an “anode-less” battery with 500 Wh/kg and 80% capacity retention after 300 cycles.

Collaborations. While this project has a single PI, B. McCloskey will leverage the collaborative battery research environment at LBNL and coordinate with other LBNL PIs in the BMR Program for materials and experimental development.

Milestones

1. Establish polymer synthesis by making two neat TFSI-containing polymers. (Q1, FY 2022; Completed)
2. Measure conductivity of two polymers using Li-Li symmetric cells. (Q2, FY 2022; Delayed – completion anticipated early May 2022)
3. Measure interfacial impedance evolution of polymer in a Li-Li cell. (Q3, FY 2022; On schedule)
4. Synthesize a series of four copolymers with various ratios of TFSI monomer and a film-forming monomer. (Q4, FY 2022)

Progress Report

This quarter, the team developed a reversible addition–fragmentation chain-transfer (RAFT) polymer synthesis procedure to reliably produce poly((trifluoromethanesulfonyl)imide lithium methacrylate) (PLiMTFSI) at a controlled molecular weight. They have produced 20,000 g/mol and 60,000 g/mol molecular weight PLiMTFSI, with molecular weight confirmed by ^1H NMR end-group analysis and gel permeation chromatography (GPC). NMR was also used to characterize the reaction kinetics of the 20 K PLiMTFSI and determine conversion and molecular weight as a function of time, as shown in Figure 54. The molecular weight predicted by conversion was verified by NMR end-group analysis and GPC. No melting was detected via DSC, indicating the lack of crystalline domains in the PLiMTFSI. XRD results confirmed the amorphous nature of polymer, with only a broad XRD peak evident, as shown in Figure 55. No glass transition temperature (T_g) was detected via initial DSC test within the range of -80°C to 250°C ; however, further DSC studies will be necessary to rule out any glass transition behavior in this temperature range.

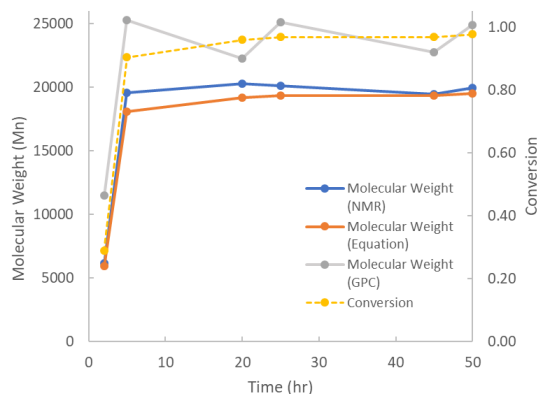


Figure 54. Conversion and molecular weight data from a 20 K PLiMTFSI synthesis.

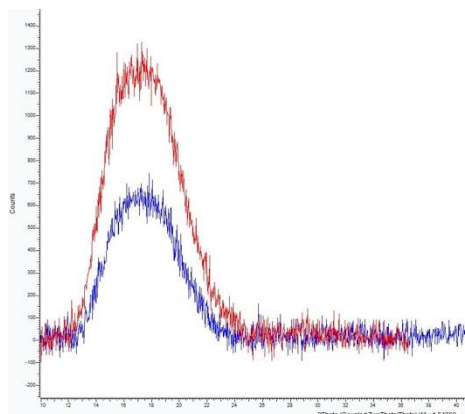


Figure 55. X-ray diffraction data showing characteristic amorphous peak for both the 60 K (red) and 20 K (blue) PLiMTFSI.

Once the team successfully synthesized these PLiMTFSI polymers, they cast free-standing films to begin measuring conductivity of their neat polymers. Solvent choice and polymer concentration were found to be important, with 30 wt% PLiMTFSI in methanol the best solution composition for film casting. Drop casting directly onto stainless steel led to usable films for conductivity measurements, but they were unable to remove films from the stainless steel after drop casting. They attempted to create a free-standing film using solvent casting with a doctor blade to control the thickness. After casting onto a Teflon surface, they were able to remove the PLiMTFSI; however, the film was brittle and difficult to transfer to an electrochemical cell without it breaking. Next quarter, the team plans to pursue several options to produce free-standing films with better mechanical integrity, including exploring polymer blends with plasticizing agents as well as using crosslinking agents. Once they find a solution that allows them to form these free-standing films, they will begin conductivity measurements using both stainless-steel symmetric cells and Li-Li symmetric cells.

Patents/Publications/Presentations

The project has no patents, publications, or presentations to report this quarter.

Task 1.22 – Inorganic-Polymer-Composite Electrolyte with Architecture Design for Lithium-Metal Solid-State Batteries (Enyuan Hu, Brookhaven National Laboratory)

Project Objective. This project targets the following goal: the composite electrolytes will be thin ($< 100 \mu\text{m}$) and have high Li-ion conductivity ($\geq 10^{-3} \text{ S/cm}$ at room temperature), low interfacial impedance, and desirable mechanical properties. When used in the SE Li-metal battery, a current density $> 1 \text{ mA/cm}^2$ and an aerial capacity of $2\text{-}3 \text{ mAh/cm}^2$ can be achieved with more than 300 cycles. The constructed $\text{LiNi}_x\text{Mn}_y\text{Co}_{1-x-y}\text{O}_2$ (NMC) / LiCoO_2 || composite electrolyte || Li-metal cell can be operated at up to 4.5 V versus Li^+/Li . The SE will also be compatible with high loading cathodes in achieving high energy density at the coin or pouch-cell level.

Impact. The results of this project will lead to advancement of SSBs, a beyond Li-ion battery option with better safety characteristics and higher energy density. The project will also provide valuable knowledge to U. S. industries in scaling up SSB production for vehicle applications, thus providing solutions to the clean energy strategy.

Approach. The project approaches are as follows: (1) design and synthesize polymer with anion-tether strategy for high transference number, (2) through theories and experiments, design hierarchical inorganic electrolyte for suppressing lithium dendrite penetration, (3) optimize the composite electrolyte composition and structure, (4) use additives for Li-metal anode and NMC cathode protection, and (5) use synchrotron and cryo-EM characterization to understand the bulk electrolyte and interphases.

Out-Year Goals. The out-year goals are to synthesize single ion conducting SPE with high transference number and conductivity; to design hierarchical inorganic electrolyte with high ionic conductivity and good mechanical/electrochemical stability; and to use synchrotron total scattering to study the structure of ceramic/polymer electrolyte.

Collaborations. This project PI will work closely with co-PI H. Xin of University of California, Irvine, and co-PI X. Li of Harvard University.

Milestones

1. Synthesize single ion conducting SPE with high transference number and conductivity. Achieve formulation optimization to achieve transference number > 0.5 . (Q1, FY 2022; Completed)
2. Design hierarchical inorganic electrolyte with high ionic conductivity and good mechanical/electrochemical stability. Develop inorganic electrolytes (sulfides, halides) with ionic conductivity $> 1 \text{ mS/cm}$ and a hierarchy of voltage stability up to 4.5 V and down to near 0 V in cyclic voltammetry (CV) tests. (Q2, FY 2022; delayed, completion anticipated by May 2022).
3. Optimize composition for plastic hybrid electrolyte. Tune the SPE and inorganic electrolyte composition to enable compatibility. (Q3, FY 2022)
4. Use synchrotron total scattering to study the structure of ceramic/polymer electrolyte. Complete synchrotron pair distribution function (PDF) analysis of the ceramic/polymer electrolyte. (Q4, FY 2022)

Progress Report

This quarter, the UCI team has established an ultraviolet (UV)-polymerization platform to synthesize the single Li-ion conducting PE (referred to here as SIC), as shown in Figure 56a. An anionic monomer with ionizable Li^+ counter-cation was co-polymerized with a crosslinking reagent to adjust the Li^+ concentration and regulate the mechanical properties. The role of the plasticizer is to facilitate the solvation and dissociation of Li^+ to improve the ionic conductivity. In sharp contrast to conventional PEs, all the anions in SIC were covalently tethered to the polymer backbones, and the Li^+ is the sole charge carrier. As a result, the unique polymer architecture design has delivered a high Li^+ transference number (t_{Li^+}) of 0.86 (Figure 56b), which is four-fold higher than the conventional PEO SPE. The benefit from this high t_{Li^+} is that the migration and accumulation of electrochemically non-reactive anions at the SPE-electrode interface are largely avoided. Figure 56c shows the voltage-time curve of Li/SIC-SPE/Li cell at different cycling times. The SIC-SPE exhibits total overpotential of 100 mV, and a low concentration overpotential of 10 mV when cycling at 0.2 mA/cm^2 and 22°C (Figure 56c). For comparison, the team also synthesized a mixed ion-conducting SPE containing free-mobile anions. The Li^+ concentration, crosslinking degree, and plasticizer content of mixed ion-conducting SPE were controlled to be the same as SIC, while a much lower t_{Li^+} of 0.39 (Figure 56d) was observed. As expected, the Li-Li symmetric cell with mixed ion-conducting SPE also showed a high concentration overpotential of $\sim 50 \text{ mV}$ (Figure 56e). The above results preliminarily revealed the critical role of t_{Li^+} in dominating the electrochemical behavior of SSBs. They will investigate its effect on dendrite suppression, SEI formation, and full cell durability in the next stage.

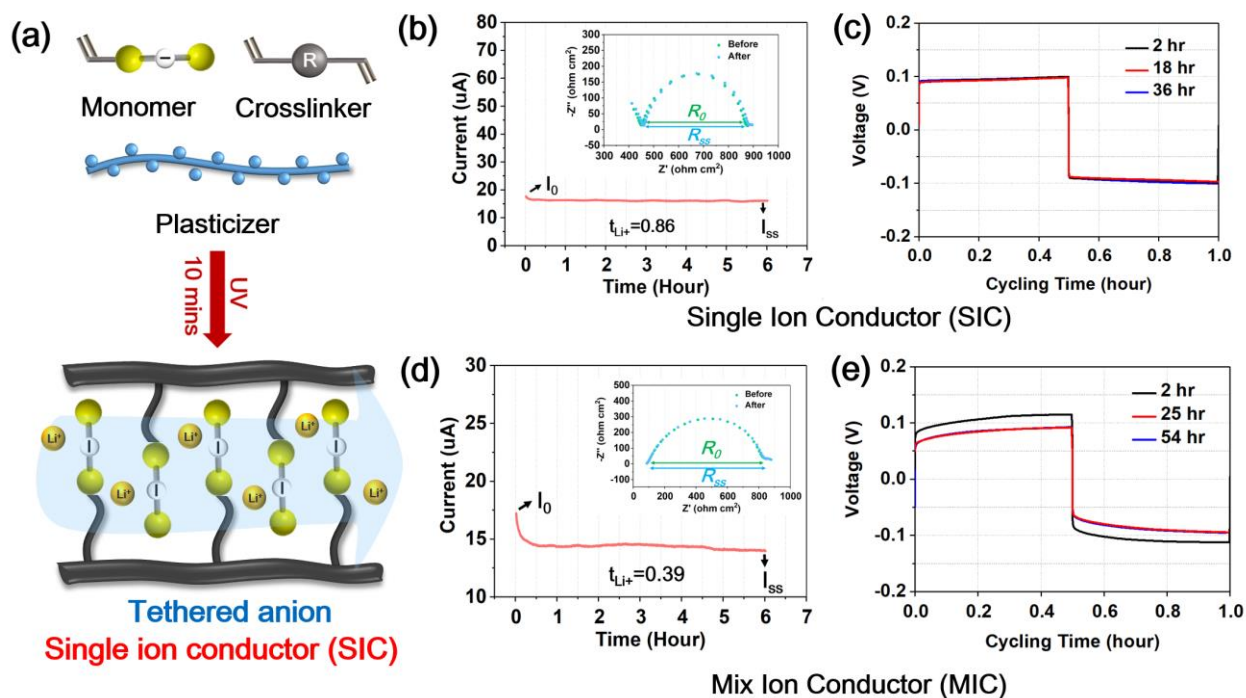


Figure 56. (a) Schematic illustration showing the UV-polymerization route to synthesize the single Li-ion conducting (SIC) solid polymer electrolyte (SPE) from the anionic monomer, crosslinker, and plasticizer. (b) Li^+ transference number measured by the potentiostatic polarization method of SIC-SPE. (c) Voltage-time profile of the Li-Li symmetric cells when cycling at 0.2 mA/cm^2 and 0.1 mAh/cm^2 showing the concentration overpotential of SIC-SPE. (d) Li^+ transference number measured by the potentiostatic polarization method of mixed ion-conducting SPE. (e) Voltage-time profile of the Li-Li symmetric cells when cycling at 0.2 mA/cm^2 and 0.1 mAh/cm^2 showing the concentration overpotential of mixed-ion conducting SPE.

Patents/Publications/Presentations

The project has no patents, publications, or presentations to report this quarter.

Task 1.23 – Solid-State Batteries with Long Cycle Life and High Energy Density through Materials Design and Integration (Gerbrand Ceder, University of California, Berkeley)

Project Objective. This project aims to create solid-state Li-metal batteries (SSLMBs) with high specific energy, high energy density, and long cycle life using scalable processing techniques. The team will achieve this by addressing fundamental challenges associated with (1) interfacial reactivity, (2) Li-metal plating, and (3) cathode loading. Addressing these challenges supports the broader VTO goal of SSBs with increased cycle life and energy density.

Impact. Ultimately, this project will develop an understanding of how to prevent interfacial reactions, make uniform Li-metal plating, and increase cathode loading significantly. The knowledge obtained from this project will be used to design SSLMBs with high specific energy of 500 Wh/kg, 80% capacity retention for at least 300 cycles, and $CCD > 1 \text{ mA/cm}^2$.

Approach. This project addresses several fundamental challenges and makes the SSLMB competitive, surpassing the specific energy, energy density, and cycle life of Li-ion batteries:

- Create homogeneous lithium deposition on the anode without penetration of lithium metal through the separator to achieve high cycle life and high safety. The team will achieve this with the use of an active buffer layer (ABL) that combines active and inactive components to homogenize lithium plating and to keep the lithium plating potential away from the SE separator.
- Limit chemical reactivity and mechanical decohesion between the SE, carbon, and cathode material in the composite cathode so that high cycle life can be achieved. The team will limit chemical reactivity by protecting the carbon from the SE, by using novel cathode coatings designed to be stable to high voltage and that do not react with the SE, by using novel solid halide catholyte conductors, and by using inorganic/organic solid composite electrolytes in the cathode.
- Achieve high volumetric loading of the active cathode material in the composite cathode to achieve high energy density and high specific energy. The team will achieve high volumetric cathode loading by creating thin highly porous conductor scaffolds that are infiltrated with cathode, by tailored particle size distributions of deformable lightweight conductors, and by the use of organic/inorganic hybrids.
- Create inexpensive materials and processes to fabricate SSBs so that they can be cost-competitive with Li-ion batteries. The team will create solution-processable organic/inorganic hybrids to be used as separator and to blend in the composite cathode; they will use inexpensive, scalable ceramics processing techniques to create high loading composite cathodes.

Out-Year Goals. The ultimate project goal is to develop SSLMBs that achieve high specific energy of 500 Wh/kg, 80% of capacity retention after 300 cycles, and $> 1 \text{ mA/cm}^2$ of critical density.

Collaborations. This project collaborates with the following co-PIs: H. Kim, V. Battaglia, G. Chen, M. M. Doeff, G. Liu, M. Scott, M. Tucker, and J. Urban, all at LBNL.

Milestones

1. Demonstration of use of ABL in Li-metal cell with active component other than silver. (Project start in Q2, FY 2022; Completed)
2. Integration of $\text{LiNi}_x\text{Mn}_y\text{Co}_{1-x-y}\text{O}_2$ (NCM) into 3D carbon framework with CAM loading $> 80 \text{ wt}\%$. (Q3, FY 2022; In progress)
3. Model studies to assess compatibility of cathode components. (Q3, FY 2022)

Progress Report

A critical role of ABL is to physically separate the SE and Li-metal anode to avoid detrimental interphase formation. The ideal ABL will lead the Li-metal plating at the interface between the current collector and ABL. However, it is unclear what properties of ABL determine where Li-metal plating occurs: current collector/ABL interface versus ABL/SE interface. This quarter, the team investigated how lithium diffusivity in the ABL affects Li-plating behavior. They tested and compared two distinct types of carbon: amorphous carbon (Super P) and graphite (natural graphite with particle size of $\sim 20 \mu\text{m}$) as ABLs. These two carbon materials will have very different lithium diffusion behavior when they are in thin-electrode form. The sphere-like amorphous carbon will have 3D lithium diffusion pathways once it is lithiated. In this respect, amorphous carbon ABL can provide lithium diffusion and electron transport pathways between SE and current collector (Figure 57a). In contrast, in the plate-like graphitic carbon, lithium ions can transport rapidly along *ab*-plane, but lithium migration along the *c*-direction is infeasible because of the very high migration barrier greater than 8 eV.^[1] In the electrode film, the graphitic carbon particles stack on top of each other because of their two-dimensional (2D) morphology. Therefore, the graphitic carbon electrode film will have very low lithium diffusivity along the *c*-direction while maintaining high electrical conductivity (Figure 57b). Thus, the amorphous carbon can represent an ABL with high lithium diffusivity and high electrical conductivity, while the graphitic carbon can represent the ABL with low lithium diffusivity but with high electrical conductivity. In their experiments, the team prepared the ABL by mixing carbon (amorphous carbon and graphitic carbon) and PTFE binder in 70 wt% (carbon) : 30 wt% (PTFE) ratio and a subsequent roll pressing method. The Li_3PS_4 SE is pressed under 500 MPa to make a dense pellet. Then, an asymmetric lithium half-cell is prepared with a Li_3PS_4 SE pellet, as shown in Figure 57c. They used a copper film as a current collector. The asymmetric cells are discharged for 60 hours under a constant current of $27.3 \mu\text{A}$ (0.115 mA/cm^2). Figure 57d shows the discharging profile of the asymmetric cell. Figure 57e-f shows the optical microscope images of amorphous carbon and graphitic carbon after lithium plating. The team found that lithium plating preferentially occurs on the interface between the amorphous carbon and copper current collector. Figure 57e shows the amorphous carbon ABL film facing the copper current collector, where they found a shiny lithium metal on the carbon surface. In contrast, it is clearly visible that lithium metal is plated at the interface between graphitic carbon and Li_3PS_4 SE (Figure 57f). The goldish color of the ABL indicates that lithium ions intercalate into graphitic carbon. They speculate that the lithium plating occurs first, and the plated lithium metal is squeezed in the pores of the graphitic carbon electrode. Therefore, lithiation to graphitic carbon can occur along the *ab*-plane. This work demonstrates that lithium diffusivity along the direction that is perpendicular to the current collector serves an important role in determining lithium plating behaviors.

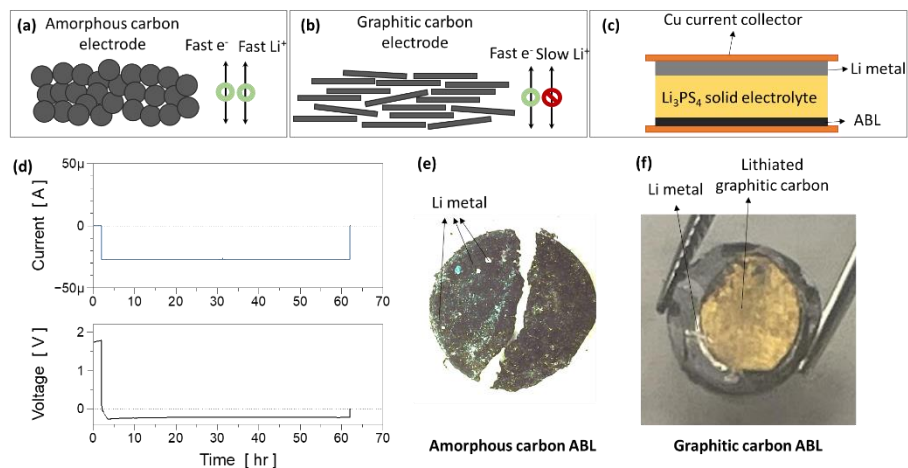


Figure 57. Schematics of (a) amorphous carbon and (b) graphitic carbon electrodes. (c) Schematic of an asymmetric cell with active buffer layer (ABL). (d) Discharging profile of the asymmetric cell. (e-f) Optical microscopy images of (e) amorphous carbon and (f) graphitic carbon ABLs after lithium plating.

Reference

- [1] Thinius, S., et al. *Journal of Physical Chemistry C* 118 (2014): 2273.

Patents/Publications/Presentations

The project has no patents, publications, or presentations to report this quarter.

Task 1.24 – Low-Pressure All-Solid-State Cells (Anthony Burrell, National Renewable Energy Laboratory)

Project Objective. The goal of this project is to develop ASSBs using four classes of SSEs, and/or electrode modifiers, that can be used to achieve the final 500 Wh/kg cell target. These materials will be down selected using full-cell testing and advanced characterization to achieve cell targets at cell pressures less than 100 psi.

Impact. Many factors limit ASSB performance, and this project seeks to address the interface stability of both the lithium interface and the high-voltage cathode. The combination of multiple ionic conductors coupled is specifically targeted to allow solution processing, and low-pressure cell outcome will enable lower cost deployment of solid-state cells in automotive applications.

Approach. To achieve the goal of low-pressure ASSBs, the team is utilizing three classes of solid ion conductors, sulfide materials, melt-processable lithium carboranes, and multinary metal halides. These materials can be chemically modified to optimize ionic conductivity and voltage stability in single conductor modes or in combinations to effect interface modification for full-cell development. Specifically, the use of flexible ionic conductors at the cathode interface will enable the mechanical effects of cathode expansion and contraction to be mitigated. In combination with the materials discovery work, the project has an extensive characterization team to help determine the impacts of interface, chemical, electrochemical, and mechanical factors on system performance. Full-cell assembly and development, targeting approaches that are readily scalable and compatible with roll-to-roll process, will drive the materials innovation and development.

Out-Year Goals. The out-year goal is demonstration of 2 Ah cells that achieve 500 Wh/kg and lifetimes exceeding 300 cycles at functional pressures below 100 psi.

Collaborations. There is a joint effort for this project between National Renewable Energy Laboratory (NREL), M. Toney at the University of Colorado, and A. Maughan at the Colorado School of Mines.

Milestones

1. Prepare electrochemical cells using lithium carboranes. (Q1, FY 2022; Delayed)
2. Prepare electrochemical cells using Li_yMCl_z . (Q2, FY 2022; Delayed).
3. Prepare electrochemical cells using sulfur-polymer-coated cathodes. (Q3, FY 2022; Completed)
4. Demonstrate full-cell design that enables accurate, repeatable internal pressure control for ASSBs. (Q4, FY 2022; Completed)

Progress Report

Last quarter, supply chain issues impeded progress on carboranes and Li_yMCl_z systems; these milestones should be complete by the end of next quarter. This delay in materials has freed resources for development of the test cell; as a result, the third and fourth quarter milestones have been completed.

Materials

This quarter, the team developed methods to coat a sulfide-based argyrodite $\text{Li}_6\text{PS}_5\text{Cl}$ (LPSCI) SE powder with a novel ionically conductive sulfur polymer (PolyS structure, as shown in Figure 58a) that can be solubilized in non-polar solvents and that is chemically compatible with LPSCI (10% to 90% by mass ratio of PolyS to LPSCI). It has been previously reported that LPSCI is chemically stable with non-polar solvents and polymeric binders such as polyisobutene (PolyIB, as shown in Figure 58c), but will degrade when used with polar solvents and polymeric binders.^[1-2] This coated LPSCI powder was then used to assemble an In-metal symmetric cell (Figure 58b) to evaluate the ionic conductivity of the composite material. Next, the team fabricated a composite using PolyIB and LPSCI (10% to 90% by mass ratio of PolyIB to LPSCI) to compare to the PolyS-based composite, and used this material to fabricate an analogous indium symmetric cell as shown in Figure 58d.

This quarter the team also developed a new tool to measure the electrochemical impedance of materials as a function of applied cell stack pressures. Figure 58e compares the ionic conductivity of the two composites. In the pressure region below ~ 2.5 MPa (highlighted with a grey colored box), the PolyS-coated composite exhibits significantly improved ionic conductivity in comparison to the PolyIB composite. At stack pressures above ~ 3.5 MPa, the PolyIB-based composite exhibits improved ionic conductivity in comparison to the PolyS composite. Therefore, these results indicate that this type of novel sulfur polymer can be used to effectively boost the ionic conductivity of a composite SSB layer at low stack pressures (< 2.5 MPa).

Next quarter, the team will focus on examining the Li-metal compatibility and electrochemical stability of these composite materials. Specifically, they will galvanostatically cycle lithium symmetric cells and will compare the rate of electrochemical degradation between the PolyS and PolyIB composites. Moreover, they will examine the degradation products of each composite at the lithium electrode interface using XPS and other spectroscopic techniques. Finally, during the third and fourth quarters, the team will continue to develop methods to fabricate a cathode layer using the sulfur polymer as an interfacial coating and catholyte that can increase effective ionic conductivity within the catholyte at low cell stack pressures.

Characterization

Virtual-Electrode (VE) XPS (G. Teeter)

Over the past several years, NREL staff have developed the VE-XPS approach, shown in Figure 59, to enable *in situ* / *operando* XPS measurements on ASSB materials and exposed interfaces. VE-XPS measurements quantify the evolution of composition and chemical states in ASSB samples versus extent of lithiation. Additionally, XPS binding-energy shifts in response to applied VE current bias provide a means for assessing

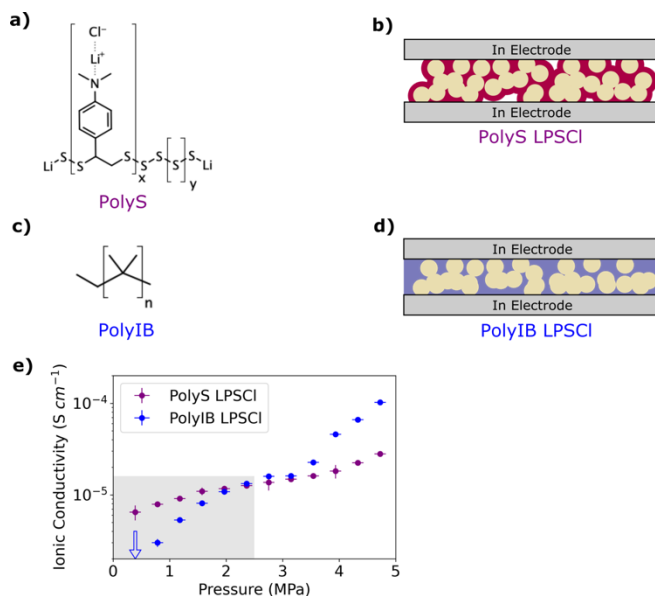


Figure 58. Materials and structural concepts for polymer incorporation in solid-state electrolytes.

chemically resolved overpotentials for individual phases detected in interfacial layers. A closely related approach uses the VE concept to drive electrochemical currents during scanning Auger microscopy (SAM) measurements. NREL has previously used the standard SAM scanning electron excitation source to perform VE measurements, but this source typically operates at 5-10 keV, and thus tends to deposit charge quite deeply into materials. Consequently, plans are being developed to incorporate a low-energy electron gun source on the SAM system, which will provide much gentler *in situ* cycling conditions. Beginning next quarter with planned studies on a sulfur polymer / LPSCI SE composite, the team will correlate elemental and phase composition of interfacial layers in ASSB materials with phase-resolved contributions to interfacial impedances from VE-XPS measurements. These results will be complemented by high-spatial resolution VE-SAM measurements of morphology and composition to provide feedback to materials synthesis and interface stabilization approaches that are being explored within the project.

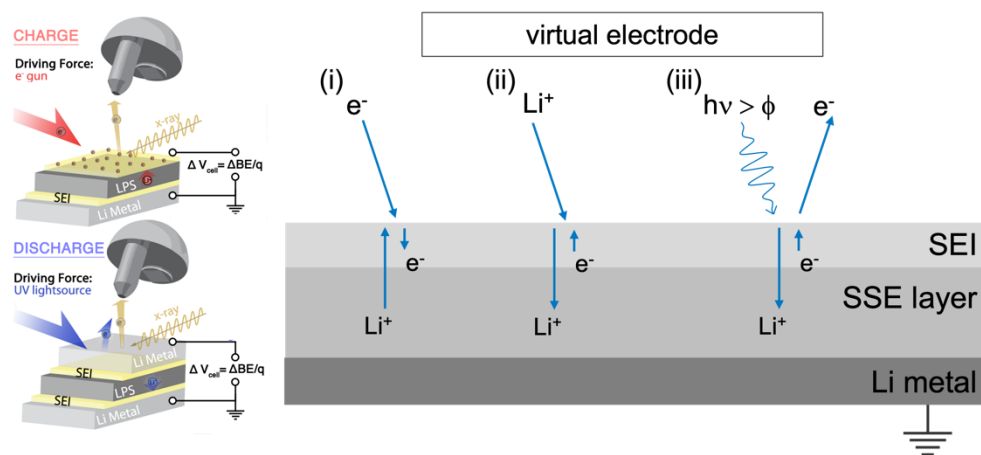


Figure 59. Schematic illustration of the virtual electrode (VE) X-ray photoelectron spectroscopy (XPS) approach for studying solid-state electrolyte (SSE) materials. The VE-XPS approach employs (1) low-energy electron and (2) Li^+ ion gun sources to drive electrochemical currents at the surface of exposed battery materials and structure. Additionally, various ultraviolet (UV) and vacuum UV (VUV) light sources are available to extract electrons from the valence-band of the exposed surface. By combining these current-bias sources, it is possible to perform electrochemical cycling on all-solid-state battery materials to probe the formation and evolution of electrochemical properties of the SEI that forms at the Li/SSE interface.

X-Ray Nano-CT of SSBs (D. Finegan)

An Alliance Partner University Program (APUP) agreement is being made with Colorado University, Boulder, to partly sponsor a PhD student who will focus on characterization of SSB degradation mechanisms. Deciding on a research plan and creating this agreement has spanned the past two months and is under way. As part of this research plan, the student will apply X-ray nano-CT to solid-state cells to explore mechanical degradation mechanisms such as delamination of the SE from the active material particles and voids forming at the lithium electrode interface.

In anticipation of the student starting to work at NREL, the team is designing an *in situ* electrochemical cell that facilitates high-quality nano-CT images, electrochemical control, and compression control. The greatest challenges are as follows: (1) facilitating motion/displacement control of the electrode terminals with accuracy of sub-micrometer control, and (2) making a cell with no more than 100- μm diameter for optimal image quality. Figure 60 shows the first iteration of design that consists of a piezo-electric motor with 50-nm step-motion control. The enclosure allows for independent motion of the two electrodes while maintaining a seal around the micro-cell. However, this design still has too much matter in the field of view, which would lead to sub-optimal image quality. The next iteration will focus on thinning the enclosure material and minimizing excess electrolyte in the field of view to improve image quality.

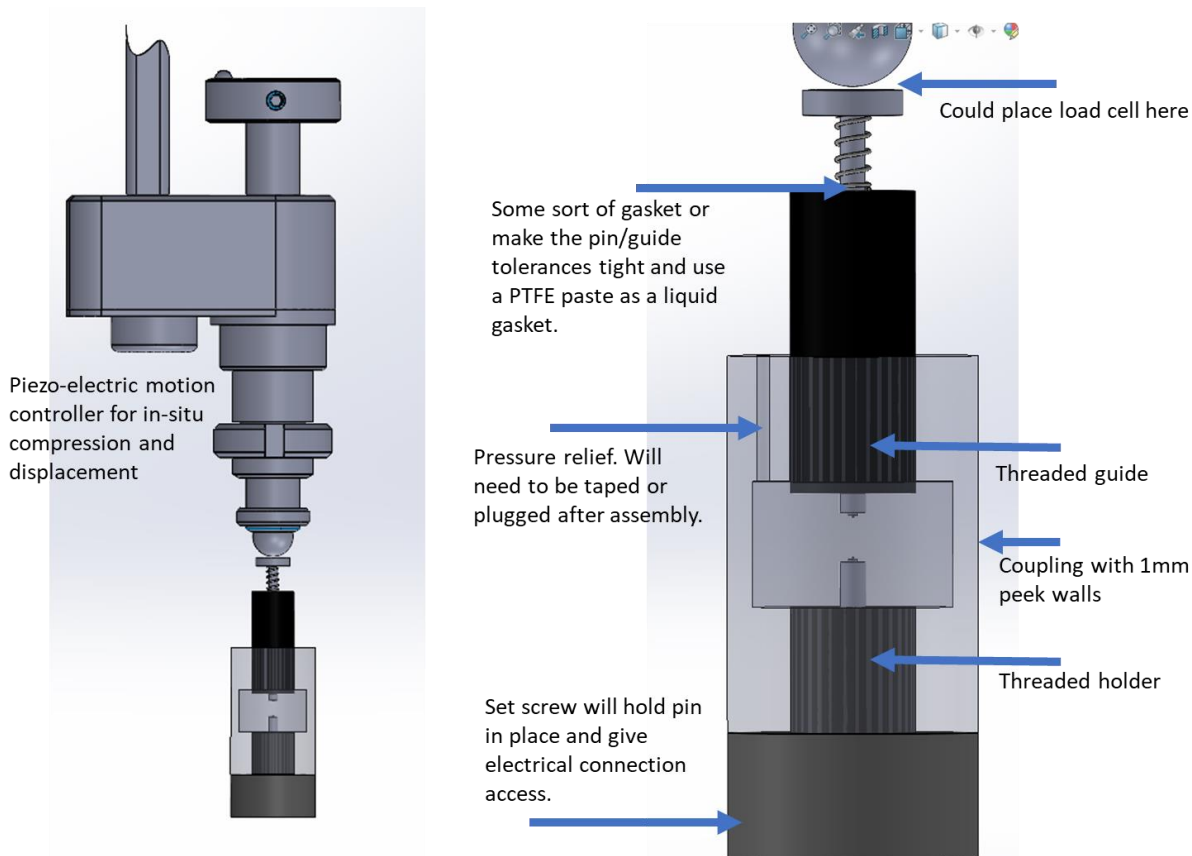


Figure 60. First iteration of design for an *in situ* nano – computed tomography cell with (left) a full view of *in situ* cell with piezo-electric motion controller on top and (right) a magnified view of the cell enclosure.

Characterizations by Atomic Force Microscopy (AFM)-Based Nano-Probes (C-S. Jiang)

The team has developed multiple SSB-oriented nm-scale ionic, electronic, and electrical characterizations based on AFM, including the following: (1) ionic and electronic transport imaging (Figure 61a), and (2) potential imaging on space charges at interfaces (Figure 61b), as well as air-free sample preparation using ion-milling and sample transfers needed for the characterizations. These nanoprobes are readily set up for assisting SSB development.

SEs with state-of-the-art ionic conductivity are made of polycrystalline materials and their composites. Because of the highly crystalline orientation-dependent ionic transport, ionic conductivity is expected to be highly nonuniform through the SE. Further, the inhomogeneous interfaces (for example, the interfaces between the anode and SE and between the active cathode particles and SE) make the ionic transport even more nonuniform. This nonuniform conductivity can be a major factor, inducing lithium dendrite and causing device failure. To characterize the ionic transport, the team has developed a transport imaging technique, by applying a positive bias voltage (V_s) to the SE side.^[3] The measured current flowing through the AFM probe in this case is the sum of ionic and electronic currents (right panel, Figure 61a). To separate the electronic leaking current from the dominant ionic current, a negative V_s is applied, and the current is only the electronic current in this V_s polarity because no lithium supply is available from the probe side (left panel, Figure 61a) and a small V_s (< 1.5 V) cannot make a lithium reduction reaction from the SE. A working SE should flow ionic current dominantly in many orders of magnitude larger than electronic current. However, an inferior or a degraded SE by cycling can have comparable electronic current. The team has developed an imaging technique using a wide range (10^{-15} - 10^{-4} A) current sensor to enhance the detection sensitivity of ionic and electronic transport where current can differ by several orders of magnitude. Resolution is comparable to the probe size, ~ 20 nm.

In another nanoprobe-based characterization, the team aimed to image the space-charge layers by the nm-scale kelvin probe force microscopy (KPFM) potential mapping. Space-charge regions around the active-material/SE interface should exist, and can significantly affect Li-ion transport across the interface.^[4] Fermi-level alignment requires an ionic charge transfer across the interface between the ion conductors that build an electric field around the interface. Highly inhomogeneous space-charge regions are expected in SSB. This space-charge region has been proposed theoretically, but direct measurement of the electrical potential has been reported only by this team to its knowledge.^[5] They have developed the SSB-oriented potential imaging based on a home-developed KPFM with the state-of-the-art ~ 30-nm spatial resolution and ~ 10 mV sensitivity. An initial test on NMC/LPSCI interface demonstrated the highly nonuniform potential distribution in both amplitude of 300-500 mV and spatial 1-2 mm. These unique nm-scale ionic and electrical characterizations developed at NREL will be actively applied for assisting SSB development.

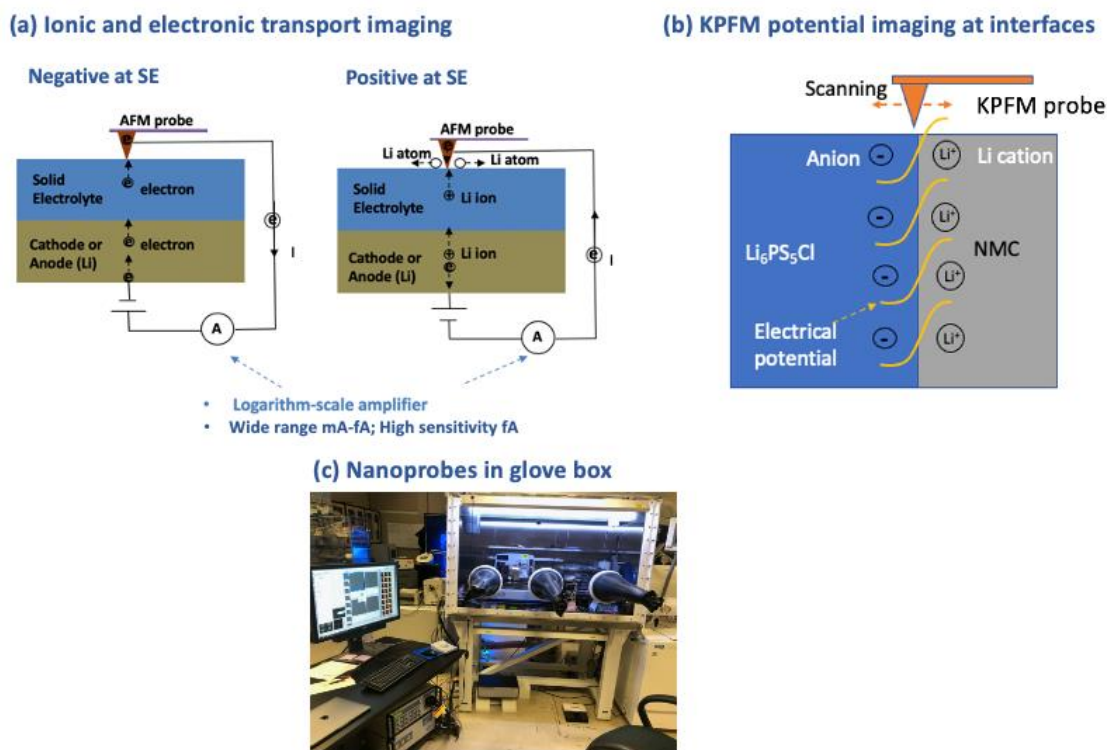


Figure 61. Schematics of (a) the nm-scale ionic and electronic transport imaging and (b) kelvin probe force microscopy (KPFM) potential imaging on space charges at interfaces. (c) Photograph of the atomic force microscopy – based nanoprobes set up in an argon glove box.

Characterizing Changes in Chemical Environment during Charging (M. Toney)

To achieve the goal of measuring changes in the chemical environment of SSEs, the team is beginning by ensuring that they can reproducibly make SSBs using commercial SSEs. This quarter, they have been building the team's knowledge on preparing SSBs, with help from A. Maughan (Colorado School of Mines) and training from C. Ban's students at Colorado University, Boulder.

With D. Finegan, the team is building connections with M. Pasta (University of Oxford, UK) and P. Shearing (University College London, UK), part of the Faraday Institute, whose knowledge and experience in making SSBs the team hopes to leverage in the short term, forming longer-term collaborations as the project becomes more established.

Cell Development

In this first year, the SSE cell build team is developing techniques to fabricate large-area single-layer pouch cells using casting techniques suitable for high-volume manufacturing. Typically, solid-state cells have been limited to very small active areas ($\leq 1 \text{ cm}^2$) and made by mixing small amounts of dry powders and mechanically consolidating using an extreme amount of pressure ($\sim 1 \text{ GPa}$). This is unsuitable for high-volume manufacturing or implementation into high-energy-density modules/packs with limited mechanical constraints. Further, these cells often have separators on the order of 1-mm thick, resulting in low cell-level energy density. Presently, the team is casting solid separator and composite electrodes to be able to assemble 30 cm^2 single-layer pouch cells. Initially, cells will be constructed with anodes using lithium/graphite active material and cathodes with coated LCO, and also using a commercial chloride argyrodite electrolyte. These cells will be tested under moderate pressures of $\sim 10 \text{ MPa}$. Electrical isolation has been achieved with separators about $100\text{-}\mu\text{m}$ thick. As the project progresses, energy density of cells will increase and required pressure will decrease using novel electrolytes/interfaces developed by the materials team. For instance, LCO will be replaced with a high nickel cathode having $> 200 \text{ mAh/g}$, and more compliant active material / electrolyte interfaces will reduce required stack pressure.

The SSE cell build team focused on two main tasks this quarter:

- Establish Protocols for Fabricating Solid-State Cathodes, Anodes, and Electrolyte Separators via Slurry Printing, and Assembling them into Full-Cell Stacks for Electrochemical Testing.** Anode and cathode composite slurries have been formulated with the following compositions: 65 wt% active material (graphite or LCO), 30 wt% SSE ($\text{Li}_6\text{PS}_5\text{Cl}$), 5 wt% conductive carbon, and 5 wt% polymer binder (Oppanol). These were cast onto a copper foil (Figure 62a, graphite anode) or aluminum foil (Figure 62b, LCO cathode), then subsequently coated by SSE-only layer comprising 95 wt% SSE and 5 wt% Oppanol binder, as shown in Figure 62a-b. For Li-metal anodes, lithium metal can also be rolled to form thin films on stainless-steel foils, as shown in Figure 62c. Finally, freestanding SSE separator layers were fabricated by printing a SSE slurry onto a mylar backing or nonwoven fabric, as shown in Figure 62d, and laminated into a full-cell stack with anode and cathode composites later, using either a hot-roll press or *in situ* during application of pressure to a sealed cell stack. The slurry compositions and coating procedures can be modified to incorporate novel materials from other teams into the cell stack for electrochemical testing.

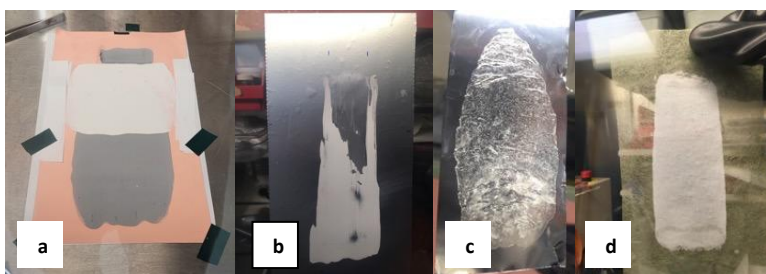


Figure 62. (a) Graphite composite anode with solid-state electrolytes (SSE) overlayer. (b) Coated LCO composite cathode with SSE overlayer. (c) Thin Li-metal film rolled onto stainless-steel foil. (e) SSE layer printed onto non-woven fabric.

- Building Equipment Capability for Testing $5 \times 6 \text{ cm}$ Area Single-Layer Solid-State Pouch-Cell Batteries under Known Pressures and Temperatures.** Load frames were fabricated to allow high pressures to be measured and applied to $5 \text{ cm} \times 6 \text{ cm}$ all-solid-state pouch cells. The frames are shown in Figure 63 and have been designed to apply up to 20 MPa or 50 MPa maximum pressures to the 30 cm^2 cell stack area. Digital load cell washers around each of the four load frame bolts will allow applied pressure to be measured. Compliant layers such as a dense foam or rubber sheets can be used to keep the applied pressure as uniform as possible. Next quarter, pouch cells will be placed into the load frame, and the team will apply measured pressure of $\sim 10 \text{ MPa}$. The frames can then be loaded into a temperature-controlled chamber, and the team can measure the electrochemical performance of the cell under known temperatures and pressures.

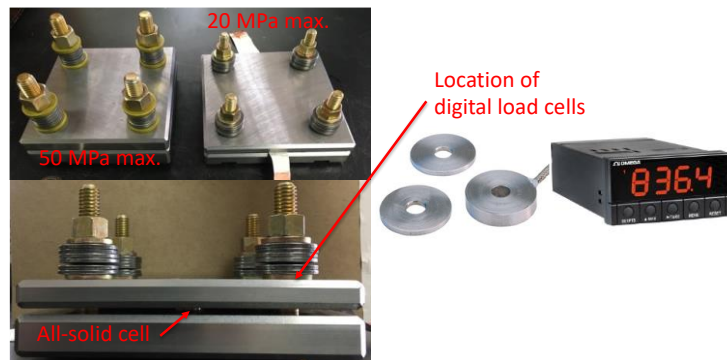


Figure 63. Load frames for applying digitally measured pressure to all-solid-state pouch or coin-cell batteries.

References

- [1] Sen, S., E. Trevisanello, E. Niemöller, B. X. Shi, F. J. Simon, and F. H. Richter. *Journal of Materials Chemistry A* 9 (2021): 18701–18732.
- [2] Riphaut, N., P. Strobl, B. Stiaszny, T. Zinkevich, M. Yavuz, J. Schnell, S. Indris, H. A. Gasteiger, and S. J. Sedlmaier. *Journal of The Electrochemical Society* 165 (2018): A3993–A3999.
- [3] Jiang, C.-S., N. Dunlap, Y. Li, H. Guthrey, P. Liu, S.-H. Lee, and M. M. Al-Jassim. *Advanced Energy Materials* 10 (2020): 2000219.
- [4] Haruyama, J., K. Sodeyama, L. Han, K. Takeda, and Y. Tateyama. *Chemistry of Materials* 26, (2014): 4248.
- [5] Jiang, C. S., K. Park, A. K. Burrell, and M. M. Al-Jassim. *The Electrochemical Society Meeting Abstract*, V. MA2020-02, Section A05 (2020): 934.

Patents/Publications/Presentations

The project has no patents, publications, or presentations to report this quarter.

Task 1.25 – Precision Control of the Lithium Surface for Solid-State Batteries (Andrew Westover, Oak Ridge National Laboratory)

Project Objective. The overall goal of this project is to understand and engineer the surface and purity of thin Li-metal anodes to enable batteries with an energy density of 500 Wh/kg and a cycle life > 300 cycles.

Impact. The knowledge of lithium surface engineering and the implications for cell design of Li-metal-batteries will improve commercialization efforts for SSLMBs. There is very little standard knowledge about variations in the impurity level in different lithium sources, the surface chemistry of different lithium surfaces, and their impact on performance. Furthermore, the strategies developed to engineer the surface of the lithium metal for integration into Li-metal batteries will provide significant performance increases, ideally enabling successful commercialization.

Approach. This project is broken into two parts. First, the team is focused on thoroughly understanding the purity, mechanics, and surface chemistry of multiple lithium sources and how these parameters impact performance. Second, they will focus on intentional engineering of the lithium purity and surface chemistry to control the mechanical properties, electrochemical stability, and electrochemical performance. They will explore three approaches to engineer the surfaces: gas-phase passivation, deposition of thin metal coatings, and deposition of thin inorganic coatings. To test electrochemical performance, they will use standard ceramic and polymer electrolytes to demonstrate the impact of purity and surface chemistry. The program will also employ a range of standard and specialized characterization techniques, including a significant focus on understanding the mechanics of lithium metal using nanoindentation and adhesion measurements using surface probe microscopy.

Out-Year Goals. In FY 2023, the program plans to finish gaining a deep understanding of different lithium sources, purity, and surface conditions, and of how they affect performance in Li-metal cells with both ceramic and polymer electrolytes. In FY 2024 through FY 2027, the primary goal is to develop strategies to carefully control and engineer the surface of lithium metal to optimize performance, enabling batteries that can achieve 500 Wh/kg and cycle for more than 300 cycles at mid-to-high current densities.

Collaborations. The primary collaborator for this project is E. Herbert at Michigan Technological University (MTU), who is focused on mechanical measurements of Li-metal anodes and electrolytes in inert environments. The project also includes R. Sahore, S. Kalnaus, W-Y. Tsai, and R. Sacci of ORNL. The team anticipates the BMR program will also foster significant collaborations with other teams who have a complementary focus on lithium metal. H. Meyer from ORNL helped with the XPS measurements and data analysis this quarter.

Milestones

1. Obtain lithium sources. (Q1, FY 2022; Completed)
2. Conduct chemical characterization of lithium surfaces. (Q2, FY 2022; Completed).
3. Conduct nanoindentation of various lithium sources. (Q3, FY 2022; In progress)
4. Establish baseline electrochemical performance of multiple lithium sources. (Q4, FY 2022; In progress)

Progress Report

This quarter, the team's work focused on obtaining and characterizing the surface of multiple thin lithium sources. They studied five lithium sources labeled Supplier #1, Supplier #2, Supplier #3, and Supplier #4, and ORNL (evaporated lithium produced in-house). The lithium from Suppliers #1-#4 are rolled Li-metal foils with a thickness of $\sim 40 \mu\text{m}$, except for the Supplier #2 lithium, which had a thickness of $\sim 500 \mu\text{m}$. Each of the purchased lithium sources was stored in its original packaging in an Ar-filled glovebox with minimal oxygen and H_2O content before characterization. The Supplier #1, Supplier #2, and Supplier #3 lithium films were freestanding, while the Supplier #4 lithium was laminated onto copper foil. The ORNL lithium was evaporated in a custom-designed chamber using an Alfa Aesar rolled-Li foil as the precursor. The Alfa Aesar foil was placed into a tantalum crucible and evaporated onto copper foil at $\sim 170 \text{ \AA/s}$. After deposition, the chamber and all the associated lithium were allowed to cool for several hours before a 95% Ar/ 5% CO_2 (99.9999% pure) was used to vent the system before bringing the evaporated lithium metal into the same glove box used to store the other lithium foils. To perform the initial characterization of the films, the team performed infrared (IR) spectroscopy measurements in the same Ar-filled glovebox using a Bruker Alpha II Fourier transform infrared (FTIR) spectrometer with an attenuated total reflection (ATR) diamond crystal module. The data are presented in Figure 64. As can be seen in the data, all the lithium films have some amount of lithium oxide and lithium carbonate on the surface, as seen by the characteristic lithium oxide / lithium / salt peaks from $\sim 400\text{-}700 \text{ cm}^{-1}$ and the characteristic lithium carbonate peaks at 800 cm^{-1} and $1400\text{-}1600 \text{ cm}^{-1}$. In addition, the rolled foils all have some amount of hydrocarbon, indicated by the series of peaks between 2800 cm^{-1} and 3000 cm^{-1} . The Supplier #2 lithium has an especially intense hydrocarbon peak, suggesting a hydrocarbon coating on the surface that may or may not be intentional. On the other hand, the Supplier #4 lithium has a faint but distinct silicone-based hydrocarbon signature, with the characteristic Si-H peak at 780 cm^{-1} and Si-O-Si peaks between $900\text{-}1100 \text{ cm}^{-1}$. While the Supplier #3 and Supplier #1 lithium do not have intense hydrocarbon peaks, the Supplier #1 lithium has a particularly intense lithium carbonate signature, and the Supplier #3 lithium has a particularly intense lithium oxide signature. The ORNL lithium only has relatively low-intensity lithium oxide and lithium carbonate peaks.

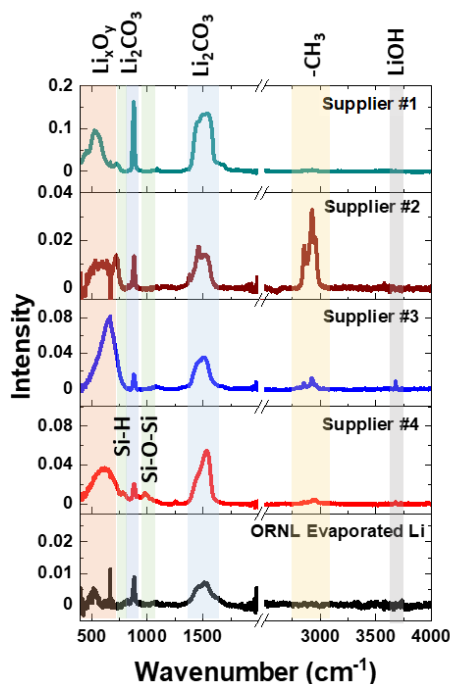


Figure 64. FTIR-ATR data of the five lithium sources studied: Supplier #1, Supplier #2, Supplier #3, Supplier #4, and ORNL evaporated lithium, from 400 cm^{-1} to 4000 cm^{-1} .

The team further characterized the samples using XPS, as shown in Table 5 and Figure 65. Table 5 presents the relative composition from an initial survey scan. All the samples have a significant amount of oxygen and carbon on the surface, with the ORNL evaporated lithium having the highest lithium concentration. Other trace impurities, including nitrogen, fluorine, sulfur, silicon, and chlorine, are found in trace amounts throughout a few samples, but are not significant enough to merit much discussion except for the silicon concentration in the Supplier #4 samples. There is an appreciable amount of silicon in the Supplier #4 lithium, amounting to ~ 1.6 at%. The data corroborate and support the IR data, which show the characteristics of a Si-based hydrocarbon such as silicone. A detailed look at the lithium 1s, carbon 1s, and oxygen 1s (Figure 65) reveals the presence of a significant amount of lithium carbonate, C-C based material, a small amount of lithium oxide, and a small amount of lithium carbide in the ORNL evaporated lithium. The carbon 1s data are particularly intriguing. The data suggest that lithium carbonate-based species dominate the surface layer of the ORNL lithium and Supplier #1 lithium, but that the Supplier #2, Supplier #3, and Supplier #4 lithium are dominated by the C-C species, likely a hydrocarbon. This observation aligns with the IR data where there are distinct hydrocarbon species in the Supplier #2, Supplier #3, and Supplier #4 lithium samples. The lack of significant lithium oxide peaks in the initial scan deviates from the IR data. It suggests that the lithium oxide components prevalent in much of the IR data come from species that are deeper under the surface, as IR probes several hundred nm at once. Still, XPS only probes the few nanometers on the very outer surface.

Table 5. Surface composition from X-ray photoelectron spectroscopy (at%) before etching.

	Li	O	C	F	Si	S	N	Cl
Supplier #1	30.4	43.1	26.3	0.1	0.1	0.0	0.0	0.1
Supplier #2	18.8	16.6	64.6	0.0	0.0	0.0	0.0	0.0
Supplier #3	22.3	21.9	55.2	0.2	0.0	0.0	0.4	0.0
Supplier #4	24.8	32.1	41.4	0.2	1.6	0.0	0.0	0.0
Evap. Li	34.7	37.0	28.0	0.1	0.1	0.1	0.0	0.0

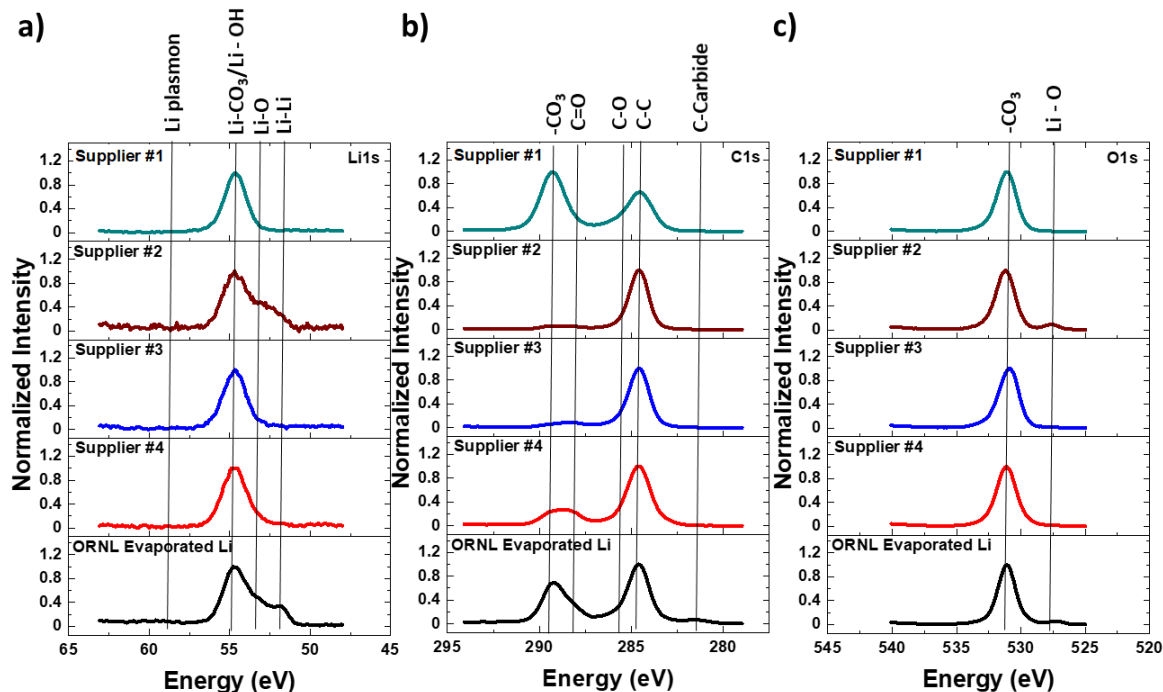


Figure 65. Initial X-ray photoelectron data of the five lithium sources studied: Supplier #1, Supplier #2, Supplier #3, Supplier #4, and ORNL evaporated lithium focused on the (a) lithium 1s, (b) carbon 1s, and (c) oxygen 1s peaks.

To get a better picture of the surface composition of the Li-metal sources and how they change a function of depth, the team used the etching capability integrated into the XPS system, where they can sputter off the surface and explore the surface composition as a function of depth. These data are presented in Figure 66, focusing on the lithium 1s, carbon 1s, and oxygen 1s in Figure 66a-c. The carbon-based surface species quickly disappear in all the samples after < 60 seconds of etching. The lone exception to this is the Supplier #1 lithium, where the C-C based peak immediately disappears, but the lithium carbonate peak remains for 250 seconds of etching (~ 50 nm). While the carbon species are etched away relatively quickly, rather than a pure Li-metal signal appearing, a distinct Li-oxide signal appears in all the lithium samples. This oxide is also etched away after ~ 300 seconds (~ 60 nm) for the evaporated lithium, 1500 seconds (~ 300 nm) for the Supplier #4 lithium, 1500 seconds (~ 300 nm) for the Supplier #3 lithium, 2000 seconds (~ 400 nm) for the Supplier #2 lithium, and 3200 seconds (~ 640 nm) for the Supplier #3 lithium. While the Supplier #4, Supplier #2, and ORNL lithium all have a quick decline in intensity, suggesting a more mixed composition, the Supplier #1 and Supplier #3 lithium both have a very distinct Li-oxide layer that persists for > 1000 seconds of etching followed by a more gradual decay in the Li-oxide content. This buried oxide directly aligns with the IR data.

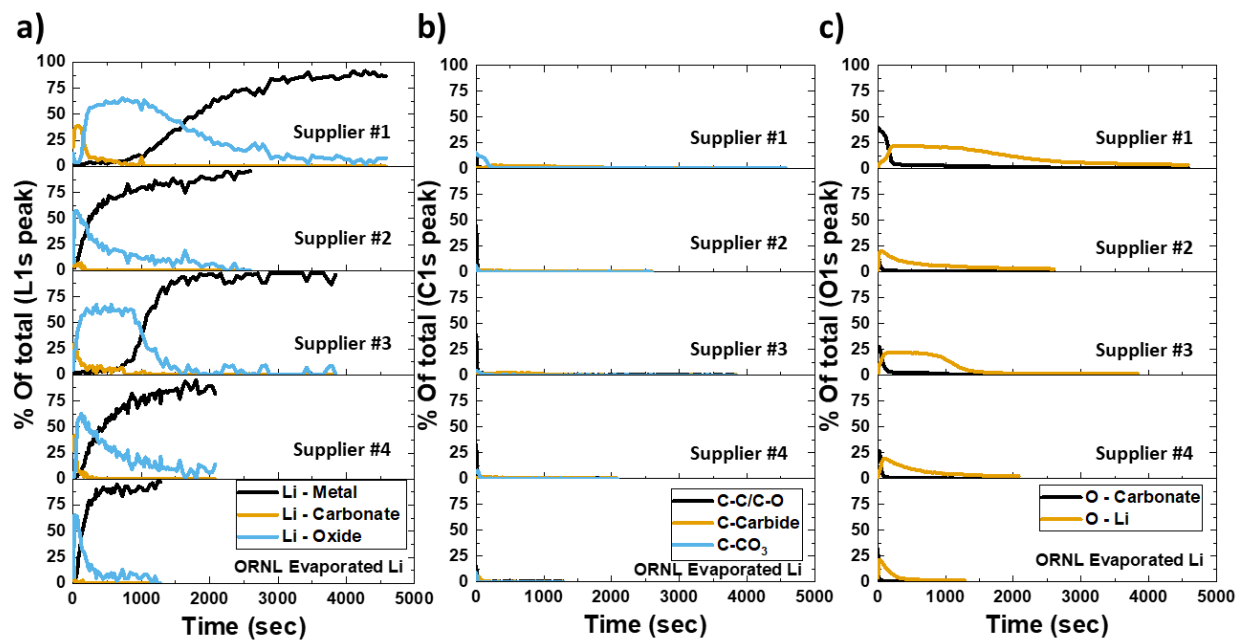


Figure 66. Depth profiling X-ray photoelectron spectroscopy data of the 5 lithium sources studied: Supplier #1, Supplier #2, Supplier #3, Supplier #4, and ORNL evaporated lithium, focused on the lithium 1s (a), the carbon 1s (b), and the oxygen 1s (c) peaks with the different lithium, carbon, and oxygen species denoted as a function of etching time. The estimated etching rate based on a SiO₂ standard was 12 nm/min for an estimated etch depth of ~ 200 nm per 1000s.

After the lithium etching was completed, the team again took survey scans of each lithium sample. The dominant signal was lithium metal at greater than 97% in all cases. Each of the samples had some residual oxygen due to the outgassing of oxygen from the XPS chamber walls. All other impurities, including the carbon and silicon, were eliminated from the samples. The most notable impurity is sodium, which appeared in appreciable amounts in both the Supplier #3 and Supplier #1 lithium. As sodium is the most common impurity in lithium metal, this is likely a real impurity. Based on the atomic percentages from XPS, this would place the Supplier #3 and Supplier #1 lithium at ~ 99.6% pure. There were trace amounts of copper identified for the Supplier #4 supplies and the ORNL evaporated lithium, but this is an artifact of the etching process, as both have copper substrates. A small amount of re-sputtering of copper onto the surfaces is not unexpected.

In summary, the team has identified that lithium supplied by Supplier #1 is passivated with a Li-carbonate layer, the Supplier #2 lithium is passivated with a hydrocarbon, the Supplier #3 lithium is likely also passivated with a hydrocarbon in combination with a carbonate, the Supplier #4 lithium is passivated with a Si-based hydrocarbon, and the ORNL lithium has a Li-carbonate passivation layer. In addition, all lithium samples have

a significant Li-oxide layer underneath the surface passivation that can range in thickness from < 50 nm (for ORNL evaporated lithium) to > 500 nm for the Supplier #1 lithium. Perhaps one of the most important findings was that even for thin lithium samples, a simple etching process could eliminate virtually all surface species, leaving mostly clean lithium surfaces. As the significant surface species present on Li-metal films will undoubtedly impact battery performance, great care needs to be taken in the choice of lithium source, the characterization of the surface species, and the pretreatment before use.

Table 6. X-ray photoelectron spectroscopy surface composition (at%) after etching.

	Li	O	C	Cu	Na
Supplier #1	96.8	2.8	0.0	0.0	0.4
Supplier #2	97.8	2.2	0.0	0.0	0.0
Supplier #3	98.2	1.3	<0.1	0.0	0.3
Supplier #4	98.0	2.0	0.0	<0.1	0.0
Evap. Li	98.6	1.3	0.0	0.1	0.0

Patents/Publications/Presentations

The project has no patents, publications, or presentations to report this quarter.

TASK 2 – DIAGNOSTICS

Team Lead: Guoying Chen, Lawrence Berkeley National Laboratory

Summary and Highlights

To meet the goals of the Vehicle Technologies Office programs on next-generation electric vehicles, low-cost and abuse-tolerant batteries with higher energy density, higher power density, better safety, and longer lifetimes are needed. In pursuit of these goals, high cell operating voltages and demanding cycling conditions are used, which leads to unprecedented chemical and mechanical instabilities in cell components. Successful implementation of promising electrode materials (such as silicon anode and high-voltage cathodes) and new cell chemistry (such as high-energy Li-metal cells combined with solid-state electrolytes, or SSEs) requires better understanding of fundamental processes, especially those at the interface/interphase of both anode and cathode. Identifying and understanding structure-property-electrochemical performance relationships in materials and various failure modes in cell chemistry are therefore more pressing than ever, not only in guiding battery development activities but also the scale-up efforts needed for commercialization.

This Task takes on these challenges by combining model systems, *ex situ*, *in situ*, and *operando* approaches, with an array of state-of-the-art analytical and computational tools. Numerous subtasks are tackling the chemical processes and reactions at the electrode/electrolyte interfaces in Li-metal batteries. Researchers at Lawrence Berkeley National Laboratory (LBNL) use surface- and bulk-sensitive techniques, including Fourier transform infrared (FTIR), attenuated total reflectance – FTIR, near-field IR and Raman spectroscopy/microscopy, and scanning probe microscopy to characterize changes in materials and the physicochemical phenomena occurring at the interface of Li-metal electrode. General Motors is developing *in situ* diagnostic techniques, including atomic force microscopy, nano-indentor, dilatometer, and stress-sensor, to be combined with atomic/continuum modeling schemes to investigate the coupled mechanical/chemical degradation of the solid electrolyte interphase layer as well as the microstructural evolution at the interface/interphase of Li-metal anode. University of Houston is developing multidimensional diagnostic tools, including focused ion beam – scanning electron microscopy (SEM), time-of-flight – secondary ion mass spectrometry, and in-SEM nanoindentation, to probe structural, chemical, and mechanical evolution at the interfaces of solid-state lithium batteries. At LBNL, model systems of electrode, SSE, and their interfaces with well-defined physical attributes are being developed and used for advanced diagnostic and mechanistic studies at both bulk and single-particle levels. These controlled studies remove the ambiguity in correlating a material's physical properties and reaction mechanisms to its performance and stability, which is critical for further optimization. Subtasks at Brookhaven National Laboratory (BNL) and Pacific Northwest National Laboratory (PNNL) focus on the understanding of fading mechanisms in electrode materials, with the help of synchrotron-based X-ray techniques (diffraction and hard/soft X-ray absorption spectroscopy) at BNL and high-resolution transmission electron microscopy (HRTEM) / scanning transmission electron microscopy (STEM) and related spectroscopy techniques at PNNL. The final subtask at Stanford University / Stanford Linear Accelerator Center develops and utilizes an integrated X-ray characterization toolkit to investigate and generate insights on solid-state batteries, by tracking the evolution of nanoscale chemistry as well as structure, microstructure, and transport properties. The diagnostics team not only produces a wealth of knowledge key to developing next-generation batteries, but also advances analytical techniques and instrumentation with a far-reaching effect on material and device development in various fields.

Highlights

The highlights for this quarter are as follows:

- The LBNL (G. Chen) group demonstrated stable cycling of all-solid-state Li-metal battery cells employing an uncoated single-crystal NMC-811 cathode, Li_3YCl_6 solid electrolyte, and a Li-In anode for over 1000 cycles. The formation of an interlayer between the electrolyte and anode was revealed in the cycled cell.

- The BNL (X-Q. Yang / E. Hu) team used cryogenic transmission electron microscopy to demonstrate the ability of LiNO₃ additive in suppressing lithium dendrites. The cryogenic conditions reduce beam damage on deposited materials, allowing observation of uniformly spheric versus dendritic lithium formations with and without LiNO₃, respectively.

Task 2.1 – Characterization and Modeling of Lithium-Metal Batteries: Model-System Synthesis and Advanced Characterization (Guoying Chen, Lawrence Berkeley National Laboratory)

Project Objective. This project will use a rational, non-empirical approach to design and develop SSE materials and interfaces for next-generation Li-metal batteries. Combining a suite of advanced diagnostic techniques with carefully prepared model-system samples, the project will perform systematic studies to achieve the following goals: (1) obtain understanding on the role of SSE grain and GBs on ion conduction and dendrite formation, (2) obtain fundamental knowledge on rate- and stability-limiting properties and processes in SSEs when used in Li-metal batteries, (3) investigate the reactivities between SSE and electrodes, and gain insights on the dynamic evolution of the interfaces, and (4) design and synthesize improved SSE materials and interfaces for safer and more stable high-energy Li-metal batteries.

Impact. The project will focus on fundamental understanding of SSE and relevant interfaces to enable its use in Li-metal batteries. Knowledge gathered from model-system-based studies will guide the design and engineering of advanced materials and interfaces. The use of the non-empirical, rational-design approach will develop high-energy battery systems with improved commercial viability.

Approach. The project will combine model-system synthesis and advanced diagnostic studies to investigate ion conduction and interfacial chemistry of SSE in Li-metal batteries. Single crystalline (SC), polycrystalline (PC), and amorphous model SSE samples with various grain and GB properties will be synthesized. Model interfaces between the SSE and electrodes with controlled properties will also be developed. Both bulk-level and single-grain-level characterization will be performed. Global properties and performance of the samples will be established from the bulk analyses, while the single-grain-based studies will utilize time-resolved and spatially-resolved analytical techniques to probe the intrinsic redox transformation processes and failure mechanisms under battery operating conditions.

Out-Year Goals. In the out years, the project will deliver fundamental knowledge on the role of SSE microstructure in Li^+ conduction and lithium dendrite formation/propagation. Insights on performance-limiting physical properties and phase transition mechanisms as well as dynamic evolution of SSE/electrode interfaces will be obtained. Mitigating approaches, such as use of surface coating or a “buffer layer” in stabilizing SSE/electrode interfaces, will be evaluated. Further, advanced SSE materials and interfaces for improved high-energy Li-metal batteries will be designed and synthesized.

Collaborations. This project collaborates with the following PIs: G. Ceder, K. Persson, M. M. Doeff, B. McCloskey, R. Kostecki, and R. Prasher (LBNL); W. Yang (Advanced Light Source, ALS); D. Nordlund and Y. Liu (Stanford Synchrotron Radiation Lightsource, SSRL); C. Wang (PNNL); and J. Nanda (ORNL).

Milestones

1. Develop SSE/cathode model systems for studying the cathode interfaces. (Q1, FY 2022; Completed)
2. Synthesize SSE model samples and model SSE/cathode interfaces. (Q2, FY 2022; Completed)
3. Advanced diagnostic studies of SSE/cathode interfaces. (Q3, FY 2022; On schedule)
4. Obtain mechanistic understanding and deliver design strategies to improve SSE/cathode interfaces. (Q4, FY 2022; On schedule)

Progress Report

Last quarter, the team constructed model systems to investigate interfacial chemistry in ASSB cells. Cathode composites were prepared by combining NMC-811, Li_3YCl_6 (LYC), and carbon black in a weight ratio of 57 : 40.5 : 2.5. Both PC and SC NMC-811 were directly used as cathode active material, or CAM, without a coating, which consists of large secondary particles ($\sim 10\ \mu\text{m}$) with primary grains of $\sim 0.5\ \mu\text{m}$ and discrete single grains of 3-5 μm , respectively (Figure 67a-b). All solid-state NMC-811 LYC | LYC | Li-In cells were assembled and cycled between 3.0 V and 4.3 V (V versus Li^+/Li). Figure 67c-d compares the electrochemical performance when cycled at 0.5 C at room temperature. While the PC cell delivered a discharge capacity of $\sim 110\ \text{mAh/g}$, the SC cell delivered $\sim 150\ \text{mAh/g}$ on initial cycling, a net gain of 36%. Gradual capacity decrease was observed in both cells, with a capacity retention of $\sim 70\%$ after 820 cycles and $\sim 90\%$ after 1000 cycles, respectively (Figure 67e). The rate capability comparison is shown in Figure 67f. As expected, both cells showed relatively poor rate performance due to the absence of any LE. The cells with the SC NMC-811 active material, however, significantly outperformed the PC counterpart in cycling stability and rate capability testing.

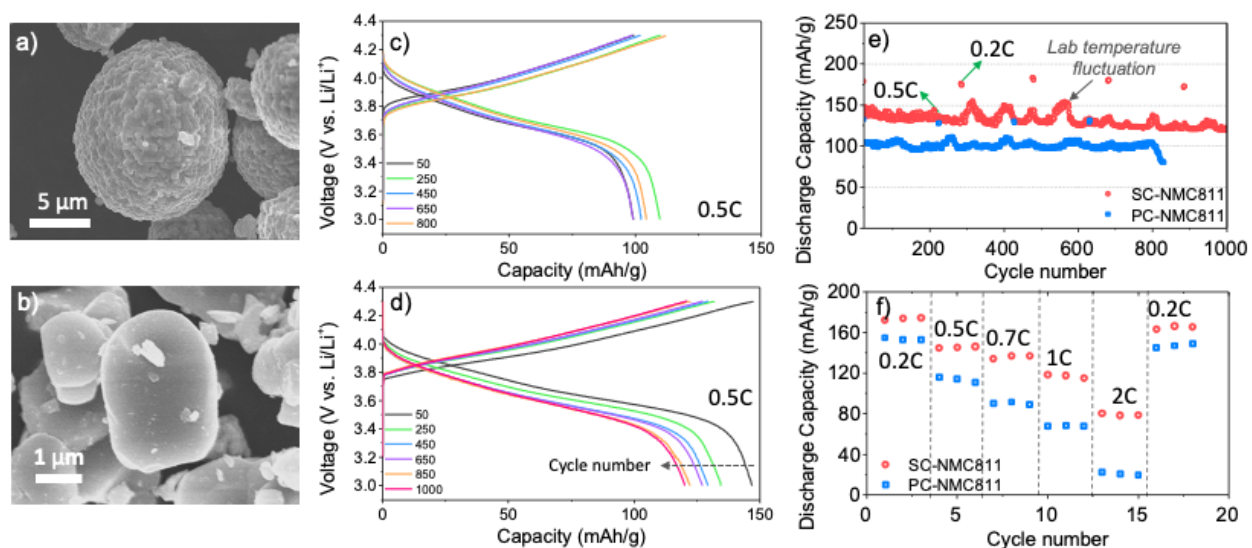


Figure 67. (a-b) Scanning electron microscopy images of polycrystalline (PC) NMC-811 and single crystalline (SC) NMC-811 particles, respectively. (c-d) Voltage profiles collected on PC NMC-811 and SC NMC-811 cells cycled at 0.5C. Li_3YCl_6 was used as electrolyte and Li-In alloy used as anode. (e) Comparison of discharge capacity as a function of cycle number. (f) Rate capability comparison of the cells.

The excellent cycling stability of the project's SC NMC-811 cell represents one of the best performances reported to date on ASSB cells with an NMC cathode and a Li-metal based anode. The team wishes to note that previous theory studies have predicted reduction of LYC to yttrium metal, Y_2Cl_3 , and LiCl at the Li-metal anode interface. Without effective protection, cells with a LYC SE are expected to have poor cycle life, as metallic yttrium leads to an increase in electronic conduction and cell shorting over cycling. To this end, they performed post-mortem analysis to understand interface evolution at the anode. Figure 68 shows results collected at the cross-section of the cycled ASSB anode interface. A distinct interface layer was found between LYC electrolyte and Li-In anode after cycling (Figure 68a), indicating reactivity at the anode. The SEM image shows an average interlayer thickness of $\sim 8\ \mu\text{m}$ after 1000 cycles. EDS analysis (Figure 68b-d) reveals that the chemical composition of the interlayer includes indium, yttrium, and chlorine, although lithium may also exist that was not detectable by EDS.

To further investigate the chemical nature of the interface layer, hard XAS and micro-XRF mapping were used to analyze yttrium oxidation state at the cycled anode interface. After removing the composite cathode and LYC layers, the sample was sandwiched between two Kapton tapes for measurements. The experiments

were carried out at beam line 2-3 at SSRL. Figure 68e compares the XANES profiles collected on the cycled interface as well as pristine LYC and yttrium metal standard for comparison. There is a white-line crossover between the pristine LYC and the cycled sample, indicating slight differences in atomic environment of yttrium. However, the yttrium oxidation state largely remains at $3+$, and metallic yttrium was not detected after extensive cycling. This is further shown in the chemical map obtained by XRF (Figure 68f), where a multi-energy map collected at 17053.99 eV, 17058.29 eV, and 17180 eV was analyzed by linear combination fitting of yttrium XAS data collected from yttrium metal and YCl_3 references. The oxidation state map of yttrium shows uniform distribution of Y^{3+} , as well as the absence of metallic yttrium in the entire area examined. The team believes this discovery is significant, as in this case the interlayer likely provided passivation between LYC and lithium anode and enabled the extraordinarily stable cycling of the ASSB cell.

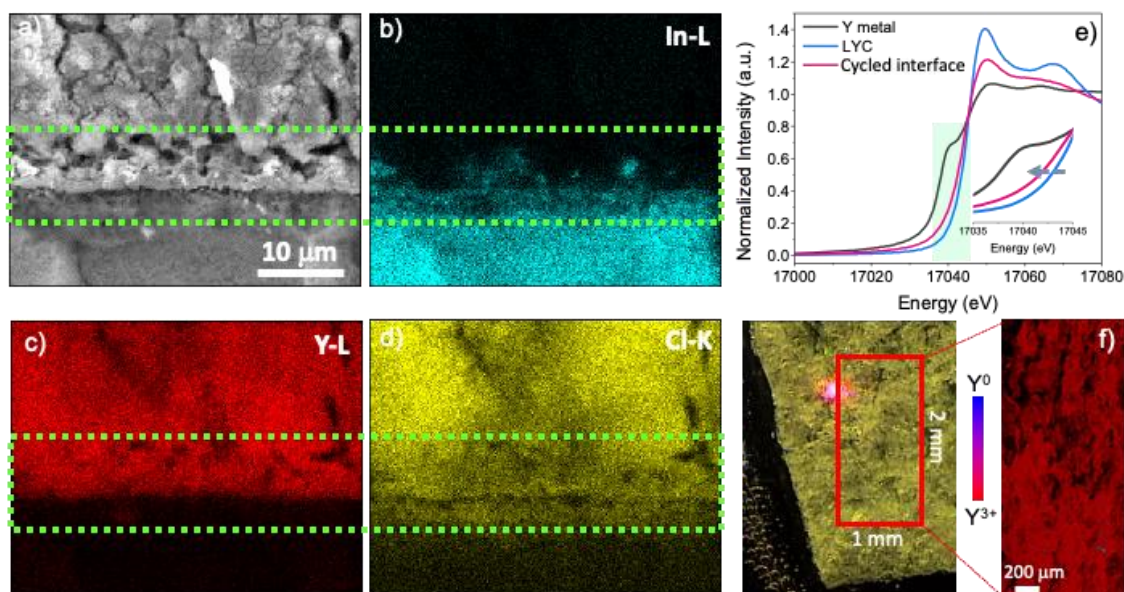


Figure 68. Post-mortem analysis of the interface between Li_3YCl_6 (LYC) and Li-In anode after 1000 cycles. (a) Cross-sectional scanning electron microscopy image. (b-d) Energy-dispersive X-ray spectroscopy maps of In-Li, Y-Li, and Cl-K, respectively. (e) Yttrium K-edge X-ray absorption spectra collected on yttrium metal, pristine LYC, and the interface after cycling. (f) Chemical map obtained from X-ray fluorescence imaging.

Patents/Publications/Presentations

Presentation

- U. S. – U. K. Battery Technology Research and Innovation Summit, Virtual (February 2022): “VTO Cathode Overview”; G. Chen. Invited.

Task 2.2 – Interfacial Processes – Diagnostics (Robert Kostecki, Lawrence Berkeley National Laboratory)

Project Objective. The project objective is to establish specific design rules toward the next generation of low-impedance Li-metal rechargeable batteries that are capable of performing 1000 deep discharge cycles at CE > 99.9% and suppressing lithium dendrite formation at high current densities (> 2 mA/cm²). This project aims at the following: (1) establishing general rules between Li⁺ transport properties in novel liquid/solid electrolytes, and (2) determining the mechanism of the SEI layer (re)formation. The other goal is development and application of far- and near-field optical probes and synchrotron-based advanced X-ray techniques to obtain insight into the mechanism of Li⁺ transport and interfacial reactions in lithium/liquid model systems. Through an integrated synthesis, characterization, and electrochemistry effort, this project aims to develop a better understanding of lithium/LE interface so that rational decisions can be made as to their further development into commercially viable Li-metal cells.

Project Impact. Chemical instability and high impedance at the interface of Li-metal electrodes limit electrochemical performance of high-energy-density batteries. A better understanding of the underlying principles that govern these phenomena is inextricably linked with successful implementation of high-energy-density materials in Li-metal-based cells for PHEVs and EVs. New state-of-the-art techniques to identify, characterize, and monitor changes in materials structure and composition that take place during battery operation and/or storage will be developed and made available to BMR participants. The work constitutes an integral part of the concerted effort within the BMR Program, and it supports development of new electrode materials for high-energy, Li-metal-based rechargeable cells.

Approach. Pristine and cycled composite electrode and model thin-film electrodes will be probed using various surface- and bulk-sensitive techniques, including FTIR, ATR-FTIR, near-field IR and Raman spectroscopy/microscopy, and scanning probe microscopy to identify and characterize changes in materials structure and composition. Novel *in situ* / *ex situ* far- and near-field optical multi-functional probes in combination with standard electrochemical and analytical techniques are developed to unveil the structure and reactivity at interfaces and interphases that determine electrochemical performance and failure modes of materials.

Out-Year Goals. In the out-years, the project aims to achieve the following: (1) understand factors that control performance and degradation processes, (2) unveil structure and reactivity at hidden or buried interfaces and interphases that determine electrochemical performance and failure modes, and (3) propose effective remedies to address inadequate Li-metal-based battery calendar/cycle lifetimes for PHEV and EV applications.

Collaborations. Diagnostic studies will be carried out in sync with other diagnosticians (that is, G. Chen, B. McCloskey, R. Prasher, and L-W. Wang) and theory/computational scientists (that is, G. Ceder and K. Persson).

Milestones

1. Fundamental physicochemical and electrochemical characterization of the considered primary and secondary Li-metal cell chemistries. (Q1, FY 2022; Completed)
2. *In situ* nano-FTIR spectroscopy experimental setup for probing Li/LE interface designed, built, and tested. Preliminary tests and results delivered. (Q2, FY 2022; Completed)
3. Near- and far-field optical and XPS characterization of the baseline Li-metal cell chemistries and relevant interfacial phenomena and processes completed. (Q3, FY 2022; In progress)
4. Correlation of electrolyte chemistry and Li/SEI compositional structure in Li-metal baseline LE and SE systems determined. (Q4, FY 2022; In progress)

Progress Report

This quarter's milestone was successfully completed. In addition, progress advanced toward the third and fourth quarter milestones.

To address this quarter's milestone, the team adopted a liquid cell design their lab has previously utilized successfully,^[1] which generally enables characterization of electrically biased solid/liquid interfaces, *in situ* and nondestructively, via near-field infrared nanospectroscopy (nano-FTIR). The experimental setup is illustrated in Figure 69, where an atomically thin and IR transparent carbon membrane (graphene) functions as both an optical window and working electrode, while a metalized AFM probe opposite and adjacent to the interface enhances and confines incident IR light. In this way, collection of nano-FTIR spectra from nanoscopic volumes subsurface to graphene (the interfacial region) are readily performed.

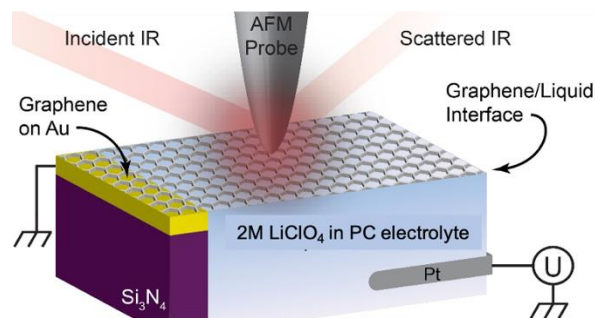


Figure 69. Schematic of experimental and device setup for graphene-liquid electrochemical *in situ* cell for infrared near-field imaging and nanospectroscopy, previously used by this team.

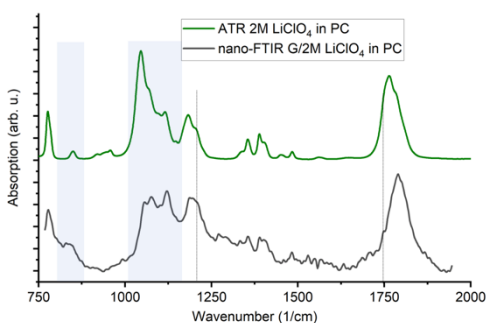


Figure 70. Comparison of attenuated total reflectance – Fourier transform infrared (ATR-FTIR) of 2 M LiClO₄ in propylene carbonate (top, green trace) and nano-FTIR spectra of the graphene / 2 M LiClO₄ in propylene carbonate interface (bottom, black trace). Light blue bars and black vertical lines highlight measured differences in infrared absorption between the bulk and interface.

It is clear by direct comparison that the molecular environment of the bulk and interface must be significantly different. Contributing to this discrepancy is likely the difference in average ion solvation between the bulk and interface. These measurements confirm that the device and experimental setup are capable of characterizing the interface, *in situ*.

Following the *in situ* methodology described, spatially-dependent nano-FTIR spectra were collected along the graphene/LE interface at roughly 100 nm separations (and ca. 20-nm resolution), while in an open circuit state. These spectra are plotted in Figure 71a, and possess subtle differences in a few regions, such as ~ 1200 cm⁻¹ and 1750 cm⁻¹ (note the ~ 1700-1900 cm⁻¹ region corresponds to the carbonyl C = O group for PC^[2-3]). The modest heterogeneities in absorption may arise from *local* variations in (1) the concentration of free propylene carbonate molecules, (2) the solvation state of interfacial ionic species, (3) orientations of physisorbed ClO₄⁻, and (4) structure and composition of the electric double and diffuse layers. In any case, ultimately, these naturally occurring nanoscale heterogeneities in the IR absorption

Beyond the designing, building, and testing of the device, the milestone plans include conducting preliminary experiments that would build toward the eventual probing of the Li/LE interface in future milestones. As a natural progression to this end, the team opted to use an electrolyte that is less chemically complex than GEN2: 2M LiClO₄ in propylene carbonate. First, ATR-FTIR of the bulk electrolyte was collected (Figure 70, green trace) and compared with nano-FTIR absorption of the graphene/LE interface (Figure 70, black trace). It is clear by direct comparison that the molecular environment of the bulk and interface must be

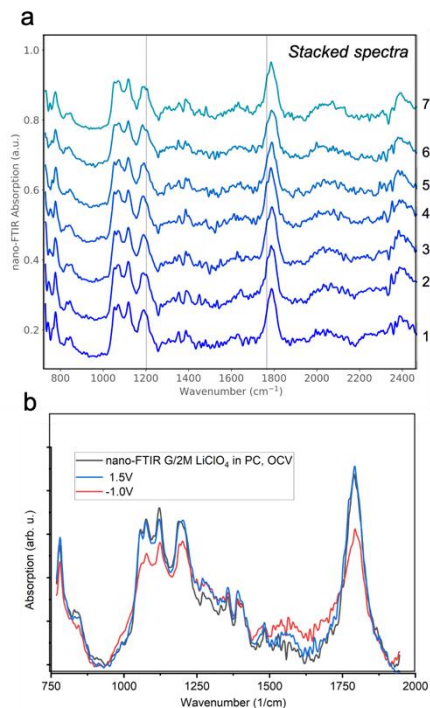


Figure 71. (a) Spatially-resolved nano – Fourier transform infrared (nano-FTIR) spectra across the graphene / 2 M LiClO₄ in propylene carbonate interface. Noted with the black lines are changes in the shoulder of the peaks (b) biased nano-FTIR data collected over single location

spectra certainly point to *nanoscale* heterogeneities in the local molecular environments which together comprise the interface. As shown in the team's recently published work for PE systems,^[4] these heterogeneities may be the source for additional subsequent heterogeneities in lithium plating and interphase formation—though additional work to verify this is needed.

Lastly, gold contacts to the graphene enable the biasing of the graphene working electrode with respect to a thin-diameter wire of choice that can be inserted into the LE reservoir (a few microliters in volume). For these preliminary measurements focused on demonstrating device functionality and methodological transferability to a multiplicity of chemistries, the team chose to conduct basic potential step experiments, to ensure the device was diffusion limited. Once a steady state was reached, they collected nano-FTIR. To accomplish these *in situ* bias-dependent measurements, they chose a silver wire. As the graphene electrode is biased, and charge is transferred to/from graphene proceeds, the graphene/liquid interface should respond, including the local distribution and concentration of electrolyte solution components. These changes should be observable in the nano-FTIR if it is indeed primarily probing the interface. Such findings are reflected in the bias-dependent nano-FTIR spectra the team collected (Figure 71b).

References

- [1] Lu, Y-H., J. M. Larson, A. Baskin, X. Zhao, P. D. Ashby, D. Prendergast, H. A. Bechtel, R. Kostecki, and M. Salmeron. *Nano Letters* 19, no. 8 (2019): 5388–5393.
- [2] Battisti, D., G. Nazri, B. Klassen, and R. Aroca. *The Journal of Physical Chemistry* 97, no. 22 (1993): 5826–5830.
- [3] Barthel, J., R. Buchner, and E. Wismeth. *Journal of Solution Chemistry* 29, no. 10 (2000): 937–954.
- [4] He, X., J. M. Larson, H. A. Bechtel, and R. Kostecki. *Nature Communications* 13, no. 1 (2022): 1398.

Patents/Publications/Presentations

The project has no patents, publications, or presentations to report this quarter.

Task 2.3 – Advanced *In Situ* Diagnostic Techniques for Battery Materials (Xiao-Qing Yang and Enyuan Hu, Brookhaven National Laboratory)

Project Objective. The primary objective of this project is to develop new advanced *in situ* material characterization techniques and to apply these techniques to support development of new cathode and anode materials with high energy and power density, low cost, good abuse tolerance, and long calendar and cycle life for beyond Li-ion battery systems to power PHEVs and battery electric vehicles (BEVs). The diagnostic studies will focus on issues relating to capacity retention, thermal stability, cycle life, and rate capability of beyond Li-ion battery systems.

Project Impact. The VTO Multi-Year Program Plan describes the goals for battery: “Specifically, lower-cost, abuse-tolerant batteries with higher energy density, higher power, better low-temperature operation, and longer lifetimes are needed for development of the next-generation of HEVs [hybrid electric vehicles], PHEVs, and EVs.” The results of this project will be used for development of technologies that will significantly increase energy density and cycle life, and reduce cost. This will greatly accelerate deployment of EVs and reduce carbon emission associated with fossil fuel consumption.

Approach. This project will use a combination of SXRD and pair distribution function (x-PDF) and of neutron diffraction and pair distribution function (n-PDF); X-ray spectroscopies including hard/soft XAS, X-ray photon emission spectroscopy (PES); and imaging techniques including XRF microscopy, transmission X-ray microscopy (TXM), and transmission electron microscopy (TEM).

Out-Year Goals. The out-year goals are to develop spectro-tomography, XRD, XAS, and PDF techniques, and to apply these techniques on Li-ion battery cathode, Na-ion battery cathode, and SSE.

Collaborations. The BNL team will work closely with material synthesis groups at ANL (Y. Shin and K. Amine) for the high-energy composite, at PNNL for the S-based cathode and Li-metal anode materials, and with ORNL on neutron scatterings. This project will also collaborate with industrial partners, as well as with international collaborators.

Milestones

1. Complete XRD and X-ray PDF studies on SSE $\text{Li}_7\text{P}_2\text{S}_8\text{I}_{0.5}\text{Br}_{0.5}$ to understand its degradation mechanism at high voltage. (Q1, FY 2022; Completed)
2. Complete cryo-EM study to understand the positive role of LiNO_3 additive in SEI formation on Li-metal anode. (Q2, FY 2022; Completed)
3. Complete many-particle TXM studies on $\text{LiNi}_{0.8}\text{Mn}_{0.1}\text{Co}_{0.1}\text{O}_2$ cathode to understand its chemical and morphological heterogeneities at the electrode level. (Q3, FY 2022; In progress)
4. Complete *ex situ* XAS and TXM studies on polymeric sulfur cathode to understand its redox mechanism and morphological evolutions during cycling. (Q4, FY 2022; In progress)

Progress Report

This quarter, the second milestone was completed. BNL has been focusing on developing advanced diagnostic techniques to achieve a thorough understanding of high-energy-density, long-cycle-life electrode materials. Li-metal anode is regarded as one of the most promising anode materials for next-generation lithium batteries because of the high theoretical capacity. However, the degradation of Li-metal anodes related to unfavored interphase behaviors during electrochemical cycling is still a setback for its practical applications on EVs. Great efforts have been devoted to solving the interphase problem for the Li-metal anode by developing novel electrolytes in the past few years. For example, LiNO_3 has been widely used as an additive for the Li-metal anode. However, the mechanism of how LiNO_3 improves the SEI for lithium metal is still unclear, which greatly slows down the novel additive development. Therefore, an investigation of the effects of LiNO_3 on the Li-metal anode was planned by using cryogenic transmission electron microscopy (cryo-TEM). A cryo-EM study was carried out on the lithium metal plated in the electrolyte with and without the LiNO_3 additive by the BNL team. The cryogenic condition can greatly enhance the beam tolerance of lithium metal and the SEI, therefore reducing beam damage on the samples. As shown in Figure 72a-b, the lithium plated in the baseline electrolyte without LiNO_3 are in dendritic form. On the other hand, with LiNO_3 added, the lithium are plated as uniform spheric lithium particles, and lithium dendrite formation is greatly suppressed. Moreover, uniform and conformal SEI is formed with the help of LiNO_3 additive, which could be correlated with the improved capacity retention for LiNO_3 -added electrolyte. The fast Fourier transform (FFT) pattern on a selected SEI area shows three inorganic components in the SEI formed with LiNO_3 -added electrolyte.

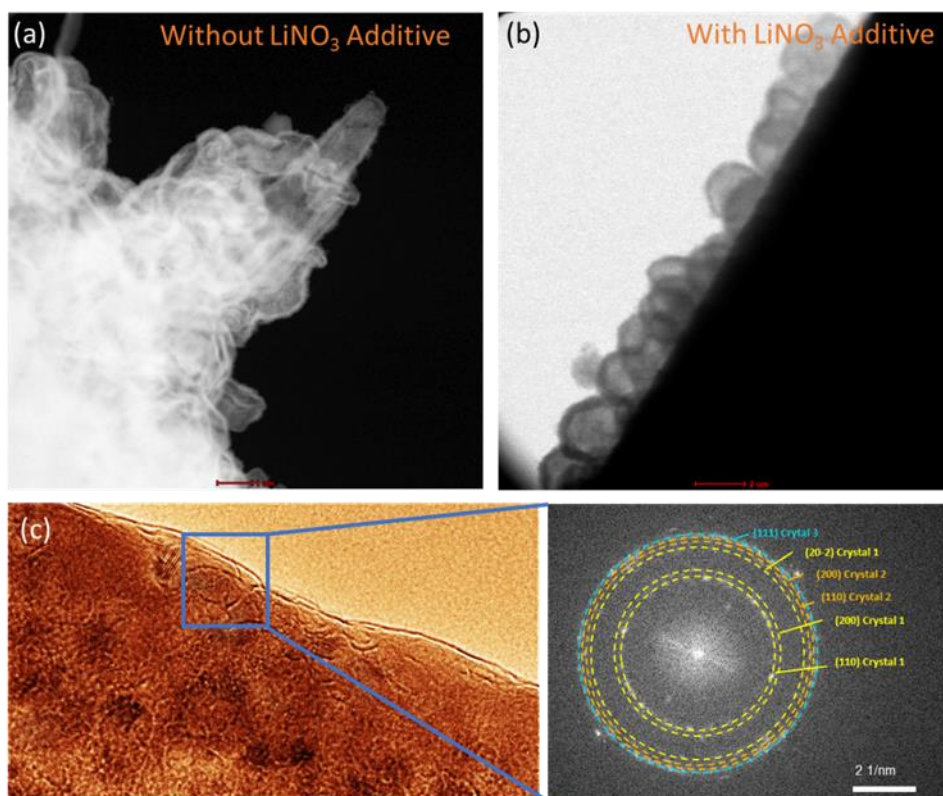


Figure 72. (a) Cryo – high-angle annular dark field (HAADF) scanning transmission electron microscopy (STEM) of plated lithium dendrite in baseline electrolyte without LiNO_3 additive. (b) Cryo – bright field STEM of plated lithium particles in electrolyte with LiNO_3 additive. (c) Cryo – transmission electron microscopy and selected area diffraction of the SEI formed in electrolyte with LiNO_3 additive.

Patents/Publications/Presentations

The project has no patents, publications, or presentations to report this quarter.

Task 2.4 – Probing Interfacial Processes Controlled Electrode Stability in Rechargeable Batteries (Chongmin Wang, Pacific Northwest National Laboratory)

Project Objective. The main objective is to explore interfacial phenomena in rechargeable Li-ion batteries of both SSE and LE configuration, to identify the critical parameters that control the stability of interface and electrodes as well as SE. The outcome will be establishing correlations between structural-chemical evolution of active components of batteries and their properties. These correlations will provide insight and guidance to battery materials development groups for developing high-performance battery materials.

Project Impact. The proposed characterization work focuses on atomic-level structural and chemical analysis and direct correlation with battery fading properties. The work can be directly used to guide design of electrode materials with tailored microstructure and chemistry for enhanced properties of increasing the energy density of Li-ion batteries and to accelerate market acceptance of EVs, especially for PHEVs as required by the EV Everywhere Grand Challenge.

Approach. The project will use integrated advanced microscopic and spectroscopic techniques, including *in situ* and *ex situ* STEM, environmental STEM, cryo-EM, and *in situ* liquid secondary ion mass spectrometry (SIMS), in collaboration with theoretical modeling, to directly probe the structural and chemical information of active materials in rechargeable batteries. Cryo-STEM with analytical tools, such as EDS and EELS, will be used to gain chemical and electronic structural information at the interface between lithium metal and electrolyte of both solid-state and liquid configuration, which will allow direct correlation between the morphology and chemistry. STEM – high-angle annular dark-field (HAADF) atomic-level imaging and EDS/EELS will be used to probe the interface and bulk lattice stability of cathode and SE in SSB. The work will be in close collaboration with the battery development group within the BMR and U. S.–Germany Collaboration on Energy Storage.

Out-Year-Goals. This project has the following out-year goals:

- Atomic-level multi-scale *ex situ* / *in situ* and *operando* STEM and cryo-STEM investigation on the fading mechanisms of energy-storage materials and devices in the system of both LE and SE; gain a fundamental understanding of electronic and ionic transport characteristics and kinetics in energy-storage system.
- Develop new *in situ* and *ex situ* STEM capability for probing challenging questions related to energy storage technology for both SSE and LE energy storage systems.

Collaborations. This project collaborates with G. Chen (LBNL); J. Nanda (ORNL); Y. Yao (UH); K. Amine (ANL); D. Wang (PSU); A. Manthiram (University of Texas, or UT, Austin); W. Tong (LBNL); Y. Cui (Stanford University); J. Zhang (PNNL); J. Liu (PNNL); P. Le (PNNL); W. Xu (PNNL); X. Jie (PNNL); D. Lu (PNNL); X. Xiao (GM); and M. S. Whittingham (State University of New York, Binghamton).

Milestones

1. Measure electronic properties of SEI layer and electrical double layers (EDLs), identifying their effects on electrochemical properties. (Q1, FY 2022; Completed)
2. Identify correlation between electrical properties of SEI layer and lithium structural features, such as how mossy lithium and crystalline lithium form. (Q2, FY 2022; Completed)
3. Reveal the nature of reaction product between cathode and S-based SE. (Q3, FY 2022)
4. Measure mechanical properties of SEI layer and its correlation with the lithium morphology. (Q4, FY 2022)

Progress Report

The biggest challenges for Li-metal electrode are controlled deposition and stripping. Existing knowledge indicates that the morphologies of lithium deposits are affected by pressure, temperature, current density, electrolyte composition, and physical/chemical properties of the SEI layer. Consequently, various approaches, mostly empirical in nature, have been explored intending to suppress irregular lithium growth, including reducing local reaction rate, electric field regulation, and electrolyte modification. Although remarkable progress has been achieved in stabilizing lithium electrodeposition, an in-depth and comprehensive understanding of the underlying mechanism of lithium nucleation and growth is still under-developed; however, such an understanding is crucial for practical use of Li-metal batteries.

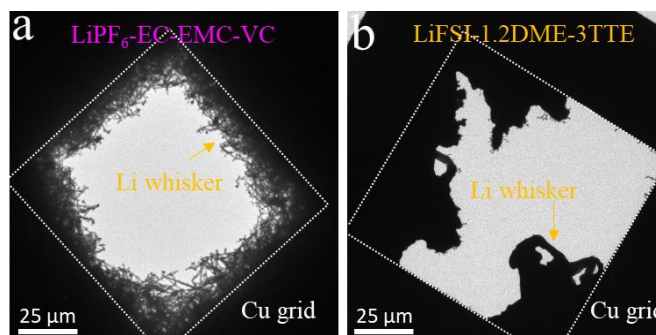


Figure 73. Low-magnification transmission electron microscopy images of lithium deposits in (a) carbonate-based electrolyte and (b) ether-based localized high-concentration electrolyte.

The team uses cryo-TEM to probe, at atomic level, the features of SEI on lithium whisker formed in the carbonate-based electrolyte [LiPF₆ – EC – ethyl methyl carbonate (EMC) – vinylene carbonate (VC)] and ether-based localized high-concentration electrolyte (LHCE) with Li-bis(fluorosulfonyl)imide (LiFSI)-1.2DME-3TTE. Figure 73 shows a low magnification TEM image of Li-metal deposits formed after the first electrochemical deposition. They reveal that, with the carbonate-based electrolyte, most of the lithium whiskers have a length of several micrometers, as shown in Figure 73a.

Select area electron diffraction (SAED) pattern (Figure 74a, inset) acquired from the lithium whisker indicates that the lithium deposit is crystalline lithium metal, which is further substantiated by the high-resolution TEM (HRTEM) image taken from the whisker stem region and tip region, as shown in Figure 74b-c. The SEI layer on the lithium whisker stem region has a smooth surface, with a thickness of ~ 18 nm, as shown by the atomically resolved TEM image in Figure 74b. The HRTEM image and corresponding FFT pattern (Figure 74b, blue coded color) indicate the amorphous structure. The interface between lithium whisker and SEI is atomically sharp (Figure 74b). Similarly, the SEI layer on the lithium tip region also exhibits amorphous structure, but with greater thickness (22 nm).

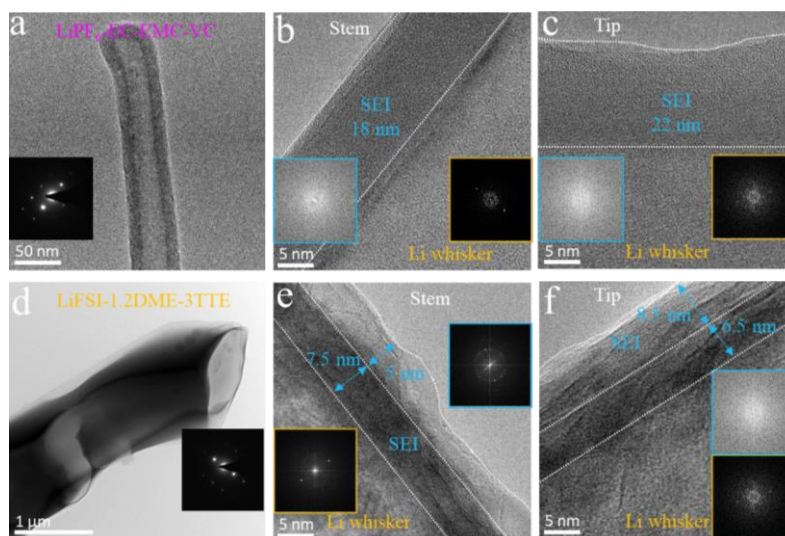


Figure 74. Microstructure of lithium deposits and SEI formed in the different electrolytes. (a-c) Cryogenic – transmission electron microscopy (cryo-TEM) images of lithium deposits formed in the carbonate-based electrolyte: (a) TEM image of lithium deposits with whisker morphology. (b) High-resolution TEM (HRTEM) images acquired from the stem region of the lithium whisker. (c) HRTEM images acquired from the tip region of the lithium whisker. (d-f) Cryo-TEM images of lithium deposits formed in the ether-based LHCE: (d) TEM image of lithium deposits with whisker morphology. (e) HRTEM images acquired from the stem region of the lithium whisker. (f) HRTEM images acquired from the tip region of the lithium whisker.

The lithium deposit structure formed in LHCE is different from those formed in the carbonate-based electrolyte (Figure 73a), featuring particle-shaped morphology except for very few lithium whiskers, which is consistent with previous reporting that the ether-based LHCE primarily leads to formation of large lithium particles during deposition. For lithium deposits formed in the ether-based LHCE, the SAED pattern (Figure 74d, inset) and the atomically resolved TEM images (Figure 74e-f) indicate that the whisker-shaped lithium deposits are single-crystalline lithium metals.

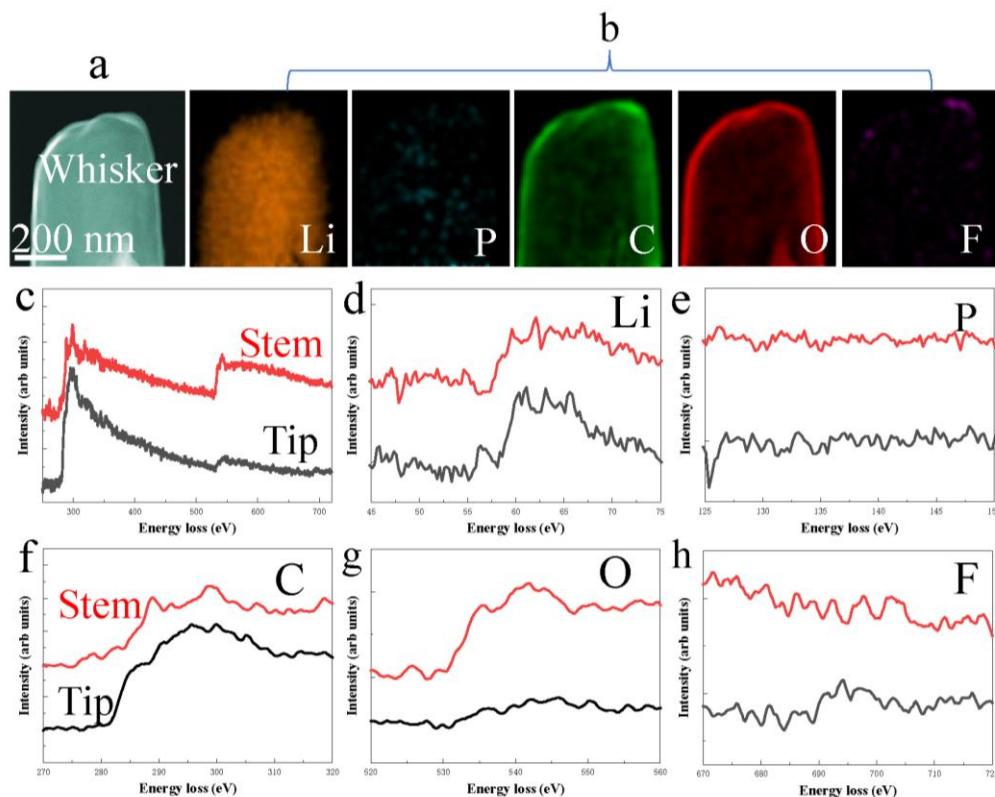


Figure 75. Structure and elemental composition of lithium deposits and their SEIs formed in the carbonate-based electrolyte. (a) Scanning transmission electron microscopy – high-angle annular dark field image showing the lithium whisker. (b) Electron energy loss spectroscopy (EELS) elemental mapping showing the elemental distribution of SEI. (c) EELS acquired from stem and tip region of the whisker. (d) EELS of lithium. (e) EELS of phosphorus. (f) EELS of carbon. (g) EELS of oxygen. (h) EELS of fluorine.

The SEI layer on the lithium whisker stem and tip region shows bilayer structure, which is characterized by an amorphous inner layer of 7.5 nm and a mosaic outer layer of 5 nm on the stem and by an amorphous inner layer of 6.5 nm and a mosaic outer layer of 8.5 nm on the tip. The mosaic outer layer is featured with an amorphous matrix dispersed with Li_2O particles (Figure 74e-f).

The team further investigated the chemical composition and fine structure of SEI layers by EELS, revealing the elemental distribution and electronic structure with high spatial resolution. Compositionally, the EELS maps (Figure 75) indicate that the SEI layers on the lithium whisker stem and tip region formed in the carbonate-based electrolyte are similarly composed of oxygen, carbon, fluorine, and phosphorus (Figure 75), with oxygen and carbon as the dominant components, indicating that the SEI is mainly derived from solvent reduction. However, the relative ratio of oxygen and carbon on the stem is different from that on the tip, as shown in Figure 75f-g. In addition, the tip region is rich of fluorine, which indicates more lithium salt decomposition happens in the tip region. Considering the difference on the reduction potential between solvent and lithium salt, especially the LiPF_6 that has higher reduction potential than solvent, more lithium salt decomposition at the tip region is associated with the potential difference between stem and tip region. It would be expected that the tip region has higher potential distribution than that at the stem region.

While in the ether-based LHCE, the SEI layer on the tip region (Figure 76a) and stem region (Figure 76b) of the whisker are similarly composed of sulfur, fluorine, oxygen, and nitrogen, but different in carbon. A high concentration of sulfur indicates the SEI is mainly from reductive decomposition of lithium salt, while carbon concentration near the whisker tip region indicates enhanced solvent reduction on the tip region. The difference of the composition of SEI layer at the tip and the stem of the whisker in those two electrolytes clearly shows the nonuniform formation of SEI on lithium whisker. This indicates the close correlation between the morphology of the whisker and SEI composition.

The team reveals that the composition of the SEI formed on the tip and stem regions of a lithium whisker is different. In contrast to the stem region, an enhanced electrical field at the tip region will lead to preferential decomposition of certain components in the electrolyte, such as LiPF_6 salt around the tip region. Further, an enhanced electrical field will also lead to preferential deposition of lithium at the tip region, leading to a scenario of a self-amplification effect for lithium whisker growth. The observation of the distinctive difference of SEI on the tip and stem regions of lithium whisker delineates insight on the direct correlation between features of the SEI layer and lithium morphology, leading to insight on possible tuning of crucial structural and chemical features of SEI to regulate the morphology of lithium deposit.

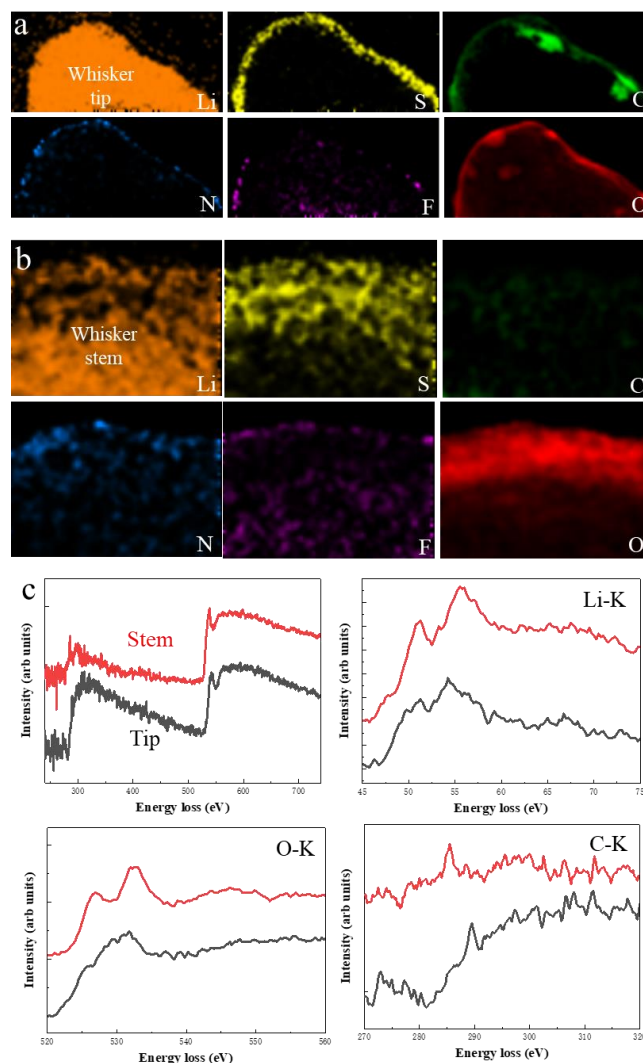


Figure 76. Composition of lithium deposit and SEI layer formed in the ether-based localized high-concentration electrolyte (LHCE). (a) Electron energy loss spectroscopy (EELS) elemental maps from the *tip region* of the whisker showing distribution of lithium, sulfur, carbon, nitrogen, fluorine, and oxygen. (b) EELS elemental maps from the *stem region* of the whisker showing distribution of lithium, sulfur, carbon, nitrogen, fluorine, and oxygen. (c) Comparison of EELS of lithium K-edge, oxygen K-edge, and carbon K-edge from the stem and tip region of the lithium whisker.

Patents/Publications/Presentations

Publications

- Jia, H., Y. B. Xu, L. F. Zou, P. Y. Gao, X. H. Zhang, B. Taing, B. E. Matthews, M. H. Engelhard, S. D. Burton, K. S. Han, L. R. Zhong, C. M. Wang, and Wu Xu. “Sulfone-Based Electrolytes for High Energy Density Lithium-Ion Batteries.” *Journal of Power Sources* 527 (2022): 231171.
- Kim, J-M., Y. B. Xu, M. H. Engelhard, J. T. Hu, H-S. Lim, H. Jia, Z. J. Yang, B. E. Matthews, S. Tripathi, X. H. Zhang, L. R. Zhong, F. Lin, C. M. Wang, and W. Xu. “Facile Dual-Protection Layer Enhancing Performances of Cobalt-Free/Nickel-Rich Cathodes in Lithium-Ion Batteries.” *ACS Applied Materials & Interfaces* 14, no. 15 (2022): 17405–17414.
- Sebti, E., H. A. Evans, H. N. Chen, P. M. Richardson, K. M. White, R. Giovine, K. P. Koirala, Y. B. Xu, E. Gonzalez-Correa, C. M. Wang, C. M. Brown, A. K. Cheetham, P. Canepa, and R. J. Clément. “Stacking Faults Assist Lithium-Ion Conduction in a Halide-Based Superionic Conductor.” *Journal of the American Chemical Society* 144 (2022): 5795.

Task 2.5 – Integrated Atomic-, Meso-, and Micro-Scale Diagnostics of Solid-State Batteries (Yi Cui, William Chueh, and Michael Toney; Stanford University / SLAC National Accelerator Laboratory)

Project Objective. By developing a characterization toolkit that tackles length scales (Å to mm), cell pressure (1-100 bars), and dynamics (during synthesis, fabrication, and cycling), the project aims to generate insights to engineer SSBs for deployment in EVs. This interdisciplinary team aims to achieve this objective by merging a broad range of characterization approaches as well as modeling to track the evolution of nanoscale chemistry and structure, microstructure, and transport.

Project Impact. The project will have an impact in several areas: (1) accelerate rational design of coatings and artificial SEIs in SSBs; (2) inhibit the root causes leading to cell shorting, and enable high current cycling; (3) accelerate design of cathode coating and composite electrode architectures; and (4) reduce degradation and variability during SSB manufacturing via composition and surface engineering.

Approach. The project has a multi-fold approach that will encompass the following: (1) resolve nanoscale structure and chemistry of SEIs via cryo-TEM; (2) track SE and lithium microstructure evolution in 3D via X-ray micro and diffraction tomography; (3) visualize nanoscale ionic and electronic transport at GBs via conducting AFM; (4) map current distribution in cathodes via scanning TXM; and (5) monitor nanoscale SE evolution with gas impurity via *in situ* environmental TEM.

Out-Year Goals. The project will develop an integrated characterization toolkit to characterize SSBs within a single cycle and over hundreds of cycles, spanning a wide range of relevant length scales.

Collaborations. Project collaborations include work with SSRL, ALS, and APS synchrotron light sources.

Milestones

1. Quantify the effect of microindentation pressure on fracture formation of LLZO SE using *in situ* electrochemical SEM. (Q1, FY 2022; Completed)
2. Quantify the degree of H/Li exchange for acid-treatment LLZO before and after heat treatment. (Q2, FY 2022; Completed)
3. Characterize the chemical nature of the Ag-LLZO interface via cryo-TEM. (Q3, FY 2022; In progress)
4. Characterize lithium plating on LLZO coated with five metallic electrodes using *in situ* electrochemical SEM. (Q4, FY 2022; In progress)

Progress Report

C. Monroe and J. Newman argued that SSEs with a shear modulus > 8 GPa should suppress Li-metal intrusion due to the changes in electrochemical potential for stressed lithium. Building on this model, recent theoretical works have showed that the morphological stability of SEs is also a function of the partial molar volume of lithium ions in the material. However, experiments of lithium plating on ceramic SSEs with shear moduli much larger than 8 GPa have demonstrated intrusion growth at relatively low current densities. Indeed, the most studied oxide SE (that is, LLZO, with a shear modulus of ~ 60 GPa), still exhibits intrusion growth at current densities well below 1 mA cm^{-2} (averaged across the electrode), even lower than that for LEs. However, it is also possible to obtain much higher current densities, with some authors reporting up to 10 mA cm^{-2} , highlighting the large uncertainty in the understanding of intrusion growth in LLZO.

In this work, the initiation mechanism for lithium intrusions on chemically pristine LLZO surfaces was examined using *operando* SEM microprobe. Figure 77 presents an overview of the experiment setup, a representative current-voltage curve, and *operando* SEM images of the Li-plating process. The cumulative probability of intrusion initiation as a function of lithium whisker diameter was shown to follow a Weibull distribution, close to an exponential distribution. This finding suggests that the intrusion initiation process is facilitated by localized defects on the surface of LLZO. In addition, the team discovered that the probability distribution could be dramatically shifted by adjusting the contact force between the microprobe and LLZO surface, with a contact force of 5 mN causing a decrease in characteristic failure diameter by nearly a factor of 3, compared to the low-contact-force case. *Ex situ* diamond-tip indentation showed significant deviation from an elastic-plastic response, suggesting that microcracking is occurring in the sample. Finite element method (FEM) analysis of the microprobe-LLZO contact suggests that plastic deformation in LLZO is unlikely due to the yielding of the tungsten microprobe. Based on these results, the team concludes that microcracks (which are either pre-existing in the material or generated via external loads) are the origin of Li-metal intrusions in LLZO. They emphasize that these microcracks are difficult to observe using standard microscopy techniques such as SEM or optical imaging, and encourage development of advanced characterization methods to study these defects. Overall, the mechanisms examined here provide a foundation for understanding the complex interactions between the chemical, electrical, and mechanical forces that govern Li-intrusion processes in SSEs.

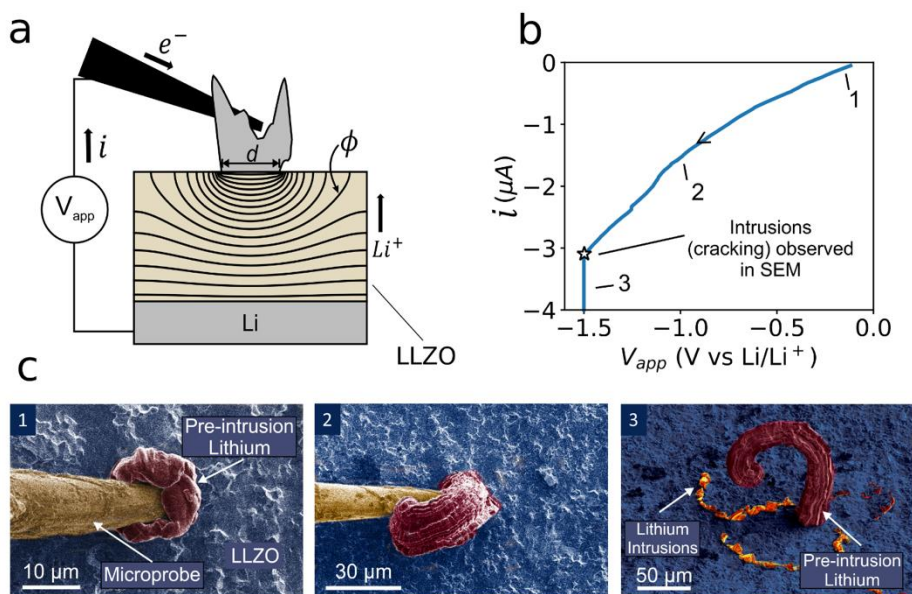


Figure 77. (a) Schematic of scanning electron microscopy (SEM) microprobe Li-metal deposition experiment showing electrostatic potential profile contours. (b) Example linear sweep voltammetry experiments from SEM experiment. (c) Colorized SEM images of lithium plating experiments outlined in (a), with each image corresponding to the positions on plot (b).

Patents/Publications/Presentations

Presentations

- ACS Spring Meeting, Virtual (March 20, 2022); “*Operando* Nanoscale Microscopy of Electrochemical Redox Processes: Interplay between Composition and Kinetics”; W. C. Chueh.
- ACS Spring Meeting, Virtual (March 23, 2022); “The Dynamic Local Chemistry of Cathodes: During Synthesis, Operations & Aging”; W. C. Chueh.

Task 2.6 – Fundamental Understanding of Interfacial Phenomena in Solid-State Batteries (Xingcheng Xiao, General Motors)

Project Objective. The project objective is to develop a comprehensive set of *in situ* diagnostic techniques combined with atomic/continuum modeling schemes to investigate and understand the coupled mechanical/chemical degradation associated with dynamic interfacial phenomena in SSBs. Specifically, *in situ* observations and characterizations of lithium plating-stripping processes, lithium dendrite formation, interphase formation, and the induced interfacial stresses, as well as the mechanical and electrochemical properties of interfaces and interphases, are paramount. The study will provide useful guidelines for optimizing cell structure design and engineering interfaces and interphases to enable SSBs.

Project Impact. The project will provide fundamental understanding of the dynamic interfacial phenomena and the coupled mechanical and chemical degradation. In addition, it will establish a critical guideline to design safe and durable SSBs with energy density > 500 wh/kg for EV applications.

Approach. The multi-scale *in situ* diagnostic tools, including AFM, nanoindentation, dilatometer, stress sensors, and pressure cells, will be used to investigate mechanical behavior and microstructure evolution at interface/interphase during lithium plating and stripping. The information (along with Li-ion transport properties and microstructure evolution obtained using the advanced spectroscopic ellipsometry, and *in situ* TEM) will be correlated with electrochemical performance toward high cycle efficiency and dendrite-free SSBs. The goal of this understanding is to develop strategies for surface and interface engineering, apply them to commercially available SEs (including powder, pellets, and foils), and assemble SSBs for further validation and optimization, eventually extending cycle life for EV application.

Out-Year Goals. The project seeks to develop SSB model systems to capture critical mechanical properties and probe the coupled mechanical-chemical degradation by further developing comprehensive *in situ* diagnostic tools. All results obtained from these *in situ* studies, combined with advanced *postmortem* analysis and modeling, will be correlated with the cycling stability of SSBs. The *in situ* tools developed will be applied to the following two periods to deeply understand the coupled mechanical and chemical degradation of interface/interphase.

Collaborations. The co-PIs involved in experiments and simulation will be as follows: B. W. Sheldon and Y. Qi (Brown University), and Y-T. Cheng and A. Seo (University of Kentucky).

Milestones

1. Artificial interlayer can regulate mechanical/chemical properties of interfaces. (Q1, FY 2022; Completed)
2. Artificial interphase has good ionic conductivity and chemical stability. (Q2, FY 2022; Completed)
3. Model to predict the governing mechanical and material properties of interfaces responsible for failures. (Q3, FY 2022)
4. Pouch cells of SSBs with optimized interlayers with energy density > 350 Wh/kg and cycle life > 500 cycles. (Q4, FY 2022)

Progress Report

Mechanical Characterization of Interlayer for Stabilizing the Interface between Lithium Metal and SE

Determining the mechanical properties of interlayer materials is vital for long-term cycling in Li-metal batteries. It has been proposed that the shear modulus of SE in a SSLMB is an important parameter for preventing dendritic growth, for instance.^[1] The measured elastic modulus of nanoindentation experiments on thin films can be influenced by the substrate. To see the influence of the substrate, environmental nanoindentation was performed on two different samples of dip-coated thin films grown on lithium foil using a Berkovich tip. Figure 78 shows that the average modulus decreased as the dip-coat time increased, and that the modulus of the maximum dip-coat time sample of 2 hours is similar to the average results for the 1-hour sample. These results provide more confidence that the previous results found are probing the polymer film. Figure 79 shows histograms representing the spread of the data comparing each sample with lithium foil.

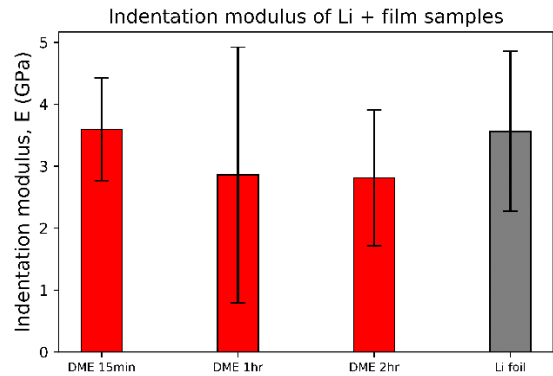


Figure 78. Indentation modulus results on different thin films on lithium foil.

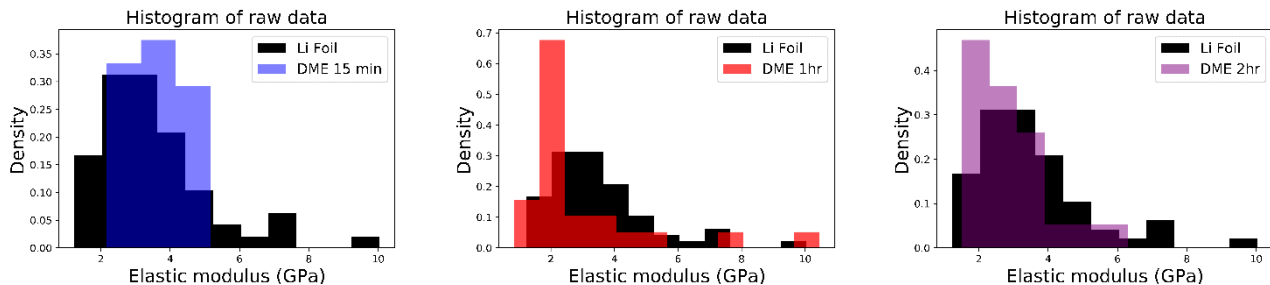


Figure 79. Histogram of the moduli in Figure 78.

The error bars in Figure 78 show that the measured modulus varies significantly across every sample. For lithium foil, this may be explained by how lithium has a very high anisotropy factor,^[2] and since lithium foil is polycrystalline, it is expected to see moduli ranging by 17 GPa. It is proposed that one reason for such large variations in the thin film samples has to do with variations in the morphology of the film. Figure 80 shows an example of three AFM images taken at different locations on the DME 15-minute sample, showing differences in the local morphology of the film at different locations.

It is also plausible that the sharpness of the Berkovich tip makes it difficult to detect the surface of such a soft polymer layer, as reported previously.^[3] To build more confidence in these results, flat punch indentation will be performed next. Creep studies will also be performed with this indenter to extract the time-dependent modulus to characterize the viscous behavior of the polymer film. These results will aim to better understand why coated Li-metal anodes outperform uncoated ones during long-term cycling tests. Finally, FEM will be applied to this system to determine whether the results presented here are in isolation of the substrate.

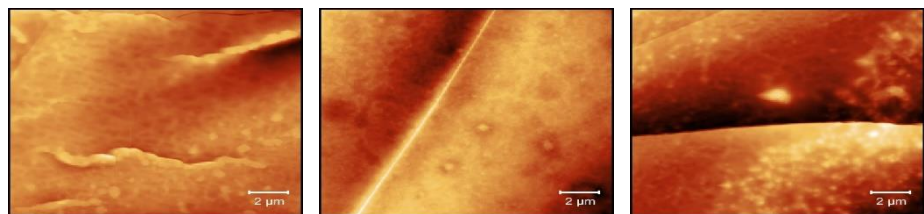


Figure 80. Three atomic force microscopy images at different locations of the DME 2-hour sample.

References

- [1] Monroe, C., and J. Newman. “The Impact of Elastic Deformation on Deposition Kinetics at Lithium/Polymer Interfaces.” *Journal of The Electrochemical Society* 152, no. 2 (2005): A396.
- [2] Herbert, E. G., et al. “Nanoindentation of High-Purity Vapor Deposited Lithium Films: The Elastic Modulus.” *Journal of Materials Research* 33, no. 10 (2018): 1335–1346.
- [3] VanLandingham, M. R., et al. “Nanoindentation of Polymers: An Overview.” *Macromolecular Symposia* 167, no. 1 (2001): 15–44.

Patents/Publications/Presentations

Publication

- Cho, J. H., K. Kim, S. Chakravarthy, X. Xiao, J. L. M. Rupp, and B. W. Sheldon. “An Investigation of Chemo-Mechanical Phenomena and Li Metal Penetration in All-Solid-State Lithium Metal Batteries Using *In Situ* Optical Curvature Measurements.” *Advanced Energy Materials* 12, no. 19 (2022): 2200369. doi: 10.1002/aenm.202200369.

Task 2.7 – Multidimensional Diagnostics of the Interface Evolutions in Solid-State Lithium Batteries (Yan Yao, University of Houston)

Project Objective. The project objective is to develop a platform combining FIB-SEM tomography, TOF-SIMS, and in-SEM nanoindentation-based stiffness mapping for structural, chemical, and mechanical characterizations in SSLBs. Assessment of the influence of cell design and testing conditions (that is, external pressure, current density, and temperature) on the evolutions of interfaces will be performed.

Project Impact. The consolidated *in situ* structural–chemical–mechanical diagnostic platform established in this project will provide unprecedented insights into the failure mechanisms of SSLBs.

Approach. Space- and time-resolved structural, chemical, and mechanical characterizations of the cathode-electrolyte and anode-electrolyte interfaces will be performed on lithium ASSBs using FIB-SEM, TOF-SIMS, and in-SEM nanoindentation. Tasks include the following: (1) development of solid-state cell thin stacks and test-cell configurations that are suitable for *in situ* characterizations; (2) quantitative characterization and *in situ* tracking of interfacial voids formation within composite cathode and electrolyte layer; (3) identification and *in situ* tracking of the chemical composition, spatial distribution, and mechanical properties of electrolyte decomposition products at the lithium- and cathode-electrolyte interfaces; and (4) visualization, chemo-mechanical properties detection, and *in situ* tracking of lithium dendrites grown within the SE layer.

Out-Year Goals. In the out years, the project will develop thin-stack solid-state cells, micro-cells, in-SEM nanoindentation, and testing protocols. The correlation between structural evolution, electrolyte decomposition, and interfacial resistance increase will be investigated.

Collaborations. The UH team (Y. Yao, Z. Fan, and Y. Liang) works closely with the Rice University team (J. Lou and H. Guo).

Milestones

1. Multi-scale structural investigations. (Q1, FY 2022; Completed)
2. Composition and spatial distribution study. (Q2, FY 2022; Completed)
3. Selected region mechanical property probing. (Q3, FY 2022; Completed)
4. Real-time monitoring of structural evolutions. (Q4, FY2022; Ongoing)

Progress Report

The project objective is to develop a platform combining structural, chemical, and mechanical characterizations in SSLBs. To investigate chemical information at the interface, a custom-built TOF-SIMS stage was designed for *in situ* biasing of the specimen inside TOF-SIMS (Figure 81). The *in situ* biasing stage allows for simultaneous electrochemical biasing and TOF-SIMS imaging. For conducting *operando* TOF-SIMS diagnosis, a solid cell with the structure of Cu/Ag-C/LPSCI/Li was fabricated and polished with an Ar-ion polisher. The cell was mounted on the stage vertically and protected during sample transfer from a glovebox to the TOF-SIMS by employing an air-free transfer vessel.

The TOF-SIMS mapping of the pristine sample is shown in Figure 82. The Ag^+ image clearly shows the distribution of the Ag-C layer, while the Li_3S^+ mapping shows that of the LPSCI electrolyte. The team can clearly observe that Li^+ exists solely in the LPSCI phase. Imaging the Li^+ distribution during charge and discharge is critical for a better understanding of how the Ag-C functions during operation and how the Ag-C works as an effective interfacial layer in SSBs. Cell discharge was performed on the biasing stage to test the *operando* feasibility in the TOF-SIMS. As demonstrated in Figure 83, the voltage dropped from 2.1 V to 0.01 V with a current discharge density of 0.1 mA/cm^2 ; however, the cell failed during the charging process.

Systematic *operando* TOF-SIMS measurements will be conducted and reported next quarter. The capability to monitor the chemical evolutions using high-mass-resolution mass spectra at varied state-of-charges is very attractive. Furthermore, high-resolution secondary ions images of the interfaces will provide useful information of interfacial species distribution and lithiation kinetics.

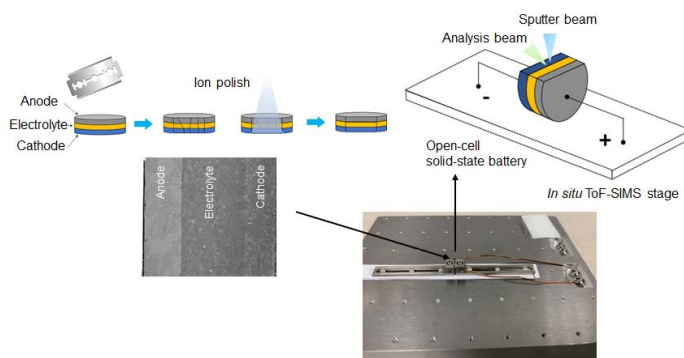


Figure 81. Schematic illustration of an *in situ* time-of-flight – secondary ion mass spectrometry stage and open-cell setup on the stage.

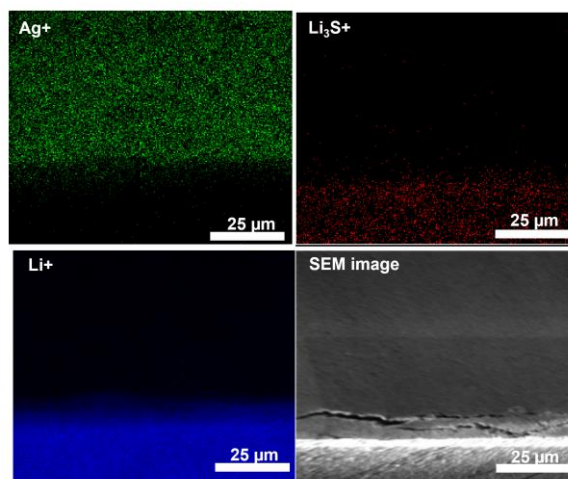


Figure 82. Time-of-flight – secondary ion mass spectrometry (TOF-SIMS) and scanning electron microscopy characterization of Cu/Ag-C/LPSCI/Li cell inside TOF-SIMS.

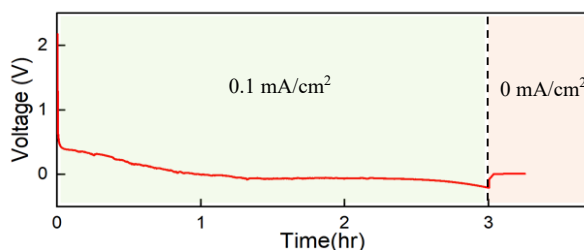


Figure 83. Electrochemical measurements of Cu/Ag-C/LPSCI/Li cell mounted on a biasing stage inside time-of-flight – secondary ion mass spectrometry.

Patents/Publications/Presentations

Presentations

- Solid-State Battery Colloquium, Virtual (January 26, 2022): “Multiscale Characterizations for Solid-State Lithium Batteries”; Y. Yao. (Invited)
- Chemistry and Biochemistry Department Seminar, George Mason University, Virtual (February 11, 2022): “Next-Generation Batteries for Electric Vehicles and Stationary Storage”; Y. Yao. (Invited)
- Mechanical Science and Engineering, University of Illinois, Urbana-Champaign (March 29, 2022): “Next-Generation Batteries for Electric Vehicles and Stationary Storage”; Y. Yao. (Invited)
- Materials Science and Applied Physics, KAUST, Virtual (March 31, 2022): “Next-Generation Batteries for Electric Vehicles and Stationary Storage”; Y. Yao. (Invited)

TASK 3 – MODELING

Team Lead: Venkat Srinivasan, Argonne National Laboratory

Summary and Highlights

Achieving the performance, life, and cost targets outlined by the Vehicle Technologies Office will require moving to next-generation chemistries, such as higher capacity Li-ion intercalation cathodes, silicon and other alloy-based anodes, Li-metal anode, and sulfur cathodes. However, numerous problems plague development of these systems, from material-level challenges in ensuring reversibility to electrode-level issues in accommodating volume changes, to cell-level challenges in preventing cross talk between the electrodes. In this task, a mathematical perspective is applied to these challenges to provide an understanding of the underlying phenomenon and to suggest solutions that can be implemented by the material synthesis and electrode architecture groups.

The effort spans multiple length scales, from *ab initio* methods to continuum-scale techniques. Models are combined with experiments, and extensive collaborations are established with experimental groups to ensure that the predictions match reality. Efforts also focus on obtaining parameters needed for the models, either from lower-length scale methods or from experiments. Projects also emphasize pushing the boundaries of the modeling techniques used to ensure that the task stays at the cutting edge.

A major focus of the effort is around Li-metal-based solid-state batteries. While these chemistries hold promise, numerous challenges such as reactivity, conductivity, and mechanical stability prevent their commercialization. Mathematical models are ideal to provide the guidance and insights needed to solve these issues.

In the area of Li-metal anodes, the focus is on understanding how materials can be designed to prevent dendrite growth using continuum modeling approaches, combined with calculations on mobility in solid conductors. The results are used to guide materials development by providing the properties needed to prevent dendrites, while also achieving the energy and power goals. Models examine the role of the solid electrolyte interphase on the morphology of the dendrite and describe the mechanical-electrochemical coupled effects that are critical for dendrite formation. Finally, efforts are focused on discovery of new solid ion conductors with properties that far exceed existing materials. The focus is on using these models as a guide before embarking on extensive experimentation.

Lithium metal with solid electrolytes (SEs) will be paired with cathode materials, often intercalative in nature. Models are being developed to examine the solid-cathode interface in Li-metal-based systems, where side reactions and interface debonding issues are known to limit cycling. These models are being used to understand how to prevent chemo-mechanical failure at the interface. Coatings, an effective strategy for high-voltage operation, are being explored with the aim of providing a rational design approach for new coating materials. In addition, focus is paid to porous electrodes with cathode particles to predict the impact of heterogeneities on electrode behavior.

Highlight. The instability of SE against lithium metal remains a significant bottleneck for commercialization of Li-metal-based batteries. Using *ab initio* molecular dynamics (AIMD) simulations, the P. Jena group at Virginia Commonwealth University has shed light into this issue. AIMD simulations on the reactivity of $\text{Li}_6\text{PS}_5(\text{BH}_4)$ SE against lithium metal showed that the thermodynamically favored breakup of BH_4^- units does not occur due to large kinetic barrier originated from the strong B-H covalent bonding. Rather, the instability is due to the PS_4^{3-} species in $\text{Li}_6\text{PS}_5(\text{BH}_4)$.

Task 3.1 – Characterization and Modeling of Lithium-Metal Batteries: First-Principles Modeling and Machine Learning (Kristin Persson, Lawrence Berkeley National Laboratory)

Project Objective. This project supports VTO programmatic goals by developing next-generation, high-energy cathode materials and enabling stable cathode operation at high voltages through target particle morphology design, functional coatings, and rational design of electrolytes. The end-of-project goals include the following: (1) understanding of the factors that govern charge transport in nonaqueous, superconcentrated LEs, (2) critical surface and coating design and optimization strategies that will improve cycling of Li-ion battery cathodes by reducing cathode degradation from oxygen loss, and (3) simulation and machine learning (ML) of the early formation of the SEI on Li-metal electrodes.

Project Impact. This project is aimed at providing fundamental insights into the atomistic mechanisms underlying surface reactivity and performance of Li-ion cathode materials and electrolytes, with the ultimate goal being to suggest improvement strategies, such as coatings, surface protection, novel electrolyte formulations, and particle morphology design. Transport modes as a function of solvent and salt concentrations will be clarified, and a data-driven reaction network framework will be designed and implemented to predict early SEI formation on lithium metal.

Approach. First-principles calculations, both static and dynamic approaches, are used to model SSE material thermodynamics and kinetics. LEs are modeled through coupled classical molecular dynamics (CMD) and first-principles methods to accurately capture solvation structure as well as reactivity of the liquid system. The reaction network is built on large-scale first-principles data, using graph theory and ML models.

Out-Year Goals. Electrolyte work will be aimed toward understanding the atomistic interactions underlying performance of lithium electrolytes, specifically elucidating conductivity (as a function of salt concentration) and impact on the charge transport mechanisms at play. Amorphous coatings will be evaluated based on ionic transport metrics and thermodynamic stability. The reaction network will be tested against known interfacial species forming on lithium metal in LiPF₆/EC electrolytes.

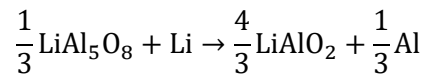
Collaborations. This project is highly collaborative between BMR PIs G. Chen (LBNL), G. Ceder (University of California, Berkeley, or UCB), and R. Kostecki (ANL). Improved coating formulations will be examined by Chen and Ceder, and interfacial reactivity insights will be corroborated by Kostecki.

Milestones

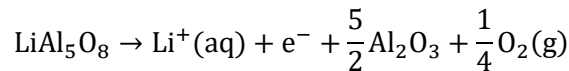
1. Correlate electrolyte chemistry and Li/SEI compositional structure determined for Li-EC-based electrolyte. (Q1, FY 2022; Completed)
2. Determine sensitivity of molecular dynamics (MD) parameters to diluent effect on transport in at least one superconcentrated electrolyte. (Q2, FY 2022; In progress)
3. Develop HT infrastructure for MD simulations. (Q3, FY 2022, In progress)
4. Determine chemistry and structural motifs that control cathode amorphous coating performance, screening over 50,000 compositions. (Q4, FY 2022; In progress)

Progress Report

This quarter, the team reports the method they have used to calculate the electrochemical stability window of amorphous coatings. The method combines formation energies calculated by DFT in the Materials Project,^[1] experimental thermochemical data for gaseous species, and experimental electrochemical data for solvated ions.^[2] The procedure is similar to the Pourbaix diagram formalism outlined by Persson et al.^[3] To estimate the reaction potential (versus lithium metal) in HT fashion, they make the following approximations: (1) for solid phases, they assume the entropy and $P\Delta V$ contributions to the Gibbs free energy of a reaction are negligible; (2) they assume a one-step single ion dissolution: $A = A^{n+} + ne^-$; and (3) they assume a unity of activity for condensed phases and all solvated ions. The electrochemical stability window consists of a reduction limit (V_{red}) at which the material starts lithiation during discharge and an oxidation limit ($-V_{ox}$) at which the material starts delithiation/decomposition during charge. Here, the team takes Al_2O_3 and $LiAl_5O_8$ as examples to illustrate their method in calculating the electrochemical stability window of Li-containing and non-Li-containing compounds. The lithiation compound of $LiAl_5O_8$ can be directly identified from a Li-Al-O phase diagram (see Figure 84a). Its discharge reaction can be expressed as:

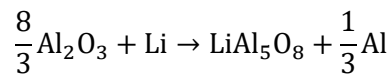


As all the reactants and products are in their solid phases, $V_{red} = -\frac{\Delta G}{zF} = -\frac{\Delta H}{zF} = 0.79 V$ versus lithium metal, where z is the number of electrons transferred in the reaction and F is the Faraday's constant. As $LiAl_5O_8$ is a Li-containing compound, its delithiation takes place via a dissolution of Li^+ . From the Li-Al-O phase diagram, the delithiation reaction of $LiAl_5O_8$ can be expressed as:

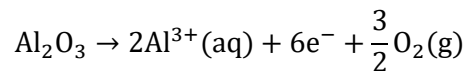


As the reaction involves oxygen gas evolution, the team includes the entropy value of O_2 taken from the JANAF tables.^[4] Thus, $V_{ox} = -\frac{\Delta G}{zF} = -\frac{\Delta H - TS}{zF} = -3.96 V$ versus lithium metal. Therefore, the electrochemical stability window of $LiAl_5O_8$ can be estimated as: $[V_{red}, -V_{ox}] = [0.79, 3.96]$.

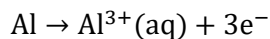
Similar to $LiAl_5O_8$, the lithiation compound of Al_2O_3 can also be directly identified from a Li-Al-O phase diagram (see Figure 84b). Its discharge reaction can be expressed as:



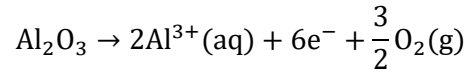
As all the reactants and products are in their solid phases, $V_{red} = -\frac{\Delta G}{zF} = -\frac{\Delta H}{zF} = 1.26 V$ versus lithium metal. As Al_2O_3 is a non-Li-containing compound, they assume its oxidation takes place via a dissolution of Al^{3+} . From the Li-Al-O phase diagram, the decomposition reaction of Al_2O_3 can be expressed as:



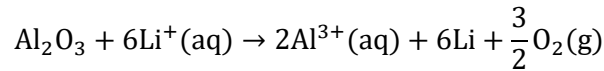
As the reaction involves oxygen gas evolution, they include the entropy value of O_2 . Thus, $\Delta G_1 = \Delta H - TS = 16.18 eV$. Next, they add the standard free energy of Al^{3+} formation, ΔG_2 , to ΔG_1 .



$\Delta G_2 = -nFE_{Al^{3+}}^0 = -4.99 eV$ where n is the valence state of Al^{3+} and $E_{Al^{3+}}^0$ is the standard oxidation potential of Al^{3+} versus standard hydrogen electrode (SHE) taken from the International Union of Pure and Applied Chemistry publication.^[5]



$\Delta G_3 = \Delta G_1 + 2\Delta G_2 = 6.21 \text{ eV}$. Next, they reference the above equation to Li/Li^+ to calculate the reaction potential with respect to the lithium metal: $\text{Li}^+(\text{aq}) + \text{e}^- \rightarrow \text{Li}$:



The standard oxidation potential of Li^+ is $E_{\text{Li}^+}^0 = 3.04 \text{ V}$ versus SHE. Thus, $\Delta G_4 = \Delta G_3 + 6nFE_{\text{Li}^+}^0 = 24.45 \text{ eV}$. Finally, the reaction potential V_{ox} can be obtained using the Nernst equation: $V_{\text{ox}} = -\frac{\Delta G_4}{zF} = -4.07 \text{ V}$. Therefore, the electrochemical stability window of Al_2O_3 can be estimated as: $[V_{\text{red}}, -V_{\text{ox}}] = [1.26, 4.07]$.

It should be noted that the actual dissolution process may involve multi-step/multi-ion dissolutions. Therefore, this method merely serves as an approximation that aims at broadly capturing the dissolution tendencies in HT fashion.

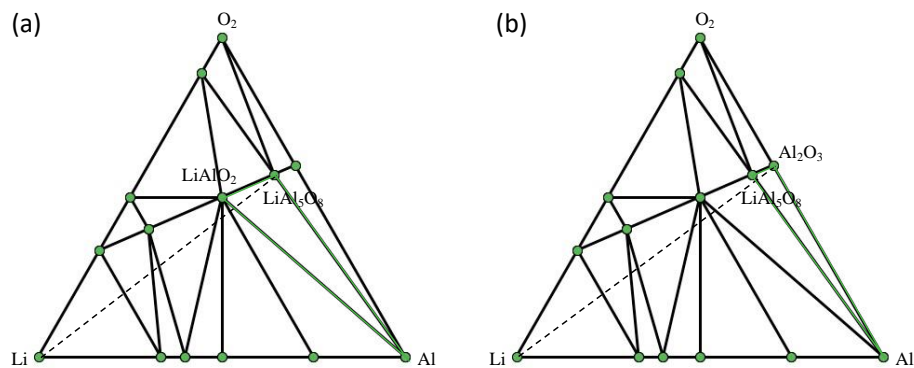


Figure 84. Li-Al-O phase diagrams. (a) The first phase-region (green triangle) formed by LiAlO_2 , LiAl_5O_8 , and aluminum for LiAl_5O_8 lithiation. The dash line represents the lithiation path of LiAl_5O_8 . (b) The first phase-region (green triangle) formed by LiAl_5O_8 , Al_2O_3 , and aluminum for Al_2O_3 lithiation. The dash line represents the lithiation path of Al_2O_3 .

References

- [1] Jain, A., et al. “Commentary: The Materials Project: A Materials Genome Approach to Accelerating Materials Innovation.” *APL Materials* 1 (2013).
- [2] Aykol, M., et al. “High-Throughput Computational Design of Cathode Coatings for Li-Ion Batteries.” *Nature Communications* 7 (2016): 13779.
- [3] Persson, K. A., B. Walwick, P. Lazić, and G. Ceder. “Prediction of Solid-Aqueous Equilibria: Scheme to Combine First-Principles Calculations of Solids with Experimental Aqueous States.” *Physical Review B: Condensed Matter and Materials Physics* 85 (2012): 235438.
- [4] Chase, M. W., et al. JANAF Thermochemical Tables, 1982 Supplement. *Journal of Physical and Chemical Reference Data* 11 (1982): 695–940.
- [5] Bard, A. J., R. Parsons, and J. Jordan. *Standard Potentials in Aqueous Solution*. New York: Routledge, 2017. doi: 10.1201/9780203738764.

Patents/Publications/Presentations

Publication

- Self, J., et al. “A Theoretical Model for Computing Freezing Point Depression of Lithium-Ion Battery Electrolytes.” *The Journal of The Electrochemical Society* 168 (2021): 120532.

Task 3.2 – Electrode Materials Design and Failure Prediction (Venkat Srinivasan, Argonne National Laboratory)

Project Objective. The main project objective is to develop computational models for understanding the various degradation mechanisms for next-generation Li-ion batteries. This year's goal is to use the continuum-based mathematical model to estimate the conduction pathway through the SEs and investigate interfacial stability between Li-metal electrodes and SEs during deposition and dissolution of lithium under externally applied currents. Electrolytes comprised of soft polymers, hard ceramics, and a combination of the two in the form of polymer-ceramic composites, will be investigated. SEs are expected to enable high-energy-density and liquid-free, safe, next-generation Li-ion batteries, while combined with thin Li-metal anodes. During charge, lithium dendrites are observed through the SEs, which are supposed to occur because of the non-uniform current distribution at the Li/electrolyte interface. Due to their lack of conformability, hard-ceramic-based SEs (such as LLZO and LATP) are expected to experience loss of electrochemically active surface area during lithium plating and stripping, which can eventually lead to current focusing and subsequent dendrite growth. Sulfide-based soft ceramics (LPS and LPSCI), and/or polymer-ceramic composite electrolytes are expected to maintain better contact with the Li-metal electrode because of their higher deformability. The possibility of stabilizing the lithium deposition with composite electrolytes consisting of PEO-based soft-polymer matrix and LLZO-type hard ceramic fillers will be studied. Proper conduction pathways through the polymer and ceramic domains, and their influence on the effective conductivity of the SE, will be elucidated. Other soft SEs, such as SEO polymer and sulfide-based soft ceramics, will be investigated for their capability to stabilize the lithium deposition on metallic anodes.

Project Impact. Findings from this research will give a better understanding of the ion transport mechanism within the polymer and ceramic domains of the composite SEs, and will help elucidate the factors influencing the deposition of lithium at the electrode/electrolyte interface.

Project Approach. In the present project, mesoscale models are developed based on mass conservation, charge balance, and force balance relations at the continuum level to describe the physical processes occurring in the electrochemical systems during charge and discharge, which is then compared with the experimental observations for appropriate validation. The models are then used to provide insights and guidance for strategizing new design concepts and materials for the stabilization of Li-metal anodes.

Out-Year Goals. In this project, a computational framework will be presented that can capture the ionic transport through composite electrolytes and predict lithium deposition at the electrode/electrolyte interface.

Collaborations. This project collaborates with L. A. Curtiss, A. T. Ngo, S. Tepavcevic, and Y. Zhang at ANL.

Milestones

1. Investigating the current, focusing on the interface between Li-metal electrode and polymer/ceramic composite electrolyte. (Q1, FY 2022; Completed)
2. Elucidating ion transport mechanism through the polymer and ceramic phases in a composite electrolyte. (Q2, FY 2022; Completed)
3. Deciphering the influence of stress state on the exchange current density experienced by Li-metal electrodes in contact with SPEs during lithium deposition and stripping processes. (Q3, FY 2022; In progress)
4. Understanding the impact of GBs in soft inorganic SEs on the lithium deposition process and subsequent dendrite growth. (Q4, FY 2022)

Progress Report

Elucidation of Ion Transport Mechanism through the Polymer and Ceramic Phases in a Composite Electrolyte. Composite electrolytes, consisting of polymer matrix and ceramic particles, are expected to possess higher transport parameters than polymer phase due to high ionic conductivity of ceramics. Lithium ions can transport through only polymer phase and through polymer and ceramic phase in composite electrolyte (Figure 85a). Transport of lithium ions through the polymer/ceramic interphase layer is not taken into consideration. The higher ionic conductivity of lithium ions can only be achieved by enabling Li-ion transport through the ceramic particles. The charge transfer resistance between polymer and ceramic, R_{CT} , plays a very important role in facilitating Li-ion transfer through ceramic particle. At the surface of the ceramic particle, polymer chain motion gets impeded. This near-surface region is defined as interphase and can possess lower conductivity than that of bulk, which is quantified by $k_{interphase}$ (Figure 85a). At low R_{CT} , with increasing ceramic particle content, effective conductivity and transference number of the composite electrolyte increases. However, as R_{CT} value increases, this effect reverses and negatively affects the effective conductivity and transference number (Figure 85b-d). At higher ceramic particle content (30-40 % volume fraction), interphase volume fraction is comparable with the polymer and significantly contributes to effective conductivity. Lastly, interphase conductivity, $k_{interphase}$, dictates quantification of the composite electrolyte conductivity, but the positive or negative effect of the ceramic particle content is dictated by R_{CT} . Interplay between $k_{interphase}$ and R_{CT} is necessary to predict the transport parameters of the composite electrolyte. The present study of PEO-LATP composite system can meet the required targets of conductivity and transference number for EV application only at very low R_{CT} ($<10^{-6} \Omega m^2$); see Figure 85e. Experimentally observed R_{CT} values at the PEO-LATP interface are $\sim 0.004 \Omega m^2$ (denoted by the yellow asterisk in Figure 85e), which is around three orders of magnitude larger than the desired charge transfer resistances. This completes the second-quarter milestone.

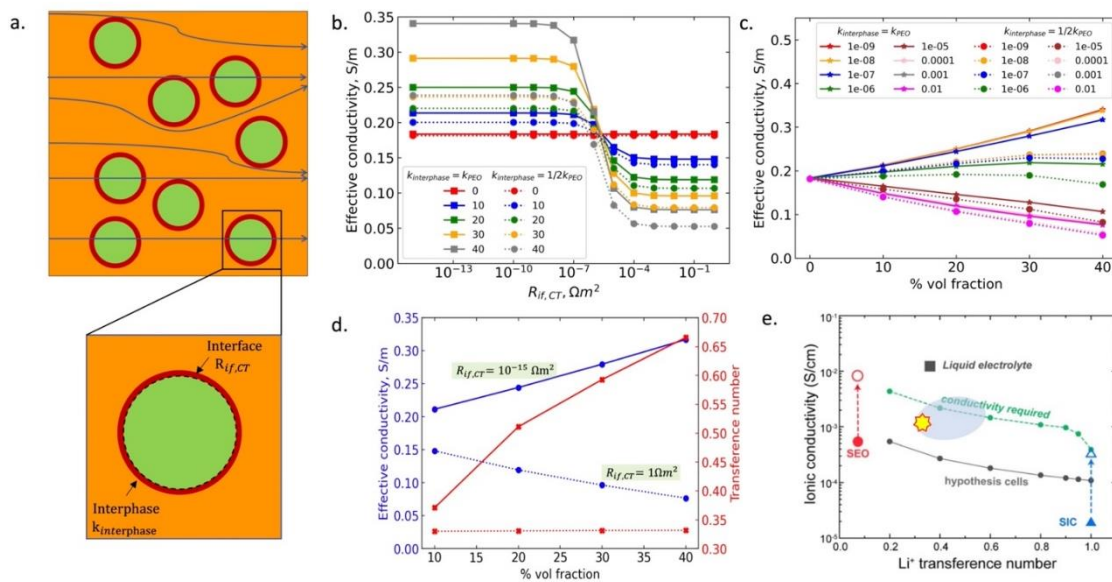


Figure 85. Li-ion transport mechanism study in PEO-LATP composite electrolyte at temperature 90°C. (a) Schematic representation of polymer and ceramic particles in composite electrolyte. Ceramic particles, polymer, and interphase are represented in green, orange, and red, respectively. The zoomed-in view of ceramic particle depicts ceramic and polymer interface and interphase region near ceramic particle surface. (b) Effective conductivity of the composite electrolyte at a varying interface charge transfer resistance for different volume fractions of ceramics in polymer matrix. Solid lines represent case 1: $k_{interphase} = k_{PEO}$, and dotted lines represent case 2: $k_{interphase} = (1/2)k_{PEO}$. (c) Effective conductivity of the composite electrolyte at varying volume fractions of ceramics in polymer matrix at different interface charge transfer resistance. Solid lines represent case 1: $k_{interphase} = k_{PEO}$ and case 2: $k_{interphase} = (1/2)k_{PEO}$. (d) Transference number and effective conductivity at low (solid line) and high (dotted line) interfacial charge transfer resistance. (e) Required ionic conductivity for polymer electrolytes at different transference number for electric vehicle applications. Composite electrolytes are represented by the blue oval patch. A yellow asterisk represents the current state of LATP-PEO system for $R_{CT} = 0.004 \Omega m^2$.

Patents/Publications/Presentations

The project has no patents, publications, or presentations to report this quarter.

Task 3.3 – Modeling of Amorphous Solid-State Conductors (Gerbrand Ceder, University of California, Berkeley)

Project Objective. SSEs are promising to achieve high energy density. The project objective is to determine the design principles needed to create SSEs with high Li-ion conductivity, while also achieving stability against common Li-ion cathodes and Li-metal anodes.

Project Impact. The project will lead to understanding the factors that control Li-ion motion in crystalline and amorphous solids and will develop strategies to create stable interfaces against lithium metal and high-voltage cathode materials. The understanding of such processes is necessary to determine design principles to develop reliable ASSBs.

Approach. HT computation is used to screen suitable SE with high electrochemical stability and high ionic conductivity, by incorporating nudged elastic band (NEB) and an AIMD method. Meanwhile, DFT is used to calculate bulk elastic constants of materials, surface energies, and interface decohesion energies of GBs. Thermodynamic interface stability is assessed from *ab initio* computed grand potential phase diagrams in which the lithium voltage can be controlled. Kinetic limits for SE decomposition are assessed by topotactic lithium insertion and removal from the SE.

Out-Year Goals. Future goals include the following: (1) gain insight into what creates high Li-ion conduction in sulfide and oxide solids, and (2) develop stable, processable solid-state conductors that can be applied in ASSBs.

Collaborations. There are no collaborative activities this quarter.

Milestones

1. Investigate lithium diffusion mechanism in activated network structures. (Q1, FY 2022; Completed)
2. Conduct diffusion network analysis in low-density structures. (Q2, FY 2022; Completed)
3. Perform detailed lithium transport modeling in one novel conductor. (Q3, FY 2022; In progress)
4. Conduct stability analysis of novel LIC. (Q4, FY 2022; In progress)

Progress Report

Novel SEs from Corner-Sharing (CS) Frameworks with a Highly Distorted Lithium Environment

A typical LIC has a crystal structure, with its anion serving as a backbone hosting the mobile lithium ions and immobile non-Li cations. By observing the crystal structure of well-known oxide-based superionic conductors (Figure 86), such as NASICON-type $\text{Li}_{1+x}\text{Al}_x\text{Ti}_{2-x}(\text{PO}_4)_3$,^[1] LiTa_2PO_8 ,^[2] and $\text{Li}_{1+x}\text{Ta}_{1-x}\text{Zr}_x\text{SiO}_5$,^[3] the team identified structural commonality among them. The non-Li cation polyhedrons in these materials are connected by a single oxygen anion vertex and have no edge- or face-sharing among the polyhedrons.

The team defines the CS framework as a framework where all of the non-Li cation polyhedrons share one or less vertex. Correspondingly, a non-CS framework is a framework that has at least one edge- or face-sharing within the framework. The team then compares the lithium environment provided in the CS frameworks and non-CS frameworks. They employ a metric of distortion, continuous symmetry measure (CSM), which is 0 for a perfectly symmetric polyhedron and reaches a maximum value of 100 for completely distorted polyhedrons. In Figure 87, they classify all of the quaternary lithium oxides from the Materials Project database,^[4] based on whether they have CS or non-CS frameworks. Then, they investigate the distortion level of the lithium environment being provided in each framework. As shown in Figure 87, while the majority of lithium environments in structures with non-CS frameworks are highly symmetric, with CSM values peaked near 0, the structures with CS frameworks tend to provide a wide range of distorted lithium environments. The team identifies the highly distorted lithium environment provided in CS frameworks as a major factor that may lead to low activation energy and high ionic conductivities.

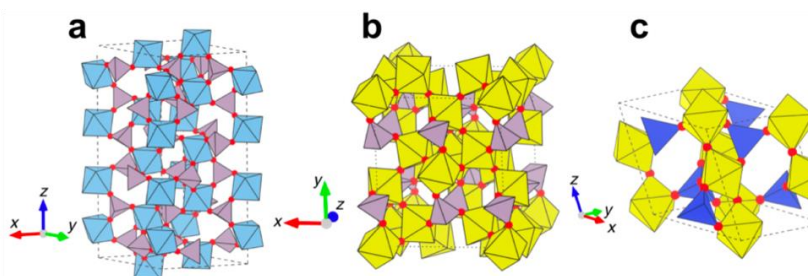


Figure 86. Typical crystal structures of known superionic conductors with corner-sharing frameworks. (a) Structure of $\text{Li}_{1+x}\text{Al}_x\text{Ti}_{2-x}(\text{PO}_4)_3$. (b) Structure of LiTa_2PO_8 . (c) Structure of $\text{Li}_{1+x}\text{Ta}_{1-x}\text{Zr}_x\text{SiO}_5$.

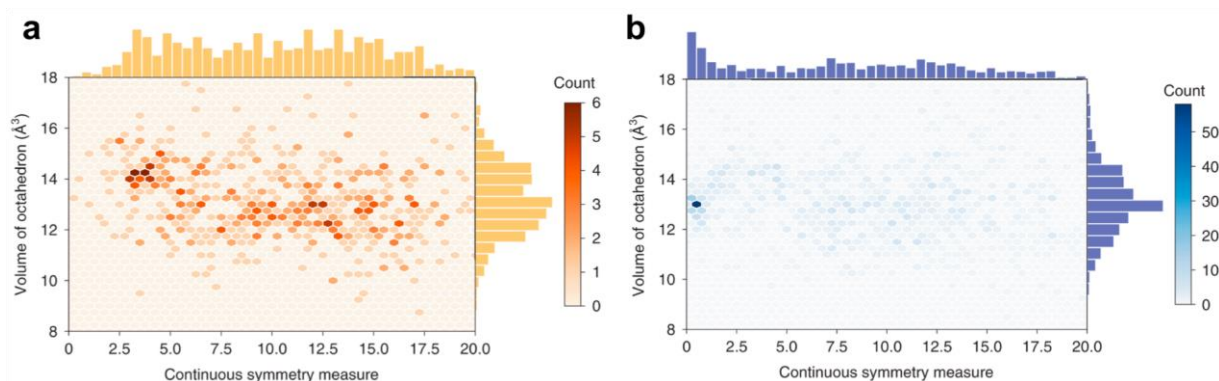


Figure 87. Degree of distortion of octahedral lithium environment in quaternary lithium oxide materials with (a) corner-sharing framework, and (b) non-corner-sharing frameworks.

References

- [1] Aono, H. *Journal of The Electrochemical Society* 137 (1990): 1023.
- [2] Kim, J. et al. *Journal of Materials Chemistry A* 6 (2018): 22478–22482.
- [3] Xoing, S. et al. *Advanced Energy Materials* 9 (2019): 1803821.
- [4] Jain, A. et al. *APL Materials* 1 (2013): 011002.

Patents/Publications/Presentations

Publication

- Jun, K., Y. Sun, Y. Xiao, Y. Zeng, R. Kim, H. Kim, L. J. Miara, D. Im, Y. Wang, and G. Ceder. “Lithium Superionic Conductors with Corner-Sharing Frameworks.” *Nature Materials* (2022).

Task 3.4 – *In Situ* and *Operando* Thermal Diagnostics of Buried Interfaces in Beyond Lithium-Ion Cells (Ravi Prasher, Lawrence Berkeley National Laboratory)

Project Objective. Transport at various interfaces in beyond Li-ion cells will play a major role in electrochemical performance and reliability. It has not yet been possible to thermally profile a Li-metal cell during operation to provide a spatially resolved map of thermal transport properties throughout the cell. The objective of this research is to create a metrology capable of spatially resolved *in operando* thermal property profiling, and then to relate thermal property to the quality of electrodes and interfaces, and to use the developed thermal metrology to understand electrochemical processes in Li-metal batteries, such as dendrite growth, interface kinetics, and ionic transport.

Project Impact. Characterizing electrochemical processes in Li-metal cells such as lithium deposition and dendrite growth at interfaces is of great significance for understanding and enhancing their electrochemical performance and reliability. *In situ* and *operando* micro electrothermal sensors can provide significant information regarding the impact of buried interfaces as a function of time, material, voltage, current, temperature, etc. Therefore, it is important to develop *operando* micro electrothermal sensors and develop models relating those signals to electrochemical performance for beyond Li-ion cells. The physics-based model relating thermal and electrochemical properties based on these measurements can facilitate future design of Li-metal batteries.

Approach. To accomplish project goals, the team will utilize an in-house adapted 3-omega (3ω) technique to probe thermal properties of a Li-metal cell while it is in operation, without affecting the operation of the cell. The 3ω sensors will be deposited and fabricated on Li-metal cells based on previous learning on 3ω sensor fabrication. The characteristic depth of the thermally probed region is defined by the wave's "thermal penetration depth," $\delta_p = \sqrt{D/2\omega}$, where D is the sample's thermal diffusivity, and 2ω is the heating frequency of the thermal wave. By depositing the project's 3ω sensors on the battery's outer surface and adjusting ω , the team controls δ_p to span the full range from the top to the bottom layer, thereby noninvasively probing the thermal transport in subsurface layers and interfaces within the bulk of the battery. Thermal transport can be related to quality of the interfaces. By doing concurrent thermal transport and electrochemical performance measurements, the team plans to relate thermal transport to electrochemical performance. As frequency-based thermal measurement techniques provide excellent spatial resolution within the cell, the team also plans to study heat generation at the electrolyte / Li-metal interface and to relate the thermal signals to the interface kinetics and ionic transport. The frequency dependence of heat generated due to transport resistance is different from that due to kinetic resistance. The team plans to utilize this difference to separate the contributions of kinetic and transport resistance at the interface, which will enable understanding of interface kinetics and transport at the Li-metal / SSE interface.

Out-Year Goals. The project will design, build, and implement the adapted 3ω metrology to examine thermal properties and a general frequency-dependent thermal metrology to examine heat generation. This will involve developing and testing the metrology itself along with accompanying theory, designing compatible battery samples, and applying the technique to live cells. The team will measure thermal transport properties of battery materials provided by collaborators. Combined with the electrochemical performance measurement, this will provide significant information relating the thermal signal to the electrochemical process.

Collaborations. This project collaborates with two LBNL groups: V. Battaglia's for cell assembly for 3ω studies, and R. Kostecky's for pristine battery active material growths for studies of thermal signals related to electrochemical process.

Milestones

1. Identification of theoretical model relating the interface morphology to thermal contact resistance (TCR). (Q1, FY 2022; Completed)
2. Measured change to TCR/morphology with cell cycling correlated with EIS. (Q2, FY 2022; Completed)
3. *Ex situ* characterization of interface morphology to validate the theory relating the morphology to TCR. (Q3, FY 2022; In progress)
4. Effect of temperature on TCR and self-heating study of thermally insulated LLZO cycling. (Q4, FY 2022; In progress)

Progress Report

This quarter, the team worked on measuring the TCR at the lithium-LLZO interface in symmetric solid-state cells. They studied the effect of pressure and cell cycling on the contact resistance, and correspondingly extracted the interface morphology related to the thermal measurements. Figure 88 shows the evolution of the TCR (panel a) and the extracted contact spot size (panel b) and the contact number density (c) as a function of pressure on symmetric solid-state cells. The pressure versus interface resistance trend is in good agreement with the interface resistance model developed by M. R. Sridhar and M. M. Yovanovic.^[1] The team also performed simultaneous EIS measurement (Figure 88d) to extract the electrochemical interface resistance and observed no significant change; this is most likely because the electrolyte was sputtered with gold before the cell fabrication, and the effective electrical contact between the lithium and the electrolyte was defined by the gold-electrolyte contact, which did not change with pressure.

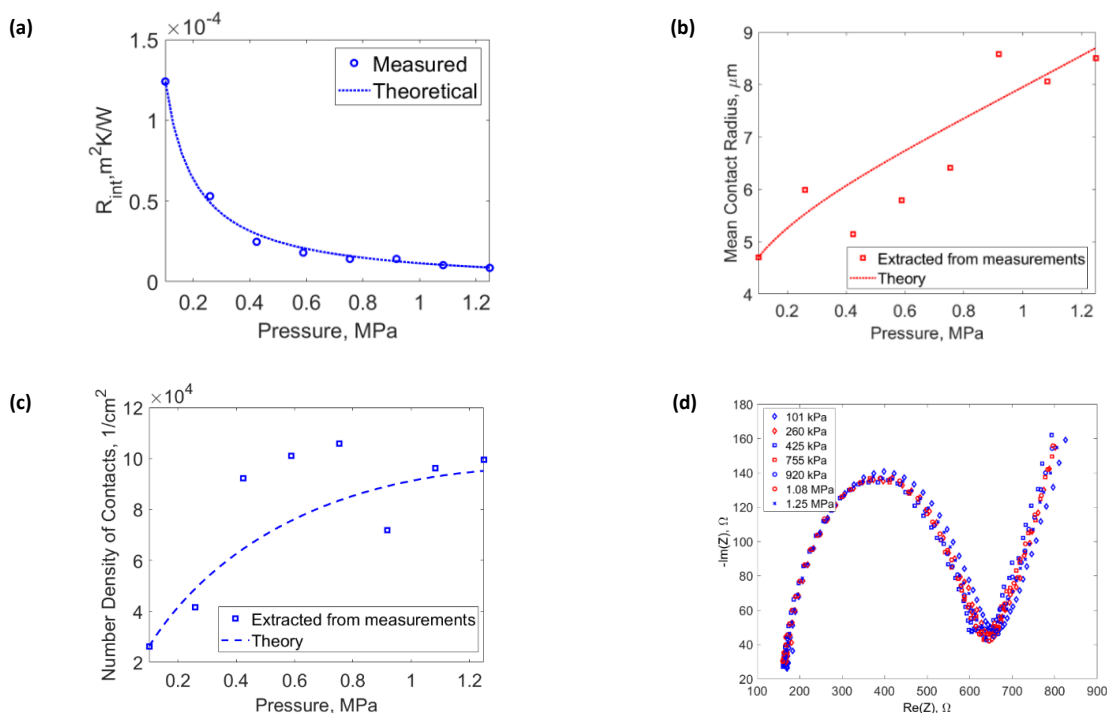


Figure 88. (a) Variation of the thermal contact resistance with pressure in good agreement with the contact resistance model (M. R. Sridhar and M. M. Yovanovich; see Reference [1]). Extracted mean contact spot size (b) and contact number density (c) from the model of Yovanovich, and (d) the electrochemical impedance spectroscopy Nyquist plot at different stack pressure showing no significant pressure dependence.

Additionally, the team also observed the thermal interface resistance as a function of cell cycling and extracted the corresponding interface morphology (average contact size and density). As shown in Figure 89, with cycling, the thermal interface resistance increases; subsequently, the number density decreases, while the average contact size increases. This most likely indicates preferential lithium deposition at specific sites as lithium cycling progresses.

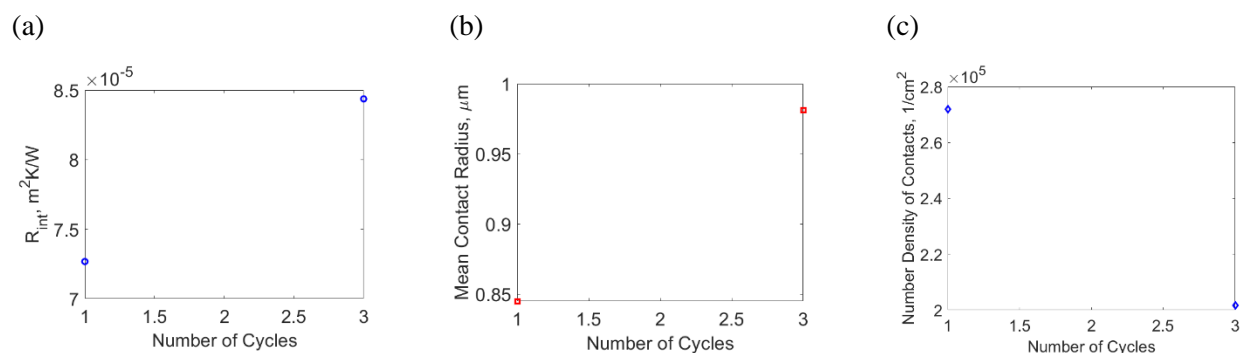


Figure 89. (a) Variation of the thermal contact resistance with cell cycling and the extracted mean contact spot size (b) and contact number density (c). With cycling, the number of contacts decreases while the mean contact spot size increases, indicating preferential lithium deposition.

They also worked on verifying their thermal wave sensing approach involving heat generation signatures from electrochemical processes, which they have named multiharmonic electrothermal spectroscopy (METS). This quarter, they were able to fabricate a symmetric cell with lithium metal and LE to extract the electrochemical interface resistance related to kinetics and transport at the interface along with the entropic coefficient associated with the charge transfer reaction. The results from METS were compared to the results from EIS, showing good agreement. Additionally, from METS the team was able to independently isolate the contribution of transport resistance at the SEI with the kinetic overpotential at the interface, which is not possible with EIS alone. Further, from the first harmonic thermal signature, they were able to extract the entropic potential associated with the entropy change of a single charge transfer reaction at an electrode, which in their knowledge has not been measured before.

METS fitting and parameter extraction for different harmonics of heat generation are presented in Figure 90, and the results are summarized in Table 7.

Table 7. Summary of the electrochemical impedance spectroscopy (EIS) and multiharmonic electrothermal spectroscopy (METS) measurements.

Quantity	Value	Method
Exchange Current Density (i_e)	8.82 A/m^2	2w METS
	8.44 A/m^2	EIS
Electrolyte Resistance (R_t)	0.46 Ω	EIS
SEI Resistance (R_{SEI})	0.1 Ω	2w METS
Entropic Coefficient ($\frac{dU}{dT}$)	0.53 $\frac{mV}{K}$	1w METS

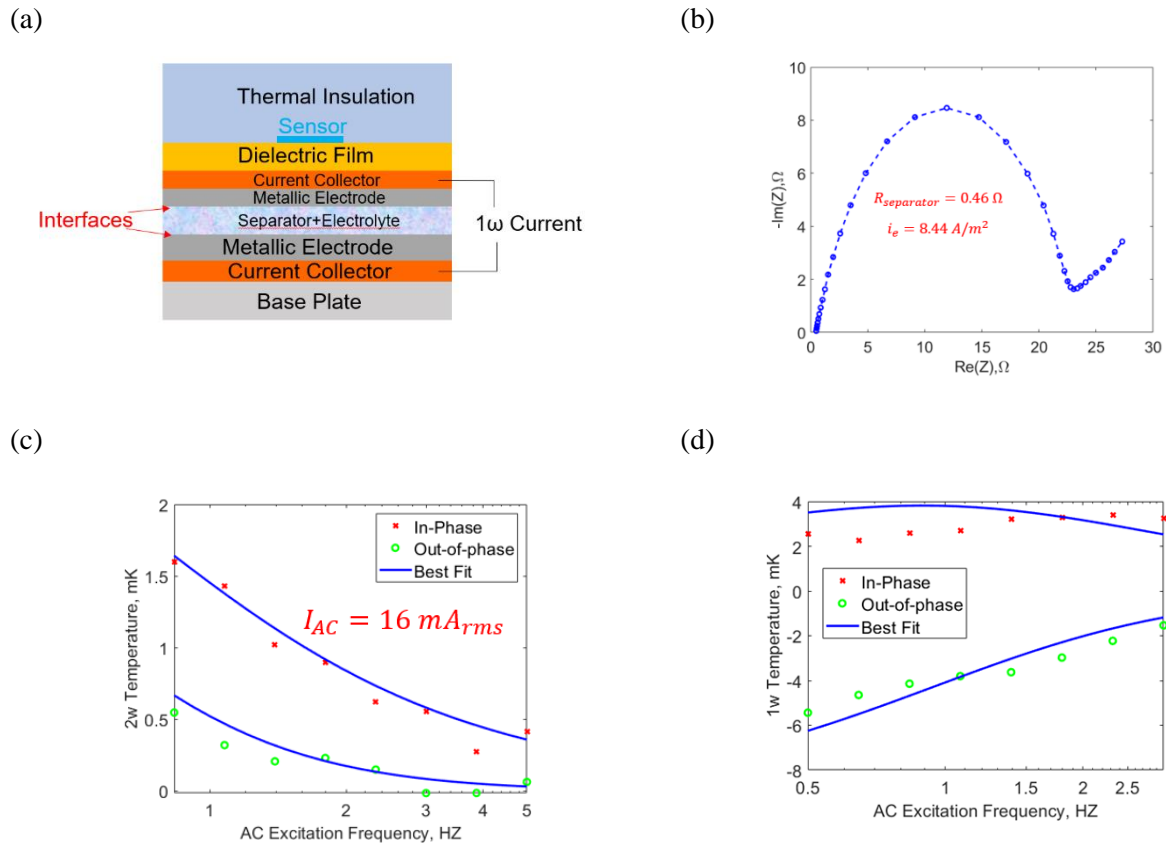


Figure 90. (a) Schematic of the symmetric cell. (b) Electrochemical impedance spectroscopy Nyquist plot of the cell impedance. (c) 2ω multiharmonic electrothermal spectroscopy (METS) fitting related to the resistances at the interface and the transport in the electrolyte. (d) 1ω METS fitting related to the entropy change of the charge transfer reaction.

Reference

- [1] Sridhar, M. R., and M. M. Yovanovich. *Journal of Heat Transfer* 118, no. 1 (1996): 3–9.

Patents/Publications/Presentations

The project has no patents, publications, or presentations to report this quarter.

Task 3.5 – Multi-Scale Modeling of Solid-State Electrolytes for Next-Generation Lithium Batteries (Anh Ngo, Larry A. Curtiss, and Venkat Srinivasan, Argonne National Laboratory)

Project Objective. This project is part of a multi-scale modeling effort to obtain an in-depth understanding of the interaction of the electrode and the SE aimed at developing highly efficient SSE batteries for vehicle applications. Input parameters needed for mesoscale (continuum) level calculations are being obtained from atomistic calculations including DFT and CMD simulations. This atomistic input will enable a multi-scale computational procedure for SSEs that is capable of successfully capturing the physicochemical aspects during charge and discharge process, including lithium transport mechanisms, interfacial phenomena during the insertion and extraction of lithium ions, and mechanical deformation of SSE.

Project Impact. A major safety concern experienced with commercially available Li-ion batteries under some scenarios is leakage of the LE, which can potentially catch fire. Replacement of the LE is necessary to decrease the fire hazard and improve safety associated with present-day Li-ion batteries. In addition, use of SEs provides a path to prevent dendrites in Li-metal anodes, thereby leading to batteries with significantly higher energy density. The impact of this project will be to help in development of good SSEs as a replacement for the commercially used organic LEs to improve safety and energy density in Li-ion batteries.

Approach. Parameters needed for mesoscale modeling of grain interior, GB, and electrode-electrolyte interface will be calculated by DFT-based calculations along with Monte Carlo (MC) and MD simulations. The calculations will be used to determine properties of the electrode with the SE as well as in GB regions of the SE. This will include calculations of structure, stability, ionic conductivity, Young's modulus, fracture toughness, exchange current density, and other properties.

Out-Year Goals. The out-year goals of this work are to calculate other properties such as fracture toughness and include other SSEs and coatings in the multi-scale modeling.

Collaborations. This project collaborates with Y. Cui at Stanford.

Milestones

1. Determine the stable phase of $\text{Li}_7\text{P}_3\text{S}_{11}$ amorphous/disordered glass-ceramic SSE and S-C cathode / $\text{Li}_7\text{P}_3\text{S}_{11}$ interface. (Q1, FY 2022; Completed)
2. Conduct AIMD study of an electrochemical interface between S-C cathode / amorphous $\text{Li}_7\text{P}_3\text{S}_{11}$ interface. (Q2, FY 2022; Completed)
3. Investigate Li-ion transport of the S-C cathode / amorphous $\text{Li}_7\text{P}_3\text{S}_{11}$ interface. (Q3, FY 2022; Initiated)
4. Compute the exchange current density associated with charge transfer from amorphous $\text{Li}_7\text{P}_3\text{S}_{11}$ glass-ceramic SSE to the S-C cathode. (Q4, FY 2022; Initiated)

Progress Report

Li-S batteries have been under investigation for several decades due to the low-cost S-based cathode materials and demonstration of high specific capacity. In LE system during the discharge process, the reduction reaction between lithium and sulfur occurs through a multistep process. The sulfur gets dissolved into the LE and forms polysulfide chains of various lengths before reacting with the lithium cations. These negatively charged polysulfide chains can easily migrate and diffuse through the LE toward the anode side and react with the lithium electrode surface to form a passivation layer that can effectively minimize capacity and enhance resistance of the cell. This detrimental shuttling of polysulfide chains can substantially limit the performance of Li-S batteries with LEs. To prevent this polysulfide shuttling mechanism, SEs have been invoked that can potentially prevent the dissolution of negatively charged polysulfides into the SE and their movement toward the anode during the discharge process.

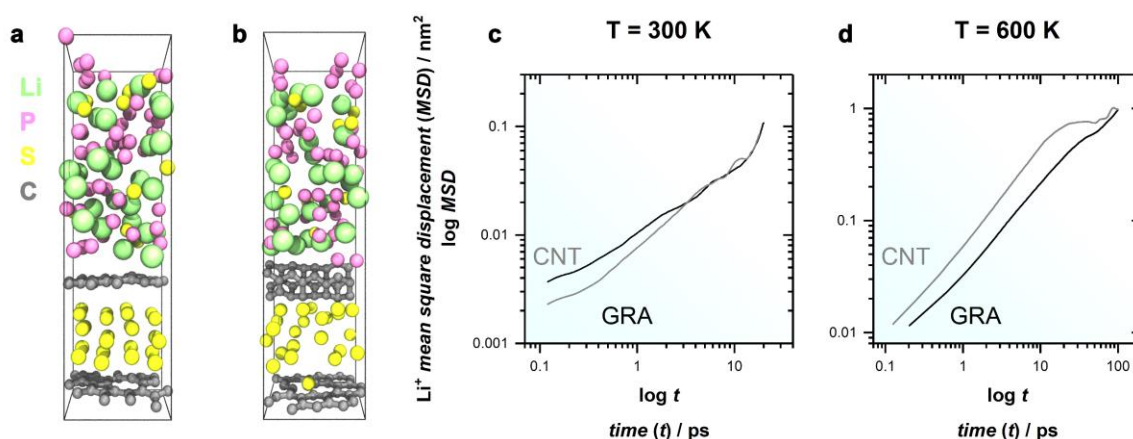


Figure 91. The snapshots of the interface between a S-C cathode and a $\text{Li}_7\text{P}_3\text{S}_{11}$ amorphous glass-ceramic solid-state electrolyte (a) S-graphene (GRA) and (b) S-carbon nanotube (CNT) based systems and mean square displacement of Li^+ in system GRA and CNT calculated by means of *ab initio* molecular dynamics simulation at (c) 300 K and (d) 600 K.

Successful operation of an electrochemical Li-S cell depends not only on the reaction between lithium and sulfur, but also on various ion and charge transfer processes occurring within the bulk of the electrode and electrolyte materials and at their interfaces. This quarter, the team has calculated atomistic-level properties of the bulk and interfaces needed for mesoscale simulations of Li-S cells conducted at larger length scales. This will be used to understand the impact of these transport mechanisms, and their impact on overall cell resistance. Since most of the bulk and interfacial phenomena occurring within an electrochemical cell are usually taken into consideration in the continuum-level simulations, it is always easier to compare the model predictions from larger length scales with the experimental observations. They are calculating various parameters needed by the large-scale simulations, such as ionic conductivity in the bulk, reaction rate constants at the interface, and equilibrium potentials where electrochemical reactions occur, as input to the model. All these material and interface specific thermodynamic and transport parameters are being calculated at atomistic-length scales using electronic structure calculations. The information from these calculations will be used in multiscale computations for predicting the performance curve and understanding the various reaction pathways in Li-S batteries with SEs.

In the team's calculations, they have focused on lithium transport across the S-C cathode bulk and the $\text{Li}_7\text{P}_3\text{S}_{11}$ amorphous interface. They have investigated the dynamics of the S-C cathode and $\text{Li}_7\text{P}_3\text{S}_{11}$ amorphous glass-ceramic interface by carrying out AIMD calculations at different temperatures for two interfacial models. From these simulations, they calculated the lithium mean square displacements (MSD). A summary of the results is shown in Figure 91. The MSDs of Li^+ in S-graphene (GRA) and sulfur-carbon nanotube (CNT)

systems were calculated at 300 K and 600 K. From these calculations, the team obtained $D_{\text{Li}^+}(\text{GRA}, T = 300 \text{ K}) = 4.5 \times 10^{-6}$; $D_{\text{Li}^+}(\text{GRA}, T = 600 \text{ K}) = 13.8 \times 10^{-6}$; $D_{\text{Li}^+}(\text{CNT}, T = 300 \text{ K}) = 10.3 \times 10^{-6}$; and $D_{\text{Li}^+}(\text{CNT}, T = 600 \text{ K}) = 21.7 \times 10^{-6} \text{ cm}^2 \text{ s}^{-1}$ for use in mesoscale modeling. They are performing another series of *AIMD* calculations to investigate the stability of the interface and Li-ion transport channels. The calculated structure of the interface and the Li-ion migration barrier will be used for calculation of the exchange current density for use in mesoscale modeling. This approach will provide input for continuum-level modeling of the interface.

Patents/Publications/Presentations

The project has no patents, publications, or presentations to report this quarter.

Task 3.6 – First-Principles Modeling of Cluster-Based Solid Electrolytes (Puru Jena, Virginia Commonwealth University)

Project Objective. The objective of the project is to use cluster-ions, which are stable atomic clusters that mimic the chemistry of individual atoms, as the building blocks of new SEs for Li-ion batteries and the corresponding battery system. The advantages of using cluster-ions to replace elemental ions is that the size, shape, and composition of the former can be tailored to achieve higher superionic conductivity, electrochemical stability, and charge transfer across the solid-state ions (SSIs) than the conventional materials. More specifically, the goal is to develop superior SEs based on cluster-ions and to model these SEs and their interfaces with electrodes, especially with the Li-metal anode, for successful integration into high-performance SSBs for EVs. The team will model and screen cluster-based solid electrolytes (CSEs) that, compared to conventional SEs, have low activation energies, practical room-temperature ionic conductivities, wide electrochemical stability windows, and desired mechanical properties that, for example, can inhibit the Li-metal anode dendrite growth. They will provide a fundamental understanding of the ionic conduction mechanism in the newly developed CSEs and will identify means to further improve property metrics via chemical and defect engineering. The team will model the interfacial properties, such as the structural, chemical, electrochemical, and ion/charge transfer properties, between the CSEs and electrodes at the atomic level, as well as find the interfacial coating materials with desired properties. Based on accumulated data from modeling, they will establish links between the basic parameters of the cluster-ions and the bulk/interface properties, which can directly guide experiments. Meanwhile, the team will work closely with experimentalists in the BMR Program to complement the project's theoretical efforts and to guide them in focused development of the predicted CSEs and the interfaces.

Project Impact. The proposed project will open a new avenue for guiding experiments in the synthesis of SSBs equipped with CSEs and capable of operating over a wide temperature range. Modeling and understanding of the ionic conduction of CSEs and their interfacial properties with electrodes, especially with Li-metal anode, will enrich current battery science and also train the future workforce in SSB development for next-generation EVs by supporting postdoctoral fellows.

Approach. This project will employ multi-scale theoretical methods and computational techniques.

Out-Year Goals. The out-year goals involve modeling development of new CSE materials and database.

Collaborations. The team is working with J. Nanda of ORNL, Y. Wu of Ohio State University (OSU), and D. Mitlin of UT, Austin, on SEs.

Milestones

1. Complete phase analysis for interfaces between the CSE and electrodes. (Q1, FY 2022; Completed)
2. Model structural properties of CSE interfaces. (Q2, FY 2022; Completed)
3. Model chemical/electrochemical and transport properties of CSE interfaces. (Q3, FY 2022; In progress)
4. Identify potential coating materials, and model electrolyte-coating-electrode interfaces. (Q4, FY 2022; In progress)

Progress Report

This quarter, the team has conducted explicit simulations at the electrolyte-electrode interface. Interface models between the studied CSEs and the Li-metal anode are obtained. Each model is constructed as a coherent heterointerface, which allows both the SE and the Li-metal anode supercell lattices to form periodicities along the interfacial plane. The interface models are then optimized and subjected to AIMD simulations for their structural evolutions at finite temperatures.

Specifically, slabs of the SEs and the Li-metal anode are cleaved according to different Miller indices (hkl). Then, the lattices of each slab couple are matched according to the epitaxial constraint with the restriction of maximal surface area of 300 \AA^2 , maximal lattice length mismatch of 0.03 \AA , and maximal lattice angle mismatch of 0.01 radians. For each as-built interface, there are still a few different configurations with different terminal species at the interface. The initial distances between the electrolyte slab and the anode slab are set to about 60% of the sum of van der Waals radii of the terminal elements in the closest contact. A vacuum padding greater than 12 \AA is also included in each model structure to minimize the interactions between the cell image perpendicular to the interface. Given the low crystalline symmetry of the studied CSEs, a resulting interface model usually contains about 300 and more atoms, testing the limit of a regular *ab initio* calculation. To make the computation affordable, only those interface models with the lowest matching surface areas are selected for further investigation.

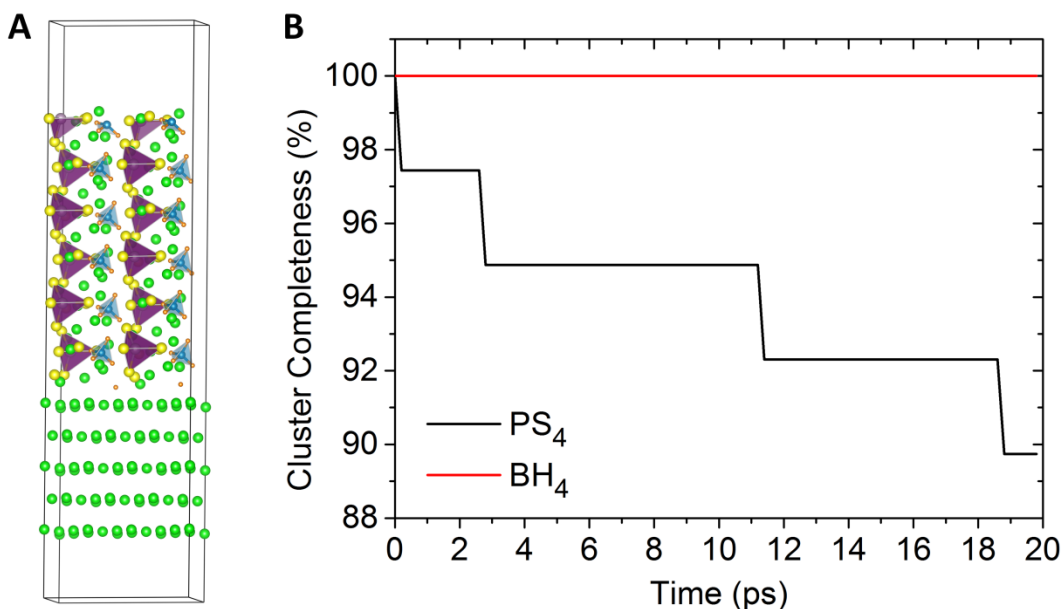


Figure 92. (a) Interface model between $\text{Li}_6\text{PS}_5(\text{BH}_4)$ and Li-metal anode with terminal atoms of H_2 at the interfacial contact. Lithium atoms are in green, BH_4 units are in light blue with hydrogen in pink, and PS_4 units are in purple with sulfur in yellow. (b) Evolution of P-S and B-H bonds versus simulation time.

To demonstrate this, the team uses the CSE $\text{Li}_6\text{PS}_5(\text{BH}_4)$ as the example here. It is found that the (111) surface of $\text{Li}_6\text{PS}_5(\text{BH}_4)$ and the (001) surface of Li-metal anode can form a coherent epitaxial interface with the minimum surface area of 114.67 \AA^2 . The interface exhibits a very low misfit strain (measured by the von Mises strain) of 0.008. The interface model contains 12 formula units of $\text{Li}_6\text{PS}_5(\text{BH}_4)$ and five atomic layers of the lithium metal. There are three configurations of the interface model with different types of terminal groups at the interface, including H_2 , B, and LiS. Figure 92a shows the model with the terminal atoms of H_2 .

Based on the optimized (in both the lattice and ionic position) interface model, AIMD simulations were conducted, and the resulting interfacial structures characterized by the evolution of local bonding structure and the interphase along the simulation time. It is found that the major interfacial reaction is reduction of

phosphorus, as suggested by the continuing disintegration of the PS_4 units represented by the progressive P-S bond breaking. As shown in Figure 92b, more than 10% P-S bonds are broken within 20 ps. On the other hand, the cluster-ions BH_4^- introduced in the SE maintain their completeness throughout the time, as shown in Figure 92b. This is different from the results of the phase diagram based on phases at full thermodynamic equilibrium, where decomposed phases such as LiB and LiH are predicted at the interface based on the premise that the BH_4^- units will disintegrate. In practice, the BH_4^- units are unlikely to break due to large kinetic barrier originated from the strong B-H covalent bonding. Thus, the instability of $\text{Li}_6\text{PS}_5(\text{BH}_4)$ against Li-metal anode is not due to the introduced cluster-ion BH_4^- that can greatly enhance the low-temperature ionic conductivity. Rather, the instability is due to the PS_4^{3-} species already included in the argyrodite system.

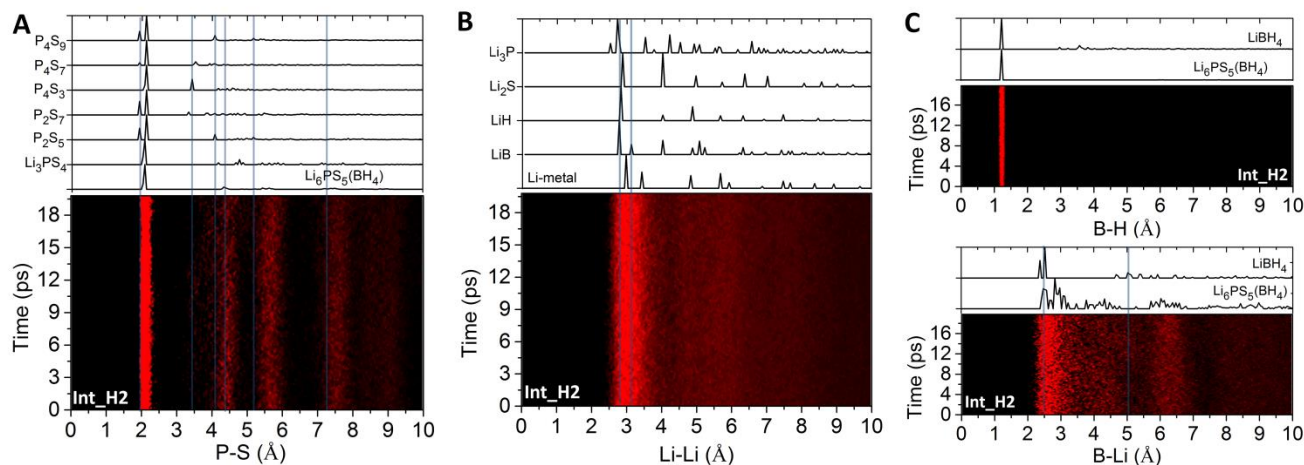


Figure 93. (a) Calculated radial distribution function of P-S at the interface compared to those of the bulk $\text{Li}_6\text{PS}_5(\text{BH}_4)$ and the stable polysulfide phases in the Li-P-S chemical space. (b) Calculated radial distribution function of Li-Li at the interface compared to those of its decomposition phases predicted under full thermodynamic equilibrium. (c) Calculated radial distribution function of B-H and B-Li at the interface compared to those of the bulk $\text{Li}_6\text{PS}_5(\text{BH}_4)$ and LiBH_4 .

Indeed, the radial distribution function analyses further indicate this. As shown in Figure 93a, at the interface (lower panel), more and more P-S signals (in red) appear toward the peaks (around 3.5-4.0 Å) found in P_xS_y polysulfide phases with reduced phosphorus versus that in PS_4^{3-} , diverging over time from the main peak around 4.5 Å found in the bulk $\text{Li}_6\text{PS}_5(\text{BH}_4)$. As shown in Figure 93b, the Li-Li radial distribution at the interface lacks the peaks around 4.0 Å for LiB and LiH, but shows peaks similar to those of Li_3P . This suggests that, unlike PS_4^{3-} , the BH_4^- units are unlikely to disintegrate due to interfacial reactions. Figure 93c indicates that, instead of LiB and LiH, the likely interphase by involving the cluster-ion BH_4^- is LiBH_4 that contains the BH_4^- cluster ions.

Note that, compared to the semiconducting LiH and electrically conductive LiB, LiBH_4 is a good insulator and has much better electrochemical stability as well as ionic conductivity. This suggests that the CSE $\text{Li}_6\text{PS}_5(\text{BH}_4)$ should have much better electrochemical stability against Li-metal anode than that evaluated by only considering the thermodynamic equilibrium phases. This points to the value of the explicit simulation of the interface and the importance of combining different levels of modeling in the electrolyte-electrode interfacial study.

Patents/Publications/Presentations

Publication

- Fang, H., and P. Jena. “Argyrodite-Type Advanced Lithium Conductors and Transport Mechanisms Beyond Peddle-Wheel Effect.” *Nature Communications* 13 (2022). doi: 10.1038/s41467-022-29769-5.

Presentation

- American Physical Society Meeting, (March 16, 2022): “Multi-Mechanistic Strategies for Novel Solid Electrolytes with Superior Properties”; H. Fang and P. Jena.

Task 3.7 – Predictive Engineering of Interfaces and Cathodes for High-Performance All-Solid-State Lithium-Sulfur Batteries (Badri Narayanan, University of Louisville)

Project Objective. The primary project goal is to leverage data-driven methods and ML strategies to develop accurate multi-physics models for ASSLSB materials that can capture electrochemical and transport phenomena over atomic-to-mesoscopic length/timescales; these models will be rigorously validated by synthesis and advanced characterization experiments. The team will leverage the predictive power of these models, alongside synthesis/characterization experiments and battery fabrication, to address longstanding issues at the electrode/electrolyte interfaces in ASSLSBs. The project’s proposed technology involves the following: (1) halide-doped solid sulfide electrolytes that can concurrently provide high Li^+ ion conductivity and suppress dendrite growth; (2) novel mesoporous cathode composed of interconnected carbon nano-cages (CNCs) co-infiltrated with sulfur and sulfide electrolyte, which hold potential to allow high sulfur loading and optimal ion/electron pathways; and (3) functionalization of sulfide electrolyte with ILs to improve physical contact and minimize impedance at the CEI.

Project Impact. ASSLSBs remain far from commercialization due to poor understanding of fundamental electrochemical/chemical and transport processes that occur at the interfaces, especially at atomic to mesoscopic scales. Successful development of proposed predictive models (at multiple scales) will bridge this knowledge gap and will advance fundamental understanding of reaction chemistry, kinetics, charge transfer, and dendrite growth at electrified SSIs. This will enable predictive design of effective strategies to mitigate interfacial problems in ASSLSBs, including poor interfacial contact, interfacial impedance to Li^+ ion transport, and poor electron/ion conduction within cathodes. Ultimately, the fundamental knowledge gained will lead to development of high-performance ASSLSBs that meet DOE targets of specific energy (350 Wh/kg @C/3), sulfur loading ($> 6 \text{ mg/cm}^2$), and high cycle life (1000).

Approach. The project brings together innovative solutions in multi-scale materials modeling, electrolyte synthesis, fabrication of cathode architecture, and electrolyte functionalization to overcome the issues at electrode/electrolyte interfaces in ASSLSBs. The central idea is to employ a data-driven and ML-based approach to develop accurate multi-physics battery models at atomic-to-mesoscopic scales. This approach overcomes critical problems with existing model development methods by foregoing the need for pre-defined functional forms, introducing deep-learning technique to describe reactivity, and employing optimization methods that do not require human intuition. Multi-scale simulations based on the newly developed models will provide insights into electrochemical phenomena at electrode/electrolyte interfaces.

Out-Year Goals. In Year 3, the goal is to optimize the composite cathode, functionalize CEI, and understand interfacial reactions to design ASSLSBs with high-sulfur loading ($> 4 \text{ mg/cm}^2$) and good capacity retention ($\sim 1000 \text{ mAh/g}$, 100 cycles @C/10).

Collaborations. The team collaborates with the groups under A. Ngo and L. A. Curtiss at ANL for quantum simulations of battery systems; they plan to collaborate with J. Nanda at ORNL for advanced spectroscopic *in situ* characterization of interfaces.

Milestones

1. Optimize cathode architecture to achieve good sulfur utilization at high sulfur loading. (Q1, FY 2022; Completed)
2. Develop composite cathodes and optimize CEI to achieve good electrochemical performance at high sulfur loading using insights from simulations and experiment. (Q2, FY 2022; In progress)

- Utilize reactive MD and advanced sampling to gain insights into defect chemistry, microstructural evolution, and interfacial processes. (Q3, FY 2022; In progress)
- Fabricate batteries that meet performance metrics. (Q4, FY 2022; In progress)

Progress Report

Last quarter, the team successfully developed mesoporous architecture for cathodes (based on super-P carbon) that provide good sulfur utilization even at high sulfur loading by adding optimized amounts of acetylene black (AB) and multi-walled CNT. They found that addition of 7% AB and 9% CNT (by weight) to the super-P cathode enables excellent percolation of carbon network within the cathode; and drastically improves its electrical conductivity. This, in turn, provided high initial capacity of ~ 1100 mAh/g at 4 mg/cm² sulfur loading with traditional glyme-based LEs. However, their coin cells using this optimized cathode (with 4 mg/cm² sulfur loading), lithium anode, and Li₆PS₅F_{0.5}Cl_{0.5} SSE yielded lower initial discharge capacity (~ 500 mAh/g)—less than half obtained with traditional LE—even on ensuring stable contact between cathode and SSE using their optimized IL 40 μ L of 2 M LiTFSI in Py : 1,3-dioxolane (DOL) (1:3) functionalizing agent (developed by the team in FY 2021). This diminished initial capacity is mainly due to the lower ionic (Li⁺) conductivity within the sulfur cathode at higher sulfur loading.

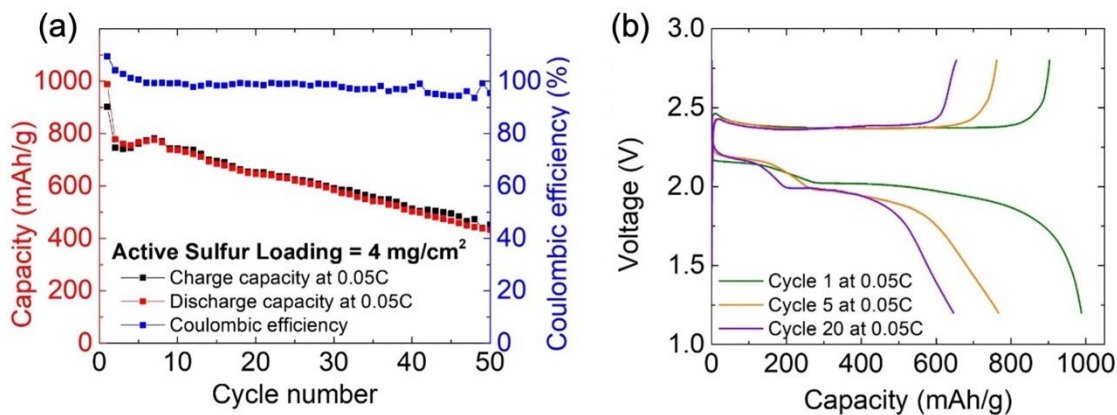


Figure 94. Electrochemical performance of quasi-solid-state Li-S battery at high-S loading (4 mg/cm²). (a) Cycling behavior and (b) discharge curves at selected cycles are shown for a quasi-solid-state Li-S battery made up of Li-anode, Li₆PS₅F_{0.5}Cl_{0.5} SSE, and super-P cathode with sulfur loading of 4 mg/cm² containing 2 wt% AB + 9 wt% CNT, and 2 wt% LTP. The battery was cycled at C/20.

To increase the Li⁺ ion conductivity within the sulfur cathode, the team added LTP glass ceramic into the optimized Super P-S cathode. They note that they could not merely add SSE used in this work, that is, Li₆PS₅F_{0.5}Cl_{0.5} argyrodite, since it is not compatible with the water-based binder chemistry. They tested the electrochemical performance of a quasi-solid-state Li-S battery with a cathode that consisted of lithium anode, a composite cathode with 4 mg/cm² sulfur loading [SP-S (1:3) 81.5 wt%, CMC 4 wt%, SBR 0.5 wt%, AB 7 wt%, CNT 5 wt%, and LTP 2 wt%], and Li₆PS₅F_{0.5}Cl_{0.5} argyrodite SSE (Figure 94). They functionalized the cathode/SSE interface with 40 μ L of IL 2 M LiTFSI in Py:DOL (1:1) to ensure good contact, and cycled the battery at C/20 under ambient conditions. The higher Li⁺ conductivity facilitated by LTP yielded a substantial improvement in initial discharge capacity to ~ 1000 mAh/g (Figure 94a), which drops to ~ 420 mAh/g after 50 cycles. Importantly, the discharge curves show two distinct plateaus, which indicates reduction through higher order polysulfides; the behavior lies in between the expected curves for a solid-state and a conventional battery with LE.

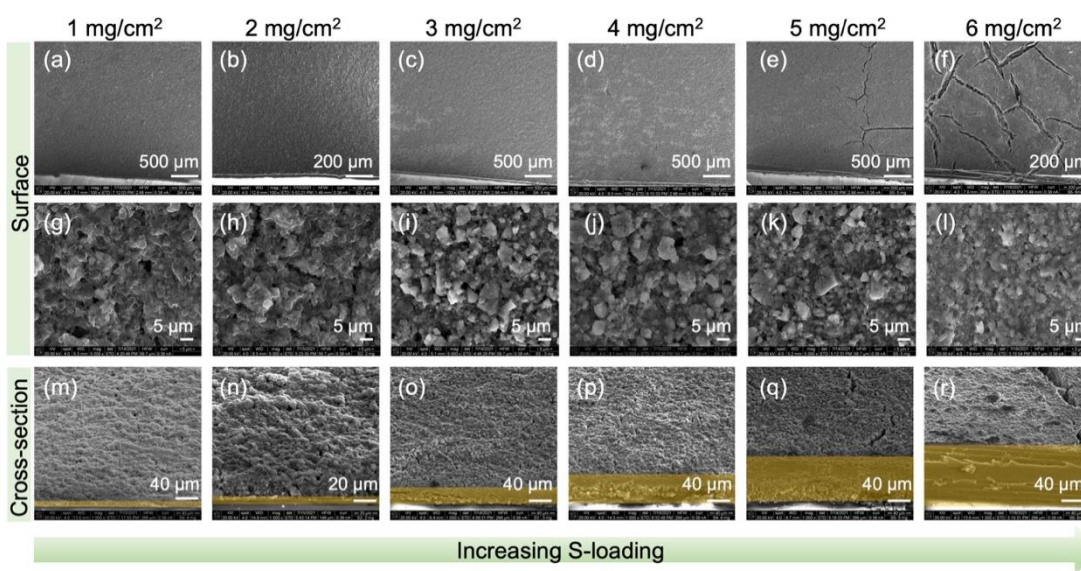


Figure 95. Scanning electron microscopy characterization of SP-S cathodes (with AB 7 wt%, CNT 5 wt%) at various sulfur loadings. (a-f) Low-magnification images, (g-l) high-magnification images, and (m-r) cross-sectional view taken at 60° tilts.

To understand the microstructure of the SP-based cathodes, the team performed SEM of representative cathodes without any LATP (that is, only AB 7 wt%, CNT 5 wt%) at different sulfur loading coated on glass substrates (Figure 95). The SEM images of the surface show that the coating is smooth up to 4 mg/cm² sulfur loading (Figure 95a-d), while cracks begin to appear at sulfur loading > 5 mg/cm² (Figure 95e-f). Furthermore, porosity of the cathode reduces progressively with increase in sulfur loading (Figure 95g-l). The cross-sectional view again shows systematic increase of the thickness (marked in yellow) for increasing sulfur loading (Figure 95m-r).

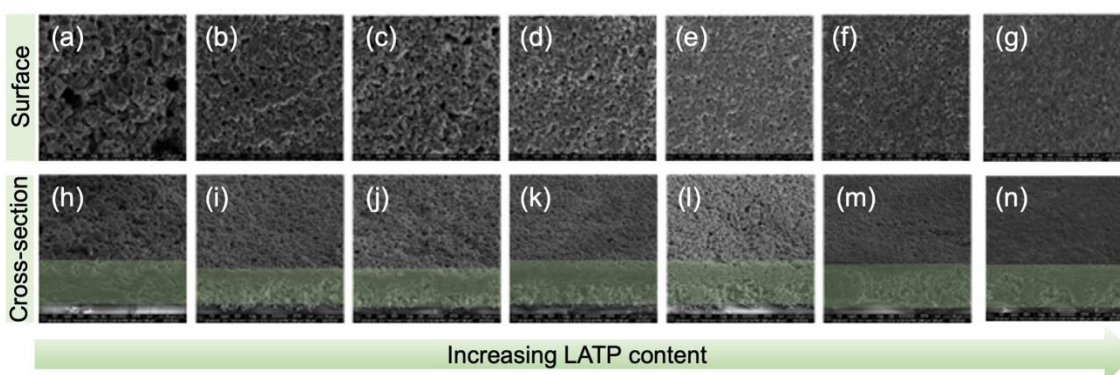


Figure 96. Scanning electron microscopy characterization of SP-S cathodes (with AB 7 wt%, CNT 5 wt%) with (a/h) no LATP, (b/i) 0.5 wt%, (c/j) 1 wt%, (d/k) 1.5 wt%, (e/l) 2 wt%, (f/m) 2.5 wt%, and (g/n) 5 wt%. (a-g) Images of the surface. (h-n) Cross-sectional view taken at 60° tilts.

Similarly, SEM characterization shows that addition of LATP also leads to a systematic decrease in porosity (as well as particle size) with increasing amounts of LATP (Figure 96). This opens a new opportunity to optimize the porosity of the cathodes by varying amounts of solid-state Li-conductor, AB, and CNT to obtain the best combination of electronic/ionic conduction. Although the team has achieved a high initial discharge capacity by adding LATP, they still need to increase capacity retention over battery cycling. Efforts are under way to optimize the amount of LATP, AB, and CNT to obtain desired porosity, as well as to reduce the amount of functionalizing liquid to obtain discharge characteristics that are closer to an ASSB.

Patents/Publications/Presentations

Publication

- Arnold, W., V. Shreyas, Y. Li, M. Koralalage, J. Jasinski, A. Thapa, G. Sumanasekera, A. Ngo, B. Narayanan,* and H. Wang.* “Synthesis of Fluorine-Doped Lithium Argyrodite Solid Electrolytes for Solid-State Lithium Metal Batteries.” *ACS Applied Materials and Interfaces* 14 (2022): 11483. doi: 10.1021/acsami.1c24468.

Presentation

- Materials Theory Group Seminar Series, Center for Nanoscale Materials, ANL: “Understanding Ion-Transport and Interfacial Stability in Argyrodite Electrolytes for Solid-State Lithium Batteries”; B. Narayanan. Invited.

Task 3.8 – Predicting the Nucleation and Evolution of Interphases in All-Solid-State Lithium Batteries (Sabrina (Liwen) Wan, Lawrence Livermore National Laboratory)

Project Objective. The goal of this project is to develop and apply a suite of new computational tools to predict early-stage formation of metastable interphases in SSBs. To achieve this goal, this project focuses on meeting three primary objectives corresponding to different regimes within the early-stage interphase formation: (1) identify chemical motifs for pre-nucleation; (2) predict possible interphase structures; and (3) model the kinetics of interphase formation.

Project Impact. Degradation of SSE and formation of undesired secondary interphases at the solid electrolyte/electrode interfaces are some of the key issues that limit SSB technology from practical applications. The computational tools developed in this project will allow modeling of nucleation and formation of interphases with quantum-level accuracy as well as significantly improved efficiency compared to currently available methods. Completion of this project will also provide valuable insights into the correlation between local chemistry and interphase formation, which can be used to inform design of interfacial structures to lower interfacial resistance, and to extend cycling life of SSBs.

Approach. The project approach centers on close integration of *ab initio* simulations, ML, and stochastic methods to probe chemistry and nucleation across broad ranges of time and length scales. First, the team will identify chemical motif, which acts as chemical precursor for pre-nucleation based on ML and large-scale AIMD simulations. Second, they will predict possible interphase structures based on stochastic minimizations of population-weighted chemical motifs identified from the MD simulations. Third, they will model the kinetics of interphase formation and evolution using metadynamics and solid-state NEB (SS-NEB) methods. To test the general applicability of the proposed computational methods, the team considers various commercially viable SE and cathode materials, including cubic LLZO and LiPON SEs, and LCO and LFP cathodes. These materials also represent a range of degrees of stability arising from their intrinsic properties—in particular, LiPON|LCO, LLZO|LCO, and LLZO|LFP are expected to form stable, less stable, and reactive interfaces, respectively.

Out-Year Goals. The future goal is to predict practical strategies either (1) to facilitate formation of the desired interphase that allows for fast Li⁺ diffusion and is stable on cycling, or (2) to suppress formation of undesired interphase to reduce interfacial impedance of ASSBs.

Collaborations. There are no collaborative activities this quarter.

Milestones

1. Establish a library of meta-stable interphase structures. (Q1 FY 2022; Complete)
2. Identify initial phase transformation pathways. (Q2, FY 2022; In progress)
3. Obtain lowest energy phase transformation pathways. (Q3, FY 2022; In progress)
4. Extract phase transformation kinetics as a function of composition. (Q4, FY 2022; On schedule)

Progress Report

This quarter, the team continued efforts to identify distinct stable secondary compounds that might be formed at the LLZO|LCO interfaces. Building on the LaCoO_3 phase identified in previous quarters, they expanded their phase identifications to other La-Co-O compositions. For example, they have surveyed the complex potential energy surface of La_2CoO_4 using the Basin Hopping approach and have identified several crystal structures as highlighted in Figure 97. They further fully relaxed these metastable structures that correspond to local minima on the potential energy surface to identify the most stable atomic configurations. From over 200 local minima structures obtained during the Basin Hopping runs, they predicted 5-10 unique, relatively stable structures (with a 0.01 eV/atom energy difference among them). As shown in Figure 97b, their predicted most stable structure of La_2CoO_4 matches closely with the ground state structure predicted in the Materials Project. The other two dominant structures identified during the Basin Hopping search are also shown in Figure 97; these are at slightly higher energy states, yet may still be relevant as metastable or intermediate phases formed at the LLZO|LCO interfaces.

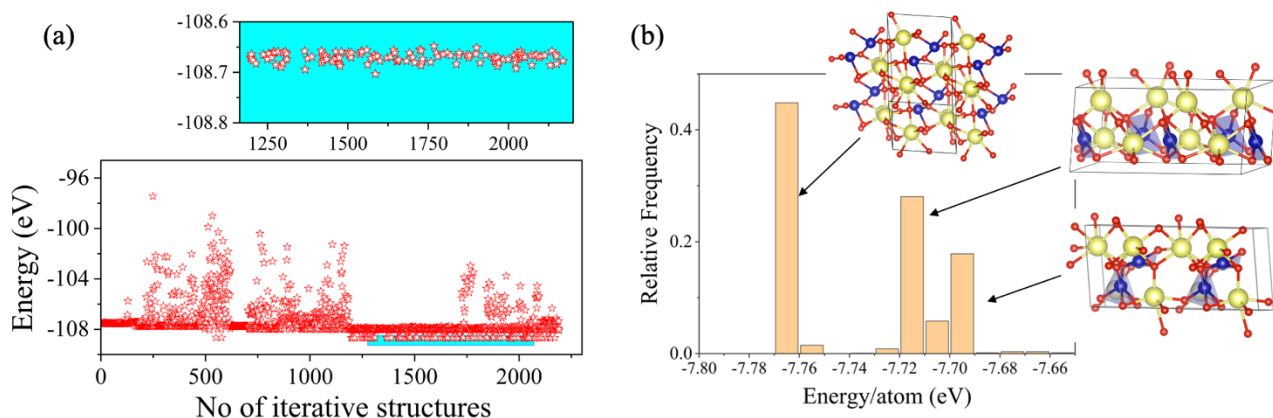


Figure 97. (a) Example energy variation plot for different iterative structures sampled for La_2CoO_4 using the Basin Hopping approach. (b) Distribution of energies, with corresponding atomic structures for selected local minima (highlighted region) from the energy variation plot. Lanthanum, cobalt, and oxygen are represented by yellow, blue, and red spheres, respectively, in the structure representation.

Apart from these experimentally proposed LaCoO_3 and La_2CoO_4 compositions, they have also explored the quaternary phases of these compounds with the addition of lithium, that is, Li-La-Co-O. Given the charge and local coordination constraints, they focused on the $\text{Li}_{1.5}\text{La}_{0.5}\text{CoO}_3$ and $\text{Li}_{1.5}\text{LaCo}_{0.5}\text{O}_3$ compositions. Figure 98 highlights some of the obtained stable structures of $\text{Li}_{1.5}\text{La}_{0.5}\text{CoO}_3$ (shown in panels a-c) and $\text{Li}_{1.5}\text{LaCo}_{0.5}\text{O}_3$ (shown in panels d-e), respectively. Although the structures shown in Figure 98 are very similar in energies (within 0.05 eV/atom), they exhibit distinct local coordination environments, such as for cobalt and lanthanum, which implies that lithium incorporation in LaCoO_3 may follow different kinetically driven pathways. The team is performing additional simulations to examine the kinetic stabilities of these phases and how lithium is dynamically incorporated into LaCoO_3 . In addition, it would be beneficial to study Li-ion transport behavior in these metastable La-Co-O compounds and to address whether or to what extent formation of such secondary phases at the LLZO|LCO interface contributes to the observed high interfacial impedance.

The team has obtained a library of more than 5-10 distinct structures for each of the distinct secondary phase compositions (LaCoO_3 , La_2CoO_4 , $\text{Li}_{1.5}\text{La}_{0.5}\text{CoO}_3$, $\text{Li}_{1.5}\text{LaCo}_{0.5}\text{O}_3$, etc.). A quantitative understanding of the kinetic energy barrier for phase nucleation would help to differentiate fast and slow nucleating pathways to form these predicted secondary phases. This quarter, they have performed SS-NEB calculations to determine the kinetic activation energies for phase nucleation starting from the random nuclei identified from the AIMD simulations of the LLZO|LCO interface to the stable structure obtained from Basin Hopping. They evaluated the kinetic energy barrier for over 10 different nucleation pathways to form LaCoO_3 , and the results

are summarized in Figure 99. Large variations in nucleation kinetics are observed, among which 50% of the pathways show activation energy barrier < 1.2 eV. The pathways with kinetic energy barriers above 1.5 eV are highly unlikely to contribute toward phase nucleation and thus will be neglected for further investigation. The lowest energy barrier pathway corresponds to the one wherein gradual variation in cell volume is observed during the phase nucleation process. The team is performing additional SS-NEB runs to identify kinetic energy barrier for other distinct secondary phases, as discussed previously. A comparison between the calculated kinetic energy barrier would provide a quantitative understanding of possible fast and slow nucleating processes at the LLZO|LCO interface for the formation of secondary phases.

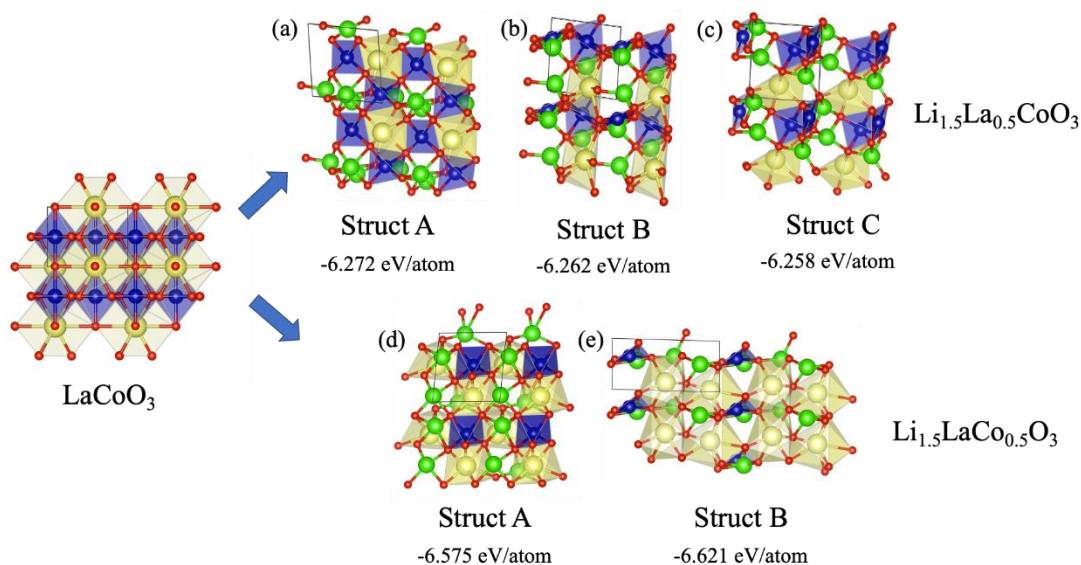


Figure 98. Example of stable structures obtained for (a-c) $\text{Li}_{1.5}\text{La}_{0.5}\text{CoO}_3$ and (d-e) $\text{Li}_{1.5}\text{LaCo}_{0.5}\text{O}_3$. Lithium, lanthanum, cobalt, and oxygen ions are represented by green, yellow, blue, and red spheres, respectively, in the structure representations.

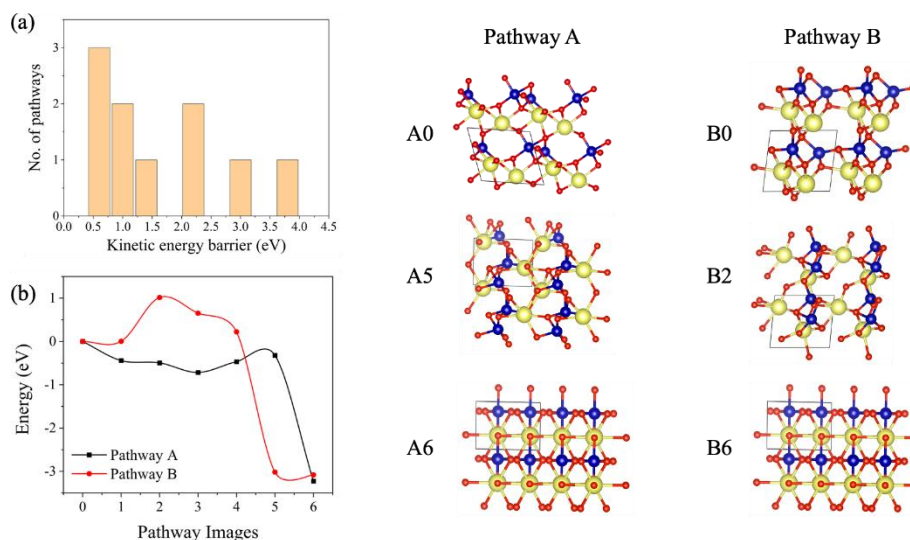


Figure 99. (a) Distribution of calculated kinetic energy barrier for 10 distinct nucleation pathways to form LaCoO_3 . (b) Examples of relatively low-energy and high-energy nucleation pathways. The structural evolutions along these two nucleation pathways are also presented from the starting nuclei to the stable structure predicted for LaCoO_3 .

Patents/Publications/Presentations

Presentation

- ACS Spring Meeting, San Diego, California (March 2022): “Towards Understanding the Electrolyte-Cathode Interfaces in Solid-State Batteries”; A. M. Dive, K. Kim, W. Jeong, M. Wood, B. C. Wood, and L. Wan.

Task 3.9 – Design of Strain Free Cathode – Solid-State Electrolyte Interfaces Using Chemistry-Informed Deep Learning (Hakim Iddir, Argonne National Laboratory)

Project Objective. The main objective of this project is to use state-of-the-art ML techniques and high-performance computing (HPC) to model complex oxide materials that will allow the team to develop cathode / SE interfaces that exhibit minimal or no strain as well as provide chemical stability at the interface between the cathode material and the SSE. A deep understanding and control of the cathode/SSE interface (including its chemical and mechanical stability) is needed to develop an effective SSB. The active cathode material changes volume during cycling, particularly at high task state of charge (SOC). This volume change leads to strained interfaces triggering loss of contact and delamination, and hence reduction/elimination of electron and ion transport pathways. The increased strain could also generate cracks within the SSE, creating new paths for lithium dendrite growth channels. These structural changes degrade the electrochemical performance of the battery. Several strategies have had limited success in alleviating these drawbacks, including mixed SSE, buffer layers between the cathode and the SSE, and dopants to improve chemical stability of the interface. These approaches, although promising, could not resolve issues with both the chemical and mechanical stability of the interface. In this project, the team proposes a new approach that takes advantage of well-established ML techniques and HPC to screen for candidate dopants of high-Ni-content NMC cathodes that would both reduce the volume expansion and the chemical reactivity (mixing) at the interface, with minimum impact on electrochemical performance and energy density of the cathode.

Project Impact. Structure-property relationships are at the heart of most fundamental scientific approaches. However, the link between structure and property remains a challenge in the materials science of complex systems, such as the oxides that form battery components. In particular, the chemical and mechanical stability of the cathode-SSE interface presents a challenge to development of SSBs. High-performance DFT calculations provide the necessary framework to understand such systems. Unfortunately, given the limited number of atoms and time scales accessible by the method, along with the myriad calculations required to achieve satisfactory results, the computational cost of simulating all the possible configurations of a multicomponent oxide is prohibitive. In this work, the team augments the DFT data with ML (especially deep learning) techniques that allow them to access the large system sizes and longer time scales necessary to build thermodynamic models. They focus on understanding the nature of benchmark $\text{Li}_{1-\alpha}\text{Ni}_{1-x-y-z}\text{Mn}_x\text{Co}_y\text{M}_z\text{O}_2$ structures (M dopant, $\alpha, x, y, z < 1$), their volume change with lithium content, the nature and concentration of the dopants, and chemical stability of the SSE-cathode interface. The DFT and ML approach will provide new cathode compositions that will reduce the strain of the SSE-cathode interface and hence improve its mechanical and chemical stabilities.

In this project, the team aims at developing a methodology that will allow them to explore and expand the configurational space using HPC approaches in a systematic and efficient way. The methodology will encompass DFT, AIMD, MD, and ML. The methodology will also take advantage of various software already developed at ANL and at other DOE laboratories (for example, Balsam) to automate, manage, and control the large number of calculations needed to achieve the project goal.

Approach. All calculations will be performed by spin-polarized DFT as implemented in the Vienna *ab initio* simulation package (VASP). After geometry optimization within the DFT+U framework, electronic relaxation will be performed using a single-point calculation with the hybrid functional HSE06. For production calculations, they will use the message-passing interface (MPI) parallelized version of VASP.

Exploration of the potential energy surface is needed to predict the structure of solid materials and interfaces. Such calculations are infeasible using MD or DFT calculations alone. Thankfully, the potential energy surface of a system can be represented by the sum of the energies of the local neighborhoods surrounding each atom. This enables the use of ML surrogate models trained with DFT calculations to capture the energies in local

neighborhoods. The input to the ML surrogate must be a unique representation of the system under study. Consequently, the local environment of each ion is described using a local environment descriptor that renders the atomic configuration invariant to rotations, translations, and permutations of the atoms. In recent years, several different descriptors have come to prominence with advantages and disadvantages. Once the ML surrogate is trained, the total energy and forces over all the ions of any structural configuration can be determined. Such information can be used for atomistic simulations, namely, MD and MC.

In this project, the team proposes to use the open-source DeepMDkit python/C++ package to construct the ML potential energy surface and force field (FFs). The promise of DeepMDkit in this work is to provide near-DFT accuracy at orders-of-magnitude lower computational expense, comparable to traditional MD simulations. Efficiency in training is facilitated through integration with TensorFlow and MPI / graphics processing unit support.

One of the challenges of developing ML potential energy surface is achieving accurate predicted forces and energies across the entire configurational space, while minimizing the total number of calculations required for training. In recent years, active learning has been highlighted for its ability to target training examples most likely to improve the model quality or to achieve some other objective (that is, maximizing a predicted material property). DP-GEN, an open-source python package based on DeepMDkit, implements a similar active learning scheme with HPC support, and has been employed to construct ML potential energy surface with accuracy approaching DFT and sometimes exceeding embedded atom potential for experimentally measured properties of interest. In this work, the team proposes to leverage DeepMDkit and DP-GEN to efficiently generate ML potential energy surfaces for cathode-electrolyte systems including a variety of dopants.

Out-Year Goals. One out-year goal involves developing a DFT-trained ML model on NMC/LLZO interface, ready to use for large screening of new cathodes, SSE compositions, and cathodes/SSE interfaces. A second is to provide fundamental understanding on critical parameters limiting performance and stability of the cathode/SSE interface and hence of the SSB.

Collaborations. Project collaborators include J. Croy, C. Johnson, and E. Lee from ANL Chemical Sciences and Engineering Division for the synthesis phase of the project.

Milestones

1. Determine cationic distribution in $\text{LiNi}_{0.8}\text{Mn}_{0.1}\text{Co}_{0.1-y}\text{X}_y\text{O}_2$ (NMCX) for X (Ti, Zr, Al, Fe, Ca, Mg, Y, W, Nb, B, La). (Q1, FY 2022; Completed)
2. Determine elemental segregation, volume changes, and phase transformation during charging of doped (including fluorine anionic substitution) NMC-811 using the developed DFT-trained ML model. (Q2, FY 2022; DFT completed, ML trained modeling in progress)
3. Determine doped NMC-811-LLZO interface reactivity and structural stability. (Q3, FY 2022; In progress)
4. Screen for compositions with low interfacial strain, and elemental mixing (NMCX-LLZO). (Q4, FY 2022)

Progress Report

As a first step toward the evaluation of the volume changes on delithiation of NMC-811 with added dopants, DFT calculations were performed to provide training data for the DeepMDkit machine learning force fields (MLFFs). The potential energy surface was thoroughly explored to determine the most likely cation configurations and provide high-quality data for the MLFFs. Figure 100 shows the probability of occurrence for the tested conformations with one and two dopants (zirconium case) in the simulation cell (3.7% and 7.4% TM at%). The probability of occurrence for each configuration is computed using DFT energies, configurational density of states, and the Boltzmann factor at three different temperatures. The configurational entropy increases the probability of occurrence of high-energy configurations with regard to the ground state computed at 0 K, and dopant concentration seems to impact the probability distribution. The volume change on delithiation to a very high SOC (2%, see publications section) shows a volume decrease by ~ 7% for pure LiNiO₂. A decrease of ~ 6.5% in volume for the doped (Al, B, Fe, Nb, Ti, W, Zr) NMC-811 cathode is calculated, showing a minimal impact. However, dopants (La, Mg, Ca) with a preference for the lithium layer sites, presented a smaller decrease (~ 4%). Dopants in the lithium layer act as pillars, avoiding the lattice inter-slab space collapse. The data are being processed to be presented in a publication.

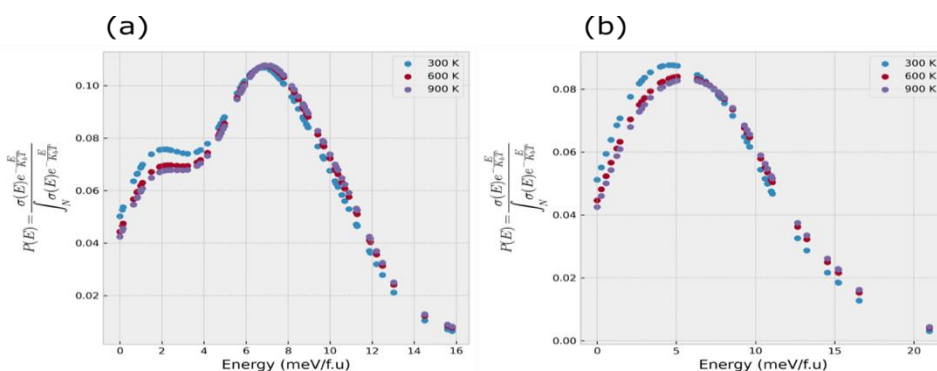


Figure 100. Probability of occurrence of a given configuration of Zr-doped LiNi_{0.8}Mn_{0.1}Co_{0.1}O₂: (a) one dopant per cell [3.7% of total transition metal content], and (b) two dopants per cell [7.4% of total transition metal content].

Aluminum and magnesium dopants were selected for preliminary study to demonstrate the methodology. For a given NMC volume, the cobalt dopant atoms were replaced with either 1, 2, or 3 aluminum or magnesium atoms. The dopants were placed in the TM layer or the lithium layer. From these DFT calculation results, an ensemble of five MLFFs were trained for both aluminum and magnesium. Ensembles were successfully trained for each dopant type with R² values of 0.987 and 0.998 for aluminum and magnesium, respectively. These ensembles can be employed to estimate the uncertainty in MLFF predictions and are therefore a critical component in the use of Bayesian optimization to identify low energy structures (as in the team’s previous work with LiNiO₂). Next quarter, these MLFF ensembles will be employed to identify the lowest energy configurations for each dopant type and concentration (for a total of six structures), and then to determine the volume change with delithiation with estimated uncertainties. Figure 101 shows parity plots for MLFF predictions of energies compared with DFT data for aluminum and magnesium (as representative examples of the data).

It is important to highlight that the major issues in SSBs happen under the extreme conditions of high SOC. Structural changes in Li_xNiO₂, as lithium is removed during charging, are known to cause damage to microcrystallites of Li_xNiO₂, limiting the lifetime and SOC in Ni-rich Li-ion batteries. The stacking of NiO₂ layers has been observed to change from O3 to O1 in the limit of zero lithium (NiO₂). Theoretically, the energy difference between O1 and O3 stacking in NiO₂ is too small to predict reliably with DFT. Different levels of DFT theory will predict different relative energetics for O1 and O3. However, DFT predicts larger, more reliable energy differences between the stacking of layers in NiO₂ with defects and can be used to rationalize why the stacking of Li_xNiO₂ changes when x approaches zero.

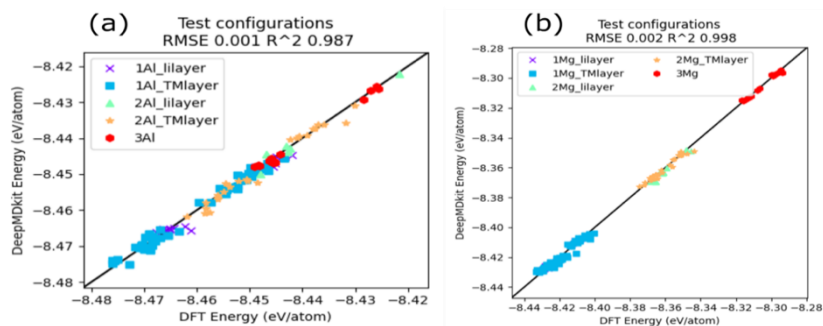


Figure 101. Parity plots of machine learning model energies for (a) Al-doped NMC-811 and (b) Mg-doped NMC-811.

This team and others have examined the relative energy of O1 and O3 stacking in NiO₂ with several flavors of DFT. In general, they observe that gradient corrected DFT with van der Waals terms favor O1 stacking, while DFT+U, meta-functionals, or hybrid exchange favors O3 stacking. Their results are presented in Table 8.

Table 8. Comparison of density functional theory calculated NiO₂ oxygen stacking relative energy and structural parameters.

	O1 NiO ₂				O3 NiO ₂				
	a	b	Volume	Energy	a	c	volume	Energy	E(O1-O3)
	(Å)	(Å)	(Å ³)	(eV/cell)	(Å)	(Å)	(Å ³)	(eV/cell)	(eV/cell)
Experiment ^[1]	2.822	13.04	89.93						
optB86b-vdW	2.808	12.834	87.63	-31.8204	2.806	13.061	89.08	-31.8080	-0.0124
optB86b-vdW+U	2.779	13.082	87.51	-19.6138	2.779	13.200	88.26	-19.6139	0.0001
R2SCAN+DFTd4	2.785	13.119	88.10	-80.5317	2.784	13.218	88.75	-80.5350	0.0033
HSE06+DFTd4	2.765	13.253	87.74	-69.0278	2.766	13.238	87.72	-69.0341	0.0063

Although the optB86b-vdW agrees with experiment for structural parameters for layered materials, strong correlation is needed to predict accurate energies with changes in oxidation state associated with charging Li_xNiO₂. The team decided to use the R2SCAN+DFTd4 meta-functional because it includes a significant amount of strong correlation and avoids issues with metastable states found in DFT+U and hybrid functionals.

In comparing to experiment, one should keep in mind that the magnitude of the energy difference between O1 and O3 stacking is less than 1.3 meV/atom in every case. This is too small of an energy difference for DFT to predict accurately. The team believes that O1 and O3 stacking in perfect NiO₂ has essentially the same energy. C. P. Grey et al. observed that “due to a combination of a lower thermodynamic driving force, sluggish kinetics, and the presence of antisite defects, O1 structured NiO₂/Li_xNiO₂ is only rarely observed.”^[2]

Following up on the suggestion by Grey et al. that the formation of the O1 phase during delithiation of Li_xNiO₂ “could potentially be an artifact of proton insertion which can assist the stacking sequence change,”^[2] the team has considered the effect of protons on the O3 and O1 stacking in NiO₂. They find that a proton favors O1 stacking over O3 in a Ni₃₆O₇₂ supercell by 90 meV/supercell. This represents a change of 126 meV in the relative energies of O1 and O3 stacking in Ni₃₆O₇₂, where O3 stacking is favored by 36 meV. This energy difference is due to H-bonding between the proton and the oxygens in the NiO₂ layer above the hydroxyl defect. For O1 stacking, the O-H bond points

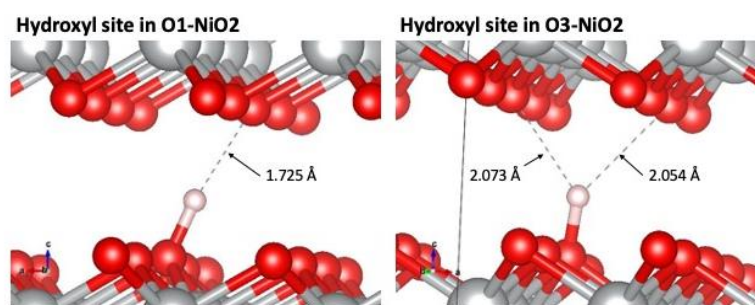


Figure 102. Comparison of the hydroxyl bonds for the proton defect in NiO₂ for O1 stacking and O3 stacking. The dashed line shows the hydrogen bonding between layers.

directly at an oxygen atom in the layer above the hydroxyl. However, for O3 stacking, the proton points between two oxygen atoms above the hydroxyl. This leads to shorter (1.725 Å) and stronger H-bonds for O1 stacking than O3 stacking (see Figure 102)

Proton defects are often present in samples of NiO₂. They are introduced through exposure to moisture and decomposition of the electrolyte during charging. Recently, M. C. Hersam et al. showed that oxygen vacancies also favor O1 stacking in NiO₂ and argued that oxygen vacancies drive the change from O3 to O1 stacking in NiO₂.^[3] The team believes that oxygen vacancies, protons, and other defects drive the formation of O1 stacking in NiO₂. Modifications to Li_xNiO₂ suppressing these defects will help preserve the high-voltage capacity and improve the performance of batteries that use this cathode material. They have completed a series of NEB calculations to determine the barrier to diffusion of a proton in NiO₂. The barrier for a proton moving between layers is relatively low at 290 meV, which is 2.7 times higher than the barrier for proton transfer in water at 108 meV.^[4] This implies proton will diffuse slowly in O1 NiO₂ at room temperature.

References

- [1] Croguennec, L., C. Poullierie, A. N. Mansour, and C. Delmas. “Structural Characterization of the Highly Deintercalated Li_xNi_{1.02}O₂ Phases (with $x \leq 0.30$).” *Journal of Materials Chemistry* (2001): 131–141.
- [2] Xu, C., P. J. Reeves, Q. Jacquet, and C. P. Grey. “Phase Behavior during Electrochemical Cycling of Ni-Rich Cathode Materials for Li-Ion Batteries.” *Advanced Energy Materials* 11, no. 7 (2021): 2003404.
- [3] Park, K-Y., Y. Zhu, C. G. Torres-Castanedo, H. J. Jung, N. S. Luu, O. Kahvecioglu, Y. Yoo, J-W. T. Seo, J. R. Downing, H-D. Lim, M. J. Bedzyk, C. Wolverton, and M. C. Hersam. “Elucidating and Mitigating High-Voltage Degradation Cascades in Cobalt-Free LiNiO₂ Lithium-Ion Battery Cathodes.” *Advanced Materials* 34, no. 3 (2022): 2106402.
- [4] Lee, S. H., and J. C. Rasaiah. “Proton Transfer and the Mobilities of the H⁺ and OH⁻ Ions from Studies of a Dissociating Model for Water.” *Journal of Materials Chemistry* 135, No. 12 (2011): 124505.

Patents/Publications/Presentations

Publication

- Garcia, J. C., J. Gabriel, N. H. Paulson, J. Low, M. Stan, and H. Iddir. “Insights from Computational Studies on the Anisotropic Volume Change of Li_xNiO₂ at High States of Charge ($x < 0.25$).” *Journal of Physical Chemistry C* 125, no. 49 (2021): 27130–27139. doi: 10.1021/acs.jpcc.1c08022.

Task 3.10 – Tackling Solid-State Electrochemical Interfaces from Structure to Function Utilizing High-Performance Computing and Machine-Learning Tools (Shinjae Yoo, Feng Wang, and Deyu Lu, Brookhaven National Laboratory; Nongnuch Artrith and Alexander Urban, Columbia University)

Project Objective. This project aims at elucidating the structural evolution and other dynamic properties of the interphases at the SSIs in SSBs under processing and electrochemical cycling conditions that strongly impact cell performance. By leveraging synergies of first-principles theory, HPC, ML, and computational/experimental spectroscopy, this project involves a comprehensive investigation of SE systems and SSIs that may enable the practical use of lithium anodes and high-Ni NMC cathodes in SSBs. Specific project objectives are as follows: (1) develop realistic atomic-scale structure models of the heterostructural SSIs, (2) determine the impact of structural evolution on stability and transport properties of SSIs, and (3) identify the coating/doping chemistry that may stabilize SSIs during formation and electrochemical cycling.

Project Impact. Interfacial properties and the dynamical evolution of interphase structures are crucial for the stability and performance of SSBs. This project will lead to fundamental understanding of current materials limits and will identify key materials parameters for optimizing the performance of SSBs. By corroborating atomic-scale theory with experiment, the project will identify structure–property relationships of the heterostructural SSIs in SSB systems that are relevant for EVs. The outcomes of this project will therefore accelerate development of high-energy-density, safe SSBs for EVs.

Approach. Accurate ML potentials will be trained on an extensive database from DFT calculations to simulate the structure evolution and electrochemical properties of the SSIs. Using a second ML model, key physical descriptors will be extracted from EELS and XAS measurements. This spectral fingerprinting will enable the automated interpretation of spectroscopy measurements, thereby bridging between atomistic modeling and experiment. An experimental platform will be developed to integrate experimental/computational spectroscopy and modeling of SSIs. In combination, the two ML models and the spectroscopic data will facilitate the construction of a physics-based model to unravel the structure-property relationships of the SSIs.

Out-Year Goals. The project will progress toward establishing dynamic composition-structure-property relationships for interface stability and transport within and across the electrochemical SSIs in SSBs. The ML approach will be further developed to a general model for thermodynamic and transport properties of dynamic heterostructural electrochemical interfaces and will eventually be applied to the practical SSB systems.

Collaborations. The project is collaborating with Y. Du at BNL.

Milestones

1. Determine electrochemical stability of LPS/Li interfaces during cycling through spectroscopy characterization aided by ML, data-analysis, and modeling. (Q1, FY 2022; Completed)
2. Analyze impact of halide-substitution on chemical and electrochemical stabilities of LPS-X (X = Cl, Br, I) systems in contact with lithium metal. (Q2, FY 2022; In progress)
3. Identify key limitations to interfacial stability of LPS and LPS-X systems in contact with lithium metal through combined computational/experimental investigations. (Q3, FY 2022; In progress)
4. Establish doping/coating-based approaches for enabling long cycling stability of the LPS-X based half and full cells at high current density. (Q4, FY 2022; In progress)

Progress Report

This quarter, the team has combined electrochemical, spectroscopic, and computational techniques to study the oxidation stability of argyrodite sulfide electrolytes $\text{Li}_6\text{PS}_5\text{X}$ ($\text{X} = \text{Cl}, \text{Cl}_{0.5}\text{Br}_{0.5}, \text{Br}$; LPSX), characterize the microscopic structure changes on oxidation, and identify the oxidative decomposition products. They have found that LPSX compounds start to oxidize at ≈ 2.4 V versus Li^+/Li . Like LPS, sulfur atoms in argyrodites are likely to form bridging sulfur bonds during delithiation. However, the change in the phosphorus K-edge XAS spectra is small compared with that in LPS, indicating that the local atomic environments of phosphorus atoms do not change significantly during delithiation. The stabilization of the local structures could originate from the halide substitution. The chlorine K-edge XAS shows the formation of LiCl at the interface, which may also help to prevent destruction of PS_4 local structures. These findings reveal that the better stability of LPSX than LPS comes from more stable local structures around the phosphorus atom. In future work, these findings could provide guidance for controlling macroscopic reactions by microstructure engineering in electrolyte design.

CV Study of Electrochemical Stability of LPSX

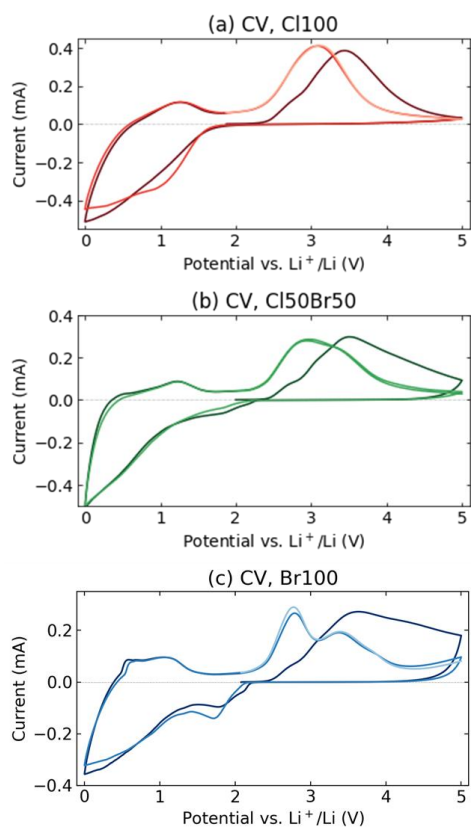


Figure 103. Cyclic voltammetry (CV) profiles of (a) $\text{Li}_6\text{PS}_5\text{Cl}$, (b) $\text{Li}_6\text{PS}_5\text{Cl}_{0.5}\text{Br}_{0.5}$, and (c) $\text{Li}_6\text{PS}_5\text{Br}$. Cycle range is 0-5 V, and voltage sweep rate is 0.1 mV/s. In each experiment, the voltage sweep starts first from open-circuit voltage (~ 2 V) toward the higher voltage, hence the oxidation (delithiation) direction.

from that of the later cycles. The CV profile is also influenced by the halide species. Adding bromine hinders surface passivation in the 1st delithiation cycle, as evidenced by the larger current at 5 V in Figure 103c compared to Figure 103a. For the 100% bromine sample, there are two major oxidation peaks

Argyrodite-type electrolytes $\text{Li}_6\text{PS}_5\text{X}$ ($\text{X} = \text{Cl}, \text{Br}$) with bromine and chlorine substitutions of sulfur show good ionic conductivity (10^{-3} S/cm) compared to LPS (10^{-4} S/cm).^[2] The conductivity of $\text{Li}_6\text{PS}_5\text{I}$ is lower than its chlorine and bromine counterparts because the large size of I increases the activation energy of Li^+ transport.^[3] Like LPS, argyrodite sulfides also suffer from interface issues between the electrode and the SE, including electrolyte decomposition outside the stability window, reaction with cathode/anode materials, and formation of high-resistance interphase layers.

The team focused on the intrinsic redox behavior of argyrodite sulfide electrolytes, and studied the stability of the electrolyte with respect to different halide substitutions. They first probed the electrochemical stability window of LPSX compounds using CV. They employed an LPSX-C composite working electrode consisting of LPSX particles and carbon black to focus on the intrinsic redox reaction of LPSX. The battery used an LPSCl pellet as the SE and Li-In alloy as the counter/reference. More details on this setup can be found in the FY 2021 fourth quarter report. Figure 103 shows the CV curves for LPSCl, $\text{LPSCl}_{0.5}\text{Br}_{0.5}$, and LPSBr, with a scan range of 0-5 V and voltage sweep rate of 0.1 mV/s. All experiments start with increasing the voltage from OCV to 5 V versus Li^+/Li . The batteries were cycled until they reached 5 V for the third time. As shown in Figure 103, the oxidation onset voltage of LPSX is ~ 2.4 V versus Li^+/Li for all three electrolytes.

The team notes that in all experiments, the curves of the 1st cycle differ from those of the 2nd and 3rd cycles, but the current profiles of the 2nd and 3rd cycles are similar, as are the following cycles (not shown). This implies that the redox reaction in the 1st cycle differs

above OCV at 2.8 V and 3.4 V in the 2nd and 3rd cycle, while the 100% chlorine sample shows only a single peak. Additionally, the 100% bromine samples show a reduction peak at ~ 1.7 V and a small oxidation peak at 0.6 V. The 50% bromine – 50% chlorine sample shows an intermediate behavior between the 100% bromine and 100% chlorine samples. The origin of these redox peaks in CV is not fully understood and requires further study.

XAS to Resolve LPSX Redox Reactions

The team measured the phosphorus, sulfur, and chlorine K-edge XAS of pristine and cycled LPS and LPSX samples. The characterization was performed in partial electron yield mode at the NSLS-II SST-2 (7-ID-2) beamline. The sulfide SE-carbon composite electrodes were cycled and disassembled in an argon glovebox, and then transferred into the UHV chamber at the beamline under argon to avoid oxidation and reaction with moisture in the ambient air. Figure 104 shows the XANES spectra of the four sulfides [that is, LPS (black), LPSCl (red), LPSCl_{0.5}Br_{0.5} (green), and LPSBr (blue)], with solid and dashed lines representing pristine and cycled samples, respectively. The cycled samples were harvested after the batteries were cycled to 5 V for the third time.

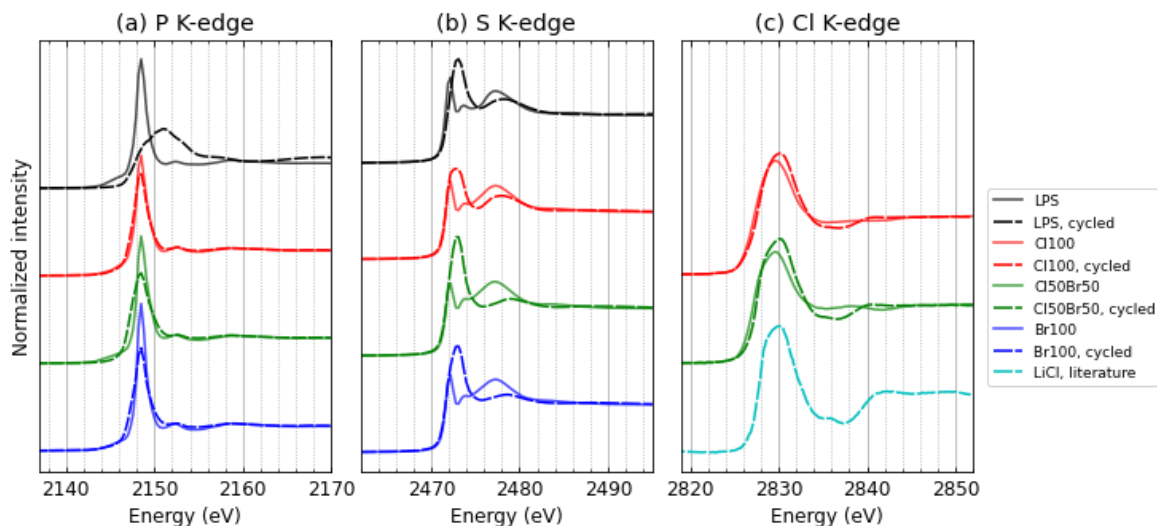


Figure 104. (a) Phosphorus K-edge, (b) sulfur K-edge, and (c) chlorine K-edge X-ray absorption spectra of sulfide electrolytes before and after cycling. In each panel, the black, red, green, and blue curves are from Li₃PS₄, Li₆PS₅Cl, Li₆PS₅Cl_{0.5}Br_{0.5}, and Li₆PS₅Br, respectively, with solid lines representing the pristine samples and dashed lines representing cycled samples. The cyan curve in (c) is a reference chlorine K-edge spectra of LiCl compound from Reference [1].

In pristine samples, the phosphorus K-edge spectra of argyrodite sulfides are similar to those of LPS because the local structures of phosphorus atoms are PS₄ tetrahedra in both LPS and LPSX. However, the phosphorus spectra of cycled LPSX exhibit large differences from cycled LPS. In LPSX, the intensity of the white line peak at 2148.5 eV decreases and the peak broadens, which may indicate a slight lattice distortion.^[4] In contrast, the phosphorus spectra of cycled LPS varies significantly from the pristine spectra: a new peak appears at 2151 eV, and only a shoulder remains at the position of the original white line peak. This new peak indicates the oxidation and local atomic structure changes of phosphorus after delithiation. The local structural change is also reflected in extended X-ray absorption fine structure (EXAFS) data (Figure 105). In the cycled LPS, the intensity of the first shell of phosphorus atom (~ 1.6 Å in R-space) decreases, indicating that the PS₄ tetrahedral structure is no longer preserved. The absence of large changes in phosphorus XANES spectra of LPSX electrolytes shows argyrodite sulfides have better oxidation stability. The better performance may come from the halide substitution, which stabilizes the structure due to the large-size halide ions and could also possibly lead to the formation of LiCl at the interface.

The sulfur K-edge spectra of LPSX are similar to LPS for both pristine and cycled samples. On delithiation, a new peak appears at 2473 eV with a higher intensity than the original white line feature at 2472 eV and becomes

the dominant feature. This new peak is attributed to the formation of bridging sulfur bonds.^[5-6] The origin of this peak was explained in last quarter's report and is consistent with the team's XANES simulation results (see the fourth quarter FY 2021 report).

Chlorine K-edge XAS of LPSCl and LPSCl_{0.5}Br_{0.5} samples are shown in Figure 104c. Comparing the pristine and cycled spectra with the standard LiCl spectrum from Reference [1], the cycled spectra show similar characteristic features to the LiCl spectrum, including a similar peak shape at 2830 eV, the small bulge at 2836 eV, and a small peak at 2841 eV. Therefore, they conclude that LiCl is an oxidation product of LPSCl and LPSCl_{0.5}Br_{0.5}. Along the same line, this indicates LiBr formation during delithiation of LPSCl_{0.5}Br_{0.5} and LPSBr; however, they did not measure bromine edge to obtain direct spectral evidence for LiBr. LiCl is thermodynamically stable on (de)lithiation and can passivate the surface of the electrolyte, so the formation of LiCl can act as a buffer layer to prevent further decomposition of the sulfide, which may contribute to the better stability of LPSX.

In summary, the team has studied the structural and compositional changes of argyrodite electrolytes after delithiation via XAS and CV. Compared with LPS, the PS₄ tetrahedral structure in LPSX appears to be preserved after cycling, which may be the origin of good stability. By tuning the composition and structure of sulfide SEs, the microscopic local structure of the electrolyte can be preserved during the redox process, thus improving the macroscopic interfacial stability.

References

- [1] Kiguchi, M., R. Arita, G. Yoshikawa, Y. Tanida, M. Katayama, K. Saiki, A. Koma, and H. Aoki. *Physical Review Letters* 90 (2003): 196803.
- [2] Lian, P-J., B-S. Zhao, L-Q. Zhang, N. Xu, M-T. Wu, and X-P. Gao. *Journal of Materials Chemistry A* 7 (2019): 20540.
- [3] Yu, C., S. Ganapathy, N. J. de Klerk, I. Roslon, E. R. van Eck, A. P. Kentgens, and M. Wagemaker. *Journal of the American Chemical Society* 138 (2016): 11192.
- [4] Ye, L., et al. *Advanced Energy Materials* 10 (2020).
- [5] Koerver, R., I. Aygün, T. Leichtweiß, C. Dietrich, W. Zhang, J. O. Binder, P. Hartmann, W. G. Zeier, and J. Janek. *Chemistry of Materials* 29 (2017): 5574.
- [6] Swamy, T., X. Chen, and Y-M. Chiang. *Chemistry of Materials* 31 (2019): 707.

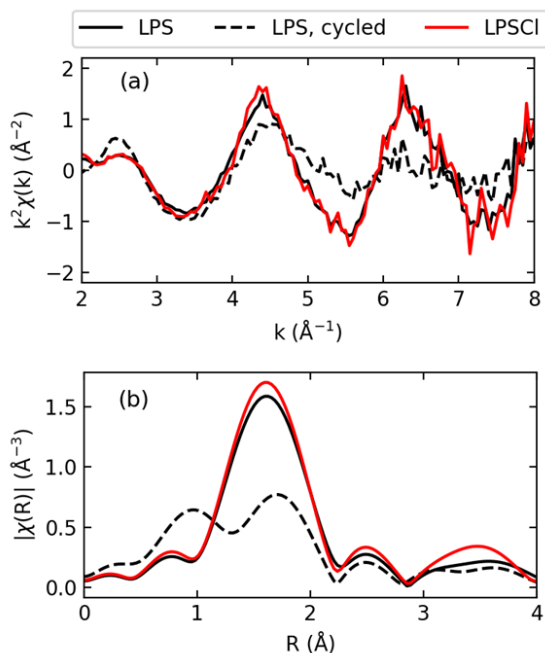


Figure 105. (a) The k-space and (b) R-space extended X-ray absorption fine structure of phosphorus K-edge. Black curve: Li₃PS₄; red curve: Li₆PS₅Cl; and black dashed curve: cycled Li₃PS₄.

Patents/Publications/Presentations

Publication

- Li, X., Q. Wang, H. Guo, N. Artrith, and A. Urban. "Understanding the Onset of Surface Degradation in LiNiO₂ Cathodes." *ACS Applied Energy Materials* (accepted 2022). <https://arxiv.org/abs/2112.04697>.

Task 3.11 – Integrated Multiscale Model for Design of Robust, Three-Dimensional, Solid-State Lithium Batteries (Brandon Wood, Lawrence Livermore National Laboratory)

Project Objective. This project is developing and applying multiscale, multiphysics models that connect composition, microstructure, and architecture to mechanical integrity in 3D-SSBs. The models integrate multiple computational methods, informed and validated through collaborations with complementary experimental efforts. The project scope addresses three objectives: (1) develop multiphysics, multiscale chemomechanics models; (2) assess interface- and microstructure-induced mechanical failure thresholds; and (3) simulate chemomechanical evolution under battery operating conditions.

Impact. This project will deliver multiscale, multiphysics models that connect composition, microstructure, and architecture to mechanical integrity in 3D SSBs. The tools will be used to examine common interfaces in commercially viable electrolyte and cathode materials and to provide design principles for maintaining mechanically robust operation. The modeling framework will address the shortcomings of existing modeling strategies that either lack coupling of the multiphysics nature of various processes active in 3D batteries or fail to incorporate processes at different length scales to understand function. Connections will be made to understand the limits of operability and to co-optimize ionic conductivity and mechanical robustness in solid electrolyte-cathode matrix composites.

Approach. The project approach integrates atomistic, mesoscale, and continuum simulation methods to predict chemomechanical properties of interfaces in ceramic (LLZO) and halide-based SEs. Both internal GBs and interfaces with LiCoO₂ (LCO) and NMC cathode materials are considered. The project is aligned along three tasks, each of which uses simulations to probe a different fundamental length scale relevant to the performance of 3D-SSB architectures. First, atomic-scale interfacial properties are computed using DFT and ML approaches. These include local bond strength and mechanical response, as well as stress distributions associated with formation of cracks. Second, using digital reproductions of 3D electrodes and electrolytes, the local stress distributions and stress hotspots in SEs and cathode-electrolyte composites are computed within a mesoscale model. Third, materials performance is coupled to cycling conditions within an operating device by incorporating phase-field models that can simulate rate-dependent fracture likelihood under cycling and extract microstructure-fracture-transport relationships.

Out-Year Goals. The team will focus on the following out-year goals: use *ab initio* methods to generate models for GBs and CEIs; compute local bond strength and mechanical response of model interfaces; reconstruct microstructures of electrodes and electrolytes using phase-field models; and develop a phase-field model for cathode-induced volume evolution on cycling.

Collaborations. This project collaborates with N. Adelstein from San Francisco State University on atomistic diffusion modeling, and J. Ye from Lawrence Livermore National Laboratory (LLNL) on 3D printing of SSB materials. They also partner with T. Danner and A. Latz from Deutsches Zentrum für Luft- und Raumfahrt (DLR) on impedance modeling and electro-chemo-mechanical interface models, with P. Zapol from ANL on modeling of interfaces in LLZO, and with D. Fattakhova-Rohlfing from Forschungszentrum Jülich (FZJ) and E. Wachsman from UMD on properties of LLZO with varying densities and microstructures as part of the U. S.–Germany partnership on SSB research.

Milestones

1. Complete atomistic CEI models. (Q1, FY 2022; In progress)
2. Determine composition profiles of CEIs. (Q2, FY 2022; In progress)

3. Set up model for local stress mapping. (Q3, FY 2022; In progress)
4. Train MLFFs for disordered interfaces. (Q4, FY 2022; Completed)

Progress Report

ML Interatomic Potentials for Accelerated Atomistic Simulations. This quarter, the team has prioritized the research activities of ML potential development work (scheduled for the fourth quarter of FY 2022) for paper submission as well as providing necessary inputs for the U. S. – Germany collaboration. They have extended the tests to their previously developed ML potential of LLZO for predicting phase transitions and have also applied it to compute Li-ion diffusivities with response to mechanical stress/strain fields. They simulated the thermal transition behavior of LLZO using npt [that is, constant number of atoms (N), pressure (P), and temperature (T)] MD simulations of a supercell with 1536 atoms. Figure 106a shows that the solid-solid (*s/s*) transition from tetragonal to cubic and the melting transition are observed at 850 K and 1800 K, respectively. The predicted *s/s* transition temperature matches closely to the experimental observation of 923 K, which again validates the general applicability of the LLZO potential. They further applied this ML potential to analyze lithium transport with hydraulic pressure and mechanical strain in LLZO. They found that the diffusivity increases with larger volume under hydraulic pressure due to wider migration channel (Figure 106b). With mechanical strain, the diffusivity along the strain axis decreases significantly with compression, whereas the increase in diffusivity is negligible with elongation (Figure 106c). The team is performing additional MD simulations for Li-ion diffusivity as a function of strain/stress, and the results will be used to parameterize the mesoscale model for the evaluation of strain/stress impact on microstructure evolution and the overall Li-ion conductivity in polygranular LLZO.

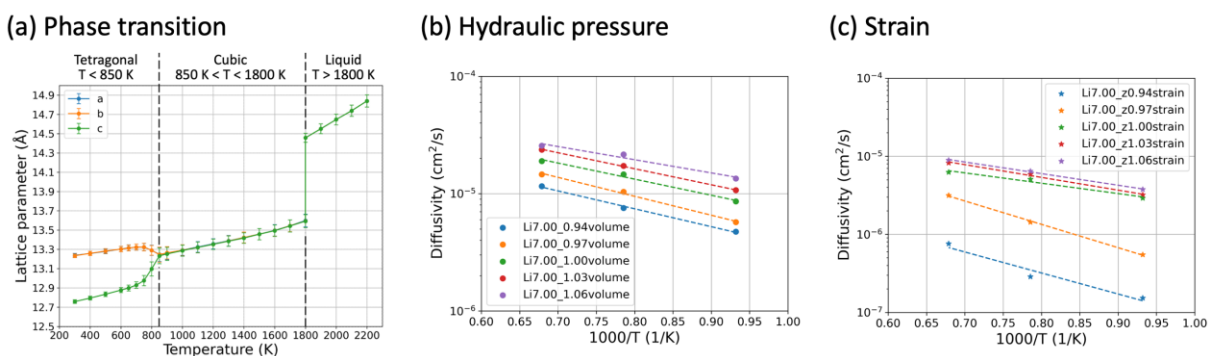


Figure 106. (a) Lattice parameters. (b) Total lithium diffusivity under hydraulic pressures. (c) Lithium diffusivity along strain axis under mechanical strain of LLZO as a function of temperature.

The team has also developed ML potential for Li_xCoO_2 (LCO) cathode, which is validated by radial distribution functions (RDFs) and lithium diffusivity compared against DFT calculation. They further applied the ML potential to compute Li-ion diffusivity at the GBs of LCO. These again are critical parameters to develop the mesoscale models for the extraction of effective Li-ion conductivity in the SE/cathode composites. As shown in Figure 107a, the ML potential predicted RDF peaks and intensities of bulk $\text{Li}_{0.75}\text{CoO}_2$ are very close to those calculated from AIMD simulations. In addition, the lithium diffusion behavior sampled by the ML potential is almost identical to that observed in AIMD simulations (Figure 107b), suggesting the quantum-level accuracy of the ML potential for LCO. They applied this ML potential to analyze lithium transport at eight different GB structures. For example, Figure 107c shows a stoichiometric LCO $\Sigma 2(-1104)/[11-20]$ tilt GB model with 4800 atoms. They performed MD simulations using ML potential (that is, MLMD) and tracked lithium atoms that stayed at the GB regions. Figure 107d presents the histogram of diffusivities of each lithium: this library can be used to obtain the in-plane and out-of-plane diffusivities. The team is calculating lithium diffusivity at different GBs, which again will be used to parameterize mesoscale models.

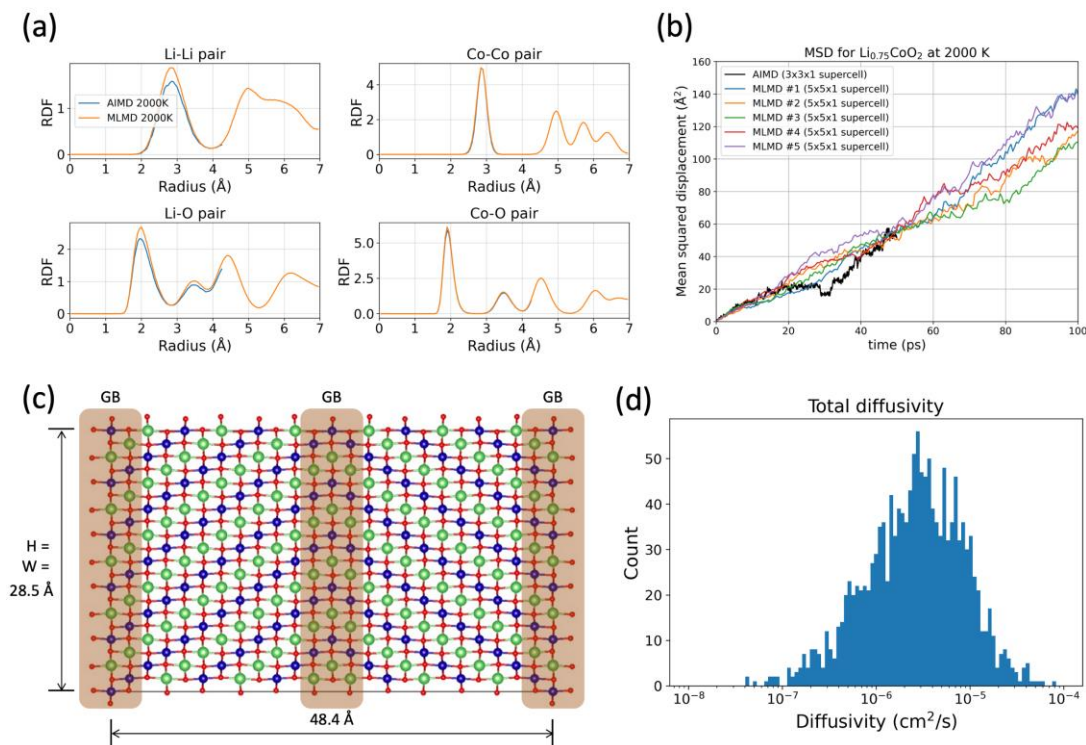


Figure 107. (a) Radial distribution functions and (b) mean squared displacement of bulk $\text{Li}_{0.75}\text{CoO}_2$ at 2000 K. (c) LCO $\Sigma 2(-1104)/[11-20]$ tilt grain boundary (GB) model. (d) Histogram of diffusivity of lithium atoms that stayed at GB area.

Mesoscale Modeling of SE-Cathode Particulate Composite Microstructures. This quarter, the team’s mesoscale modeling effort has focused on developing a new workflow to efficiently generate digital representations of realistic microstructures of SE-cathode particles mixture. These are key inputs for their LLNL *MesoMicro* code framework for computing effective elastic and ionic transport properties of the two-phase, composite cathode (for example, LLZO-LCO particles mixture). Their previous approach for generating digital microstructures of polycrystalline LLZO is based on the phase-field grain-growth model, which has limitations in controlling topological features of porous two-phase microstructures such as porosity, particle size distribution, particle dispersion, and so forth. In contrast, the new workflow has unique advantages over the previous approach in three aspects: (1) it allows for generating porous microstructures consisting of two or more phases; (2) it enables the team to better control the microstructural topology (that is, particle shape, particle size distribution of each phase, and porosity), which is critical for generating experimentally relevant digital microstructures; and (3) it is much more efficient in generating 3D particulate microstructures, which typically takes less than one minute on a personal computer in contrast to several hours for a typical phase-field grain-growth simulation on a supercomputer.

The new workflow consists of three major steps, as shown in Figure 108. The first step utilizes an open-source software package, *Particula*, which was originally developed for geoscience research to generate packings of irregular particles with prescribed size distributions. With *Particula*, they can assign different size distributions for different phases constituting the composite cathode; see Figure 108a as an example of two separate Gaussian distributions for the LLZO and LCO particles. By default, *Particula* generates a series of stereolithography mesh format for the 3D realization of the stack of particles, which is not directly compatible with the *MesoMicro* code based on uniform 3D grid discretization. Therefore, in the second step, they convert the data format using their script that voxelizes the structure and labels individual grains of each phase (Figure 108b). The resolution of the voxelization can be tuned depending on the computational demand and resources. In the third step, the voxelized and labeled microstructure is fed into the *MesoMicro* code, which enables further refinement of the microstructure by relaxing the interface structure based on phase-field simulations, as well as

final calculations of the effective ionic transport and elastic properties (Figure 108c). Based on preliminary numerical testing for single-phase porous microstructures, they are further improving the numerical convergence for computing the effective properties of the two-phase microstructures. In particular, they are developing a more robust algorithm to assign local properties to each grain and phase and improving the numerical iteration scheme for better accounting for spatially inhomogeneous systems. Moreover, the implementation of a self-consistent treatment of the chemo-mechanical coupling effect is also under way, which can yield better numerical stability and more accurate evaluation of the chemo-mechanical effect within the *MesoMicro* code framework.

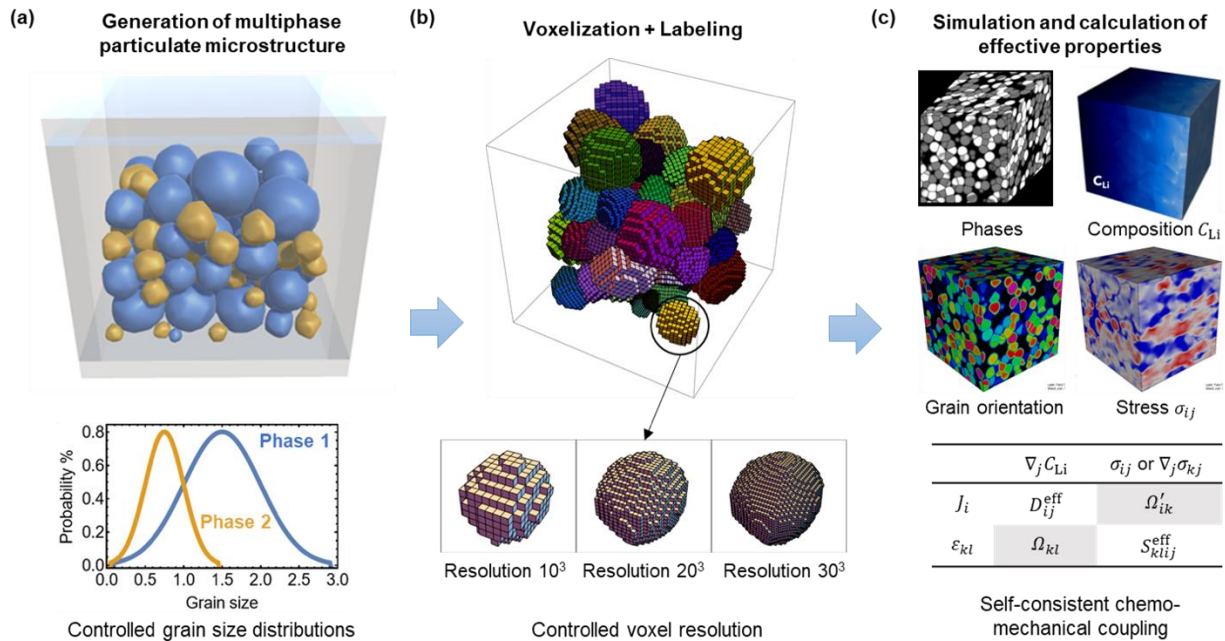


Figure 108. A workflow for generating two-phase particulate microstructures for modeling the composite cathode consisting of LLZO solid electrolyte and LCO active particles. (a) Generation of multiphase particulate microstructure with controlled size distributions of two-phase mixtures using the open-source software *Particula*. (b) Voxelization and labeling of the two-phase particulate microstructure to convert it into a readable format for *MesoMicro*. (c) Simulation of the transport of lithium in the composite cathode and calculation of the effective diffusivity and mechanical elastic modulus by a self-consistent model considering chemo-mechanical couplings.

Patents/Publications/Presentations

The project has no patents, publications, or presentations to report this quarter.

TASK 4 – METALLIC LITHIUM

Team Lead: Jagjit Nanda, Oak Ridge National Laboratory

Summary and Highlights

The use of a metallic lithium anode is required for advanced battery chemistries like Li-ion, Li-air, and Li-S to realize dramatic improvements in energy density, vehicle range, cost requirements, and safety. However, use of metallic lithium with liquid and solid polymer or ceramic electrolytes has so far been limited due to parasitic solid electrolyte interphase reactions and dendrite formation that eventually short circuit the battery. Adding excess lithium to compensate for such losses negates the high-energy-density advantage of a Li-metal anode and leads to further concern for battery safety. For a long lifetime and safe anode, it is essential that no lithium capacity is lost either (1) to physical isolation by roughening, dendrites, or delamination processes, or (2) to chemical isolation from side reactions. The key risk, and current limitation, for this technology is the gradual loss of lithium over the cycle life of the battery.

BMR, Battery500, and other U. S. Department of Energy programs are addressing this challenge with many innovative and diverse approaches. Key to all is the need for a much deeper analysis of the degradation processes and new strategies to maintain a dense, fully connected lithium and a dendrite-free electrolyte so that materials can be engineered to fulfill the target performance metrics for EV application, namely 1000 cycles and a 15-year lifetime, with adequate pulse power. Projecting the performance required in terms of just the lithium anode, this requires a high rate of lithium deposition and stripping reactions, specifically about 30 μm of lithium per cycle, with pulse rates up to 10 and 20 nm/s (15 mA/cm²) charge and discharge, respectively, with little or no excess lithium inventory. This is daunting in the total mass and rate of material transport that must be achieved without failures.

The efficient and safe use of metallic lithium for rechargeable batteries is then a great challenge, and one that has eluded research and development efforts for years. This project takes a broad look at this challenge for both solid-state batteries and batteries continuing to use liquid electrolytes (LEs). The electrolytes reported here include conventional LEs including localized high-concentration electrolytes, gel-type polymer-in-a-salt, composites of ceramic polymer phases, common and novel polymer electrolytes, and both oxide and sulfide ceramic electrolytes. Researchers are typically working toward cycling of full cells with relevant and balanced capacities using both thin lithium metal and anode free configuration, prelithiation methods, and post-cycling observation of the disassembled cell components to assess stability of the Li-metal/electrolyte interface.

Highlights

The highlights for this quarter are as follows:

- The Stanford University / Stanford Linear Accelerator Center team (Y. Cui) developed a method of fabricating porous lithium mesh to optimize and control pre-lithiation of silicon anodes. Their results show that 70% porous lithium mesh (1.5 mAh cm⁻²) fully compensates for the initial capacity loss and improves the initial Coulombic efficiency (CE) to a nearly ideal 100%. This approach has advantages compared to using thick lithium foil due to significant capacity mismatch between the lithiating electrodes.
- The Pacific Northwest National Laboratory team (J. Zhang) has developed an electrochemical test protocol to address the issue of capacity loss during lithium plating in anode-free lithium batteries (AFLBs). As part of the protocol, the assembled cells were rested at 1.5 V for wetting to avoid the copper redox reaction at open circuit voltage (~ 3 V), and CE of the AFLB cell was monitored at different cut-off voltage. Test results on Cu/NMC-622 AFLBs show optimal balance of energy density, and cycling stability lies in the range of 3.5-3.6 V.

Task 4.1 – Lithium Dendrite Prevention for Lithium Batteries (Wu Xu and Ji-Guang Zhang, Pacific Northwest National Laboratory)

Project Objective. The objective of this project is to enable lithium metal to be used as an effective anode in Li-metal batteries with good thermal stability and safety. The investigation in FY 2022 will focus on the following aspects: (1) continuing evaluation of separators with high thermal stability in Li-metal batteries, (2) developing 3D-structured, lightweight, flexible current collectors for Li-metal anode and Li-metal batteries, and (3) obtaining mechanistic insight on Li-metal deposition/stripping behavior.

Project Impact. Lithium metal is an ideal anode material for next-generation, high-energy-density, rechargeable batteries. However, the application of Li-metal anode has been hindered by concern for safety and short cycle life. The safety concern regarding Li-metal batteries mainly arises from lithium dendrite growth and electrolyte flammability; the short cycle life is largely associated with the high reactivity of lithium metal with electrolyte and the lithium loss due to formation of SEI and electrochemically inactive or “dead” lithium during cycling. Although much progress has been achieved in suppressing lithium dendrites and increasing lithium CE in LEs in recent years, the intrinsic problems of Li-metal anode still exist. This fiscal year, the PNNL team will continue to evaluate the effectiveness of separators with high thermal stability in improving the thermal stability of Li-metal batteries. Meanwhile, the team will develop 3D porous current collectors for Li-metal anode to suppress lithium dendrite growth, increasing the utilization of lithium metal and consequently extending the cycle life of Li-metal batteries. The success of this project will increase safety and cycle life of lithium batteries and accelerate market acceptance of EVs, as required by the EV Everywhere Grand Challenge.

Approach. The approach will encompass the following areas: (1) continue comparative evaluation of separators with high thermal stability in Li||NMC-622 cells during cycling and heating process, (2) develop current collectors with 3D structure for Li-metal anode to suppress lithium dendrite growth, increase lithium utilization, and extend cycle life of Li-metal batteries, and (3) conduct mechanistic studies on lithium deposition behavior to lay groundwork for future improvement of Li-metal batteries.

Out-Year Goals. The long-term goal of the proposed work is to enable Li-metal and Li-ion batteries with a specific energy of > 350 Wh/kg (in cell level), 1000 deep-discharge cycles, 15-year calendar life, and less than 20% capacity fade over a 10-year span to meet the goal of the EV Everywhere Grand Challenge.

Collaborations. This project collaborates with C. Wang of PNNL on characterization by TEM/SEM; K. Xu and M. Ding of U. S. Army Research Laboratory (ARL) on DSC measurements; A. Bates, Y. Preger and L. Torres-Castro of Sandia National Laboratory (SNL) on DSC microcell tests; and Y. Zhang and A. Simmons of ANL on electrospinning polyimide, polysulfone, and polycarbonate porous membranes.

Milestones

1. Evaluate thermal properties of polyimide and polyethylene separators in Li||NMC cells during heating. (Q1, FY 2022; Completed)
2. Evaluate cell performance and thermal properties of other separators in Li||NMC cells. (Q2, FY 2022; Completed)
3. Fabricate 3D-structured current collectors and characterize their physical properties; elucidate influencing factors on lithium deposition/stripping behavior by *in situ* characterization. (Q3, FY 2022; On schedule)
4. Evaluate effect of new separator and 3D-structured current collector on cycling performance of Li||NMC cells. (Q4, FY 2022; On schedule)

Progress Report

Last quarter, the team discovered that the pore structure and morphology of a separator regulate the Li-ion flux and hence the lithium deposition behavior and the cycling life of Li-metal batteries. Li||NMC-622 cells using the combination of a 7- μm -thick polyethylene separator and an 11- μm -thick polyimide porous membrane outperform the cells using a 20- μm -thick single-layer polyethylene separator, due to the better pore structure of the 7- μm -thick polyethylene in the dual separator. This quarter, the thermal properties of cells using the single-layer polyethylene separator and the polyethylene – polyimide dual separator were evaluated by DSC. Apart from the polyethylene – polyimide dual separator, the applicability of separators based on polysulfone and polycarbonate with 7- μm -thick polyethylene in Li-metal batteries was also investigated.

Thermal Properties of Li||NMC-622 Cells Using Single-Layer Polyethylene and Polyethylene – Polyimide Dual Separator

To verify the safety enhancement of the polyethylene – polyimide dual separator, the team performed DSC measurements on Li||NMC-622 micro cells comprising a single-layer polyethylene and also polyethylene – polyimide. The DSC curves of micro cells containing the studied separators are shown in Figure 109. Both cells show two small endothermic peaks, one at $\sim 95^\circ\text{C}$ (for evaporation of 1,1,2,2-tetrafluoroethyl -2,2,3,3-tetrafluoropropyl ether, or TTE, diluent) and another at $\sim 128^\circ\text{C}$ (for the melting of polyethylene separator). Starting at $\sim 130^\circ\text{C}$, both cells exhibit exothermic behavior, probably due to the reactions of electrodes and electrolyte. Counterintuitively, there is no serious exothermic reaction in the cell using the single-layer 20- μm -thick polyethylene separator. The possible reason might be the lack of mechanical pressure between NMC-622 and lithium. Even after the polyethylene separator shrank or even melted at 128°C , the cell shorting between lithium and NMC-622 was not observed in the micro cell for DSC measurement. However, such contact is almost inevitable in real cells. Mechanical pressure will be introduced into the micro cells to simulate the environment of real Li-metal batteries as part of the next-step investigation.

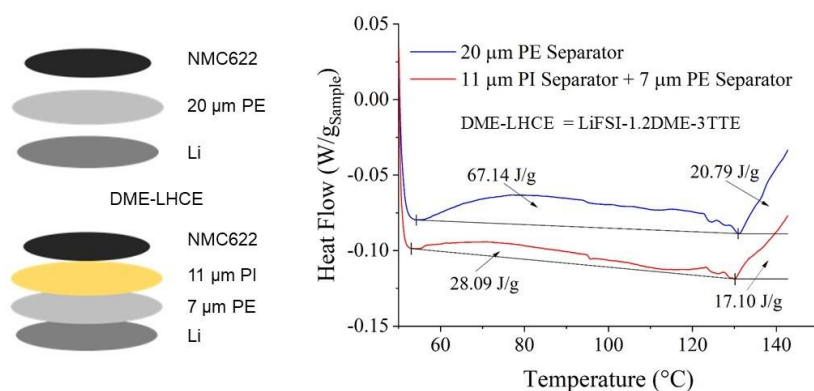


Figure 109. Differential scanning calorimetry curves of Li||NMC-622 cells using a single-layer 20- μm polyethylene separator and 7 μm polyethylene + polyimide separator. (NMC-622 was charged to 4.4 V.)

Applicability of Polysulfone and Polycarbonate in Dual Separators for Li-Metal Batteries

The thermal stability and cycling performance of dual separators based on polycarbonate and polysulfone were evaluated. A 20- μm -thick polyethylene separator was selected as the reference. As shown in Figure 110a, polyethylene separator suffers from significant shrinkage due to its low melting point. The thermal instability of polyethylene separator poses a safety hazard to Li-metal batteries since the shrinkage during thermal runaway readily leads to internal shorting, which inevitably leads to aggravated heat generation. In comparison, both polycarbonate and polysulfone exhibit superior thermal stability (Figure 110b-c). The preliminary cycling performance of Li||NMC-622 cells with polyethylene and polysulfone or polycarbonate dual separator was evaluated and is shown in Figure 110d. Polyethylene – polysulfone dual separator achieved comparable cycling performance to 20- μm -thick single-layer polyethylene. In contrast, cells using polyethylene – polycarbonate suffered from significant capacity loss, which is mainly due to poor anodic stability of polycarbonate at ~ 3.7 V versus Li/Li⁺.

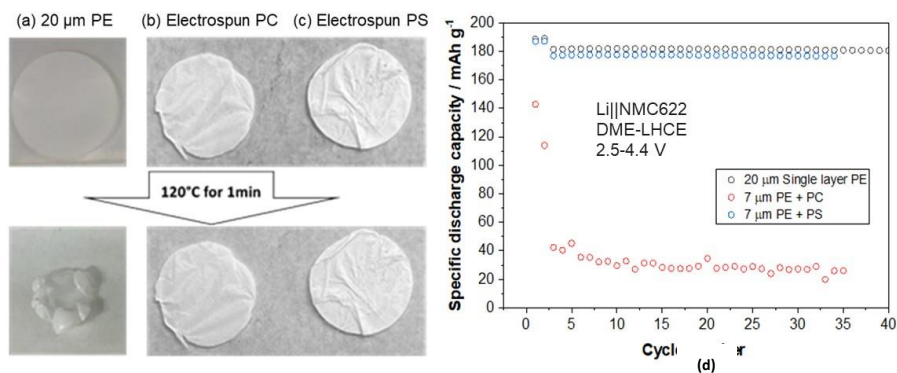


Figure 110. Thermal stabilities of (a) 20- μm single-layer polyethylene, (b) electrospun polycarbonate, and (c) electrospun polysulfone separators. (d) Cycling performance of Li||NMC-622 cells using 20- μm single-layer polyethylene, 7- μm polyethylene + polycarbonate, and 7- μm polyethylene + polysulfone dual separators.

Patents/Publications/Presentations

Publication

- Jia, H., and W. Xu.* “Electrolytes for High-Voltage Lithium Batteries.” *Trends in Chemistry* (May 13, 2022). doi: 10.1016/j.trechm.2022.04.010.

Task 4.2 – Prelithiation for High-Energy Lithium-Ion Batteries (Yi Cui, Stanford University)

Project Objective. Prelithiation of high-capacity electrode materials is an important means to enable those materials in high-energy batteries. This study pursues three main directions: (1) development of facile and practical methods to increase 1st-cycle CE of anodes, (2) synthesis of fully lithiated anode to pair with high-capacity, Li-free cathode materials, and (3) prelithiation from the cathode side.

Project Impact. Prelithiation of high-capacity electrode materials will enable those materials in the next generation of high-energy-density Li-ion batteries. This project's success will make high-energy-density Li-ion batteries for EVs.

Approach. Silicon electrode film will be prepared by coating the slurry of silicon nanoparticles (NPs), carbon black, and binder mixture on copper foil through a doctor-blading method. The silicon electrode film will be prelithiated by pressing a Li-metal foil on top of it and heating it in an argon glovebox for a certain time. Then, Li_xSi electrode film can be obtained by removing the redundant lithium foil through a peeling-off approach. The redundant lithium foil is reusable for the next prelithiation. The structure, morphology, and other properties can be analyzed by SEM, TEM, XPS, Raman spectroscopy, XRD, etc. In the first year, the team aims to fabricate Li_xSi freestanding electrode film and improve its air stability. In the second year, the team aims to improve the electrochemical stability in full cells.

Out-Year Goals. Materials containing a large quantity of lithium will be synthesized for pre-storing lithium ions inside batteries. Materials and processes will be developed to be compatible with battery electrode and cell fabrication. First-cycle CE of anodes will be improved and optimized by prelithiation materials. Materials for prelithiation from the cathode side will be developed.

Collaborations. This project engages in collaboration with the following: BMR PIs; SLAC: M. Toney (*in situ* X-ray); and Stanford University: W. Nix (mechanics).

Milestones

1. Demonstrate a new solvent-free dry prelithiation strategy through *in situ* prelithiation. (Q1, FY 2022; Completed)
2. Demonstrate that the *in situ* prelithiation strategy can delicately control the prelithiation amount. (Q2, FY 2022; Completed)
3. Demonstrate that the *in situ* prelithiation strategy can achieve uniform prelithiation. (Q3, FY 2022; In progress)
4. Investigate the prelithiation kinetics in the *in situ* prelithiation strategy. (Q4, FY 2022; On schedule)

Progress Report

Substantial improvements on energy density of Li-ion batteries require the development of high-capacity electrodes. Silicon anodes that have high theoretical capacities (3579 mAh/g)—ten times higher than the conventional graphite anodes (372 mAh/g)—hold great potential for application in high-energy Li-ion batteries. However, silicon anodes exhibit a low initial CE of 50-80%, which means 20-50% of battery capacity will be lost after 1st cycle due to side reactions. Therefore, a strategy to compensate the initial active lithium loss and improve initial CE is urgently needed to prevent battery capacity degradation.

In previous reports, the team has presented a new solvent-free *in situ* prelithiation method. Prelithiation reagents are added to the battery in the battery assembly step, and prelithiation *in situ* takes place in the cell resting period based on shorting mechanism. This *in situ* prelithiation process addresses the challenges of cell reassembly and solvent compatibility in traditional prelithiation methods. In this report, they present further development of *in situ* prelithiation by designing lithium meshes as prelithiation reagents. Through designing lithium meshes with different porosity levels, they achieve controllable prelithiation capacity and initial CE improvement of silicon anodes to around 100%.

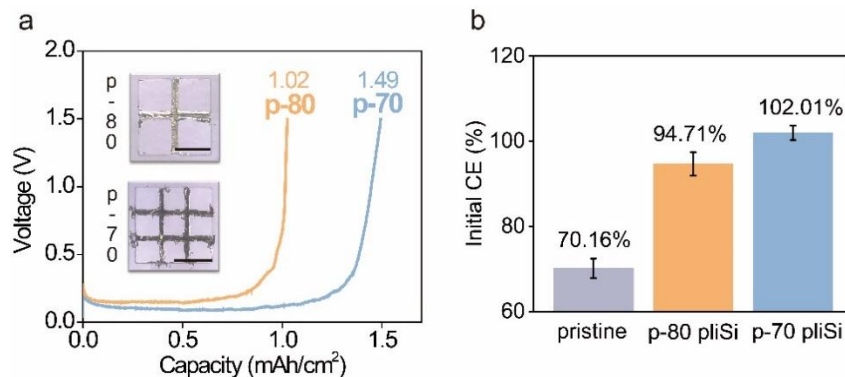


Figure 111. (a) Digital photos of the designed prelithiation reagents with porosity of 80% and 70%, respectively, and their corresponding capacity. (b) The initial Coulombic efficiency of silicon anode with and without prelithiation.

In situ prelithiation is a promising dry one-step prelithiation strategy without the concern of cell reassembly and solvent compatibility. This prelithiation approach takes one step to insert prelithiation reagents above silicon anode in fabrication and allows prelithiation *in situ* to take place during the battery resting period based on shorting mechanism. Due to no extraction of lithium out of the cell after prelithiation, the inserted lithium amount must be carefully controlled to match the desired prelithiation amount. However, presently commercialized lithium foils have thickness over 25 μm , providing capacities higher than 5 mAh cm⁻². This capacity is much higher than the initial capacity loss in common battery systems. To avoid excessive lithium, the team designs porous lithium meshes as prelithiation reagents for *in situ* prelithiation. As shown in Figure 111a, lithium mesh with porosity of 80% (p-80) and 70% (p-70) is designed and produced. 25- μm lithium foils are used to fabricate lithium mesh. The p-80 and p-70 meshes have capacity of ~ 1 mAh cm⁻² and 1.5 mAh cm⁻², respectively. The team uses these two lithium meshes to prelithiate silicon anodes through an *in situ* prelithiation method. Silicon anodes with capacity of ~ 5 mAh cm⁻² are used here. Figure 111b shows that silicon anodes without prelithiation have low initial CE of $\sim 70.16\%$, indicating the initial capacity loss is ~ 1.5 mAh cm⁻². Through prelithiation with p-80 lithium mesh (~ 1 mAh cm⁻²), initial capacity loss is partially compensated, and initial CE is improved to $\sim 94.71\%$. Meanwhile, prelithiation with p-70 lithium mesh (1.5 mAh cm⁻²) fully compensates initial capacity loss and improves initial CE to a nearly ideal 100%. These results suggest that through tuning the porosity of lithium mesh, the team is able to achieve controllable prelithiation capacity. By further matching lithium mesh capacity with the desired prelithiation capacity of anode materials, they fully compensate initial capacity loss and achieve a nearly ideal 100% initial CE.

Patents/Publications/Presentations

The project has no patents, publications, or presentations to report this quarter.

Task 4.3 – Anode-Free Lithium Batteries (Jiguang Zhang and Xia Cao, Pacific Northwest National Laboratory)

Project Objective. The main objective of this project is to explore the feasibility of anode-free lithium batteries (AFLBs) for high-energy-density energy storage systems. An AFLB is an extreme case of Li-metal battery and Li-ion battery, where all active lithium is stored in cathode in the as-assembled batteries. Because of the many similarities among AFLBs, Li-metal batteries, and Li-ion batteries, extensive experiences and approaches developed for Li-metal and Li-ion batteries can be applied to AFLBs. Likewise, new approaches and knowledge to extend the cycle life and calendar life of AFLBs can also be used for development of Li-metal and Li-ion batteries, thus accelerating the market penetration of Li-based rechargeable batteries.

Project Impact. The ever-increasing need for EVs continually pushes the boundary of high-density energy storage systems. To date, the state-of-the-art Li-ion batteries consisting of graphite anode and high-voltage lithium intercalation cathodes cannot satisfy the energy demand from these applications. By replacing graphite anode with Li-metal anode, the specific energy density of Li-metal batteries can increase by more than 50% because Li-metal anode has a much higher specific capacity (3820 mAh g^{-1}) than that of graphite (372 mAh g^{-1}). To further increase the energy density of lithium batteries, the concept of AFLBs has been explored. An as-assembled or fully discharged AFLB consists of a cathode and an anode current collector (such as copper). All lithium source is stored in cathode. This cell design not only increases energy density of the battery, but also improves battery safety because no lithium metal is present in the battery in its as-assembled or discharged state. However, the cycle life of AFLBs is still very limited due to loss of active lithium during the cycling process. Therefore, there is an urgent need to understand the correlation between lithium CE, cathode CE, and electrolyte (including its electrochemical properties and consumption), as well as lithium dendrite growth and the formation of “dead” lithium, so that AFLBs and Li-metal batteries can be designed to achieve desired energy density and cycle life. In the end, the combination of these two efforts will accelerate the understanding and application of high-energy-density rechargeable batteries for EV applications.

Approach. This task will investigate the main factors affecting the performance of AFLBs and identify the solutions to enable long-term cycling and safety of these batteries. The lithium loss due to SEI formation and “dead” lithium generation by dendrite growth in the lithium deposition and stripping processes will be analyzed. The lithium dendrite suppressing principles and strategies for both liquid and solid-state AFLBs, ranging from materials design (electrolytes, cathodes, and current collectors), cell fabrication, operation controls (pressure, temperature, and cycling protocol) will also be investigated.

Out-Year Goals. The long-term goal of the proposed work is to enable lithium batteries with a specific energy of $> 350 \text{ Wh/kg}$ (in cell level), 1000 deep-discharge cycles, 15-year calendar life, and less than 20% capacity fade over a 10-year span to meet the goal of the EV Everywhere Grand Challenge.

Collaborations. This project collaborates with the following: C. S. Wang of UMD on approaches to improve the CE of lithium cycling; C. M. Wang of PNNL on characterization by TEM/SEM; and Battery500 PIs on understanding and approaches to improve the calendar life of lithium batteries.

Milestones

1. Optimize cycling parameters of AFLBs to improve cycle life using LHCE electrolyte with high CE and safety. (Q1, FY 2022; Completed)
2. Develop approaches to treat copper substrate to minimize lithium loss during cycling. (Q2, FY 2022; Completed)
3. Improve CE efficiency of electrolyte by forming a lithiophobic SEI layer. (Q3, FY 2022; In progress)
4. Extend the cycle life of AFLBs to be more than 100 cycles. (Q4, FY 2022; In progress)

Progress Report

AFLB shares many similarities with Li-metal batteries, as the AFLB is actually an extreme case of a Li-metal battery where there is no lithium stored on the anode current collector in the as-assembled cells. However, beyond the issues associated with Li-metal anode in Li-metal batteries, AFLB has additional challenges related to the absence of lithium on copper anode of as-assembled cells. These problems include the following: copper redox reaction at the OCV of the cell, especially at their as-assembled condition; repeated lithium nucleation on copper anode at the beginning of each cycle; and the increased lithium galvanic corrosion caused by the Li||Cu galvanic cells at the early state of lithium plating. All these undesired reactions occur at a certain voltage range that results in the loss of active lithium and an increase of cell resistance, which in turn leads to fast capacity decay of the AFLB. Therefore, the testing protocol has a significant influence on AFLB performance.

In this work, all as-assembled cells used a LHCE, that is, LiFSI-DME-TTE (1:1.2:3 in molar ratio). They were rested at 1.5 V for wetting to avoid the copper redox reaction at OCV (~3 V), and the team applied different DOD to avoid the repeated lithiation nucleation and minimize lithium galvanic corrosion.

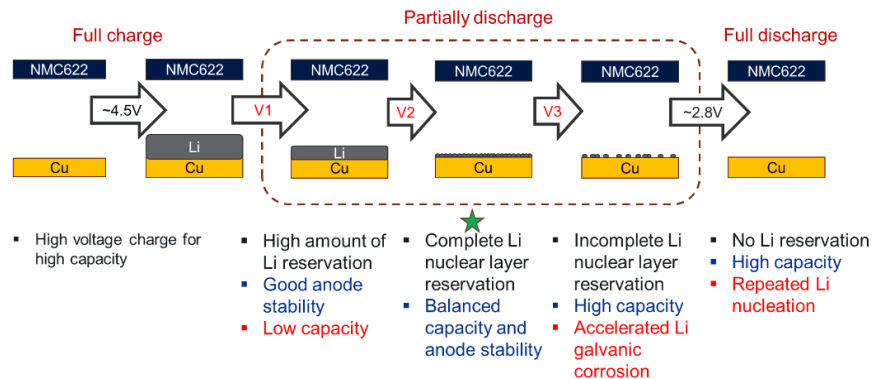


Figure 112. Schematic of lithium reserve on copper (lithium from cathode) by voltage optimization.

The schematic in Figure 112 shows lithium reserve on copper at different DOD. A complete lithium nucleation layer was covered on the copper substrate after the initial cycle. At this condition, the Cu||NMC-622 cell has the best balance between the energy and cycling stability. Figure 113 shows the electrochemical performance of Cu||NMC-622 cells. With the increase of cut-off voltage (lower DOD), cells deliver decreased capacity while their cycling stabilities increase. The cell-performance details are summarized in Table 9. Voltage of 3.5 and 3.6 can be considered as optimized, with balanced energy and energy retention. The team is investigating the effects of other factors on AFLB performance.

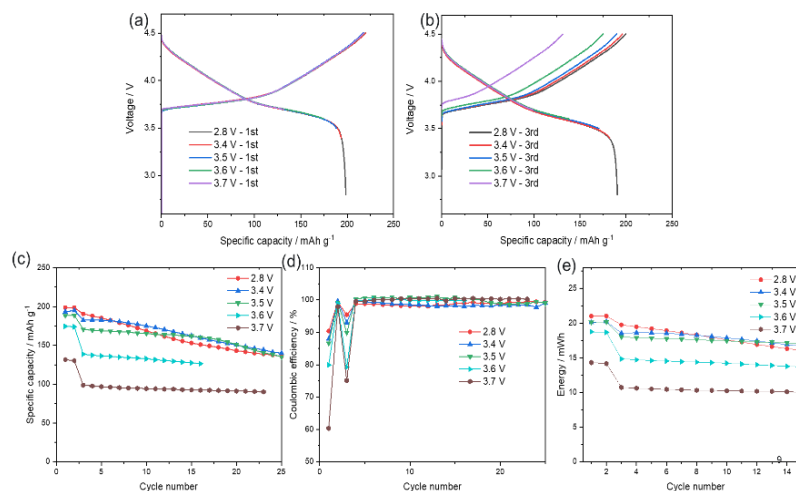


Figure 113. Cu||NMC-622 cell performance at different cutoff-discharge voltages.

Table 9. Summarized performance of Cu||NMC-622 cell at different cutoff-discharge voltages.

Cut-off voltage / V	Formation cycle		Cycling			
	Initial cap. / mAh g ⁻¹	Initial CE / %	Initial cap. / mAh g ⁻¹	Initial CE / %	Cap. Retention / % (25 cycles)	Average CE / %
2.8	198.6	90.42	190.6	95.46	71.30	98.82
3.4	193.4	87.98	182.3	93.01	76.85	98.59
3.5	188.3	86.66	170.6	89.95	79.25	100.07
3.6	174.5	79.9	138.6	79.22	91.20 (16 cyc.)	99.94
3.7	131.6	60.35	98.6	75.14	91.34 (23 cyc.)	100.22

Patents/Publications/Presentations

The project has no patents, publications, or presentations to report this quarter.

TASK 5 – LITHIUM-SULFUR BATTERIES

Team Lead: Prashant N. Kumta, University of Pittsburgh

Summary

The collected work of the projects in this Task encompasses the following areas:

- Conducting focused fundamental research on the mechanism of “shuttle effect” inhibition for rechargeable Li-S batteries.
- Developing electrode and electrolyte systems that can mitigate the “shuttle effect” so the low self-discharge and long cycle life can be achieved.
- Synthesizing sulfur composite materials with an emphasis on polymer sulfur composite materials.
- Developing creative electrode-making processes to improve processability and aerial capacity; for example, polymeric sulfur composites may not be suitable for the traditional slurry casting process.
- Developing a novel S_xSe_y cathode material for rechargeable lithium batteries with high energy density and long life, as well as low cost and high safety.
- Delivering an electrochemically responsive self-formed hybrid Li-ion conductor as a protective layer for Li-metal anodes, enabling them to cycle with high efficiency.
- Developing high-energy, low-cost Li-S batteries with long lifespan.

Highlights

The highlights for this quarter are as follows:

- K. Amine’s group at Argonne National Laboratory continued their work on microporous carbon with double-end binding sites as sulfur host (3d-omsh/ZnS, Co-N-C/S cathode) by fabricating pouch cells of high sulfur loading under lean electrolyte conditions of 4 $\mu\text{L}/\text{mg}$. They fabricated a 4-layer Li-S pouch cell with areal sulfur loading of $\sim 6.25 \text{ mg}/\text{cm}^2$ (6 mm \times 8 mm) and total sulfur amount of 1.2 g. The electrolyte used in the test was conventional 1,3-dioxolane / 1,2-dimethoxyethane (DOL/DME)-based electrolyte. The assembled cell could deliver a high specific capacity of $> 1200 \text{ mAh}/\text{g}$ at 41.67 mA/g, yielding a practical energy density of 317 Wh/kg. When the current density was increased 4-fold, the specific capacity decreased to $\sim 950 \text{ mAh}/\text{g}$ with increased voltage polarization. The system nevertheless exhibited a Coulombic efficiency (CE) of $> 95\%$ and stable cycling to 80 cycles with $\sim 74\%$ capacity retention, suggesting need for further improvement. The results reported thus far represent a significant advancement and demonstrate the potential of the electrode configuration and cathode system for enabling high-energy-density Li-S batteries.
- D. Lu and J. Liu’s group at Pacific Northwest National Laboratory have demonstrated use of low porosity, large secondary particles of S/C electrodes with elongate Li-polysulfide diffusion pathways that could help mitigate the polysulfide shuttling effect. To further reduce electrode porosity, they proposed a single-particle-layer electrode approach. With this single-particle electrode layer, a high discharge capacity of 1100 mAh/g was obtained with high sulfur loadings of $> 4 \text{ mg}/\text{cm}^2$, a sulfur content $> 70\%$, and porosity $< 35\%$ at lean electrolyte conditions of electrolyte-to-sulfur (E/S) ratio of 4 $\mu\text{L}/\text{mg}$. By controlling wet coating thickness and appropriate electrode calendaring, the large S/C secondary particles of 50 μm were distributed uniformly to form a single-particle layer with low-tortuosity in both vertical and planar directions, enabling uniform electrolyte transport while also benefiting homogeneous reaction with electrode containing 90% sulfur content. As a result, uniform SEI is formed on the Li-anode side, extending

cycle life. However, when they switched to a multi-layer stacking of small particles $< 20 \mu\text{M}$, the cell exhibited poor capacity due to exacerbation of wetting caused by high tortuosity and inhomogeneous plating and stripping of lithium. The particle size effects nevertheless demonstrate the potential of achieving high energy density in Li-S batteries.

- Dr. Y. Cui's group at Stanford University report on their continuing work on all-solid-state lithium-sulfur batteries (ASSLSBs), exploring the reaction mechanisms of redox mediators of 1,5-bis(2-(2-methoxyethoxy)ethoxy)ethoxy anthra-9,10-quinone (AQT) to oxidize Li_2S . They performed *operando* X-ray absorption spectroscopy (XAS) measurements for lithium sulfide (Li_2S) electrodes in polymer-based ASSLSBs. The XAS studies validated that during charge, the Li_2S is gradually converted to elemental sulfur, while no extra pre-edge feature corresponding to the terminal sulfur of lithium polysulfides is observed; this indicates absence of detectable lithium polysulfides. At the end of the first charge, all peaks corresponding to Li_2S are lost, with only sulfur phase existing. Hence, the team proposed that Li_2S is gradually consumed and directly converted to sulfur through a solid-solid reaction in the first charging process, showing the sluggish Li_2S oxidation in ASSLSBs. The *operando* XAS studies showed that with the incorporation of AQT, Li_2S is converted to lithium polysulfides not observed for bare Li_2S . They also observed that the average chain length of lithium polysulfides at different charge stages changed from ~ 4 to 8, with progression of the electrochemical reaction ultimately showing the formation of only elemental sulfur, which suggests a different reaction mechanism for the Li_2S cathodes containing AQT compared to pure Li_2S . The results show the promising use of reaction mediators for realization of ASSLSBs.
- Dr. E. Hu's group at Brookhaven National Laboratory, in partnership with Dr. D. Qu at the University of Wisconsin, Milwaukee, continued their studies using the organic dipentamethylenethiuram hexasulfide (PMTH) as organo-sulfur cathode in an ASSLSB. They demonstrated that the PMTH cathode attained a capacity of $\sim 600 \text{ mAh/g}$ with excellent cyclability, retaining 80.8% capacity after 500 cycles, which is a significant advancement in the organic cathode area. They also showed with an active mass loading of 17 mg/cm^2 , the PMTH cathode displays an areal capacity of 10.4 mAh/cm^2 . The cell with this high mass loading also retained 96.2% of capacity after 50 cycles with a CE of nearly 100%. The electrode level energy density was 376.2 Wh/kg , which is also the highest among sulfide-based all-solid-state sulfur batteries. They plan to reduce the solid-state electrolyte (SSE) fraction within the composite cathode by adopting more Li-ion conducting sulfide-based SSEs. The demonstration of the use of PMTH organic cathode in ASSLSBs is a very promising achievement, providing credence to the realization of a practical ASSLSB.
- G. Liu's group at the University of California, Berkeley, focused their work on exploring methods to optimize the sulfur electrode and increase the sulfur loading while also preventing polysulfide dissolution reactions. They have used a nickel foam to formulate a high-loading sulfur electrode utilizing multiwalled carbon nanotubes along with polyvinylidene (di)fluoride (PVDF) binder to formulate the sulfur composite electrode on the nickel foam to deliver up to 6 mAh/cm^2 areal capacity with sulfur utilization to give a specific capacity of 1000 mAh/g . They also plan to use a polyamic acid salt of lithium as a polysulfide retaining agent. The polyamic acid is coated on a thin glass separator to be only on the surface of the fiber, but not to block the transport through the pores, allowing only lithium salt to pass while blocking the large polysulfides. They plan to demonstrate the efficacy of the above process and the influence of polysulfide dissolution and transport to the anode side. The proposed work could potentially have a strong implication on the realization of high-energy-density Li-S batteries.
- Y. S. Meng's group at University of California, San Diego, continued work on developing high-energy-density ($> 500 \text{ Wh/kg}$) and low-cost ($< 65\$/\text{kWh}$) Li-S pouch cells using the hexaazatrinaphthylene polymer – sulfur composite (HATN-S) electrode. They have shown the ability to scale up synthesis of the HATN polymer, and they have also benchmarked performance of high-loading HATN-S electrodes with the baseline electrolyte. Finally, they have shown preliminary results of developing a new electrolyte system for Li-S batteries without LiNO_3 to address capacity fade under lean electrolyte conditions. They have shown the ability to scale up from 1-g to 10-g batches. They have shown that the new scale-up version can exhibit areal capacity of $\sim 10 \text{ mAh/cm}^2$ of HATN-S cathode.

Furthermore, they have shown that the use of LiNO_3 in the electrolyte causes lithium losses under lean electrolyte conditions due to consumption of limited LiNO_3 . The new electrolyte contains a new additive to replace LiNO_3 . The C/S electrode displays a capacity of ~ 1000 mAh/g at 0.05C rate with an E/S ratio of $10 \mu\text{L}/\text{mg}$, sustaining stable cycling with a capacity retention of $\sim 68\%$ after 170 cycles. These results demonstrate the potential of the new HATN-S system combined with the new electrolyte strategy for realizing high-energy-density Li-S batteries.

- P. N. Kumta's group at the University of Pittsburgh focused their work on fabrication of new sulfur confinement cathodes as well as exploring new anode architectures. In the former case, they modified the catholyte architectures using functional additives to finetune the dissolution of polysulfides. At the same time, they explored redox active porous inorganic-organic framework materials as sulfur confinement systems. Both systems exhibit initial capacities of ~ 875 mAh/g for a sulfur loading of $3.8 \text{ mg}/\text{cm}^2$ in the former and as high as ~ 800 mAh/g for a sulfur loading of $2.6 \text{ mg}/\text{cm}^2$ in the latter, giving areal capacities of $\sim 3.3 \text{ mAh}/\text{cm}^2$ and $2.1 \text{ mAh}/\text{cm}^2$ with stable cycling response for > 25 cycles. They plan to improve the specific capacity by incorporating Li-ion conductors and effective electrocatalysts. In the anodes, they used density functional theory to identify multicomponent alloy (MCA) as current collectors to demonstrate formation of uniformly disordered, metastable, *bcc* solid solutions with lithium. They have shown the ability of MCA anodes to incorporate large amounts of lithium (> 50 at%) without formation of lithium dendrites; specifically, FMCA2 containing lightweight alloying elements exhibiting the metastable *bcc* phase can incorporate more than 60 at% lithium, resulting in $> 15 \text{ mAh}/\text{cm}^2$ areal specific capacity without formation of dendrites pending experimental validation which is under way. Results of these studies show the promise of engineering new confinement sulfur cathodes and new MCA dendrite-free Li-anode substrates for high-energy-density Li-S batteries.
- D. Wang's group at Pennsylvania State University focused on developing Generation 1 sulfur polymerized composite (SPZ) derived active materials (SPZ-G-1) and demonstrated its cathode performance with high discharge capacity of > 500 mAh/g based on cathode weight at an E/S ratio of $< 10 \mu\text{L}/\text{mg}$. Different types of SPZ-G-1 active materials were designed and tested in conventional ether-based electrolytes, showing capacities of ~ 632.4 mAh/g with the optimal system exhibiting capacity of 660.8 mAh/g. Based on this, they also developed heteroatoms introduced into the backbone and side chains of the SPZ materials and tested initially with carbonate electrolytes, demonstrating an initial capacity of ~ 530 mAh/g. The heteroatoms have higher electronic conductivity and exhibit better binding sites for sulfur species. However, the specific capacity is limited. With an optimal system, they have shown that the heteroatom containing SPZ system can attain a capacity of ~ 530 mAh/g as well as more desirable cycling stability. These initial studies show the promise of engineering improved sulfur cathodes for demonstrating high-energy-density Li-S batteries.

Task 5.1 – Novel Chemistry: Lithium Selenium and Selenium Sulfur Couple (Khalil Amine, Argonne National Laboratory)

Project Objective. The project objective is to develop novel S_xSe_y cathode materials and advanced LEs for rechargeable lithium batteries with high energy density and long life, as well as low cost and high safety.

Project Impact. Development of a new battery chemistry is promising to support the goal of PHEV and EV applications.

Approach. The dissolution of lithium polysulfides in nonaqueous electrolytes has been the major contribution to the low energy efficiency and short life of Li-S batteries. In addition, insulating characteristics of both end members during charge/discharge (sulfur and Li_2S) limit their rate capacity. To overcome this problem, sulfur or Li_2S is generally impregnated in a carbon-conducting matrix for better electronic conductivity. However, this makes it difficult to increase the loading density of practical electrodes. It is proposed to solve these barriers using the following approaches: (1) partially replace sulfur with selenium, (2) nano-confine the S_xSe_y in a nanoporous conductive matrix, and (3) explore advanced electrolytes with suppressed shuttle effect.

Out-Year Goals. This new cathode will be optimized with the following goals:

- A cell with nominal voltage of 2 V and energy density of 600 Wh/kg.
- A battery capable of operating for 500 cycles with low capacity fade.

Collaborations. This project engages in collaboration with the following: C. Sun and X. Zuo of APS at ANL, Y. Liu of the Center for Nanoscale Materials at ANL, and L. Cheng of the Materials Science Division at ANL.

Milestones

1. Fabrication of single-layer Li-S pouch cell with stable cycle life and *in situ* diagnostics. (Q1, FY 2022; Completed)
2. TOF-SIMS studies on the cycled lithium metal and sulfur cathode. (Q2, FY 2022; In progress)
3. Development of 1 Ah Li-S pouch cell with a cell energy density of > 300 Wh/kg and stable cycle life. (Q3, FY 2022; In progress)
4. Optimization of Li-S pouch cells: cell-level diagnostic, electrolytes, and interlayer optimization. (Q4, FY 2022; In progress)

Progress Report

This quarter, the team has been focusing on fabrication of Ah-level Li-S pouch cell with high cell energy density and stable cycle life. They have calculated the cell energy density of Li-S pouch cell as a function of areal sulfur loading and electrolytes/sulfur (E/S) ratio, see Figure 114a. The results show that to achieve the goal of 300 Wh/kg, the E/S ratio should be maintained below 4 $\mu\text{l}/\text{mg}$ and areal capacity should be at least 6 mAh/cm^2 . The team therefore proposed a multilayer, interdigitated type of battery for pouch-cell stacking (Figure 114b). As a result, they have fabricated a four-layer Li-S pouch cell using their sulfur/macroporous host with double-end binding (DEB) cathode with an areal sulfur loading of $\sim 6.25 \text{ mg}/\text{cm}^2$ ($6 \text{ mm} \times 8 \text{ mm}$) and total sulfur amount of 1.2 g. The test utilizes conventional DOL/DME-based electrolytes, and the E/S ratio is controlled at 4 $\mu\text{l}/\text{mg}$. The negative/positive capacity ratio is ~ 2.6 .

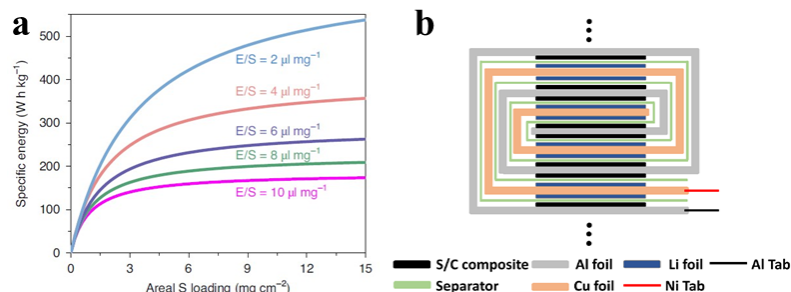


Figure 114. (a) Calculated specific energy versus areal sulfur loading for Li-S pouch cells with different E/S ratios assuming that the specific capacity and the average discharge voltage are 1,000 mAh/g and 2.05 V, respectively. (b) Configuration of interdigitated type battery winding for the pouch cell stacking.

Figure 115a shows the charge/discharge curves of a 1.2-g-sulfur pouch cell at different current densities. As shown, the as-assembled cell could deliver a high specific capacity of $> 1200 \text{ mAh}/\text{g}$ at 41.67 mA/g , indicating high sulfur utilization even under operation with a lean electrolyte and high areal sulfur loading condition. The specific energy of the pouch cell was evaluated based on equation (1):

$$Eg = \frac{vc}{\sum m_i} \quad (1)$$

where Eg is the cell specific energy (Wh/kg), V is the output voltage (V), C is the output capacity (mAh), and m_i is the weight (g) of each component of the pouch cell. The total weight taken into consideration includes the weight of the cathode (including sulfur, binder, carbon black, and carbon host), Li-metal foil (100 μm),

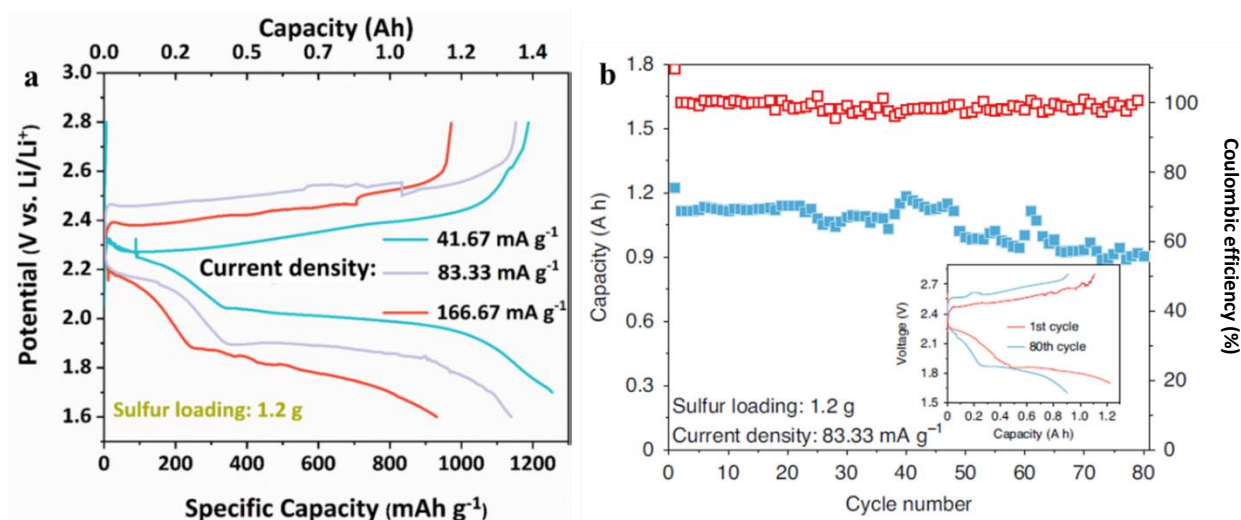


Figure 115. (a) Charge/discharge curves of 1.2 g-sulfur pouch cell using sulfur/macroporous host with double-end binding cathode under different current densities ranging from 41.67 mA/g to 166.67 mA/g . (b) Cycling performance of 1.2-g-sulfur pouch cell using sulfur/macroporous host with double-end binding cathode at 83.33 mA/g .

electrolyte ($\rho_{\text{electrolyte}} = 1.0 \text{ g/cm}^3$), separator ($\rho_{\text{separator}} = 0.95 \text{ g/cm}^3$), aluminum foil ($\rho_{\text{Al}} = 2.70 \text{ g/cm}^3$) current collector, and copper foil ($\rho_{\text{Cu}} = 8.96 \text{ g/cm}^3$) current collector. The weight percentage of each component is summarized in Figure 116. As a result, it could enable a high practical cell energy density of 317 Wh/kg.

When the current density was increased by four times, the specific capacity was decreased to $\sim 950 \text{ mAh/g}$ with increased voltage polarization. This should be due to the insufficient ion transport in the thick cathode under lean electrolyte condition, indicating further improvement is needed to boost performance at higher current densities. Figure 115b shows the corresponding cycling performance of the Li-S pouch cell at 83.33 mA/g and E/S ratio of 4 $\mu\text{l/mg}$. Surprisingly, even under the influence of side reactions between the bare lithium metal and the ether-based electrolyte, the

team's A-h-level Li-S pouch cell still delivered high CE ($> 95\%$) and stable cycling performance for 80 cycles ($\sim 74\%$ capacity retention), supporting the effectiveness of the double-end binding sites in immobilizing polysulfides and eliminating Li-metal corrosion. The team's comparison of their results with reported performance in literature demonstrates that—in terms of specific energy, cycle life, and capacity retention—their Li-S pouch cell based on the macroporous host with DEB site design clearly represents a significant advancement. It should be noted that there is still fluctuation in capacity observed after tens of cycles, which should be attributed to the inherent instability of lithium metal with the conventional ether electrolytes. With additional lithium metal protection (for example, host design or electrolyte modulation) and cell configuration optimization (for example, internal pressure), the team believes that performance could be further improved.

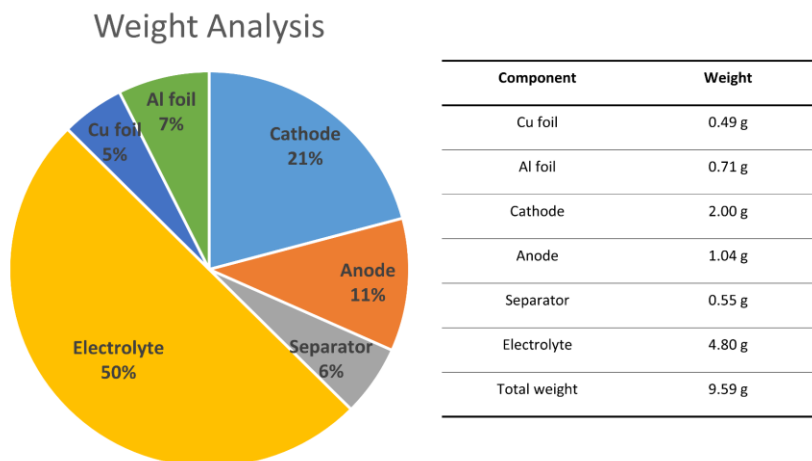


Figure 116. Weight analysis pie chart of the 1.2-g-sulfur pouch cell through interdigitated type battery winding.

Patents/Publications/Presentations

Presentation

- 39th Annual International Battery Seminar & Exhibit, Orlando, Florida (March 28–31, 2022): “Advanced Cathode and Electrolytes Design for High-Energy Li-S Pouch Cells”; G-L. Xu and K. Amine. Invited.

Task 5.2 – Development of High-Energy Lithium-Sulfur Batteries (Dongping Lu and Jun Liu, Pacific Northwest National Laboratory)

Project Objective. The project objective is to develop high-energy, low-cost Li-S batteries with long lifespan. All proposed work will employ thick sulfur cathode ($\geq 4 \text{ mg/cm}^2$ of sulfur) at a relevant scale for practical applications. The diffusion process of soluble polysulfide out of thick cathode will be revisited to investigate cell failure mechanism at different cycling. The fundamental reaction mechanism of polysulfide under the electrical field will be explored by applying advanced characterization techniques to accelerate development of Li-S battery technology.

Project Impact. The theoretical specific energy of Li-S batteries is $\sim 2300 \text{ Wh/kg}$, which is almost three times higher than that of state-of-the-art Li-ion batteries. The proposed work will design novel approaches to enable Li-S battery technology and accelerate market acceptance of long-range EVs required by the EV Everywhere Grand Challenge.

Approach. The project proposes the following approach: (1) to identify and address key issues of applying high-energy sulfur cathodes including materials, binders, electrode architectures, and functional electrode additives, (2) to advance the mechanism study of sulfur cathode and electrolyte by using *in situ* / *ex situ* techniques and custom-designed hybrid cell setup, and (3) to verify effectiveness of the new approaches with coin/pouch cells by using high-loading electrodes ($> 4 \text{ mg/cm}^2$), limited lithium ($< 200\%$ lithium excess), and lean electrolyte (E/S ratio $< 4 \text{ }\mu\text{L/mg}$).

Out-Year Goals. This project has the following out-year goals:

- Fabricate Li-S pouch cells with thick electrodes to understand sulfur chemistry/electrochemistry in environments similar to those witnessed in real application.
- Leverage the Li-metal protection project funded by the DOE and PNNL advanced characterization facilities to accelerate development of Li-S battery technology.
- Develop Li-S batteries with a specific energy of 400 Wh/kg at cell level, 1000 deep-discharge cycles, improved abuse tolerance, and less than 20% capacity fade over a 10-year period to accelerate commercialization of EVs.

Collaborations. This project engages in collaboration with the following: X-Q. Yang (BNL), M. Cai (GM), J. Bao (PNNL), P. Khalifah (BNL), and Z. Liu (Thermo Fisher Scientific).

Milestones

1. Build 3D electrode models to understand electrolyte transport and sulfur reactions in high-loading and low-porosity sulfur electrodes. (Q1, FY 2022; Completed)
2. Optimize S/C material and electrode architecture to realize sulfur utilization $> 1100 \text{ mAh/g}$ in high loading electrode ($> 4 \text{ mg S/cm}^2$) with sulfur content $> 70\%$ and porosity $< 35\%$. (Q2, FY 2022; Completed)
3. Study impacts of electrode architecture and topography on sulfur utilization rate and cell cycling. (Q3, FY 2022; In progress)
4. Process high-loading ($> 4 \text{ mg/cm}^2$) and dense ($< 35\%$ porosity) sulfur electrodes at a relevant scale for pouch-cell fabrication. (Q4, FY 2022; On schedule)

Progress Report

Last quarter, the team performed 3D electrode simulation and experimentally demonstrated that using larger particles helps to improve electrode wetting and enhance electrolyte distribution in low-porosity S/C electrodes. Moreover, the large secondary particles with elongated Li-polysulfide diffusion pathways can help mitigate the polysulfide shuttling effect. To further reduce electrode porosity, they proposed a single-particle-layer electrode approach, which was validated this quarter through materials optimization and electrode characterization. With the single-particle-layer electrodes, a high discharge capacity of 1100 mAh/g can be obtained in high loading electrodes ($> 4 \text{ mg S/cm}^2$) with sulfur content $> 70\%$ and porosity $< 35\%$ at lean electrolyte conditions (E/S ratio = $4 \text{ } \mu\text{L/mg}$).

As illustrated in Figure 117a, to realize single-particle-layer coating, the diameter of the S/C secondary particles should be equal or slightly larger than the designed electrode thickness. By controlling the wet coating thickness followed by appropriate electrode calendaring, the large S/C secondary particles will be distributed evenly to form a single-particle-layer electrode, featuring a low-tortuosity electrode structure in both vertical and planar directions. This unique electrode structure not only enables uniform electrolyte transport among the cathode particles, but also benefits the sulfur reaction homogeneity, which promotes uniform SEI formation on the Li-anode side and hence extends the cycle life. Based on the team's calculation, to prepare the 4 mg/cm^2 electrodes with 70% sulfur content and 35% porosity, electrode thickness should be $\sim 45 \text{ } \mu\text{m}$. Accordingly, $50\text{-}\mu\text{m}$ S/C secondary particles (Figure 117b) were specifically synthesized, and the sulfur content in S/C composite was controlled as high as 90%. After adding carbon additive and binder, the electrode

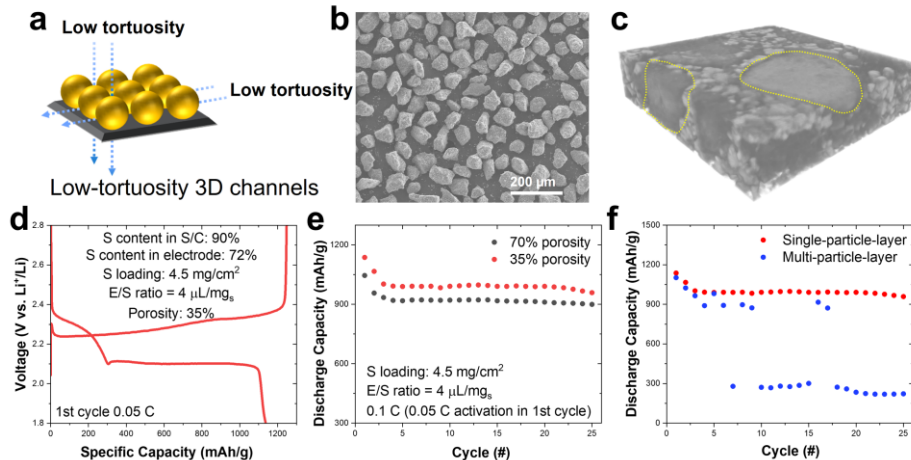


Figure 117. (a) Schematic of a single-particle-layer electrode with low tortuosity in vertical and planar direction. (b) Scanning electron microscopy image of sulfur/carbon materials around $50 \text{ } \mu\text{m}$. (c) Reconstructed micro-computed tomography image of single-particle-layer electrode. (d) Discharge and charge curves of the single-particle-layer electrode during 1st cycle. (e) Cycling performance of single-particle-layer electrode at different porosity. (f) Cycling performance of single-/multi-particle-layer electrodes.

with a S/C:carbon:binder mass ratio of 8:1:1 and 72% sulfur in the whole cathode was prepared. Electrode porosity was reduced from 70% to 35% through calendaring. The single-particle-layer electrode structure was characterized by micro-CT and reconstructed into a 3D image (Figure 117c). Individual S/C particles are highlighted with a yellow dotted line. Clearly, the large particles occupied the electrode from the bottom to the very top and formed through-pores between the particles. Such through-pores have low tortuosity and provide diffusion channels for quick electrolyte infiltration and distribution. Benefiting from sufficient electrolyte wetting, the single-particle-layer electrode can deliver a high sulfur utilization rate of 1100 mAh/g (at 0.05 C) even under harsh low porosity and lean electrolyte conditions. Compared to 70% porosity electrode, the 35% porosity electrode shows better overall performance in terms of sulfur utilization rate and capacity retention. This suggests that reduced porosity of single-particle-layer electrode does not affect sulfur reaction kinetics. However, when switched to a multi-particle-layer electrode composed of relatively smaller particles ($< 20 \text{ } \mu\text{m}$), the cell suffered from obvious capacity fluctuation and readily failed after 20 cycles. The poor performance is due to the highly tortuous electrode structure formed by multi-layer stacking of small particles. In addition, the cathode wetting issue leads to heterogeneous lithium stripping/plating on Li-anode side, exaggerating electrolyte depletion or further leading to internal short circuits.

Patents/Publications/Presentations

The project has no patents, publications, or presentations to report this quarter.

Task 5.3 – Nanostructured Design of Sulfur Cathodes for High-Energy Lithium-Sulfur Batteries (Yi Cui, Stanford University)

Project Objective. The charge capacity limitations of conventional TM oxide cathodes are overcome by designing optimized nano-architected sulfur cathodes. This study aims to enable sulfur cathodes with high capacity and long cycle life by developing sulfur cathodes from the perspective of nanostructured materials design, which will be used to combine with Li-metal anodes to generate high-energy Li-S batteries. Novel sulfur nanostructures as well as multi-functional coatings will be designed and fabricated to overcome issues related to volume expansion, polysulfide dissolution, and the insulating nature of sulfur.

Project Impact. The capacity and cycling stability of sulfur cathodes will be dramatically increased. This project's success will allow Li-S batteries to power EVs and decrease the high cost of batteries.

Approach. The approach involves three main efforts:

- Advanced nanostructured sulfur cathodes design and synthesis, including (1) engineer empty space into sulfur cathode to solve the problem of electrode volume expansion, (2) develop novel sulfur nanostructures with multi-functional coatings for confinement of S/Li polysulfides to address issues of active materials loss and low conductivity, (3) develop/discover optimal nanostructured materials that can capture the polysulfide dissolved in the electrolyte, (4) develop space-efficiently-packed nanostructured sulfur cathode to increase volumetric energy density and rate capability, and (5) identify interaction mechanism between sulfur species and different types of oxides/sulfides, and find optimal materials to improve capacity and cycling of sulfur cathode.
- Structure and property characterization, including *ex situ* SEM, XPS analysis, and *in operando* XRD and optical microscopy.
- Electrochemical testing including coin cells and pouch cells as well as a set of electrochemical techniques.

Out-Year Goals. The cycle life, capacity retention, and capacity loading of sulfur cathodes will be greatly improved (200 cycles with 80% capacity retention, > 0.3 mAh/cm² capacity loading) by optimizing material design, synthesis, and electrode assembly.

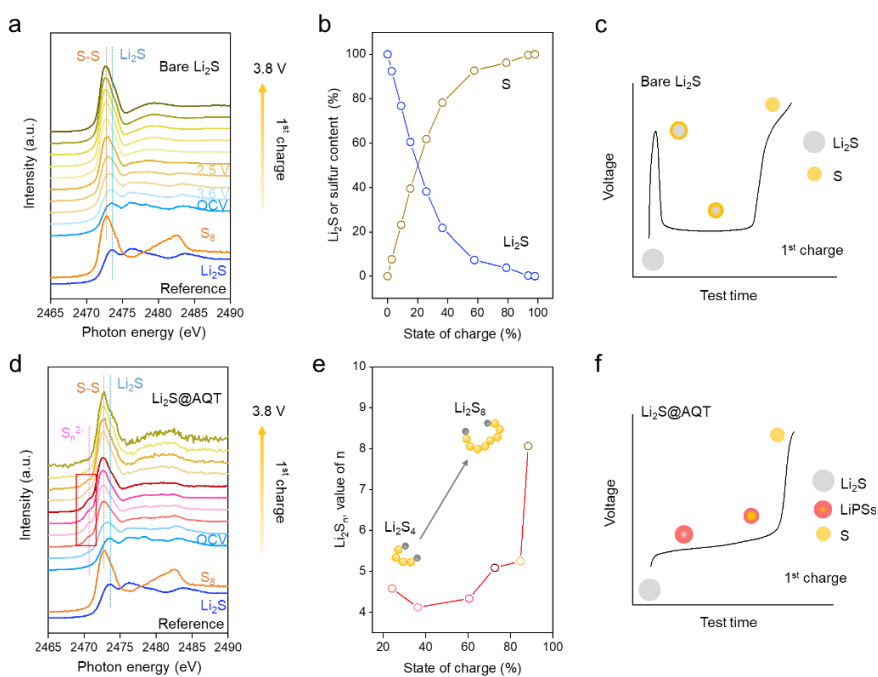
Collaborations. This project collaborates with the following: BMR PIs; SLAC: M. Toney (*in situ* X-ray); and Stanford University: W. Nix (mechanics) and Z. Bao (materials).

Milestones

1. Designing redox mediators (RMs) to facilitate Li₂S activation for ASSLSBs. (Q1, FY 2022; Completed)
2. Understanding redox chemistry in ASSLSBs using *operando* XAS measurements. (Q2, FY 2022; Completed)
3. Demonstrating cycling performance of ASSLSBs with designed RMs. (Q3, FY 2022; In progress)
4. Enabling ASSLSBs with high area capacity and high energy density. (Q4, FY 2022; In progress)

Progress Report

To understand the roles of effective RMs, the team performed the *operando* XAS measurements for lithium sulfide (Li_2S) electrodes in polymer-based ASSLSBs. Figure 118a shows the *operando* XAS results on a Li_2S -Li cell during the first galvanostatic electrochemical cycle. At OCV, the XAS spectrum for Li_2S cathodes shows a feature at 2473.5 eV, indicating pure Li_2S at the pristine state. As the charging process proceeds, an additional peak at 2472.7 eV, assigned to the sulfur 1s to 3p transition of elemental sulfur, appears and gradually becomes stronger with continued delithiation. Meanwhile, no extra pre-edge features corresponding to the terminal sulfur of lithium polysulfides at 2470.7 eV are observed, indicating no detectable lithium polysulfide formation. To further quantify the content change of Li_2S and sulfur during the first charging process, the two-phase fitting for the *operando* XAS spectra was conducted. As shown in Figure 118b, the content of Li_2S decreases monotonously as the charging proceeds, while that of sulfur is increased. At the end of the first charging process, all Li_2S disappears, and only the sulfur phase exists. Therefore, the team proposed that Li_2S is gradually consumed and directly converted to sulfur through a solid-solid reaction in the first charging process (Figure 118c), showing the sluggish Li_2S oxidation in ASSLSBs.



To understand the redox chemistry after incorporating 1,5-bis(2-(2-(2-methoxyethoxy)ethoxy)ethoxy) anthra-9,10-quinone (AQT) RM, the team conducted *operando* sulfur K-edge XAS measurements for $\text{Li}_2\text{S}@AQT$ electrodes. The feature of elemental sulfur at 2472.7 eV shows a gradual increase, indicating the transformation from Li_2S to sulfur during the charging process. Particularly, typical features of lithium polysulfides are observed from the XAS spectra in the red rectangle in Figure 118d, while they are not observed for bare Li_2S cathodes during the whole first charge process. The team further calculated the average chain length of lithium polysulfides at different charge stages based on the area ratio of main-edge peaks to pre-edge peaks. Figure 118e shows the average chain length of lithium polysulfides (n) as a function of SOC. At the beginning of charging, the value of n is ~ 4 and then significantly increases to 8 as the electrochemical reaction proceeds. At the end of the charge process, the pre-edge feature of lithium polysulfides disappears, while the main-edge feature of the elemental sulfur (2472.7 eV) becomes more prominent. These results indicate Li_2S cathodes with AQT undergo a different Li-S reaction mechanism with bare Li_2S for the activation cycle, as proposed in Figure 118c/f.

Patents/Publications/Presentations

The project has no patents, publications, or presentations to report this quarter.

Task 5.4 – Investigation of Sulfur Reaction Mechanisms (Enyuan Hu, Brookhaven National Laboratory; Deyang Qu, University of Wisconsin, Milwaukee)

Project Objective. The primary objectives are as follows:

- To optimize and down select polymeric sulfur electrode. The team will focus on the overall dissolution of polysulfide in an electrolyte and effectiveness of polymeric sulfur electrodes.
- To develop small organosulfur materials for all SE Li-S batteries.
- To continue developing alternative anode materials having low reactivity with dissolved polysulfide ions.
- To continue investigating the interaction of polysulfides in the cathode solid phase.

Project Impact. The results of this project will be used for development of technologies that will significantly increase energy density and cycle life and will reduce the cost of beyond Li-ion battery systems. This will greatly accelerate deployment of EVs and reduce carbon emission associated with fossil fuel consumption and help in the direction of building the U. S.-based energy storage manufacture chains.

Approach. The team will first down select the cross-linked polymerized sulfur compounds, in which sulfur are attached to the conductive backbone with covalent bonds; therefore, the polysulfides can be immobilized within the matrix. They will also explore the small organosulfur molecules in ASSLSBs. They will continue exploring alternative anode materials that can cycle well and do not react with dissolved polysulfide and sulfur in the electrolyte to mitigate the “shuttle effect.” In addition, they will continue to engage in fundamental *in situ* electrochemical investigations of the sulfur redox mechanisms to guide material and engineering designs. They will also continue optimizing alternative electrode fabrication processes.

One-Year Goals. The interim goal is to develop a Li-S battery with S-containing cathode of 600-800 mAh/g capacity with mitigation of the “shuttle effect.”

Collaborations. The PI works closely with beamline scientists at synchrotron facilities to develop novel Li-S characterization tools. The PI and co-PI collaborate closely with top scientists at ANL, LBNL, and PNNL, as well as U. S. industrial collaborators at GM, Duracell, Clarios, etc. The PI and co-PI also collaborate with scientists in China, Japan, and South Korea. These collaborations will be strengthened and expanded to give this project a vision on both today’s state-of-the-art technology and tomorrow’s technology in development, with feedback from the material designer and synthesizers upstream and from industrial end users downstream.

Milestones

1. Selection of small organosulfur compounds and complete design of all-solid-state testing. (Q1, FY 2022; Completed)
2. Complete initial testing of prelithiated tin anode. Complete initial testing of small organo-sulfur molecules in ASSLSB. (Q2, FY 2022; Completed)
3. Complete testing of full Li-S cell with alternative prelithiated anode. Complete synthesis of potential polymeric sulfur materials. (Q3, FY 2022; In progress)
4. Complete testing full cell with selected polymeric sulfur, small organosulfur cathodes, and alternative anode. (Q4, FY 2022; In progress)
5. Complete the investigations of sulfur redox reaction mechanism in the solid phase in cathode and the interplay between dissolved polysulfide ions in electrolyte and sulfide compounds in the solid. Complete and continue testing of polymeric sulfur cathode, small organosulfur cathode, and alternative anode in full cell format. (Annual milestone; In progress)

Progress Report

Last quarter, the team reported the application of dipentamethylenethiuram hexasulfide (PMTH) as organo-sulfur cathode in ASSLSBs. A discharge capacity of $\sim 600 \text{ mAh g}^{-1}$ was obtained under 82 mA g^{-1} at 25°C . The cell retained 80% of its capacity for 250 cycles at 0.12 mA cm^{-2} . On cycling, an electrochemically reversible cathode/electrolyte interface was revealed.

This quarter, to explore the practical applicability of PMTH cathode, a prolonged cycling test under a higher current ($\sim 0.3\text{C}$, 200 mA g^{-1}) was carried out. All cells were cycled under 60°C , aiming to improve the reaction kinetics and interfacial contact within the cell. Figure 119a displays an attainable capacity of $\sim 600 \text{ mAh g}^{-1}$ and an excellent cyclability, retaining 80.8% of capacity after 500 cycles, which is record-breaking for Li-organic ASSBs to date.

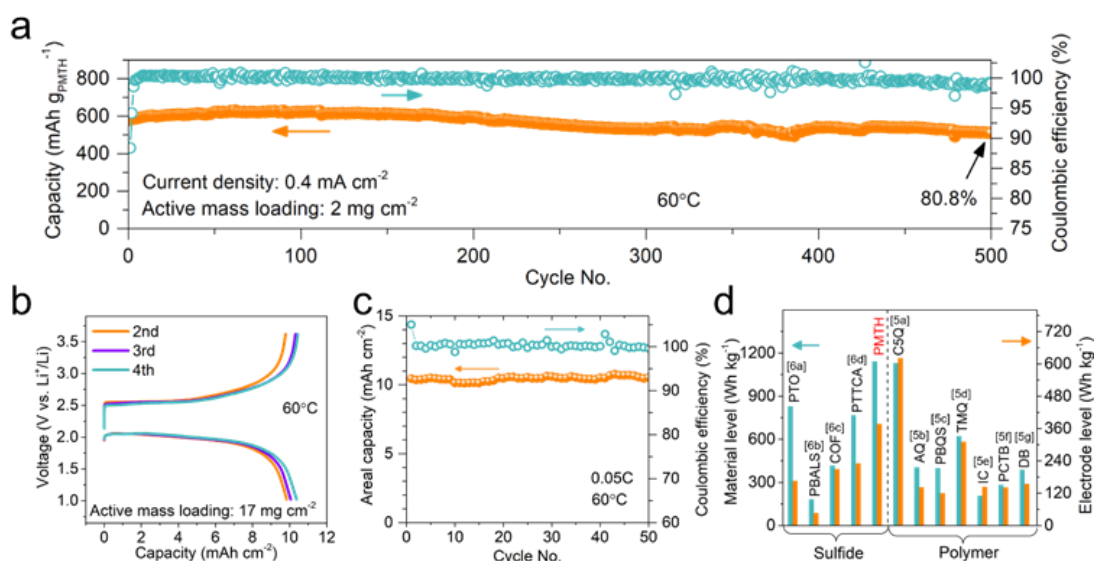


Figure 119. (a) Prolonged cycling performance at 60°C . (b) Galvanostatic voltage profiles of high active mass loading PMTH cathode and (c) its cycling performance at 0.05 C . (d) Energy density comparison of the state-of-the-art organic cathodes reported in Li-organic all-solid-state batteries.

In addition, the performance of a high mass loading PMTH cathode is investigated. With an active mass loading of 17 mg cm^{-2} , the PMTH cathode in Figure 119b displays an ultrahigh areal capacity of 10.4 mAh cm^{-2} . The voltage profiles are similar to those of the cells with a moderate active loading (2 mg cm^{-2}). The applied current is relatively small (0.05 C), which aims to promote the SOC distribution within the composite cathode and also prevent potential vibrant stress change caused by the two electrodes. The high mass loading cell in Figure 119c retained 96.2% of capacity after 50 cycles and possessed nearly 100% CE throughout cycling.

Figure 119d compares the gravimetric energy density of PMTH with previously reported organic cathodes for Li-organic ASSBs. The material-level energy density was 1140 Wh kg^{-1} , surpassing the records reported in all literature. The theoretical capacity of organosulfide could be further improved by devising the end caps and increasing the number of linear sulfur atoms. The electrode-level energy density was 376.2 Wh kg^{-1} , which was the highest among sulfide-based ASSBs, but the second highest when compared with SPE-based ASSBs. This is due to the lightweight property of SPEs compared with the sulfide electrolytes. To further enhance the electrode-level energy density of PMTH, future work can reduce the SSE fraction within the composite cathode through adopting more ionically conducting sulfide SSEs.

Patents/Publications/Presentations

Publications

- Ji, W., X. Zhang, D. Zhang, H. Huang, T. Lambert, and D. Qu.* “Practically Accessible All-Solid-State Batteries Enabled by Organosulfide Cathodes and Sulfide Electrolyte.” *Advanced Functional Materials* (2022): 2202919.
- Zheng, D., D. Qiu, T. Ding, and D. Qu.* “Examining the Chemical Stability of Battery Components with Polysulfide Species by High Performance Liquid Chromatography and X-Ray Photoelectron Spectroscopy.” *Industrial & Engineering Chemistry Research* 61 (2022): 3055–3062.

Task 5.5 – New Electrolytes for Lithium-Sulfur Battery (Gao Liu, Lawrence Berkeley National Laboratory)

Project Objective. The project objective is to develop new electrolytes, additives, and electrode compositions for Li-S battery with high ion-conductivity, stable toward polysulfide, and promoting the polysulfide affiliation with the electrode substrate to prevent polysulfide dissolution.

Project Impact. This work will address the high cost and low energy density of Li-ion rechargeable batteries. The emerging Li-S batteries could feature both high energy density and low cost. This project enables applications of the low-cost, abundant sulfur element as a major chemical component for electrical energy storage. This project will develop new approaches for electrolytes and electrode compositions of Li-S rechargeable batteries.

Approach. This project aims to develop new electrolytes and additives for Li-S battery. The properties of the ideal electrolyte for sulfur electrode would be high ion conductivity, stable toward polysulfide, and promoting the polysulfide affiliation with the electrode substrate to prevent polysulfide dissolution. The project is designed to first understand the electrode substrate interaction with the polysulfides in different electrolytes. This will lead to better understandings of the polysulfide nucleation and precipitation mechanisms in common electrolytes. The second stage of the project will focus on chemically modifying the structures of the solvent and salt electrolyte molecules to increase electrolyte stability and ionic conductivity, to prevent polysulfide dissolution, and to promote polysulfide precipitation.

Out-Year Goals. The team will also investigate the contribution of Li-metal electrodes to overall Li-S battery performance and will develop methods to stabilize Li-metal surface.

Collaborations. This project collaborates with J. Guo and C. Zhu (ALS/LBNL), A. Minor (National Center for Electron Microscopy, or NCEM, at LBNL/UCB), G. Nagy and W. Heller (Neutron National Science User Facility/ORNL), and P. B. Balbuena (Texas A&M University).

Milestones

1. Synthesize and formulate amphiphilic electrolytes using combination solvents, salts, and ILs. (Q1, FY 2022; Completed)
2. Optimize sulfur positive electrode to balance ionic and electronic conductivity, as well as dissolution and precipitation properties. (Q2, FY 2022; Completed)
3. Implement at least one strategy to stabilize Li-metal anode electrode. (Q3, FY 2022; In progress)
4. Combine the electrolyte, sulfur electrode, and lithium metal stabilization strategies to achieve stable cell cycling. (Q4, FY 2022; On schedule)

Progress Report

This quarter, the team explored methods to optimize the sulfur electrode to increase sulfur loading, and to further prevent polysulfide dissolution reactions. Two approaches are used and reported here. The first focuses on increased loading of the sulfur electrode. A nickel foam is used to formulate a high-loading sulfur electrode. To form large pores and good electric connection within the nickel foam electrode, multiwalled carbon nanotube (MWCNT) is used along with PVDF binder to formulate the sulfur composite electrode on nickel foam, resulting in a highly interconnected electrically conductive CNT-based thicker nickel foam electrode, which can deliver up to 6 mAh/cm² areal capacity with sulfur utilization ~ 1000 mAh/g (Figure 120). The second approach is to develop a barrier layer to prevent polysulfides from escaping from the cathode side (Figure 121a). The larger cathode pores created by the CNT do not contain well the polysulfides (Figure 121a). Therefore, an interlayer with a polysulfide retention agent has been developed to prevent polysulfides from crossing to the Li-anode side. Polyamic acid lithium salt is used as polysulfide retaining agent. The polyamic is coated on a thin glass fiber separator. The coating was controlled to be on the surface of fiber but not to block the transport through pores entirely, so the large polysulfides can be retained, but smaller lithium salt can freely pass through (Figure 121b-c).

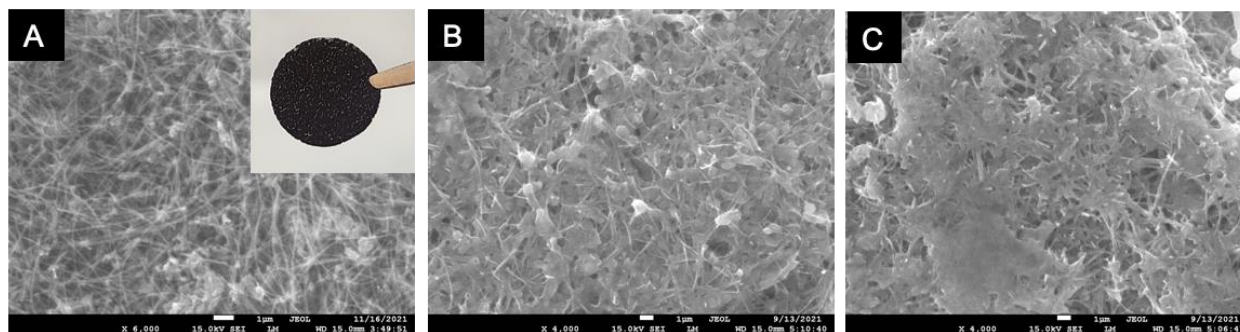


Figure 120. (a) The scanning electron microscopy surface image of nickel foam and multiwalled carbon nanotube composite electrode. The inset is optical photo of the electrode. (b) The composite electrode after first full charge. (c) The electrode after first full discharge.

The polysulfide retaining effect is clearly demonstrated in both the charged and discharged electrode. In the discharged electrode, there is extensive Li₂S precipitation, whereas in the charged electrode, the sulfur precipitate also covered the entire electrode surface (Figure 120b-c). The barrier layer is very effective in retaining polysulfides in the cathode side of the electrode. The polysulfide dissolution and transport to the anode side also has a major effect on the lithium morphology, which is the focus of next quarter's study.

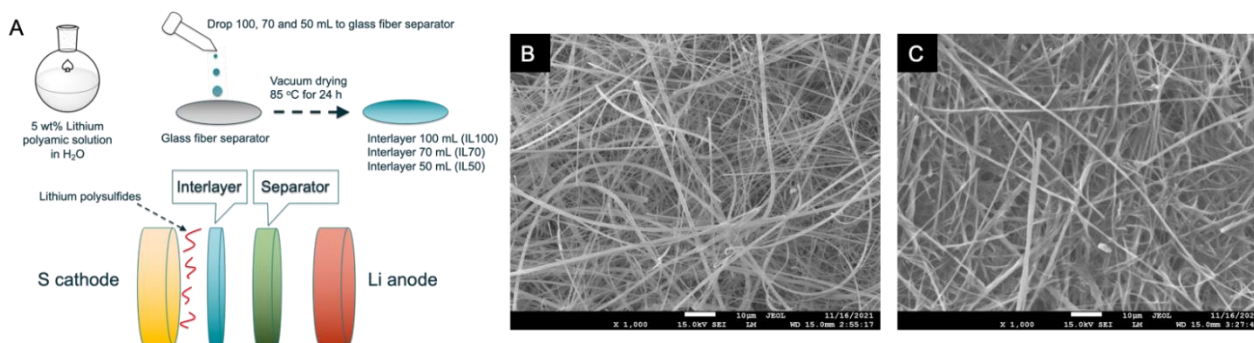


Figure 121. (a) Schematics of preparing the polysulfide retaining interlayer. (b) Scanning electron microscopy image of the surface of the glass fiber separator. (c) The polyamic-coated glass fiber separator interlayer.

Patents/Publications/Presentations

The project has no patents, publications, or presentations to report this quarter.

Task 5.6 – Strategies to Enable Lean Electrolytes for High Loading and Stable Lithium-Sulfur Batteries (Y. Shirley Meng, University of California, San Diego)

Project Objective. The project aims to develop high energy density (> 500 Wh/kg) and low cost (< 65 \$/kWh) Li-S pouch cells.

Impact. The project focuses on addressing the fundamental bottleneck in enabling high-energy-density Li-S batteries. This has been identified as the need to reduce LE excess and enable high areal loading electrodes. The challenges are overcome via the use of a dense polymer-S electrode composite, which significantly reduces electrode porosity in conventional C-S systems while improving capacity retention. These capabilities, combined with project collaborator Ampcera’s material scaling and collaborator GM’s pouch prototyping capability using thin lithium metal, will result in breakthroughs in next-generation Li-S battery chemistries that meet the energy density (> 500 Wh/kg) and cost goals ($< \$65$ /kWh) of this project.

Approach. Novel electrode architectures using hexaazatrinaphthylene polymer-S composite (HATN-S) electrode will be explored to reduce the porosity and increase the active loading of the composite electrode. Additionally, advanced electrolyte systems and optimization of Li-metal anode will be applied to further increase energy density of the Li-S pouch cell. If successful, the proposed HATN-S electrode should have less than 20% porosity with high areal capacities of > 15 mAh cm⁻², which will enable lean electrolyte conditions < 2 g/Ah in the full Li-S pouch cell.

Out-Year Goals. The out-year goals involve demonstration of baseline cell chemistries with reduced cathode porosity and increased cathode areal loading pairing with limited electrolyte and lithium inventory. The conventional electrode drying process (solvent evaporation) limits sulfur loading in the electrode. Thus, the HATN-S electrode will be prepared by optimizing the electrode architecture to increase sulfur loading and reduce electrode porosity. The electrolyte system will be optimized to reduce lithium usage (low N/P ratio) and improve cell stability.

Collaborations. Project collaborators include GM and Ampcera. This quarter, the work has been accomplished by UCSD. Ampcera and GM have started the preparations for synthesis of hexaazatrinaphthylene (HATN) monomer and polymer, thick conventional C/S cathode and the thin lithium metal (100 μ m).

Milestones

1. Achieve a benchmark performance metric of 80% capacity retention of HATN-S electrodes after 200 cycles using baseline electrolyte system. (Q1, FY 2022; Completed)
2. Process synthesis to demonstrate HATN-S electrode with reduced porosity and increased areal loading. (Q2, FY 2022; Completed)
3. Demonstrate cyclability of optimized HATN-S electrode with limited electrolyte and lithium inventory. (Q3, FY 2022; In progress)
4. Demonstrate stable cycling of optimized HATN-S electrode, which should be able to cycle with limited electrolyte (< 2 g/Ah) and low N/P ratios (< 1.2). (Q4, FY 2022; In progress)

Progress Report

Introduction

The project objective is to develop high-energy-density (> 500 Wh/kg) and low-cost (< 65 \$/kWh) Li-S pouch cells. To achieve that, novel electrode architectures using the HATN-S electrode will be explored to reduce the porosity and increase the active loading of the composite electrode. Additionally, advanced electrolyte systems and optimization of Li-metal anode will be applied to further increase energy density of the Li-S pouch cell. If successful, the proposed HATN-S electrode will achieve less than 20% porosity with high areal capacities of > 10 mAh cm⁻², which will enable lean electrolyte conditions < 2 g/Ah in the full Li-S pouch cell. This quarter, major activities include the following: scaling up synthesis of HATN polymer; benchmarking the electrochemical performance of high-loading HATN-S electrodes with the baseline electrolyte; and developing a new electrolyte system for Li-S batteries to address capacity fade under lean electrolyte conditions.

Specifically, a 10-g batch synthesis for the HATN monomer and the polymer has been established, representing an increase of more than ten-fold from the previous < 1 -g synthesis procedure. A high areal capacity of ~ 10 mAh cm⁻² of HATN-S cathode (low porosity of $\sim 29.8\%$) was achieved, and cells were tested using baseline electrolyte, and by pairing the high loading cathode with 100- μ m Li-metal foils received from the collaborators at GM. This report describes cell construction and performance results. Following the work conducted last quarter, new results reveal that lithium losses are more severe under lean electrolyte conditions due to consumption of the limited LiNO₃ reservoir in lean electrolyte conditions. As LiNO₃ is required to form a passivation layer that protects lithium from polysulfide shuttle, a stable alternative is necessary to avoid continuous depletion of its critical function. Thus, a new electrolyte system is proposed to avoid reliance on LiNO₃, using an alternative additive that is stable at the Li-metal anode. In applying this new electrolyte system to the C/S cathode, stable cell cycling with a capacity retention of $\sim 68\%$ after 170 cycles is achieved using lean electrolyte conditions, compared to the baseline LiNO₃-containing electrolyte that shows severe degradation after 75 cycles.

Process Synthesis of HATN Polymer and HATN-S Cathode for Li-S Battery (UCSD & Ampcera)

To meet the scale-up targets (50-g batch in Year 1) by Ampcera, it is vital to modify previous synthesis steps that are suited for small batches (< 1 g) to be compatible with larger batches. First, the UCSD and Ampcera team designed a new procedure to enable 10-g batch production of the HATN-polymer in the laboratory, and the designs are transferred to Ampcera's production site to scale it toward larger volumes. In Figure 122, the HATN monomer was synthesized using round bottom flasks, which can yield > 10 -g product batches when a larger flask is used. After synthesis, all the monomers were transferred to a vacuum system for HATN polymerization steps. While monomer synthesis can be scaled using larger flasks relatively easily, scaling the vacuum system design for polymerization is highly challenging at the laboratory scale with a limit of 10 g per batch (Figure 122b). To this end, Ampcera's high volume vacuum sealing setups will be used for subsequent scaling steps.

Ampcera has assembled a lab-scale synthesis similar to that in Figure 122a as part of the scale-up process to establish a baseline synthesis. Several trials have been carried out to optimize the monomer synthesis process to obtain the monomer (yellow-green) product. A preliminary batch of HATN monomer has been sent to UCSD for NMR evaluation. Using a proprietary polymerization process, Ampcera has been able to form what is believed to be the HATN monomer, which will be validated by UCSD using FTIR and BET analysis next quarter. Once the baseline is established, the monomer synthesis will be scaled to deliver 50-g batches by the end of the first year.

After polymerization, the next steps include active sulfur material incorporation to produce the HATN-S composite. This is done by sulfur melt infusion into the HATN polymer. Figure 122c shows the field emission scanning electron microscopy (FESEM) image of a single HATN-S particle after the melt infusion step, showing its highly-dense-packed nature. The EDS spectrum (Figure 122d) measured within the circled region shows strong sulfur signals within the composite, indicating a high sulfur content within. Then, HATN-S composite was mixed with carbon additives and binders in a slurry to produce a cathode electrode sheet, which contains a sulfur content of 64% (in the entire cathode). A low porosity of $\sim 30\%$ was calculated, and a high loading of $\sim 10 \text{ mg}_{\text{sulfur}} \text{ cm}^{-2}$ was achieved, meeting the target areal loading milestones of the project. To evaluate the material under realistic conditions, the electrochemical performance of high-loading HATN-S cathode electrode was paired against the 100- μm Li-metal foil obtained from the team's collaborators at GM (N/P ratio of ~ 2) and a lean electrolyte (E/S ratio of $\sim 5 \mu\text{l mg}_{\text{sulfur}}^{-1}$) in the baseline electrolyte [1 M LiTFSI in a DOL/DME mixture (1:1, v/v) with 2 wt% LiNO_3]. As shown in Figure 122e, the HATN-S cathode electrode delivers an areal capacity of close to 10 mAh cm^{-2} with a high specific capacity of $\sim 900 \text{ mAh g}^{-1}$ at a current density of 0.5 mA cm^{-2} . Subsequent sections of this report will cover the capacity retention of the high loading electrode, along with root causes of capacity fade investigated in the same conditions described above.

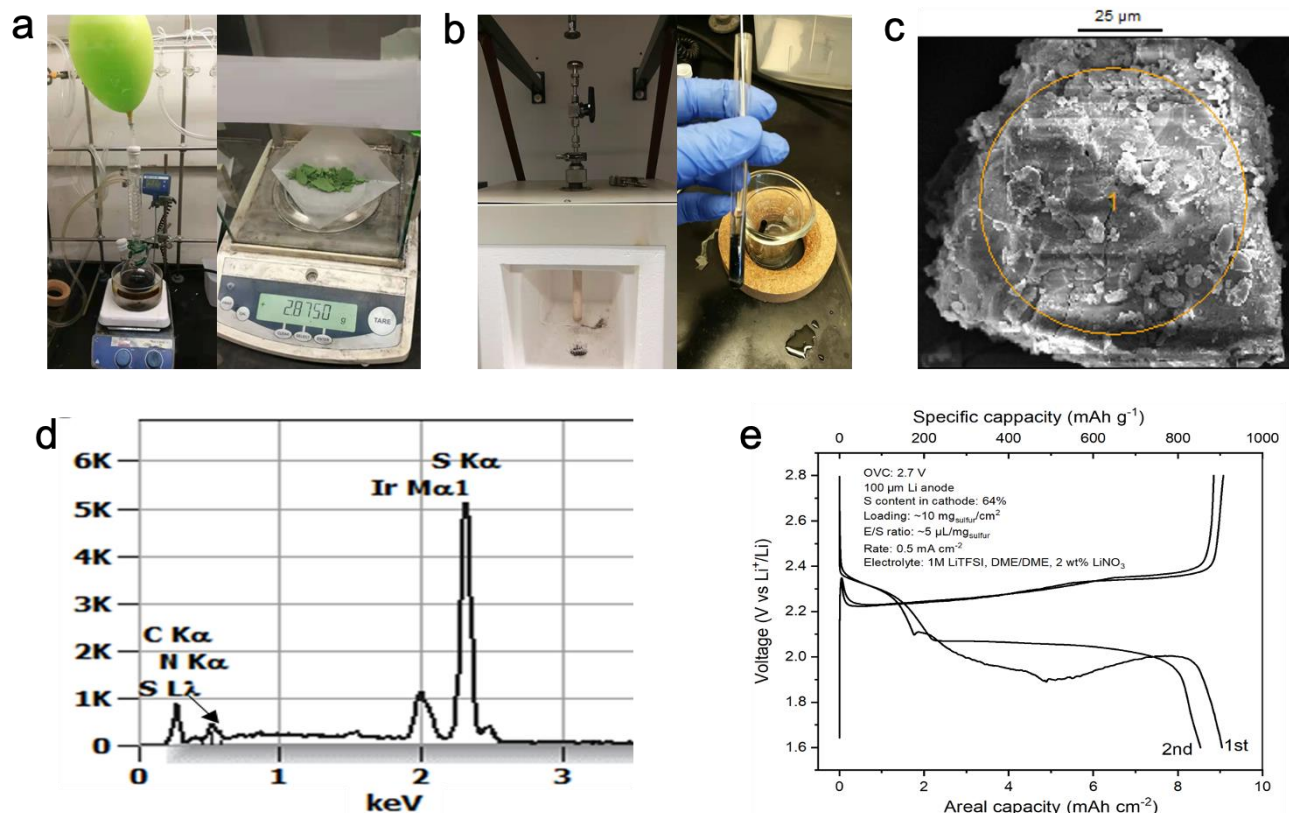


Figure 122. The laboratory synthesis setup of the (a) HATN monomer and (b) polymer. (c) The field emission scanning electron microscopy image of HATN-S composite and (d) the energy dispersive X-ray spectrum of the yellow circled area. (e) Voltage profiles of high-loading HATN-S cathode in lean lithium and electrolyte conditions, showing the high areal loadings achieved.

Benchmarking Electrochemical Performance of High-Loading HATN-S Electrodes (UCSD/GM)

To establish a reference for comparison, the HATN-S electrodes will be tested against the conventional C/S electrode composite. Figure 123a shows the charge-discharge curves of C/S composite cathode at different C-rates using a 100- μm Li-metal foil anode and E/S ratio of $\sim 10 \mu\text{l mg}_{\text{sulfur}}^{-1}$. Based on literature studies, as well as recommendations through findings at the Battery500 Consortium, a lean electrolyte condition is achieved when electrolyte excess is kept at $< 5 \mu\text{l mg}_{\text{sulfur}}^{-1}$. However, as the C/S is unable to cycle consistently

under such lean electrolyte conditions, a slightly higher E/S ratio is used for this specific case. The C/S composite cathode delivers areal capacities of 3 mAh cm⁻², 2.5 mAh cm⁻², and 2 mAh cm⁻² at 0.05 C, 0.1 C, and 0.2 C, respectively. The initial discharge plateaus are observed to be lower compared to cells operating with large excess electrolyte, as sulfur redistribution in cathode is prohibited due to slower polysulfide diffusion in lean electrolyte conditions. This phenomenon is also observed in HATN-S cathode (as reported last quarter and seen in Figure 122e for this quarter). The C/S cathode cycles at 0.2 C for less than 100 cycles (Figure 123b) before complete failure. Interestingly, severe degradation is observed at the 74th and 75th cycles, wherein the cell displayed an abnormal charge voltage profile, likely due to severe polysulfide shuttle (Figure 123b, inset). Such phenomena are not observed in Li-S cells when large excess electrolytes are used, highlighting the need to understand its root causes for practical Li-S cells to be realized.

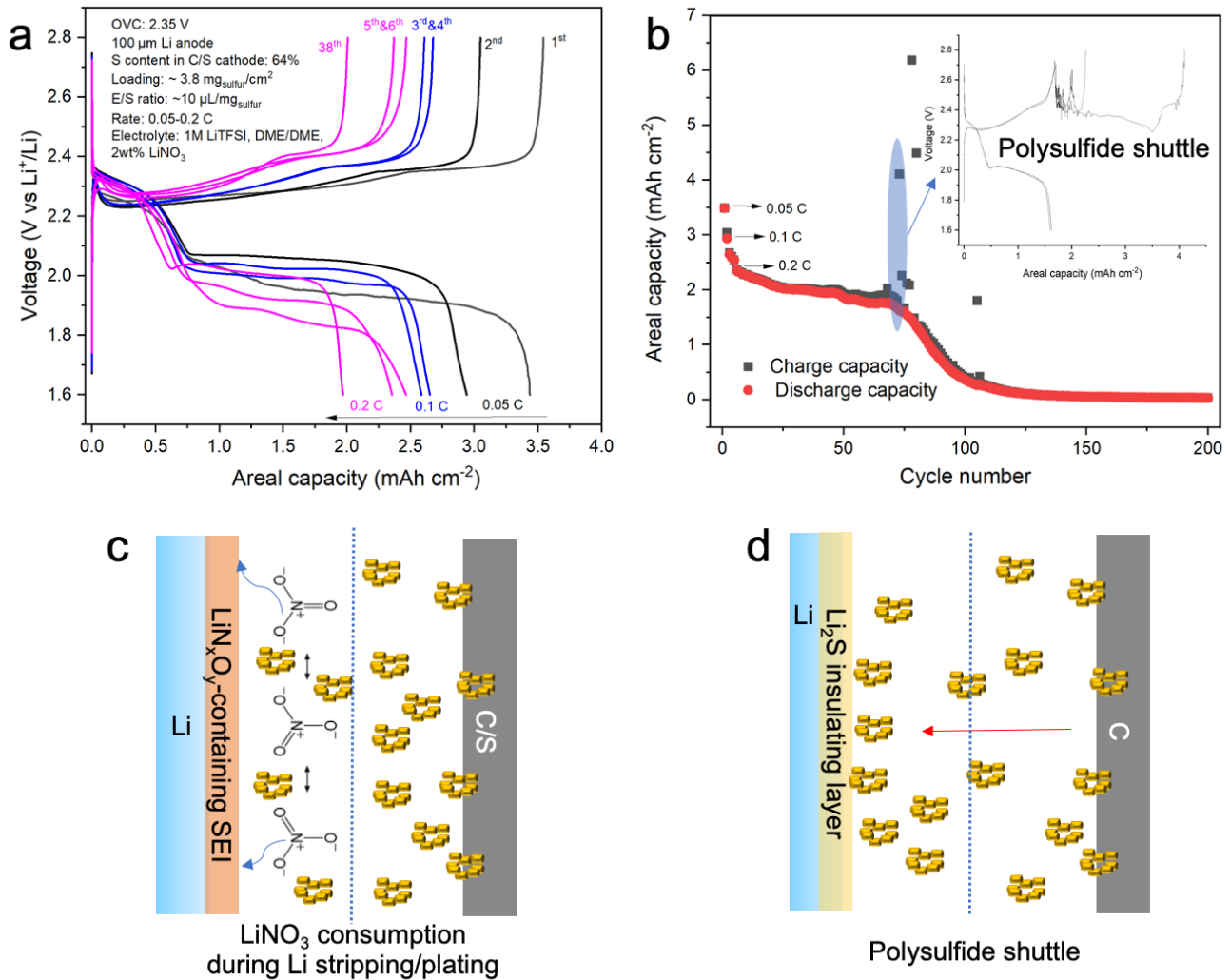


Figure 123. (a) Voltage profiles of C/S composite electrodes at different C-rates using 100 μm lithium and E/S ratio of 10 μL mg_{sulfur}⁻¹ and (b) the corresponding cycling stability. (c) Schematic of passivation layer originated from LiNO₃ consumption and (d) the formation of insulating layer due to polysulfide shuttle.

One major distinction between lean versus excessive electrolyte conditions is the amount of LiNO₃ reservoir present in the cell. LiNO₃ protects lithium from polysulfide shuttle and corrosion (high polysulfide concentration in lean electrolyte) by forming a lithium passivation layer containing Li_xO_y as a result of LiNO₃ decomposition, as illustrated in Figure 123c. However, repeated lithium stripping/plating gives rise to the destruction/reformation of this layer, causing continuous consumption of LiNO₃. Under large excess electrolyte

conditions, the large LiNO_3 reservoir allows sustained consumption over an extended cell cycling period, giving a perceived stable performance of the Li-S cell. However, under lean electrolyte conditions, the limited LiNO_3 reservoir is quickly consumed within the first 100 cycles. In this scenario, polysulfide will shuttle to the now exposed Li-metal anode side and form a thick insulating lithium sulfide layer that blocks further lithium deposition or stripping (Figure 123d). This polysulfide reaction results in both lithium and sulfur inventory losses that eventually result in cell failure. In the previous report, the team reported that active sulfur inventory losses remain as the major bottleneck limiting long cycle performance of Li-S batteries, an observation that aligns with most literature studies using excess electrolyte conditions. However, this conclusion needs to be re-evaluated under lean electrolyte conditions as well. To identify which active material species (lithium or sulfur) is depleted first, the lithium and sulfur losses are quantified in the next section. Additionally, an alternative strategy to overcome the LiNO_3 depletion problem is discussed following that.

Quantifying Lithium Inventory Losses in Lean Electrolyte Li-S System

To quantify lithium inventory losses, the team used the baseline C/S composite electrode system because it undergoes a quicker and more severe failure route to facilitate analysis. Previously, the team successfully developed the titration gas chromatography (TGC) method to quantify the metallic lithium mass in the cycled electrodes. The TGC method has been expanded recently to accommodate the Li-S system. A new calibration curve with a range up to 2.5 mg of lithium was established for measuring larger quantities of lithium used in this project. With the new calibration curve, the remaining metallic lithium mass in the cycled Li-metal electrode from Li-S cells can be quantified. Figure 124a shows the polysulfide shuttled lithium metal (yellow residues of sulfur species) that undergoes a large lithium inventory loss of 47%, which was quantified by TGC (Figure 124b). A calculated total of $\sim 10 \text{ mAh cm}^{-2}$ lithium anode capacity is lost in the cycled cell despite a total cathode capacity of only $\sim 2 \text{ mAh cm}^{-2}$, indicating that the polysulfide shuttle can induce a disproportionate amount of lithium inventory losses in the cell. Figure 124c shows the reacted lithium after the TGC experiment (brown solution), indicating not only the consumption of lithium metal but also the trapped sulfur species within Li-metal matrix. This is also verified from Figure 124d, which shows no polysulfide on the part of the cycled C/S cathode when immersed into DOL/DME solvents. Therefore, it can be inferred that without sufficient lithium passivation, polysulfides will shuttle to the Li-anode side, inducing a combination of both lithium and sulfur inventory losses. Thus, a potentially effective approach to mitigate both lithium and sulfur inventory losses would be to protect lithium using an additive more stable and effective than LiNO_3 , which will be discussed later.

Quantifying Sulfur Inventory Losses in Lean Electrolyte Li-S System

Last quarter, the team established TGA to be a valid tool for quantification of sulfur mass, and in turn, sulfur inventory losses with cycling. This quarter, they proceeded to conduct analysis on the sulfur inventory loss of the cycled electrode materials under lean electrolyte conditions. To do so, the cycled electrode at the charged state from Figure 124d was extracted and its sulfur content analyzed using TGA. From an initial sulfur mass of 3 mg at the pristine state, only 0.6 mg of active sulfur was found after 200 cycles, as shown in Figure 124e. The TGA measured for C/S cathode illustrates a drastic sulfur inventory loss (80%), a contrasting conclusion from what was previously reported using large excess of electrolyte. These initial results indicate that capacity fade in the Li-S cells is due to both lithium and sulfur inventory losses, with more severe depletion of sulfur inventory under lean electrolyte conditions. Thus, the consumption of LiNO_3 in lean lithium and electrolyte Li-S system might be the pivotal factor that limits Li-S cycling performance. Therefore, it is significant to develop a new electrolyte system to replace LiNO_3 or to protect lithium from polysulfide shuttle without continuous electrolyte consumption. Next quarter, the same quantification using high areal capacity HATN-S cathode will be conducted to verify the limiting factor for battery fading under extreme conditions like low E/S and N/P ratios.

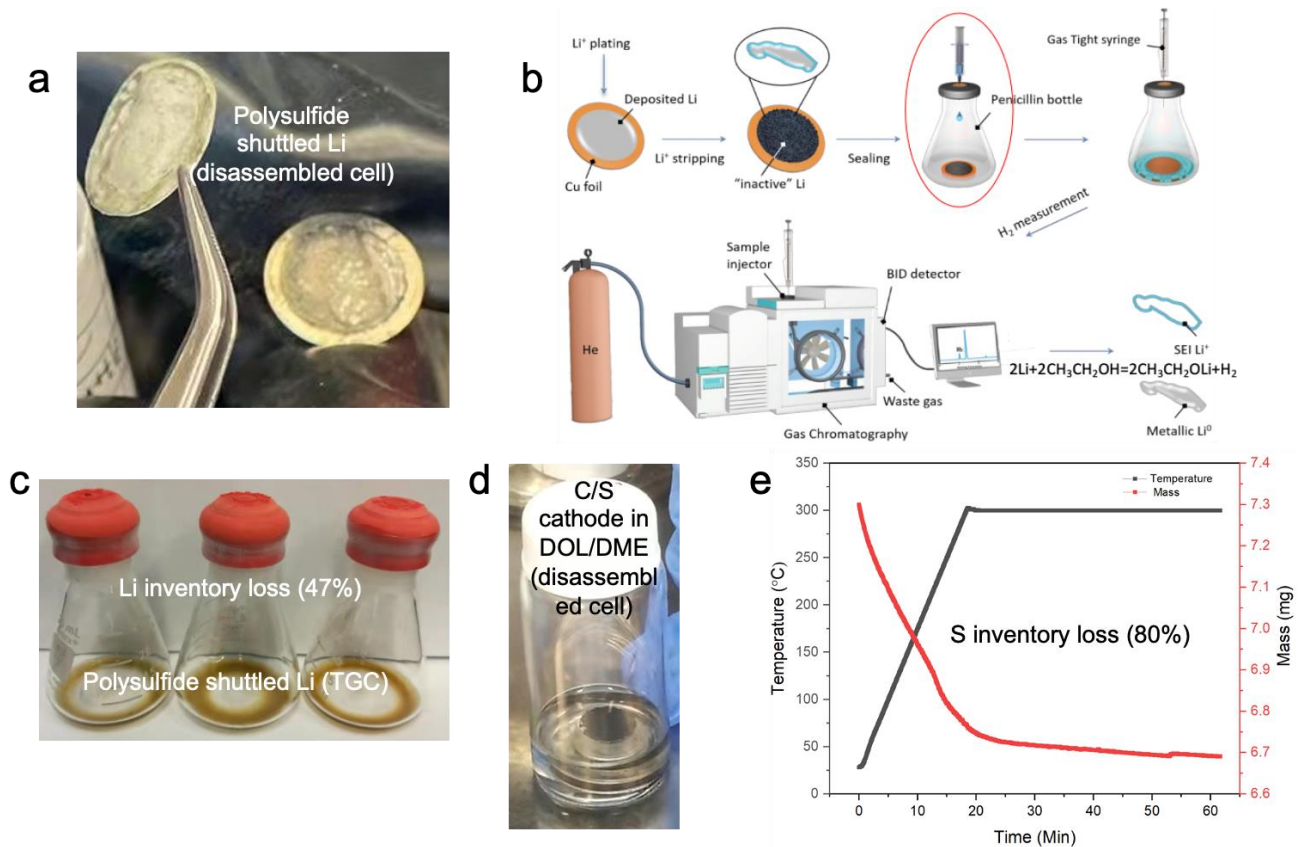


Figure 124. (a) Photo of lithium metal from the disassembled cell after 200 cycles. (b) Schematic of titration gas chromatography quantification of lithium metal loss. (c) Sample of lithium metal by polysulfide shuttle. (d) Photo of C/S cathode from the disassembled cell after 200 cycles and immersed in DOL/DME solvents. (e) Thermal gravimetric analysis curves.

In the benchmarking scope of work, all the C/S baseline composite electrodes were studied using low electrode loading. Compared to the high loading HATN-S ($> 10 \text{ mAh cm}^{-2}$) electrodes demonstrated earlier, the loadings of the C/S reference electrodes need to be increased for meaningful comparisons. However, due to the limitations of slurry-based casing of low-density C/S based composites, it is difficult to achieve such high-loading cast layers at the laboratory scale. To this end, GM has produced C/S cathode electrodes with high loading $> 5 \text{ mg-sulfur/cm}^2$ by developing both new slurry coating technology (for example, plasma treatment of aluminum substrate) and further optimizing slurry compositions. This has been scaled up to kg-scale coating using a roll-to-roll coater, as shown in Figure 125a. Cracking-free and flexible sulfur cathode electrodes with high loading of $5.2 \text{ mg-sulfur/cm}^2$ have been demonstrated, as shown in Figure 125b.

Figure 126 shows the potential versus specific capacity retention curves of the sulfur electrode with $5.2 \text{ mg-sulfur/cm}^2$. The areal discharge capacity can reach up to $\sim 6 \text{ mAh/cm}^2$ initially under first C/20 formation cycle with E/S ratio of $8 \mu\text{L/mg}$, which quickly stabilizes at 4 mAh/cm^2 after switching to C/10 discharge current rate for the following cycles. The cell lasts for about 50 cycles until the discharge capacity decreases to below 60% retention. Next quarter, UCSD will use the high-loading C/S cathode from GM for comparison.

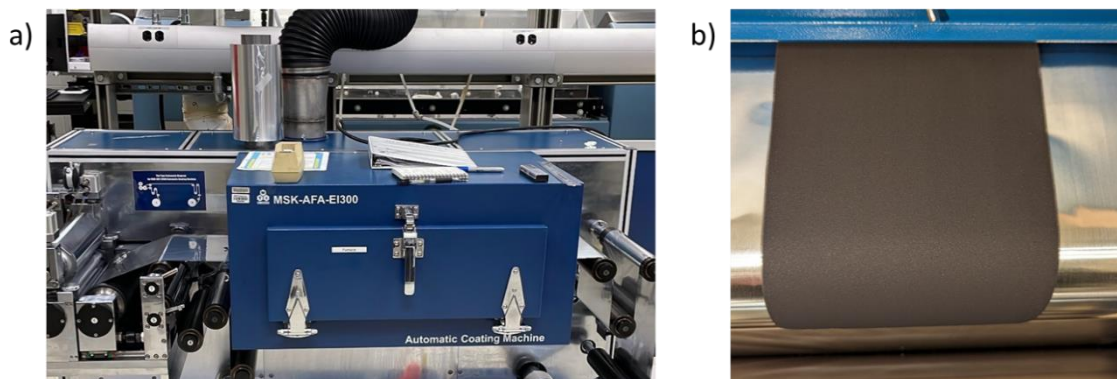


Figure 125. (a) Image of MTI E1300 roll-to-roll coater for kg-scale coating at GM. (b) Image of sulfur cathode electrode with areal sulfur loading of ~ 5.2 mg-sulfur/cm².

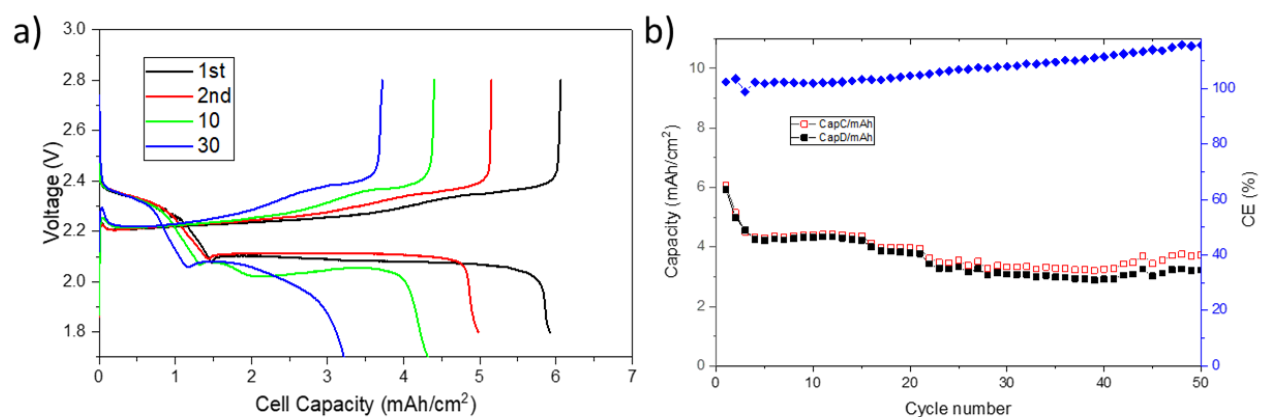


Figure 126. Electrochemical performance of 5.2 mg-sulfur/cm² sulfur cathode electrode (a) charge-discharge profiles, and (b) discharge-discharge capacities and Coulombic efficiency versus cycle number.

Developing New Electrolyte System to Address Capacity Fade (UCSD)

To improve the electrochemical performance of Li-S batteries, alternative electrolytes were also explored with the considerations for Li-metal passivation and polysulfide solubility. Last quarter, a promising electrolyte candidate, the LHCE with composition of LiFSI:DME:TTE with 1:1.2:3 molar ratio, was explored. This electrolyte was found to produce large granular lithium deposition morphology and delivered high CE. However, the voltage profile of Li-S battery using LHCE shows a large polarization and limited capacity during the 1st cycle. The incompatibility of LHCE in the Li-S system highlights the need for a new electrolyte system to be compatible with both the anode and the cathode.

One of the main designing principles of LE for Li-S system is to passivate the Li-metal surface and terminate the polysulfide shuttle. As the team has shown in this report, in the baseline electrolyte, the decomposition of LiNO₃ can successfully achieve the goal of passivating lithium metal. Herein, they also demonstrate the consequences if no LiNO₃ is added in LE for Li-S battery (Figure 127a). It shows that the charging cycle cannot complete when there is no formation of LiN_xO_y containing layer to passivate the lithium surface and prevent the polysulfide shuttle. However, the passivation of the lithium surface will eventually fail when all the LiNO₃ in the electrolyte is consumed. Thus, it is crucial for the team to design a new electrolyte system that can passivate the Li-metal surface but does not rely on decomposition of certain electrolyte components. This quarter, the team designed a new electrolyte that does not contain LiNO₃ (Figure 127b). A new type of N-containing salt is synthesized in lab, and the resulting electrolyte shows high chemical compatibility with

lithium metal, verified from the shiny lithium kept in the electrolyte for 48 hours (Figure 127b, inset). In Figure 127b, C/S cathode can successfully charge and discharge in this new electrolyte with no polysulfide shuttle, delivering a similar specific capacity of $\sim 1000 \text{ mAh g}^{-1}$ at 0.05 C with a low E/S ratio of $10 \mu\text{L mg}_{\text{sulfur}}^{-1}$, compared to that of baseline electrolyte (Figure 123a). Finally, C/S cathode can sustain stable cycling with a capacity retention of $\sim 68\%$ after 170 cycles (ongoing) using lean new electrolyte (Figure 127c), while the cells can only cycle for ~ 75 cycles before sudden capacity drop in the baseline electrolyte (Figure 123b). Next quarter, the quantification of lithium and sulfur loss in new electrolyte will be conducted using both C/S and HATN-S cathodes to identify the capacity loss root cause.

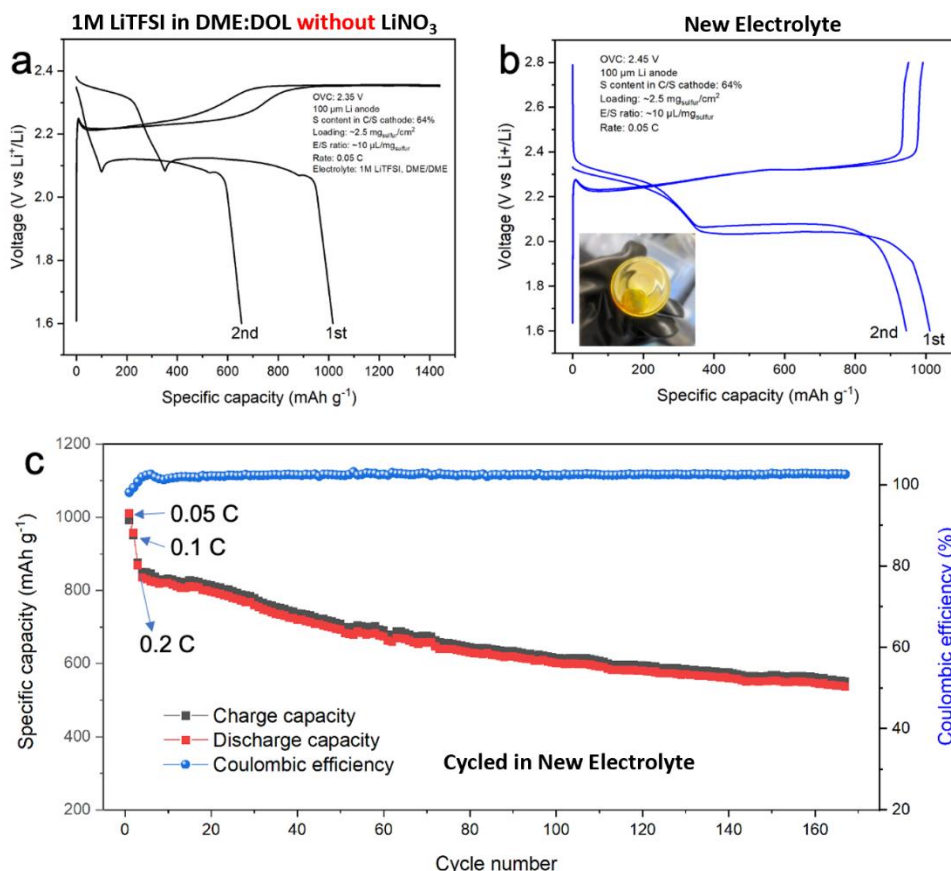


Figure 127. (a) The charge-discharge curves of C/S cathode in 1 M LiTFSI in a DOL/DME mixture (1:1, v/v) and in (b) New Electrolyte, using (c) cycling performance of C/S cathode cycling in New Electrolyte.

Patents/Publications/Presentations

The project has no patents, publications, or presentations to report this quarter.

Task 5.7 – New Engineering Concepts to High-Energy-Density Lithium-Sulfur Batteries (Prashant N. Kumta, University of Pittsburgh)

Project Objective. The major objectives of this project are to develop a Li-S pouch cell with a cell capacity > 300 mAh with energy density ≥ 500 Wh/kg, ≥ 750 Wh/L with cycling over 1000 cycles @C/3 rate, cycle life of 1000 at C/3 and $\leq 20\%$ fade in energy @ C/10-C/3, and $\leq \$80$ /kWh. To achieve the proposed objectives, the following major goals will be successfully attained over the first year of the project: (1) identification of effective electrocatalysts and LICs lowering the activation barrier; (2) *in situ* synthesis of electrocatalysts and LICs dispersed complex carbon-based framework material (CFM) and sulfur nanocomposite with sulfur content ≥ 90 wt%; (3) ~ 15 mAh/cm² areal capacity of sulfur electrode with sulfur loading ≥ 10 mg/cm²; (4) Li-containing structurally isomorphous alloy (Li-SIA) of ≥ 1000 cycles with 15 mAh/cm² areal capacity @C/3 rate; and (5) identification of optimal electrolyte compositions giving Li⁺ conductivities $\sim 10^{-2}$ S/cm and polysulfide dissolution < 1 ppm.

Impact. The work from this project will have a strong impact on development of high-energy-density Li-S batteries. The results of this work will lead to new knowledge on identification and generation of high-capacity sulfur cathodes and dendrite-free Li-metal anodes using scalable synthesis and fabrication approaches. Both fundamental and applied knowledge will be gathered from the study. Systematic characterization will provide new scientific insights into the mechanisms contributing to the corresponding response in coin-cell and pouch-cell formats. Results of this work also will likely have an impact on other fields such as electrocatalysts for water splitting and fuel cells and other fields engaged in electrochemistry. Plans are also in place to engage under-represented minority undergraduate students to gain research experience in various aspects of the project. With new materials identified as the project is executed, opportunities will emerge for filing invention disclosures, and provisional/non-provisional patent applications. The training and opportunities presented by this project to undergraduate and graduate students as well as postdoctoral research associates will foster next-generation work force training, equipping workers with the necessary skillsets to transform the quality of life all over the globe by generating high-energy-density systems that can be deployed in EVs as well as in laptops and cell phones including innumerable portable and wireless devices, opening the doors to a new green and sustainable energy environment improving overall quality of life.

Approach. Work involves executing a theory-driven study directed at identification of electrocatalysts for efficient conversion of polysulfides to Li₂S during the forward discharge process and backward charge process to elemental sulfur and lithium. Also, first-principles computational approaches will be applied to identify solid-state LICs with conductivity $> 10^{-4}$ S/cm. Employing expertise in the PI's laboratory, suitable low-temperature (< 240°C) scalable synthesis techniques will be used to generate theoretically identified electrocatalysts and LICs. Low polysulfide solubility and stable SEI forming electrolytes will then be prepared from commercially available solvents, additives, and salts. The effectiveness of the electrocatalysts and LICs to improve the polysulfide to Li₂S transformation kinetics and the ability to achieve the targeted specific capacity by trapping polysulfides, including desired structural transformation during charging/discharging, will be assessed; accordingly, suitable modification of electrocatalysts and LICs will be performed to generate the ideal microstructures. Suitable modification if required of lithium alloy as anode will also be performed by alloying with other metals to improve the Li-ion diffusivity kinetics and the Gibbs-Thomson parameter. The scalable approaches developed will be further refined to optimize sulfur utilization in the cathode, engineer the surface and bulk structure of the novel Li-SIA and lithium multicomponent alloy (Li-MCA) anodes to yield the desired areal capacity with optimal CE, and finally optimize the electrolyte structure to minimize and eliminate polysulfide dissolution with desired Li⁺ conductivities. Finally, the developed systems will be scaled up, fabricated, and tested in pouch-cell configurations.

Out-Year Goals. The following goals will be achieved in subsequent years: (1) determine optimal cell component design parameters such as electrode thickness and porosity exhibiting minimal polarization while maintaining cathode capacity ≥ 1500 mAh/gS; (2) demonstrate excellent cycle life of > 1000 cycles with $> 80\%$ capacity retention; (3) electrochemically test cells with dendrite-free Li-alloy anodes comprising Li-SIA and Li-MCA of areal capacity of ~ 15 mAh/cm²; (4) electrochemically test cells with modified electrolytes at charge-discharge rates of C/3 as well as other C-rates of C/10-C/3; (5) fabricate > 300 -mAh pouch cell giving energy density of greater or equal to 500 Wh/kg at C/3 rate and demonstration of acceptable performance at other C-rates of C/10-C/3; and (6) demonstrate cyclability of a minimum of 1000 charge/discharge cycles with $< 20\%$ fade rate for operation in -40°C to $+40^{\circ}\text{C}$ temperature ranges with temperature measured external to the pouch cell.

Collaborations. The project involves collaboration with G. E. Blomgran of Blomgren Consulting Services, Ltd.

Milestones

1. Computational identification of electrocatalysts and LICs will be completed: 80% lower activation barrier of polysulfide to Li₂S transformation and a 10-times improvement of reaction kinetics will be achieved. (Q4, FY 2022; In progress, October 2022)
2. Synthesis and characterization of ~ 20 -nm-sized electrocatalysts and LICs homogeneously dispersed in the CFM/S will be completed. (Q1, FY 2023; In progress, January 2023)
3. Dendrite-free growth study will be completed, and ≥ 1000 cycles cyclability tests @C/3 rate will be completed for dendrite-free anode technology innovation. (Q2, FY 2023; In progress, April 2023)
4. Modified electrolyte with high Li-ion conductivity ($\sim 10^{-2}$ S/cm) and minimum polysulfide solubility (< 1 ppm) will be achieved. (Q3, FY 2023; In progress, July 2023)

Progress Report

This quarter, the team reports preliminary work initiated in the fabrication of new sulfur confinement cathodes. With the goal of generating advanced cathode architectures, they attempted to modify the catholyte using functional additives. These functional monomer additives not only can finetune the dissolution of polysulfides, but also can modify the electrolyte/electrode interface on the lithium anodes. Therefore, additives can play a vital role in improving the cycle life of Li-S batteries. In this report, accordingly, the use of functional monomer additive molecule (FAM) as a promising stabilizer for use in Li-S batteries to improve the cycle life is described. It was observed that the FAM short-chain polysulfides complexes formed during charge-discharge processes not only modify the kinetics of formation of short-chain polysulfides but also reduce polysulfide dissolution. The results highlight the importance of use of appropriate amounts of FAM and carbon matrix serving as the sulfur host material for the efficient functioning of the FAM in Li-S batteries. Figure 128 shows the electrochemical cycling performance of sulfur-infiltrated carbon-based complex framework materials, termed as CFM-S cathodes containing the FAM, tested in Li-S battery. The CFM-S cycled at 0.05C with an average electrode loading of 3.8 mg cm⁻² electrode area. The CFM-S shows an initial discharge capacity of ~ 875 mAh g⁻¹, which stabilizes at ~ 625 mAh g⁻¹ after the 6th cycle. On prolonged cycling, the CFM-S shows a very stable capacity of ~ 550 mAh g⁻¹ for over 26 cycles. The E/S ratio was 4 $\mu\text{L mg}^{-1}$. Efforts to increase the sulfur loadings with use of LICs and electrocatalysts to enhance the specific capacity are in progress.

Another system that was studied included the synthesis of redox-active porous inorganic-organic framework materials (IOFM) as cathode in Li-S battery. These systems serve as a Li_2S_x reactive-type hosts to regulate polysulfide electrochemistry, facilitating its transformation into nanostructured Li_2S and sulfur within the porous IOFM matrix. IOFM was selected because it provides good surface area of $\sim 1000 \text{ m}^2 \text{ g}^{-1}$, which enables compact electrode preparation with high sulfur loading on carbon-coated aluminum foil. Thus, the IOFM/S cathode was tested for Li-S battery performance, and the electrochemical cycling performance of IOFM-S is shown in Figure 129. The IOFM-S cells were cycled at 0.05C with an average electrode loading of 2.6 mg cm^{-2} electrode area. The IOFM-S shows an initial discharge capacity of $\sim 500 \text{ mAh g}^{-1}$, which stabilizes at $\sim 650 \text{ mAh g}^{-1}$ after the 4th cycle. The low initial discharge capacity observed and the subsequent increase are likely due to wettability issues due to low E/S ratio of $4 \mu\text{L mg}^{-1}$. On prolonged cycling, the IOFM-S shows a stable capacity of $\sim 550 \text{ mAh g}^{-1}$ for over 25 cycles. Efforts to increase the sulfur loading with use of LICs and appropriate electrocatalyst to increase the specific capacity of these systems are under way.

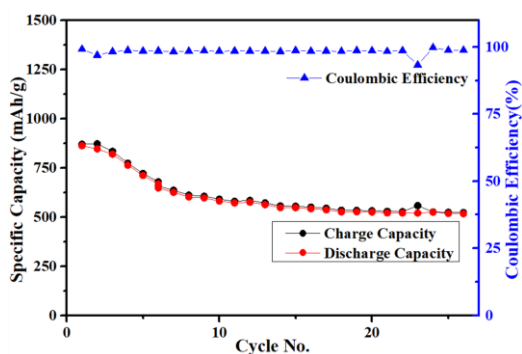


Figure 128. Electrochemical cycling performance and Coulombic efficiency of *complex framework materials – sulfur* cycled between 1.7-2.8 V.

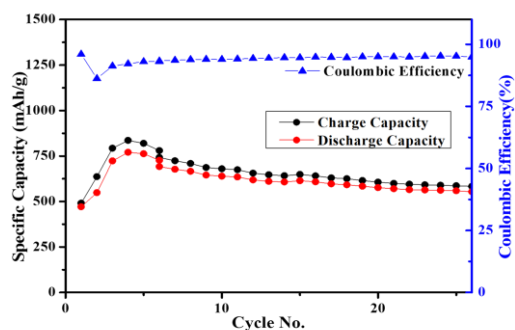
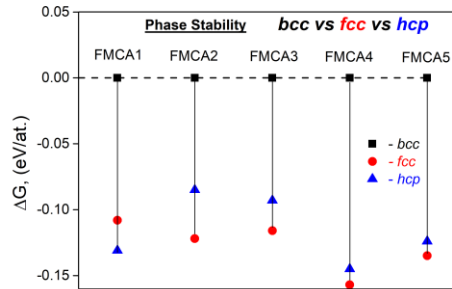


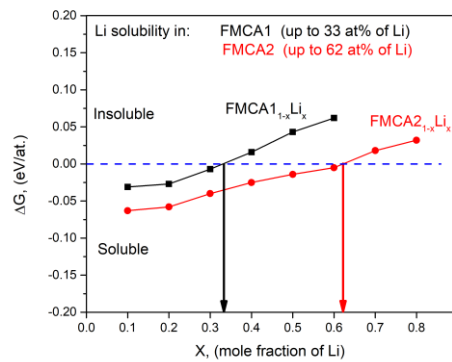
Figure 129. Electrochemical cycling performance and Coulombic efficiency of *inorganic-organic framework materials – sulfur* cycled between 1.7-2.8 V.

Furthermore, computational study was conducted with the goal to identify multi-component alloy (MCA) anodes. These MCA anodes were identified using DFT methods to demonstrate formation of uniformly disordered, metastable, *bcc* solid solution. Based on theory, the ability of the MCA anodes to incorporate large amounts of lithium ($> 50 \text{ at}\%$) was studied this quarter. The aim is that these systems will be able to electrochemically alloy theoretically demonstrated amounts of lithium ($> 50 \text{ at}\%$) during electrochemical cycling without the formation of lithium dendrites. Additionally, the project goal is to explore the ability of the system to cycle > 100 cycles attaining a targeted specific capacity of $> 15 \text{ mAh cm}^{-2}$. In the previous experimental study, the synthesis of a specific Fe-based MCA, FMCA1 was demonstrated, exhibiting an areal specific capacity of 4 mAh cm^{-2} without dendrite formation up to 300 cycles at C/2 rate. The low areal specific capacity is due to insufficient amounts of lithium that are accommodated or alloyed by the host alloy, FMCA1, with *bcc* crystal structure preventing this material from widespread use as an anode in the Li-ion batteries. Thus, there is a need to identify better alloys with lower atomic weight and stronger ability of the base alloy structure to accept high lithium content without inducing phase separation and intermetallic phase formation.

Calculation of phase stability shown in Figure 130 indicates that the metastable FMCA1 alloy exhibiting the *bcc* phase can accommodate only up to $\sim 33 \text{ at}\%$ of lithium without causing phase separation (Figure 130b, black line and arrow), which is insufficient to yield the target specific capacity of 15 mAh cm^{-2} . To achieve this target capacity, there is a need to incorporate at least $50 \text{ at}\%$ of lithium and use lighter constituent elements to reduce the total weight of the assembled anode and the ensuing fabricated full battery. Thus, in the present computational study, lighter elements were selected, and the corresponding phase stability of the several compositions studied was calculated. Figure 130a shows calculated phase stability of the various non-lithiated alloy compositions studied. As seen from Figure 130a, the FMCA2 alloy has better relative stability of the metastable *bcc* phase. Moreover, it can incorporate $> 60 \text{ at}\%$ of lithium (Figure 130b, red line and arrow), resulting in $> 15 \text{ mAh cm}^{-2}$ areal specific capacity. Experimental validations of these theoretical findings are in progress.



(a)



(b)

Figure 130. (a) Non-lithiated phase stability of alloys. (b) Lithiated phase stability.

Patents/Publications/Presentations

The project has no patents, publications, or presentations to report this quarter.

Task 5.8 – Development of Lithium-Sulfur Battery Cells with High Energy Density and Long Cycling Life (Donghai Wang, Pennsylvania State University)

Project Objective. The objective of this project is to develop a new soluble-polysulfide-free sulfur cathode with a high sulfur content (> 50 wt%) and high discharge specific capacity (> 700 mAh g^{-1} , based on the weight of the whole cathode), and demonstrate performance of the sulfur electrode at high electrode capacity (> 7 mAh cm^{-2}), low N/P ratio (< 2), and low E/S ratio (< 2.5 μL mg^{-1}). Prototype Li-S pouch cells with predicted energy density of 400 Wh kg^{-1} and 80% capacity retention for over 300 cycles using conventional electrolyte and Li-metal anodes with a protective layer developed by the team will be demonstrated.

Impact. This project aims to develop new sulfur composite active materials and functional polymer binders that enable polysulfide-free, high-performance, low-cost sulfur cathode. The use of these high-performance and low-cost sulfur cathodes, in turn, enables Li-S batteries with high energy density and long cycle life. Such Li-S batteries, made using the developed cathodes paired with a Li-metal anode, can lead to 50% greater energy density than conventional Li-ion batteries. Meeting the technical targets will potentially develop high-energy-density lithium batteries, promote increased adoption of EVs and PHEVs, and reduce petroleum consumption in the transportation sector by helping battery-powered vehicles become accepted by consumers as a reliable source of transportation.

Approach. The overall approach will focus on synthesizing and optimizing a novel polysulfide-free sulfur composite active material and functional binders. Specifically, approaches to realize the project objectives include the following: (1) development of novel polysulfide-free sulfur composite active materials, (2) development of new functional polymer binders to facilitate Li^+ transport and trap residual lithium polysulfide; and (3) diagnostics, characterization, theoretical simulation, and cell tests on the developed materials in Li-S batteries.

Out-Year Goals. The out-year goals are as follows: (1) develop new sulfur composite active materials, and (2) conduct characterization, simulation, and performance tests on material and electrode levels. The *Go/No-Go Decision* will be demonstration of Li-S batteries using the developed sulfur composite active materials with an initial discharge specific capacity > 600 mAh g^{-1} (based on cathode weight) at an areal capacity of 4 mAh cm^{-2} and E/S ratio < 8 μL mg^{-1} .

Collaborations. PSU will collaborate with the University of Illinois at Chicago (UIC) on theoretical simulation.

Milestones

1. Demonstrate sulfur cathode using sulfur composite active material (generation 1) with an initial discharge capacity > 500 mAh g^{-1} (based on cathode weight), at E/S ratio < 10 μL mg^{-1} . (Q1, FY 2022; In progress)
2. Demonstrate sulfur cathode using sulfur composite active material (generation 2) with an initial discharge capacity > 500 mAh g^{-1} (based on cathode weight), at E/S ratio < 10 μL mg^{-1} . (Q2, FY 2022; In progress).
3. Demonstrate sulfur cathode using sulfur composite active material (generation 1) with an initial discharge capacity > 600 mAh g^{-1} (based on cathode weight), at E/S ratio < 10 μL mg^{-1} . (Q3, FY 2022; In progress)
4. Demonstrate sulfur cathode using sulfur composite active material (generation 2) with an initial discharge capacity > 600 mAh g^{-1} (based on cathode weight), at E/S ratio < 10 μL mg^{-1} . (Q4, FY 2022; In progress)

Progress Report

Development of Sulfur Composite Active Material (Generation 1)

This quarter, the team developed Generation 1 of the sulfur polymerized composite (SPZ) derived active material (SPZ-G-1) and demonstrated its cathode performance with a high initial discharge capacity of $> 500 \text{ mAh g}^{-1}$ (based on cathode weight) at an E/S ratio $< 10 \text{ } \mu\text{L mg}^{-1}$. Based on their SPZ-G-1, they further demonstrated sulfur cathode using the SPZ-derived active material (generation 2, SPZ-2) with an initial discharge capacity $> 500 \text{ mAh g}^{-1}$ (based on cathode weight) at an E/S ratio $< 10 \text{ } \mu\text{L mg}^{-1}$. Therefore, they first worked on the design, synthesis, and evaluation of the electrochemical performance for SPZ-G-1 materials.

Different types of SPZ-G-1 active materials have been designed and synthesized. First, synthesis conditions and chemical compositions were optimized. The team then evaluated the electrochemical performance of some of the developed SPZ-G-1 active materials. In detail, sulfur cathodes using SPZ-1a, SPZ-1b, and SPZ-1c were fabricated with 80 wt% of active material and an areal loading $\sim 2 \text{ mg SPZ cm}^{-2}$. Their electrochemical performances were tested in conventional ether-based electrolytes and illustrated in Figure 131. The initial discharge specific capacity of the SPZ-1a cathode after activation could reach $632.64 \text{ mAh g}^{-1}$ (based on the weight of the whole cathode). Such discharge specific capacity fulfills the target for this reporting period. Two voltage plateaus at 2.35 V and 2.15 V were observed, indicating the generation of lithium polysulfides. Cycling performance was evaluated as well. Among SPZ-1a, SPZ-1b, and SPZ-1c composite active materials, SPZ-1c cathode shows the highest initial discharge specific capacity of 660.8 mAh g^{-1} and best cycling stability.

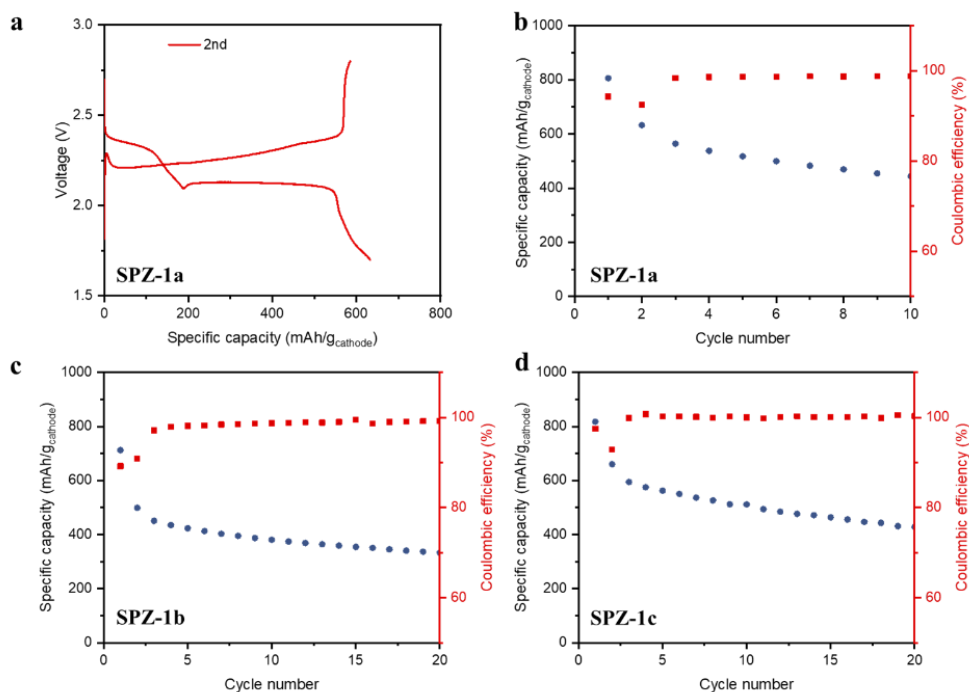


Figure 131. (a) Galvanostatic discharge-charge curves of SPZ-1a cathode at different cycles. (b-d) Cycling performance of (b) SPZ-1a, (c) SPZ-1b, and (d) SPZ-1c cathodes. The areal active material loading is $\sim 2 \text{ mg cm}^{-2}$. The cells were activated at 0.03 A g^{-1} (based on composite weight) for the 1st cycle and then cycled at 0.1 A g^{-1} .

Development of Sulfur Composite Active Material (Generation 2)

In the team's proposed SPZ-2 materials, heteroatoms are introduced to modify the backbones and side chains of previously reported SPZ-1 materials. The type of heteroatoms determines their binding energy with sulfur atoms and thus the reversibility of conversion reactions in Li-S batteries. Therefore, three types of heteroatoms (denoted as a, b, and c) were first introduced into the synthetic routes of the SPZ-2 materials (denoted as SPZ-2a, SPZ-2b, and SPZ-2c) and then screened by the initial specific capacity of the yielded batteries. Cathodes based on SPZ-2a, b, and c were fabricated with 80 wt% of active material and areal loading $\sim 2 \text{ mgSPZ-2 cm}^{-2}$. The Li-S batteries based on the above cathodes were tested in carbonate-based electrolyte because it is safer, cheaper than the ether-based electrolyte, and proves to contribute a polysulfide-free conversion reaction with improved cycling performance. As a result, batteries based on SPZ-2a cathodes demonstrated the highest initial specific capacity ($\sim 530 \text{ mAh g}^{-1}$) over their counterparts, including batteries based on SPZ-2b, and SPZ-2c cathodes (Figure 132a). Such discharge specific capacity meets the target for this reporting period. The selected heteroatom-a has better electronic conductivity than sulfur, demonstrates good compatibility with carbonate electrolyte, and can serve as extra bond sites for sulfur species to enhance sulfur utilization. However, the theoretical capacity of heteroatom-a is limited. Therefore, the trade-off between the amount of heteroatom-a in SPZ-2a and the yielded capacity needs to be clarified for optimized electrochemical performance. In this regard, SPZ-2a containing various weight percentages of heteroatom-a (that is, 2 wt%, 6 wt%, and 10 wt%, denoted as SPZ-2a2, 2a6, and 2a10) were synthesized and evaluated in full cells (Figure 132b-d). Consequently, among SPZ-2a2, SPZ-2a6, and SPZ-2a10 composite active materials, SPZ-2a6 cathode shows the highest initial discharge capacity of $\sim 530 \text{ mAh g}^{-1}$ as well as more desirable cycling stability.

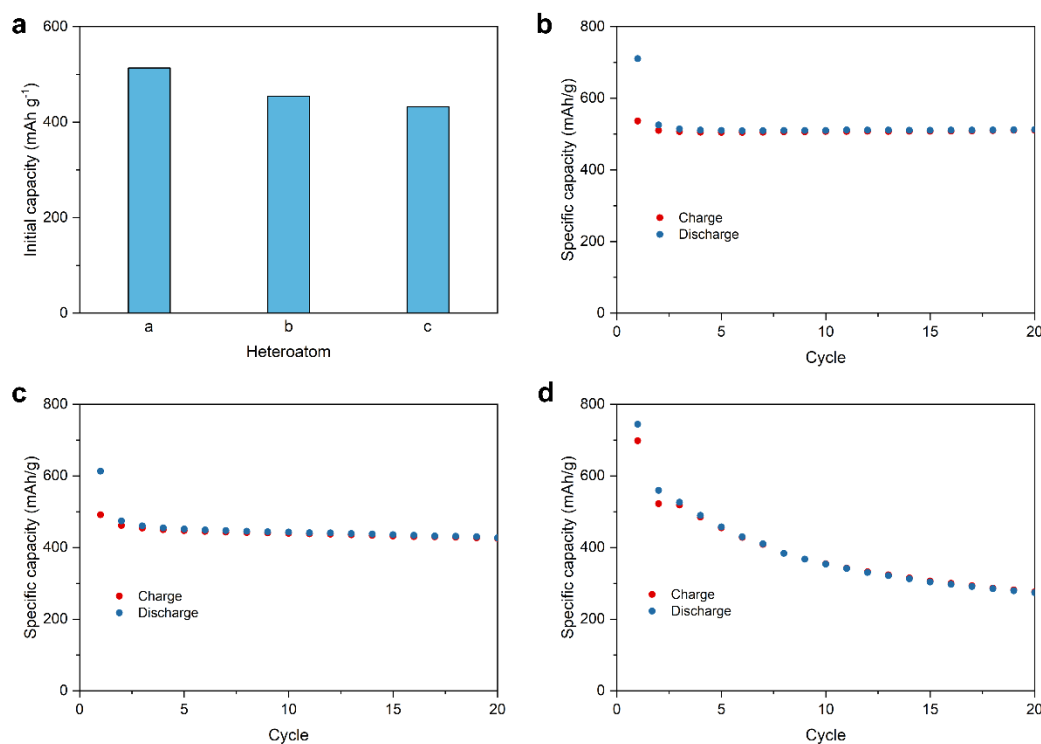


Figure 132. (a) Initial capacities of SPZ-2a, SPZ-2b, and SPZ-2c cathodes. (b-d) Cycling performance of (b) SPZ-2a2, (c) SPZ-2a6, and (d) SPZ-2a10 cathodes in carbonate electrolytes. The areal active material loading is $\sim 2 \text{ mg cm}^{-2}$. The cells were activated at 0.05 A g^{-1} (based on composite weight) for the 1st cycle and then cycled at 0.1 A g^{-1} .

Next quarter, the team will screen and optimize the electrolyte for the designed SPZ-2 materials and further improve the specific capacities of SPZ-1 materials in both carbonate and ether electrolytes. The milestone for the next quarter would be to demonstrate sulfur cathode using sulfur composite active material (generation 1) with an initial discharge capacity $> 600 \text{ mAh g}^{-1}$ (based on cathode weight) at an E/S ratio $< 10 \text{ } \mu\text{L mg}^{-1}$. In addition, the team will continue optimizing the synthetic parameters of both SPZ-1 and SPZ-2 cathode materials.

Patents/Publications/Presentations

The project has no patents, publications, or presentations to report this quarter.

TASK 6 – LITHIUM-AIR BATTERIES

Team Lead: Ji-Guang Zhang, Pacific Northwest National Laboratory

Summary and Highlights

The Task objective is to develop rechargeable Li-O₂ batteries with long-term cycling stability through in-depth research on more stable electrolytes and highly efficient catalysts for air electrodes, protection of Li-metal anodes, and deeper understanding on the oxygen reduction reaction and oxygen evolution reaction mechanisms behind the electrochemical performance of Li-O₂ cells.

Highlights

The highlights for this quarter are as follows:

- The Argonne National Laboratory (ANL) team studied the chemistry of the solid electrolyte interphase (SEI) layer at various stages of its processing and application using attenuated total reflectance – Fourier transform infrared spectroscopy. They confirm that the species the SEI is generating is soluble in the electrolyte. The results of X-ray photoelectron spectroscopy further indicate that the functioning mechanism of the SEI entails the deposition of a non-toroidal like Li₂O₂ with a weaker structure that can be more easily delithiated.
- The ANL / University of Illinois, Chicago (UIC) team used density functional theory calculations to explain several aspects of the tin sulfide (SnS) catalyst developed last quarter. They found that whether the disproportionation occurs in solution or on the surface, the formation mechanism will involve nucleation and growth of the discharge product on the surface of the cathode. In the case of the SnS catalyst and the dimethylsulfoxide (DMSO)-based electrolyte, the morphology of the Li₂O₂ is toroids, similar to what has been found in other studies.
- The UIC group further studied the combination of (NbTa)_{0.5}BiS₃ as a cathode catalyst and a ZnI₂ additive with ionic-liquid-based electrolyte at the higher current rate of 0.5 mA/cm². They found that at such a high current density, the battery can operate up to 125 cycles with the capacity of 0.25 mAh/cm² (corresponding to 2500 mAh/g) and up to 50 cycles with the capacity of 0.5 mAh/cm² (corresponding to 5000 mAh/g).

Task 6.1 – Lithium-Air Batteries (Khalil Amine, Larry A. Curtiss, and Jun Lu; Argonne National Laboratory)

Project Objective. This project will develop new cathode materials and electrolytes for Li-air batteries for long cycle life, high capacity, and high efficiency. The goal is to obtain critical insight that will provide information on the charge and discharge processes in Li-air batteries to enable new advances to be made in their performance. This will be done using state-of-the-art characterization techniques combined with state-of-the-art computational methodologies to understand and design new materials and electrolytes for Li-air batteries.

Project Impact. The instability of current nonaqueous electrolytes and degradation of cathode materials limits performance of Li-air batteries. The project impact will be to develop new electrolytes and cathode materials that are stable and can increase energy density of electrical energy storage systems based on lithium.

Approach. The project is using a joint theoretical/experimental approach for design and discovery of new cathode and electrolyte materials that act synergistically to reduce charge overpotentials and increase cycle life. Synthesis methods, in combination with design principles developed from computations, are used to make new cathode architectures. Computational studies are used to help understand decomposition mechanisms of electrolytes and how to design electrolytes with improved stability. The new cathodes and electrolytes are tested in Li-O₂ cells. Characterization, along with theory, is used to understand the performance of materials used in the cell and to make improved materials.

Out-Year Goals. The out-year goals are to find catalysts that promote discharge product morphologies that reduce charge potentials and to find electrolytes for long cycle life through testing and design.

Collaborations. This project engages in collaboration with K. C. Lau (University of California, Norridge), Y. Wu (OSU), and R. Shahbazian-Yassar (UIC).

Milestones

1. Design functionalized cathodes to achieve high electrochemical performance of Li-O₂ batteries. (Q1, FY 2022; Completed)
2. Characterize cathode materials and investigate electrochemical behaviors. (Q2, FY 2022; In progress)
3. Gain understanding of the processes of oxygen reduction reaction (ORR) and oxygen evolution reaction (OER) of these materials and reveal the possible parasitic reactions. (Q3, FY 2022; On schedule)
4. By understanding the effects, engineer new catalysts with improved catalytic performance and suppressed side reactions. (Q4, FY 2022; On schedule)

Progress Report

In last quarter's report, the team summarized their finding of a new metal-free catalyst platform for enabling low overpotential charge of Li-O₂ batteries across various current densities and types of carbon-based substrate materials. This platform was based on what is traditionally called SEI, an organic/inorganic interphase that is formed by the reduction of electrolyte components. The team showed that the mechanism of the low charge potential is due to some catalytic mechanism stemming from species produced by the SEI layer during oxidation. This quarter, they specifically investigated the functional groups present in these species.

To study the chemistry of the SEI layer at various stages of its processing and application, the team employed ATR-FTIR. They first sampled the SEI right after formation (Figure 133a), which revealed a relatively featureless spectrum in comparison to when the SEI is exposed to O₂ (Figure 133b). After exposure to O₂, peaks at ~1621 cm⁻¹ and 1670 cm⁻¹ increased, suggesting that lithium carboxylate and lithium oxalate groups appeared. Interestingly, after Li₂O₂ deposition the peaks disappeared, indicating either some elimination of the carboxylate species or a coverage of these species (Figure 133c). After oxidation/delithiation, the peaks reappeared, suggesting that the process is quite reversible. Importantly, the separator present in the cell used for oxidizing the Li₂O₂-SEI cathode, also exhibited some peaks at ~1620 cm⁻¹. In alignment with last quarter's report, they confirm that the species the SEI is generating is soluble in the electrolyte.

The team also used XPS to investigate how the SEI reacts to O₂ exposure. Figure 134a shows the carbon 1s spectrum for the pristine SEI and after exposure to oxygen. Reaction of the SEI to O₂ seems to decrease the proportion of C = O and increase the proportion of O-C = O, which aligns well with ATR-FTIR analysis. Furthermore the oxygen 1s analysis revealed that the R-C = O groups appeared to have increased, while the R-C-O decreased. It is, therefore, clear that the functioning mechanism of the SEI entails first the deposition of a non-toroidal like Li₂O₂ with a weaker structure that can be more easily delithiated. The benefit of the morphology of the Li₂O₂ is further compounded by the generation of some soluble catalyst that can diffuse and assist in oxidation of Li₂O₂.

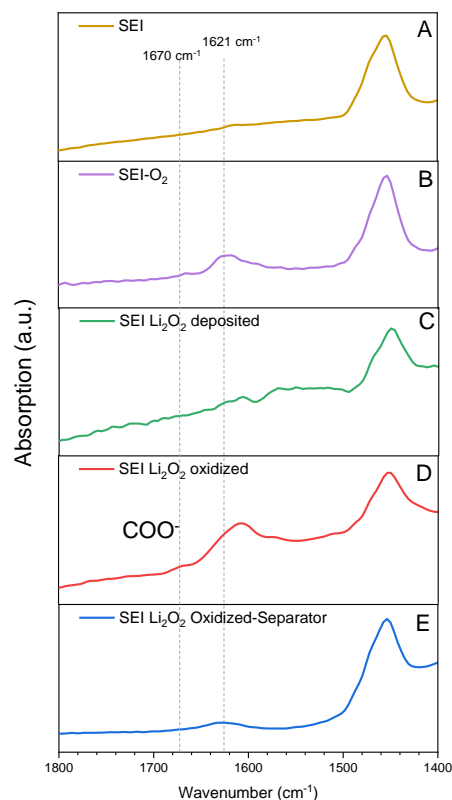


Figure 133. Attenuated total reflectance – Fourier transform infrared spectroscopy of (a) as-formed SEI catalytic layer, (b) SEI exposed to oxygen for 6 hours, (c) SEI deposited with Li₂O₂, (d) SEI with Li₂O₂ delithiated, and (e) the separator used in the cell of panel (d).

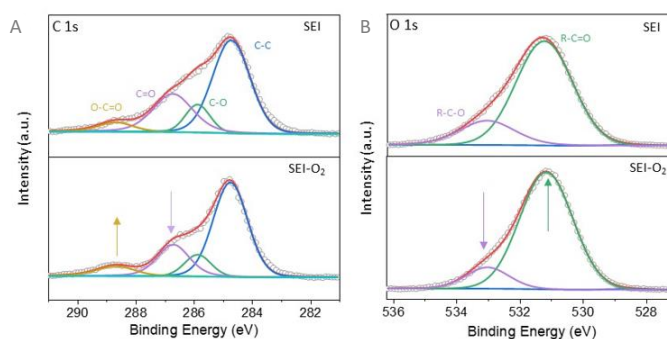


Figure 134. X-ray photoelectron spectroscopy of the SEI-coated cathode before and after exposure to O₂ at (a) carbon 1s and (b) oxygen 1s.

Patents/Publications/Presentations

The project has no patents, publications, or presentations to report this quarter.

Task 6.2 – Lithium Oxygen Battery Design and Predictions

(Larry A. Curtiss / Anh Ngo, Argonne National Laboratory; Amin Salehi-Khojin, University of Illinois, Chicago)

Project Objective. The objective of this work is to develop new materials for Li-O₂ batteries that give longer cycle life and improved efficiencies in an air environment. New electrolyte blends and additives will be investigated that can reduce clogging and at the same time promote the cathode functionality needed to reduce charge overpotentials. New cathode and anode materials will be investigated that can work in conjunction with the electrolytes to improve cycle life in the presence of air components.

Project Impact. Li-air batteries are considered as a potential alternative to Li-ion batteries for transportation applications due to their high theoretical specific energy. The major issues with the existing Li-O₂ systems include degradation of the anode electrode, reactions with air components, clogging of the cathode, and electrolyte instability. Thus, this project is using a comprehensive approach to improve cycle life and efficiency through developing new materials for electrodes, anodes, and electrolytes that work in synergy.

Approach. The experimental strategy is to use cathode materials based on 2D transition metal dichalcogenides (TMDs) that the team has found to be among the best ORR/OER catalysts. These cathode materials will be combined with new electrolyte blends and additives that work in synergy to reduce charge potentials and increase stability of the Li-air system. DFT and AIMD simulations are used to gain insight at the electronic structure level of theory of the electrolyte structure, and function both in bulk and at interfaces with the cathode, anode, and discharge product. CMD is used to obtain understanding at longer length and time scales of processes occurring in the electrolyte and growth mechanisms of discharge products. The team will also utilize a HT screening strategy based on experiment and theory to develop a large database of properties and outcomes of electrolyte combinations that can be analyzed using ML to predict electrolytes and additives with the best performance.

Out-Year Goals. The out-year goals are to find electrolytes that give high capacities and long cycle life in an air atmosphere using HT screening.

Collaborations. This project engages in collaboration with R. Assary, J. G. Wen, and S. Tepavcevic of ANL; B. Narayanan of University of Louisville; T. Li of Northern Illinois University; and F. Khalili-Araghi and R. Klie of UIC.

Milestones

1. Investigation of a highly active tin sulfide (SnS)-based catalyst for high-rate Li-O₂ battery performance. (Q1, FY 2022; Completed)
2. Computational studies of the active sites and electronic structure of the SnS catalyst. (Q2, FY 2022; Completed)
3. Development of new electrolyte RMs that work with the SnS catalyst to decrease charge potentials and computational studies. (Q3, FY 2022; On schedule)
4. Investigation of new Li-anode coatings for longer life Li-O₂ batteries with high rates. (Q4, FY 2022; On schedule)

Progress Report

Li-air batteries are considered as strong candidates for the next-generation energy storage systems designed for electrical transportation. However, low cyclability and low current rates are two major drawbacks that hinder these batteries from actual use as batteries. These issues necessitate discovery of novel electrocatalytic processes to significantly enhance the formation and decomposition of the products during battery cycling. The team is working on a system comprised of SnS nanoflakes (NFs) / reduced graphene oxide (rGO) as a solid catalyst. The goal of this work is to develop a system that enables operating the battery at high current rates of up to $1\text{mA}/\text{cm}^2$. It was reported previously that the catalytic activity of a SnS NFs/rGO catalyst for both ORR and OER occurring during the discharge and charge, respectively, far exceed those of state-of-the-art catalysts from carbon, noble metal, and TMD families. This quarter, the team has investigated using density functional calculations for explaining several aspects of the SnS catalyst.

The adsorption of O_2 and formation of O_2^- by reduction on the catalyst surface is an important factor in determining the rate at which oxygen reduction occurs and thus the efficiency of the discharge process. The team investigated six possible adsorption sites for O_2 on the SnS surface, as shown in Figure 135. In five of the six (C1-C5), the binding energy is about 1 eV, which is large enough to support oxygen reduction. The O_2 binds to tin in these five cases. The O_2 binds weakly on the surface in the sixth site (C6). The result of this study is significantly different from their previous study of MoS_2 in a Li- O_2 battery, where the molybdenum edge was found to be so reactive from DFT calculations that the O_2 dissociated on the molybdenum edges. This would result in driving the reaction toward full oxidation of the molybdenum edge and poisoning of the catalyst. To avoid this, an IL was used as the electrolyte because it was hypothesized that it can effectively prevent O_2 from dissociating on the electrode. The DFT calculations showed that the strong electrostatic interaction between the IL (EMIM^+ ions) prevents interaction with more than one molybdenum at a time to prevent complete O_2 dissociation on the molybdenum edge and leads to formation of an effective oxygen reduction site. This is unnecessary in the case of SnS as the interaction with O_2 is not nearly as strong, as shown in Figure 135; however, the SnS catalyst provides good charge transfer for oxygen reduction.

In a through solution discharge mechanism, Li_2O_2 can form by disproportionation of LiO_2 , either in solution or on the surface after deposition of LiO_2 on the surface, that is, $2\text{LiO}_2 \rightarrow \text{Li}_2\text{O}_2 + \text{O}_2$. The reaction pathway for disproportionation in solution of a LiO_2 dimer was computed for the dimethylsulfoxide (DMSO) electrolyte, assuming a dielectric constant of DMSO for the continuum level calculation. The reaction pathway computed using the accurate G4MP2 quantum chemical method, which is shown in Figure 136, indicates small barrier and favorable thermodynamics formation of Li_2O_2 in solution.

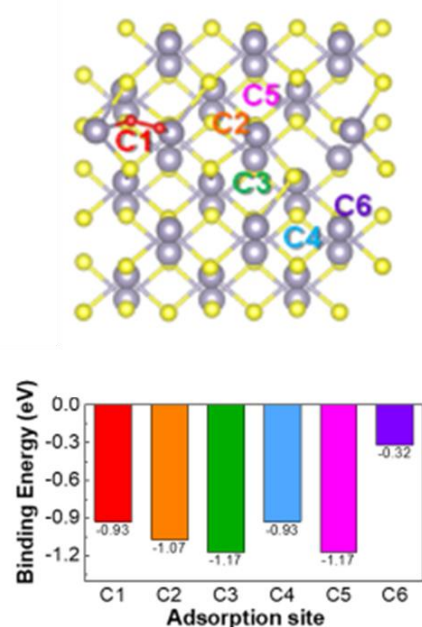


Figure 135. Density functional theory calculations for six O_2 adsorption sites on tin sulfide (SnS). (top) Example of O_2 adsorption structure is given for C1 site. (bottom) O_2 adsorption energies for the six sites shown for SnS surface (top figure).

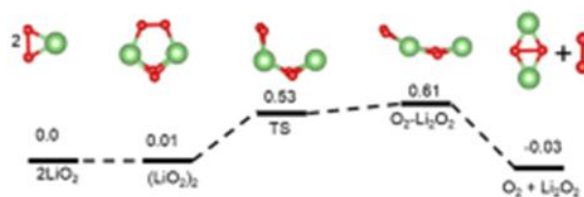


Figure 136. G4MP2 free energies for LiO_2 disproportionation to Li_2O_2 in DMSO solvent.

Whether the disproportionation occurs in solution or on the surface, the formation mechanism will involve nucleation and growth of or the discharge product on the surface of the cathode. In the case of the SnS catalyst and the DMSO-based electrolyte, the morphology of the Li_2O_2 is toroids, similar to what has been found in other studies.

In future work, the team will be developing and characterizing a new additive for the SnS catalyst to reduce the charge potential. Computational studies will be used to understand the performance of the additive. The additive will involve a liquid catalyst that can be oxidized at a lower potential and then act as a catalyst to decompose the Li_2O_2 . In addition, an additive is needed to provide lithium anode protection for longer cycling life.

Patents/Publications/Presentations

The project has no patents, publications, or presentations to report this quarter.

Task 6.3 – Development of a High-Rate Lithium-Air Battery Using a Gaseous CO₂ Reactant (Amin Salehi-Khojin, University of Illinois, Chicago)

Project Objective. The main objective of this project is to develop a novel strategy to enable operation of Li-CO₂ batteries at high-capacity high-rate with a long-cycle-life. The experiments will be performed in both Swagelok and pouch cells. In the former case, the team will use: (1) a novel co-catalyst system comprised of inexpensive and earth-abundant TMD materials that work in synergy with IL-based electrolytes to enhance efficiency of reactions during discharge and charge processes, (2) a solution-based catalyst (RM) to reduce charge overpotential and increase energy efficiency of the battery, (3) high porosity cathode electrodes to increase electrode surface area, gas permeability, stability, electrical conductivity, and lifetime of battery operation, and (4) SEI layer to protect the anode against oxidation without affecting the ionic transport of Li⁺ species in the system. At the pouch-cell level, the team will design and construct a stackable pouch cell to deliver a capacity of > 200 mAh.

Impact. Li-air batteries are considered as a potential alternative to Li-ion batteries for transportation applications due to their high theoretical specific energy. Most work in this area focuses on use of O₂ as the reactant. However, newer concepts for using gaseous reactants, such as CO₂ that has a theoretical specific energy density of 1,876 Wh/kg, provide opportunities for further exploration. This project will produce a thorough understanding of key chemical and electronic parameters that govern the operation of Li-CO₂ batteries in realistic conditions. Achieving the project objectives will generate a library of fundamental properties of TMD- and IL-based electrolytes with the most promise for Li-CO₂ battery applications. The methodologies employed, and the insight generated, will also be valuable beyond advancing the field of Li-CO₂ batteries.

Approach. The above targets will be achieved through an integrated approach based on materials synthesis, testing, characterization, analysis, and computation. The team will synthesize catalysts and test them in cells along with developing new electrolytes and additives. These cathode materials with new electrolyte blends and additives will work in synergy to reduce charge potentials and increase battery stability. DFT and AIMD simulations will be performed to understand battery operation and make predictions of new materials for the Li-CO₂ battery.

Out-Year Goals. The out-year goals are to find novel 2D catalysts and IL-based electrolytes that give high capacities and long cycle life in a CO₂ atmosphere.

Collaborations. This project collaborates with L. A. Curtiss (ANL), F. Khalili-Araghi (UIC), A. Subramanian (UIC), and Z. Huang (Stockholm University).

Milestones

1. Successful synthesis and characterization of bulk and 2D forms of six alloy TMDs for electrocatalysis and battery experiments. (Q1, FY 2022; Completed)
2. Successful exfoliation of TMD alloys with desired lateral sizes for battery experiments. (Q2, FY 2022; Completed)
3. Initiation of electrolyte blend development and characterization for battery experiments. (Q3, FY 2022; On schedule)
4. Charge transfer properties of different TMD alloys. (Q4, FY 2022; On schedule)

Progress Report

Most current research in energy storage for electric vehicles and flights is focused on incremental advances in Li-ion batteries. In recent years, research has also focused on new concepts that go beyond Li-ion batteries, with many challenges in making the new concepts feasible. Considerable effort has been spent on batteries based on chemical transformations including Li-S and Li-air batteries based on oxygen (Li-O_2), with the latter having the highest theoretical energy density (3500 Wh/kg). Another chemical transformation involving air components that has been less studied is batteries based on a CO_2 reactant, that is, the Li- CO_2 battery. Such a battery has a theoretical energy density of 1876 Wh/kg.

A Li-air battery based on a CO_2 reactant has major advantages over batteries based on O_2 , including: (1) the gaseous component CO_2 is less reactive than O_2 , making battery operation safer, (2) they avoid the lithium superoxide intermediate that can induce electrolyte detrimental reactions, (3) the Li_2CO_3 discharge product is more stable and less reactive than the Li_2O_2 product in the Li- O_2 battery, and (4) the reaction mechanisms during discharge and charge processes are not as complex as in Li- O_2 batteries. Moreover, the Li-air battery based on a CO_2 reactant has a potential for reversible carbon fixation for energy storage systems.

Last quarter, the team discovered a novel combination of transition metal chalcogenide, $(\text{NbTa})_{0.5}\text{BiS}_3$, as a cathode catalyst, and a ZnI_2 additive that works in synergy with IL-based electrolyte to operate the battery at the high rate of 0.3 mA/cm^2 (Figure 137a). This quarter, they further studied this combination of materials at the higher current density of 0.5 mA/cm^2 . Their results indicate that at such a high current density, the battery can operate up to 125 cycles with the capacity of 0.25 mAh/cm^2 (corresponding to 2500 mAh/g) and up to 50 cycles with the capacity of 0.5 mAh/cm^2 (corresponding to 5000 mAh/g); see Figure 137b-c. The current attenuation (rate capability) results are demonstrated in Figure 137d. The current density of the battery was increased from 0.1 mA/cm^2 to 0.5 mA/cm^2 during discharge and swept back to the original discharge value. The voltage difference between initial and final values is negligible (less than 5 mV) after 0.25 mAh/cm^2 discharge capacity, confirming the robustness of the cathode catalyst and electrolyte blend during discharge process.

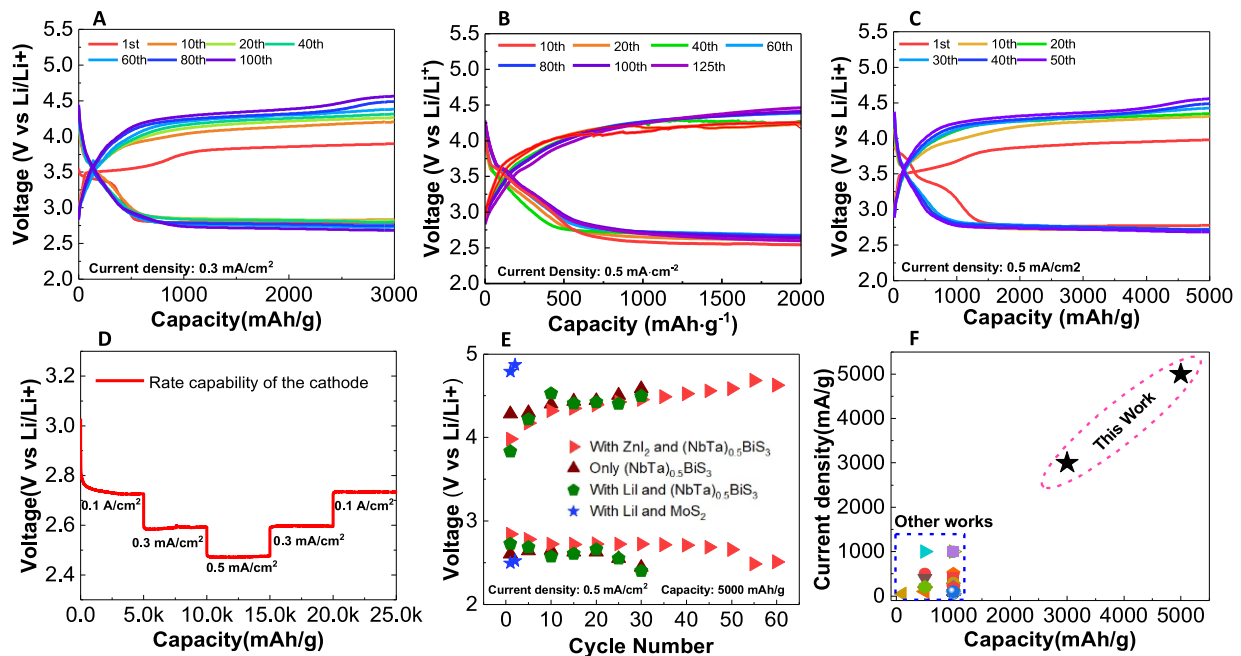


Figure 137. Electrochemical performance of Li- CO_2 battery. (a) Discharge/charge curves at current density and capacity of 0.3 mA/cm^2 and 0.3 mAh/cm^2 (corresponding to 3000 mAh/g), respectively. (b) Discharge/charge curves at current density of 0.5 mA/cm^2 and capacity of 0.2 mAh/cm^2 (2000 mAh/g). (c) Discharge/charge curves in CO_2 chamber at the current density of 0.5 mA/cm^2 and capacity of 0.5 mAh/cm^2 (5000 mAh/g), respectively. (d) Rate capability results of $(\text{NbTa})_{0.5}\text{BiS}_3$. (e) Cycling stability of batteries with $(\text{NbTa})_{0.5}\text{BiS}_3$ with ZnI_2 , only $(\text{NbTa})_{0.5}\text{BiS}_3$, $(\text{NbTa})_{0.5}\text{BiS}_3$ with LiI, and MoS_2 with LiI. (f) Comparison of current density versus capacity of the Li- CO_2 battery for the team's work (black stars) with other references.

Figure 137e shows the results of control battery experiments collected at the current density of 0.5 mA/cm^2 with the capacity of 5000 mAh/g (0.5 mAh/cm^2). For the case of $(\text{NbTa})_{0.5}\text{BiS}_3$ catalyst without ZnI_2 , the battery was able to run for 30 cycles before dropping the discharge potential below 2.4 V. However, the battery can run up to 50 cycles with ZnI_2 . On the other hand, the battery with $(\text{NbTa})_{0.5}\text{BiS}_3$ and LiI RM can only run for 25 cycles before the discharge voltage decreases to 2.4 V. The team notes that the polarization gap for all batteries is similar. These results suggest that ZnI_2 does not have RM role in reducing charge potential. Thus, they conclude that: (1) $(\text{NbTa})_{0.5}\text{BiS}_3$ solid catalyst is only responsible for all reactions, (2) the role of ZnI_2 is limited to SEI layer formation on the Li-anode surface, and (3) the Li_2CO_3 SEI layer that usually forms on the Li-anode surface in presence of CO_2 species through a chemical process is not effective in such a high current rate operation of the battery; thus, the role of Zn-based SEI layer to protect the anode surface is significant.

Other data in Figure 137e also indicate the battery with MoS_2 can only operate 3 cycles, while it can operate up to 500 cycles at the low current density of 0.05 mA/cm^2 based on the team's published paper in *Advanced Materials 2019*. Their detailed analysis uncovers that it loses its structural integrity at high current rates verified by the Raman spectroscopy experiments, which is not the case with $(\text{NbTa})_{0.5}\text{BiS}_3$. Figure 137f illustrates a comparison between this work and other studies in literature. Both current density and capacity were improved significantly, with an achieved current density of 5-50 times and a capacity of 5-100 times compared to other works.

Patents/Publications/Presentations

The project has no patents, publications, or presentations to report this quarter.

TASK 7 – SODIUM-ION BATTERIES

Team Lead: Xiao-Qing Yang, Brookhaven National Laboratory

Summary

The Na-ion battery will require investigations to identify optimal electrode materials, electrolytes, separators, and binders to reach full potential. The BMR program will therefore have a limited effort directed toward identifying Na-ion battery materials that have potential value for vehicle applications. Progress on these projects this quarter is described in this report.

Highlights

The highlights for this quarter are as follows:

- The Argonne National Laboratory team investigated and determined that Fe-predominate cathodes (1) are inherently unstable to the ester carbonate LiPF_6 electrolytes; (2) have a tendency to form large regions of P3 from synthesized O3 materials with air exposure and the expulsion of Na_2CO_3 from the Na-layers (water insertion), and (3) create nominally oxidized nickel as a result of sodium cation expulsion. High utilization of iron in layered cathodes will require surface coatings and doping for stabilization.
- The Brookhaven National Laboratory team completed *in situ* X-ray diffraction (XRD) studies on a new P3-structured $\text{Na}_{0.66}[\text{Cu}_{0.33}\text{Mn}_{0.67}]\text{O}_2$ cathode material for Na-ion batteries during charge-discharge cycling. They also discovered the highly reversible voltage and capacity in $\text{Na}_{2/3}\text{Cu}_{1/3}\text{Mn}_{2/3}\text{O}_2$, indicating the oxygen 2p holes can be stabilized by forming localized bound state with singly occupied Cu dx^2-y^2 . These findings open new approaches to design and explore cathode materials utilizing reversible lattice oxygen redox beyond the widely adopted A-O-A (A is an alkali metal) configuration.
- At Lawrence Berkeley National Laboratory, an *in situ* synchrotron XRD experiment during heating was carried out on a nonstoichiometric lepidocrocite sodium titanate. Dehydration occurs at low temperatures, and then the material undergoes a series of phase transformations to various layered structures. Above 700°C, the tunnel compound $\text{Na}_2\text{Ti}_6\text{O}_{13}$ is formed.
- The Pacific Northwest National Laboratory team developed a low-solvation electrolyte, sodium bis(fluorosulfonyl)imide : 1,2-dimethoxyethane : tris(2,2,2-trifluoroethyl) phosphate (NaFSI:DME:TFP) (1:1.5:2 in mole), to suppress the solid electrolyte interphase dissolution and extend the long cycling performance of high energy Na-ion batteries. The $\text{HC}||\text{NaNi}_{0.68}\text{Mn}_{0.22}\text{Co}_{0.1}\text{O}_2$ (NaNMC) full cells using NaFSI : dimethyl carbonate : TFP (NaFSI:DMC:TFP) electrolyte with charge limit of 4.2 V demonstrated 94% capacity retention after 300 cycles. Such correlation between the electrochemical performance of Na-ion cell and the electrode/electrolyte interphase stability provides valuable guidance for new electrolyte development.

Task 7.1 – Exploratory Studies of Novel Sodium-Ion Battery Systems (Xiao-Qing Yang and Enyuan Hu, Brookhaven National Laboratory)

Project Objective. To meet the challenges of powering PHEVs and BEVs, new rechargeable battery systems with high energy and power density, low cost, good abuse tolerance, and long calendar and cycle life need to be developed. The primary objective of this project is to develop new advanced synchrotron-based material characterization techniques and apply these techniques to study the new rechargeable battery systems beyond the Li-ion batteries, namely the Na-ion battery systems for EVs.

Project Impact. The results of this project will be used for developing technologies that will significantly increase the energy density and cycle life and reduce the cost of beyond Li-ion battery systems. This will greatly accelerate deployment of EVs and reduce carbon emission associated with fossil fuel consumption and will help in the direction of building U. S.-based energy storage manufacture chains.

Approach. This project will use synchrotron-based *in situ* X-ray diagnostics such as *in situ* XRD and *in situ* XAS tools, combined with TEM, STEM, and TXM imaging techniques developed at BNL to evaluate the new materials and redox couples to obtain in-depth understanding of the reaction mechanisms of these materials, aiming to improve existing materials and to provide guidance for new materials and new technology development for Na-ion battery systems.

Out-Year Goals. The out-year goal is to complete the SXRD, XAS, and XANES studies of new cathode materials of NaMnFeCoNiO₂ (NMFCN) and P2- Na_{0.66}[Cu_{0.33} Mn_{0.67}]O₂ for Na-ion batteries.

Collaborations. The BNL team has been closely working with top scientists on new material synthesis at ANL, LBNL, and PNNL, with U. S. industrial collaborators at GM and Johnson Controls, and with international collaborators.

Milestones

1. Complete XRD and TEM studies on a high-capacity and high-C rate multi-component sodium cathode materials NMFCN at pristine and after 1st charge state to study the structural changes of this material. (Q1, FY 2022; Completed)
2. Complete *in situ* XRD studies on a new P2-structured Na_{0.66}[Cu_{0.33} Mn_{0.67}]O₂ cathode material for Na-ion batteries during charge-discharge cycling. (Q2, FY 2022; Completed)
3. Complete *in situ* copper and manganese K-edge XAS studies on P2-structured Na_{0.66}[Cu_{0.33} Mn_{0.67}]O₂ materials during charge-discharge cycling to understand the redox contributions of copper and manganese of this material. (Q3, FY 2022; In progress)
4. Complete the soft XAS studies of Na_{0.66}[Cu_{0.33} Mn_{0.67}]O₂ materials at pristine and charged to 3.6 V and 4.1 V states to understand the redox contribution of oxygen. (Q4, FY 2022; In progress)

Progress Report

This quarter, the second milestone was completed at BNL. Advanced diagnostic techniques have been successfully applied to the studies of the new sodium cathode materials, P3-type $\text{Na}_{2/3}\text{Cu}_{1/3}\text{Mn}_{2/3}\text{O}_2$. Half of the Na^+ in this compound (corresponding to the nominal oxidation of Cu^{2+} to Cu^{3+}) can be reversibly extracted/inserted at two different plateaus with minimum voltage hysteresis. Detailed structure and electronic structure investigation reveal that charge compensation at the 3.5 V plateau is mainly contributed from the oxidation of p-d hybridized states, leading to the increase of p-d hybridization. In contrast, holes are predominantly created on a state with primary oxygen 2p parentage at the 4.1 V charge plateau. The highly reversible voltage and capacity in $\text{Na}_{2/3}\text{Cu}_{1/3}\text{Mn}_{2/3}\text{O}_2$ highlights that oxygen 2p holes can be stabilized by forming localized bound state with singly occupied Cu dx^2-y^2 . These findings open new routes to design and explore cathode materials utilizing reversible lattice oxygen redox beyond the widely adopted A-O-A (A is an alkali metal) configuration.

High-resolution *in situ* XRD data were collected to monitor the structural evolution during the initial charge and discharge with the up cut off voltages set to 4.1 V. During the initial charge, a two-phase reaction is identified for the 3.55 V plateau (Figure 138). The (001) and (002) reflections (in the monoclinic setting, corresponding to the (003) and (006) reflections in the conventional P3 type structure) shift toward lower angle during charging. These Bragg peaks indicate the dimension along crystallography *c*-axis, and the shifts suggest the expansion of the interlayer spacing after Na^+ extraction. In contrast, the (10-2) and (20-2) reflections shift to higher angle during charging. The position of these peaks is determined by both *a* and *c* axes. Considering that *c* expands during this process, the only possibility for peaks shifting to lower angle is that *a* axis shrinks. Interestingly, the (031) reflection remains almost unchanged. This peak is associated with the dimensions along both *b* and *c* axes, but the peak position is more sensitive to the former than the latter. Therefore, the behavior of (031) peak suggests that *b* axis is mostly unchanged during the 3.55 V plateau.

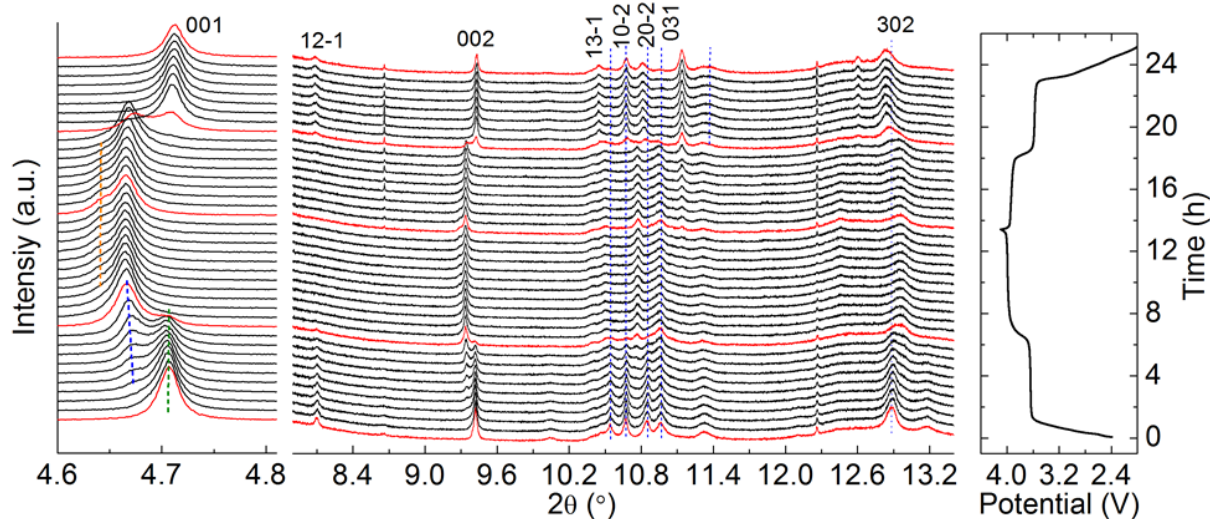


Figure 138. *In situ* X-ray diffraction with up cut-off voltage of 4.1 V.

Patents/Publications/Presentations

Publication

- Ali, G., M. Islam, D. S. Bhange, Y. H. Jung, M. Ge, Y. S. Chu, K-W. Nam, Y. Du, X-Q. Yang, H-G. Jung, S-M. Bak,* and K. Y. Chung.* “Self-Standing $\text{Co}_{2.4}\text{Sn}_{0.6}\text{O}_4$ Nano Rods as High-Performance Anode Materials for Sodium-Ion Battery and Investigation on Its Reaction Mechanism.” *Chemical Engineering Journal* 439 (2022): 135791. doi: 10.1016/j.cej.2022.135791.

Task 7.2 – Development of a High-Energy Sodium-Ion Battery with Long Life (Chris Johnson and Khalil Amine, Argonne National Laboratory)

Project Objective. The project objective is to develop a high-energy Na-ion battery with long life. Moreover, the battery chemistry should utilize low-cost materials. The energy density target is 200 Wh/kg and/or 500 Wh/L, wherein the anode and cathode capacity targets are 600 mAhg⁻¹ and 200 mAhg⁻¹, respectively.

Project Impact. A Na-ion battery on par with the energy density of a Li-ion battery can have a high impact in the transportation sector with the assumption that the cost is significantly below \$85/kWh and that the battery pack provides a 300-mile range. The consumer is not concerned about the battery chemistry employed if these metrics can be met. Development of these battery chemistries will situate the United States in a strong position as relates to new low-cost energy storage systems beyond lithium ion.

Approach. In a team approach, the Na-ion battery group will create a versatile Na-ion battery chemistry with beneficial advantages such as low cost, safety, recycling, and sustainability of materials used. The team will work synergistically so that the final design is the culmination of advances in phosphorus carbon composites mated with optimized lead or other highly dense metalloids, such as tin and/or antimony and derivatives thereof, for the recyclable anode. Synthesis and optimization of such blended composite anodes will be conducted in parallel to diagnostic characterization of structures, phase formation, and cycling stability. Cathode work will begin at the end of the first year and will involve gradient cathodes consisting of Fe-Mn compositions, as well as intergrowths of layer stacking sequenced oxides. If resources allow, the team also will attempt to stabilize cathode surfaces using ALD methods, particularly for the benefit of staving off dissolution of manganese and iron / electrolyte reactivity. Electrolytes will be partly procured from H. Li at PNNL.

Out-Year Goals. The state-of-the-art Na-ion battery in the literature has now been surpassed by this team, but performance is still too low for commercialization. Thus, the goal is to move forward and continually invent the most superior Na-ion battery chemistry that can compete worldwide through work output from this project.

Collaborations. Researchers from PNNL who are developing electrolytes for Na-ion batteries will provide this project with formulations to test with the various electrode combinations investigated at ANL.

Milestones

1. Investigate effect of native structural defects on high-voltage stability of sodium layered cathodes. (Q1, FY 2022; Complete)
2. Develop high-capacity single-crystal Ni-rich layered oxide cathodes with > 150 mAh/g and stable cycle life of > 100 cycles. (Q2, FY 2022; In progress)
3. Develop engineered surface for better air-storage and high-voltage stability. (Q2, FY 2022; In progress)
4. Develop concentration gradient layered oxide cathode with 130 mAh/g and stable cycle life of > 200 cycles. (Q3, FY 2022; In progress)
5. Investigate novel local atomic structural features to stabilize high oxidation state of iron active species. (Q4, FY 2022; In progress)
6. Optimize structure/electrolytes to enhance cycling stability of high-areal-capacity phosphorus anode and layered oxide cathodes. (Q4, FY 2022; In progress)

Progress Report

One of the critical concerns in layered sodium TM oxides (Na_xMO_2) is their poor ambient air storage stability. The hygroscopic nature of the sodium cathodes leads to hydration, sodium extraction, and degradation on the air-exposed surface, which in turn cause practical process and performance issues such as gas evolution, slurry gelation, and electrolyte decomposition. These could incur additional costs for material storage, transportation, and manufacturing in the battery manufacturing. Recently, it has been noticed that Fe-containing layered oxides have improved air stability over Fe-free counterparts.^[1-2] Naturally, Fe-containing compounds would be critically needed and should be incorporated in the cathode composition for low cost, essentially eliminating nickel. Although both $\text{Na}(\text{Ni},\text{Mn})\text{O}_2$ and NaFeO_2 are known to have moisture-sensitivity and poor storage properties, the solid solution compounds of $\text{Na}(\text{Ni},\text{Mn},\text{Fe})\text{O}_2$ have shown better storage stability. The role of iron in improving the air storage stability of $\text{Na}(\text{NiMnFe})\text{O}_2$ remains unclear. This quarter, the team reports on the systematic evaluation results of the air-storage stability of $\text{Na}(\text{Ni},\text{Mn},\text{Fe})\text{O}_2$ cathodes as a function of iron content.

A series of layered $\text{Na}[(\text{Ni}_{0.5}\text{Mn}_{0.5})_{1-x}\text{Fe}_x]\text{O}_2$ cathode materials was synthesized using co-precipitation and solid-state reaction method. The powder samples were exposed to ambient air for several days, and the degree of degradation was evaluated by XRD in Figure 139. The as-synthesized pristine cathodes have an O3-type layered structure with stoichiometric sodium content ($\text{O3-Na}_{1.0}\text{MO}_2$). After being air-exposed, the XRD data exhibit changes in the O3 structure and the formation of degradation products. The Fe0 sample shows the most significant structural degradation among the samples (Figure 139a). The parent O3 layered phase transformed to P3 structure, indicating a significant amount of sodium extraction from the layered structure ($\text{P3-Na}_{1-y}\text{MO}_2$), and new peaks corresponding to Na_2CO_3 and NiO appeared. In striking contrast, the Fe2/3 sample preserves the O3 layered structure better; the XRD pattern shows only a slight peak shift corresponding to c-axis expansion and a-axis contraction, indicating less sodium extraction ($\text{O3-Na}_{1-y}\text{MO}_2$). In Figure 139d, the lattice parameter changes for the air-exposed cathodes reveal a clear trend of suppressed sodium extraction and structural degradation with increasing iron content.

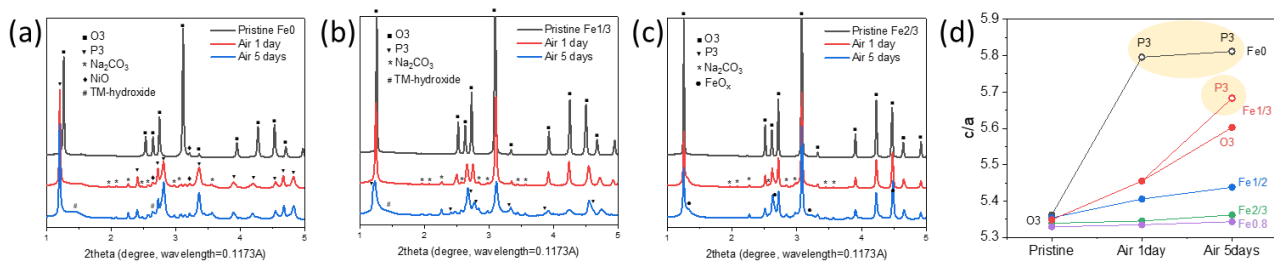


Figure 139. (a-c) Powder X-ray diffraction patterns of $\text{Na}[(\text{Ni}_{0.5}\text{Mn}_{0.5})_{1-x}\text{Fe}_x]\text{O}_2$ ($x = 0, 1/3,$ and $2/3$), and (d) changes in the c/a lattice parameter ratio before and after air-exposure.

Figure 140 compares the particle morphologies before and after the air exposure. All the pristine samples show similar secondary particle morphologies comprising aggregated plates of primary particles. After being exposed to ambient air for five days, the surface of low-Fe cathodes (Fe0, Fe1/3) is fully covered by a thick layer of residual sodium species, Na_2CO_3 . In contrast, the high-Fe cathodes (Fe1/2, Fe2/3, Fe0.8) better preserve the pristine surface morphology, and Na_2CO_3 grows as rod-shaped crystals rather than surface covering.^[2] The lower Na_2CO_3 quantity in the high-Fe cathodes was confirmed by both XPS and TGA data (not shown). The team presumes that a slower surface degradation and sodium extraction rate of the high-Fe cathodes provide a suitable condition for the growth of rod-shaped Na_2CO_3 crystals.

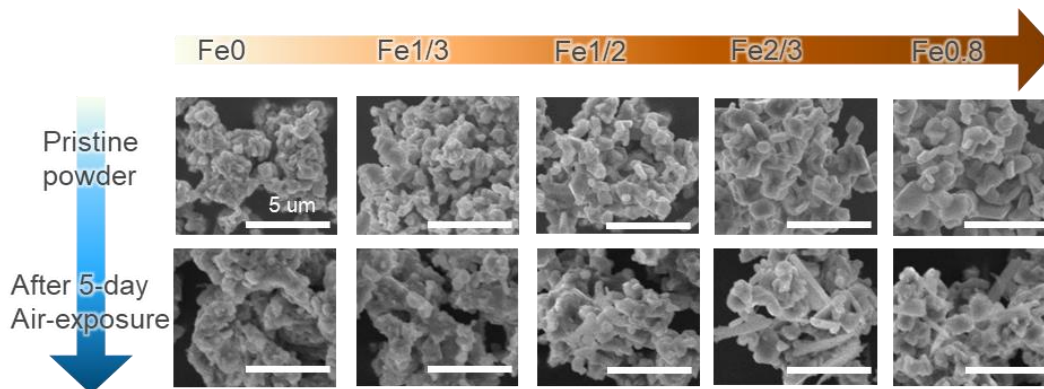


Figure 140. Scanning electron microscopy particle morphologies of $\text{Na}[(\text{Ni}_{0.5}\text{Mn}_{0.5})_{1-x}\text{Fe}_x]\text{O}_2$ ($x = 0, 1/3, 1/2, 2/3,$ and 0.8) before and after air-exposure for five days.

It can be postulated from the above observations that the sodium extraction from the stoichiometric O3- NaMO_2 triggers the cathode degradation during the ambient storage. There are two possible mechanisms by which the sodium deficient layered oxide phase maintains charge neutrality: TM oxidation ($\text{Na}_{1-y}\text{M}^{\text{III,IV}}\text{O}_2$), and proton exchange ($\text{H}_y\text{Na}_{1-y}\text{M}^{\text{III}}\text{O}_2$).^[3] The O3 to P3 phase transition shown in the low-Fe compounds corresponds well with the typical phase transition during the electrochemical sodium deintercalation from O3- NaMO_2 materials. However, phase degradation via the proton exchange mechanism cannot be completely ruled out because P3-type layered structure can also be stabilized in the proton exchanged layered H_yMO_2 .^[4] To better understand the degradation mechanism, the team has examined the oxidation states of TMs after air exposure. As shown in Figure 141a-c, the oxidation state of nickel increases to a higher value after air exposure, supporting the TM oxidation mechanism. (Note that manganese and iron remain in their pristine oxidation states, Mn^{IV} and Fe^{III} .) This result suggests the air stability of layered NaMO_2 cathodes is closely correlated with their oxidation potential. Figure 141d exhibits that the OCV for $\text{Na}_{1-y}[(\text{Ni}_{0.5}\text{Mn}_{0.5})_{1-x}\text{Fe}_x]\text{O}_2$ linearly increase with iron content, x . Therefore, the improved air-storage stability of the high-Fe compounds can be attributed to their higher oxidation barrier, which suppresses the sodium extraction from the lattice and the subsequent cascades of phase degradation.

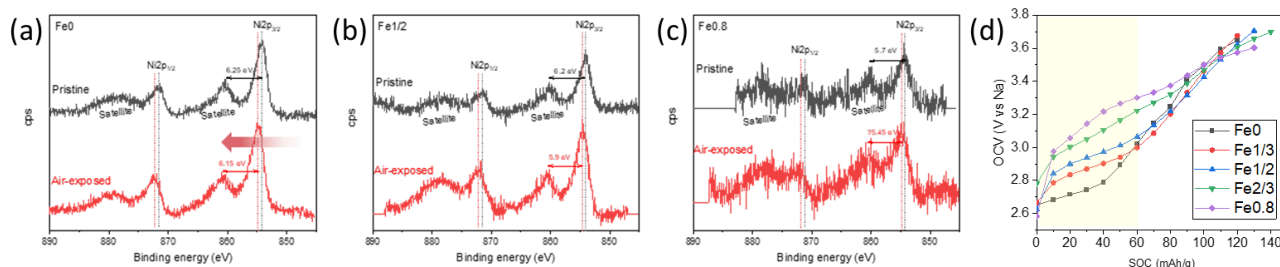


Figure 141. X-ray photoelectron spectroscopy nickel 2p spectra of the pristine and air-exposed (a) $\text{Na}[\text{Ni}_{0.5}\text{Mn}_{0.5}]\text{O}_2$, (b) $\text{Na}[\text{Ni}_{0.25}\text{Mn}_{0.25}\text{Fe}_{0.5}]\text{O}_2$, and (c) $\text{Na}[\text{Ni}_{0.1}\text{Mn}_{0.1}\text{Fe}_{0.8}]\text{O}_2$. (d) Open-circuit voltage profiles of $\text{Na}[(\text{Ni}_{0.5}\text{Mn}_{0.5})_{1-x}\text{Fe}_x]\text{O}_2$.

References

- [1] Yao, H-R., Y-G. Guo, et al. *ACS Applied Materials Interfaces* 11 (2019): 22067.
- [2] Sun, Y., Z-F. Ma, et al. *ACS Applied Energy Materials* 4 (2021): 2061.
- [3] Zuo, W., Y. Yang, et al. *Nature Communications* 11 (2020): 3544.
- [4] Robertson, A., and P. G. Bruce. *Chemistry of Materials* 15 (2003): 1984.

Patents/Publications/Presentations

Publications

- Park, J., K. Ku, S-B. Son, J. Gim, Y. Kim, E. Lee, and C. Johnson. “Effect of Electrolytes on the Cathode-Electrolyte Interfacial Stability of Fe-Based Layered Cathodes for Sodium-Ion Batteries.” *Journal of The Electrochemical Society* 169 (2022): 030536.
- Gabriel, E., D. Hou, E. Lee, and H. Xiong. “Multiphase Layered Transition Metal Oxide Positive Electrodes for Sodium Ion Batteries.” *Energy Science & Engineering* 10, no. 5 (2022): 1672–1705. doi: 10.1002/ese3.1128.
- Xu, G. L., X. Liu, X. Zhou, C. Zhao, I. Hwang, A. Daali, Z. Yang, Y. Ren, C. J. Sun, Z. Chen, Y. Liu, and K. Amine. “Native Lattice Strain Induced Structural Earthquake in Sodium Layered Oxide Cathodes.” *Nature Communications* 13 (2022): 1-12.

Presentation

- 14th American Institute of Chemical Engineers (AIChE) Midwest Regional Conference, Chicago, Illinois (March 1–2, 2022); “Electrolyte Engineering to Stabilize Cathode Electrolyte Interface of Na_{1-x}FeO₂ Cathode for NaIon Batteries”; J. Park, et al.

Task 7.3 – Tailoring High-Capacity, Reversible Anodes for Sodium-Ion Batteries (Marca M. Doeff, Lawrence Berkeley National Laboratory)

Project Objective. The project objective is to understand the role vacancies, surface defects, and bulk structure play in determining electrochemical properties of high capacity, stepped layered titanate anodes.

Project Impact. Although several suitable cathode materials for Na-ion batteries exist, there are few suitable anode materials due to low potential instabilities. Sodium titanate anodes are a promising class of materials for this application. The electrochemical properties can be manipulated through structural and surface modifications.

Approach. The structure and surface properties of candidate stepped layered titanates will be modified through manipulation of synthetic parameters. Materials will then be characterized electrochemically and physically to understand the role that surface defects, vacancies, and bulk structure play in determining electrochemical behavior.

Out-Year Goals. The out-year goal is to achieve development of an electrode that can deliver 225 mAh/g at C/3 rate with good capacity retention (80% or better) for 100 cycles.

Collaborations. The team collaborates with beam line scientists at SSRL and the ALS at LBNL.

Milestones

1. Conduct hot stage experiments on lepidocrocite titanates. (Q1, FY 2022; Completed)
2. Complete physical and electrochemical characterization of lepidocrocite titanates. (Q2, FY 2022; Completed)
3. Attempt surface modification of lepidocrocite titanates. (Q3, FY 2022; In progress)
4. *Go/No-Go Decision:* Surface modification methods; stop if performance is not improved. (Q4, FY 2022; In progress)

Progress Report

Due to equipment issues, the team was not able to carry out the *in situ* laboratory XRD hot stage experiments last quarter. Instead, they utilized the synchrotron XRD capabilities at SSRL for this work.

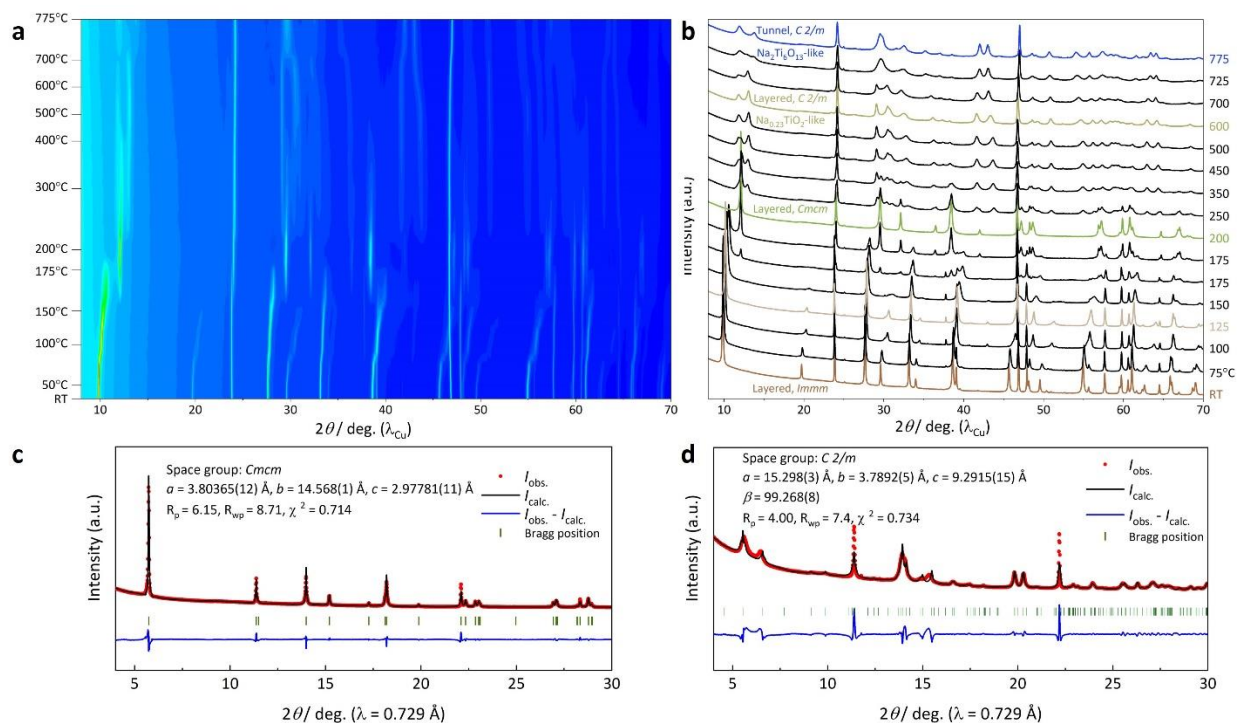


Figure 142. (a) Two-dimensional contour plot and (b) selected high-temperature synchrotron X-ray diffraction (XRD) patterns of $\text{Na}_{0.74}\text{Ti}_{1.815-0.185}\text{O}_4 \cdot n\text{H}_2\text{O}$ collected from room temperature to 775°C during the heating process in air. Le Bail fitting of XRD patterns collected at (c) 200°C using space group *Cmcm* and (d) 775°C using space group *C2/m*.

The *in situ* high-temperature synchrotron XRD measurement was conducted to elucidate the structural evolution of layered hydrous lepidocrocite (γ -FeOOH)-type sodium titanate (nominal composition of $\text{Na}_{0.74}\text{Ti}_{1.815-0.185}\text{O}_4 \cdot n\text{H}_2\text{O}$) in the temperature range from room temperature to 775°C (Figure 142a-b). Le Bail analyses of the XRD patterns suggest that the initial body centered orthorhombic *Immm* structure was largely maintained during the heating from room temperature to 150°C (Figure 143). The right-shift of the (020) diffraction line located at $2\theta = 9.86^\circ$ and decrease in intensity of (040) reflection located at $2\theta = 19.8^\circ$, agrees well with the shrinkage of the interlayer distance caused by dehydration. On further elevating the temperature, new diffraction peaks appear at $2\theta = 12.1^\circ, 29.5^\circ, 32.1^\circ,$ and 38.4° at the expense of the parent ones, eventually leading to formation of a new layered phase at 200°C. Phase transition from a hydrous *P-type* phase to the anhydrous *Cmcm* phase due to heating-induced lateral gliding was reported for other lepidocrocite-like titanates such as $\text{Na}_x[\text{Ti}_{2-x/3}\text{Li}_{x/3}]\text{O}_4 \cdot n\text{H}_2\text{O}$. A structureless Le Bail fitting on the pattern collected at 200°C using the space group of *Cmcm* led to sufficiently small R-values, and the calculated patterns agrees well with the observed one (Figure 142c). Lattice parameters are refined to be $a = 3.80365(12) \text{ \AA}$, $b = 14.568(1) \text{ \AA}$, and $c = 2.97781(11) \text{ \AA}$. The much smaller interlayer spacing of $\sim 7.284 \text{ \AA}$ as compared to that of $\sim 8.968 \text{ \AA}$ for the room-temperature hydrated phase suggests the removal of interlayer water. When the sample was further heated to higher temperatures, the (020) reflection gradually loses its intensity, along with broader shoulders appearing at both the higher- and lower- angle side. Additionally, multiple new broader peaks began to develop in the 2θ range of $28 \sim 35^\circ$ and $40 \sim 45^\circ$. These broader peaks merge, evolve, and become sharper as the temperature increases to the end of heating at 775°C. The disappearance of the (020) peak and growth of new peaks clearly indicate

that the layered *Cmcm* structure undergoes successive phase transitions. The resulting diffraction pattern at 775°C is like that of $\text{Na}_2\text{Ti}_6\text{O}_{13}$; Le Bail fitting of the pattern using the space group of $\text{Na}_2\text{Ti}_6\text{O}_{13}$ (*C 2/m*) gave a reasonably good fit (Figure 142d). Broadening of the diffraction peaks, most likely due to the structural disorder, for example, the positions of sodium ions inside the crystalline lattice, makes the profile fitting of XRD patterns collected at the intermediate temperature range difficult. Therefore, Raman spectroscopy was performed to gain additional structural information. As shown in Figure 144, similar Raman spectra were obtained for the samples heated at 60°C and 100°C, showing Raman-active modes at 125 cm^{-1} , 194 cm^{-1} , 275 cm^{-1} , 383 cm^{-1} , 440 cm^{-1} , 555 cm^{-1} , 659 cm^{-1} , 705 cm^{-1} , 796 cm^{-1} , and 908 cm^{-1} expected from the lepidocrocite structure. As the heating temperature continues to increase (350°C ~ 600°C), new bands grow in the range of 153 cm^{-1} ~ 247 cm^{-1} , indicating changes of the structure. The broad band at 796 cm^{-1} that was assigned to Ti–O–H vibrations becomes weak and finally disappears, which was likely due to the weakening/absence of OH– between TiO_6 layers caused by dehydration. The complete Raman spectrum of 600°C-heated sample is similar to that of monoclinic $\text{Na}_{0.23}\text{TiO}_2$. Le Bail fitting of the patterns collected for 500°C- heated and 600°C-heated samples using the space group of $\text{Na}_{0.23}\text{TiO}_2$ (*C 2/m*) enables a good fit of the positions of major reflection peaks (Figure 145). Raman spectra of the samples heated at 700°C and 800°C show similar characteristic Raman bands as $\text{Na}_2\text{Ti}_6\text{O}_{13}$ (Figure 144). In detail, a Raman band was seen at 871 cm^{-1} , corresponding to the vibrations of the shortest Ti–O bonds in the tunnel structure of $\text{Na}_2\text{Ti}_6\text{O}_{13}$. Raman bands at 658 cm^{-1} and 680 cm^{-1} , and 744 cm^{-1} , are characteristic of the Ti–O–Ti stretch in edge- and corner-shared TiO_6 octahedra, respectively.

Altogether, the team's *in situ* high-temperature synchrotron XRD and *ex situ* Raman results show that the layered hydrous orthorhombic structure (space group *Immm*) of lepidocrocite ($\gamma\text{-FeOOH}$)-type $\text{Na}_{0.74}\text{Ti}_{1.815}\square_{0.185}\text{O}_4 \cdot n\text{H}_2\text{O}$ firstly converts to a layered anhydrous orthorhombic *Cmcm* structure at 200°C, and eventually transforms to a $\text{Na}_2\text{Ti}_6\text{O}_{13}$ -like tunnel structure (space group *C 2/m*) at high temperatures of 700°C and above possibly via an intermediate $\text{Na}_{0.23}\text{TiO}_2$ -like layered structure (space group *C 2/m*).

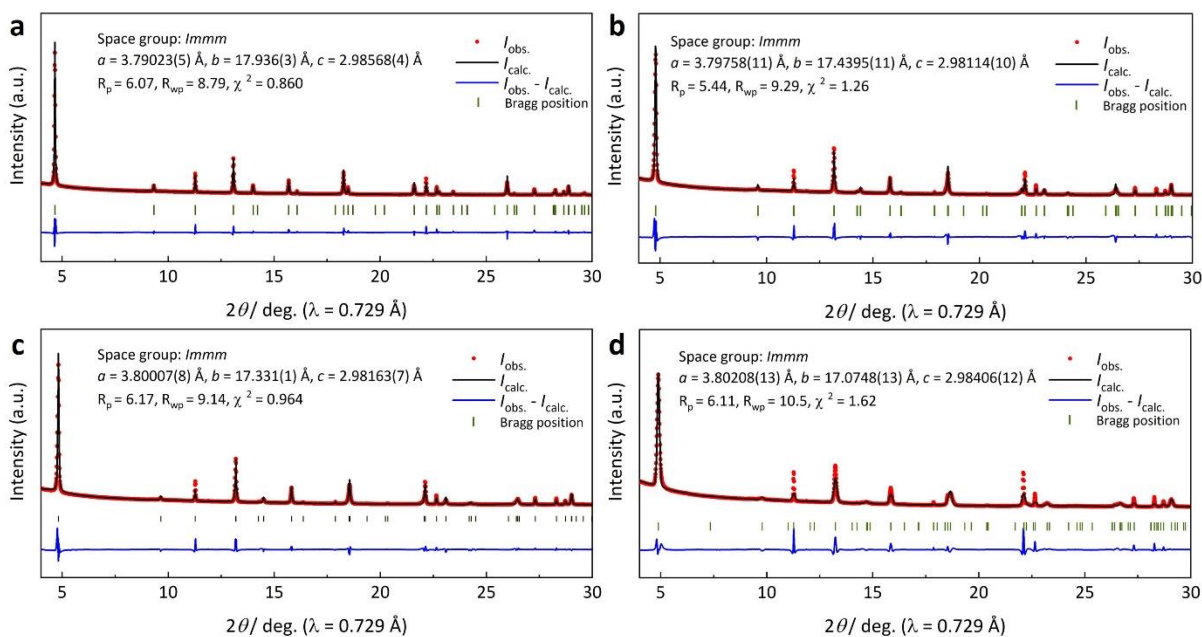


Figure 143. Le Bail fitting of X-ray diffraction (XRD) patterns collected at (a) room temperature, (b) 100°C, (c) 125°C, and (d) 150°C during the high-temperature synchrotron XRD measurement by adopting the *Immm* space group.

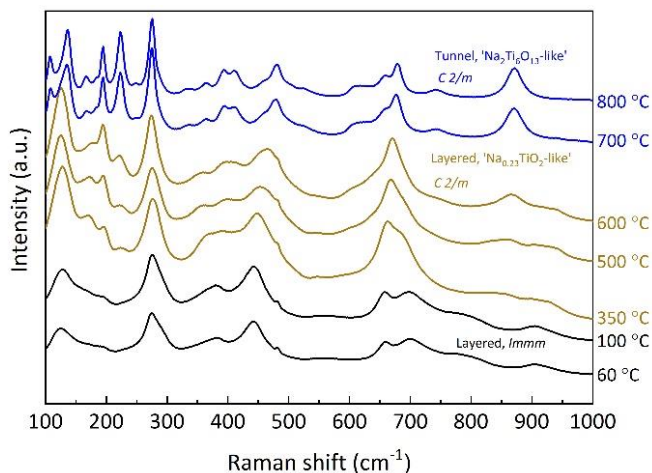


Figure 144. *Ex situ* Raman spectra of $\text{Na}_{0.74}\text{Ti}_{1.815}\square_{0.185}\text{O}_4 \cdot n\text{H}_2\text{O}$ heated in air at different temperatures.

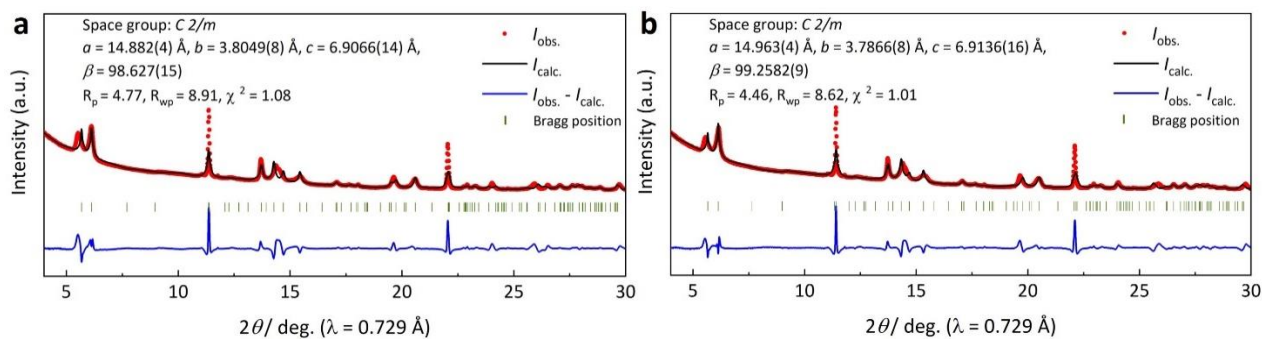


Figure 145. Le Bail fitting of X-ray diffraction (XRD) patterns collected at (a) 500 °C and (b) 600 °C during the high-temperature synchrotron XRD measurement by adopting the $C2/m$ space group.

Patents/Publications/Presentations

The project has no patents, publications, or presentations to report this quarter.

Task 7.4 – Electrolytes and Interfaces for Stable High-Energy Sodium-Ion Batteries (Phung M. L. Le, Pacific Northwest National Laboratory)

Project Objective. The Na-ion battery is a potential alternative energy source for EVs and grid applications due to the low cost and the natural abundance of sodium. The performance of Na-ion batteries largely depends on development of electrode materials and electrolytes. In recent years, a series of potential electrode materials has been developed. However, a fundamental understanding of the electrochemistry of Na-ion batteries, especially the stability of the electrode-electrolyte interface in these batteries, is still not well established. This project will develop innovative electrolytes to enable fundamental understanding on the interface between electrode and electrolyte for stable operation of high-energy Na-ion batteries. A high-capacity anode will also be developed. The proposed research will enhance the achievable capacities of both anode and cathode for Na-ion battery and improve the stability of electrodes/electrolyte interface, establish correlation (electrolyte design rule) between electrochemical performances of Na-ion batteries and the electrolyte/interface properties, and enable long cycle life and safe operation of high-energy Na-ion batteries.

Project Impact. This project will develop new electrolytes to enable long cycle life and safe operation of Na-ion batteries. If successful, the resulting improvements in energy, life, and safety will provide a solid contribution to the understanding of fundamental scientific questions and the development for Na-ion battery technology and promote its practical application as a competitive alternative to the current Li-ion batteries and greatly reduce the cost of energy storage systems for EVs.

Approach. This project will continuously optimize the electrolyte components and concentrations to develop innovative electrolytes and additives with improved electrochemical and physical properties. Ether-based electrolytes with different salts and additives will be optimized toward both anode [sodium metal and hard carbon (HC)] and cathode. Phosphate-based LHCE will be optimized to improve cycling performance of Na-ion batteries. SEI/CEI components of Na-ion battery in ether and phosphate electrolytes will be studied using XPS and SEM/TEM techniques to reveal the fundamental mechanism behind the improved stable performance of Na-ion batteries. Electrolyte additives in carbonate electrolyte will also be investigated to improve the electrochemical cathode performance. These approaches will unravel the origin of the SEI at the dynamic interface, providing guidance for the electrolyte and interface design and enabling high capacity and long life of Na-ion batteries.

Out-Year Goals. This project will select electrolyte compounds and identify formation of interfacial SEI layer on HC and CEI layer-on-layer oxide cathode and its effect on electrode materials. It will also provide guidance on electrolyte optimization and to improve CE of sodium deposition/stripping to be more than 99%.

Collaborations. This project will collaborate with leading scientists at ANL, LBNL, and other organizations in the field of cathode and anode materials for Na-ion batteries. It will also collaborate with C. Wang and M. Engelhard of PNNL for TEM and XPS characterization.

Milestones

1. Develop high-voltage electrolytes based on fluorinated solvent (≥ 4.2 V) to be compatible with high-voltage cathode material. (Q1, FY 2021; Completed)
2. Characterize CEI/SEI interphase properties in optimized electrolyte to probe the mechanism of high-voltage cycling stability of Na-ion batteries. (Q2, FY 2022; In progress)
3. Design new electrolytes to enable extremely high CE ($> 99.5\%$) of sodium stripping/plating process on different current collectors. (Q3, FY 2022; On schedule)
4. Investigate feasibility of anode-free sodium batteries using new electrolytes and $\text{Na}_3\text{V}_2(\text{PO}_4)_3$ cathode. (Q4, FY 2022; On schedule)

Progress Report

The team's target this quarter was to explore the underlying mechanism of electrochemical/chemical reaction at the electrode/electrolyte interface to correlate with the obtained electrochemical performance in the optimized electrolyte. Herein, they compare the electrochemical performance of three electrolytes: NaPF₆/EC:EMC (3:7 in vol) as the baseline carbonate electrolyte (named NaPF₆/EC:EMC), 1 M sodium bis(fluorosulfonyl) imide (NaFSI) / tris(2,2,2-trifluoroethyl) phosphate (TFP) (named NaFSI/TFP), and 1.5 M NaFSI/DMC:TFP (1.5:2 in mole or 1.6:8.4 in wt) as the advanced electrolyte (named NaFSI/DMC:TFP). As shown in Figure 146, the best with a carbonate electrolyte exhibits poor long-term cycling performance, while NaFSI/DMC:TFP electrolyte exhibited excellent cycling stability. In particular, the capacity retention is only 28.1% after 300 cycles (specific capacity of 154.3/43.4 mAh g⁻¹ for 4th/300th cycle). In contrast, the cell with optimized NaFSI/DMC:TFP electrolyte shows the best long-term cycling performance, with 94.8% capacity retention after 300 cycles (specific capacity of 153.2/145.3 mAh g⁻¹ for 4th/ 300th cycle). The initial CE is 84.49% in NaFSI/DMC:TFP electrolyte compared with 81.21% in NaPF₆/EC:EMC electrolyte, indicating less side-reactions with electrolyte during cycling.

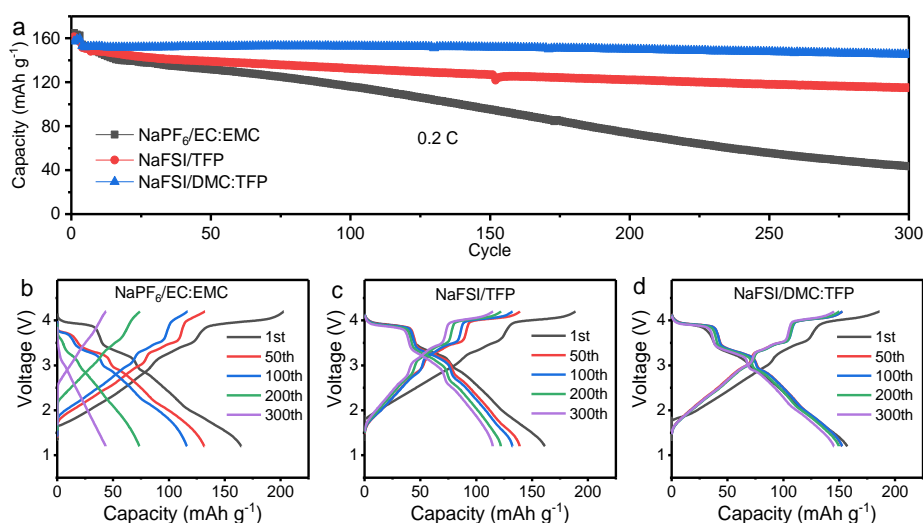


Figure 146. Electrochemical performance of hard carbon (HC) || NaNCM full cells. (a) Electrochemical stability window. (b) Cycling performance of HC||NaNCM full cells using different electrolytes cycled at 0.2 C after three formation cycles at 0.1 C. The cathode loading is 1.5 mAh cm⁻². (c–e) Voltage curves as a function of cycle number of HC||NaNCM full cells using NaPF₆/EC:EMC (c), NaFSI/TFP (d), and NaFSI/DMC:TFP (e) electrolytes.

To further explain the superior performance of NaFSI/DMC:TFP, the compositions and properties (that is, dissolution) of the SEI layer on cycled HC electrodes surface were analyzed. In a carbonate electrolyte, the preferential decomposition of carbonate solvent induces an organic-rich SEI layer. In a NaFSI/TFP electrolyte, SEI layer contains more F- and P- based components formed by the decomposition of TFP solvent. In a sharp contrast, both TFP solvent (strong fluorine 1s and phosphorus 2p peaks) and significant amount of NaFSI salt (high intensity of nitrogen 1s and sulfur 2p peaks) were decomposed in a NaFSI/DMC:TFP electrolyte and generated an inorganic-rich SEI layer.

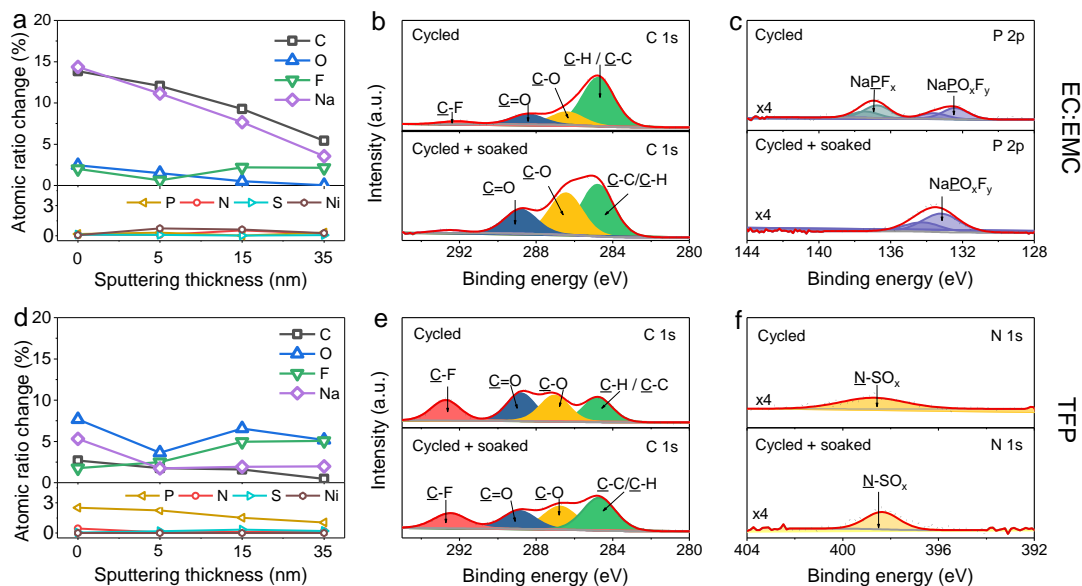


Figure 147. X-ray photoelectron (XPS) characterization to identify SEI dissolution. (a/d) The absolute value of difference of quantified SEI atomic composition ratios between the cycled and cycled-soaked hard carbon (HC) anodes as a function of the sputtering thickness. (b/e/f) XPS spectra of carbon 1s (b/e), phosphorus 2p (c), and nitrogen 1s (f) of the HC anodes (signal depth = 0 nm). The cycled HC anodes were cycled in NaPF₆ / EC:EMC (a; upper of b/c), NaFSI/TFP (d; upper of e/f) electrolytes for 100 cycles. The cycled-soaked HC anodes were soaking cycled HC electrodes with EC:EMC (a; bottom of b/c) and TFP (d; bottom of e/f) solvents for 50 hours.

The degrees of SEI dissolution are quantified by the XPS atomic ratio change (absolute value of atomic ratio difference between cycled and cycled-solvent soaked electrodes) of the SEI (Figure 147). The much lower atomic ratio change of SEI components after soaking in TFP solvent (Figure 147d) than that in carbonate EC:EMC solvent (Figure 147a) indicates excellent capability of TFP solvent to suppress the SEI dissolution due to its low dielectric constant. In high-resolution XPS spectra (Figure 147), there is obvious peak change of carbon 1s (Figure 147b) and NaPF_x peak disappearance (Figure 147c) after soaking in EC:EMC solvent, while minor intensity adjustment of carbon 1s (Figure 147e) and the same nitrogen 1s peak intensity (Figure 147f) before/after soaking in TFP solvent. Furthermore, atomic ratio change of salt derived components (N/S) are significantly lower than solvent decomposition derived components (C/P) in Figure 147d, proving the tuned SEI components from salt decomposition shows less solubility than solvent derived components, and emphasizing the necessity to tune SEI components.

Patents/Publications/Presentations

The project has no patents, publications, or presentations to report this quarter.

Innovation Center for Battery500 (Jun Liu, Pacific Northwest National Laboratory; Yi Cui, Stanford University)

Project Objective. The overall goal of the consortium is to increase the energy density of advanced lithium batteries to beyond what can be achieved in today's state-of-the-art Li-ion batteries. The Battery500 Consortium aims to increase the specific energy (up to 500 Wh kg⁻¹) and achieve 1,000 charge/discharge cycles, with cost reduction of the cells to significantly less than \$100 per kWh⁻¹. This goal directly addresses the DOE priority to achieve a carbon-free electricity sector by 2035 and to decarbonize the transportation sector by developing and manufacturing the next-generation, high-energy, low-cost batteries to enable a wide deployment of EVs in the marketplace.

Project Impact. Battery500 will develop next-generation lithium battery technologies that will significantly increase energy density, improve cycle life, and reduce cost. This will greatly accelerate deployment of EVs and reduce carbon emission associated with fossil fuel consumption. The consortium will utilize first-class expertise and capabilities in battery research in the United States and develop an integrated and multi-disciplinary approach to accelerate development and deployment of advanced electrode and electrolyte materials in commercially viable high-energy batteries. The advances made in this consortium will also benefit improvement of current Li-ion battery technologies. This project will provide tremendous opportunities for students and scientists for battery-related training that will enhance the workforce for the United States to maintain global leadership in the battery R&D field.

Approach. This project focuses on the two most promising battery chemistries: Li-metal anode with high-voltage/high-capacity metal oxide cathodes like LiNi_xMn_yCo_{1-x-y}O₂ (NMC), and lithium metal with sulfur cathodes. The project focus is to design novel electrode and cell architectures to meet the 500 Wh/kg goal. The consortium will work closely with battery/material manufacturers, suppliers, and end users / original equipment manufacturers in the United States to ensure the technologies being developed by this project are well aligned with industry needs, poised for transitioning to real production, and helpful in securing the supply chain in the United States.

Out-Year Goals. The out-year goals are to improve cycle life of the Li||NMC pouch cell with 400 Wh/kg energy density and more than 200 cycle life, and to fabricate and test the pouch cells with 450 Wh/kg energy density and cycle life of > 100.

Collaborations. Collaboration among consortium team members will be well coordinated by the leadership team, which also includes four keystone project leads and co-leads along with PIs at all member institutions. Collaboration with the community outside of this consortium and with industry will be facilitated by the executive committee and the advisory board.

Milestones

1. Complete synchrotron-based TXM studies on CEI interphase protection for NMC cathode cycled at high-voltage limit. (Q1, FY 2022; Completed)
2. Complete electrochemical AFM imaging in glovebox to study the nucleation of Li-metal anode during lithium plating. (Q2, FY 2022; Completed)
3. Complete Li-metal anode morphology studies by cryo-EM and modeling. (Q3, FY 2022; In progress)
4. Improve cycle life of Li||NMC pouch cell with 350 Wh/kg energy density with cycle life of > 800, and with 400 Wh/kg energy density with cycle life of > 200 . Fabricate and test pouch cells with 450 Wh/kg energy density and cycle life > 100. (Q4, FY 2022; In progress)

Progress Report

Keystone Project 1: Materials and Interfaces

Cathode Coating (Binghamton University)

The team has been pursuing their finding that niobium surface and bulk treatment of NMC-811 reduces the 1st cycle loss and improves capacity retention. Those studies treated commercial NMC with Nb-containing solutions followed by heating process in oxygen. For a commercially viable manufacturing process, this niobium treatment would be more practical if no additional step was involved. This quarter, the team added the niobium together with the lithium salt to an in-house synthesized 90%-nickel-content NMC. As shown in Figure 148, this niobium treatment is highly effective in improving capacity retention, but it does come with some loss of capacity. The M47 electrolyte from PNNL (right) gave improved capacity retention over the carbonate electrolyte. This improved behavior of the coated NMC-9055 can be associated with a significant suppression of impedance increase on cycling, as indicated in Figure 149.

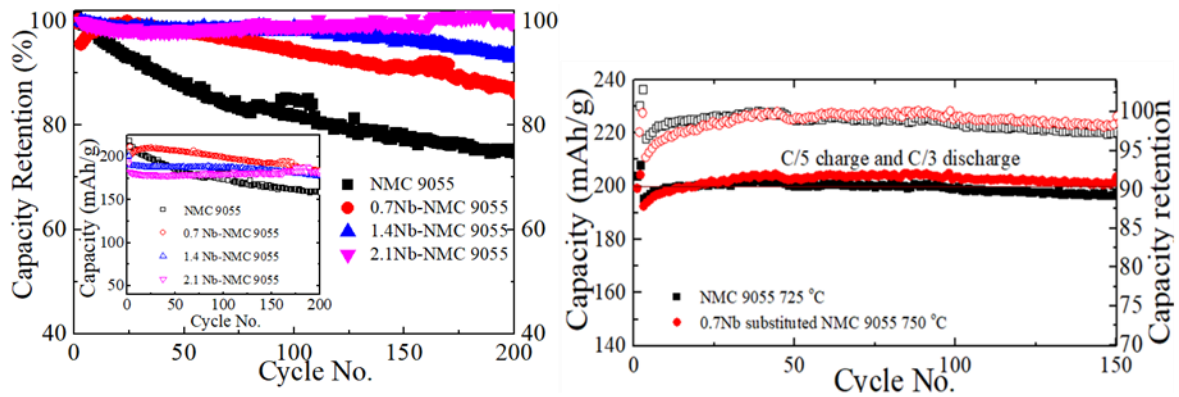


Figure 148. Capacity retention for NMC-9055 and Nb-coated/substituted NMC-9055. Cycling conditions: 2.8 V to 4.4 V, tap density 3.0 g/cm³, lithium foil as anode, (left) 1M LiPF₆ in EC/DMC, and (right) M47 electrolyte.

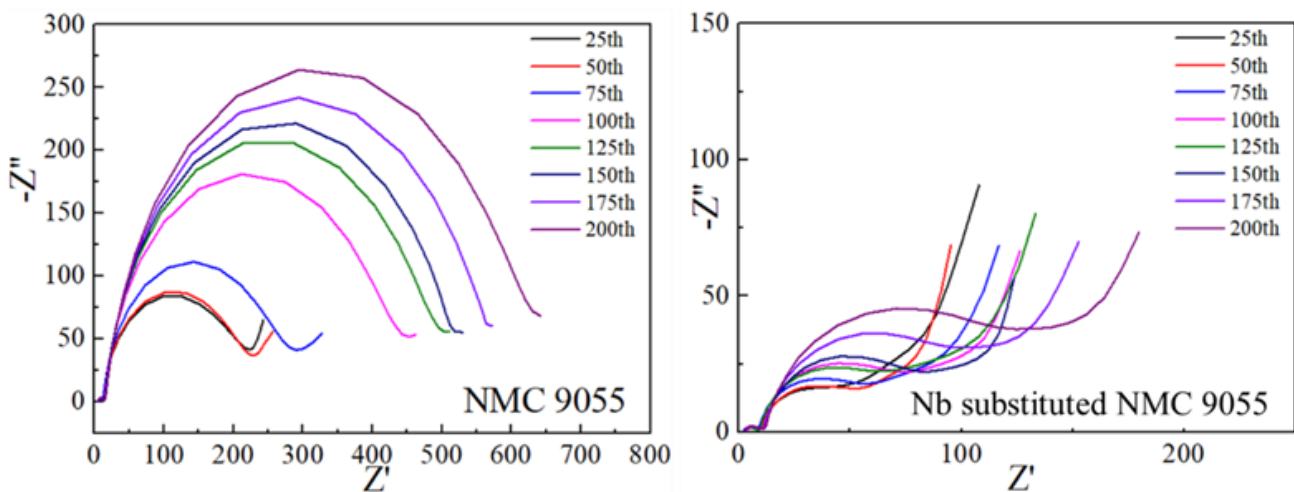


Figure 149. Evolution of the cell impedance of NMC-9055 and Nb-coated / substituted NMC-9055 during cycling in carbonate electrolyte.

Lithium Anode Coating (PNNL)

The team further evaluated an ionic conductive double-layer coating (DL-3) for Li-metal anode protection. Li-metal anode without coating was used as a baseline. Lithium was deposited at a current density of 2 mA cm^{-2} for a capacity of 4 mAh cm^{-2} using $75 \mu\text{L}$ DME-LHCE (LiFSI-1.2DME-3TTE) electrolyte in the Li||Li symmetric coin cells with a thin lithium foil ($50 \mu\text{m}$). To get the cross-sectional images of the Li-metal anodes after deposition, the UCSD team performed the cryo-FIB. The DL-3@Li shows a denser lithium layer with a bigger size of the lithium particles in the cross-sectional SEM image (Figure 150a) compared to the uncoated lithium which has a porous morphology with a larger amount of SEI layer between lithium particles, as shown in Figure 150b. In addition, the top-view image of the DL-3@Li displays a denser morphology than that of the bare lithium. Such a dense lithium deposition behavior at a high current density is proved to not only minimize the side reactions between lithium and electrolyte but also provide a uniform Li-ion flux through the ionic-conductive double-layer coating. Driven by the significant feature of the DL-3@Li, the team investigated the charge rate capability of the Li||NMC-622 cells. The charge current densities varied from C/10 to 1.5C ($1\text{C} = 4.6 \text{ mAh cm}^{-2}$), while a constant discharge current density of C/10 was used in these tests (Figure 150c). Because the DL-3 coating layer enables a uniform ion flux, the DL-3@Li has demonstrated an improved charge rate capability over the bare lithium. The DL-3@Li reaches a higher discharge capacity of 126.0 mAh g^{-1} after charging at 1.5C. This is much higher than that obtained in the case of bare lithium (94.3 mAh g^{-1}), as shown in Figure 150c. To further evaluate the increased ion transport of the DL-3@Li at a high current density, a galvanostatic intermittent titration technique (GITT) analysis was conducted. As shown in Figure 150d, the cell overpotential of DL-3@Li diminishes on repeated current stimuli [applied at a current density of 1.5C ($= 6.9 \text{ mA cm}^{-2}$) with an interruption time between the pulses of 2 hours]. The obtained internal cell resistances as a function of the state of charge are shown in the inset image of Figure 150d. Moreover, the DL-3@Li has a smoother deposition surface after charging at a current density of 1.5C (as shown by a green star in Figure 150c). In contrast, the bare lithium shows a porous morphology after being charged at similar conditions (Figure 150e-f). The charged DL-3@Li does not exhibit obvious interface between the fresh and the deposited lithium as depicted in the cross-sectional SEM image (Figure 150e). In contrast, charged bare lithium shows a huge volume change with significant interfacial cracking (Figure 150f). This indicates that the utilization of fresh lithium is reduced at a high current density when a bare lithium substrate is used. These results demonstrate that an optimized ionic conductive protection layer such as DL-3 can largely enhance the fast-charging capability of Li-metal batteries.

3D Host Lithium Anode (University of Washington, or UW)

In previous reports, the UW team systematically evaluated the 3D porous carbon as lithium hosts for high-energy rechargeable Li-metal batteries in different kinds of electrolytes. The results demonstrated that the nature of the electrolyte has a dominant effect on determining the CE and cyclability of Li-metal anode. This quarter, they have investigated the cycle performance of the copper foam as lithium hosts with three types of electrolytes: high-concentration electrolyte (HCE; LiFSI:DME = 1:1.2, by mol), LHCE (LiFSI:DME:TTE = 1:1.2:3, by mol), and fluorinated-1,2-diethoxyethanes electrolyte (F5DEE; 1.2 M LiFSI in F5DEE), which have been proved to show good compatibility with Li-metal anode. The team is trying to determine the optimum electrolyte composition for 3D hosts so that they can study the geometrical effect (that is, pore size and shape, tortuosity, specific surface area, etc.) in future studies.

Figure 151a shows the 10th charge/discharge curves of Li/Cu foam cells in the HCE, LHCE, and F5DEE electrolytes at 1 mA/cm^2 . The cell with F5DEE electrolyte shows the highest CE and the lowest overpotential, which can be attributed to the high ionic conductivity of the F5DEE electrolytes and the high efficiency of interfacial ion transport. The cycling performance of the Li/Cu cells in the HCE, LHCE, and F5DEE electrolytes is shown in Figure 151b. The cells using HCE and LHCE electrolytes need tens of activation cycles to ramp up to 99% CE. In contrast, the cell using F5DEE electrolytes exhibits a substantial improvement, with activation periods decreasing to around 10 cycles, indicating a robust and stable SEI is formed in the F5DEE electrolytes. Therefore, the optimal electrolyte for the 3D lithium host is found to be the F5DEE electrolyte, and they will study the geometrical effect of the 3D host in it to realize a high-energy-density lithium battery.

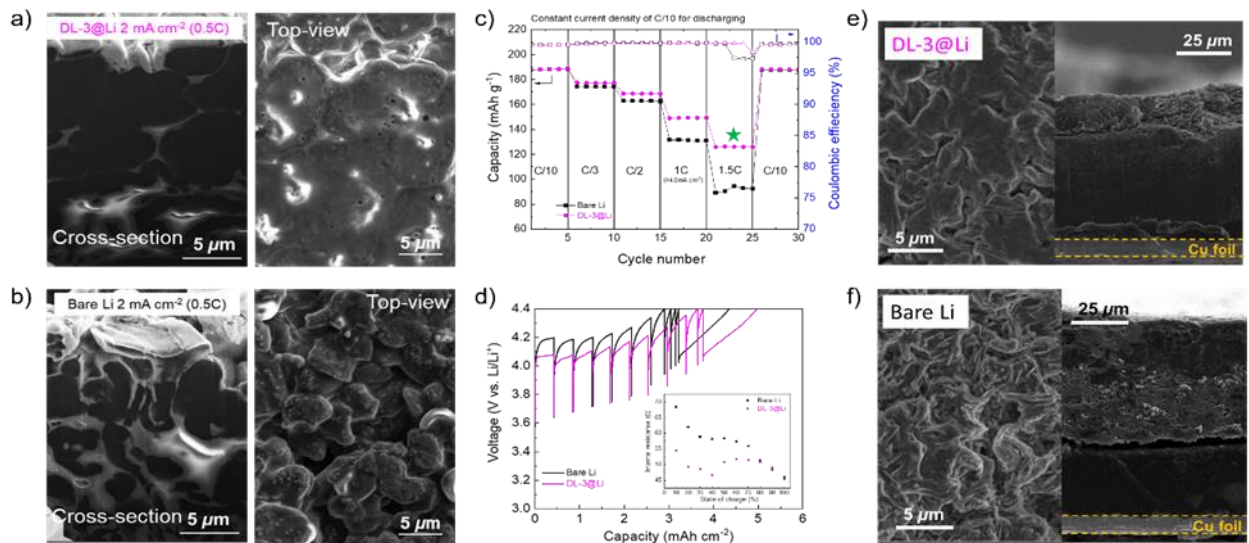


Figure 150. Cross-sectional and top-view scanning electron microscopy (SEM) images of (a) DL-3@Li and (b) bare lithium after deposition for a capacity of 4 mAh cm^{-2} at a current density of 2 mA cm^{-2} . (c) Charge rate capability of Li||NMC-622 cells at various charge current densities from C/10 to 1.5C ($1\text{C} = 4.6 \text{ mAh cm}^{-2}$) with the same constant discharge current density of C/10. (d) Galvanostatic intermittent titration technique profiles of Li||NMC-622 cells (4 mAh cm^{-2}) at a current density of 1.5C and variation in internal cell resistance as a function of state of charge. Cross-sectional and top-view SEM images of (e) DL-3@Li and (f) bare lithium after charging at 1.5C, as pointed out in panel (c).

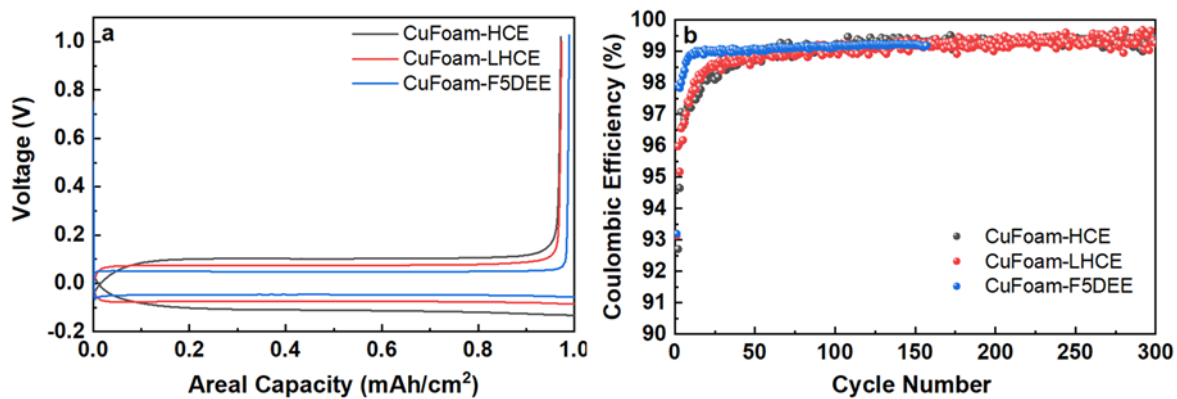


Figure 151. (a) The 10th charge/discharge curves and (b) Coulombic efficiency of Li/Cu batteries in high-concentration electrolyte, localized high-concentration electrolyte, and F5DEE electrolytes (at 1 mA cm^{-2} current density and 1 mAh cm^{-2} areal capacity).

New Electrolyte (PSU)

Last quarter, PSU researchers introduced the new novel Electrolyte C, achieving CE of 99.0%, which improved cycling performance as well as cell stability under practical conditions such as high-loading cathode NMC-811 (4 mAh.cm^{-2}), thin Li-foil (50 μm) anode, and lean electrolyte. To further demonstrate the superiority of this electrolyte, Li||NMC-811 coin cells were electrochemically evaluated between 2.8–4.3 V. After an SEI formation cycle at 0.1C, the Li||NMC-811 full cells were cycled at 0.2C for charge and 0.5 C for discharge in Electrolytes A, B, and C. All cells demonstrated similar charge/discharge voltage profiles during the formation cycle and delivered high discharge specific capacities of $\sim 210 \text{ mAh/g}$ (Figure 152a). As shown in Figure 152b, using baseline Electrolyte A, the cell decays fast and retains 80% of its original capacity after 40 cycles. In Electrolyte B, the cell shows improved cycling stability, surviving 140 cycles at capacity retention of 80%. In contrast, Electrolyte C enabled significantly improved cycling stability, delivering 80% capacity

retention after 246 cycles. The Li||NMC-811 full cells are further evaluated at an elevated temperature of 60°C, where the side reactions of electrolytes with the Ni-rich NMC-811 cathode and Li-metal anodes are more severe. Interestingly, the Li||NMC-811 full cell using Electrolyte C can still demonstrate good cycling stability with 86% capacity retention after 100 cycles (Figure 152c).

Furthermore, the EIS of the Li||NMC-811 full cells shows stable and reduced impedance using Electrolyte C, in contrast to the large and continuously increased impedance on cycling in both Electrolyte A and B (Figure 153a-c). The impedance increase is limited even after 150 cycles in Electrolyte C (Figure 153d). Collectively, these electrochemical evaluations indicate that Electrolyte C possibly contributes to forming robust interfacial layers on both Li-metal anode and NMC-811 cathode during cycling.

In conclusion, the newly developed Electrolyte C can significantly improve cycling performance of Li||NMC-811 coin cells. The EIS study reveals that Electrolyte C demonstrated the most limited impedance increasing over cycling, indicating stable interphase layers on both Li-metal anode and cathode surface. Detailed information about Electrolytes A, B, and C will be provided after publication of these results.

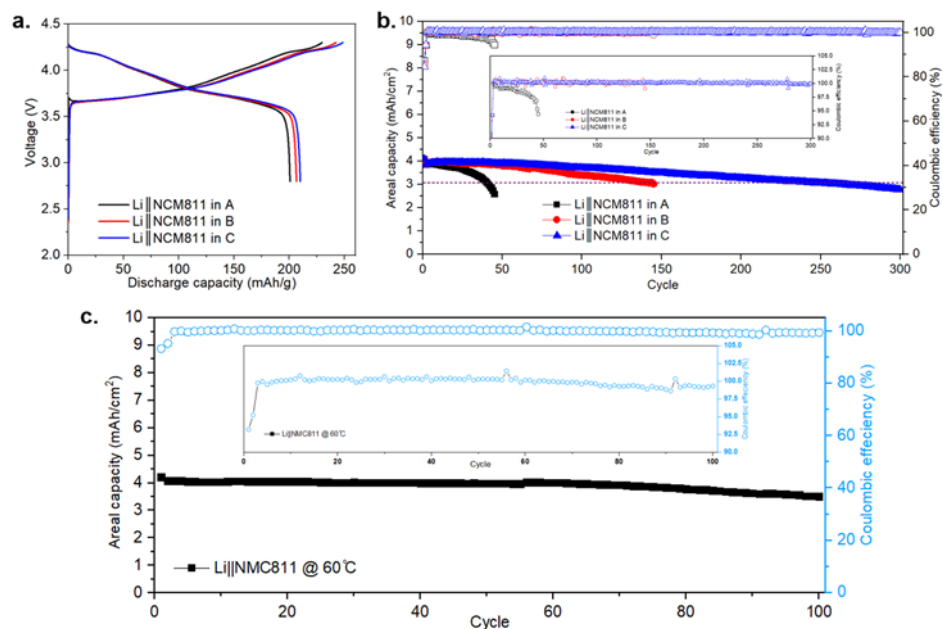


Figure 152. Electrochemical performance of Li||NMC-811 battery cells in Electrolytes A, B, and C between 2.8-4.3 V. (a) Initial voltage profiles of Li||NMC-811 coin cells at 0.1 C. (b) Cycling performance of Li||NMC-811 coin cells at 0.2C for charge and 0.5 C for discharge. (c) Cycling performance of Li||NMC-811 coin cells at 0.2C for charge and 0.5 C for discharge in Electrolyte C. 50- μ m Li-metal anode and 30 μ L of electrolytes were used. 1 C = 4 mA/cm².

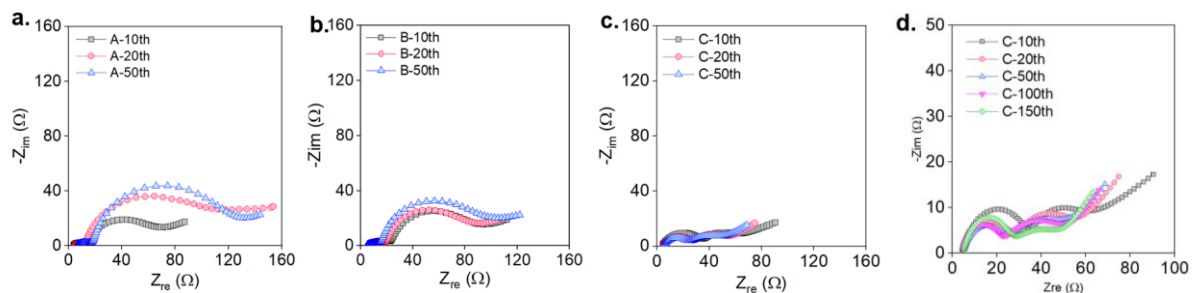


Figure 153. Nyquist plots of Li||NMC-811 coin cells in Electrolytes A, B, and C at different cycles.

High-Ni NMC (UT, Austin)

This quarter, to understand the intrinsic roles of cobalt, manganese, and aluminum dopants in high-nickel cathodes, the team synthesized a series of high-Ni cathode materials in-house, which are LiNiO_2 (LNO), $\text{LiNi}_{0.95}\text{Co}_{0.05}\text{O}_2$ (NC), $\text{LiNi}_{0.95}\text{Mn}_{0.05}\text{O}_2$ (NM), and $\text{LiNi}_{0.95}\text{Al}_{0.05}\text{O}_2$ (NA). Figure 154a illustrates that LNO, NC, NM, and NA display spherical morphology with a similar secondary particle size of $\sim 12 \mu\text{m}$. The structures of the cathode materials were characterized by powder XRD. As shown in Figure 154b, the four samples have a well-defined rhombohedral $\alpha\text{-NaFeO}_2$ structure ($R\bar{3}m$ space group) without any impurity phases detected.

As shown in Figure 154c, the electrochemical performances of the four materials are compared through a conventional way with a charging cutoff voltage of 4.4 V. The capacity retention of LNO, NC, NA, and NM is 76.9%, 77.3%, 81.5%, and 84.6%, respectively, after 150 cycles. Compared to cobalt, it is clear that aluminum and manganese are more effective in extending the cycle life of LiNiO_2 -based cathodes. However, as indicated by Figure 154d, such an increase in cycle life of NM and NA comes with a decrease in initial capacity values. With a lower capacity or SOC, the extent of surface reactivity and lattice distortion of high-Ni cathodes can be reduced and lead to better cycle life. Therefore, a critical question remains elusive: does the increased cycle life of NM or NA originate from the dopants or only from the decreased capacity? To clarify this, electrochemical tests on the four cathodes were performed with a cutoff energy density of 750 Wh kg^{-1} (Figure 154e), which incorporates both the capacity and voltage that can affect the cycle life. With the same cutoff energy density, increase in voltage and impedance growth are considered as evidence of fade as opposed to only capacity. In contrast to the conventional electrochemical tests based on a cutoff voltage (Figure 154c), the cycle life of cells based on cutoff energy density decreases in the order $\text{NC} \approx \text{LNO} > \text{NA} > \text{NM}$ with baseline LP57 electrolyte (Figure 154f) and $\text{NC} \approx \text{LNO} \approx \text{NA} > \text{NM}$ with LHCE (Figure 154g). This indicates that the extended cycle life of NM cycled between 2.8 V and 4.4 V might originate simply from a decreased capacity utilization or a lower degree of lithium extraction/insertion. Future work will focus on post-mortem experiments on the cycled cathode electrodes to unveil the real roles of critical dopants.

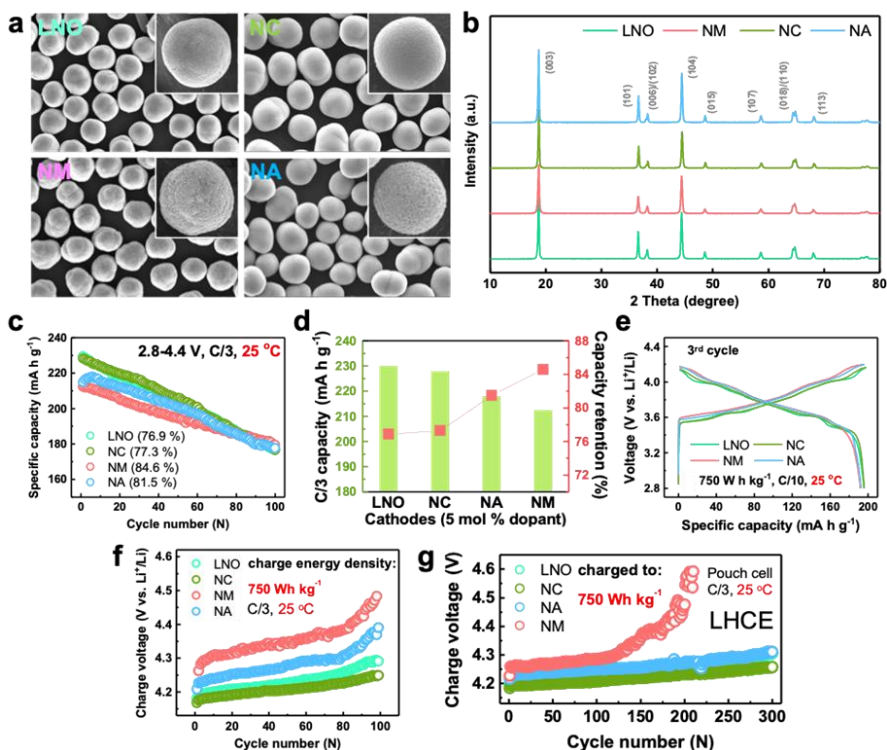


Figure 154. (a) Scanning electron spectroscopy (SEM) images and (b) X-ray diffraction patterns of LNO, NM, NC, and NA cathodes. (c) Cycling performances and (d) relationship between the specific capacities (C/3 rate) and cycle life (100 cycles) of LNO, NM, NC, and NA cathodes cycled between 2.8 V and 4.4 V. (e) Charge-discharge curves of LNO, NM, NC, and NA cathodes cycled with a cutoff energy density of 750 Wh kg^{-1} . Cyclability evaluation in (f) coin cells with baseline LP57 electrolyte for 100 cycles at a C/3 rate and in (g) pouch cells with a localized high-concentration electrolyte (LHCE) for 300 cycles at a C/3 rate with a cutoff energy density of 750 Wh kg^{-1} . The scale bars in (a) are $20 \mu\text{m}$. LHCE electrolyte in (g) consists of LiFSI, DME, and TTE with a molar ratio of 1:1.2:3.

Highlights of Keystone Project 1

The highlights for this quarter are as follows:

- The Binghamton team developed a new niobium treatment process by adding the niobium together with the lithium salt to an in-house synthesized 90%-Ni-content NMC. This niobium treatment is highly effective in improving capacity retention to reach as high as 95% capacity retention after 200 cycles for the 3.1Nb-NMC-9055 versus the 75% retention for untreated NMC-9055
- The PSU team developed a novel electrolyte achieving a CE of 99.0%, which improved cycling performance as well as cell stability under practical conditions such as high-loading cathode NMC-811 (4 mAh.cm⁻²), thin Li-foil (50 μm) anode, and lean electrolyte.

Keystone Project 2: Electrode Architecture

The goal of Keystone 2 is to design, model, fabricate, and characterize the effect of electrode architecture on electrode and cell performance in support of reaching the project goal of 500 Wh kg⁻¹ cell specific energy. Such studies include both high-capacity cathode materials such as high-Ni-content NMC and sulfurized polymer cathode, as well as Li-metal anodes. Highlighted in this report for Keystone 2 is unraveling the working mechanism for sulfurized polyacrylonitrile (SPAN) cathode (UCSD).

Unraveling the Working Mechanism for SPAN Cathode

Last quarter, J. Liu's group at UCSD characterized the impacts of synthesis temperature for the SPAN. The study shows that 450°C is the best synthesis temperature for SPAN as a cathode material in Li-metal battery. The 450°C synthesized SPAN not only ensures a high sulfur loading, but also suppresses the 1st discharge irreversible capacity loss. This quarter, in collaboration with Y. S. Meng's group at UCSD, Liu's group further characterized the correlations between the structure of SPAN and synthesis temperature. Liu's group also characterized the functional groups in SPAN and their impacts on the battery performance.

As shown in Figure 155, XPS and FTIR were applied for characterizing the structures of SPAN synthesized at different temperatures. In Figure 155a, the XPS nitrogen 1s peak shows that there are 3 nitrogen components, which are pyridine-N, graphite-N, and N-H, respectively. For sulfur, in the XPS sulfur 2p spectra, C = S, C-S, and S-S are the main sulfur components in SPAN (the additional S-O is due to surface oxidation of sulfur). In FTIR, the C-S peak can be deconvoluted into three components, indicating that the SPAN has three C-S species, which are the aromatic, non-aromatic, and bridging C-S bonds. As shown in Figure 155b, the synthesis temperature can impact the ratios of these functional groups. Figure 155c shows all of these functional groups and their molecular structures.

To further understand the roles of the components in SPAN as cathode material, several additional characterization tools had been applied by Liu and Meng's groups. First, the gas chromatography – mass spectrometry (GC-MS) analysis shows formation of H₂S during chemical lithiation of SPAN (Figure 156a). The team believes this mechanism is partially responsible for the 1st discharge irreversible capacity loss. In Figure 156b, the STEM-EELS results further probe this phenomenon. After the 1st discharge, even though the majority of sulfur is uniformly distributed in SPAN, a small amount has diffused into the super-P carbon, which might be a result of the formation of H₂S as well. In the STEM-EDS results, shown in Figure 156c, the non-uniform distribution of sulfur was also observed. After charging, this non-uniformly distributed sulfur disappeared. This can be attributed to the negative charge in the SPAN polymer matrix that would prefer to adsorb H₂S during discharge. After charge, the SPAN matrix is neutralized, thus the H₂S will be desorbed.

The sulfur 2p XPS spectra in Figure 156d show the bridging sulfur (S-S) disappeared after the 1st discharge and did not reappear after charge. The C-S bond intensity decreased, while a new component at lower binding energy appeared at ~ 162 eV. After charge, features of this new component disappeared while that of the

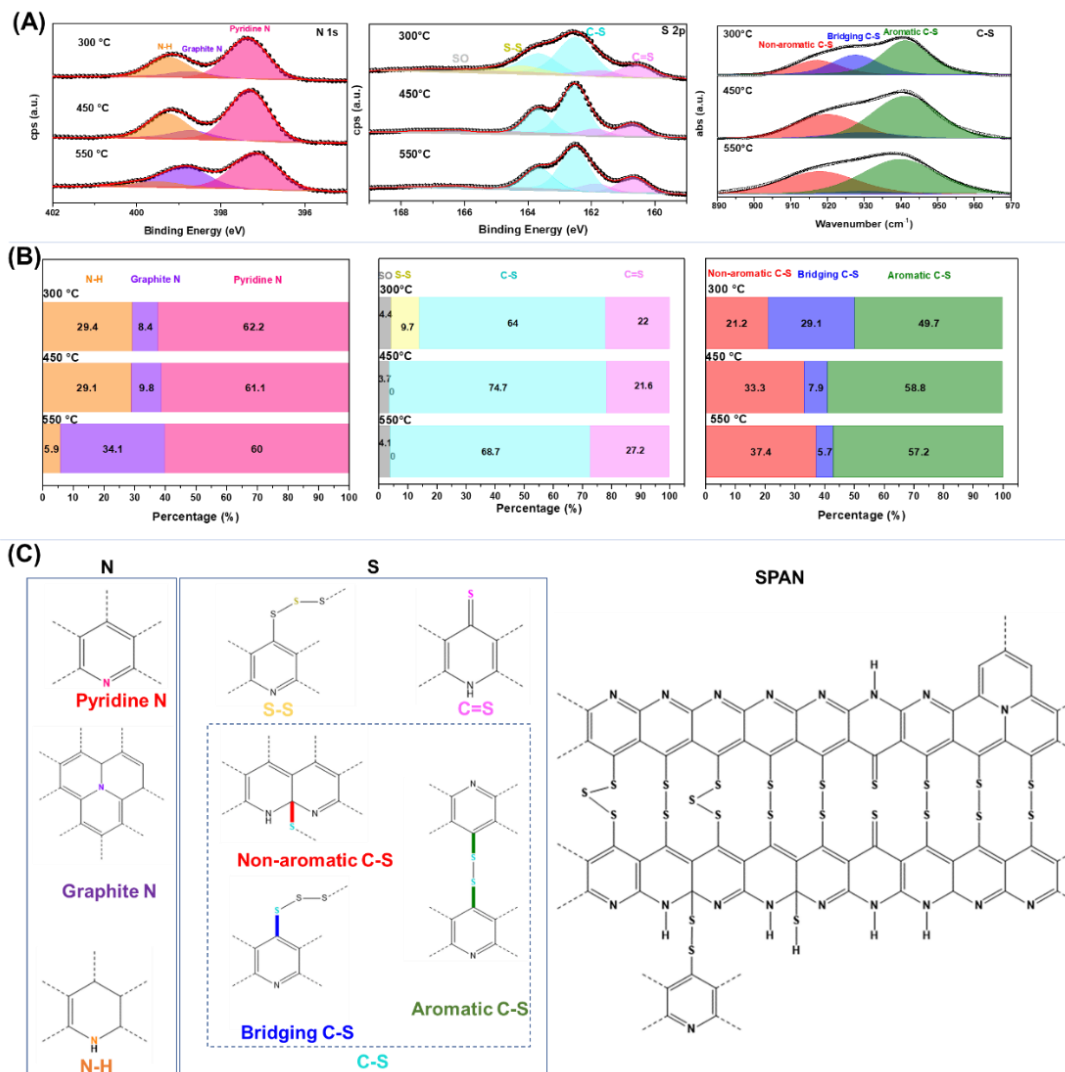


Figure 155. Functional groups and structure for sulfurized polyacrylonitrile (SPAN). (a) X-ray photoelectron spectra (XPS) for SPAN synthesized at different temperature. (b) Compositional ratio in SPAN derived from XPS results shown in (a). (c) Molecular structure of SPAN.

C-S component increases. The new component at 162 eV can be attributed to the C-S-Li, which is formed from the C-S bond capable of reversible reaction with lithium. However, as compared to the pristine SPAN, the relative intensity of C-S decreased after charge. Based on these observations, the irreversible sulfur loss might be associated with the loss of non-aromatic C-S and bridging sulfur species.

Regarding nitrogen, Figure 156e shows the disappearance of N-H on discharge. After charge, this component does not reappear. At the same time, the pyridine-N signal decreases during discharge and increases after charge. Since the chemical structure of pyridine is stable, this observation indicates that the pyridine-N might host lithium without any covalent bond formation.

Taking all these results into consideration, the team summarizes the role of each component in SPAN after the 1st discharge in Figure 156f, while Figure 156g shows the charge mechanism. In summary, aromatic C-S and pyridine-N in SPAN are the main contributors to the reversible capacity in SPAN, while other components are either involved in irreversible structural change and/or irreversible capacity loss.

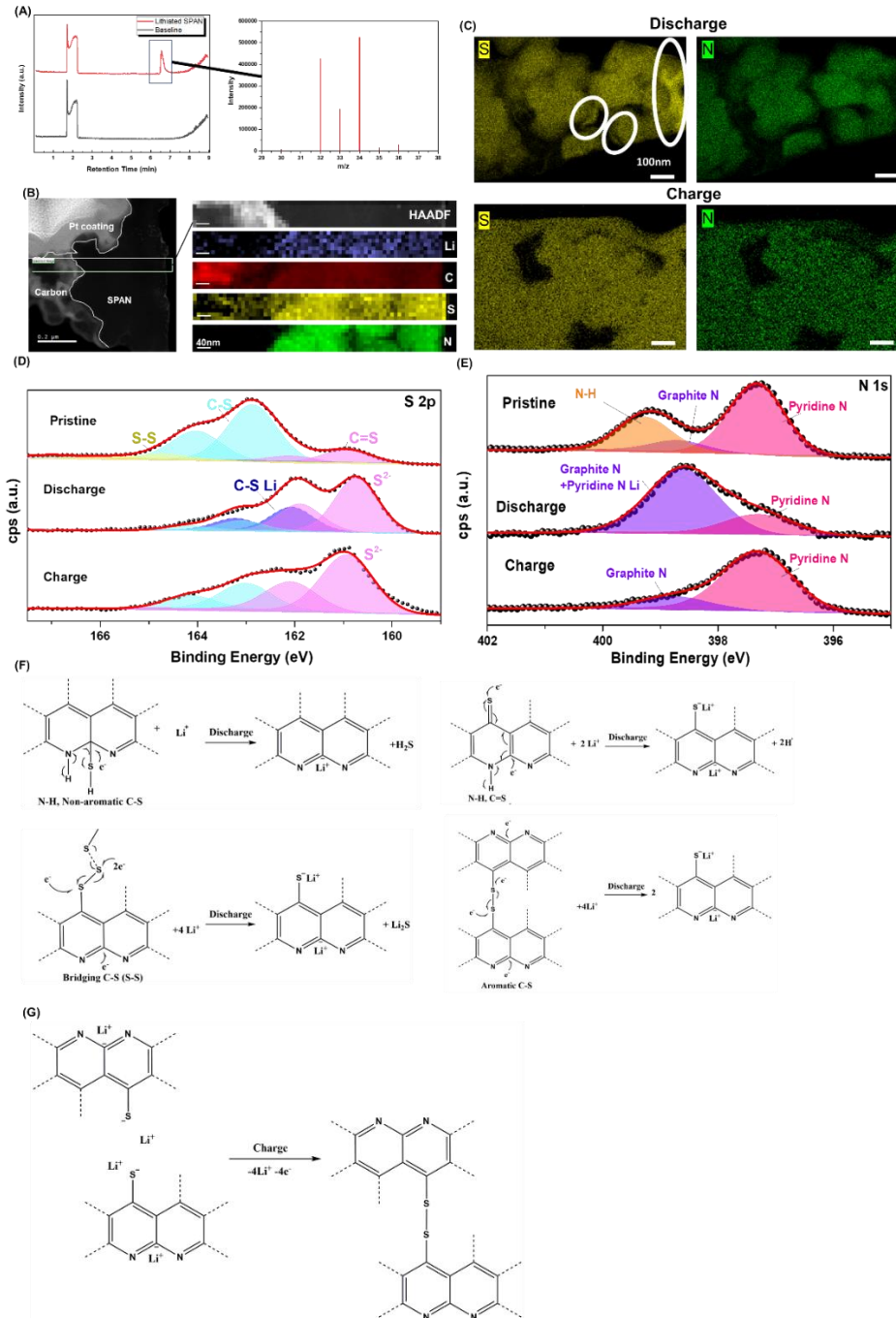


Figure 156. Roles of sulfur and nitrogen for sulfurized polyacrylonitrile (SPAN) cathode (SPAN:CMC:Super-P 8:1:1) in a Li-metal battery (a) gas chromatography – mass spectrometry of SPAN in the chemical lithiation solution. (b) Scanning transmission electron microscopy (STEM) – electron energy loss spectroscopy of the SPAN cathode after the 1st discharge in battery. (c) STEM – energy dispersive X-ray spectroscopy of the SPAN cathode after the 1st discharge and charge; X-ray photoelectron spectroscopy (d) sulfur 2p and (e) nitrogen 1s spectra for the SPAN cathode after the 1st discharge and charge. (f-g) Discharge and charge mechanism of the sulfur and nitrogen functional groups in SPAN.

Separator Coating (UW)

Progress this quarter relates to the $\text{Li}_4\text{Ti}_5\text{O}_{12}$ (LTO) coating on the anode side of the separator to improve the electrochemical performances of Li-metal batteries. Previously, the team demonstrated that $\text{Li}_{1.3}\text{Al}_{0.3}\text{Ti}_{1.7}(\text{PO}_4)_3$ (LATP) coating on the anode side of the separator has a beneficial impact on Li-metal anode cycling since the decomposition products at the Li|LATP interface are electronically insulative while ionically conductive.^[1] Compared to LATP, the spinel structured LTO has a stable structure and high ionic conductivity, as well as good compatibility with electrolytes, indicating its potential to homogenize lithium ions flux and stabilize the interface of the Li-metal anode.^[2] Here, the team reports on preparation of an LTO (~10 μm thickness) coated polyethylene (LTO@PE) separator via doctor blading and employed it in Li-metal batteries. In the Li|Cu half-cell, the CE is up to 99.4%, which is similar to the team's previous data using the PE separator, but the overpotential decreased.^[3] Furthermore, using LTO@PE in Li-metal full cell (50 μm Li|NCM-622) exhibits capacity retention of 94.4% after 130 cycles, which presents much higher cycle stability than that of using uncoated PE separator full cell.

In the first experiment of this study, the nano-sized (20 nm) LTO:PVDF with a ratio of 9:1 dissolved in 1-methyl-2-pyrrolidinone (NMP) solvent to make a slurry. The slurry was coated on one side of the PE separator via doctor blading. The thickness was controlled at ~10 μm . Then, the LTO@PE was dried under 60°C in a vacuum oven for 12 hours. Following, it was pouched in a diameter of 20 mm. The CE, cycle stability, and polarization voltage were evaluated in Li|Cu coin cell. The selected galvanotactic charge and discharge curves and CE versus cycle number are shown in Figure 157. During the initial discharge process, there is a voltage plateau at ~1.45 V versus Li/Li^+ , corresponding to Li-ion insertion into LTO frameworks. The initial CE was 67% and quickly jumped to 99% after about 20 cycles. The average CE was 99.4%.

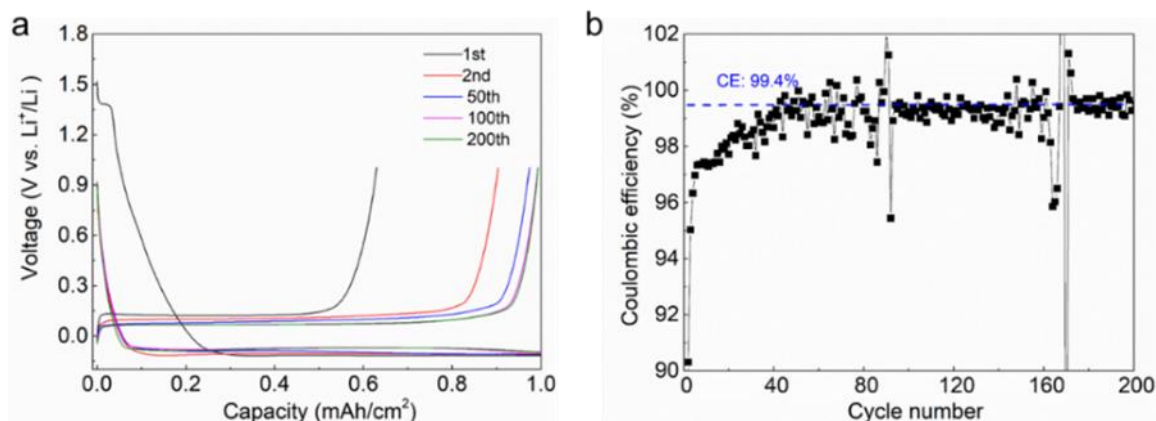


Figure 157. (a-b) Selected galvanotactic charge and discharge curves and Coulombic efficiency versus cycle number of Li|Cu coin cell using LTO@PE separator. The electrolyte is the 1.49 M lithium bis(fluorosulfonyl)imide (LiFSI) in a mixture of 1,2-dimethoxyethane (DME) and 1,1,2,2-tetrafluoroethyl-2,2,3,3-tetrafluoropropyl ether (TTE), with DME and TTE a molar ratio of 1.2:3. The deposition capacity is 1 mAh cm^{-2} at a current density of 1 mA cm^{-2} with a volume of 60 μL for each coin cell. In this testing procedure, a given amount of lithium metal is plated on a copper foil and then stripped off with a cutoff voltage of 1 V versus Li/Li^+ .

The electrochemical performance of 50 μm Li|NCM-622 (4 mAh cm^{-2}) full cells using the uncoated PE and LTO@PE separators is shown in Figure 158. The selected galvanotactic charge and discharge curves using the PE separator shown in Figure 158a indicate that the capacity is maintained at 4.7 mAh after 30 cycles at the rate of C/3 charge and C/3 discharge (the cell is still cycling). Figure 158b shows selected galvanotactic charge and discharge curves of the full cell using the LTO@PE separator under the same conditions. The capacity is maintained at 4.7 mAh after 130 cycles, corresponding to a 94.4% capacity retention rate (the cell is still cycling). The capacity versus cycle number graph shown in Figure 158c confirms the high stability of the full cell using the LTO@PE separator compared to the uncoated PE separator.

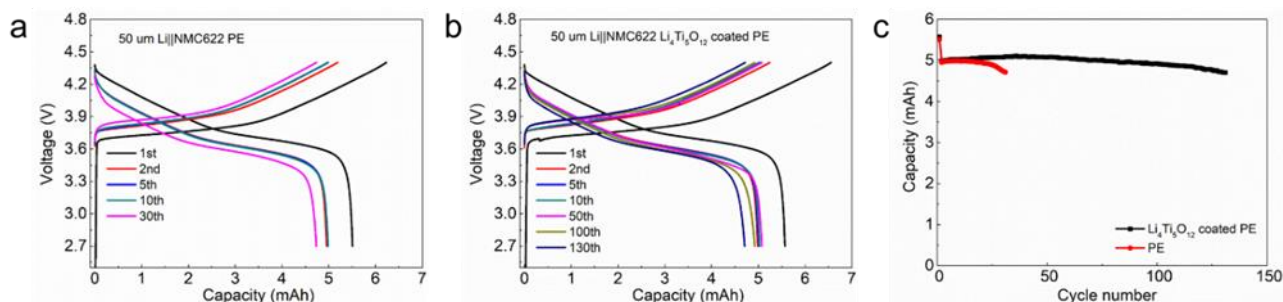


Figure 158. (a-b) Selected galvanostatic charge and discharge curves of 50 μm Li||NMC-622 (4 mAh cm^{-2}) full cell using polyethylene and LTO@PE separators. (c) Capacity versus cycle number of 50 μm Li||NMC-622 full cell. All cells were charged and discharged at C/10 for the 1st formation cycle and then cycled at a C/3 charge and discharge in the voltage window of 2.7–4.4 V. The electrolyte was localized high-concentration electrolyte, with a volume of 60 μL for each coin cell.

References

- [1] Yang, J., et al. “Battery Separator with Li-ion Conductor Coating.” International Patent Application No. PCT/US2019/037988, June 19, 2019.
- [2] Xiong, X., W. Yan, Y. Zhu, L. Liu, L. Fu, Y. Chen, N. Yu, Y. Wu, B. Wang, and R. Xiao. “Li₄Ti₅O₁₂ Coating on Copper Foil as Ion Redistributor Layer for Stable Lithium Metal Anode.” *Advanced Energy Materials* 12 (2022): 2103112.
- [3] Liu, Y., X. Wu, C. Niu, W. Xu, X. Cao, J-G. Zhang, X. Jiang, J. Xiao, J. Yang, M. S. Whittingham, and J. Liu. “Systematic Evaluation of Carbon Hosts for High-Energy Rechargeable Lithium-Metal Batteries.” *ACS Energy Letters* (2021): 1550–1559.

Computational Identification of Functional Catalysts for Li₂S₂ to Li₂S Conversion (University of Pittsburgh)

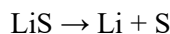
The team carried out theoretical modeling of Li₂S₂ to Li₂S conversion. Complete conversion of Li₂S₂ to Li₂S is of prime importance for the discharge process since the very sluggish kinetics of this reaction prevents full sulfur cathode utilization. The typical end products of the discharge process are Li₂S and Li₂S₂ mixtures giving greatly lower energy density and sulfur utilization opposed to pure Li₂S due to the high activation barrier of the conversion of Li₂S₂ to the desired final state of Li₂S. Thus, calculation of this barrier and identification of the appropriate electrocatalysts substantially decreasing or even leading to complete elimination of this activation barrier will result in efficient utilization of sulfur, leading to the desired high specific capacity and energy density of Li-S batteries.

Thus, the main aim of the present computational study is to identify functional catalysts that can decrease the activation barriers and promote fast conversion of Li₂S₂ to Li₂S during discharge and the backward reaction from Li₂S to Li₂S₂ during the charge process.

The overall transformation reaction for the *charge* process could be written as follows:



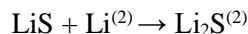
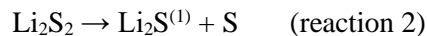
which will involve three possible elementary steps:



Similarly, for the *discharge* reaction path:



with the following corresponding elementary steps:



Out of these 6 elementary steps, reaction 1 and reaction 2 are the principal reactions, and will be considered in the present computational study

To obtain the thermodynamic properties, the DFT approaches implemented in VASP have been used, while a climbing image nudged elastic band (CNEB) method was utilized for determination of the activation energies and other pertinent kinetic parameters of the elementary reactions on the different catalytic surfaces.

The model of the functional catalyst consists of a surface slab with the most stable crystallographic orientation containing the attached Li_2S_2 or Li_2S molecules. The slab with a thickness of $\sim 5\text{-}7 \text{ \AA}$ is separated from its image perpendicular to the surface direction by $\sim 20 \text{ \AA}$ to avoid their mutual interaction. The bottom two to three layers of the slab are fixed with lattice parameters corresponding to the bulk state, while the remaining top layers along with attached polysulfide molecule are allowed to completely relax. All the species are adsorbed on the electrocatalyst surface including the lithium and sulfur atoms.

The activation barriers for the elementary reactions were estimated using the CNEB method, where five different intermediate points were chosen for calculations of the potential energy profile between the initial and final position of the Li-ion for the reaction 1 and sulfur atom for the reaction 2 at the electrocatalytic surface (totally 7 points).

All computations have been executed within the projector-augmented wave method and the generalized gradient approximation for the exchange-correlation energy functional in a form described by J. P. Perdew and Y. Wang implemented in VASP software. To maintain the high precision for all total energy and electronic structure calculations, the plane wave cutoff energy of 520 eV has been chosen. The relaxation procedure has been used to optimize the internal positions as well as the lattice parameters of atoms within the supercell. Also, the Monkhorst-Pack scheme has been used to sample the Brillouin zone and create the k-point grid for all catalytic surface slabs used in the current study. The selection of appropriate numbers of k-points in the irreducible parts of the Brillouin zone were made on the grounds of the convergence of the total energy to 0.1 meV/atom.

The calculated potential energy profiles are shown in Figure 159a for Reaction 1 and in Figure 159b for Reaction 2. One can see in Figure 159a that all the potential energy graphs for the Reaction 1 have similar profiles but with different energy values. For all considered materials in *discharge* direction (from right to left), the Reaction 1 is almost spontaneous without appreciable activation barrier and demonstrating only slight hump at the beginning (at the right side of the graph). This indicates that formation of Li_2S by grabbing Li-ion during discharge process does not hinder the overall kinetics of $\text{Li}_2\text{S}_2 \rightarrow \text{Li}_2\text{S}$ transformation.

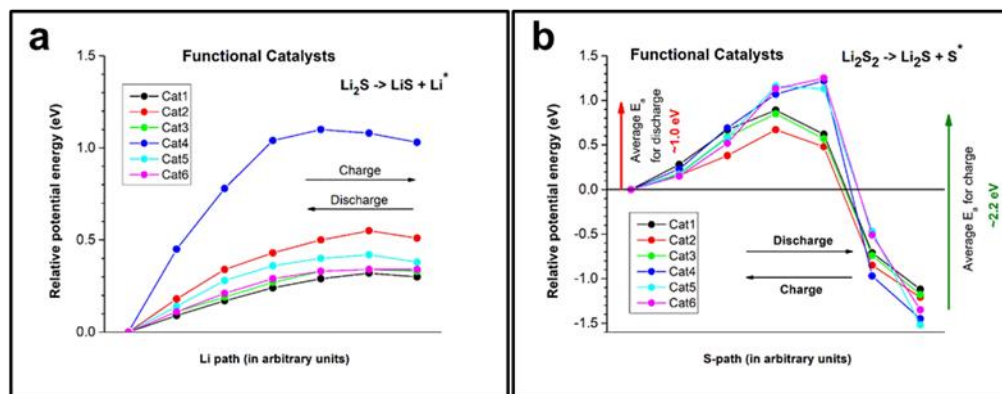


Figure 159. (a) Potential energy profile for Reaction 1 ($\text{Li}_2\text{S} \rightarrow \text{LiS} + \text{Li}$). (b) Potential energy profile for Reaction 2 ($\text{Li}_2\text{S}_2 \rightarrow \text{Li}_2\text{S} + \text{S}$).

Figure 159b demonstrates calculated energy profiles for Reaction 2, which is a decomposition of Li_2S_2 to form the end product, Li_2S and elemental sulfur. One can see that for all the probed materials Reaction 2 in the discharge direction is exothermic, as expected, with final product ($\text{Li}_2\text{S} + \text{S}$) being more energetically favorable compared to Li_2S_2 . However, in contrast to the Reaction 1, this reaction is not spontaneous with substantial activation barriers for different catalytic materials and averaged around ~ 1 eV. Due to this, the discharge process does not progress till the end product Li_2S is formed and stops at the Li_2S_2 stage, yielding only a half of the theoretical capacity value. Thus, the Reaction 2 could be considered as a rate determining step for the $\text{Li}_2\text{S}_2 \rightarrow \text{Li}_2\text{S}$ transformation and will be needed to be considered during computational screening of other potential functional catalysts to decrease or even eliminate this undesired activation barrier and, therefore, to improve the specific capacity and sulfur utilization of the Li-S batteries. These studies are under way.

Highlights of Keystone Project 2

The highlights for this quarter are as follows:

- UCSD demonstrated that the aromatic C-S and pyridine-N in SPAN are the main contributors to the reversible capacity in SPAN, while other components are either involved in irreversible structural change and/or irreversible capacity loss. These results were obtained through XPS and FTIR studies.
- UW carried out studies of using LTO coating on the anode side of the PE separator to improve the electrochemical performances of Li-metal batteries. The results show that a full cell using the LTO@PE separator was able to maintain 94.4% capacity after 130 cycles (the cell is still cycling), which is significantly higher than that using uncoated PE separator.

Keystone Project 3: Cell Fabrication, Testing, and Diagnosis

The GM team led the Li-S pouch cell sub-team including six university / national laboratory research teams. Since January 2022, a bi-weekly meeting has been scheduled for technical update of the sub-team. To help drive data consistency, the GM team provided S/C cathode to all sub-team institutions to serve as the baseline electrode for comparison with advances developed across each team's purpose. To complement the baseline electrodes, a corresponding testing protocol including component specification and testing condition/setup was also discussed, agreed on, and adopted for utilization across the sub-team.

At GM, non-destructive CT and ultrasonic transmission mapping equipment were installed, and an overall research plan was defined. These capabilities will allow the researchers to monitor lithium plating morphology and study the root causes of electrolyte degradation without tearing down the cells. At the same time,

C/S cathode formulation was optimized, and roll-to-roll coater parameter continues to be calibrated to improve the continuous double-sided coating uniformity and quality. GM was able to confirm larger batch coating quality of sulfur cathode electrodes using the roll-to-roll coater, as demonstrated in Figure 160, which shows the good electrochemical performance of cathodes with areal sulfur loading of 3.75 mgS/cm² and 5.2 mgS/cm². In addition, GM prepared a new batch coating for baseline samples and shipped out to all Li-S teams for performance verifications.

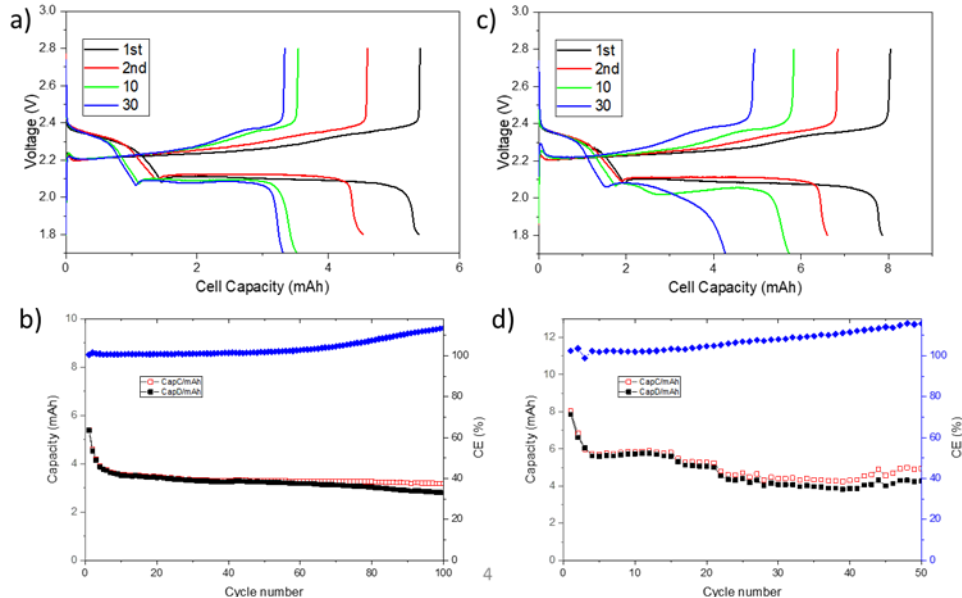


Figure 160. Electrochemical performance of sulfur cathodes with areal sulfur loading of (a-b) 3.75 mgS/cm² and (c-d) 5.2 mgS/cm².

A concept of “cycle life projection” (CLP) of rechargeable Li-metal cells has been reported by Idaho National Laboratory (INL) as part of the cross-platform comparison approach to evaluate cell performance reported by the Battery500 Consortium. This CLP approach can provide a verifiable and quantitative validation of the cycle life results from different team members in the consortium consistently and help establish a useful basis of comparison against the goal of achieving 1,000 cycles in a cell formulation and design with an “early prediction and assessment” capability. The principle and application of electrochemical analytic diagnosis (eCAD) for battery performance evaluation and failure analysis have been reported in the literature^[1-3] and illustrated in previous quarterly reports. Besides the unique capability for capacity fade analysis, recently the team also applied the eCAD technique to track lithium inventory as a new capability to quantify and qualify battery cell performance and efficiency. This approach requires a proper alignment of typical charge discharge voltage profiles with the lithium content in the cathode active material (CAM) and uses the well-defined “equilibrium open circuit voltage (OCV or V_{eq}) versus lithium content in CAM” relationship to evaluate the charge retention and lithium inventory changes during the charge discharge processes in the test.

Another important aspect of the eCAD approach is the ability to utilize a theoretical framework in the cross-platform comparisons. This aspect is somehow overlooked in past battery evaluation. Thus, a proper introduction of this framework is deemed necessary. The theoretical capacity (Q_{Th}) of the NMC composition can be calculated based on the lithium content in CAM. For NMC-622-based cells, $Q_{Th} = 276.5$ Ah/kg (or mAh/g) is obtained from the theoretical calculation based on the removal of one lithium from a fully lithiated NMC-622 stoichiometry. In general, Q_{Th} is rather constant across the entire $LiNi_xMn_yCo_zO_2$ composition, where $x+y+z = 1$, for example, from $Q_{Th} = 277.9$ Ah/kg for NMC-333 to $Q_{Th} = 275.5$ Ah/kg for NMC-811. Thus, using Q_{Th} as the basis for the cross-platform comparison is quite useful, as this method provides a reliable framework for performance evaluation, and this approach is insensitive to the formulations of CAM, electrode, cell, or configuration of the cell.

Figure 161 shows the data transformation process of the eCAD approach. Here, the formation cycle of a Li-NMC-622 coin cell is used as an example. The cell was charged and discharged between $V_{\min} = 2.5$ V and $V_{\max} = 4.5$ V at C/10 in the formation cycle. Figure 161a shows the charge-discharge voltage profiles, and with a proper determination of the IR potential of the cell, the corresponding IR-free voltage ($V_{\text{IR-free}}$) profiles in the formation cycle. The utilization of the NMC-622 capacity differs between the charge ($Q_{\text{ch}} = 198.1$ mAh/g) and the discharge segment ($Q_{\text{dis}} = 178.7$ mAh/g) with CE of 90.2% and a 1st cycle capacity loss of 19.4 mAh/g in the formation cycle. Also presented in the figure is the pseudo-OCV versus SOC profile determined from another Li-NMC-622 cell by averaging the charge and discharge voltage profiles at C/20 rate in the initial reference performance test (RPT 0) that has been validated in another experiment. The pseudo-OCV versus SOC curve has been demonstrated as a reliable and universal profile to align the $V_{\text{IR-free}}$ voltage profiles with the lithium content in the CAM consistently.^[1] Based on the RPT 0 results and the pseudo-OCV versus SOC curve, the capacity measured between 2.5 V and 4.5 V is $Q_{\text{pseudo-OCV (2.5-4.5 V)}} = 204.0$ mAh/g for NMC-622 cells. To understand the differences in the capacity utilization and the CAM utilization, the charge and discharge profiles are further analyzed by eCAD using the pseudo-OCV versus SOC curve, which has close agreement with the lithium content in the CAM. Comparing $Q_{\text{ch}} = 198.1$ mAh/g and $Q_{\text{pseudo-OCV (2.5-4.5 V)}} = 204.0$ mAh/g, hypothesizing that the difference is due to the CAM utilization, the charge profile could be corrected with the CAM utilization coefficient, which is considered as the ratio of $Q_{\text{ch}} / Q_{\text{pseudo-OCV (2.5-4.5 V)}}$; the resulting charge $V_{\text{IR-free}}$ profile is shown in Figure 161b. The same procedure was used for the discharge segment, and the discharge $V_{\text{IR-free}}$ profile is also shown in Figure 161b. The excellent agreement among the charge, discharge $V_{\text{IR-free}}$ profiles and the pseudo-OCV versus SOC curve in Figure 161b indicates the voltage profiles all aligned consistently with the lithium content in CAM. Once lithium content alignment was achieved, the capacity utilization of CAM in each polarization regime is clearly quantified in correspondence with the lithium content change in the CAM composition. In other words, the correspondence between the capacity utilization and the CAM utilization is clearly validated, as shown in Figure 161b. From this example, the CAM utilization coefficient can be expressed in a general term as

$$\text{CAM Utilization Coefficient} = Q_{\text{measured}} / Q_{\text{pseudo-OCV (} V_{\min} - V_{\max} \text{)}} \quad (1)$$

which is defined by the rate of the polarization and V_{\min} and V_{\max} in the test protocol.

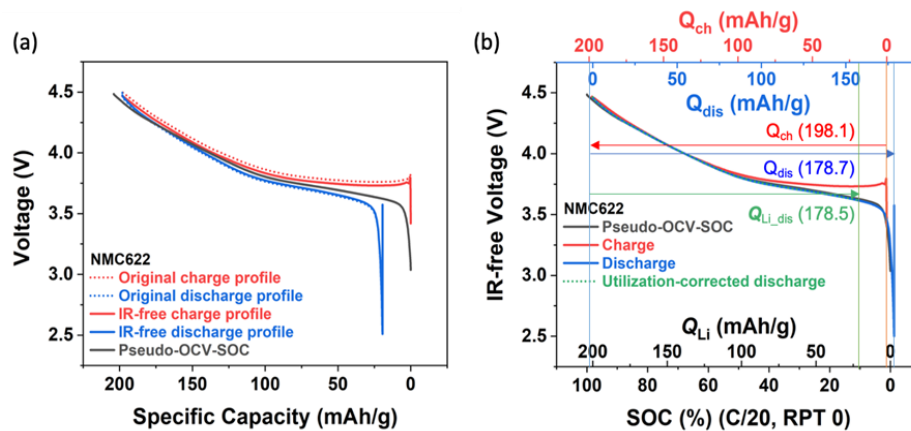


Figure 161. Analysis of the formation cycle of a Li-NMC-622 cell using the eCAD technique. (a) The charge and discharge voltage profiles and the associated infrared-free voltage ($V_{\text{IR-free}}$) profiles. Also presented is the pseudo – open circuit voltage versus state-of-charge (SOC) curve, which is obtained from a validated Li-NMC-622 cell during an initial reference performance test at C/20. (b) The reconciled charge and discharge $V_{\text{IR-free}}$ versus SOC profiles in correspondence with the lithium content in NMC-622.

Figure 162 shows the results of the cycle aging test on the Li-NMC-622 cell. The specific capacity of the cell from RPT 0 to RPT 2 is shown as a function of cycle number in Figure 162a. Based on the charge capacity retention over cycles, the useful cycle life (> 80% initial capacity) under cycle aging can be projected as shown in Figure 162b. Depending on the cycling rate, the capacity retention could exhibit different fade rate, so the

useful life projections could be rate dependent, as shown. The useful life projection based on the early fade rate is ~ 212 cycles for C/20, 209 cycles for C/10, 87 cycles for C/3, and 124 cycles for C/3, which was measured immediately after the C/20 charge discharge cycles in three RPTs. The C/3 cycles that came after RPTs represent scenarios of a long rest period for the cell to recuperate during the C/20 cycling in RPT. Using the eCAD analysis, the useful life projections are shown in Figure 162c based on the CAM utilization. Based on the same cutoff criterion for the end-of-life condition, the useful life projection for each rate is extended to a higher cycle number: 213 cycles for C/3, 259 cycles for C/10, and 371 cycles for C/20 in terms of the CAM utilization coefficient. It is quite well studied and accepted in the literature that the lithium diffusion and transport limitation in the NMC cathodes are the dominant factors that determine capacity.^[4-9] This cause also explains the origin of the CAM utilization fade even at the slow rate of C/20 if an insufficient rest period prevents CAM from full recovery of the lithium content in equilibrium because the lithium concentration gradient still exists or the inhomogeneous distribution of the lithium content in the bulk persists. If this hypothesis pertains to the observation, the useful life projection at C/20 by CAM utilization implies that the useful life will still suffer from this cause. As the rate increases, the severity of the useful life reduction from the same cause will amplify for C/10 and C/3.

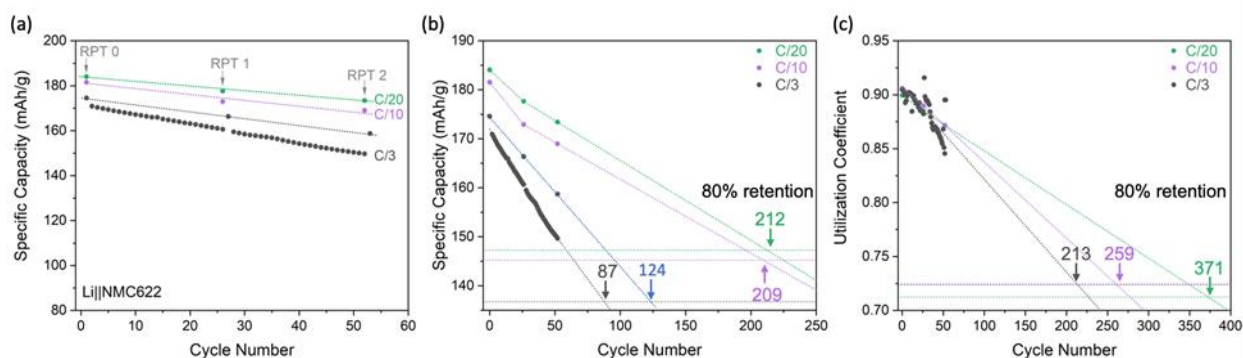


Figure 162. (a) Charge capacity retention curve of the Li-NMC-622 cell in the cycle aging test. (b) Projections of useful life based on charge capacity retention as a function of cycle number. (c) Projections of useful life based on the lithium inventory retention and cathode active material utilization as a function of cycling rate.

References

- [1] Zhang, Y., Q. Wang, B. Liaw, S. C. Nagpure, E. J. Dufek, and C. C. Dickerson. "A Quantitative Failure Analysis on Capacity Fade in Rechargeable Lithium Metal Cells." *Journal of The Electrochemical Society* 167 (2020): 090502. doi: 10.1149/1945-7111/ab6cf4.
- [2] Zhang, Y., Q. Wang, B. Liaw, S. C. Nagpure, E. J. Dufek, and C. C. Dickerson. "Cell Qualification—A Performance Metric-Based Approach." *Journal of Physics: Energy* 2 (2020): 034003. doi: 10.1088/2515-7655/ab979b.
- [3] Zhang, Y., R. Nguyen, and B. Liaw. "Status and Gaps in Li-Ion Battery Supply Chain: Importance of Quantitative Failure Analysis." *Special Issue on Electric and Hybrid Vehicles* (Invited), eds. T. Mi, et al. *Proceedings of the IEEE* 109 (2021): 1029–1038. doi: 10.1109/JPROC.2020.3047880.
- [4] Kasnatscheew, J., M. Evertz, B. Streipert, R. Wagner, R. K. Klopsch, B. Vortmann, H. Hahn, S. Nowak, M. Amereller, A-C. Gentschev, P. Lamp, and M. Winter. "The Truth about the 1st Cycle Coulombic Efficiency of LiNi_{1/3}Co_{1/3}Mn_{1/3}O₂ (NCM) Cathodes." *Physical Chemistry Chemical Physics* 18 (2016): 3956–3965.
- [5] Choi, J., and A. Manthiram. "Investigation of the Irreversible Capacity Loss in the Layered LiNi_{1/3}Co_{1/3}Mn_{1/3}O₂ Cathodes." *Electrochemical and Solid-State Letters* 8 (2005): C102–C105.
- [6] Zhang, S. S., K. Xu, and T. R. Jow. "Formation of Solid Electrolyte Interface in Lithium Nickel Mixed Oxide Electrodes during the First Cycling." *Electrochemical and Solid-State Letters* 5 (2002): A92–A94.
- [7] Lee, K.-K. and K-B. Kim. "Electrochemical and Structural Characterization of LiNi_{1-2y}Co_yO₂ (0 ≤ y ≤ 0.2) Positive Electrodes during Initial Cycling." *Journal of The Electrochemical Society* 147 (2000): 1709–1717.
- [8] Arai, H., S. Okada, Y. Sakurai, and J-I. Yamaki. "Reversibility of LiNiO₂ Cathode." *Solid State Ionics* 95 (1997): 275–282.
- [9] Zhou, H., F. Xin, B. Pei, and M. S. Whittingham. "What Limits the Capacity of Layered Oxide Cathodes in Lithium Batteries?" *ACS Energy Letters* 4 (2019): 1902–1906.

Highlights of Keystone Project 3

The highlights for this quarter are as follows:

- The GM team led the Li-S pouch cell sub-team including six universities and national laboratories. They provided S/C cathode to all sub-team institutions; a testing protocol including component specification and testing conditions was adopted across the sub-team.
- The INL team developed a method for useful life predictions using testing data from multiple cycling with different rates and eCAD.

Keystone Project 4: Cross-Cutting Efforts

The goal of the Cross-cutting team is to develop and deploy advanced characterization tools in support of the three Keystone efforts, with a focus on probing specific materials and interfaces for Keystone 1, probing individual electrodes for Keystone 2, and probing the whole cell for Keystone 3. This quarter, the Cross-cutting team completed a milestone to study electrolyte additive functionality on lithium and sulfur deposition on Li-metal anode using XRF imaging technology in Li-SPAN system (BNL and UCSD). SLAC/Stanford completed its milestone of electrochemical AFM imaging in glovebox to study the nucleation of Li-metal anode during lithium plating. Further computational studies of SEI properties have been carried out by Texas A&M. In an additional collaboration between these two institutions, it was demonstrated that changes in bonding in the non-crystalline SPAN cathode material can be followed using PDF methods. UCSD has also been developing characterization methods for quantifying the sulfur inventory in Li-S batteries; in separate studies, they have demonstrated that the rate of Li-metal corrosion is strongly dependent on its porosity.

Structural Changes of SPAN Cathode Cycled in Different Electrolytes Using PDF Methods

The BNL team (in close collaboration with UCSD) applied x-PDF characterization techniques to study the bulk structure changes of SPAN cathodes in Li-S batteries during cycling in different electrolytes. SPAN is a promising material due to the confinement of the small molecular sulfur in the conductive polymer network, capable of mitigating polysulfide shuttling. Carbonate electrolytes are widely employed for the Li-SPAN battery, exhibiting excellent chemical compatibility with the SPAN cathode. However, the use of carbonate-based electrolytes results in poor cycling stability with the Li-metal anode. On the other hand, ether-based electrolytes provide much more stable Li-metal anode cycling; the mixed solvent of DME and DOL has been employed in most Li-metal anode battery research, including Li-S batteries. It has been reported that DME/DOL-based electrolytes cause the dissolution of lithium polysulfides from the SPAN, and the resulting polysulfide shuttle effect typically cancels out any benefits offered by the usage of SPAN. Several prior unsuccessful attempts were made to improve the stability of SPAN in ether electrolytes by increasing the salt/solvent ratio or introducing additives. Recently, it was found by the Battery500 team at UCSD that LHCE not only efficiently passivates Li-anode surface, but also suppresses polysulfide dissolution in a dilute DME/DOL-based electrolyte. However, the effects of different electrolytes on the structural changes of SPAN during electrochemical cycling are not yet known and should be studied.

The UCSD team developed a new LHCE electrolyte that was used for this study and will be referred to as the UCSD electrolyte. The electrochemical performance of SPAN in UCSD electrolyte and in DOL/DME baseline electrolyte (1 M LiTFSI in DOL/DME) is compared in Figure 163. The areal capacity of the SPAN electrode is $\sim 1 \text{ mAh cm}^{-2}$. The volume of the electrolyte is 70 μL . SPAN shows stable cycling in the UCSD electrolyte at C/10 between 1 V and 3 V, consistent with previous reports. The electrode maintains a reversible capacity of $\sim 600 \text{ mAh g}^{-1}$ during the 50 cycles (Figure 163a). However, in the ether-based DOL/DME baseline electrolyte, the SPAN electrode does not cycle well. There is a long charge plateau at $\sim 2.4 \text{ V}$, indicating that the shuttling reaction of Li_2S_n takes place in this ether-based electrolyte, resulting in sulfur loss from the SPAN and low CE (Figure 163b). Long-term stability and CE comparison are shown in Figure 163c-d. A high

CE (~ 100%) and an excellent capacity retention of ~ 98.4% (based on the capacity of the 1st cycle) were achieved with the UCSD electrolyte. In contrast, the Li||SPAN cell with the DOL/DME electrolyte only delivered a capacity of ~ 355 mAh g⁻¹ at the 50th cycle, corresponding to low capacity retention of 39.6%.

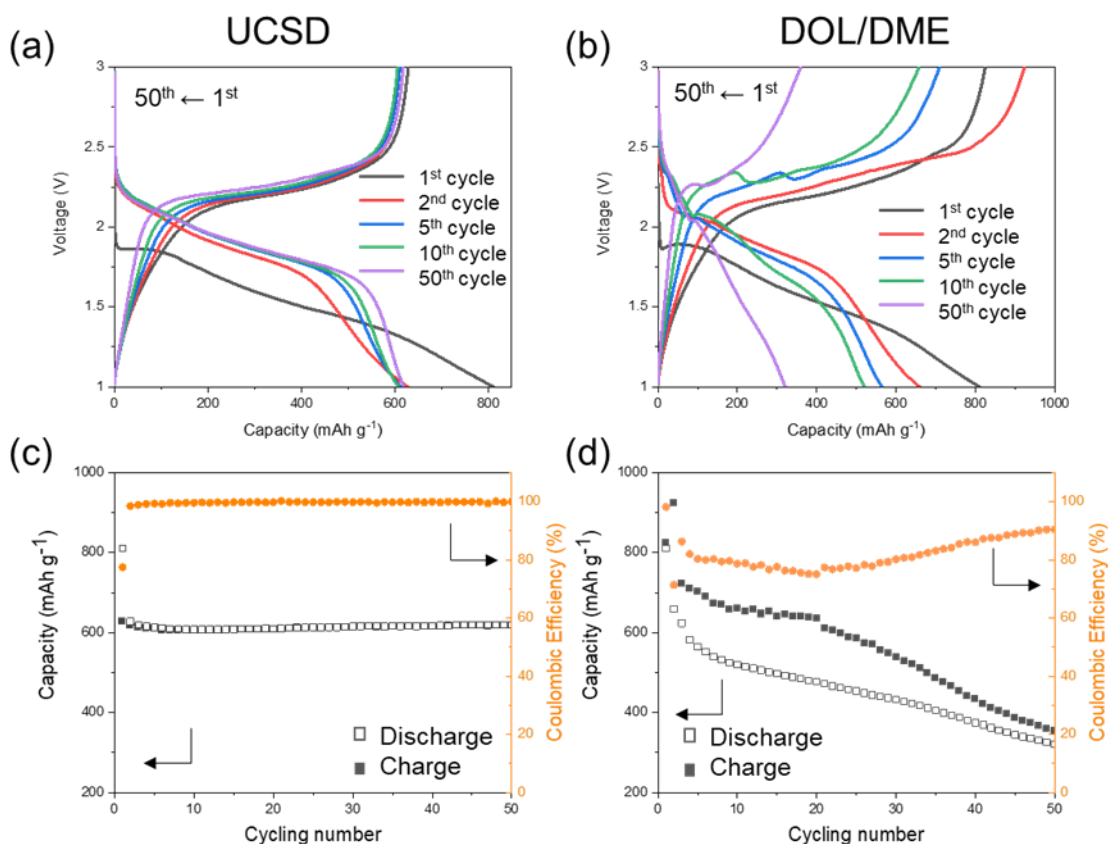


Figure 163. Galvanostatic charge and discharge voltage profiles of Li||SPAN coin cell across 50 cycles using (a) UCSD electrolyte and (b) baseline electrolyte: 1 M LiTFSI in DOL/DME. Cycling performance and Coulombic efficiency of Li||SPAN battery cycling in (c) UCSD electrolyte and (d) 1 M LiTFSI in DOL/DME electrolyte. Cells were cycled at C/10 (1C = 550 mA h g⁻¹).

The BNL team used x-PDF methods to study the structure changes of SPAN in different electrolytes, since it is an ideal tool for studying atomic pairs in non-crystalline solids and liquid. PDF is basically a histogram of all the atomic pairs whose corresponding peak intensity is weighted by the abundance of the pairs and the X-ray scattering power of involved atoms. In this manner, it was possible to directly monitor the evolution of bonds and interactions of interested atom pairs during electrochemical cycling in different electrolytes. Figure 164 shows the PDF data of pristine SPAN and SPAN after the 1st discharge, 1st charge, 2nd charge, and 50th charge, with an arrow indicating the peak corresponding to the C-S bond. The C-S peak shifted to larger r values after the 1st discharge (lithiation), which is likely caused by the C-S-Li interactions. These changes were reversible, with a return to the pristine distance after completion of the 1st charge. After 50 cycles, the C-S length for SPAN cycled in DOL/DME baseline electrolyte was slightly longer than after the 2nd cycle, while that for SPAN cycled in UCSD electrolyte was almost the same as after the 2nd cycle, indicating the better reversibility of SPAN cycled in UCSD electrolyte.

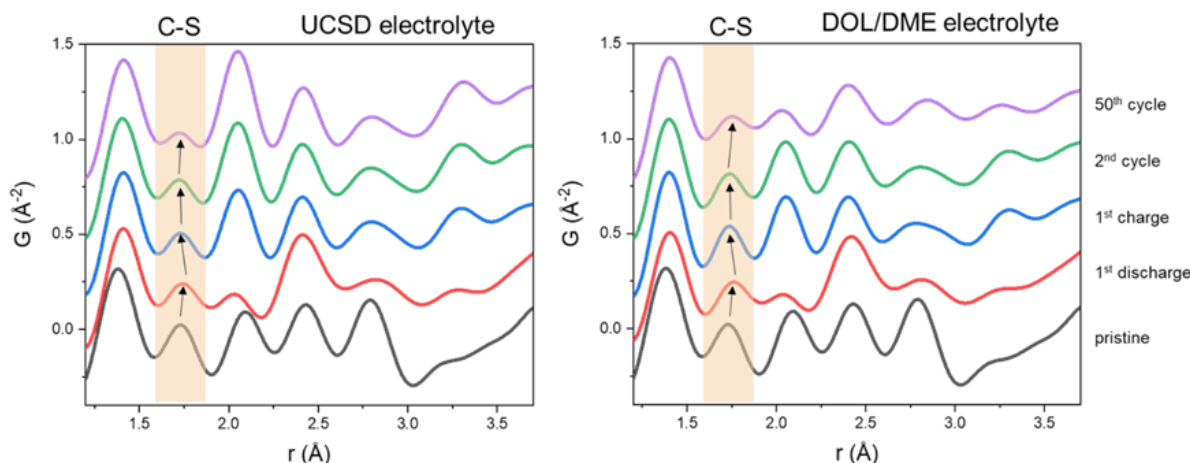


Figure 164. Pair distribution function results comparing SPAN structural changes during cycling in the UCSD electrolyte (left) and the DOL/DME electrolyte (right), with the peak corresponding to the C-S bond distance highlighted.

In addition to providing information about the C-S bond, the PDF data also provide information about the S-S bond changes that are central to the energy storage of this material (Figure 165a-b). For both electrolytes, the length of the nearest neighbor S-S bond [denoted (S-S)₁] increased after the first discharge, indicating the effects of lithiation (and the concomitant sulfur reduction) on the S-S bond length. In addition, a new peak ~ 3.3 Å appeared after the 1st cycle. This peak is assigned to the second nearest-neighbor sulfur-sulfur distance [denoted (S-S)₂], as illustrated in Figure 165c. Its appearance indicates that after 1st charge, the polysulfide chains of S₃ (or longer), which were not present in the pristine SPAN, were formed on electrochemical cycling, as illustrated in Figure 165d. In the 1st cycle, the breaking and reconstitution of (S-S)₁ bonds are mostly reversible for both UCSD and DOL/DME electrolytes, as indicated by the reversible (S-S)₁ peak intensity change. However, in the following cycles, the behavior of (S-S)₁ bond is very different between these two electrolytes. For UCSD electrolyte, the peak intensity of (S-S)₁ bond and (S-S)₂ remained strong during cycling, indicating well preserved sulfur inventory. In contrast, for DOL/DME baseline electrolyte, the intensities of (S-S)₁ peak gradually decreased after multiple cycling, suggesting the loss of sulfur. The peak intensity of the (S-S)₂ for second nearest-neighbor evolves similarly as (S-S)₁. For the UCSD electrolyte, the short sulfur chains of S₃ are likely preserved during cycling. However, for the DOL/DME baseline electrolyte, the chain experienced considerable loss, possibly due to sulfur inventory loss.

Based on the PDF results, a proposed C-S and S-S evolution pathway in the Li||SPAN cell is given in Figure 165d. In the pristine SPAN structure, there are C-S and S-S nearest-neighbor (S-S)₁ bonds. After the 1st discharge, formation of C-S-Li and breakage of the S-S bond contribute to the energy storage. During the charge process, the SPAN structure undergoes two pathways. Route 1 is the reversible S-S bond reformation, as demonstrated by intensity recovery of the (S-S)₁ peak. Route 2 is the C-S breakage and short sulfur chain (-S₃-) formation, causing the intensity decrease of C-S peak and appearance of the second nearest-neighbor (S-S)₂ peak with ~ 3.3 Å distance. Also, it should be noted that the appearance (S-S)₂ peak is at the cost of C-S breakage. For example, after the 1st charging process, lower intensity C-S peak is observed when using UCSD electrolyte, while a higher second-nearest-neighbor (S-S)₂ peak occurs. In contrast, when using the DOL/DME electrolyte, a higher C-S peak and lower second-nearest-neighbor (S-S)₂ signal is seen. These results provide valuable information about the C-S and S-S bonding changes, clearly demonstrating that synchrotron-based PDF is a powerful tool to study structural changes of SPAN during discharge-charge cycling.

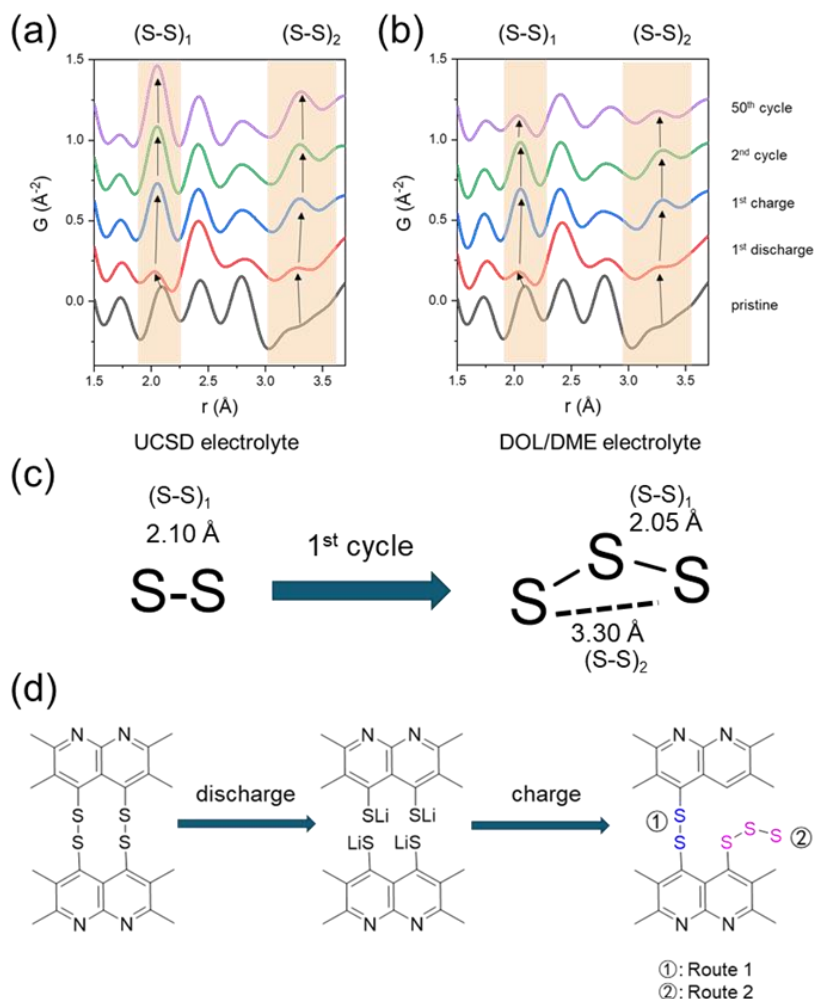


Figure 165. Pair distribution function results for S-S bonding changes while cycling SPAN (a) in UCSD electrolyte and (b) in DOL/DME baseline electrolyte. (c) Illustration of interatomic distances in S-S and S-S-S. (d) Proposed structural changes in SPAN during 1st cycle, providing insights into two different charge storage mechanisms.

Effects of LiNO₃ Additive on Morphology and Chemistry of Lithium SEI using XRF and XAS

The BNL team, in collaboration with PNNL and UCSD Battery500 consortium members, applied synchrotron-based XRF mapping and XAS to study the effects of a LiNO₃ additive on the morphology and chemistry of the Li-metal SEI. This was investigated in a Li||Cu coin cell for two electrolytes: the baseline electrolyte using 1 M LiTFSI dissolved in the solvents of DOL-DME (1:1 by volume), and with 1% LiNO₃ added to the baseline electrolyte. Figure 166a shows the lithium stripping plating capacity at the 10th cycle, indicating the electrolyte with LiNO₃ delivers substantially more capacity than that by the baseline electrolyte. Figure 166b compares the XRF results collected on the surface of copper at an excitation energy of 2482 eV. The field of view is $\sim 5 \text{ mm} \times 5 \text{ mm}$ with a spatial resolution of $\sim 30 \mu\text{m}$. As this energy is just above the sulfur K-edge, the fluorescence signal is proportional to the concentration of sulfur species. In general, the two SEIs formed in different electrolytes showed similar heterogeneity in the distribution of sulfur species in XRF maps. However, complementary XAS data that can reveal the specific sulfur oxidation state indicate there is a large difference between these two electrolytes. As shown in Figure 166c, the sulfur species in the SEI of baseline electrolyte are mostly in a reduced form, containing a considerable amount of polysulfides (2472 eV) and Li₂S (2476 eV). There are also some SO₃²⁻ and COSO₂⁻ species found. When LiNO₃ additive is used in the electrolyte, the sulfur species in the SEI become more oxidized. Polysulfides are mostly absent, and the Li₂S formation is strongly

suppressed. There is even some formation of sulfate species (2483 eV). These observations suggest that LiNO_3 changes the sulfur chemistry in the SEI due to the oxidizing capability of LiNO_3 . The removal of polysulfides and the suppression of Li_2S are believed to be beneficial for stable SEI and help to improve electrochemical performance.

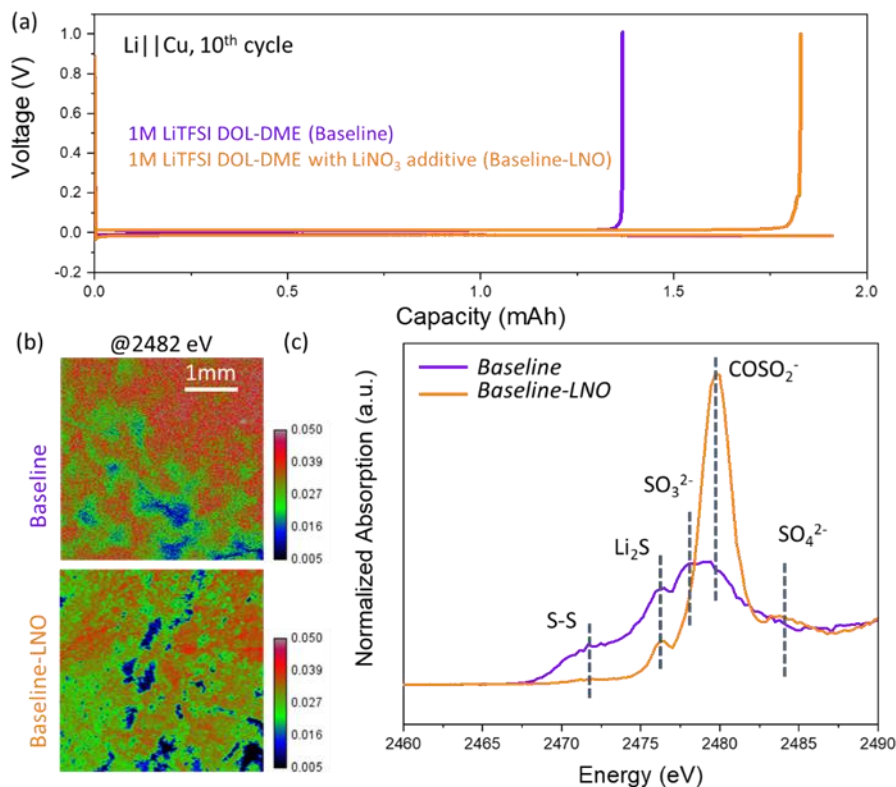


Figure 166. (a) Comparison of electrochemical performance for Li||Cu cell in baseline electrolyte with and without LiNO_3 additive. (b) X-ray fluorescence mapping of copper electrode after cycling. (c) X-ray absorption results of SEI from electrolytes with and without LiNO_3 additive.

The Texas A&M team has implemented a simulation method that combines CMD and AIMD to follow the evolution of the SEI in timeframes that go well beyond the AIMD capabilities while keeping the AIMD accuracy. In the new simulation scheme, AIMD is used to describe the localized electrochemical reactions, while CMD addresses the longer-range and longer-time chemical reactions in the electrolyte along with the mass transfer. In this way, the team has demonstrated the SEI morphology evolution as a function of salt concentration for LiFSI in DMC. One of the findings is the formation of a stratified morphology with well-defined regions of amorphous LiO_x (predominantly), LiF_x , and LiS_xN_y . Figure 167 illustrates the amorphous LiO_x SEI morphology found in 5 M LiFSI in DMC electrolyte. The effects of electrolyte/anode ratio and solvent chemistry on the SEI morphology and properties have been identified. It was found that the compactness of the amorphous Li-oxide phase has a maximum as a function of the electrolyte/anode ratio. The nature of the solvent also affects the SEI density due to the formation of wet or dry regions. The team expects these properties to affect Li-ion transport through the SEI. In a parallel study, they are investigating ion transport through a Li_2S film on lithium metal. They have detected ion and charge transport mechanisms occurring when reactions are taking place on the surface of the film-covered lithium surface. The main findings include spontaneous ion-hopping mechanisms driven by electron transfer from the lithium anode through the Li_2S SEI. Current work investigates the link between SEI morphology and chemistry with Li-ion transport mechanisms.

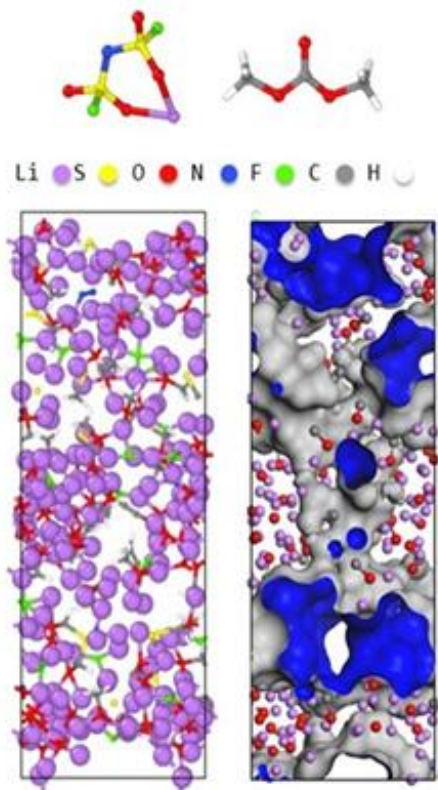


Figure 167. Evolution of SEI morphology at the Li-metal surface in 5 M LiFSI in DMC solution from *ab initio* molecular dynamics / classical molecular dynamics simulations. (left) Well-defined regions of amorphous lithium oxide connected by less dense regions of LiF_x and LiS_xN_y structures. (right) Blue and gray are outer and inner surfaces enclosing lithium oxide volumes.

Quantification of Lithium and Sulfur Inventory Loss in Li-S Batteries

Previously, Y. S. Meng's UCSD group developed an analytical method based on TGC to quantify inactive (dead) Li^0 in Li-metal batteries and to correlate lithium inventory losses with CE. It has been observed in Li-S batteries that drastic decay in specific capacity during cycling occurs along with the formation of soluble and insoluble polysulfides, but it has been hard to correlate their formation with the cycling CE. It is therefore crucial to quantify both the sulfur and lithium inventory losses during cycling and find key reasons for the capacity decay in the Li-S batteries.

High-performance liquid chromatography (HPLC) was used to differentiate and quantify each individual polysulfide species in the electrolyte, building on prior work by D. Qu in a BMR project. HPLC is an analytical technique widely used to quantify individual species in mixtures by separating them based on their polarity using a gradient of mobile phases. Through HPLC-UV, it is possible to quantify dissolved elemental sulfur and also to probe the distribution of derivatized polysulfides qualitatively. Additionally, it is possible to quantify the relative distribution of derivatized polysulfides using HPLC-MS. To quantify dissolved sulfur concentration in the electrolyte, HPLC-UV ($\lambda = 210$ nm) was first used to establish a calibration curve of elemental sulfur in DME (Figure 168a-b), which exhibited good linearity ($R^2 = 0.9998$). In-house standards consisting of elemental sulfur dissolved in DME were used for this purpose. Separate peaks for DME and sulfur could be observed when using pure methanol as the mobile phase.

Polysulfides are harder to analyze due to their metastable and dynamic nature. One approach is to use a derivatizing agent that does not change the distribution of these polysulfide species significantly but can instead stabilize them in the solution so that individual derivatized species can be quantitatively probed. In-house mixtures of polysulfides were made by mixing elemental sulfur and Li_2S in DME. Methyl triflate was then used to derivatize a small amount of the diluted polysulfide mixture. These species were later analyzed using HPLC-UV at $\lambda = 230$ nm (Figure 168c), and peak assignments were made based on prior literature. The team used a gradient of water and methanol for better separation of derivatized polysulfides. It was found that the retention time of different derivatized polysulfides had a nearly logarithmic dependence on the number of sulfur

atoms in the chain (Figure 168d). These results demonstrate that the separation of polysulfides in the mixed solution through HPLC-UV is possible. Next quarter, these methodologies will be further developed to quantify the concentration of each individual polysulfide species in the mixed solution.

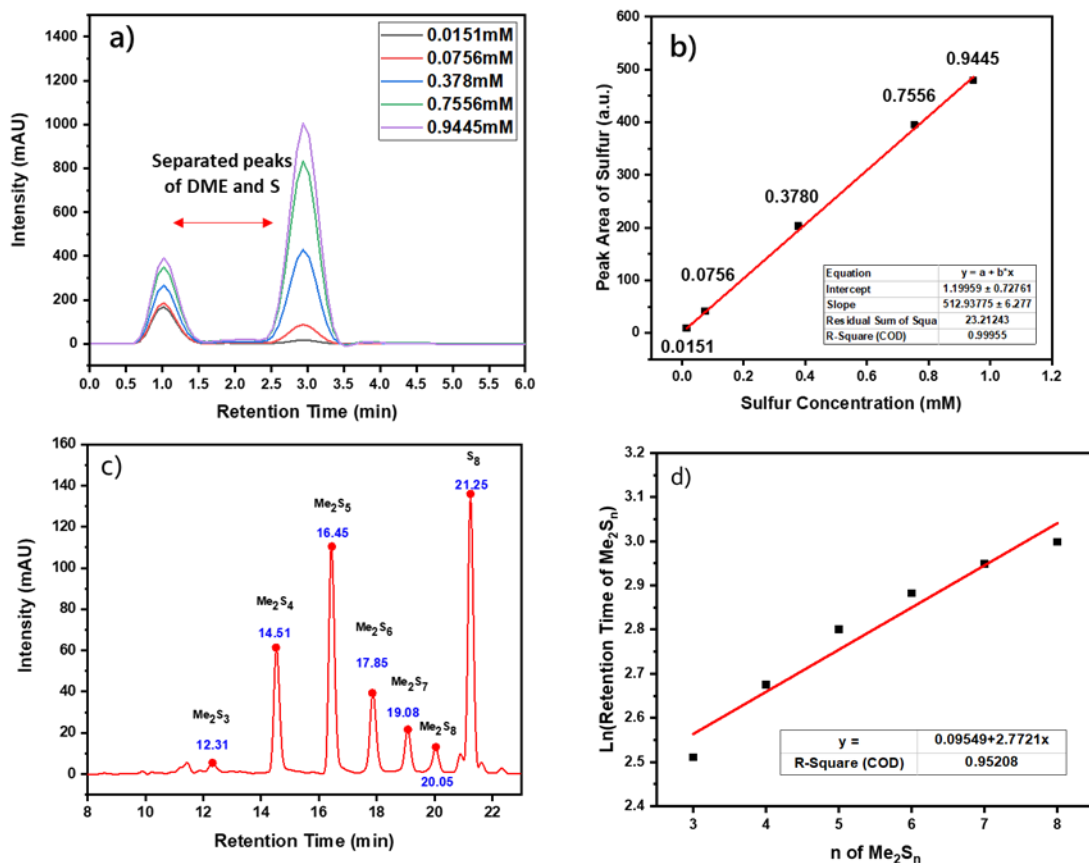


Figure 168. (a) High-performance liquid chromatography – ultra violet (HPLC-UV) chromatograms of five different standards of elemental sulfur in DME: 0.0151 mM, 0.0756 mM, 0.378 mM, 0.7556 mM, and 0.9445 mM. (b) Calibration curve obtained by plotting the area under the sulfur peak in HPLC-UV chromatogram against the sulfur concentration. (c) HPLC-UV chromatogram of derivatized polysulfides using methyl triflate as a derivatization agent. (d) Plot of logarithm of retention time of a particular derivatized polysulfide against the number of sulfur atoms in it.

Last quarter, Meng's group found that the porosity of plated lithium plays a major role in controlling the corrosion rate of lithium in LEs. When optimized stack pressure is applied during the lithium plating process, nearly 100% dense lithium is achieved, even with Gen 2 electrolyte (1 M LiPF_6 in EC:EMC). The dense lithium exhibited slower corrosion than porous lithium when resting in electrolyte. This quarter, the effect of porosity on the corrosion rate of lithium was further explored.

To test if the lithium electrode porosity is the dominating factor of corrosion rate, the team selectively deposited lithium in Gen 2 electrolyte under a range of stack pressures, allowing the controlled deposition of lithium with systematically varying porosities. Pressure control was accomplished using a split cell together with a pressure sensor. Cryo-FIB/SEM was used to obtain a 3D reconstruction of the plated lithium and to determine its porosity (Figure 169). With an optimized stack pressure of 350 kPa, the deposited lithium has a porosity of only 0.68%. On decreasing the stack pressure to 250 kPa, 150 kPa, and 50 kPa, the resulting lithium has porosities of 8.6%, 37%, and 44%, respectively. After measuring the porosity of the different lithium samples, the as-plated lithium was then immersed into the Gen 2 electrolyte for three weeks. The Li^0 mass loss was used to calculate the corrosion rate of the lithium using the equation $R = \Delta m / (A_s T)$, where Δm is the change in mass, A_s is the electrode area, and T is the corrosion time. As shown in Figure 169e, the lithium corrosion rate directly correlates with the porosity of the plated lithium. These results further validate the team's hypothesis that the

porosity of the plated lithium is the major factor in determining the lithium corrosion rate. It can be concluded that the lithium corrosion only takes place at the interface between lithium and the electrolyte. If the porosity of the lithium can be strictly controlled, the corrosion of lithium should also be largely mitigated. Next quarter, the role of surface chemistry in the corrosion of lithium metal will be studied in detail.

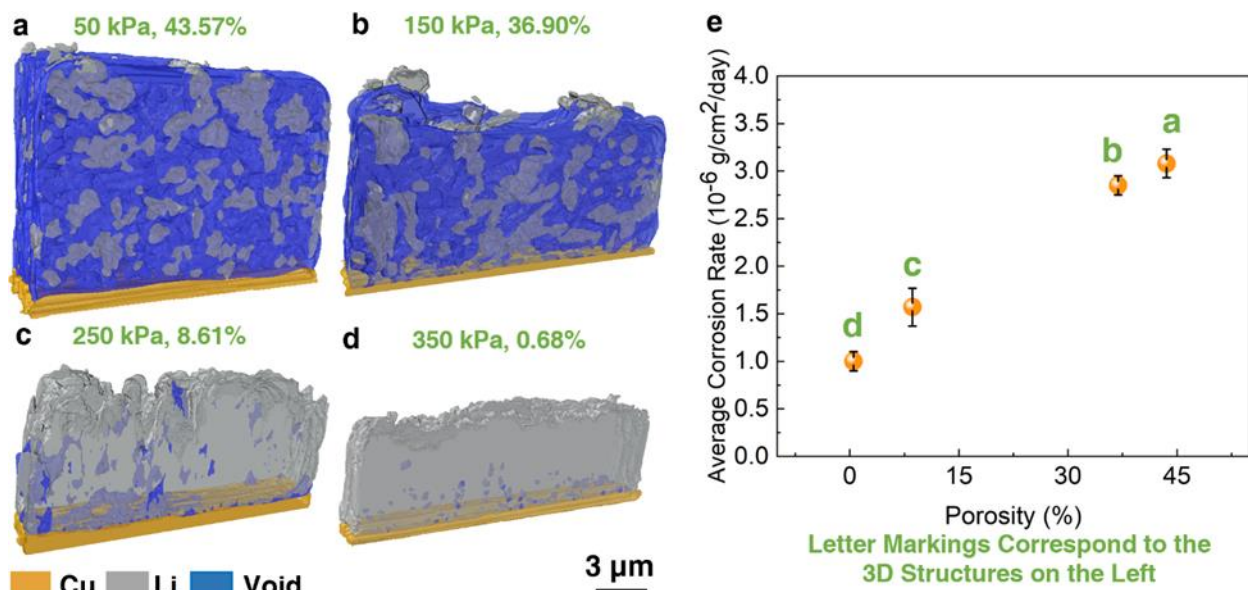


Figure 169. 3D reconstruction of deposited lithium metal plated under different stacking pressures resulting in different lithium porosities: (a) 50 kPa and 43.57% porosity; (b) 150 kPa and 36.90% porosity; (c) 250 kPa and 8.61% porosity, and (d) 350 kPa and 0.68% porosity. (e) Li-metal corrosion rate and its correlation with the porosity of the freshly deposited lithium. All lithium is plated in Gen 2 electrolyte. A total amount of 0.318 mAh of lithium is plated at a rate of 0.5 mA/cm² for each sample.

Nucleation of Li-Metal Anode during Lithium Plating

The SLAC / Stanford University team (W. Chueh and Y. Cui) completed the second quarter milestone of developing *operando* electrochemical atomic force microscopy (EC-AFM) to study lithium plating. This capability is now available to the Battery500 Consortium to carry out *operando* study of microstructural evolution during lithium plating in various electrolyte systems. Briefly, *operando* EC-AFM is used to investigate lithium plating at approximately 1 nm spatial resolution (x, y, and z). The microstructure of initial SEI formation on copper, the nucleation events during the early stage of lithium plating, and the growth morphology during a later stage in lithium plating are captured dynamically at a time resolution of several seconds per μm². This technique is complementary to *ex situ* cryo-EM studies, providing dynamics information to complement the high spatial and chemical resolution of cryo-EM. Similarly, *operando* AFM is also complementary to *operando* XRD studies by providing local nanostructure information.

For their technique development, the team investigated three stages of lithium plating: (1) SEI growth on copper, (2) lithium nucleation, and (3) lithium growth. They have deployed an Asylum Cypher environmental EC-AFM inside a temperature-controlled Ar-filled glovebox. A pressure-free liquid cell, consisting of a large, ring electrode (lithium metal) serves as a quasi-reference electrode; a copper foil serves as the working electrode. To eliminate mass transport effects (migration of lithium ions from the center of the cell to the ring counter electrode at the edge of the cell), the copper foil is masked such that ~ 1 mm disc is available to deposit lithium. This configuration eliminates a distribution of resistances and overpotential during lithium plating, thereby assuring uniformity. They have successfully conducted *operando* AFM for over 100 hours in a single experimental run, demonstrating the robustness of the measurement setup. For development purposes and to simplify the experiment, they selected the Gen2 electrolyte (1 M LiPF₆ in EC:EMC). Work is ongoing to investigate other electrolytes being studied by Battery500.

Figure 170a shows the initial SEI growth on copper at the potential of 30 mV versus Li/Li⁺ over 25 hours recorded by *operando* AFM. This potential was chosen so that they can monitor the pre-plating SEI growth. Two morphologies are clearly observed in the SEI: sub-50-nm “grains” and > 200-nm “particles.” Over the measurement period, both types of microstructures grew in size. The large SEI particle eventually grew to be ~ 250-nm wide and 80-nm tall. Figure 170b shows the subsequent lithium nucleation at 1 μAh cm⁻² of charge passed. Immediately evident is the wide distribution of nucleus size, which subsequently grew at different rates. Finally, Figure 170c shows the later-stage lithium growth at 0.5 mAh cm⁻² of charge passed. There, nanoscale faceting and roughening (feature size ~ 50 nm) of large lithium particles (~ 500 nm) were observed. The recorded lithium plating dynamics, from the pre-plating SEI growth stage to the lithium nucleation stage to the later lithium particle growth stage, provide quantitative information on the microstructure evolution, which directly impacts the CE and reversibility of lithium plating/stripping.

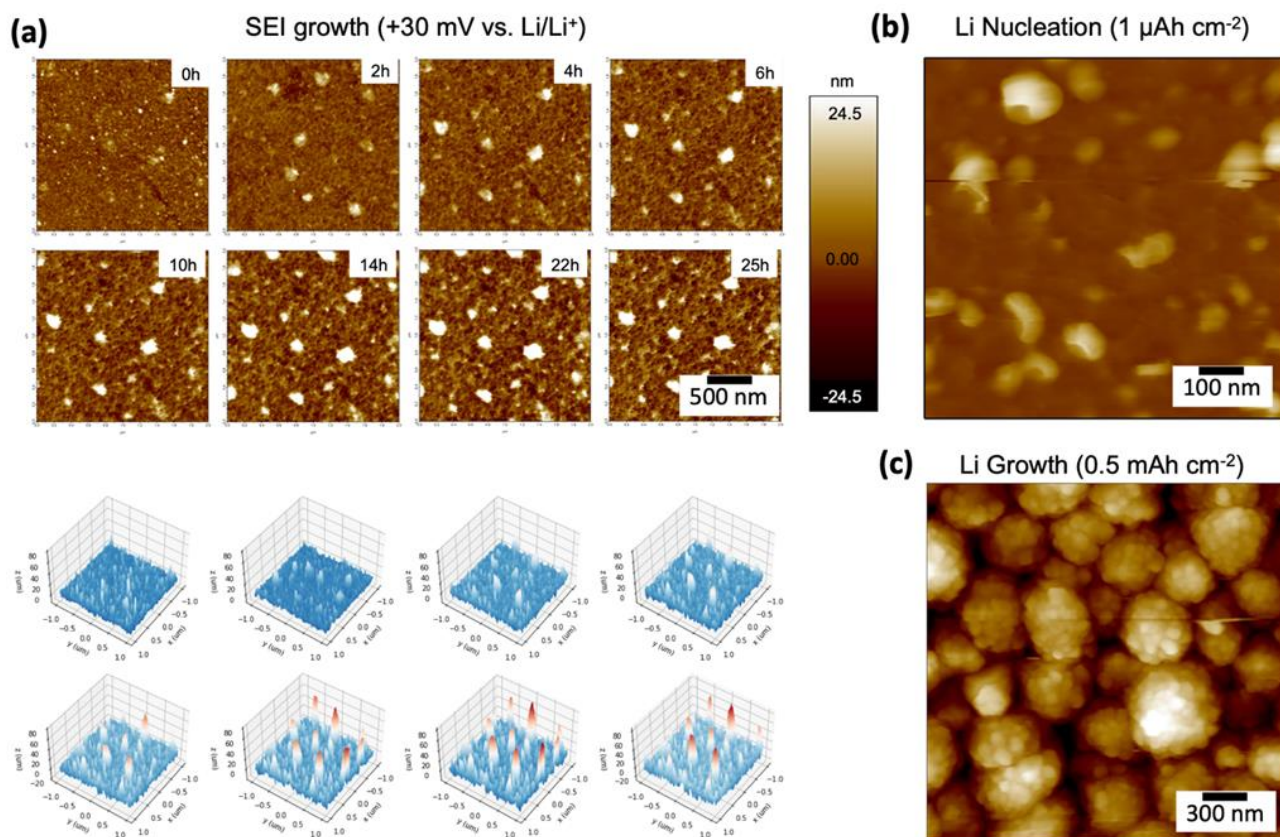


Figure 170. *Operando* atomic force microscopy of lithium plating in three stages. (a) SEI growth on copper at +30 mV versus Li/Li⁺ potential prior to lithium plating. Measurement over 25 hours reveals dual microstructure (grain + particles) that roughens with time. (b) Lithium nucleation showing a broad distribution of nuclei sizes. (c) Later-stage lithium growth showing faceted grain structure. The amount of charge passed is indicated.

Highlights of Keystone Project 4 (Cross-Cutting Efforts)

The highlights for this quarter are as follows:

- The BNL team (in close collaboration with UCSD) applied x-PDF characterization techniques to study the bulk structure changes of SPAN cathodes in Li-S batteries during cycling in different electrolytes. The UCSD electrolyte preserved desired S-S bonding, while the DOL/DME baseline electrolyte suffered considerable sulfur inventory loss. This technique provides a new tool to monitor the structural changes of SPAN during cycling.

- The Texas A&M team (P. Balbuena and J. M. Seminario) has implemented a simulation method that combines CMD and AIMD to follow the evolution of the SEI in timeframes that go well beyond the AIMD capabilities while keeping the AIMD accuracy. The main findings include spontaneous ion-hopping mechanisms driven by electron transfer from the lithium anode through the SEI.
- The UCSD team (Y. S. Meng) selectively deposited lithium in Gen 2 electrolyte under a range of stack pressures that resulted in the controlled deposition of lithium with systematically varying porosities. The as-plated lithium was then immersed into the Gen 2 electrolyte for three weeks to study the corrosion rate. It was concluded that the porosity of the plated lithium is the major factor in determining the lithium corrosion rate. If the porosity of the lithium can be strictly controlled, the corrosion of lithium should also be largely mitigated.
- The SLAC/Stanford team (W. Chueh and Y. Cui) has developed a new *operando* EC-AFM to study lithium plating. This capability is now available to the Battery500 Consortium to carry out *operando* study of microstructural evolution during lithium plating in various electrolyte systems with ~1 nm spatial resolution (x, y, and z). The microstructure of initial SEI formation on copper, the nucleation events during the early stage of lithium plating, and the growth morphology during later stage in lithium plating are captured dynamically.

Patents/Publications/Presentations

Publications

- Su, L., H. Charalambous, Z. Cui, and A. Manthiram. “High-Efficiency, Anode-Free Lithium-Metal Batteries with a Close-Packed Homogeneous Lithium Morphology.” *Energy & Environmental Science* 15 (2022): 843–854. doi: 10.1039/d1ee03103a.
- Shin, W., and A. Manthiram. “A Facile Potential Hold Method for Fostering Inorganic-Rich Solid-Electrolyte Interphase for Anode-Free Lithium-Metal Batteries.” *Angewandte Chemie* 61, no. 13 (2022): e202115909. doi: 10.1002/anie.202115909.
- Ren, Y., W. Shin, and A. Manthiram. “Operating High-Energy Lithium-Metal Pouch Cells with Reduced Stack Pressure through a Rational Lithium-Host Design.” *Advanced Energy Materials* 12, no. 19 (2022): 2200190. doi: 10.1002/aenm.202200190.
- Galvez-Aranda, D. E., and J. M. Seminario. “Li-Metal Anode in a Conventional Li-Ion Battery Electrolyte: Solid Electrolyte Interphase Formation using *Ab Initio* Molecular Dynamics.” *Journal of The Electrochemical Society* 169 (2022): 030502. doi: 10.1149/1945-7111/ac55c8.
- Xu, K., W. Xu, and S. S. Zhang. “Austen Angell’s Legacy in Electrolyte Research.” *Journal of Non-Crystalline Solids: X* 14 (2022): 100088. doi: 10.1016/j.nocx.2022.100088.
- Tan, S., H. Liu, Z. Wu, C. Weiland, S.-M. Bak, A. Ronne, P. Liu, M. S. Whittingham, Z. Shadike,* E. Hu,* X.-Q. Yang.* “Isoxazole-Based Electrolytes for Lithium Metal Protection and Lithium-Sulfurized Polyacrylonitrile (SPAN) Battery Operating at Low Temperature.” *Journal of The Electrochemical Society* 169 (2022). doi: 10.1149/1945-7111/ac58c5.
- Cosby, M. R., G. M. Carignan, Z. Li, C. M. Efaw, C. C. Dickerson, L. Yin, Y. Ren, B. Li, E. J. Dufek, and P. G. Khalifah. “*Operando* Synchrotron Studies of Inhomogeneity during Anode-Free Plating of Li Metal in Pouch Cell Batteries.” *Journal of The Electrochemical Society* 169, no. 2 (2022): 020571. doi: 10.1149/1945-7111/ac5345.

- Yu, S., Z. Wu, J. Holoubek, H. Liu, E. Hopkins, Y. Xiao, X. Xing, M. H. Lee, and P. Liu. “A Fiber-Based 3D Lithium Host for Lean Electrolyte Lithium Metal Batteries.” *Advanced Science* (2022): 2104829. doi: 10.1002/advs.202104829.
- Holoubek, J., Q. Yan, H. Liu, E. J. Hopkins, Z. Wu, S. Yu, J. Luo, T. A. Pascal, Z. Chen, and P. Liu. “Oxidative Stabilization of Dilute Ether Electrolytes via Anion Modification.” *ACS Energy Letters* 7 (2022): 675–682. doi: 10.1021/acsenergylett.1c02723.
- Holoubek, J., K. Kim, Y. Yin, Z. Wu, H. Liu, M. Li, A. Chen, et al. “Electrolyte Design Implications of Ion-Pairing in Low-Temperature Li-Metal Batteries.” *Energy & Environmental Science* 15 (2022): 1647–1658. doi: 10.1039/d1ee03422g.
- Yu, Z., P. E. Rudnicki, Z. Zhang, Z. Huang, H. Celik, S. T. Oyakhire, Y. Chen, X. Kong, S. Kim, X. Xiao, H. Wang, Y. Zheng, G. A. Kamat, M. Kim, S. F. Bent, J. Qin, Y. Cui, and Z. Bao. “Rational Solvent Molecule Tuning for High-Performance Lithium Metal Battery Electrolytes.” *Nature Energy* 7 (2022): 94–106. doi: 10.1038/s41560-021-00962-y.
- Kim, M. S., Z. Zhang, P. E. Rudnicki, Z. Yu, J. Wang, H. Wang, S. T. Oyakhire, Y. Chen, S. C. Kim, W. Zhang, D. T. Boyle, X. Kong, R. Xu, Z. Huang, W. Huang, S. F. Bent, L. Wang, J. Qin, Z. Bao, and Y. Cui. “Suspension Electrolyte with Modified Li⁺ Solvation Environment for Lithium Metal Batteries.” *Nature Materials* 21 (2022): 445–454. doi: 10.1038/s41563-021-01172-3.
- Wang, H., Z. Yu, X. Kong, S. Kim, D. T. Boyle, J. Qin, Z. Bao, and Y. Cui. “Liquid Electrolyte: The Nexus of Practical Lithium Metal Batteries.” *Joule* 6 (2022): 588–616. doi: 10.1016/j.joule.2021.12.018.
- Zhang, Z., Y. Li, R. Xu, W. Zhou, Y. Li, S. T. Oyakhire, Y. Wu, J. Xu, H. Wang, Z. Yu, D. T. Boyle, W. Huang, Y. Ye, H. Chen, J. Wan, Z. Bao, W. Chiu, and Y. Cui. “Capturing the Swelling of Solid-Electrolyte Interphase in Lithium Metal Batteries.” *Science* 375 (2022): 66–70. doi: 10.1126/science.abi8703.
- Xiao, J., C. Anderson, X. Cao, H-J. Chang, R. Feng, Q. Huang, Y. Jin, H. Job, J-M. Kim, P. M. L. Le, D. Liu, L. Seymour, N. Shamim, L. Shi, and B. Sivakumar. “Electrochemistry in Understanding and Designing Electrochemical Energy Storage Systems.” (Invited for Women in Electrochemistry Special Issue.) *Journal of The Electrochemical Society* 169 (2022): 010524. doi: 10.1149/1945-7111/ac4a55.

Presentations

- International Conference on Energy Materials and Devices, Banarus Hindu University, Varanasi, India, (January 11–12, 2022): “Sustainable Next-Generation Battery Technologies”; A. Manthiram. Plenary.
- University of Utah, Denver, Colorado (January 26, 2022): “Sustainable Battery Chemistries for Electrical Energy Storage”; A. Manthiram.
- Gyeongsang National University, Jinju, South Korea (February 7, 2022): “Sustainable Battery Chemistries for Electrical Energy Storage”; A. Manthiram. Invited.
- International Virtual Conference on Advanced Materials for Sustainable Energy and Environment, Coimbatore, India (February 16, 2022): “Sustainable Battery Chemistries for a Cleaner Environment”; A. Manthiram. Inaugural address.
- Spotlights in Advanced Science/Small Science: Advances in Smart Materials and Energy Research Webinar, Wiley Publisher, Weinheim, Germany (March 15–16, 2022): “A Path Forward for Sustainable Battery Chemistries”; A. Manthiram. Invited.
- Battery Conference, Korea Battery Industry Association, Seoul, South Korea (March 17–19, 2022): “Towards Practically Viable Lithium–Sulfur Batteries”; A. Manthiram. Invited.
- The 2022 International Conference on Hierarchical Green Energy, Taiwan (January 15, 2022): “Energy Storage is Key to Attainment of Fossil-Free Energy”; M. Stanley Whittingham.

- Global Young Scientists Meeting, Singapore (January 17, 2022): “The Critical Role of Storage for Renewable Energy and Climate Change”; M. S. Whittingham.
- Arkema (February 3, 2022): “The Challenges Facing Lithium Batteries as They Address Climate Change”; M. S. Whittingham.
- Seminar at Dalhousie University, Nova Scotia, Canada (March 24, 2022): “Electrochemical Energy Storage: An Integration of Materials Science, Electrochemistry and Engineering”; J. Xiao.
- ACS Spring Meeting (March 21, 2022): “Single Crystal Ni-Rich Cathode Materials for Advanced Li-Ion Batteries”; J. Xiao.
- Lithium Metal Battery Symposium, Military Power Sources Committee Symposium Series, Virtual (March 3, 2022): “Battery500 Consortium Overview”; J. Xiao.
- U. S. – U. K. Battery Technology Research and Innovation Online Summit, Virtual (February 1, 2022): “Battery500 Consortium Overview”; J. Xiao.

APPENDIX – ACRONYM GUIDE

Acronym	Full Description
1,4-DX	1,4-dioxane
1D	one-dimensional
2D	two-dimensional
3D	three-dimensional
3DOM	three-dimensional ordered microporous
3D-OMSH	three-dimensionally ordered microporous sulfur host
AB	acetylene black
ABL	active buffer layer
AC	alternating current
ACN	acetonitrile
ACS	American Chemical Society
AFLB	anode-free lithium battery
AFM	atomic force microscopy
AIMD	<i>ab initio</i> molecular dynamic
AIR	areal interfacial resistance
ALD	atomic layer deposition
ALS	Advanced Light Source
ANL	Argonne National Laboratory
ANN	artificial neural network
AOM	amphipathic organic molecules
APS	Advanced Photon Source
APUP	Alliance Partner University Program
AQC	anthraquinone-2-carboxylic acid
AQT	1,5-bis(2-(2-(2-methoxyethoxy)ethoxy)ethoxy) anthra-9,10-quinone
ARC	accelerating rate calorimetry
ARL	U. S. Army Research Laboratory
ASR	area specific resistance
ASSB	all-solid-state battery
ASSLB	all-solid-state lithium battery
ASSLMB	all-solid-state Li-metal battery
ASSLSB	all-solid-state Li-S battery
ATR	attenuated total reflectance
β -LPS	β -phase Li_3PS_4
BBP	benzyl butyl phthalate
BE	baseline electrolyte
BEV	battery electric vehicle
BL	bottom layer
BMIM	1-butyl-3-methylimidazolium
BMR	Advanced Battery Materials Research Program
BNL	Brookhaven National Laboratory
BTFE	bis(2,2,2-trifluoroethyl) ether
BV	Butler-Volmer
c-AIMD	constrained – <i>ab initio</i> molecular dynamics

Acronym	Full Description
CA	chronoamperometry
CAM	cathode active material
CC	carbonized cotton
CCCV	constant current / constant voltage
CCD	critical current density
CCD ^{plating}	plating critical current density
CCD ^{stripping}	stripping critical current density
CE	Coulombic efficiency
CEI	cathode electrolyte interface
CFM	carbon-based framework material
CLP	cycle life projection
CMC	carboxymethyl cellulose
CMD	classical molecular dynamics
CN	coordination number
CNC	carbon nano-cage
cNEB	climbing image nudged elastic band
CNM	Center for Nanoscale Materials
CNT	carbon nanotube
COP	critical overpotential
CPE	composite polymer electrolyte
cryo	cryogenic
cryo-EM	cryogenic electron microscopy
cryo-FIB	cryogenic – focused ion beam
cryo-STEM	cryogenic – scanning transmission electron spectroscopy
cryo-TEM	cryogenic – transmission electron microscopy
CS	corner-sharing
CSE	cluster-based solid electrolyte
CSM	continuous symmetry measure
CT	computed tomography
CV	cyclic voltammetry
DBE	dibutyl ether
DB-ML-FF	density-based machine-learning force field
DC	direct current
DCA	dicyanamide
DEB	double-end binding
DEC	diethyl carbonate
DEE	1,2-diethoxyethane
DEGDME	diethylene glycol dimethyl ether
DEMS	differential electrochemical mass spectrometry
DFE	defect formation energy
DFT	density functional theory
DiPE	diisopropyl ether
DIW	direct ink writing
DLR	Deutsches Zentrum für Luft- und Raumfahrt
DMC	dimethyl carbonate
DME	1,2-dimethoxyethane

Acronym	Full Description
DMF	dimethyl formamide
DMSO	dimethylsulfoxide
DOD	depth-of-discharge
DOE	U. S. Department of Energy
DOL	1,3-dioxolane
DOS	density of states
dP/dV	differential pressure
dPEO	dynamic bonds between polymer chains
dQ/dV	differential capacity
DRT	distribution of relaxation times
DSC	differential scanning calorimetry
E/C	electrolyte/capacity
EC	ethylene carbonate
eCAD	electrochemical analytic diagnosis
EC-AFM	electrochemical atomic force microscopy
ECS	The Electrochemical Society
EDL	electrical double layer
EDLi	electrochemically deposited lithium
EDS	energy-dispersive X-ray spectroscopy (also known as EDX)
EELS	electron energy loss spectroscopy
eGF	exfoliated graphene fluoride
EIS	electrochemical impedance spectroscopy
eLi	engineered lithium
EM	electron microscopy
EMC	ethyl methyl carbonate
EMIM-BF ₄	1-ethyl-3-methylimidazolium tetrafluoroborate
eNMR	electrophoretic nuclear magnetic resonance
EO	ethylene oxide
EPR	electron paramagnetic resonance
EQ-SANS	extended Q-range small-angle neutron scattering diffractometer
E/S	electrolyte/sulfur
EV	electric vehicle
EXAFS	extended X-ray absorption fine structure
F5DEE	fluorinated-1,2-diethoxyethanes electrolyte
FAM	functional monomer additive molecule
FDMB	fluorinated 1,4-dimethoxybutane
FDMH	fluorinated 1,6-dimethoxyhexane
FDMO	fluorinated 1,8-dimethoxyoctane
FDMP	fluorinated 1,5-dimethoxypentane
FEC	fluoroethylene carbonate
FEM	finite element method
FESEM	field emission scanning electron microscopy
FF	force field
FFT	fast Fourier transform
FIB	focused ion beam
fs	femtosecond

Acronym	Full Description
FSI	bis(fluorosulfonyl)imide
FTIR	Fourier transform infrared
FZJ	Forschungszentrum Jülich
GB	grain boundary
<i>gc</i>	glass/ceramic
GC-MS	gas chromatography – mass spectrometry
GCPL	galvanostatic cycling with potential limitation
GDL	gas diffusion layer
GE	gel electrolyte
GITT	galvanostatic intermittent titration technique
GM	General Motors
GOMD	Glass & Optical Materials Division
GP	Gaussian process
GPC	gel permeation chromatography
Gr	graphene
GSE	glassy solid electrolyte
HAADF	high-angle annular dark-field
HATN	hexaazatrinaphthylene
HATN-S	hexaazatrinaphthylene polymer – sulfur composite
HC	hard carbon
HCE	high-concentrated electrolyte
HEV	hybrid electric vehicle
HEXRD	high-energy X-ray diffraction
HFB	hexafluorobenzene
HFE	hydrofluoroether
HFP	hexafluoropropylene
HG	hand grinding
HOPG	highly oriented pyrolytic graphite
HPC	high-performance computing
HPLC	high-performance liquid chromatography
HRTEM	high-resolution transmission electron microscopy
HT	high throughput
IBA	International Battery Materials Association
IEEE	Institute of Electrical and Electronics Engineers
IL	ionic liquid
INL	Idaho National Laboratory
IOFM	inorganic-organic framework material
IPA	isopropanol
IR	Infrared
ISEL	Israel Electrochemical Society
ISU	Iowa State University
KAIST	Korea Advanced Institute of Science and Technology
KB	Ketjenblack
KMC	kinetic Monte Carlo
KPFM	kelvin probe force microscopy
LATP	Li-Al-Ti-P, such as $\text{Li}_{1+x}\text{Al}_x\text{Ti}_{2-x}(\text{PO}_4)_3$ or $\text{Li}_{1.3}\text{Al}_{0.3}\text{Ti}_{1.7}(\text{PO}_4)_3$

Acronym	Full Description
LBNL	Lawrence Berkeley National Laboratory
LBO	Li-B-O, such as Li_3BO_3
LBS	Li-B-S
LCE	low-concentration electrolyte
LCO	LiCoO_2
LCRC	Laboratory Computing Resource Center
LDBE	1.8 M LiFSI in dibutyl ether
LDEE	1.8 M LiFSI in diethyl ether / BTFE
LDiPE	1.8 M LiFSI in diisopropyl ether
LDME	1.8 M LiFSI in 1,2-dimethoxyethane
LE	liquid electrolyte
LFP	lithium iron phosphate
LGPS	Li-Ge-P-S, such as $\text{Li}_{10}\text{GeP}_2\text{S}_{12}$
LHCE	localized high-concentration electrolyte
LHS	left-hand side
LIB	Li-ion battery
LIC	Li-ion conductor
LiFSI	Li-bis(fluorosulfonyl)imide
Li-MCA	lithium multicomponent alloy
Li-NMC	lithium – nickel manganese cobalt oxide
LIPS	Li_7PS_6
Li-SIA	Li-containing structurally isomorphous alloy
LiTFSI	lithium bis(trifluoromethanesulfonyl)imide
LLNL	Lawrence Livermore National Laboratory
LLTO	Li-La-Ti-O, such as $\text{Li}_{3x}\text{La}_{2/3-x}\text{TiO}_3$
LLZ	Li-La-Z
LLZO	Li-La-Z-O, such as $\text{Li}_7\text{La}_3\text{Zr}_2\text{O}_{12}$
LLZTO	Li-La-Zr-Ta-O, such as $\text{Li}_{6.75}\text{La}_3\text{Zr}_{1.75}\text{Ta}_{0.25}\text{O}_{12}$
LMR-NMC	Li- and Mn-rich Ni-Mn-Co
LNO	LiNiO_2
LOB	Li-O battery
LPC	large particle cathode
LPS	Li-P-S, such as Li_3PS_4
LPSB	Li-P-S-Br, such as $\text{Li}_3\text{PS}_4 + \frac{1}{2}\text{LiBr}$
LPSBI	Li-P-S-Br-I, such as $\text{Li}_7\text{P}_2\text{S}_8\text{Br}_{0.5}\text{I}_{0.5}$
LPSBr	Li-P-S-Br, such as $\text{Li}_6\text{PS}_5\text{Br}$
LPSCI	Li-P-S-Cl, such as $\text{Li}_6\text{PS}_5\text{Cl}$
LPSI	Li-P-S-I, such as $\text{Li}_3\text{PS}_4 + \frac{1}{2}\text{LiI}$
LPSIB	Li-P-S-I-Br, such as $\text{Li}_7\text{P}_2\text{S}_8\text{I}_{0.5}\text{Br}_{0.5}$
LSiPCI	Li-Si-P-Cl, such as $\text{Li}_{9.54}\text{Si}_{1.74}\text{P}_{1.44}\text{S}_{11.7}\text{Cl}_{0.3}$
LSnS	Li-Sn-S, such as $\text{Li}_{3.85}\text{Sn}_{0.85}\text{Sb}_{0.15}\text{S}_4$
LSV	linear sweep voltammetry
LTO	$\text{Li}_4\text{Ti}_5\text{O}_{12}$
LYC / LYCI	Li-Y-Cl, such as Li_3YCl_6
MC	Monte Carlo
MCA	multicomponent alloy

Acronym	Full Description
MD	molecular dynamics
METS	multi-harmonic electrothermal spectroscopy
MGF	mixed glass former
MIC	molecular ionic composite
ML	machine learning
MLFF	machine learning force field
MLMD	molecular dynamics simulation with machine-learning potential
MOF	metal-organic framework
MOS	mixed oxy-sulfide
MOSN	mixed oxy-sulfide nitride
MPI	message-passing interface
MRS	Materials Research Society
MS	mass spectrometry
MSD	mean square displacement
MSE	mean squared error
MTU	Michigan Technological University
MWCNT	multi-walled carbon nanotube
MYEGA	Mauro–Yue–Ellison–Gupta–Allan model
NA	$\text{LiNi}_{0.95}\text{Al}_{0.05}\text{O}_2$
NaFSI	sodium bis(fluorosulfonyl)imide
NaNMC	Na-N-Mn-Co, such as $\text{NaNi}_{0.4}\text{Mn}_{0.4}\text{Co}_{0.2}\text{O}_2$ and $\text{NaNi}_{0.68}\text{Mn}_{0.22}\text{Co}_{0.1}\text{O}_2$
nano-FTIR	Fourier transform infrared nano-spectroscopy
NASICON	sodium super ionic conductor
NATM	Ni-Al-Ti-Mg, such as $\text{LiNi}_{0.93}\text{Al}_{0.05}\text{Ti}_{0.01}\text{Mg}_{0.01}\text{O}_2$
NBO	nonbridging oxygen
NBR	nitrile butadiene rubber
NBS	nonbridging sulfur
NC	Ni-Co, such as $\text{LiNi}_{0.94}\text{Co}_{0.06}\text{O}_2$
NCEM	National Center for Electron Microscopy
NCM	Ni-Co-Mn
NCM-85105	$\text{LiNi}_{0.85}\text{Co}_{0.10}\text{Mn}_{0.05}\text{O}_2$
NCSE	non-calendered sulfur electrode
ND	di-coordinated nitrogen
NEB	nudged elastic band
NF	nanoflake
NLNMF	Na-Li-Ni-Mn-Fe, such as $\text{Na}_{0.85}\text{Li}_{0.1}\text{Ni}_{0.175}\text{Mn}_{0.525}\text{Fe}_{0.2}\text{O}_2$
NM	$\text{LiNi}_{0.95}\text{Mn}_{0.05}\text{O}_2$
NMC	Ni-Mn-Co
NMC-111	$\text{LiNi}_{1/3}\text{Mn}_{1/3}\text{Co}_{1/3}$
NMC-622	$\text{LiNi}_{0.6}\text{Mn}_{0.2}\text{Co}_{0.2}$
NMC-811	$\text{LiNi}_{0.8}\text{Mn}_{0.1}\text{Co}_{0.1}$
NMDC	Nanotechnology Materials and Devices Conference
NMF	nonnegative matrix factorization
NMFCN	Na-Mn-Fe-Co-Ni
NMP	N-methyl-pyrrolidone
NMR	nuclear magnetic resonance

Acronym	Full Description
NN	neural network
N/P ratio	capacity ratio between anode (negative electrode) and cathode (positive electrode)
NP	nanoparticle
NPCE	nonflammable polymer composite electrolyte
n-PDF	neutron diffraction and pair distribution function
NPT	constant number of atoms (N), pressure (P), and temperature (T)
NREL	National Renewable Energy Laboratory
ns	nanosecond
NSLS	National Synchrotron Light Source
NT	tri-coordinated nitrogen
NTO	sodium titanate
NVE	constant number (N), volume (V), and energy (E)
NVT	constant temperature, constant volume ensemble
OCV	open circuit voltage
OER	oxygen evolution reaction
OMSH	ordered microporous sulfur host
ORNL	Oak Ridge National Laboratory
ORR	oxygen reduction reaction
OSU	Ohio State University
PAH	polycyclic aromatic hydrocarbon
PAN	polyacrylonitrile
PAQS	poly (anthraquinonyl sulfide)
PBDT	poly(2,2'-disulfonyl-4,4'-benzidine terephthalamide)
PC	propylene carbonate
PCA	principal component analysis
PCC	Pearson correlation coefficient
PC-LCHE	polymeric colloidal localized high-concentration electrolyte
PDF	pair distribution function
PDMS	polydimethylsiloxane
PE	polyelectrolyte, or polymer electrolyte
PEEK	polyether ether ketone
PEG	poly(ethylene glycol)
PEGDA	poly(ethylene glycol) diacrylate
PEGMA	poly(ethylene glycol) methacrylate
PEGMEA	poly(ethylene glycol) methyl ether acrylate
PEI	polyethylenimine
PEM	poly(ethylene malonate)
PEO	poly(ethylene oxide)
PES	photon emission spectroscopy
PETEA	pentaerythritol tetraacrylate
PFG	pulsed field gradient
PFIB	plasma focused ion beam
PFPE	perfluoropolyether
PGE	polymer gel electrolyte
PHEV	plug-in hybrid electric vehicle

Acronym	Full Description
PHM	poly(hexylene malonate)
PI	principal investigator
PI-G	polyimide-graphene
PLiMTFSI	poly((trifluoromethanesulfon)imide lithium methacrylate)
PM	planetary mill
PMMA	polymethyl methacrylate
PMTH	dipentamethylenethiuram hexasulfide
PNNL	Pacific Northwest National Laboratory
POSS	polyhedral oligomeric silsesquioxane
PP	polypropylene
ppm	parts per million
PPM	poly(pentylene malonate)
PS-SEI	polymer-supported solid electrolyte interphase
PST	partially sintered tape
PSTFSI	poly(4-styrenesulfonyl(trifluoromethanesulfonyl)imide)
PSU	Pennsylvania State University
PTFE	polytetrafluoroethylene
PTFSI	triflimide-based polyion
PTM	poly(trimethylene malonate)
PVB	polyvinyl butyral
PVDF	polyvinylidene (di)fluoride
PVP	polyvinylpyrrolidone
Py	pyrrolidinium
PyTFSI	pyrrolidinium (trifluoromethanesulfon)imide
RAFT	reversible addition-fragmentation chain-transfer
RDF	radial distribution function
ReaxFF	reactive force field
RF	random forest
rGO	reduced graphene oxide
RHS	right-hand side
RM	redox mediator
RMSE	root mean square error
RP	red phosphorus
RPT	reference performance test
SAED	select area electron diffraction
SAEP	salt affinitive electrolyte phobic
SAM	scanning Auger microscopy
SANS	small angle neutron scattering
SASP	salt affinity solvent phobic
SAXS	small angle X-ray scattering
SBR	styrene-butadiene rubber
SC	single crystalline
SE	solid electrolyte
SEB	single-end binding
SEI	solid electrolyte interphase
SEM	scanning electron microscopy

Acronym	Full Description
SEO	polystyrene- <i>b</i> -poly(ethylene oxide) block copolymer
SERS	surface-enhanced Raman spectroscopy
SFSU	San Francisco State University
SHE	standard hydrogen electrode
SIA	structurally isomorphous alloy
SIC	single ion conductor
SIL	solvate ionic liquid
SIMS	secondary ion mass spectrometry
SLAC	Stanford Linear Accelerator Center
SLD	scattering length density
SNL	Sandia National Laboratory
SnS	tin sulfide
SOC	state of charge
SPAN	sulfurized polyacrylonitrile
SPC	small particle cathode
SPE	solid polymer electrolyte
SPM	scanning probe microscopy
SPZ	sulfur polymerized composite
SQUID	superconducting quantum interference device
SRO	short-range order
SS	stainless steel
SSB	solid-state battery
SSE	solid-state electrolyte
SSI	solid-state ion
SSLB	solid-state lithium battery
SSLMB	solid-state Li-metal battery
SS-NEB	solid-state nudged elastic band
SSPC	Solid-State Proton Conductors Conference
SSRL	Stanford Synchrotron Radiation Lightsource
S-SSE	sulfide-based solid-state electrolyte
STEM	scanning transmission electron microscopy
SWCNT	single-walled carbon nanotube
SXRD	synchrotron-based X-ray diffraction
T _c	glass crystallization temperature
TCR	thermal contact resistance
TEGDME	tetraethylene glycol dimethyl ether
TEM	transmission electron microscopy
TEMPO	2,2,6,6-tetramethyl-1-piperidinyloxy
TEP	triethyl phosphate
TES	tender energy X-ray absorption spectroscopy
TFC	thin-film composite
TFP	tris(2,2,2-trifluoroethyl) phosphate
TFSI	(trifluoromethanesulfonyl)imide
T _g	glass transition temperature

Acronym	Full Description
TGA	thermal gravimetric analysis
TGC	titration gas chromatography
THF	tetrahydrofuran
TL	top layer
TM	transition metal
TMD	transition metal dichalcogenide
TMS	tetramethylsilane
TOF-SIMS	time-of-flight secondary ion mass spectrometry
TRL	technology readiness level
TTE	1,1,2,2-tetrafluoroethyl-2,2,3,3-tetrafluoropropyl ether
TXM	transmission X-ray microscopy
UCB	University of California, Berkeley
UCSD	University of California, San Diego
UH	University of Houston
UHV	ultrahigh vacuum
UIC	University of Illinois, Chicago
UM	University of Michigan
UMD	University of Maryland
UT	University of Texas
UV	ultraviolet
UW	University of Washington
UWM	University of Wisconsin, Madison
VASP	Vienna <i>ab initio</i> simulation package
VBM	valence band maximum
VC	vinylene carbonate
VE	virtual electrode
VE-SAM	virtual electrode scanning Auger microscopy
VE-XPS	virtual-electrode X-ray photoelectron spectroscopy
VTO	Vehicle Technologies Office
XAFS	X-ray absorption fine structure
XANES	X-ray absorption near-edge structure
XAS	X-ray absorption spectroscopy
x-PDF	synchrotron X-ray diffraction and pair distribution function
xPEO	crosslinked poly(ethylene oxide)
XPS	X-ray photoelectron spectroscopy
XRD	X-ray diffraction
XRF	X-ray fluorescence
XRT	X-ray tomography